

Institut für physikalische und theoretische Chemie  
Lehrstuhl für Einzelmolekül-Biophysik

Imaging-Systems for Localization-Based Super-Resolution  
Light-Microscopy in Physical Biology: Design and Applications

Dissertation  
zur Erlangung des Doktorgrades  
der Naturwissenschaften

Vorgelegt beim Fachbereich Biochemie, Chemie und Pharmazie  
der Johann Wolfgang Goethe-Universität  
in Frankfurt am Main

von  
Sebastian Malkusch

geboren in Dortmund

---

Frankfurt am Main 2014

Vom Fachbereich Biochemie, Chemie und Pharmazie der  
Johann Wolfgang Goethe - Universität als Dissertation angenommen.

Mitglieder der Promotionskommission:

Dekan: Prof. Dr. Thomas Prisner

Gutachter: Prof. Dr. Mike Heilemann

Gutachter: Jun. Prof. Dr. Martin Grininger

Datum der Disputation:

---

Die Arbeit wurde zu gleichen Teilen in den folgenden Arbeitsgruppen unter Anleitung von Prof. Dr. Mike Heilemann durchgeführt:

1. Angewandte Laserphysik und Spektroskopie im Fachbereich Physik der Universität Bielefeld
2. Biotechnologie und Biophysik im Fachbereich Biologie der Universität Würzburg
3. Physikalische und theoretische Chemie im Fachbereich Biochemie, Chemie und Pharmazie der Universität Frankfurt am Main

---

## EHRENWÖRTLICHE ERKLÄRUNG

Ich erkläre hiermit an Eides Statt, dass ich die vorliegende Dissertation über  
*Imaging-Systems for Localization-Based Super-Resolution Light-Microscopy in Physical Biology:  
Design and Applications*  
selbstständig angefertigt und mich anderer Hilfsmittel als der in ihr angegebenen nicht  
bedient habe, insbesondere, dass alle Entlehnungen aus anderen Schriften mit Angabe  
der betreffenden Schrift gekennzeichnet sind.

Ich versichere, nicht die Hilfe einer kommerziellen Promotionsvermittlung in Anspruch  
genommen zu haben

Frankfurt am Main, April 2014

Sebastian Malkusch



---

**Algorithm 1:** The Feynman Problem-Solving Algorithm by Murray Gell-Mann<sup>1</sup>

---

- 1 write down the problem;
  - 2 think very hard;
  - 3 write down the answer;
-

---

## Zusammenfassung

Die physikalische Biologie beschäftigt sich mit der Erhebung quantitativer Daten aus biophysikalischen und molekularbiologischen Experimenten unterschiedlicher Komplexität. Diese Daten können als Eingangsparameter für mathematische Modelle des zu untersuchenden biologischen Systems dienen. Solche systembiologischen Modelle bilden die relevanten Interaktionen zwischen Molekülen ab und erlauben das Verhalten des Systems auf externe Stimuli zu beschreiben.

Ein essentieller Bestandteil biophysikalischer Untersuchungen von Zellen bis zu Organismen ist die Fluoreszenzmikroskopie. Sie zeichnet sich durch eine Vielzahl stetig weiterentwickelter, spezifischer Markierungsstrategien, sowie ein breites Spektrum an Fluoreszenzfarbstoffen aus. Durch eine geringe Invasivität ist sie geeignet, um Untersuchungen selbst an lebenden Zellen oder Organismen durchzuführen. Die hohe Sensitivität moderner Photosensoren erlaubt es selbst einzelne Fluoreszenzsonden mit einer Genauigkeit von ca. 10 nm zu detektieren.

In den letzten 2 Jahrzehnten wurde ein breites Ensemble an einzelmolekülsensitiven Mikroskopie- und Spektroskopie-Methoden entwickelt. Der Einsatz photoschaltbarer Farbstoffe (*direct Stochastic Optical Reconstruction Microscopy*, dSTORM), sowie photoaktivierbarer Fluoreszenzproteine (*Photoactivated Localization Microscopy*, PALM), ermöglicht die zeitliche Separation räumlich überlagerter Fluoreszenzsignale und somit die Erhebung quantitativer Einzelmoleküldaten von großer Komplexität selbst in dicht markierten Bereichen. Diese können wiederum verwendet werden, um hochaufgelöste Bilder zu rekonstruieren, Diffusionskoeffizienten einzelner Moleküle zu ermitteln oder die Bindungskonstanten von Biomolekülen zu bestimmen.

Die Generierung quantitativer Daten aus Fluoreszenzbildern wird durch den Einsatz von Imaging-Systemen ermöglicht. Diese kombinieren sensitive Fluoreszenzmikroskope mit leistungsstarker Computer Hardware und Software und werden heutzutage meist in der konventionellen Weitfeldmikroskopie eingesetzt. In dieser Arbeit wird die Entwicklung von einzelmolekülsensitiven Imaging-Systemen für die Anwendung in der physikalischen Biologie über die Generierung quantitativer Daten bis hin zur Aufstellung eines ersten minimalen systembiologischen Modells für den Membranrezeptor TNF-R1 beschrieben.

Zur Einschätzung der Güte quantitativer Daten aus Einzelmolekülmikroskopieexperimenten muss zunächst die Sensitivität des Mikroskops charakterisiert werden. Dies geschieht an Hand von drei Eigenschaften: dem Auflösungsvermögen des Mikroskops, der örtlichen Stabilität der Probe über den Messzeitraum und der Registrierungsgenauigkeit mehrerer Kanäle. Um das Auflösungsvermögen des Mikroskops zu bestimmen, soll zunächst der

---

Begriff der Lokalisationsgenauigkeit eingeführt werden. Er definiert, wie genau der Aufenthaltsort eines einzelnen Fluorophores an Hand seiner Abbildungsfunktion bestimmt werden kann. Bisher wurde entweder die theoretisch erreichbare Lokalisationsgenauigkeit eines Fluorophores gleichen Emissionsspektrums, sowie gleicher detektierter Photonenzahl, errechnet oder experimentell über die Verteilung multipler Lokalisationen vereinzelter Fluorophore exemplarisch für einen Bruchteil der detektierten Fluoreszenzsonden bestimmt. Mit dem neuen Verfahren NeNA (*Nearest Neighbor Approach*) wurde ein Verfahren entwickelt, welches die mittlere Lokalisationsgenauigkeit aller detektierten Fluorophore eines Einzelmolekülmikroskopieexperiments aus der Nahordnung ihrer räumlichen Verteilung bestimmt. Hiermit konnte für das mit Alexa-Fluor 647 markierte Tubulinskelett einer HeLa-Zelle eine mittlere Lokalisationsgenauigkeit von  $8.6 \pm 0.1$  nm gemessen werden. Da die Aufnahme eines Einzelmolekülmikroskopiedatensatzes mehrere Minuten in Anspruch nimmt, ist die Qualität der Daten weiterhin von der festen Position der Probe abhängig. Um die Verschiebung der Probe von ihrem ursprünglichem Aufenthaltsort über den Zeitraum einer Messreihe zu quantifizieren, wurde ein Verfahren entwickelt, Referenzproben mit stabilem Fluoreszenzsignal innerhalb einer hydrophilen Gel-Matrix in einer zufälligen Verteilung um die Probe herum zu fixieren. Mit Hilfe eines Zielverfolgungsalgorithmus wurde die Verschiebung des Referenzprobenensembles über den Messzeitraum bestimmt. Durch die Messung einer genügend hohen Anzahl von Referenzproben kann über diese Methode die Verschiebung der Probe zurückgerechnet werden. Durch Einsatz multispektraler Referenzproben konnte diese Methode verwendet werden, um bei der Registrierung verschiedener Datensätze Aberrationen zu korrigieren. Korrigierte Datensätze zeichnen sich durch eine schlechtere Lokalisationsgenauigkeit aus als unbehandelte Daten, da es durch die Korrekturalgorithmen zu einer Fehlerfortpflanzung kommt.

Einzelmolekülmikroskopiedaten unterscheiden sich in ihrer Struktur grundlegend von den Daten, die mit herkömmlicher Weitfeldmikroskopie erhoben werden. Bei den Rohdaten handelt es sich um eine Liste mit Informationen der detektierten Fluorophore. Diese Listen setzen sich üblicherweise aus den Koordinaten des Fluorophores, der Detektionszeit und der Anzahl an detektierten Photonen zusammen. Somit sind Einzelmolekülmikroskopiedaten nicht mit herkömmlichen Bildverarbeitungsalgorithmen der Lichtmikroskopie kompatibel. Zur Generierung quantitativer Daten wurden spezifische Bildverarbeitungsalgorithmen entwickelt, beziehungsweise aus anderen koordinatenbasierten Analysen adaptiert. Ripley's K-Funktion ist eine häufig in der Ökologie eingesetzte statistische Verteilungsfunktion zweiter Ordnung. Sie prüft die Homogenität einer zweidimensionalen Verteilung und charakterisiert

---

diese mit der mittleren Größe ihrer Heterogenität. Ripley's K-Funktion wurde verwendet, um die Dichteverteilung verschiedener Populationen von Membranproteinen miteinander zu vergleichen. Als Beispiel seien hier, die verschiedenen Organisationsformen viraler Proteine an der Zellmembran einzelner humaner T-Zellen genannt, sowie die Reorganisation von Arrestin2/3-Proteinen an der Zellmembran von CHO-Zellen, die durch externe Stimuli G-Protein-gekoppelter Rezeptoren mit verschiedenen RANTES Analoga induziert wurden.

Ferner wurde ein koordinatenbasierter Kolokalisationsalgorithmus (CBC) entwickelt, um speziell die Kolokalisation einzelner Moleküle zweier unterschiedlich markierter Kanäle zu bestimmen. Ähnlich wie Ripley's K-Funktion basiert der Algorithmus auf der Verteilung von Lokalisationen. Abhängig von der Verteilung der Lokalisationen beider Kanäle um eine bestimmte Lokalisation wird dieser ein Kolokalisationswert zugeschrieben. Diese Prozedur wird für jede Lokalisation wiederholt. Somit ermöglicht der CBC-Algorithmus, die Lokalisationsdaten später nach Kolokalisationswerten zu sortieren, um Subpopulationen gesondert voneinander zu untersuchen. Mit Hilfe dieser Methode wurden an HeLa-Zellen membrangebundene TNF-R1 Moleküle mit TNF $\alpha$ -Molekülen kolokalisiert und in inaktivierte und aktivierte Rezeptororganisationseinheiten unterteilt.

Kolokalisiert man einen Kanal mit sich selbst, so kann der Algorithmus verwendet werden, um Bereiche von hoher Lokalisationsdichte zu identifizieren. Dies wurde für die nähere Charakterisierung von Arrestin2/3-Molekülen an der Membran von CHO-Zellen nach Aktivierung der G-Protein-gekoppelten Rezeptoren genutzt.

Mit Hilfe von Einzelmolekülmikroskopieaufnahmen fluoreszenzmarkierter TNF-R1-Fusionsproteine wurde die laterale Proteindiffusion innerhalb der Membran lebender HeLa-Zellen direkt betrachtet. Die Fusionsproteine waren mit photoaktivierbaren Fluoreszenzproteinen markiert und konnten für die Dauer ihrer Fluoreszenzperiode verfolgt werden. Ihre Bewegung über diesen Zeitraum wurde mit einer Trajektorie beschrieben. Mit Hilfe des Modells der lateralen Brown'schen Bewegung konnten aus den Trajektorien quantitative Daten über die Diffusionskoeffizienten der einzelnen Moleküle und deren Verteilung erhoben werden. Die Daten wurden mit Hilfe zuvor publizierter Fluoreszenzkorrelationsspektroskopiedaten verifiziert. Die hohe Ortsauflösung der Einzelmolekülmikroskopie ermöglichte die Erstellung hochaufgelöster Diffusionskarten der Membran einzelner Zellen.

Die entwickelten Imaging-Systeme wurden zur Untersuchung von drei verschiedenen biologischen Systemen im Kontext humaner Erkrankungen eingesetzt. Die Verteilung von HIV-1 Gag Strukturproteinen wurde an Membranen fixierter humaner T-Zellen untersucht. Es wurden drei verschiedene Organisationsformen identifiziert: eine diffuse Verteilung, kleine Foki

---

mit einer hohen Dichte an HIV-1 Gag Molekülen und runde HIV-1 Gag Ansammlungen mit einem einheitlichen Radius von ca. 70 nm und einheitlicher Lokalisationsdichte. Vergleiche mit zuvor veröffentlichten Daten aus der Elektronenmikroskopie legen den Schluss nahe, dass es sich bei den runden HIV-1 Gag Ansammlungen um sich bildende Viruspartikel handelt. Zweifarbenmessungen mit HIV-1 Gag und HIV-1 Env ergaben eine spezifische Anordnung der HIV-1 Env Moleküle um die sich bildenden Viruspartikel, ohne dabei mit den HIV-1 Gag Proteinen zu kolokalisieren. Durch Mutationen der beiden Proteine konnte die MA-Domäne der HIV-1 Gag Proteine, sowie die CT-Domäne der HIV-1 Env Proteine, als essentiell für die spezifische Rekrutierung von Hiv-1 Env in Viruspartikeln identifiziert werden.

Die zweite untersuchte biologische Fragestellung ist die Rekrutierung von Arrestin2/3 Molekülen durch ligandeninduzierte Aktivierung des G-Protein-gekoppelten C-C Chemokin 5 Rezeptors (CCR5). Vorangegangene Studien haben gezeigt, dass verschiedene Analoga des CCR5 Liganden RANTES die HIV Infektion von Zellen signifikant reduzieren. In einer Einzelmolekülstudie wurde die Arrestin2/3 Rekrutierung von CCR5 nach Rezeptoraktivierung durch verschiedene RANTES-Analoga verglichen und mit quantitativen Daten aus zuvor veröffentlichten Studien über die Intensität der induzierten G-Protein Signalkaskade, sowie die CCR5 Internalisierung, gegenübergestellt. Mit RANTES 5P14 wurde ein erster Hinweis auf einen Liganden gefunden, der lediglich Arrestin2 rekrutiert, nicht jedoch Arrestin3.

Als drittes biologisches System wurde der Einfluss von  $TNF\alpha$  auf die Dynamik von TNF-R1 Molekülen an der Zellmembran von HeLa Zellen untersucht. Diffusionsmessungen an lebenden Zellen ergaben keine signifikante Änderung der mittleren Rezeptordiffusion nach Applikation des Liganden, zeigten jedoch das Verschwinden einer langsam diffundierenden Fraktion. Vergleiche der Rezeptorverteilung mit der Verteilung des trimeren Modellsystems VSVG ergaben eine vornehmliche Organisation der TNF-R1 Moleküle in Dimeren. Anhand zuvor veröffentlichter Strukturdaten von TNF-R1 und  $TNF\alpha$ , sowie der erhobenen quantitativen Einzelmolekül Daten, wurde ein minimales systembiologisches Modell zur Beschreibung der ligandeninduzierten Umstrukturierung der TNF-R1 Organisationseinheiten aufgestellt. Das Modell beschreibt eine Umstrukturierung der TNF-R1 Moleküle zu höheren Organisationsformen eingeleitet durch die Applikation von  $TNF\alpha$ . Die Vorhersage der Simulation konnte in einem weiteren Versuch über den Vergleich der TNF-R1 Verteilung nach der Applikation mit  $TNF\alpha$  mit VSVG verifiziert werden.

Die Arbeit beschreibt die Entwicklung und Anwendung von Einzelmolekül-Imaging-Systemen zur Erhebung quantitativer Daten auf Basis einzelner Zellen und mit der Auflösung einzelner Biomoleküle. Diese Daten dienen als Eingabeparameter für systembiologische Modelle von

---

geringem Abstraktheitsgrad. In naher Zukunft werden systembiologische Modelle eine immer größere Rolle in der Erforschung humaner Erkrankungen finden. Die Modellvorhersagen werden mit steigender Genauigkeit der Eingabeparameter verlässlicher werden. Diese Arbeit gibt einen Einblick, welches Potential quantitative Daten aus Einzelmolekül-Imaging-Systemen als Eingabeparameter solcher Modelle inne haben.

---

## Summary

Physical Biology is a field of life sciences dealing with the extraction of quantitative data from biophysical or molecular biological experiments with different levels of complexity. Such data are further used as parameters for mathematical models of the biological system. These models allow to predict reactions on external stimuli by describing the relevant molecular interactions and are therefore used for example to generate a deeper comprehension of complex human diseases. An essential technique in biophysical research on human diseases is fluorescence microscopy. This is a constantly developed toolbox comprising a large number of specific labeling strategies, as well as a broad spectrum of fluorescent probes. It is further minimal invasive and therefore suitable for measurements in living cells or organisms. The sensitivity of modern photo-detectors even allows for the detection of a single fluorescent probe with an accuracy of approximately 10 nm.

A broad ensemble of single-molecule-sensitive localization-microscopy (SMLM) or spectroscopy was developed during the last 2 decades. By using photo-switchable fluorophores (dSTORM) or photo-activatable fluorescent proteins (PALM), spatially overlapping fluorescent signals can be separated temporally and therefore allow the extraction of quantitative data even in densely labeled specimens. These data can further be used to reconstruct super-resolved images, to calculate diffusion coefficients of single molecules, or to determine the dissociation constant of biomolecules.

Generating quantitative data from fluorescence images is performed by imaging-systems. These comprise a sensitive fluorescence microscope, a powerful computer hardware and data post processing software. Nowadays they are mostly used in the field of conventional wide-field microscopy. Here, the development of SMLM imaging-systems for use in physical biology from the determination of quantitative data to the set up of a first minimal systems-biological model is described.

In order to estimate the quality of quantitative data obtained from SMLM experiments the sensitivity of the microscope setup was characterized in three categories: the resolution of the microscope, the spatial stability of the sample during the time of measurement, as well as the registration accuracy of different channels. To characterize the resolution of the microscope setup, the localization accuracy shall be introduced. It defines how accurate the position of a fluorophore can be determined from its imaging function. Up to now either the theoretical achievable localization accuracy is determined from the detected number of photons, or the experimental local accuracy is determined from multiple localizations of isolated fluorophores. Here, the NeNA algorithm (*Nearest Neighbor Approach*) was developed to determine the aver-

---

age localization accuracy over all detected fluorophores by investigating the short range order of the spatial localization distribution around each localization. SMLM data sets of tubulin filaments labeled with Alexa-Fluor647 of HeLa-cells with a localization accuracy of  $8.6 \pm 0.1$  nm were measured. As recording SMLM data might take several minutes, the quality of the data is also depending on the fixed position of the sample. In order to quantify the sample displacement during measurements, fiducial marker with a stable fluorescence signal over time were used. By embedding the sample within a hydrophilic gel matrix, a random distribution of fiducial markers around the sample was achieved allowing to quantify the sample displacement by a tracking algorithm. Distributing a sufficient number of fiducial markers around the sample allocates enough information to correct the SMLM data set for drift. By introducing multi-spectral fiducial markers, this approach can also be used to register different channels and correct for aberrations. Drift-correction or channel-registration leads to a decrease in localization accuracy, due to an error propagation during the localization and the drift-correction algorithm.

SMLM data comprise a list of information about the detected fluorophores, as the localization coordinates, the detection time, and the number of detected photons. Therefore, they differ from conventional light microscopy data and are not compatible with most image post-processing algorithms. To determine quantitative data from experiments, specific post-processing algorithms were developed or adapted from other coordinate based analysis algorithms. In the field of ecology, Ripley's K-function is a frequently used approach to calculate the second order distribution function of plant positions in order to test a spatial distribution for homogeneity. The distribution is further characterized by the size of its mean heterogeneity. Ripley's K-function was used to compare the density allocation obtained for various membrane proteins: the organization of viral proteins at the cell membrane of human T-cells were identified and characterized, as well as the reorganization of arrestin2/3 proteins at the cell membrane of CHO-cells upon stimulation of G-protein-coupled receptors with different RANTES-analogues.

A coordinate-based colocalization (CBC) algorithm was developed, to determine the colocalization of two channels at the molecular level. Similar to Ripley's K-function, CBC analyzes the spatial distribution of localizations. By correlating the localization distribution of two channels within the short range order of a specific localization a colocalization value is determined. This procedure is repeated for each localization. Therefore, the CBC algorithm allows to sort localizations into different subpopulations by their CBC-value. The method was used to sort the population of TNF-R1 molecules at the cell membrane of HeLa-cells after ligand application



---

into two subpopulations: colocalized, or not colocalized with the ligand TNF $\alpha$ . The colocalization of a channel with itself is a way to investigate for heterogeneities comprising a high localization density, termed cluster. This kind of coordinate-based cluster analysis was used to characterize the cluster size of arrestin2/3 assembly sites after stimulation of G-protein-coupled receptors of CHO-cells.

Dynamical single-molecule measurements of fluorescently-labeled TNF-R1 proteins revealed the lateral protein diffusion at the cell membrane of HeLa-cells. The receptor was fused to a photo-convertible fluorescent protein, and tracked at the plasma membrane. These experiments are therefore termed single-particle tracking PALM (sptPALM) and result in a list of trajectories. By fitting the dynamic information obtained from the single-molecule trajectories to a model of lateral Brownian motion, the diffusion coefficient of each molecule is determined. The obtained data for lateral TNF-R1 diffusion was verified by fluorescence-correlation spectroscopy data available in literature. The high lateral localization accuracy of SMLM data enabled the reconstruction of diffusion maps of the whole cell.

The developed imaging-systems were further used to investigate three biological questions which are in context of complex human diseases. The distribution of HIV-1 Gag structural proteins at the cell-membrane of fixed human T-cells was characterized to appear in three different organization forms: a diffuse random distribution, an organization in small dense, and round clusters, and circular adhesion foci with a mean radius of 70 nm, comprising equidistantly distributed HIV-1 Gag molecules. Comparison to previously published electron microscopy data indicates that the focal adhesion points of HIV-1 Gag molecules represent virus-like particles. Two-color experiments of the HIV-1 proteins Gag and Env reveal a specific recruitment of Env around Gag adhesion foci without a significant colocalization. SMLM experiments with mutants of both proteins identify the MA-domain of Gag, and the CT-domain of Env being essential for the specific Env recruitment of virus particles.

Second, the recruitment of arrestin2/3 at the cell-membrane of CHO-cells by ligand-induced activation of the G-protein-coupled receptor C-C chemokine-receptor 5 (CCR5) was investigated for different analogues of the CCR5-ligand RANTES. Previous studies revealed that different RANTES analogues reduce HIV infection significantly. The arrestin2/3 distribution at the cell membrane after application of different RANTES-analogues was characterized by SMLM experiments and plot against quantitative information about CCR5 internalization, or G-protein signaling cascade intensities of previous studies. The study revealed indices of RANTES-5P14 to be the first known ligand that only induces arrestin2 recruitment.

In a third study, the influence of TNF $\alpha$  on the lateral dynamic of TNF-R1 at the cell-membrane

---

of HeLa-cells was investigated. Measuring single-molecule diffusion-coefficients on living cells revealed no significant change upon ligand application, but the vanishing of a slow diffusing subpopulation. Further the comparison of the TNF-R1 distribution to the distribution of the model-protein VSVG, which is known to form a trimer, reveals a primarily dimeric organization of non-stimulated TNF-R1 proteins. Based on previously published structural studies of TNF-R1 and TNF $\alpha$ , and on the determined quantitative SMLM data, a minimal rule-based model was introduced, to predict the ligand-induced reorganization of TNF-R1. The model predicts a reorganization of TNF-R1 towards higher order oligomers after ligand application. The model-prediction was further verified by two color SMLM experiments.

In this work the development and application of imaging-systems are described which provide quantitative data with single-molecule resolution for systems biological model approaches with a low degree of abstractness. In the near future, the impact of mathematical models in the research field of complex human diseases will increase. The predictions of these models will be more exact, the more detailed and accurate the input parameters will become. This work gives an impression of how quantitative data obtained by SMLM may serve as input parameters for mathematical models at the single-cell level.

---

# Contents

<b>1</b>	<b>Introduction</b>	<b>1</b>
1.1	Single Molecule Biophysics . . . . .	1
1.2	Aim of this Thesis . . . . .	6
<b>2</b>	<b>Theory:</b>	
	<b>Fluorescence at the Single Molecule Level</b>	<b>7</b>
2.1	Physical Interpretation of the Interaction Between Light and Matter . . . . .	7
2.2	Characteristics of Luminescence . . . . .	10
2.2.1	The Franck Condon Principle . . . . .	11
2.2.2	Lifetime and Quantum Yield of Luminescence . . . . .	14
2.3	Quenching of Luminescence . . . . .	15
2.3.1	Dynamic Quenching . . . . .	15
2.3.2	Static Quenching . . . . .	16
2.3.3	Comparison of Dynamic and Static Quenching . . . . .	16
2.3.4	Photoinduced Electron Transfer . . . . .	18
2.3.5	Molecular Oxygen in Solution . . . . .	19
2.4	Fluorescence Resonance Energy Transfer . . . . .	20
2.5	Fluorescent Probes . . . . .	21
2.5.1	Conjugated Electronic Systems . . . . .	21
2.5.2	Organic Fluorophores . . . . .	23
2.5.3	The Fluorescence Emission of Organic Fluorophores . . . . .	24
2.5.4	Redox Chemistry of Organic Fluorophores . . . . .	26
2.5.5	Fluorescent Proteins . . . . .	29
2.6	Microscope Optical Systems . . . . .	32
2.6.1	Abbe's Theory of Image Formation . . . . .	33
2.7	Fluorescence Microscopy . . . . .	36

2.8	Illumination Schemes . . . . .	38
2.8.1	Wide Field Illumination scheme . . . . .	39
2.8.2	Confocal Illumination Scheme . . . . .	41
2.9	Imaging Single Molecules . . . . .	43
2.9.1	Single Molecule Localization Microscopy . . . . .	45
2.9.2	Imaging Single Molecules in Densely Labeled Structures . . . . .	46
2.9.3	Astigmatism Based Optical Sectioning . . . . .	48
2.10	Single Molecule Diffusion Theory . . . . .	48
2.10.1	Fluorescence Correlation Spectroscopy . . . . .	51
2.10.2	Single Particle Tracking PALM . . . . .	53

### 3 Material and Methods:

	<b>Imaging single molecule fluorescence</b>	<b>55</b>
3.1	Labeling of Proteins . . . . .	55
3.2	Single Molecule Surfaces . . . . .	56
3.3	Cell Culture . . . . .	58
3.3.1	A3.01 Cell Line . . . . .	58
3.3.2	CHO Cell Line . . . . .	58
3.3.3	COS-7 Cell Line . . . . .	59
3.3.4	HeLa Cell Line . . . . .	59
3.3.5	U2OS Cell Line . . . . .	59
3.4	Labeling Cellular Structures . . . . .	59
3.4.1	Formaldehyde Fixation . . . . .	59
3.4.2	Glutaraldehyde Fixation . . . . .	60
3.4.3	Immunohistochemistry . . . . .	60
3.4.4	Actin Labeling with Phalloidin . . . . .	60
3.4.5	Click Chemistry . . . . .	61
3.5	Transient Transfection . . . . .	61
3.5.1	Transient Transfection with Turbofect . . . . .	62
3.5.2	Transient Transfection with FugeneHD . . . . .	62
3.5.3	Transient Transfection by Electroporation . . . . .	62
3.6	Optical Setups . . . . .	63
3.6.1	Wide Field Setup . . . . .	63
3.6.2	Ensemble Spectrometer . . . . .	65

3.6.3	Confocal Setup . . . . .	65
3.7	Acquisition of Single Molecule Localization Microscopy Data . . . . .	67
3.7.1	Composition of dSTORM Switching Buffer . . . . .	67
3.7.2	Acquisition of dSTORM Data . . . . .	67
3.7.3	Acquisition of PALM Data . . . . .	68
3.7.4	Acquisition of sptPALM Data . . . . .	69
3.8	Single Fluorescent Probe Localization Algorithms . . . . .	69
3.8.1	The rapidSTORM Algorithm . . . . .	70
3.8.2	The PALM Tracer Algorithm Part I . . . . .	70
3.8.3	The PALM Tracer Algorithm Part II . . . . .	70
3.9	Acquisition of FCS Data . . . . .	74
<b>4</b>	<b>Results and Discussion I:</b>	
	<b>Publications</b>	<b>75</b>
<b>5</b>	<b>Results and Discussion II:</b>	
	<b>SMLM Setup Performance</b>	<b>171</b>
5.1	Localization Accuracy . . . . .	171
5.1.1	Theoretical Localization Accuracy . . . . .	171
5.1.2	Experimental Localization Accuracy . . . . .	171
5.2	Sample Drift Quantification . . . . .	173
5.2.1	Drift Correction . . . . .	174
5.2.2	Error Estimation . . . . .	175
5.2.3	A Hydrophilic Gel Matrix for Spatial Drift Correction . . . . .	175
5.3	Multi Color Imaging . . . . .	176
5.3.1	Fluorescent Proteins under switching buffer conditions . . . . .	176
5.3.2	Channel Registration . . . . .	177
<b>6</b>	<b>Results and Discussion III:</b>	
	<b>Post-Processing of SMLM Data</b>	<b>179</b>
6.1	Cluster Analysis . . . . .	179
6.1.1	Image Reconstruction . . . . .	179
6.1.2	Morphological Cluster Analysis . . . . .	180
6.1.3	Ripley's K-Function . . . . .	180
6.2	Coordinate Based Colocalization . . . . .	184

6.2.1	CBC-mediated cluster analysis . . . . .	186
6.3	Single Particle Diffusion Analysis . . . . .	187
<b>7</b>	<b>Results and Discussion IV:</b>	
	<b>Applied Cell Biology and Biophysical Projects</b>	<b>189</b>
7.1	Morphology of HIV-1 Assembly Sites and Specific Recruitment of the Envelope Protein . . . . .	189
7.2	Arrestin Clustering Upon Stimulation of the C-C Chemokine Receptor 5 with RANTES Analogues . . . . .	192
7.3	sptPALM reveals morphological and dynamical heterogenities of membrane-bound TNF-R1 at the single molecule level . . . . .	194
<b>8</b>	<b>Outlook:</b>	
	<b>From Single Molecule Biophysics to Systems Biology</b>	<b>198</b>
8.1	Interpreting Static Single-Molecule Data by Rule-Based Modeling . . . . .	198
8.1.1	Pre-Ligand TNF-R1 Organization . . . . .	199
8.1.2	Binding Affinity of TNF $\alpha$ for TNF-R1 . . . . .	199
8.1.3	Ligand-Induced Reorganization of TNF-R1 . . . . .	199
8.1.4	A Rule-Based Model for Ligand-Induced TNF-R1 Reorganization . . . . .	200
8.2	Interpreting Dynamic Single-Molecule Data by Hidden Markov Modeling . . . . .	201
<b>A</b>	<b>Acronyms</b>	<b>205</b>
<b>B</b>	<b>References</b>	<b>210</b>
<b>C</b>	<b>Acknowledgements</b>	<b>230</b>
<b>D</b>	<b>Curriculum Vitae</b>	<b>232</b>

# List of Figures

2.1	Interactions of light and matter . . . . .	9
2.2	Franck Condon principle . . . . .	13
2.3	Jablonski diagram . . . . .	13
2.4	Dynamic and static quenching . . . . .	17
2.5	Photoinduced electron transfer . . . . .	18
2.6	Contribution of molecular oxygen to photo-induced triplet quenching . . . . .	19
2.7	Overlap integral of Atto488 and Atto647N . . . . .	20
2.8	Particle in a box . . . . .	22
2.9	HMM for the fluorescence emission of single organic fluorophores . . . . .	26
2.10	Co-solute effects on organic fluorophores . . . . .	27
2.11	Dark state formation of Cy5 . . . . .	28
2.12	Simulated fluorescence emission time trace of organic fluorophores at the single molecule level and within an ensemble under different redox conditions . . . . .	28
2.13	HMM for the fluorescence emission of activatable/convertible single fluorescent proteins . . . . .	31
2.14	Simulated fluorescence emission time trace of activatable/convertible single fluorescent proteins at the single molecule level and within an ensemble under different redox conditions . . . . .	31
2.15	A simple microscope . . . . .	32
2.16	Abbe's theory of image formation . . . . .	33
2.17	Principle of the influence of the immersion media on the numerical aperture of the microscope objective . . . . .	37
2.18	Filter cube . . . . .	38
2.19	Beam focussing scheme . . . . .	39
2.20	Optical sectioning . . . . .	41

3.1	Wide field setup . . . . .	64
3.2	Confocal setup . . . . .	66
5.1	Determining the average single-molecule localization accuracy . . . . .	172
5.2	Nonlinear drift correction and channel registration . . . . .	174
5.3	Target registration error estimation of drift correction . . . . .	175
5.4	A hydrophilic gel matrix for three dimensional fiducial marker distributions . . .	176
5.5	Spatial stability of 3D distributed fiducial markers embedded in ECM gel . . . .	177
5.6	Image Registratio . . . . .	178
6.1	Using Ripley's H-function to identify the average cluster size . . . . .	181
6.2	Toroidal edge correction . . . . .	184
6.3	The CBC concept . . . . .	185
6.4	Calibrating the CBC algorithm . . . . .	186
6.5	CBC-mediated cluster analysis . . . . .	187
6.6	Determining diffusion coefficients from single-molecule trajectroies . . . . .	188
7.1	Quantitative cluster analysis of HIV-1 Gag distribution at he cell membrane by Ripley's K-function . . . . .	190
7.2	Determination of the average dimension of HIV-1 Gag budding sites . . . . .	191
7.3	Modeling HIV-1 Gag budding sites at different developmental stages . . . . .	191
7.4	Averaged distribution of Env in context to Gag assembly sites . . . . .	193
7.5	CBC-mediated cluster analysis of arrestin3 clusters . . . . .	194
7.6	Comparison of RANTES analogues effects on arrestin recruitment, G protein sig- naling, and CCR5 internalization . . . . .	195
7.7	Super-resolution trajectory map of single TNF-R1 molecules on a HeLa cell membrane . . . . .	196
7.8	TNF-R1 diffusion coefficients in single cells . . . . .	196
7.9	Sorting single-molecule trajectories into different diffusion states . . . . .	197
8.1	Quantitative analysis of ligand-receptor interaction . . . . .	200
8.2	Two minimal rule based models for the TNF-R1-TNF $\alpha$ interaction . . . . .	201
8.3	TNF $\alpha$ -induced TNF-R1 oligomerization by network minimal rule based modeling	202
8.4	FCS measurements of ATTO655 and TNF $\alpha$ -ATTO647N . . . . .	203





---

# Chapter 1. | Introduction

## 1.1 Single Molecule Biophysics

During the last 25 years several fluorescence techniques were developed that allow the detection of single fluorescent molecules. These techniques are able to identify temporal fluctuations and spatial inhomogeneities that would otherwise have been summarized within the average distribution of an ensemble measurement. Hereby a single fluorescent molecule, that can be approximated as a point emitter for the sake of simplicity, is imaged by an optical setup as a circular area of fluorescence intensity, called *point-spread function* (PSF). This discrepancy between the image and reality results in a loss of high spatial frequencies in the Fourier space. Based on Abbe's theory, the mathematical shape of the PSF can be determined for every fluorescent molecule type and optical setup. This knowledge allows the back calculation of the taken fluorescence image to the molecule's coordinates with high accuracy (up to 1 nm<sup>2,3</sup>). The method of detecting single molecule coordinates allows the determination of several quantitative molecular characteristics, such as position, dynamics, kinetics and possible interactions<sup>4</sup>. The advent of single molecule techniques was accompanied by a breakthrough in the understanding of single molecule photophysics and its dependence on the molecules surrounding composition. This knowledge enabled the reversible stochastic photo switching of fluorescent molecules in solution between a bright and a dark state<sup>5-7</sup>. Reducing the life time of the bright state by appropriate buffer conditions allows the measurement of samples densely packed with fluorescent molecules with overlapping PSFs, by separating the single molecules temporally. These methods are classified by their way of introducing short lived bright states (PALM<sup>8</sup>, STORM<sup>9</sup>, dSTORM<sup>10</sup>) and are further referred to as *single-molecule localization microscopy* (SMLM), as they provide information of the spatial distribution of single molecules. This technique was briefly introduced in an article in [systembiologie.de](http://systembiologie.de)<sup>11</sup>.

# fluorescence nanoscopy with photoswitchable fluorophores

## Super-resolution fluorescence microscopy and single-molecule detection offer new insights into cellular processes

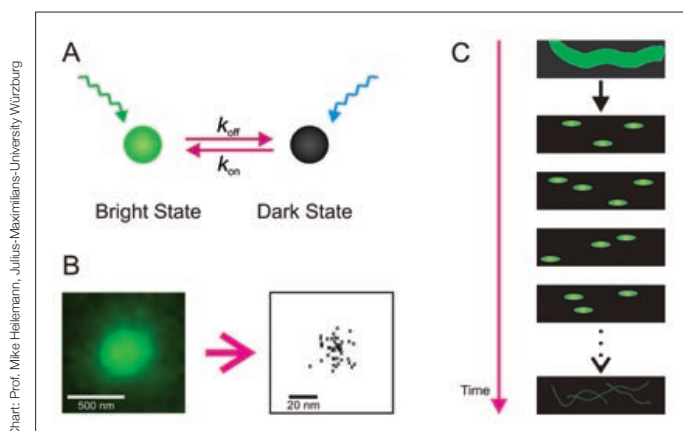
by Sebastian Malkusch, Ulrike Endesfelder, Meike Heidebreder and Mike Heilemann

Imaging biological samples is crucial for the understanding of biological function. Within the toolbox of techniques available, fluorescence microscopy is outstanding because of a number of reasons: availability of strategies for specific labeling of target structures and a large selection of fluorophores, compatibility with experiments in live cells, as well as high sensitivity which makes even the observation of single molecules possible. The newest developments in single-molecule fluorescence microscopy apply photoswitchable fluorescent probes and single-molecule localization with high precision to generate images of cellular structures with subdiffraction and near-molecular resolution and to derive quantitative data. In addition, this approach allows following dynamics of biomolecules in live cells over a long observation time, which for example allows studying the influence of an external stimulus.

Fluorescence microscopy is realized by selectively labeling a target structure with fluorescent probes and allows for the noninvasive observation of biological samples. As any light microscopy technique, the spatial resolution of fluorescence microscopy is limited to about 200 nm in the imaging plane, and to >500 nm along the optical axis. A comparison of these numbers with the biomolecular length scale illustrates that this limit in resolution hampers to resolve small (sub)cellular structures, the composition of molecular machines or viruses, or to map the precise spatial arrangement of biomolecules. This fact has been a motivation for many research groups which focus on microscopic techniques to develop new concepts that can bypass the resolution limit in light microscopy.

Among the different concepts for super-resolution fluorescence microscopy, single-molecule localization-based techniques which employ stochastically switchable fluorescent probes are of particular interest: the experimental realization is rather simple, a spatial resolution in the range of 20 nm

Fig. 1: Single-molecule localization microscopy



Photoswitchable fluorescent probes (A) can be switched between a fluorescent and a non-fluorescent state. Combining nanometer-precise localization of single molecules (B) and a temporal separation of the overall fluorescence signal (C) provides a large number of single-molecule coordinates which can be used to reconstruct a super-resolution image.

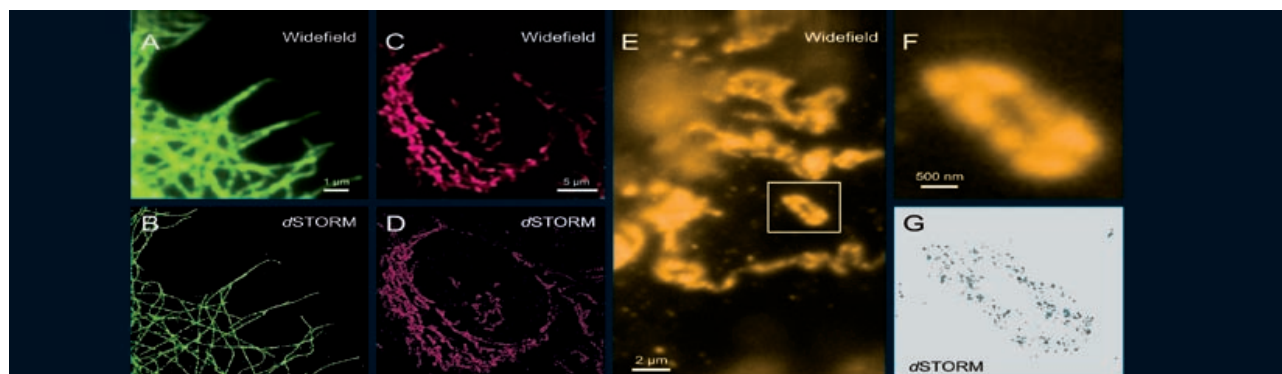


**Fig. 2:** *direct* Stochastic Optical Reconstruction Microscopy (dSTORM) of cellular structures.

Cellular structures (microtubulin (A, B), endoplasmic reticulum (C, D)) as well as protein distributions (in mitochondria (E-G)) can be imaged with near-molecular resolution using the dSTORM approach. Labeling of biological samples is performed via immunofluorescence using conventional fluorophore-labeled antibodies (Chart: Ulrike Endesfelder, Julius-Maximilians-University Würzburg).

can be achieved, and a large selection of suitable fluorescent probes and labeling techniques are readily available. As single-molecule techniques, static and dynamic heterogeneities can be resolved, and a high quality of quantitative information is provided. In analogy to classic microscopy techniques, single-molecule localization microscopy can be performed in multicolor mode and in living cells. In addition, single-molecule localization microscopy provides accurate information on both the spatial localization and time for each single molecule, which is useful beyond the generation of high-resolution images, for example to map spatial distributions of biomolecules (“biomolecular mapping”, topology), in cluster algorithms or to generate topological networks.

### Super-resolution fluorescence microscopy with photoswitchable fluorescent probes

Single-molecule localization microscopy combines three main tasks:

- 1. the application of fluorescent probes that can be photo-activated or photoswitched,
- 2. the localization of single fluorophores with a precision of a few nanometers, and
- 3. the temporal separation of the overall fluorescence signal of a sample (Figure 1).

The actual experiment starts with a “dark” sample (i.e. with all probes in their non-fluorescent state or “switched off”). In a first step, only a few fluorescent probes are activated (“switched on”) and their fluorescence signal read out, hereby making sure that the density of fluorophores per image is low enough that they are detected as single emitters. In a second step, the position of each single fluorophore is determined by approximation with a Gaussian function. The precision of localization increases with the number of photons detected, reaching <10 nm for 1000 photons. These two steps are now repeated until a sufficient number of single-molecule coordi-

ates have been collected from stochastically activated fluorophores, and can now be used to generate a reconstructed image (a “pointillistic” image) which exhibits subdiffraction spatial resolution (e.g. about 4,000 images à 20 ms for a densely labeled two-dimensional structure, or 100 images for one-dimensional filaments).

Single-molecule localization microscopy requires suitable fluorescent probes that can be switched between a fluorescent (“bright”) and a non-fluorescent (“dark”) state, e.g. by irradiation with light, through intrinsic photophysical processes or photochemical reactions. Examples for such probes are photoactivatable or photoconvertible fluorescent proteins that become fluorescent after irradiation with UV light (e.g. photoactivatable GFP, paGFP). Organic fluorophores are a second group of well-suited fluorescent probes, as they can be cycled between a “bright” and a “dark” state through photophysical or photochemical processes. One approach to photoswitch a large spectrum of organic fluorophores has been introduced with “*direct* Stochastic Optical Reconstruction Microscopy” (dSTORM), which paved the way to use conventional fluorophores that are used for a long time in cell biology e.g. in combination with immunofluorescence. dSTORM allows imaging of cellular structures in fixed cells with subdiffraction spatial resolution (Figure 2A-D), mapping of the spatial distribution of proteins (Figure 2E-G), following dynamics of single filamentous structures with a temporal resolution of 1 Hz and even super-resolution imaging inside a living cell.

Next to suitable fluorescent probes, single-molecule localization microscopy requires specific labeling strategies. While fluorescent proteins can be genetically co-expressed and integrated, labeling a biological sample with organic fluorophores can be realized with immunofluorescence or with small molecules that specifically bind to a target (e.g. phalloidin to label actin filaments). In addition, an increasing number of specific

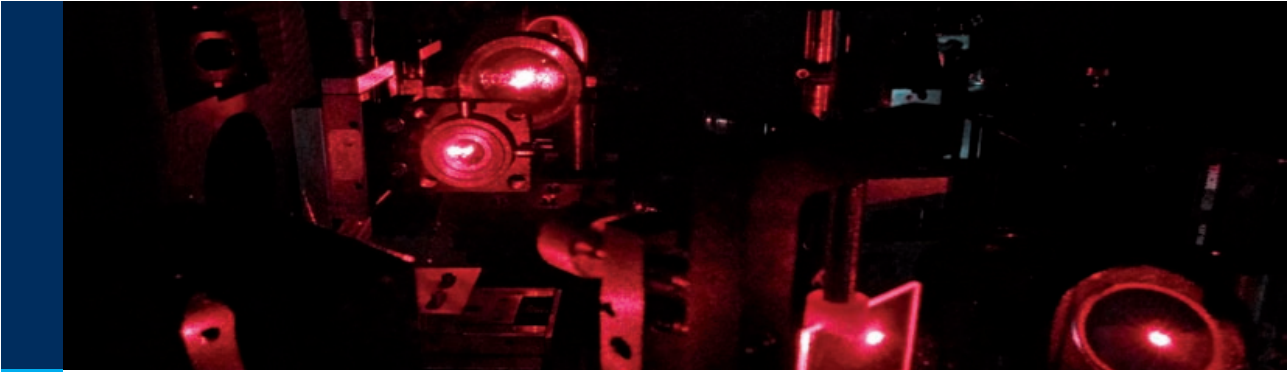


Image: Heilemann group, Würzburg

tag proteins is becoming available, which allow specific and stoichiometric labeling of biomolecules with organic fluorophores.

**Localization of single molecules: more than images**

Among the different super-resolution fluorescence microscopy methods available today, single-molecule localization is of additional interest because of the nature of the data: for each single molecule detected, nanometer-precise spatial coordinates as well as a temporal coordinate are determined. This primary data can be used straight-forward to reconstruct super-resolution images (Figure 2). Beyond that, single-molecule coordinates can further be processed by various algorithms, and information on clustering of biomolecules or trajectories in living cells can be obtained (Figure 3).

**Photoswitchable fluorescent probes and single-particle tracking**

Studies of the dynamics and the mobility of biomolecules as well as of intermolecular interactions can provide useful experimental data to establish new or to refine existing models in systems biology. An interesting and novel approach is the combination of single-particle tracking and photoswitchable fluorescent probes: different to “classical” single-particle tracking, a large pool of non-activated (“dark”) probes is available from which a small subset is activated at a given time and followed. This approach allows tracking the mobility of a fluorophore-labeled biomolecule over a long time (many minutes up to one hour), with a temporal resolution of tens of milliseconds and a spatial resolution of a few tens of nanometers. For example, the mobility of a membrane receptor before and after activation by a signal initiating molecule can be de-

Fig. 3: Single-molecule localization microscopy primary data

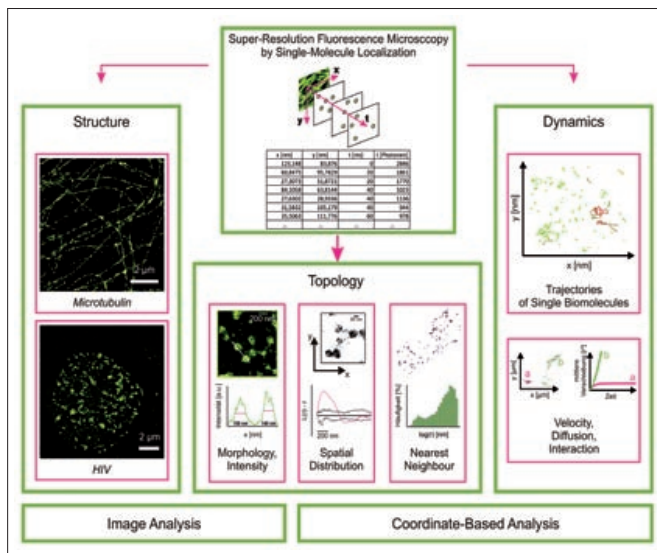
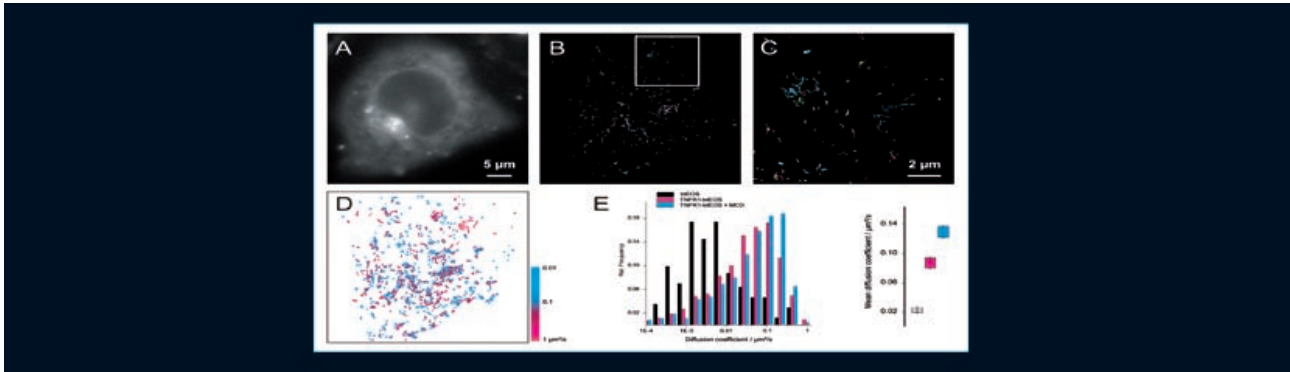


Chart: Sebastian Malkusch, Julius-Maximilians-University Würzburg

The primary data that is produced in single-molecule localization microscopy can be used to generate reconstructed images with subdiffraction resolution (left). In addition, localization data can further be processed with topological or morphological algorithms (middle) and provide quantitative information on biomolecular assemblies and clustering. On top, dynamic processes in live cells can be observed and single-molecule trajectories can be generated (right).



**Fig. 4: Photoswitchable fluorescent probes in combination with single-particle tracking.** Biomolecules that are labeled with a photoactivatable fluorescent probe (A), TNF receptor 1 labeled with the fluorescent protein tdEOS) can selectively be activated, their movement be followed in a live cell and single-molecule trajectories calculated (B, C). Further dynamic parameters such as diffusion coefficients (D, E) can be calculated from single-molecule trajectories (MCD = methylcyclodextrin). (Chart: Meike Heidebreder, Julius-Maximilians-University Würzburg).

terminated and information on aggregation, internalization and protein-protein interaction can be extracted. In addition, the mobility of membrane molecules with respect to membrane heterogeneity can be studied, and a map of diffusion coefficients can be generated (Figure 4).

#### Outlook: towards molecular resolution

The development of novel microscopic techniques has paved the way for imaging cellular structures with near-molecular resolution. The combination of super-resolution localization microscopy with single-molecule detection is a particular useful one, as it can provide a new quality of quantitative data and provide new insights into cellular structures and dynamics, biomolecular interactions, heterogeneities and subpopulations.

#### The research project in brief:

**Project name:** FORSYS-PARTNER Young Investigator „Fluorescence Techniques for Quantitative Studies of Virus-Cell Interactions“

#### Partner:

ViroQuant, Heidelberg University

#### Cooperations:

Prof. Christian Kaltschmidt, Prof. Barbara Kaltschmidt, Dr. Darius Widera, Bielefeld University;  
Dr. Jean-Baptiste Sibarita, Dr. Deepak Nair, Prof. Daniel Choquet, University of Bordeaux;  
Prof. Hans-Georg Kräusslich, PD Dr. Walter Muranyi, Heidelberg University Hospital.

#### References:

- Endesfelder, U.; van de Linde, S.; Wolter, S.; Sauer, M & Heilemann, M. (2010) Subdiffraction-Resolution Fluorescence Microscopy of Myosin-Actin Motility. *ChemPhysChem*, 11, 836-840.
- Heilemann, M. (2010). Fluorescence microscopy beyond the diffraction limit. *J. Biotech* 149, 243-251.
- Heilemann, M.; van de Linde, S.; Schüttelpe, M.; Kasper, R.; Seefeldt, B.; Mukherjee, A.; Tinnefeld, P. & Sauer, M. (2008). Subdiffraction-Resolution Fluorescence Imaging with Conventional Fluorescent Probes. *Angew. Chemie* 47, 6172-6176.
- van de Linde, S.; Sauer, M. & Heilemann, M. (2008) Subdiffraction-Resolution Fluorescence Imaging of Proteins in the Mitochondrial Inner Membrane with Photoswitchable Fluorophores. *Journal of Structural Biology* 164, 250-254.
- Wombacher, R.; Heidebreder, M.; van de Linde, S.; Sheetz, M. P.; Heilemann, M.; Cornish, V. W. & Sauer, M. (2010) Live-cell super-resolution imaging of core histones with trimethoprim conjugates. *Nature Methods* 7, 717-719.

#### Contact:

**Sebastian Malkusch** (Dipl. Biophysik)  
sebastian.malkusch@uni-wuerzburg.de

**Ulrike Endesfelder** (Dipl. Physik)  
ulrike.endesfelder@uni-wuerzburg.de

**Meike Heidebreder** (M. Sc. Biologie)  
meike.heidebreder@uni-wuerzburg.de

**Prof. Dr. Mike Heilemann**  
Single-Molecule Biology  
Department of Biotechnology & Biophysics  
Julius-Maximilians-University Würzburg  
mike.heilemann@uni-wuerzburg.de

[www.physik.uni-bielefeld.de/mh](http://www.physik.uni-bielefeld.de/mh)

## 1.2 Aim of this Thesis

The aim of this thesis was the development and design of SMLM imaging systems for biophysical applications. Hereby the quality of single molecule fluorescence experiments depends on five different factors, that had to be carved out during the work of this thesis.

1. The formulation of a qualified hypothesis on the biological target, that has to be tested by SMLM
2. Development of an optical setup for detecting single molecules
3. Development of labeling strategies with photo switchable fluorescent probes, allowing to prove/disprove the validity of the hypothesis
4. The choice of a software managing the back calculation of the fluorescent probes positions with high accuracy
5. The development of post processing software routines for localization data, allowing quantitative conclusions on the validity of the hypothesis

The biological questions that have been addressed are the spatial distribution of single membrane proteins of whole fixed cells with near molecular accuracy. Special attention was paid to human diseases such as the formation of *human immunodeficiency virus* (HIV) budding sites and the *tumor necrosis factor* (TNF)- $\alpha$  induced *tumor necrosis factor receptor type I* (TNF-R1) signaling cascade initiation. Temporal fluctuations in diffusion and spatial inhomogeneities of membrane located proteins were investigated in living cells and gave new information about the two diseases at the single molecule level.

A key objective is the implementation of quantitative SMLM data into systems biology. In particular for mathematical modeling of the initiation of transmembrane signaling cascades. As these events are localized at the cell membrane, they are easily accessible for single molecule techniques in living cells. The high accuracy of the quantitative data provided by SMLM techniques, as well as the information about molecular subpopulations that so far were masked by averaging routines of diffraction limited ensemble measurements will help to establish detailed models with a low degree of abstraction of the initiation process of transmembrane signaling processes.

---

# Chapter 2. | Theory:

## Fluorescence at the Single Molecule Level

This chapter comprises theoretical background from interaction of light and matter to the implementation of reversible photo switching of single fluorescent molecules in cutting-edge light microscopy.

### 2.1 Physical Interpretation of the Interaction Between Light and Matter

"Insofern ist für den richtigen Theoretiker nichts interessanter als eine Tatsache, die mit einer bisher allgemein anerkannten Theorie in Widerspruch steht; denn hier setzt die eigentliche Arbeit ein."

Max Planck, *Neue Bahnen der physikalischen Erkenntnis*, 1922

The basic interaction of light and matter shall be exemplified in this subsection in more detail on the basis of cavity radiation.

One of the first scientific papers about the interaction of light and matter was published by Wilhelm Ludwig Franz Hellwachs in 1888<sup>12</sup>. His work was based on the former observation of Alexandre Edmond Bacquerel who described that the exposure of one electrode within an electrolyte with light produces a potential difference between this electrode and a reference electrode within the same electrolyte (*Bacquerel Effect*). In collaboration with his mentor Heinrich Hertz, Hellwachs discovered the outer photoelectric effect. Briefly summarized, electrons of a metal plate surface may be extracted by the illumination of the plate. Hereby, the energy



of the extracted electrons is only depending on the frequency of the illuminating light. The intensity has no effect on the free electron energy, but only on the number of released electrons. In 1900 Max Planck described the experimentally determined intensity distribution  $I(\nu)$  of cavity radiation by natural oscillations of the electromagnetic field, that does not absorb arbitrary amounts of energy, but only integer multiples of  $h \cdot \nu$ <sup>13</sup>. Here,  $h$  is termed *Planck's constant* and  $\nu$  is the frequency of the emitted light. This quantum hypothesis opposed the world of classical physics but described the exact energy distribution of the cavity radiation. After Planck's hypothesis a natural oscillation containing  $n = 1, 2, 3, \dots$  photons consists of the energy  $W = q \cdot h \cdot \nu$ . This quantum hypothesis postulates that systems with two different energy states  $E_1 - E_0 = \Delta E$  are able to emit light with a frequency  $\nu$  that fulfills the constraint:

$$\Delta E = h \cdot \nu \quad (2.1)$$

$$\Delta E = \frac{h \cdot c}{\lambda} \quad (2.2)$$

$$\Delta E = \frac{1239,84}{\lambda} \text{ nm} \cdot \text{eV} \quad (2.3)$$

Here  $c$  as the speed of light and  $\lambda$  is the wavelength.

Natural oscillations  $n_i$  within the same energy state  $E_i$  of stationary systems containing  $n$  oscillations in thermal equilibrium are described by the *Maxwell Boltzmann distribution*.

$$n_i = \frac{g_i \cdot n}{q} \cdot e^{\frac{-E_i}{k \cdot T}} \quad (2.4)$$

Here,  $q$  is the systems partition function and  $g_i$  is the statistical weight of the energy state  $E_i$ ,  $T$  is the temperature, and  $k$  is the *Boltzmann constant*. For a two energy state system in thermal equilibrium, the quotient of the frequency of the natural oscillations for both energy states  $n_0$  and  $n_1$  calculates to:

$$\frac{n_1}{n_0} = \frac{g_1}{g_0} \cdot e^{-(E_1 - E_0)/(k \cdot T)} \quad (2.5)$$

$$\frac{n_1}{n_0} = \frac{g_1}{g_0} \cdot e^{\frac{-(h \cdot \nu)}{k \cdot T}} \quad (2.6)$$

Based on Planck's work, Albert Einstein described the possible interactions of light and matter<sup>14</sup>. For a two-state energy system with  $E_0 < E_1$  in a monochromatic electromagnetic field that fulfills equation (2.1), Albert Einstein postulated three possible interactions of light and matter, as depicted in figure 2.1. A molecule in the energy state  $E_0$  that absorbs a photon will be transferred to  $E_1$ , and the number of photons within the electromagnetic field will be reduced by one. The probability that one molecule absorbs a photon per second is given by  $\Gamma_{01}$ . This effect is termed *induced absorption*. A molecule in  $E_1$  may interact with the electromagnetic

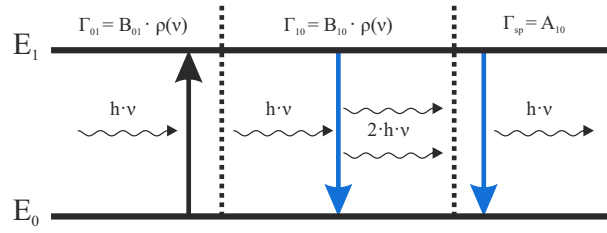


Figure 2.1: **Interactions of light and matter after Einstein**

Possible interactions and transition rates between a two-state energy system within an electromagnetic field. Transitions resulting from the absorption of a photon are depicted in black, transitions that lead to the emission of a photon are depicted in blue.

field in form of a light induced return to  $E_0$ . To conserve the systems energy the number of photons within the electromagnetic field will be amplified by one. The probability that one molecule will be induced to emit a photon per second is given by  $\Gamma_{10}$ . This effect is termed *induced* or *stimulated emission*. A molecule in  $E_1$  may also spontaneously return into  $E_0$ , even if no external electromagnetic field is interacting with the molecule. To conserve the systems energy in the case of a spontaneous transition from  $E_1$  to  $E_0$  the molecule emits a photon that fulfills equation (2.1). The probability that one molecule will spontaneously emit a photon is given by  $\Gamma_{sp}$ . This effect is termed *spontaneous emission*.  $\Gamma_{01}$  and  $\Gamma_{10}$  are both proportional to the spectral density of the electromagnetic energy of the electromagnetic field  $\rho(\nu)$ . The interaction of a two-state energy system with a electromagnetic field within the equilibrium can be described as:

$$\Gamma_{01} \cdot n_0 = (\Gamma_{sp} + \Gamma_{10}) \cdot n_1 \quad (2.7)$$

$$\Gamma_{01} = B_{01} \cdot \rho(\nu) \quad (2.8)$$

$$\Gamma_{10} = B_{10} \cdot \rho(\nu) \quad (2.9)$$

$$\Gamma_{sp} = A_{10} \quad (2.10)$$

The proportionality constants  $B_{01}$ ,  $B_{10}$  and  $A_{10}$  are termed *Einstein coefficients*. Equalizing of equation (2.7) and (2.6) yields:

$$\frac{\Gamma_{01}}{\Gamma_{sp} + \Gamma_{10}} = \frac{g_1}{g_0} \cdot e^{-\frac{h \cdot \nu}{k \cdot T}} \quad (2.11)$$

$$\frac{B_{01} \cdot \rho(\nu)}{A_{10} + B_{10} \cdot \rho(\nu)} = \frac{g_1}{g_0} \cdot e^{-\frac{h \cdot \nu}{k \cdot T}} \quad (2.12)$$

$$\rho(\nu) = \frac{A_{10}}{B_{01} \cdot \frac{g_0}{g_1} \cdot e^{\frac{h \cdot \nu}{k \cdot T}} - B_{10}} \quad (2.13)$$

For  $T \rightarrow \infty$  it is essential that  $\rho(\nu) \rightarrow \infty$ . Therefore, the relation between  $B_{01}$  and  $B_{10}$  calculates from equation (2.13) to:

$$B_{01} \cdot \frac{g_0}{g_1} \cdot e^{\frac{h \cdot \nu}{k \cdot T}} - B_{10} \rightarrow 0 \quad (2.14)$$

$$B_{01} \cdot \frac{g_0}{g_1} - B_{10} = 0 \quad (2.15)$$

$$B_{01} = \frac{g_1}{g_0} B_{10} \quad (2.16)$$

Using the serial expansion  $e^{\frac{h \cdot \nu}{k \cdot T}} = 1 + \frac{h \cdot \nu}{k \cdot T} + \dots$ , equation (2.16) calculates to:

$$\rho(\nu) = \frac{A_{10}}{B_{01}} \cdot \frac{k \cdot T}{h \cdot \nu} \quad (2.17)$$

The classical electrodynamics by Maxwell postulate a link between  $k \cdot T$  and  $\rho(\nu)$  from a linear oscillator, that is described by the law of Rayleigh-Jeans. It was experimentally confirmed for  $h \cdot \nu \ll k \cdot T$ .

$$\rho(\nu) = \frac{8 \cdot \pi \cdot \nu^2}{c^3} \cdot k \cdot T \quad (2.18)$$

Equalizing equations (2.17) and (2.18) calculates to the ratio between  $A_{10}$  and  $B_{01}$ :

$$\frac{A_{10}}{B_{01}} = \frac{8 \cdot \pi \cdot h \cdot \nu^3}{c^3} \quad (2.19)$$

Insertion of equation (2.19) into equation (2.13) calculates to:

$$\rho(\nu) = \frac{8 \cdot \pi \cdot \nu^2}{c^3} \cdot \frac{h \cdot \nu}{e^{\frac{h \cdot \nu}{k \cdot T}} - 1} \quad (2.20)$$

Equation (2.20) is termed *Planck's law* and describes the spectral density of the electromagnetic energy for cavity radiation.

## 2.2 Characteristics of Luminescence

Often interactions of light and matter occur between an electromagnetic field and multi-electron systems. These interactions are much more complicated than the single-electron two-state systems discussed in chapter 2.1, because each molecular orbital splits into several vibrational states  $v^{15,16}$ . The energy of an electronic state can be approximated mathematically by a *Morse potential*. The discrete states, a multi electron system can exist in, are described by a wave function  $\psi$  that is coupled to an energy value  $E$ . The interaction of a multi-electron system, that exists initially in the ground state  $\psi_i$ , with an electromagnetic field, results in the excitation of the multi-electron system to a higher electronic and vibrational state  $\psi_f$ . The excited molecule loses energy to its environment via collisions without emitting radiation. This

process occurs until the molecule returns to the vibrational ground state of the electronic excited state. The transition between the electronic excited state to the electronic ground state may be accompanied by the spontaneous emission of a photon as postulated by Einstein (see chapter 2.1), or by a radiationless transition termed *internal conversion* (IC). It is not possible to solve these intramolecular photo-physical mechanisms exactly but to describe them by several approximations.

### 2.2.1 The Franck Condon Principle

For further approximation for all following derivations the external electromagnetic field that causes stimulated emission will be switched off, so that  $\Gamma_{10}$  can be neglected. The remaining phenomenon  $\Gamma_{sp}$  is also termed *fluorescence*. If the energetic difference between the two eigenstates  $\psi_i$  (initial state) and  $\psi_f$  (final state) of a molecule within an external electromagnetic field fulfill equation (2.1) the molecule gets excited to the higher state. Hereby  $P$  is defined as the expectation value of the transition dipole moment operator  $\hat{\mu}$ , or transition probability.

$$P = \langle \psi_i | \hat{\mu} | \psi_k \rangle \quad (2.21)$$

$\hat{\mu}$  is defined as the summation of all charges in the molecule multiplied by the displacement to a reference point  $\hat{\mu} = q \vec{r}$ . It comprises the transition dipole moment operator for the electrons  $\hat{\mu}_e$  and the nuclei components  $\hat{\mu}_K$ . With  $e^-$  being the elementary charge of an electron,  $\vec{r}_m$  the displacements of the electrons,  $Z_n$  the proton number of the molecule, and  $\vec{R}_n$  the displacement of the nuclei it applies:

$$\hat{\mu} = \hat{\mu}_e + \hat{\mu}_K \quad (2.22)$$

$$= -e \sum_m \vec{r}_m + e \sum_n Z_n \vec{R}_n \quad (2.23)$$

The Born-Oppenheimer approximation postulates, that the electronic part and the nuclear part of the molecular wave function  $\psi$  can be separated<sup>17</sup> due to the huge difference in mass between the slowly moving nucleus and the electron. The molecular wave function is approximated as their product.

$$\psi = \psi_e(\vec{r}, \vec{R}) \cdot \chi_K(\vec{R}) \quad (2.24)$$

With  $\psi_e(\vec{r}, \vec{R})$  as the electronic wave function of the rigid molecule which depends on the  $e^-$ -coordinates  $\vec{r}$  and the nuclear configuration  $\vec{R}$ , and  $\chi_K(\vec{R})$  as the nuclear wave function which depends on the  $K^+$ -coordinates  $\vec{R}$ . Applying the separation of the dipole moment operator (equation (2.22)) and the Born-Oppenheimer approximation (equation (2.24)) to equation (2.21) leads to:

$$P = \langle \psi_{f,e} \chi_{f,K} | \hat{\mu}_e + \hat{\mu}_K | \psi_{i,e} \chi_{i,K} \rangle \quad (2.25)$$

$$= \langle \psi_{f,e} \chi_{f,K} | \hat{\mu}_e | \psi_{i,e} \chi_{i,K} \rangle + \langle \psi_{f,e} \chi_{f,K} | \hat{\mu}_K | \psi_{i,e} \chi_{i,K} \rangle \quad (2.26)$$

$$= \langle \chi_{f,K} | \chi_{i,K} \rangle \langle \psi_{f,e} | \hat{\mu}_e | \psi_{i,e} \rangle + \langle \psi_{f,e} | \psi_{i,e} \rangle \langle \chi_{f,K} | \hat{\mu}_K | \chi_{i,K} \rangle \quad (2.27)$$

For changes of the electronic and vibrational state, termed *vibronic* transitions, it applies  $\langle \psi'_e | \psi_e \rangle = 0$ , because the wave functions are orthogonal. Therefore, only the first term is non-zero<sup>18</sup>:

$$P_e = \langle \chi_{f,K} | \chi_{i,K} \rangle \langle \psi_{f,e} | \hat{\mu}_e | \psi_{i,e} \rangle \quad (2.28)$$

A *vibronic* transition of a molecule is accompanied by a reorganization of its electronic configuration. It can be described by two discrete steps: an instantaneous transition to a different electronic eigenstate followed by a slow shift of the nucleus to the new thermal equilibrium position caused by the reorganized electronic configuration via *vibrational relaxation* (VR). The transition probability between different vibrational states via VR accompanying the electronic eigenstate transition are given by their overlap integral  $\langle \chi_{f,K} | \chi_{i,K} \rangle$ , the so called Franck-Condon factor<sup>15,16</sup>. In general the vibrational relaxation to thermal equilibrium takes place  $10^4$  times faster than fluorescence<sup>19</sup>. Therefore, the transition from the first higher electronic eigenstate  $S_1$  back to the electronic ground eigenstate  $S_0$  will occur most frequently from the vibrational equilibrium  $v' = 0$  to a higher vibrational eigenstate  $v'' = n$  (with  $n=1,2,3,\dots$ ). This phenomena is also termed *Kasha's rule*<sup>19</sup>.

The intensity of the transition between two specific electronic eigenstates is given by the square of the absolute transition probability value:

$$I = |P_e|^2 \quad (2.29)$$

By plotting the energy of all possible transitions against the intensity  $|P_e|^2$  for every possible transition results in a so called absorption or emission spectrum (see figure 2.2 a). According to *Kasha's rule* the fluorescence spectrum is independent of the illuminating electromagnetic field's spectrum. As the vibrational states of  $\chi_i$  and  $\chi_f$  have approximately the same frequencies, the vibronic transitions  $\chi_{a,v''=0} \rightarrow \chi_{b,v'=n}$  and  $\chi_{b,v'=0} \rightarrow \psi_{a,v''=n}$  have approximately identical Franck-Condon factors

$$\langle \chi_{a,v''=0} | \chi_{b,v'=n} \rangle = \langle \chi_{b,v'=0} | \chi_{a,v''=n} \rangle \quad (2.30)$$

and are symmetrically localized on opposite sites of the  $v''_0 - v'_0$  transition  $h \cdot \nu_{00}$ . Therefore, the emission spectrum of a molecule is approximately a mirror image of its absorption spectrum

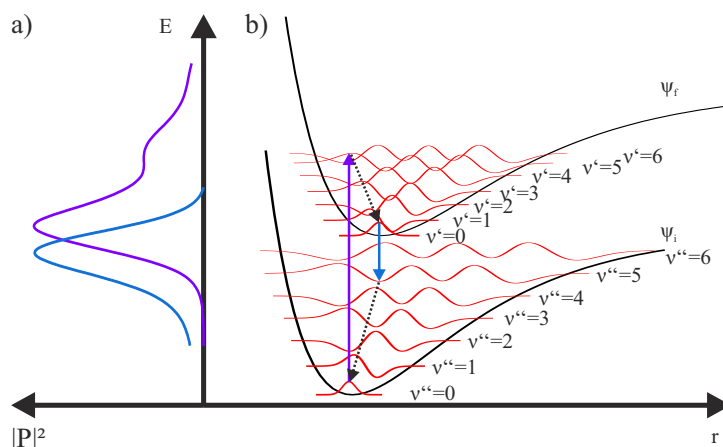


Figure 2.2: **Franck Condon principle** a) Plotting all possible state transitions within a multi electronic and vibrational state system against their transition probability results in the absorption (magenta) and emission (blue) spectrum. b) The energy  $E$  of a multi electron system plot against the nuclear coordinate  $r$ . An external electromagnetic field induces transitions between electronic ( $S_i$ ) and vibrational ( $v$ ) states. Light induced photon absorption is depicted in magenta. Spontaneous photon emission is depicted in blue. Radiationless transitions between vibrational states are indicated by dotted arrows.

(see figure 2.2 b)<sup>20</sup>.

A more simple and intuitive way to discuss the interaction of light and matter is the Jablonski diagram (see figure 2.3)<sup>21</sup>. Here, electronic and vibrational eigenstates are depicted simply by

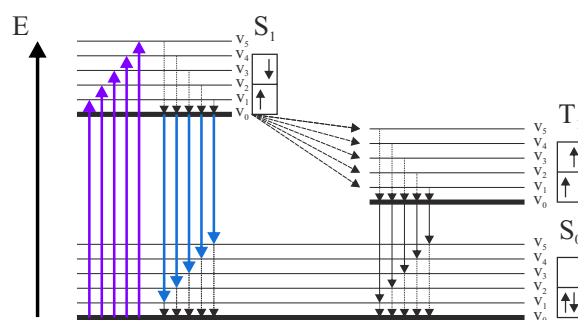


Figure 2.3: **Jablonski diagram**

Light induced photon absorption is depicted in magenta. Spontaneous photon emission is depicted in blue. Spontaneous phosphorescence is depicted in solid black arrows. Radiationless transitions between electronic and vibrational eigenstates are indicated by dotted arrows.

horizontal lines. Possible transitions between the eigenstates are illustrated by vertical arrows. Solid arrows indicate an interaction of light and matter and dotted arrows indicate radiation-

less transitions. The arrow length indicates  $\Delta E$  between the two states (see equation 2.1). Despite the emission of fluorescence, several additional ways of relaxation may occur, e.g. energy transfer via collisions to other molecules, or *Foerster resonance energy transfer* (FRET) to adjacent molecules (see chapter 2.3), the radiationless energy release to the environment via heat IC, and the transition to electronic triplet states, termed *intersystem crossing* (ISC) (see figure 2.3). IC to the electronic triplet state and the transition from the electronic triplet state to the electronic ground state are accompanied by a flip of the electron spin. Therefore, both transitions are characterized by a low transition probability, although the photophysics of ISC are not fully determined so far<sup>22</sup>. As the electronic triplet state has a higher energy level than the electronic ground state, the transition may also be accompanied by a luminescence phenomenon termed phosphorescence. Rate constants for several transition reactions are given in table 5.1.

Table 2.1: **Transition rates**

Rate constants and time scales of several transition reactions occurring during the interaction of molecules with light<sup>23</sup>

transition	transition type	rate constant	time scale [s]
$S_0 \rightarrow S_1, \dots, S_n$	absorption	$\Gamma_{0n}$	$10^{-15}$
$S_n \rightarrow S_1$	internal conversion	$k_{ic}$	$> 10^{-12}$
$S_{1,v''=n} \rightarrow S_{1,v''=0}$	vibrational relaxation	$k_{vr}$	$> 10^{-11}$
$S_1 \rightarrow S_0$	fluorescence	$\Gamma_{sp}$	$10^{-9} - 10^{-6}$
$S_1 \rightarrow S_0$	nonradiative decay	$k_{nr}$	$10^{-7} - 10^{-6}$
$S_1 \rightarrow T_1$	intersystem crossing	$k_{isc}$	$10^{-11} - 10^{-6}$
$T_1 \rightarrow S_0$	phosphorescence	$\Gamma_{ph}$	$10^{-3} - 10^2$
$T_1 \rightarrow S_0$	nonradiative triplet decay	$k_{tnr}$	$10^{-3} - 10^4$

### 2.2.2 Lifetime and Quantum Yield of Luminescence

Along with the absorption and the emission spectra, which are discussed in chapter 2.2.1 the phenomenon of luminescence is characterized by the lifetime of the excited state and the quantum yield of the process. The lifetime of an excited electronic eigenstate is the average time the molecule spends in the excited state. It is therefore depending on all processes that are depopulating the excited electronic eigenstate. In absence of an external electromagnetic field the excited electronic state is depopulated by spontaneous emission, which is described by the Einstein coefficient  $\Gamma_{sp}$  from equation (2.10) and by a sum of non-radiative transitions  $k_{nr} = \sum_i k_i$ .

A population  $[N]_0$  of molecules within an excited electronic eigenstate translates to the ground state by<sup>24</sup>:

$$\frac{d[N]}{dt} = \Gamma_{sp}[N] + k_{nr}[N] = \Gamma_{sp}[N] + \sum_i k_i[N] \quad (2.31)$$

$$[N] = [N]_0 e^{-\Gamma_{sp}t} \prod_i e^{-k_i t} = [N]_0 \cdot e^{-\frac{t}{\tau}} \quad (2.32)$$

Based on equation (2.32) the life time of the excited electronic eigenstate  $\tau_f$  calculates to:

$$\tau_f = \frac{1}{\Gamma_{sp} + k_{nr}} = \frac{1}{\Gamma_{sp} + \sum_i k_i} \quad (2.33)$$

The quantum yield is defined as the fraction between spontaneous radiative transitions to the ground state and all possible transitions to the ground state. It calculates to:

$$\Phi = \frac{\Gamma_{sp}}{\Gamma_{sp} + k_{nr}} = \tau_f \cdot \Gamma_{sp} \quad (2.34)$$

## 2.3 Quenching of Luminescence

As described briefly in chapter 2.2 non-radiative transitions from the  $S_1$  state to the ground state compete with the spontaneous radiative decay and lead to a decrease in the luminescence signal<sup>24</sup>. These intermolecular reciprocal effects are therefore termed quenching effects. Quenching effects can be split into two main groups: dynamic, and static quenching effects. Both effects have in common that a close contact between the quencher  $Q$  and the excited molecule is needed in order to quench the molecule's luminescence.

### 2.3.1 Dynamic Quenching

Dynamic quenching is defined as the transfer of the excitation energy of the excited molecule to a different molecule during collision. The excited molecule returns into the electronic ground state via non-radiative transition and the quantum yield  $\Phi$  of the excited molecule is quenched. This process can be described by building the fraction between the luminescence signal in absence  $\Phi_0$  and in presence  $\Phi_q$  of the quencher molecule:

$$\Phi_0 = \frac{\Gamma_{sp}}{\Gamma_{sp} + k_{nr}} = \tau \cdot \Gamma_{sp} \quad (2.35)$$

$$\Phi_q = \frac{\Gamma_{sp}}{\Gamma_{sp} + k_{nr} + k_{dq}[Q]} = \frac{\Gamma_{sp}}{\frac{1}{\tau} + k_{dq}[Q]} \quad (2.36)$$

$$\frac{\Phi_0}{\Phi_q} = \tau \cdot \Gamma_{sp} \cdot \frac{\frac{1}{\tau} + k_{dq}[Q]}{\Gamma_{sp}} \quad (2.37)$$

$$= 1 + \tau \cdot k_{dq}[Q] \quad (2.38)$$



with  $[Q]$  as the quencher concentration and  $k_{dq}$  as biomolecular quenching constant.

The introduction of the Stern-Volmer constant for dynamic quenching<sup>25</sup>  $K_d = \tau \cdot k_{dq}$  turns equation (2.38) into:

$$\frac{\Phi_0}{\Phi_q} = 1 + K_d[Q] \quad (2.39)$$

Equation (2.39) is termed Stern-Volmer equation for dynamic quenching. One of the most effective dynamic quencher molecules is oxygen which will be discussed in more detail in chapter 2.5.4.

### 2.3.2 Static Quenching

Static quenching is defined as the formation of a non-fluorescent complex of the luminescent molecule and the quencher. A concentration of  $[M]_0$  luminescent molecules and  $[Q]$  quencher molecules with a dissociation constant  $K_s$  calculates to:



$$K_s = \frac{[MQ]}{[M][Q]} \quad (2.41)$$

Because the absolute number of molecules is stable, the concentrations  $[M]_0$  and  $[Q]$  remain constant. Therefore,  $[MQ]$  is given by:

$$[MQ] = [M]_0 - [M] \quad (2.42)$$

Insertion of equation (2.42) into equation (2.41) gives:

$$\frac{[M]_0}{[M]} = 1 + K_s \cdot [Q] \quad (2.43)$$

With  $\frac{[M]_0}{[M]} = \frac{\Phi_0}{\Phi_q}$  equation (2.43) turns into:

$$\frac{\Phi_0}{\Phi_q} = 1 + K_s[Q] \quad (2.44)$$

### 2.3.3 Comparison of Dynamic and Static Quenching

The main difference between dynamic and static quenching is their temperature dependency. As a rise in temperature is accompanied by an increase in diffusion, it leads to a larger number of collisions and a higher rate of dynamic quenching. On the other hand a higher temperature weakens the interactions in a quencher complex and decreases the rate of static quenching<sup>24</sup>.

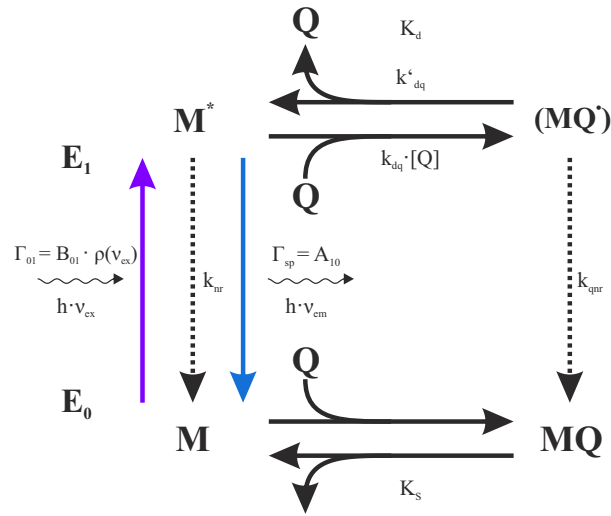


Figure 2.4: **Dynamic and static quenching**

Absorption is depicted in magenta, spontaneous emission in blue. Quenching mechanisms are depicted in black. Radiationless transitions between electronic eigenstates are indicated by dotted lines (derived from<sup>24</sup>).

In practice, one often observes a mix of both quenching mechanisms (see figure 2.4) for which the Stern-Volmer equation calculates to:

$$\frac{\Phi_0}{\Phi_q} = (1 + K_d[Q]) \cdot (1 + K_s[Q]) \quad (2.45)$$

$$= 1 + (K_d + K_s) \cdot [Q] + K_d \cdot K_s \cdot [Q]^2 \quad (2.46)$$

Collision between a fluorescent molecule and a quencher results in the formation of an encounter complex, which can perform a quenching effect with the rate  $k_{qnr}$ , or it can decompose with the back reaction rate  $k'_{dq}$  of the dynamic Stern-Volmer constant  $K_d$ . The probability that quenching occurs after a collision between a fluorescent molecule and a quencher is termed quenching efficiency  $E_q$ .

$$E_q = \frac{k_{qnr}(r)}{k' + k_{qnr}(r)} \quad (2.47)$$

With  $k_{qnr}(r) \gg k'_{dq}$  in most cases. As  $k_{qnr}(r)$  depends on the interaction of the fluorescent molecule and the quencher molecule orbitals with each other, it is highly depending on the distance  $r$  between the two molecules:

$$k_{qnr}(r) = Ae^{-B(r-r_c)} \quad (2.48)$$

With  $A$  and  $B$  being specific constants of the molecules and  $r_c$  is the closest possible distance at molecular contact.

### 2.3.4 Photoinduced Electron Transfer

Quenching of fluorescence in general depends on the formation of an encounter complex between the fluorescent molecule and the quencher. Therefore it can be modelled by the same math and is described by several mechanisms. The most frequently occurring mechanisms are ISC (see chapter 2.2.1)<sup>26</sup> and *photoinduced electron transfer* (PET)<sup>27</sup>. For SMLM-experiments the modulations of photon emission rates of fluorescent probes involves PET despite ISC (see chapter 2.5.4). The PET mechanism of fluorescence quenching is depicted in figure 2.5. It is

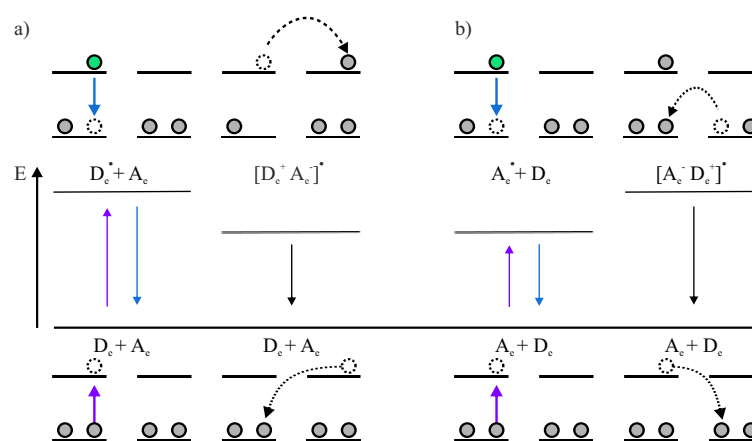


Figure 2.5: **Photoinduced electron transfer**

Two different mechanisms of PET (Absorption is depicted in magenta, emission in blue). a) The fluorescent probe serves as electron donor  $D_e$ . b) The fluorescent probe serves as acceptor  $A_e$ . Radiationless transitions between electronic eigenstates, caused by quencher interactions are indicated by dotted lines.

mediated by a redox reaction between an electron acceptor  $A_e$  and an electron donor  $D_e$ . Based on the oxidation and reduction potential of the  $S_1$  and the  $S_0$  state, the fluorescent or quenching molecule can function as  $A_e$  or  $D_e$  and vice versa. The reaction is mediated via an exciplex formation  $[ ]^*$ . The reaction requires the fluorescent molecule to be in the  $S_1$  state. If the fluorescent molecule serves as  $D_e$ , an oxidation of the excited fluorescent molecule results in the transition to a radical state  $[D_e^+ A_e^-]^*$ . The back reaction into the  $S_0$  state occurs as a reduction of the radical  $D_e^+$  (see figure 2.5 a). Vice versa, if the fluorescent molecule serves as  $A_e$ , a reduction of the fluorescent molecule results in the transition to a radical state  $[A_e^- D_e^+]^*$ . The back reaction into the  $S_0$  state occurs as an oxidation of the radical  $A_e^-$  (see figure 2.5 b). Charge transfer

exciplexes may also decay directly to the  $S_0$  state via non radiative transition  $k_{nr}$  or radiative transition  $\Gamma_{sp}$ . The exciplex exhibits a typical lifetime in the range of ns.

ISC and PET allow the exact modulation of the stochastic transition rates of fluorescent probes in solution and are the key mechanisms to SMLM techniques. Therefore, the selective manipulation of fluorescent probes in solution by the change of buffer and co-solutes conditions with respect to different single molecule fluorescent techniques will be addressed in chapter 2.5.4

### 2.3.5 Molecular Oxygen in Solution

The triplet state is characterized by a long lifetime from  $\mu\text{s}$  to  $\text{min}$ , because the  $S_1 \rightarrow T_1$  transition is accompanied by a change of the electronic spin and is forbidden by the law of quantum mechanics, as is the  $T_1 \rightarrow S_0$  transition. It is therefore considered to be a photophysically very active state. An efficient quencher of triplet states is molecular oxygen<sup>26</sup>. It is to low concentrations dissolved in aqueous solution ( $\approx 3 \text{ mM}$ )<sup>28</sup>. Molecular oxygen mediated triplet quenching occurs by the formation of an encounter complex comprising a fluorophore in the triplet state and molecular oxygen, followed by two competitive quenching mechanisms: An energy transfer from the fluorophore to the oxygen molecule, resulting in the formation of singlet oxygen ( $^1\text{O}_2$ ), and an electron transfer from the fluorophore to the oxygen molecule, resulting in the formation of super-oxidative oxygen ( $\text{O}_2^-$ , see figure 2.6 a)<sup>29,30</sup>. The byproduct of both quenching reactions are *highly reactive oxygen species* (ROS), which are involved in irreversible bleaching reactions (see figure 2.6 b)<sup>31</sup>. Decreasing the concentration of molecular oxygen within the buffer,

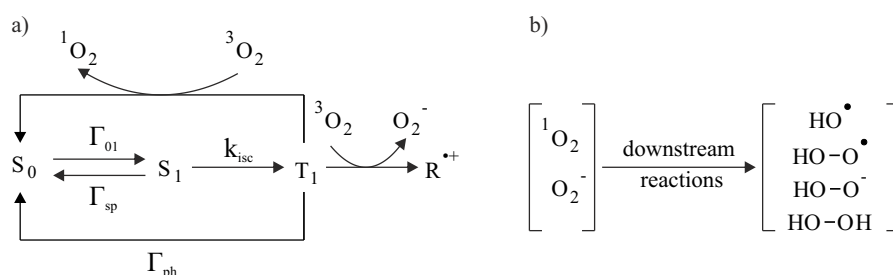


Figure 2.6: **Contribution of molecular oxygen to photo-induced triplet quenching**

a) Competitive triplet decay mechanisms ( $\text{R}^{\bullet+}$  is a long lived radical cationic state). b) Possible downstream reactions of the ROS (adapted from<sup>31</sup>).

decreases the photo-induced photobleaching and increases the triplet lifetime at the same time. As a consequence alternative  $T_1$  quencher (e.g.  $\beta$ -mercapto-ethylamine (MEA)) are added to the

buffer<sup>5,7</sup>. An excellent review about the photo-physical mechanisms during the generation and deactivation of singlet oxygen was composed by Schweitzer and Schmidt<sup>32</sup>.

## 2.4 Fluorescence Resonance Energy Transfer

Despite dynamic and static quenching mechanisms the energy of an excited molecule may also be transferred to a non-excited molecule via long distance radiationless dipole-dipole interactions. This energy transfer, like quenching, results in a decreased fluorescence signal of the originally excited molecule. This interaction is termed FRET<sup>33</sup>. An efficient FRET requires the donor's emission spectrum to overlap the acceptor's absorption spectrum in a large area, which is described by the overlap integral  $J(\lambda)$ :

$$J(\lambda) = \frac{\int_0^\infty F_D(\lambda)\epsilon_A(\lambda)\lambda^4 d\lambda}{\int_0^\infty F_D(\lambda)d\lambda} \quad (2.49)$$

Here,  $F_D(\lambda)$  describes the area-normalized donor fluorescence spectrum, and  $\epsilon_A(\lambda)$  describes the extinction coefficient of the acceptor in  $\frac{1}{\text{cm M}}$  (see figure 2.7).

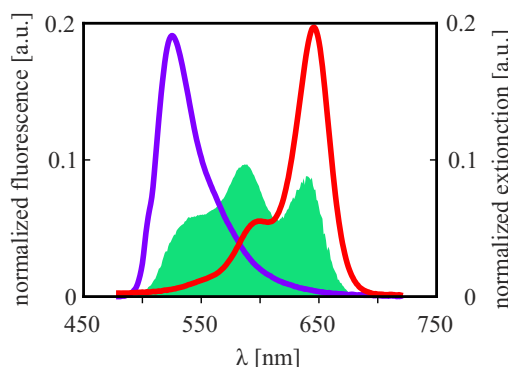


**Figure 2.7: Overlap integral of Atto488 and Atto647N**

An overlap integral (green) is calculated from the ensemble measurements from the donor (Atto488) emission spectrum (magenta) and the acceptor (Atto647N) absorption spectrum (red). The Foerster radius is determined to  $R_0 = 53$  nm (Foerster radius for the dye pair given by ATTO-TEC:  $R_0 = 51$  nm).

As FRET efficiency is highly distance-dependent, a FRET pair is usually characterized by the *Foerster radius*  $R_0$  at which the FRET efficiency reaches 0.5.

$$R_0^6 = 8.79 \cdot 10^{-5} (\kappa^2 n^{-4} Q_D J(\lambda)) [\text{Å}^6] \quad (2.50)$$

With  $\kappa$  describing the dipole-dipole orientation in space,  $n$  being the refractive index of the medium, and  $Q_D$  the donor's quantum yield. The distance-dependency of the FRET efficiency is:

$$E_{FRET}(r) = \frac{k_{FRET}(r)}{\tau_D^{-1} + k_{FRET}(r)} = \frac{R_0^6}{R_0^6 + r^6} \quad (2.51)$$

Here  $k_{FRET}(r)$  is the rate constant for FRET:

$$k_{FRET}(r) = \frac{1}{\tau_D} \cdot \left(\frac{R_0}{r}\right)^6 \quad (2.52)$$

With  $\tau_D$  characterizing the decay time of the donor in the absence of FRET.

Although dynamic and static quenching as well as FRET effects result in an additional decay of the fluorescence signal, the comparison of the distance dependencies of dynamic and static quenching (see equation 2.47) to FRET (see equation 2.51) indicate the main difference between quenching and FRET effects: At short intermolecular distances it is essential that  $E_q(r) > E_{FRET}(r)$ , whereas at long intermolecular distances it is essential that  $E_q(r) < E_{FRET}(r)$ .

## 2.5 Fluorescent Probes

The present work is exclusively based on fluorescence. In order to visualize cellular substructures and processes, different strategies based on intrinsic and extrinsic labeling with fluorescent probes are applied in the life sciences. Naturally existing fluorophores (e.g. aromatic amino acids: *tryptophan* (Trp), *tyrosine* (Tyr), *phenylalanine* (Phe) ) are termed intrinsic (for detailed information about intrinsic fluorophores see<sup>34</sup>). Extrinsic fluorescent probes are introduced by an active process of labeling into the biological sample. This includes antibody staining but also the cloning of fluorescent proteins to target proteins (for extrinsic labeling strategies see chapter 3.4).

### 2.5.1 Conjugated Electronic Systems

The ability of hydrocarbon rich organic molecules to absorb light in the visible range (400 – 800 nm) is based upon the presence of a broad conjugated electronic system. Their  $\pi$ -electrons are delocalized over multiple of p-orbitals along the carbon chain. The most simple approximation of such a system is the model of a free electron gas (see figure 2.8)<sup>35</sup>.

The  $\pi$ -electrons are supposed to move freely along the molecular skeleton of the conjugated electronic system of length L. This approximation, termed *particle in a box* model, can be described by a one dimensional potential-energy landscape  $V(r)$  with an insuperable electronic potential barrier.

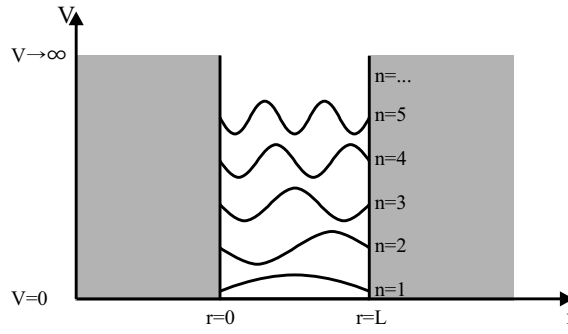


Figure 2.8: **Particle in a box**

One-dimensional potential energy landscape of a free electron gas. The wave functions of different electronic eigenstates are indicated by  $n$ .

$$V(r) = \begin{cases} 0, & \text{if: } 0 \leq r \leq L \\ \infty, & \text{otherwise} \end{cases} \quad (2.53)$$

The delocalized  $\pi$ -electrons remain only between the two energy-potential barriers in the defined space  $0 \leq r \leq L$ . The electronic eigenstates are described as standing waves. Therefore, the hamiltonian operator  $\hat{H}$ <sup>36,37</sup> for a one dimensional potential is calculated to:

$$\hat{H} = \frac{\hat{p}^2}{2m_e} + V(r) \quad (2.54)$$

Hereby  $m_e$  is the mass of the electron and  $\hat{p}$  is the one-dimensional operator of momentum:

$$\hat{p} = \frac{\hbar}{i} \frac{d}{dr} \quad (2.55)$$

With  $\hbar = \frac{h}{2\pi}$ .

This leads to the *time-independent Schrodinger equation*<sup>38,39</sup>

$$\langle r | \hat{H} | \psi \rangle = E \langle r | \psi \rangle \quad (2.56)$$

$$\langle r | -\frac{\hbar^2}{2m_e} \frac{d^2}{dr^2} + V(r) | \psi \rangle = E \langle r | \psi \rangle \quad (2.57)$$

This differential equation can be solved by:

$$| \psi \rangle = A e^{i\sqrt{\frac{2m_e E}{\hbar^2}} r} + B e^{-i\sqrt{\frac{2m_e E}{\hbar^2}} r} \quad (2.58)$$

As the *particle in the box* model postulates  $| \psi \rangle$  to represent a standing wave, equation (2.58) has to fulfill the following boundary conditions:

$$\langle r = 0 | \psi \rangle = 0 \quad (2.59)$$

$$\langle r = L | \psi \rangle = 0 \quad (2.60)$$

This leads to a family of eigenvalues ( $n = 1, 2, 3, \dots$ ) for the total energy:

$$E = \frac{n^2 \pi^2 \hbar^2}{2m_e L^2} \quad (2.61)$$

Taking equation (2.2) into account, the transition energy between the *highest occupied molecular orbital* (HOMO)  $n$  and the *lowest unoccupied molecular orbital* (LUMO)  $n + 1$  can be described by the excitation wavelength  $\lambda_{ex}$ :

$$\Delta E = \frac{hc}{\lambda_{ex}} = E_{n+1} - E_n \quad (2.62)$$

$$\lambda_{ex} = hc \frac{1}{E_{n+1} - E_n} \quad (2.63)$$

$$\lambda_{ex} = \frac{8m_e c L^2}{h} \frac{1}{2n + 1} \quad (2.64)$$

There are quite more rules to describe the absorption and emission characteristics of fluorescent probes. A review about the theoretical determination of the fluorescence characteristics of organic fluorophores, considering more complex structures, has been composed by<sup>40</sup>.

### 2.5.2 Organic Fluorophores

The class of organic fluorophores contains a broad number of fluorescent molecules with conjugated electronic systems. Three classes of photo-switchable organic dyes (cyanines<sup>10</sup>, rhodamines and oxazines<sup>41</sup>) were used for SMLM experiments in this thesis. Their photophysics are described by the maxima of excitation wavelength  $\lambda_{ex}$ , and emission wavelength  $\lambda_{em}$ , *quantum yield* (QY), molar absorption coefficient  $\epsilon$ , and *molecular weight* (MW) in table 2.2. Equation

Table 2.2: **Organic Fluorescent Probes**

List of organic fluorophores used in this thesis

Dye	Family	$\lambda_{ex}$ [nm]	$\lambda_{em}$ [nm]	QY	$\epsilon$ [M <sup>-1</sup> cm <sup>-1</sup> ]	MW
Alexa Fluor 488	Rhodamine	499	519	0.92	71,000	643
Cy 5	Cyanine	650	670	0.28	250,000	792
Alexa Fluor 647	Cyanine	652	668	0.33	239,000	1300
Atto 655	Oxazine	663	684	0.30	125,000	634

(2.64) shows a direct dependence from the wavelength  $\lambda_{ex}$  of the maximum absorption band



of the length  $L$  of the electronic system. Consisting of a nearly linear and therefore one-dimensional, conjugated electronic system, specific members of the *cyanine* (Cy) dye family are well described by the free electron-gas model<sup>35</sup>. Cy 3, Cy 5 and Cy 7 show a systematic

**Table 2.3: Conjugated Electronic Systems of Cyanine Dyes**

The elongation of the conjugated electronic system and the increasing number of  $\pi - e^-$  of organic fluorescent probes lead to a shift of  $\lambda_{calc}$  and  $\lambda_{exp}$  to longer wavelengths

Dye	Conjugated Electronic System	L [nm]	$\pi - e^-$	$\lambda_{calc}$ [nm]	$\lambda_{exp}$ [nm]
Cy 3	$R_2N^+=C-C=C-C-NR_2$	1.16	8	493	550
Cy 5	$R_2N^+=C-C=C-C-C-C-NR_2$	1.44	10	622	649
Cy 7	$R_2N^+=C-C=C-C-C-C-C-C-NR_2$	1.72	12	750	752

elongation of their conjugated electronic system in combination with an increasing number of  $\pi$ -electrons (Cy 3 < Cy 5 < Cy 7), while the residual structural features are kept (see table 2.3). Therefore, effects like changing of chemical substituents or changes in hydrophilic characteristics can be neglected in a comparison of the cyanine dyes<sup>42</sup>. Due to the principle of Pauli<sup>43,44</sup> a molecular orbital must not be occupied by electrons identical in all quantum numbers. For this reason every molecular orbital may be occupied by the maximum of two electrons that differ within their spin quantum number  $S_z$ <sup>45</sup> (one with a spin of  $S_z = +\frac{1}{2}\hbar$  and one with a spin of  $S_z = -\frac{1}{2}\hbar$ ). The 8  $\pi$ -electrons of the Cy 3 molecule occupy 4 molecular orbitals, resulting in a HOMO with  $n = 4$  and a LUMO with  $n + 1 = 5$ . With  $L = 1.16$  nm being the length of the conjugated electronic system the excitation wavelength can be calculated via equation (2.64) to  $\lambda_{calc} = 493$  nm, which is in good accordance to the experimentally determined value  $\lambda_{exp} = 550$  nm.

### 2.5.3 The Fluorescence Emission of Organic Fluorophores

The fluorescence emission of single fluorescent probes depends on the emitted number of photons per second that is based upon the stochastic processes of photon absorption and emission. As discussed in chapter 2.2 the transition rates between different electronic states vary over large time scales, as can be seen in table 5.1. The fluorescence signal of modern detection units (*exempli gratia* (e.g.) *electron multiplying charge-coupled device* (EMCCD), *photomultiplier tube* (PMT)) comprises the integration of the fluorescence emission over a certain time period. As the Nyquist-Shannon sampling theorem postulates an at least two fold higher detection rate, compared to the electronic state life time, in order to reconstruct the photo-physical tran-

sitions of a fluorophore exactly<sup>46</sup>, transitions between short lived electronic states ( $< 10^{-3}$  s) cannot be resolved by most detection units. This leads to a constant intensity signal over time (detected photons / second). While the fluorophore exists in a long lived state no radiative transition will occur and no fluorescence signal will be detected. Therefore, the detected fluorescence signal can be approximated by a two state system (the *on-state*  $\mathbb{F}$  and the *off-state*  $\mathbb{D}$ , see equation (2.65)), assuming a highly photo-stable fluorescent probe and thus neglecting the case of the irreversible destruction of the conjugated electronic system.  $\mathbb{F}$  consists of short lived states ( $S_n, n = 0, 1, 2, \dots$ ) exhibiting a high frequency of radiative transitions.  $\mathbb{D}$  is a long lived, reduced state ( $R^{\bullet+}, R^{\bullet-}$ ) characterized by a low frequency of radiative transitions. An ensemble containing a constant number of fluorescent probes  $\mathbb{N}$  existing either in the  $\mathbb{F}$  state or in the  $\mathbb{D}$  state can be described as follows:



With  $k_{\text{off}}$  and  $k_{\text{on}}$  being the rate constants. Before the time point  $t = 0$  no external electromagnetic field is applied and all  $\mathbb{N}$  exist in the ground state  $S_0$ .

$$[\mathbb{F}]_{t=0} = [\mathbb{F}]_0 = [\mathbb{N}] \quad (2.66)$$

At the time point  $t = 0$  an external electromagnetic field is applied and the time response of the system is described by

$$\frac{d[\mathbb{F}]}{dt} = -k_{\text{off}}[\mathbb{F}] + k_{\text{on}}[\mathbb{D}] \quad (2.67)$$

By considering equation (2.66) and the mass action law ( $[\mathbb{N}] = [\mathbb{F}] + [\mathbb{D}]$ ) equation (2.67) calculates to

$$\frac{d[\mathbb{F}]}{dt} = -k_{\text{off}}[\mathbb{F}] - k_{\text{on}}[\mathbb{F}] + k_{\text{on}}[\mathbb{F}]_0 \quad (2.68)$$

which can be solved to

$$[\mathbb{F}](t) = [\mathbb{F}]_0 \left( \frac{k_{\text{on}}}{k_{\text{off}} + k_{\text{on}}} + \frac{k_{\text{off}}}{k_{\text{off}} + k_{\text{on}}} e^{-(k_{\text{off}}+k_{\text{on}})t} \right) \quad (2.69)$$

By inserting  $[\mathbb{F}]_0$  and the time response of  $[\mathbb{F}](t)$  into the law of mass action, the time response for  $[\mathbb{D}](t)$  calculates to

$$[\mathbb{D}](t) = [\mathbb{F}]_0 \frac{k_{\text{off}}}{k_{\text{off}} + k_{\text{on}}} \left( 1 - e^{-(k_{\text{off}}+k_{\text{on}})t} \right) \quad (2.70)$$

For  $t \rightarrow \infty$   $\mathbb{F}$  and  $\mathbb{D}$  reach an equilibrium at

$$\lim_{t \rightarrow \infty} [\mathbb{F}] = [\mathbb{F}]_0 \frac{k_{\text{on}}}{k_{\text{off}} + k_{\text{on}}} \quad (2.71)$$

$$\lim_{t \rightarrow \infty} [\mathbb{D}] = [\mathbb{F}]_0 \frac{k_{\text{off}}}{k_{\text{off}} + k_{\text{on}}} \quad (2.72)$$

$$\lim_{t \rightarrow \infty} \frac{[\mathbb{D}]}{[\mathbb{F}]} = \frac{k_{\text{off}}}{k_{\text{on}}} \quad (2.73)$$

The behavior of a single fluorescent molecule within an external electromagnetic field can be described by a *hidden Markov model* (HMM)<sup>47–49</sup>, consisting of the two hidden states  $\mathbb{F}$ ,  $\mathbb{D}$  and four transition rates  $k_{xy}$  that compose a state transition matrix  $T$  (see figure 2.9).

$$T = \begin{pmatrix} k_{11} & k_{21} \\ k_{12} & k_{22} \end{pmatrix} \quad (2.74)$$

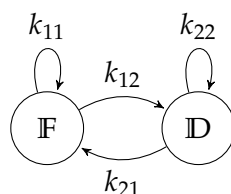


Figure 2.9: **HMM for the fluorescence emission of single organic fluorophores**

The fluorescence emission of organic fluorophores at the single molecule level is described by a two state HMM. The photosystem is switching reversibly between a fluorescent state  $\mathbb{F}$  and a dark state  $\mathbb{D}$  via the transition rates  $k_{xy}$ .

#### 2.5.4 Redox Chemistry of Organic Fluorophores

The switching behavior of organic fluorophores is influenced by quenching effects and may thus be manipulated by appropriate composition of redox buffers. In order to detect a highly stable fluorescence signal from organic fluorophores, long lasting dark states as semi-reduced radical states as well as triplet states need to be efficiently quenched. The  $S_0$  state needs to be repopulated immediately vice versa. This procedure can be achieved by a *reducing and oxidizing* (ROX) buffer, comprised of an enzymatic oxygen scavenger system (glucose oxidase, catalase and  $\beta$ -D-glucose<sup>50,51</sup>) and an oxidizing reaction agent (e.g. *trolox* (TRX), *methylviologen* (MV)) as well as an reducing reaction agent (e.g. *ascorbic acid* (AA), MEA,  $\beta$ -mercapto-ethanol (ME)). The triplet state is quenched by electron transfer reactions either caused by the oxidizing or the reducing reaction agent. Accordingly both semi-reduced radical states ( $R^{\bullet+}$  and  $R^{\bullet-}$ ) are

populated and subsequently quenched by the respective other reaction agent. This way an immediate repopulation of the  $S_0$  state is achieved (see figure 2.10 a) transferring the reaction equilibrium (see equation 2.73) towards the fluorescence state  $F^{5,7}$ .

By omitting one of the two reaction agents only one of the two semi-reduced radical states is populated, while the effective quenching of the semi reduced radical state is inhibited (see figure 2.10 b). A reduced repopulation of the  $S_0$  state is the result that leads to a shift of the

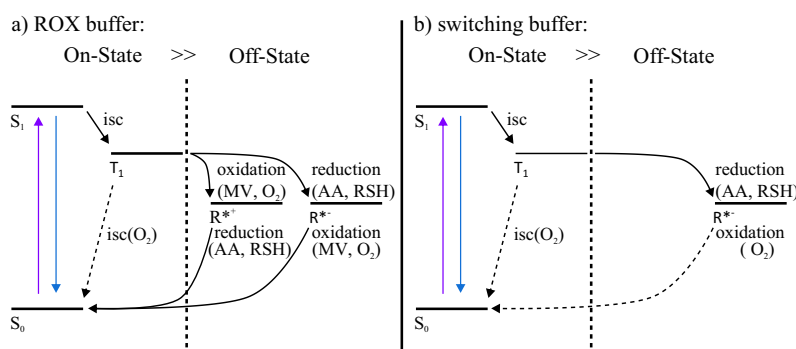
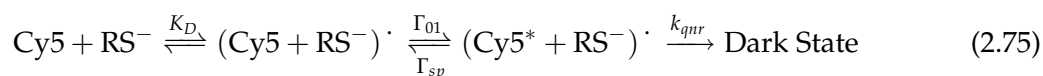


Figure 2.10: Co-solute effects on organic fluorophores

a) ROX buffer resulting in a long lasting, stable fluorescence signal. b) Switching buffer resulting in long lived dark states.

reaction equilibrium towards the dark state  $D$ . These kind of buffers are termed switching buffers, as the detected fluorescence emission signal results in blinking molecules with long lived dark states.

An alternative hypothesis of the dark state formation of carbocyanine dyes mediated by thiol (RS) as an reduction agent was determined by<sup>6</sup> to:



Equation 2.75 describes the reversible formation of an encounter complex between Cy5 and a thiol anion  $RS^-$ . A light mediated quenching reaction further forms a non-fluorescent carbocyanine-thiol adduct. Here, the lifetime of the bright state is dependent of the concentration of deprotonated thiol, which can be influenced by the concentration of the reducing reaction agent and the pH, as indicated by equation 2.75<sup>6</sup>. The dark state  $D$  results from a split  $\pi$ -electron system by an addition of the thiol anion to the polymethine bridge (see figure 2.11). The absorption spectrum of their dark state shows not only the vanish of the fluorophores absorption band but also a new absorption band occurs in the range of  $\lambda \approx 300$  nm. As a result the dark state may interact with light of shorter wavelengths by an efficient repopulation of

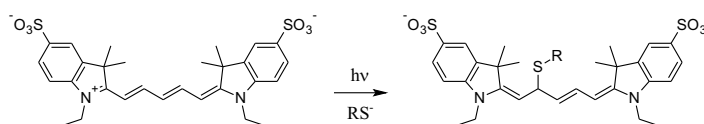


Figure 2.11: **Dark state formation of Cy5**

Light mediated formation of a non-fluorescent thiol-adduct between Cy5 and a deprotonated thiol (adapted from<sup>6</sup>).

the  $S_0$  state. Herby the repopulation rate is higher compared to thermal repopulation rates<sup>6</sup> and possesses a linear dependence on the irradiation intensity in distinct intensity ranges<sup>41,52</sup>. Therefore, the life time of the long lived dark state may be influenced by irradiation with high energetic light. Figure 2.12 a shows the photo-switching behavior of isolated organic fluo-

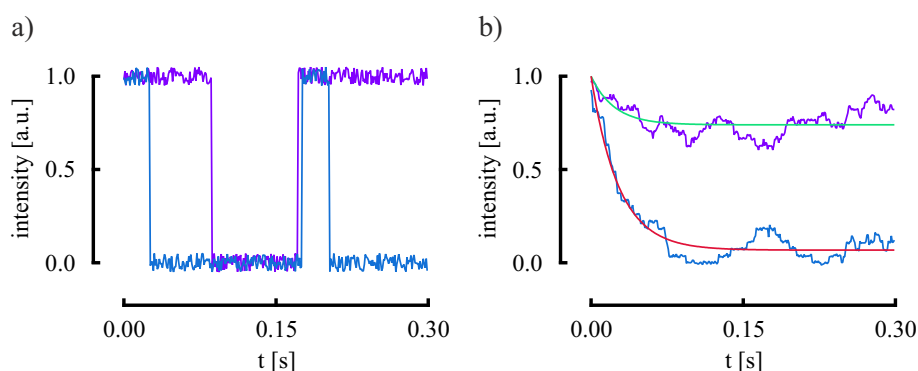


Figure 2.12: **Simulated fluorescence emission of organic fluorophores at the single molecule level and within an ensemble under different redox conditions**

Two state HMM of an organic fluorophore under different simulated buffer conditions. The experiment with fluorescence stabilizing ROX buffer ( $k_{\text{on}} = 30 \text{ s}^{-1}$ ,  $k_{\text{off}} = 10 \text{ s}^{-1}$ ) is depicted in magenta. The experiment with dark state stabilizing switching buffer ( $k_{\text{on}} = 3 \text{ s}^{-1}$ ,  $k_{\text{off}} = 30 \text{ s}^{-1}$ ) is depicted in blue. a) Single molecule fluorescence intensity time traces. b) Fluorescence intensity time traces resulting each from an ensemble of 25 molecules. By fitting the ensemble measurement with equation (2.69) the simulated rate constants were confirmed (ROX buffer:  $k_{\text{on}} = 32.3 \text{ s}^{-1}$ ,  $k_{\text{off}} = 11.4 \text{ s}^{-1}$ , switching buffer:  $k_{\text{on}} = 2,5 \text{ s}^{-1}$ ,  $k_{\text{off}} = 34.4 \text{ s}^{-1}$ ).

rophores under two different simulated buffer conditions described by a two state HMM. The fluorescence emission signal over time depicted in magenta shows a fluorophore under ROX buffer conditions (see figure 2.10 a). The fluorescence emission signal over time depicted in

blue shows a fluorophore under switching buffer conditions (see figure 2.10 b). Even at the single molecule level one can see that the dark state under switching buffer conditions is characterized by a long lifetime. Figure 2.12 b shows two ensemble measurements under the same buffer conditions, each based on 25 simulated molecules. By fitting the ensemble measurement to equation (2.69) one can obtain the switching rate constants the HMM is based on.

### 2.5.5 Fluorescent Proteins

*fluorescent protein* (FP)s are proteins characterized by the ability to absorb and emit light. The most prominent one is the *green fluorescent protein* (GFP) that was extracted from *hydromedusa Aequorea victoria*<sup>53</sup> and improved via point mutations<sup>54</sup>. By further mutating the GFP or similar proteins a broad selection of fluorescent proteins was synthesized, covering the whole visible electromagnetic spectrum. The chromophore of GFP-like FPs is formed by a tri-peptide (*Ser65 – Tyr66 – Gly67* for GFP) that is protected by an eleven-strand  $\beta$ -barrel structure with a central  $\alpha$ -helix along the axis<sup>55,56</sup>.

The point mutation (*Thr203His*) of GFP leads to a nearly non-fluorescent version that can be transformed irreversibly to a fluorescent state by irradiation with light ( $\lambda_{\text{act}} \approx 400 \text{ nm}$ )<sup>57</sup> through decarboxylation of the *Glu222* side chain. Because the fluorescent protein is activated by light it is termed *photo-activatable* (PA)-GFP.

The fluorescence characteristics of PA-FPs within an external electromagnetic field can be described by the following rate equation:



Another approach of changing the fluorescence characteristics from FPs was achieved by synthesis of *photo-convertible* (PC)-FPs (e.g. EosFP)<sup>58</sup>. Here, the irradiation with light ( $\lambda_{\text{act}} \approx 400 \text{ nm}$ ) shifts the absorption and emission spectra to longer wavelengths. The process is mediated by backbone cleavage between the  $N\alpha$  and the  $C\alpha$  atom of the first amino acid in the chromophore-forming tri-peptide. The fluorescence characteristics of PC-FPs within an external electromagnetic field can be described by the following rate equation:



Assuming that only  $\mathbb{F}(\lambda_2)$  is detected,  $\mathbb{F}(\lambda_1)$  can be assumed as the dark state  $\mathbb{D}$  and both mechanisms are described by equation (2.76) with  $k_{\text{on}} = k_{\text{con}}$ . Before the time point  $t = 0$  no external electromagnetic field is applied and all fluorescent proteins  $\mathbb{N}$  exist in  $\mathbb{D}$ .

$$[\mathbb{D}]_{t=0} = [\mathbb{D}]_0 = [\mathbb{N}] \quad (2.78)$$

At the time point  $t = 0$  an external electromagnetic field is applied and the time response of the system is described by

$$\frac{d[\text{ID}]}{dt} = -k_{\text{on}}[\text{ID}] \quad (2.79)$$

$$\frac{d[\text{IF}]}{dt} = k_{\text{on}}[\text{ID}] - k_{\text{off}}[\text{IF}] \quad (2.80)$$

$$\frac{d[\text{B}]}{dt} = k_{\text{off}}[\text{IF}] \quad (2.81)$$

The solution for  $[\text{ID}]$  is given by

$$[\text{ID}] = [\text{ID}]_0 e^{-k_{\text{on}}t} \quad (2.82)$$

Using equation (2.82)  $\frac{d[\text{IF}]}{dt}$  calculates to

$$\frac{d[\text{IF}]}{dt} = k_{\text{on}}[\text{ID}]_0 e^{-k_{\text{on}}t} - k_{\text{off}}[\text{IF}] \quad (2.83)$$

Equation (2.83) is a differential equation that can be solved by Lagrange's variation of parameters to:

$$[\text{IF}] = \left( \frac{k_{\text{on}}}{k_{\text{off}} - k_{\text{on}}} [\text{ID}]_0 e^{(k_{\text{off}} - k_{\text{on}})t} - C \right) e^{-k_{\text{off}}t} \quad (2.84)$$

$C$  is an integration constant, which with  $\lim_{t \rightarrow 0} [\text{IF}] = 0$  calculates to

$$[\text{IF}] = \frac{k_{\text{on}}}{k_{\text{off}} - k_{\text{on}}} [\text{ID}]_0 \left( e^{-k_{\text{off}}t} - e^{-k_{\text{on}}t} \right) \quad (2.85)$$

$[\text{IF}]$  is an intermediate state with  $\lim_{t \rightarrow \infty} [\text{IF}] = 0$ .

By insertion of the time response for  $[\text{ID}]$  and  $[\text{IF}]$  into the law of mass action the time response of  $[\text{B}]$  calculates to

$$[\text{B}] = [\text{ID}]_0 - [\text{ID}] - [\text{IF}] \quad (2.86)$$

$$[\text{B}] = [\text{ID}]_0 + \frac{[\text{ID}]_0}{k_{\text{on}} - k_{\text{off}}} \left( k_{\text{off}} e^{-k_{\text{on}}t} - k_{\text{on}} e^{-k_{\text{off}}t} \right) \quad (2.87)$$

At the single-molecule level within an external electromagnetic field single PA/ PC-FPs can be described by a HMM (see figure 2.13) comprising of three hidden states ( $\text{ID}$ ,  $\text{IF}$ ,  $\text{B}$ ) and nine transition rates  $k_{xy}$  that compose the transition matrix  $T$  (with  $k_{13} = k_{31} = 0$ ).

$$T = \begin{pmatrix} k_{11} & k_{21} & 0 \\ k_{12} & k_{22} & k_{32} \\ 0 & k_{23} & k_{33} \end{pmatrix} \quad (2.88)$$

Figure 2.14 a) shows the intensity time trace of the fluorescence emission of an irreversible

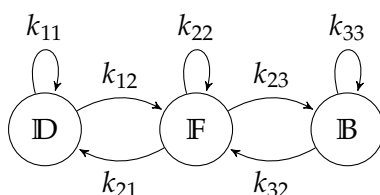


Figure 2.13: **HMM for the fluorescence emission of PA/PC-FPs**

The switching behavior of PA/PC-FPs is described by a three-state HMM. The photosystem transits irreversibly between a dark state (D), a fluorescence state (F), and a bleached state (B) via the transition rates  $k_{xy}$ .

PA/PC-FP at the single molecule level, simulated by a three-state HMM. Figure 2.14 b) shows the intensity time trace of the fluorescence emission of an fluorophore ensemble comprising 500 simulated molecules. From the ensemble simulations the fluorescent state of the FP is clearly characterized as an intermediate state. By fitting the ensemble measurement to equation (2.85) one can obtain the switching rate constants the HMM is based upon and characterize the intermediate state. A list PA/PC-FPs used in this thesis is summarized in table 2.4.

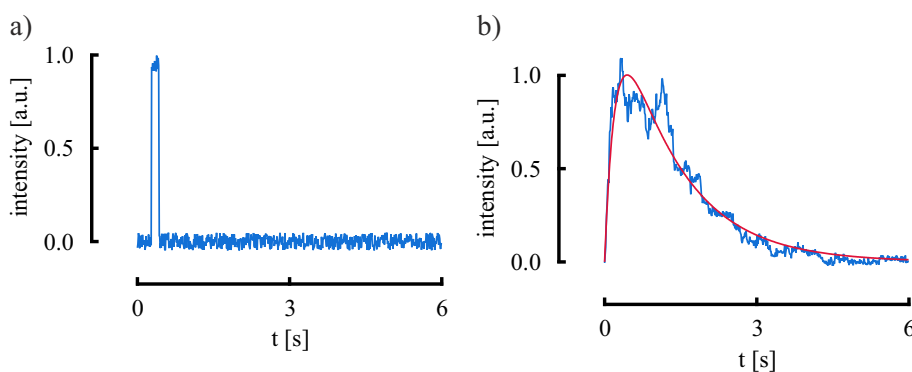


Figure 2.14: **Simulated fluorescence emission time trace of PA/PC-FPs at the single molecule level and within an ensemble under different redox conditions**

Three state HMM of an irreversible photo PA/PC-FP with simulated transition rates  $k_{xy}$  ( $k_{on} = 1 \text{ s}^{-1}$ ,  $k_{off} = 5 \text{ s}^{-1}$ ). a) Single molecule intensity time trace . b) Intensity time trace resulting from an ensemble of 500 molecules. By fitting the ensemble measurement with equation (2.85) the simulated rate constants could be confirmed ( $k_{on} = 0.8 \text{ s}^{-1}$ ,  $k_{off} = 4.7 \text{ s}^{-1}$ ).



Table 2.4: **Photophysical characteristics of photo-activatable and photo-convertible fluorescent proteins**

Dye	Transition-Type	Oligomeric State	$\lambda_{act}[nm]$	$\lambda_{ex}[nm]$	$\lambda_{em}[nm]$	Ref
bsDronpa	photo-activation	monomer	405	460	504	59
psCFP2	photo-conversion	monomer	405	400/490	468/511	60
Dendra2	photo-conversion	monomer	405/488	490/553	507/573	61
tdEos	photo-conversion	dimer	405	506/516	571/581	62
mEos2	photo-conversion	monomer	405	506/573	519/584	63
PAmCherry1	photo-activation	monomer	405	570	596	64

## 2.6 Microscope Optical Systems

A microscope is defined as an optical instrument increasing the angle of vision  $\epsilon$  of an imaging system, resulting in a magnified image ( $I$ ) of the observed object ( $O$ ). The imaging system typically consists of a single imaging lens that projects the image onto a detector (e.g. the retina or a camera). A microscope consists of two lenses, an objective lens that generates an intermediate image  $I_1$  of  $O$  and a magnifying lens within the focal distance  $f_2$  of  $O$  (see figure 2.15). According to Huygen's principle, every point of a wavefront of propagating light is the

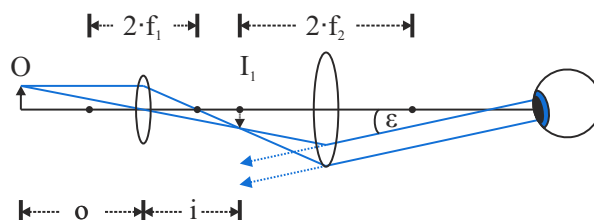


Figure 2.15: **A simple microscope**

Magnification of the angle of vision  $\epsilon$  by a two lens optical microscopic system.  $O$ : object,  $o$ : object length,  $f_1$ : focal length of lens 1,  $f_2$ : focal length of lens 2,  $I_1$ : intermediate image,  $i$ : intermediate image distance.

source of an spherical wavelet itself<sup>65</sup>. Therefore,  $I_1$  conforms to the envelope of an infinite ensemble of superimposed elementary waves. The magnifying lens generates parallel light from the spherical wavelets emanated from every point of  $I_1$ . The simple imaging system would image  $O$  in the distinct distance  $L_1$  under the angle  $\tan(\epsilon_0) = O/L_1$ . A microscope changes the angle of vision to  $\tan(\epsilon) = I_1/f_2$ . The magnification of a microscope is therefore

described by:

$$M = \frac{\tan(\epsilon)}{\tan(\epsilon_0)} = \frac{L_1 \cdot i}{o \cdot f_2} \quad (2.89)$$

With  $o$  being the distance between the objective lens and  $O$ , and  $i$  being the distance between the objective and  $I_1$ .

### 2.6.1 Abbe's Theory of Image Formation

The fact that objects can be imaged magnified with a microscope enables a more detailed observation. However, due to the diffractive nature of light the ability to resolve an object's details is limited. This diffraction limit of microscopic systems is described by Abbe's theory of image formation<sup>66</sup>. Accordingly, the field distribution  $P(x)$  at the *front focal plane* (FFP) of a convergent lens is transformed by the lens to the Fourier space at the *back focal plane* (BFP) of the lens. This can be described by a forward *Fourier transformation* (FT). For reasons of simplification this will be done for a one dimensional system. Figure 2.16 shows an optical setup comprising

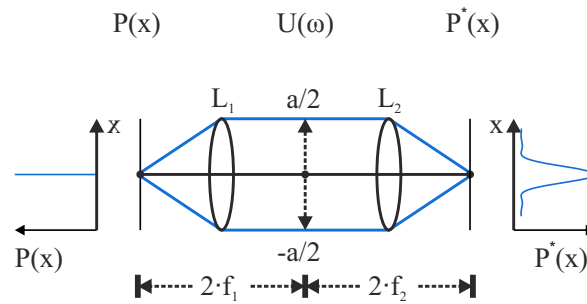


Figure 2.16: **Abbe's theory of image formation**

Special optical setup with two identical lenses ( $L_1, L_2$ ) that are placed in a distance ( $f_1 + f_2$ ), allowing the overlay of the objective back focal plane and the magnifying front focal plane.  $P(x)$ : image space,  $U(\omega)$ : frequency space.  $a$ : physical dimension of the Fourier space.

two identical convergent lenses where the BFP of the objective lens is placed onto the FFP of the magnifying lens. As the BFP of the objective lens is also the FFP of the magnifying lens, the microscope performs two successive FTs of the field distribution  $P(x)$  in the front focal plane of the objective. In the ideal case with an infinite Fourier space and two identical convergent lenses this results in the reversal original field distribution  $P^*(-x)$  located in the back focal plane of the magnifying lens.

$$P^*(-x) = \mathcal{F}\{\mathcal{F}\{P(x)\}\} \quad (2.90)$$

The field distribution of the point emitter in figure 2.16 located at  $x = 0$  is described by a Dirac delta function.

$$P(x) = \delta(x) = \begin{cases} +\infty, & x = 0 \\ 0, & \text{otherwise} \end{cases} \quad (2.91)$$

The Fourier transformation of  $P(x)$  by the objective lens calculates to:

$$U(\omega) = \int_{-\infty}^{\infty} \delta(x) e^{-ix\omega} dx = 1 \quad (2.92)$$

In the non-ideal case the Fourier space is limited by the dimensions of the BFP and higher frequencies are cut off by an *optical transfer function* (OTF)  $\mathcal{H}(\omega)$ .

$$\mathcal{H}(\omega) = \begin{cases} 1, & |\omega| \leq \frac{a}{2} \\ 0, & \text{otherwise} \end{cases} \quad (2.93)$$

The successive inverse FT of the OTF-limited frequency distribution  $U(\omega)$  to the field distribution  $P^*(x)$  in the front focal plane of the magnification lens calculates to:

$$P^*(x) = \int_{-\infty}^{\infty} U(\omega) \mathcal{H}(\omega) e^{-ix\omega} d\omega \quad (2.94)$$

$$= \int_{-\frac{a}{2}}^{\frac{a}{2}} U(\omega) e^{-ix\omega} d\omega \quad (2.95)$$

solving equation (2.95) and including equation (2.102) calculates to:

$$P^*(x) = \frac{1}{ix} (e^{ix\frac{a}{2}} - e^{-ix\frac{a}{2}}) \quad (2.96)$$

$$= a \frac{\sin(x\frac{a}{2})}{x\frac{a}{2}} \quad (2.97)$$

With the intensity  $I(x)$  defined as  $I(x) := |P^*(x)|^2$  and  $x := \frac{2\pi}{\lambda} \sin \alpha$ , equation (2.96) can be solved by:

$$I(\alpha) = |a \cdot \text{sinc}(\frac{\pi a}{\lambda} \sin \alpha)|^2 \quad (2.98)$$

The maximum of equation (2.98) occurs at  $x = 0$  and becomes zero at  $\sin(x\frac{a}{2}) = 0$  for  $x \neq 0$ .

$$\sin(x\frac{a}{2}) = \sin(\frac{\pi a}{\lambda} \sin \alpha) = 0 \quad (2.99)$$

$$\sin \alpha_{\min} = \pm \frac{n\lambda}{a} \quad \text{with } n = 1, 2, 3, \dots \quad (2.100)$$

as can be seen in figure 2.16 (right). A more realistic model would be a two-dimensional system with a field distribution  $P(x, y)$ .

$$P(x, y) = \delta^2(x, y) = \begin{cases} +\infty, & x^2 + y^2 = 0 \\ 0, & \text{otherwise} \end{cases} \quad (2.101)$$

The Fourier transformation of  $P(x)$  by the objective lens calculates to:

$$U(\omega_x, \omega_y) = \int_{-\infty}^{\infty} \int_{-\infty}^{\infty} \delta(x) e^{-ix\omega_x} \delta(y) e^{-iy\omega_y} dx dy = 1 \quad (2.102)$$

Therefore the frequencies  $\omega_x$  and  $\omega_y$  passing the Fourier plane are limited by a circular OTF  $\mathcal{H}(\omega_x, \omega_y)$  with a radius  $\Omega$ .

$$\mathcal{H}(\omega_x, \omega_y) = \begin{cases} 1, & \sqrt{\omega_x^2 + \omega_y^2} \leq \Omega \\ 0, & \text{otherwise} \end{cases} \quad (2.103)$$

In this case the inversive FT of the OTF-limited frequency distribution  $U(\omega_x, \omega_y)$  to the field distribution  $P^*(x, y)$  in the FFP of the magnification lens calculates to:

$$P^*(x, y) = \int_{-\infty}^{\infty} \int_{-\infty}^{\infty} U(\omega_x, \omega_y) \mathcal{H}(\omega_x, \omega_y) e^{-i(x\omega_x + y\omega_y)} d\omega_x d\omega_y \quad (2.104)$$

Solving equation (2.104) leads to a radially symmetric version of the one dimensional *sinc* function (2.98) known as first order Bessel function  $J_1$ .

$$I(\alpha) = \left| 2 \frac{J_1\left(\frac{\pi\Omega}{\lambda} \sin \alpha\right)}{\frac{\pi\Omega}{\lambda} \sin \alpha} \right|^2 \quad (2.105)$$

The intensity distribution described by equation (2.105) is termed the *Airy disk*<sup>67</sup>. Like equation (2.98) the Airy disk has a defined maximum at  $r = 0$  and becomes zero first at

$$\sin \alpha \simeq 1.22 \frac{\lambda}{2\Omega} \quad (2.106)$$

The higher frequency cut-off in the Fourier plane leads to a loss of information. A point light source is imaged as an imaging function spread over the BFP of the magnifying lens. This inverse FT of the circular OTF is called the PSF of the microscope.

$$PSF(x, y) = \mathcal{F}^{-1}\{\mathcal{H}(\omega_x, \omega_y)\} \quad (2.107)$$

Every elementary wave conforming a comprehensive field distribution  $P(x, y)$ <sup>65</sup>, as a large fluorescently labeled object, is imaged with a loss of information comprising a field distribution  $P^*(x, y)$  in the BFP of the magnifying lens. According to Abbe's theory of image formation,  $P^*(x, y)$  is described by a convolution of  $P(x, y)$  with the  $PSF(x, y)$  of the microscope.

$$P^*(x, y) = P(x, y) \otimes PSF(x, y) \quad (2.108)$$

According to Rayleigh, the details of two point sources are resolved if the first minimum of the Airy disk of one point source coincides with the global maximum of the second Airy disk (see equation 2.106)<sup>68</sup>. In order to resolve two point sources the minimum distance between them is defined as the lateral diffraction limit  $d_{\text{lateral}}$ .

$$d_{\text{lateral}} = 1.22 \frac{\lambda}{2n \sin \alpha} \quad (2.109)$$

$$= 0.61 \frac{\lambda}{NA}. \quad (2.110)$$

$NA = n \sin \alpha$  is the *numerical aperture* (NA) of the microscope objective,  $\lambda$  is the wavelength of the light and  $n$  the diffraction index between the object and the objective lens. Equation (2.109) illustrates that the spatial resolution can be influenced by varying the aperture angle  $\alpha$ , the refractive index  $n$ , and the wavelength of the fluorescence emission  $\lambda$ . The angle of incidence  $\alpha_1$  and the angle of refraction  $\alpha_2$  for light passing a boundary between two isotropic media with different refraction indices from  $n_1$  to  $n_2$  are related by Snell's and Descartes' law of refraction<sup>69</sup>.

$$n_1 \sin \alpha_1 = n_2 \sin \alpha_2 \quad (2.111)$$

A typical object cover glass has a refractive index of  $n_2 = 1.53$ . Typical immersion media like air ( $n_1 = 1.00$ ), and water ( $n_1 = 1.33$ ) have a lower optical density than the cover glass ( $n_1 < n_2$ ). Thus, equation (2.111) dictates that  $\alpha_1 < \alpha_2$ . This leads to a loss of resolution, as fluorescence light emitted at a large angle  $\alpha_1$  is not collected by the objective (see figure 2.17). To achieve a higher resolution, immersion oil offers the solution to match the optical density of cover glass and has a typical refraction index of  $n_1 = 1.52$ . Fluorescence light emitted at larger  $\alpha_1$  can pass the boundary layer of the two media with an infinitesimal change between  $\alpha_1$  and  $\alpha_2$  and more information is collected by the objective resulting in a higher resolution (see equation 2.109).

## 2.7 Fluorescence Microscopy

Beside the diffraction limit (see chapter 2.6.1) the information obtained from a biological sample by light microscopy is limited by the lack of contrast. Therefore, even cellular structures with a spatial dimension above the diffraction limit are hard to distinguish with conventional light microscopy techniques. This limitation was overcome by the invention of fluorescence light

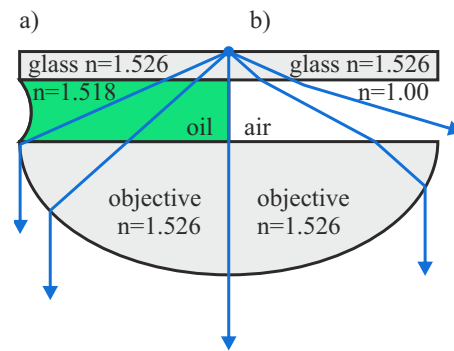


Figure 2.17: **Principle of the influence of the immersion media on the numerical aperture of the microscope objective**

Microscopic resolution enhancement based on immersion media. a) Immersion oil ( $n = 1.518$ ) matches the refractive index of glass ( $n = 1.526$ ). Therefore, even strongly inclined light is collected by the objective. b) Air ( $n = 1.000$ ) has a smaller refraction index compared to glass. Therefore, the emission light is refracted away from the perpendicular. Strongly inclined light is no longer collected by the objective, resulting in a smaller numerical aperture compared to the oil immersion objective.

microscopy<sup>70</sup>. The specific labeling of intracellular structures with fluorophores results in a huge contrast enhancement. Cutting edge fluorescence microscopes comprise a fluorophore specific light source, e.g. a *light amplification by stimulated emission of radiation* (laser), an optical excitation pathway, a filter ensemble separating the excitation light and the emission light (see figure 2.18) and an optical detection pathway focussing the emission light onto an electronic detector (e.g. EMCCD, PMT, or *avalanche photodiode* (APD)) that converts the detected photons into an electric signal. The filter ensemble comprises two filter units and a dichroic mirror (see figure 2.18). The first filter set selects a specific wavelength from the spectrum of the light source that excites the fluorophore. The heart of the filter ensemble is a dichroic mirror that is arranged in a  $45^\circ$  angle to the excitation light which is reflective to shorter wavelengths and transmissive to longer wavelengths. It directs the excitation light orthogonal to its origin electromagnetic field vector into the objective. The Stokes shifted fluorescence emission is collected by the same objective and passes the dichroic. A second filter set acts as a clean up for unspecific reflections from the excitation light and fluorescence emission from intrinsic fluorophores. The filtered fluorescence emission is directed to the detector.

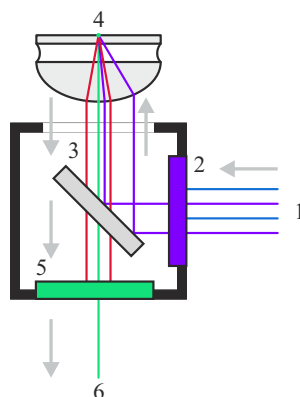


Figure 2.18: **Filter cube**

Optical path through a filter cube. The excitation light (1) is filtered by a band pass (2). The filtered excitation light is reflected by a dichroic (3) and coupled into the objective (4). The Stokes-shifted fluorescence emission passes the dichroic (3). Unspecific reflections from the excitation light and fluorescence emission from intrinsic fluorophores are filtered by an additional band pass (5). The filtered fluorescence emission is directed to the detector.

## 2.8 Illumination Schemes

Fluorescence microscopy setups are characterized by their scheme of sample illumination. The usual excitation light source is a laser with a clear Gaussian intensity profile  $I_r$ .

$$I(r) = I_0 \cdot e^{-\frac{2r^2}{w^2}} \quad (2.112)$$

$I_0$  is the intensity at the optical axis,  $r$  is the distance from the optical axis and  $w$  is defined as beam radius. Along the direction of propagation  $z$  the Gaussian beam forms a beam waist where  $w$  reaches a minimum  $w_0$  at  $z = 0$ .

$$w(z) = w_0 \sqrt{1 + \left(\frac{\Theta \cdot z}{w_0}\right)^2} \quad (2.113)$$

$z$  is the distance from  $w_0$ .  $\Theta$  is defined as the beam divergence and depends on the wavelength  $\lambda$  and  $w_0$ .

$$\Theta = \frac{\lambda}{\pi \cdot w_0} \quad (2.114)$$

Within a short interval  $l_R$  around  $w_0$ , termed the *Rayleigh length*, the beam can be approximated as parallel:

$$l_R = \frac{\pi \cdot w_0^2}{\lambda} \quad (2.115)$$

Seen from the lens, the Gaussian beam passing a convex lens with a focal length  $f$  forms a waist at  $f + l$  at the irradiation side. It will result in a Gaussian beam at the imaging side of the lens, which forms a beam waist  $w'_0$  at  $f + l'$  (see figure 2.19).

$$l' = \frac{l \cdot f^2}{l^2 + l_R^2} \quad (2.116)$$

$$(w'_0)^2 = w_0^2 \cdot \frac{l'}{l} \quad (2.117)$$

$$= w_0^2 \cdot \frac{f^2}{l^2 + l_R^2} \quad (2.118)$$

The Rayleigh length of the beam at the side of the light source  $l'_R$  calculates similar to  $l_R$ :

$$l'_R = \frac{\pi \cdot (w'_0)^2}{\lambda} \quad (2.119)$$

$$= w_0 \cdot \Theta \cdot \frac{f^2}{l^2 + l_R^2} \quad (2.120)$$

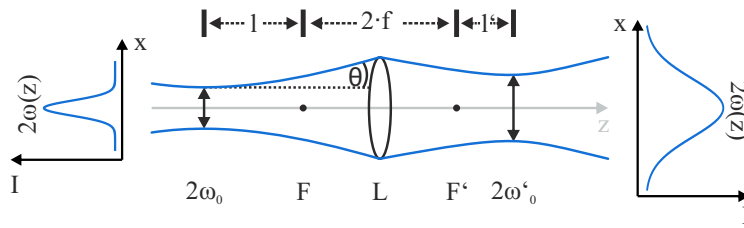


Figure 2.19: **Beam focussing scheme**

Focussing scheme of a Gaussian beam.  $w(z)$ : beam radius,  $w_0$ : beam waist on front focal side,  $F$ : front focal plane,  $L$ : Lens,  $F'$ : back focal plane,  $w'_0$ : beam waist at back focal side,  $l$ : distance between beam waist and focal plane at front focal side,  $f$ : focal length,  $l'$ : distance between beam waist and focal plane at back focal side.

### 2.8.1 Wide Field Illumination scheme

If the beam waist at the irradiation side is located at the the BFP ( $l = 0$ ) the beam will form a waist at the FFP of the imaging side ( $l' = 0$ ), which calculates from equation (2.116) with  $l = 0$ . By coupling a beam with a high divergence  $\Theta$  into the objective, the Rayleigh length of the irradiation beam will become negligible. In this special case the Rayleigh length of the imaging side beam will become large ( $l'_R \rightarrow \infty$ ) as can be seen by inserting  $l = 0$  and  $l_R \rightarrow 0$  into equation (2.120). The sample will be illuminated by a broad, nearly parallel beam, termed wide field illumination. (Further information on laser beam propagation based on geometrical optics may be found in<sup>71</sup>.)



### Optical Sectioning in Wide Field Microscopy

A wide field setup illuminates the sample with a nearly parallel Gaussian beam (see figure 2.20 a). The electromagnetic field interacting with the sample covers not only the FFP of the objective but a cylindrical volume along the axial dimension of the sample. The image on the detector results from a projection of signal emitted from all axial planes of the illuminated volume. Only fluorescence emitted from the FFP is imaged accurately by the microscope optics onto the detector. Therefore, out-of-focus light decreases the image quality especially for densely labeled, three dimensional structures. In order to detect only fluorescence emitted from the FFP, different types of optical sectioning were invented (see figure 2.20 b-c).

By parallel translation of the irradiation beam along the BFP the illumination beam on the sample side remains parallel but gets deflected according to Snell's and Descartes' law (see equation (2.111))<sup>69</sup>. This way an optical sheet with thin axial dimension  $z$  is generated that can be approximated by neglecting the beam divergence to:

$$z = \frac{w_s}{\tan \alpha_2} \quad (2.121)$$

The sample is illuminated by a *highly inclined and laminated optical sheet* (HILO), minimizing the illuminated volume in the axial dimension to a few tens of  $\mu\text{m}$  (see figure 2.20, b)<sup>72</sup>.

Further parallel translation of the irradiation beam along the BFP increases  $\alpha_1$ . Equation (2.111) dictates a critical angle  $\alpha_t$  for the deflection of light from a medium with high refractive index into a medium with low refractive index ( $n_1 > n_2$ ) at which  $\alpha_2 = 90^\circ$  and all light gets reflected totally. For an oil immersion objective the irradiation light is deflected at the interface between the object glass surface  $n_1 = 1.52$  and the aqueous solution of the sample  $n_2 = 1.33$ . The critical angle equals  $\alpha_1 = \alpha_t = 61^\circ$ . If  $\alpha_1 \geq \alpha_t$  no light is directly deflected into the sample, but an evanescent electromagnetic field occurs at the interface between the two reflective layers with an exponentially decreasing intensity distribution along the optical axis (see figure 2.20 c):

$$I(z) = I_0 \cdot e^{-\frac{z}{\delta}} \quad (2.122)$$

With  $\delta$  describing the penetration depth along the optical axis  $z$  and  $I_0$  the initial intensity at the interface of the two reflective layers.

The penetration depth depends on the angle of incidence  $\alpha_1$ , the wavelength of the electromagnetic field in the vacuum  $\lambda_0$ , and the critical angle  $\alpha_t$  which in turn depends on the refractive indices  $n_1$  and  $n_2$  of the two refractive layers.

$$\delta = \frac{\lambda_0}{4\pi \sqrt{\left(\frac{\sin \alpha_1}{\sin \alpha_t}\right)^2 - 1}} \quad (2.123)$$

*totally internal reflection* (TIR) illumination limits the irradiation volume from the cover glass surface to an axial dimension of 100 nm to 300 nm<sup>73,74</sup>. Only fluorescent probes that are located near the cover glass surface are interacting with the evanescent field.

### 2.8.2 Confocal Illumination Scheme

In the middle of the 1950ies a different illumination approach was developed in order to investigate small volumes termed confocal setup<sup>75</sup>. Confocal setups use highly collimated Gaussian beams ( $l_R \gg f$  and  $l_R \gg l$ ) with large  $w_0$  that are coupled into the objective. A small, diffraction-limited beam waist  $w'_0$  with short  $l'_R$  is generated at the FFP of the specimen side of the objective (see figure 2.20 d). For a confocal illumination scheme equation (2.118) that

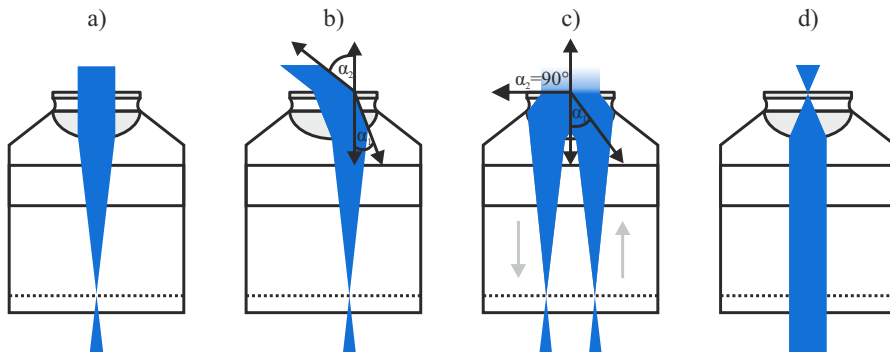


Figure 2.20: **Optical sectioning**

Possible ways of optical sectioning. The illumination beam is depicted in blue: a) wide-field, b) HILO, c) TIR, and d) confocal illumination.

describes  $w'_0$  can be approximated to:

$$w'_0 = \frac{\lambda f}{\pi w_0} \quad (2.124)$$

### Optical Sectioning in Confocal Microscopy

By introducing a pinhole to the detection optics confocal to the FFP the main part of the out-of-focus fluorescence emission is discriminated. A defined detection volume termed *confocal volume* (CV) is generated. Due to the diffractive nature of light the CV is imaged as a three dimensional PSF, that can be described by Fourier optics (see chapter 2.6.1). In contrast to the wide field setup, the confocal setup generates two images of the CV resulting in two PSFs: The first is the projection of the point shaped detection area, which is defined by the beam waist,

into the object space ( $PSF_{BW}$  as described by equation (2.105)), the second is the projection of the fluorescence emission passing the pinhole into the image space ( $PSF_{PH}$ ). The diffraction limited image of the CV ( $PSF_{CV}$ ) is therefore described by the convolution of  $PSF_{BW}$  with  $PSF_{PH}$ .

$$PSF_{CV} = PSF_{BW} \otimes PSF_{PH} \quad (2.125)$$

The CV can be described approximately by a Gaussian profile in lateral (equation (2.112)) and a Lorentz profile in axial dimension<sup>76</sup>. As the convolution to the  $PSF_{CV}$  was not derived analytically for a Gaussian-Lorentz beam profile yet, the confocal volume is usually described by a three dimensional Gaussian beam profile<sup>77</sup>.

$$I(r) = I_0 e^{-2 \frac{x^2+y^2}{w_{xy}^2}} e^{-2 \frac{z^2}{w_z^2}} \quad (2.126)$$

With  $I(r)$  being non-zero for every point in space, the CV is of infinite size. Because  $w_{xy}$  and  $w_z$  define the  $e^{-2}$  values of  $I(r)$  in the lateral and axial dimensions an effective detection volume ( $V_{eff}$ ) that differs slightly from an ellipsoid body can be defined.

$$V_{eff} = \pi^{\frac{2}{3}} w_{xy}^3 k \quad (2.127)$$

$$k = \frac{w_z}{w_{xy}} \quad (2.128)$$

With  $k$  defining the eccentricity of  $V_{eff}$ . The intensity information of the fluorescence emitted from  $V_{eff}$  is detected by a suitable detector (PMT or APD) with a high QY and fast recovery times. No additional spatial information is provided.

The lateral and axial dimensions of  $V_{eff}$  are depending on the radius of the confocal pinhole. In order to enable the derivations of  $V_{eff}$  independent of the used objective all lateral dimensions are normally expressed as multiples of the Airy disk diameter (equation (2.109)) and therefore termed *Airy unit* (AU).

$$1AU = \frac{1.22\lambda}{NA} \quad (2.129)$$

In the following the the detection volume for two exemplary values of the pinhole diameter  $D_{PH}$  shall be discussed. Pure *geometric-optical confocality* is defined at  $D_{PH} > 1$  AU. The lateral and axial dimensions of the detection volume are defined by the dimensions of the  $PSF_{BW}$ , similar to the wide field setup. The lateral and axial dimensions of the detection volume are given as *full width at half maximum* (FWHM) of the confocal volume<sup>78</sup>.

$$FWHM_{lateral} = 0.51 \frac{\lambda_{ex}}{NA} \quad (2.130)$$

$$FWHM_{axial} = 0.88 \frac{\lambda_{ex}}{n - \sqrt{n^2 - NA^2}} \quad (2.131)$$

The fact that the confocal detection volume is diffraction-limited by  $\lambda_{\text{ex}}$  and the PSF of a wide field setup is diffraction limited by  $\lambda_{\text{em}}$  leads to an increase in confocal resolution by the factor of  $\lambda_{\text{em}}/\lambda_{\text{ex}}$ , compared to a wide field setup. Pure *wave-optical confocality* is defined at  $D_{\text{PH}} < 0.25$  AU. It is dominated by diffraction effects taking place at the confocal pinhole. Thus,  $\lambda_{\text{em}}$  may no longer be neglected, which is achieved by introducing the mean wavelength  $\bar{\lambda}$ .

$$\bar{\lambda} \approx \sqrt{2} \frac{\lambda_{\text{em}} \lambda_{\text{ex}}}{\sqrt{\lambda_{\text{em}}^2 + \lambda_{\text{ex}}^2}} \quad (2.132)$$

The detection volume for pure-optical confocality is described by<sup>78</sup>:

$$FWHM_{\text{lateral}} = 0.37 \frac{\bar{\lambda}}{NA} \quad (2.133)$$

$$FWHM_{\text{axial}} = 0.64 \frac{\bar{\lambda}}{n - \sqrt{n^2 - NA^2}} \quad (2.134)$$

### Confocal Laser Scanning Microscopy

Unlike wide field setups, confocal setups provide only intensity information of the diffraction limited detection volume. Optical scanning units, like galvanometer-based raster scanning mirror systems, allow for an imaging routine termed *confocal laser scanning microscopy* (CLSM). Because the speed of the scanning unit is slow in contrast to the fluorescence life time of the fluorophores and the speed of light, the emission light passes the scanning unit in the same position as the illuminating light and is therefore de-scanned onto the detector. By dissecting the probe with the illumination beam waist, the information from the detection unit and the galvanic scanning unit is composed to an image. CLSM does not deliver snap shots like a wide field microscope, but a time series positions and intensities of the translated detection volume. The confocal pinhole enables to image defined optical sections by discriminating the fluorescence emission from out-of-focus planes. A stack of confocal images from different axial planes allows for three dimensional image reconstruction<sup>78</sup>.

## 2.9 Imaging Single Molecules

"It is not difficult to detect the fluorescence of a single molecule, but not to detect anything else"

Richard A. Keller

The key to single molecule fluorescence detection is to reduce the unspecific background fluorescence and to increase the *signal to noise ratio* (SNR) of a single fluorescent probe in a specific

volume above 1, which was first achieved in 1976<sup>79</sup>. Non negligible noise sources are unspecific background fluorescence from impurities, autofluorescence of intrinsic fluorescent probes and scattering. All can overlap with the emission spectrum of the fluorophore. The condition of detecting the specific fluorescence emission of a single Cy5 molecule shall be explained in the following gedankenexperiment, with Raman scattering of water being the only source of noise.

The relation of the fluorophore concentration and the absorption of excitation light is defined by the law of Lambert and Beer.

$$A = \log_{10} \frac{I_0}{I} = \epsilon_{\lambda} z c \quad (2.135)$$

$A$  is the absorption of the fluorophore concentration  $c$  in a solution with a path length of  $z$ .  $\epsilon_{\lambda}$  is termed the molar extinction coefficient. The integrated optical cross section of the fluorescent molecule is related to the Einstein coefficient of the stimulated absorption  $B_{ij}$  (see Chapter 2.1).

$$\sigma = \int_{\nu} \sigma_{\nu} d\nu = \frac{h\nu}{c} B_{ij} \quad (2.136)$$

$\sigma$  calculates from  $\epsilon_{\lambda}$  by

$$\sigma = 1000 \frac{\ln(10) \epsilon_{\lambda}}{N_A} \quad (2.137)$$

where  $N_A$  is Avogadro's constant.

Cy5 has an emission maximum at  $\lambda_{em} = 670$  nm, a quantum yield of  $\Phi = 0.28$ , and the optical cross section of Cy5 calculates with a molar extinction coefficient of  $\epsilon_{Cy5} = 2500000 \frac{1}{\text{mol} \cdot \text{cm}}$  to  $\sigma_{Cy5} = 9.56 \cdot 10^{-16} \text{ cm}^2$  (*GE Healthcare*). The Raman cross section of water is  $\sigma_{Ra} = 1 \cdot 10^{-28} \text{ cm}^2$  and 1 l of water contains approximately  $3.3 \cdot 10^{25}$  molecules<sup>24</sup>. The volume in which the fluorescence signal of one Cy5 molecule equals the Raman scattering noise of the surrounding water molecules calculates to:

$$V = \frac{\sigma_{Cy5} \Phi}{\sigma_{Ra} 3.3 \cdot 10^{25}} = 81 \text{ fl} \quad (2.138)$$

The dimension of a typical confocal volume is about 1 fl<sup>80</sup> and a single Cy5 molecule within  $V_{eff}$  has a theoretical  $SNR_{confocal} = 81$ . The detection volume of a wide field setup with an objective  $NA = 1.49$  in TIR illumination mode may be approximately described with cylindrical shape. The height is described by the penetration depth of the evanescent field  $\delta = 300$  nm, and the circular ground area by the Airy disk of a single Cy5 molecule (see equation 2.109). The detection volume of the wide field setup in the TIR illumination mode calculates to  $V_{TIR} = 0.002$  fl with  $SNR_{TIR} = 40500$ . This of course accounts only for Raman scattering as a source

of noise into. In reality a whole lot of different sources for additional noise will occur. But in principle this gedankenexperiment attests that both confocal and wide field setups are capable of detecting single fluorescent probes.

### 2.9.1 Single Molecule Localization Microscopy

As described in chapter 2.6.1 a single fluorescent probe can be approximated as a point emitter, that is imaged by a microscope in the form of a PSF. As the approximation of the PSF by a Bessel function is a *central processor unit* (CPU) time consuming routine due to the complex parameters, the approximation is frequently executed with the more simple Gaussian function. This approximation introduces only a negligible error, but accelerates the fitting routine significantly<sup>81</sup>.

$$I_{\text{Gaussian}}(x, y) = \frac{A}{2\pi\sigma_x\sigma_y} e^{-\frac{(x-x_c)^2}{2\sigma_x^2} - \frac{(y-y_c)^2}{2\sigma_y^2}} + B \quad (2.139)$$

With  $x_c$  and  $y_c$  being the coordinates of the function's origin, that represent the fluorescent emitters position,  $\sigma_x$  and  $\sigma_y$  are the standard deviations of the Gaussian function in both dimensions which are equal in the case of a point symmetric PSF ( $\sigma_x = \sigma_y = \sigma$ ),  $A$  is the amplitude, and  $B$  represents the offset caused by background.

The theoretical achievable accuracy of such a fitting procedure is described by equation 2.140<sup>82</sup>:

$$\Delta = \sqrt{\frac{\sigma^2 + a^2/12}{N} + \frac{8\pi\sigma^4 b^2}{a^2 N^2}} \quad (2.140)$$

The localization accuracy depends mainly on the number of detected photons ( $N$ ) and the standard deviation of the PSF ( $\sigma$ ) but also on the area imaged on one pixel of the EMCCD chip ( $a$ ), and the background signal ( $b$ ). Both  $\sigma$  and  $N$  are depending on the used fluorescence label, while  $a$  is depending on the configuration of the optical setup. Varying  $a$  by redefining the optics of the setup reveals a minimum of  $\Delta$  at:

$$a = \sigma \sqrt[4]{\frac{96\pi b^2}{N}} \quad (2.141)$$

Equation 2.141 gives an estimation of the optimal pixel size for a Gaussian based single fluorophore localization routine with respect to the fluorescent probe<sup>82</sup>. For example the PC-FP mEOS2 with an emission maximum at  $\lambda_{em} = 584$  nm and a mean number of detected photons  $N = 1500$  has an optimal pixel size of  $a \approx 160$  nm. The development of routines that calculate the localization accuracy of a single fluorescent probe is still an ongoing research field<sup>83–85</sup>, as equation 2.140 underestimates the realistic localization accuracy by about 30%.

Approximating the positions of single fluorescent probes by a Gaussian function enables to localize molecules with an accuracy down to  $1.5 \text{ nm}^2$ . Therefore, this technique is termed *fluorescence imaging with one nanometer accuracy* (FIONA)<sup>3</sup>.

### 2.9.2 Imaging Single Molecules in Densely Labeled Structures

The implementation of the Nyquist-Shannon criterium<sup>46</sup> in resolving structures beyond the diffraction limit with fluorescent probes that are imaged as broad PSFs introduces a paradox problem. On the one hand techniques like FIONA enable the precise localization of single fluorescent probe positions far beyond the diffraction limit, on the other hand a densely labeled probe is forced by the theorem of Nyquist and Shannon<sup>46</sup> to resolve fluorescently labeled structures in detail. This way multiple PSFs would overlap and could not be approximated by a point symmetric Gaussian function accurately. The whole extent of the dilemma shall be explained by the following gedankenexperiment: To resolve a structure of a plain surface with  $10 \text{ nm}$  accuracy after the Nyquist-Shannon criterium, it has to be labeled with a fluorescent probe every  $5 \text{ nm}$ . The PSF of a Cy5 molecule has a  $\sigma \approx 325 \text{ nm}$  and therefore covers an area of about  $A = \pi(\sigma/2)^2 = 83 * 10^3 \text{ nm}^2$  containing ca.  $17 * 10^3$  identical fluorescent probes with overlapping PSFs at  $5 \text{ nm}$  distance (for three dimensional extended structures the problem gets even worse). This paradox problem has been circumvented by capitalizing the photo-physical intensity fluctuations of fluorescent probes at the single molecule level. Single fluorescent probes may be switched by different mechanisms between a bright state and a dark state as described in chapter 2.5.3-2.5.5. By influencing the switching rates the number fluorescent probes that exist in the bright state at the same time can be kept sufficiently low, that simultaneously occurring PSFs do not overlap. This way the spatiotemporal separated PSFs of all fluorescent probes within the labeled structure may be detected at least once given a sufficiently measuring time. The intermediary result of a photo-switching experiment with stochastically appearing and disappearing PSFs is an image stack recorded by the EMCCD camera. In an additional step the positions of the detected fluorescent labels are determined by an approximation process as described in chapter 2.9.1 leading to the final result of the experiment: a list of information obtained from the single fluorescent probes. Typical parameters are the x and y coordinates of the origin of the Gaussian approximation at the time the PSF was detected, the detection time, the fit accuracy, and the number of photons detected from the PSF. SMLM has been recently deployed in combination with several ways of switching molecules between the bright state and the dark state such as *photo-activated localization microscopy*

(PALM)<sup>8</sup>, *fluorescence photo-activated localization microscopy* (F-PALM)<sup>86</sup>, *photo-activated localization microscopy with independently running acquisition* (PALMIRA)<sup>87</sup>, *bleaching/blinking assisted localization microscopy* (BaLM)<sup>88</sup>, *stochastic optical reconstruction microscopy* (STORM)<sup>9</sup>, *direct stochastic optical reconstruction microscopy* (dSTORM)<sup>10</sup>, *ground state depletion microscopy followed by individual molecule return* (GSDIM)<sup>89,90</sup>, etc.

During this thesis explicitly PALM and dSTORM have been used either solitarily or in combination to obtain localization information of fluorescent probes at near molecular level and shall therefore be explained in more detail.

### **direct Stochastic Optical Reconstruction Microscopy**

STORM and dSTORM experiments use a reversible photoswitching fluorophore for SMLM. In contrast to the original STORM approach, which requires two kinds of fluorophores within a distinct distance and ratio to achieve a stable photoswitching behavior, dSTORM requires only one type of fluorophore within an appropriate switching buffer (see chapter 2.5.4). In experiments with fluorescent probes switching reversibly between a bright and a dark state, an equilibrium between both states is achieved, as discussed in chapter 2.5.3.

A typical dSTORM experiment is conducted within an individual equilibrium between fluorophores existing in the bright and the dark state, at which the stochastically appearing PSFs of the single molecules are spatiotemporally separated. The conditions for the optimal equilibrium have to be determined iteratively and depend on several factors (e.g. the label density, the organization of the target protein, the compatibility with a second type of fluorescent label, and the micro environment of the fluorophore).

### **Photo-Activated Localization Microscopy**

PALM uses the serial photoactivation and subsequent bleaching of a subset of PA/PC-FPs to achieve spatiotemporally separated PSFs of the FPs ensemble within the sample. FPs in PALM experiments are transferred irreversibly from a dark state over an intermediate bright state into a photobleached state (see chapter 2.5.5). PALM experiments utilizing fluorescent probes detected only once in an experiment and characterized by an *degree of labeling* (DOL) of about 1, achieved by genetically fusing one FP to one *protein of interest* (POI), offer the opportunity to count the number of fluorescent probes within a sample<sup>91-93</sup>.



### 2.9.3 Astigmatism Based Optical Sectioning

By introducing a cylindrical lens ( $f_c = 10$  m) into the detection beam path the focal planes of the two lateral dimensions ( $x$  and  $y$ ) were decoupled resulting in an axial offset between them<sup>94</sup>. The PSF will appear with an ellipticity depending on the axial position of the fluorophore. By approximating the PSF by a two dimensional Gaussian with standard deviations ( $\sigma_x$  and  $\sigma_y$ ) independent from each other, the axial position of the fluorophore can be determined from the ratio of  $\sigma_x$  and  $\sigma_y$ . By measuring a phantom sample with fluorophores placed at known axial positions a calibration curve for the ratio of  $\sigma_x$  and  $\sigma_y$  against the axial position can be measured with an average accuracy of 50 – 60 nm, and mathematically described by:

$$\sigma_{x,y}(z) = \sigma_0 \sqrt{1 + \left(\frac{z-c}{d}\right)^2 + A \left(\frac{z-c}{d}\right)^3 + B \left(\frac{z-c}{d}\right)^4} \quad (2.142)$$

$\sigma_0$  characterizes the PSF of each dimension in the very focal plane.  $c$  gives the offset between the two focal planes  $x$  and  $y$  from the average focal plane.  $d$  characterizes the focus depth of the microscope.  $A$  and  $B$  are fit parameters of higher order terms that correct numerically for lens aberrations. By matching the ratio of  $\sigma_x$  and  $\sigma_y$  for each fluorophore detected in the experiment with the calibration curve, information on the axial position is obtained. Fluorophores appearing in between the focal planes of the  $x$  and the  $y$  dimension the PSF still appears circularly shaped but slightly broader as imaged without the cylindrical lens, resulting in a loss of lateral localization accuracy.

## 2.10 Single Molecule Diffusion Theory

Diffusion is defined as the undirected movement of particles along a gradient from a region with higher concentration to a region of lower concentration. A one dimensional diffusion flux along a gradient  $dc/dx$  is described by Fick's first law, with  $c$  being the particle concentration.

$$j(x) = -D \frac{dc}{dx} \quad (2.143)$$

The constant of proportionality  $D$  is termed the diffusion coefficient. In aqueous solution it is defined by the law of Einstein and Stokes as:

$$D = \frac{k_B T}{6\pi\eta R_0} \quad (2.144)$$

The diffusion coefficient  $D$  depends on the temperature  $T$ , the viscosity of the medium  $\eta$ , and the hydrodynamic radius  $R_0$ , which describes the diffusing particle as a solid sphere with identical diffusive characteristics within the same solvent.  $R_0$  can be estimated as

$$R_0 = \sqrt[3]{\frac{3M}{N_A 4\pi\rho}} \quad (2.145)$$

With  $M$  being the molecular weight,  $N_A$  being Avogadro's constant, and  $\rho$  being the average density of the molecule. By taking the mass action law into account the temporal change of concentration  $dc/dt$  can be coupled to the net flux of molecules into the volume  $A \cdot dx$ .

$$\frac{dc}{dt} = \frac{(j(x) - j(x + dx))}{dx} \quad (2.146)$$

$$(2.147)$$

Insertion of Fick's first law calculates to

$$\left(\frac{\partial c}{\partial t}\right)_x = D \left(\frac{d^2c}{dx^2}\right)_t \quad (2.148)$$

Eq. (2.148) is termed Fick's second law or the diffusion equation. It relates the velocity of the change in concentration at a fixed position  $x$  to the spatial variation of the concentration. For convenience eq. (2.148) will be written from now on in the form

$$c_t = Dc_{xx} \quad (2.149)$$

$$\text{with } c_t := \frac{\partial c}{\partial t} \quad (2.150)$$

$$\text{and } c_{xx} := \frac{\partial^2 c}{\partial x^2} \quad (2.151)$$

This partial differential equation can be solved by transforming both sides into the Fourier space.

$$\hat{c}_t(t, \omega) = \mathcal{F}\{c_t(t, x)\} = \int_{-\infty}^{\infty} e^{i\omega x} c_t(t, x) dx \quad (2.152)$$

$$\hat{c}_{xx}(t, \omega) = \mathcal{F}\{Dc_{xx}(t, x)\} = \int_{-\infty}^{\infty} e^{i\omega x} Dc_{xx}(t, x) dx \quad (2.153)$$

$$= -\omega^2 \int_{-\infty}^{\infty} e^{i\omega x} c(t, x) dx \quad (2.154)$$

$$= -D\omega^2 \hat{c}(t, \omega) \quad (2.155)$$

The diffusion equation in the Fourier space calculates to:

$$\hat{c}_t(t, \omega) = -D\omega^2 \hat{c}(t, \omega) \quad (2.156)$$

This differential equation can be solved by an exponential ansatz to:

$$\hat{c}(t, \omega) = \hat{c}(t = 0, \omega) e^{-D\omega^2 t} \quad (2.157)$$

In case of imaging a single diffusing molecule at the initial condition  $t = 0$  the complete concentration of single molecule localizations is exactly located in one point which can be defined as  $x = 0$ .  $c(t = 0, x)$  calculates to:

$$c(t = 0, x) = c_0 \delta(x) \quad (2.158)$$

With  $\delta(x)$  being the Delta function. The Fourier transformation of  $c(t = 0, x)$  is given by:

$$\hat{c}(t = 0, \omega) = \mathcal{F}\{c(t = 0, x)\} = \int_{-\infty}^{\infty} e^{i\omega x} c_0 dx \quad (2.159)$$

This is a Green function with the solution:

$$\hat{c}(t = 0, \omega) = c_0 \quad (2.160)$$

Inserting the initial conditions Eq. (2.160) into eq. (2.157) and transforming it back from the Fourier space gives a convolution product which is the solution of the diffusion equation (eq. (2.148)).

$$c(t, x) = \mathcal{F}^{-1}\{\hat{c}(t, \omega)\} \quad (2.161)$$

$$= \frac{1}{2\pi} \int_{-\infty}^{\infty} c_0 e^{-i\omega x} e^{-\omega^2 D t} d\omega \quad (2.162)$$

$$= \frac{c_0}{2\pi} e^{-\frac{x^2}{4Dt}} \int_{-\infty}^{\infty} e^{-(\omega\sqrt{Dt} + \frac{ix}{2\sqrt{Dt}})^2} d\omega \quad (2.163)$$

The integral can be solved by the approach of substitution.

$$\Omega := \omega\sqrt{Dt} + \frac{ix}{2\sqrt{Dt}} \quad (2.164)$$

$$\Rightarrow d\Omega = \sqrt{Dt} d\omega \quad (2.165)$$

Inserting into eq. (2.163) gives:

$$c(t, x) = \frac{c_0}{2\pi\sqrt{Dt}} e^{-\frac{x^2}{4Dt}} \int_{-\infty}^{\infty} e^{-\Omega^2} d\Omega \quad (2.166)$$

$$= \frac{c_0}{2\pi\sqrt{Dt}} e^{-\frac{x^2}{4Dt}} \sqrt{\pi} \quad (2.167)$$

$$= \frac{c_0}{\sqrt{4\pi Dt}} e^{-\frac{x^2}{4Dt}} \quad (2.168)$$

The Gaussian concentration distribution  $c(t, x)$  solves the diffusion equation eq. 2.148.

In order to describe the lateral diffusion of membrane proteins by the model of Brownian motion the cellular plasma membrane is approximated by the model of a fluid mosaic<sup>95</sup> consisting of a lipid bilayer with integrated membrane proteins. The fluidity of the membrane allows the

free lateral diffusion of membrane proteins and lipids within the bilayer. The thermic movement of all membrane components causes collisions between the molecules, leading to permanent stochastically distributed changes of directions. The diffusion coefficient of single membrane proteins fused to a fluorophore can be measured by life-cell SMLM either on a confocal, or a wide field setup.

### 2.10.1 Fluorescence Correlation Spectroscopy

A well established technique to determine  $D$  is *fluorescence correlation spectroscopy* (FCS)<sup>96</sup>. It measures the equilibrium intensity fluctuations of a solution, containing freely diffusion fluorescent probes, within a confocal volume over time. The concentration of fluorescently labeled proteins should guarantee that the average number of fluorescent probes within the confocal volume should be approximately 5 particles and does not show vast fluctuations. If the diffusion model is known, information of the diffusion behavior may be extracted from an FCS measurement, as the detected intensity fluctuations are directly linked to fluorescently labeled proteins entering and leaving the confocal detection volume<sup>24</sup>.

In brief, the number of collected photons over a distinct time interval  $\Delta t$  are given by:

$$F(t) = \Delta t Q \int I(\vec{r}) c(t, \vec{r}) dV \quad (2.169)$$

With  $I(\vec{r})$  being the intensity distribution,  $Q = q * \rho$  being the fluorescent probe specific product of the quantum yield  $q$ , and the absorption cross section  $\rho$  and  $c(t, \vec{r})$  being the particle concentration function as introduced in chapter 2.10. A confocal detection volume with an ellipsoid shape  $I(\vec{r})$  can be annealed to a three dimensional Gaussian distribution with the following Fourier transformation  $\hat{I}(q) = FT\{I(\vec{r})\}$ :

$$I(\vec{r}) = I_0 e^{-\frac{2x^2}{\omega_x^2} - \frac{2y^2}{\omega_y^2} - \frac{2z^2}{\omega_z^2}} \quad (2.170)$$

$$\hat{I}(q) = \frac{I_0 \omega_x \omega_y \omega_z}{8} e^{-\frac{\omega_x^2 q_x^2}{8} - \frac{\omega_y^2 q_y^2}{8} - \frac{\omega_z^2 q_z^2}{8}} \quad (2.171)$$

With  $I_0$  being the amplitude at the origin and  $\omega$  being the standard deviation for each dimension.

By autocorrelating  $F(t)$  over a variable time delay  $F(t + \tau)$  information about diffusion based intensity fluctuations can be obtained from the sample. The deviation of the collected photons per time from the mean is given by:

$$\delta F(t) = \langle F \rangle - F(t) \quad (2.172)$$

$$= \Delta t Q \int I(\vec{r}) \delta c(t, \vec{r}) dV \quad (2.173)$$

The autocorrelation function  $G(\tau)$  determined by comparing  $F(t)$  to  $F(t + \tau)$  averaged over all sampling intervals  $T$  and the square of the average intensity function  $\langle F \rangle^2$  calculates to

$$G(\tau) = \frac{1}{\langle F \rangle^2 T} \sum_0^{T-1} \delta F(t) \delta F(t + \tau) \quad (2.174)$$

By taking the systems ergodicity into account the temporal fluctuations may be interpreted as being representative for the state of the total system and  $t$  may be replaced with 0.

$$G(\tau) = \frac{\langle \delta F(0) \delta F(\tau) \rangle}{\langle F \rangle^2} \quad (2.175)$$

$$= \frac{\Delta t^2 Q^2}{\langle F \rangle^2} \int \int I(\bar{r}) I(\bar{r}') \langle \delta c(0, \bar{r}) c(\tau, \bar{r}') \rangle dV dV' \quad (2.176)$$

From the diffusion theory of Brownian motion the Fourier transformation of  $c(\tau, \bar{r}')$  is known to be:

$$FT\{\delta c(\tau, \bar{r}')\} = \delta \hat{c}(\tau, q) \quad (2.177)$$

$$= \delta \hat{c}(\tau, 0) e^{-D\bar{q}^2 \tau} \quad (2.178)$$

The correlation of the concentration functions may therefore be seen as an inverse three dimensional Fourier transformation:

$$\langle \delta c(0, \bar{r}) \delta c(\tau, \bar{r}') \rangle = (2\pi)^{-\frac{3}{2}} \int_{-\infty}^{\infty} e^{-i\bar{q}\bar{r}'} e^{-D\bar{q}^2 \tau} \langle \delta c(0, \bar{r}) \delta c(0, \bar{q}) \rangle dV_{\bar{q}} \quad (2.179)$$

$$= (2\pi)^{-3} \int_{-\infty}^{\infty} e^{-i\bar{q}\bar{r}'} e^{-D\bar{q}^2 \tau} dV_{\bar{q}} \int e^{i\bar{q}\bar{r}'} \langle \delta c(0, \bar{r}) \delta c(0, \bar{r}') \rangle dV \quad (2.180)$$

Assuming that two particles being at the same time  $\tau = 0$  at different places  $\bar{r}$  and  $\bar{r}'$  show no correlation,  $G(\tau)$  calculates to:

$$G(\tau) = \frac{\Delta t^2 Q^2}{\langle F \rangle^2} \int \int I(\bar{r}) I(\bar{r}') dV dV' (2\pi)^{-3} \langle c \rangle \int_{-\infty}^{\infty} e^{i\bar{q}(\bar{r}-\bar{r}')} e^{-D\bar{q}^2 \tau} dV_{\bar{q}} \quad (2.181)$$

Replacing the three dimensional Gaussian illumination profile  $I(r)$  with its Fourier transformation:

$$\hat{I}(q) = FT\{I(r)\} = \frac{1}{(2\pi)^{\frac{3}{2}}} \int e^{-iqr} I(r) dV \quad (2.182)$$

calculates  $G(\tau)$  to

$$G(\tau) = \frac{\Delta t^2 Q^2 \langle c \rangle}{\langle F \rangle^2} \int_{-\infty}^{\infty} |\hat{I}(q)|^2 e^{-Dq^2 \tau} dV_q \quad (2.183)$$

$$= \frac{\Delta t^2 Q^2 \langle c \rangle}{\langle F \rangle^2} \frac{I_0^2 \omega_x^2 \omega_y^2 \omega_z^2}{64} \int_{-\infty}^{\infty} e^{-q_x(\frac{\omega_x^2}{4} + D\tau)} e^{-q_y(\frac{\omega_y^2}{4} + D\tau)} e^{-q_z(\frac{\omega_z^2}{4} + D\tau)} dV_q \quad (2.184)$$

By solving the integral over  $dV_q$  with  $\int_{-\infty}^{\infty} e^{-ax^2} dx = \sqrt{\frac{\pi}{a}}$  and inserting

$$\langle F \rangle = (2\pi)^{\frac{3}{2}} \hat{I}(q=0) \Delta t Q \langle c \rangle \quad (2.185)$$

$$= \frac{I_0 \omega_x \omega_y \omega_z}{8} \Delta t Q \langle c \rangle \quad (2.186)$$

$G(\tau)$  calculates to

$$G(\tau) = \frac{1}{\langle c \rangle \pi^{\frac{3}{2}} \omega_x \omega_y \omega_z} \left(1 + \frac{4D\tau}{\omega_x^2}\right)^{-\frac{1}{2}} \left(1 + \frac{4D\tau}{\omega_y^2}\right)^{-\frac{1}{2}} \left(1 + \frac{4D\tau}{\omega_z^2}\right)^{-\frac{1}{2}} \quad (2.187)$$

The confocal detection volume is approximated to an ellipsoid shape  $V = \pi^{\frac{3}{2}} \omega_x \omega_y \omega_z$  with  $\omega_x = \omega_y$ . The average number of fluorescent probes within the confocal detection volume is given by  $N = \langle c \rangle V$ . With a known confocal detection volume the two-dimensional diffusion coefficient is derived by fitting the autocorrelation function to:

$$G(\tau) = \frac{1}{N} \left(1 + \frac{4D\tau}{\omega_{xy}^2}\right)^{-1} \quad (2.188)$$

### 2.10.2 Single Particle Tracking PALM

The diffusion of single membrane proteins fused to a PA/PC-FP can be measured directly at the basal membrane of living cells on a wide field setup by *single particle tracking photo-activated localization microscopy* (sptPALM)<sup>97</sup>. A small subset of FPs is transferred into the bright state and localized several times before photobleaching. This procedure results in a short snap-shot time series of the single molecule diffusion which shall be further referred to as *trajectory*.

In the ideal case every imaged diffusion step is independent from the previous one and has no influence on the following. Diffusion at the single molecule level is characterized by the *mean squared displacement* (MSD)  $\langle x^2(\tau) \rangle$  that in the one dimensional case calculates to

$$\langle x^2(\tau) \rangle = \frac{1}{T} \sum_t^T (x(t+\tau) - x(t))^2 \quad (2.189)$$

With  $T$  being the total number of diffusion steps with duration  $\tau$  within the trajectory,  $t$  being the temporal walk parameter over the diffusion steps and  $x(t+\tau)$  and  $x(t)$  being the coordinates of two localizations from the trajectory imaged within a time interval  $\tau$ . The MSD is mathematically described by the normalized concentration distribution of the stochastic diffusion processes  $p(\tau, x)$ .

$$\langle x^2(\tau) \rangle = \int_0^\infty x^2 p(\tau, x) dx \quad (2.190)$$

with

$$p(\tau, x) = \frac{c}{c_0} \quad (2.191)$$

and

$$\int_{-\infty}^{\infty} p(\tau, x) dx = 1 \quad (2.192)$$

Inserting eq. (2.168) into eq. (2.190) calculates to:

$$\langle x^2(\tau) \rangle = \frac{1}{2\sqrt{\pi Dt}} \int_{-\infty}^{\infty} x^2 e^{-\frac{x^2}{4Dt}} dx \quad (2.193)$$

$$= \frac{1}{2\sqrt{\pi Dt}} \frac{\sqrt{\pi}}{2} (4Dt)^{\frac{3}{2}} \quad (2.194)$$

$$= 2Dt \quad (2.195)$$

Which is termed as the Einstein and Smoluchowski equation of one dimensional Brownian motion. For lateral diffusion the Einstein and Smoluchowski equation gains one additional translational degree of freedom turning into:

$$\langle x^2(\tau) \rangle = 4Dt \quad (2.196)$$

By imaging a sufficiently long time interval thousands of trajectories all over the cell membrane are recorded resulting in a broad statistic of single molecule diffusion coefficients which in combination with the spatial resolution can be reconstructed to a diffusion map of the cell membrane.

---

# Chapter 3. | Material and Methods:

## Imaging single molecule fluorescence

Developing imaging-systems for SMLM and establishing their biological application is a dynamic process on all levels, as instrumentation, imaging routines, and data post processing influence each other. The instrumentation and methods described in the following chapter represent the state in the context of this work.

### 3.1 Labeling of Proteins

*N-hydroxysuccinimide* (NHS) esters of organic dyes can be covalently linked to a POI. The reactive group of the NHS ester reacts with primary amines ( $-\text{NH}_2$ ) by forming a stable amide under release of a *N*-hydroxysuccinimide. Primary amines occur at the N terminus of the polypeptide chain as well as in lysine side chains. Exposed amino groups for possible NHS-ester binding were previously identified from the POI's crystal structure. The labeled POI is purified by gel filtration and the DOL is determined by its absorption spectrum within an ensemble spectrometer (Cary 100 UV-VIS, Agilent-Technologies) by applying Lambert-Beer's law of absorption (see equation 2.135) to:

$$\text{DOL} = \frac{A_{\text{max}}/\epsilon_{\text{max}}}{A_{\text{prot}}/\epsilon_{\text{prot}}} \quad (3.1)$$

With  $A_{\text{max}}$  being the absorption maximum of the fluorescent probe at the excitation wavelength  $\lambda_{\text{abs}}$ ,  $A_{\text{prot}}$  being the absorption maximum of the protein,  $\epsilon_{\text{max}}$  being the extinction coefficient of the fluorescent probe at the absorption maximum, and  $\epsilon_{\text{prot}}$  being the extinction coefficient of the protein at the absorption maximum. The maximum absorption of a protein ( $A_{\text{prot}}$ ) is usually measured at  $\lambda = 280 \text{ nm}$  ( $A_{280}$ ), as it is mainly dominated by tryptophan. As the



absorption spectrum of the fluorophores most often also contributes to  $A_{280}$ ,  $A_{\text{prot}}$  is corrected by a fluorophore specific correction factor  $CF_{280}$  to  $A_{\text{prot}} = A_{280} - A_{\text{max}} * CF_{280}$ . The corrected DOL calculates to:

$$\text{DOL} = \frac{A_{\text{max}} * \epsilon_{\text{prot}}}{(A_{280} - A_{\text{max}} * CF_{280}) * \epsilon_{\text{max}}} \quad (3.2)$$

### Labeling of Tumor Necrosis Factor

Recombinant human soluble TNF $\alpha$  (Gibco, or Immunotools) was fluorescently labeled either with ATTO647N NHS-ester (ATTO-TEC), or Cy5 NHS-ester (GE Healthcare). The fluorophore was dissolved in dimethyl sulfoxide. TNF $\alpha$  was diluted in PBS to a final concentration of 0.25  $\mu\text{g}/\text{l}$  with a pH set to 7.4. A fluorophore-protein solution with a 10-fold molar excess of fluorophores and a pH set to 8.3 – 8.5 was prepared and incubated under gentle shaking for 2 h at room temperature. Unbound dye was removed by gravity flow columns (Illustra NAP-5, GE Healthcare) with PBS as equilibration buffer. A DOL of 0.8 was obtained for TNF $\alpha$ -ATTO647N and 1.1 for TNF $\alpha$ -Cy5. Biological activity of labeled TNF $\alpha$  was measured according to<sup>98-100</sup>.

## 3.2 Single Molecule Surfaces

To investigate the fluorescence emission of distinct single fluorophores over time their definite identification needs to be guaranteed. For that purpose fluorophores were immobilized on a surface at a concentration that guarantees for non overlapping PSFs. To avoid quenching effects between the fluorescent probe and the surface a rigid linker molecule is used to separate fluorophore and surface. This way the immobilization process does not influence the photophysics of the molecule.

### Surface Preparation

Microscope cover glass chambers were cleaned and edged with 0.5 % *hydrofluoric acid* (HF) for 10 s, and rinsed 3 times with *phosphate buffered saline* (PBS). The chambers were coated with *bovine serum albumin* (BSA)-biotin molecules by incubating in 5 mg/ml BSA (Sigma) and 1 mg/ml BSA-Biotin (Sigma) solved in PBS for 4 h at 4 °C, followed by 3 washing steps with PBS to remove remaining BSA. The coated cover glass chambers were incubated with 0.1 mg/ml streptavidin (Sigma) solved in PBS for 15 min at room temperature, followed by 3 washing steps with PBS to remove remaining streptavidin.

#### Surface Immobilization of Organic Fluorophores

Surface immobilization of organic fluorophores was performed using an established protocol<sup>101</sup>. Single stranded oligonucleotides with complementary sequences, from which one is labeled with biotin at the 3' end and the other one with an organic fluorophore at the 5' end, were obtained commercially (IBA). Biotin-streptavidin coated surfaces were incubated with the biotinylated oligonucleotide at a concentration of  $10^{-10}$  mol/l solved in PBS for 15 min at room temperature followed by incubation with the fluorescently labeled oligonucleotide. Non bound oligonucleotides were removed by three washing steps with PBS following each incubation step. For short time storage the single molecule surface was stored in PBS at 4 °C.

#### Purification and Surface Immobilization of mEOS2

*E.coli* BL21ai cells (Invitrogen) were transformed via heat shock method with pRSetA-mEOS2-6his vector (Addgene) according to manufacturer's instructions. Transformed cells were grown on ampicillin containing agar plates over night at 37 °C. Colonies were picked and grown in sterile LB-Medium (10 ml, 0.1 mmol/l ampicillin) over night at 37 °C shaking at 220 *rounds per minute* (rpm). Glycerol stocks of transformed BL21ai were stored at -80 °C for further use.

For protein expression frozen BL21ai cell stocks were thawed on ice and transferred into sterile LB-medium (0.5 ml, 0.1 mmol/l ampicillin). The preparatory culture was incubated over night at 37 °C shaking at 220 rpm. The starter culture was transferred to the main culture (100 ml, 0.1 mmol/l ampicillin) and incubated at 37 °C shaking at 220 rpm. At an optical density  $OD_{600nm} = 0.6$  the expression of mEOS2-6his was induced by the application of arabinose (10 ml, 5%, Life Technologies). The induced cells were incubated at 37°C for 80 min shaking at 220 rpm. The cells were harvested via centrifugation at 3500 g for 40 min at 4 °C. The cell pellet was stored for further use at -80 °C.

For protein purification frozen cell pellets were thawed on ice and lysed under native conditions. The cell lysate was sonicated on ice (30 GHz, 6 pulses each for 10 s) and centrifuged at 3500 g for 40 min at 4 °C. The supernatant was transferred to a Ni-NTA agarose suspension (50% in 30% ethanol, Merck Millipore) and incubated for 60 min on ice. mEOS2-6his was purified from the supernatant using the Ni-NTA purification system (Merck Millipore). The degree of mEOS2-6his purity was quantified by loading the different collected fractions onto a SDS-gel. The purified protein solution was dialyzed against PBS for 12 h at 4 °C and concentrated by using centrifugation filters (Amicon ultra 0.5 ml, 10k membrane, Merck Millipore) at 14000 g for 10 min at room temperature to a final concentration of 0.2 mg/ml. For short time storage

the purified mEos2-6his solution was stored with protease inhibitor (Sigma) at 4 °C. Purified mEos-6his proteins were biotinylated with NHS-*polyethylene glycol* (PEG) 12-biotin (Thermo Scientific) using standard protocols. 5 ml of protein stock solution (1 mg) were mixed with 3.58 µl of a 250 mmol/l NHS-Peg12-Biotin stock solution solved in amine free PBS and incubated on ice for two hours. mEos2-6his-Peg<sub>12</sub>-Biotin was applied to a biotin-streptavidin surface and incubated until the FP concentration at the surface was suitable for SMLM. Non-bound mEos2-6his-Peg<sub>12</sub>-Biotin molecules are removed by three washing steps with PBS. For short time storage the single molecule surface was stored in PBS containing protease inhibitor (Sigma) at 4 °C.

### 3.3 Cell Culture

During this thesis permanent or immortal cell lines have been used explicitly. The cell lines have either been cultured from carcinoma tissue or have been further stably transfected, to achieve a tumor like infinite splitting potential, for example with viral oncogenes like the Epstein-Barr virus. Immortal cell lines are characterized by a permanent availability and a lower dependency on specific growth factors than primary cell lines and are therefore comparatively easy to handle in cell culture.

#### 3.3.1 A3.01 Cell Line

A3.01 is a human T-cell line, explicitly developed for the study of acquired immune deficiency syndrome associated with retro viruses like the HIV. The cells are grown in *Roswell Park Memorial Institute* (RPMI) 1640 medium (Invitrogen, Grand Island, NY, USA) with 10% *fetal bovine serum* (FBS) (Gibco, Grand Island, NY, USA), 100 units/ml penicillin (PAA Laboratories GmbH) and 100 µg/ml streptomycin (PAA Laboratories GmbH) and incubated at 37 °C and 5% CO<sub>2</sub>. Confluent cells are split 1:4 every 3-4 days.

#### 3.3.2 CHO Cell Line

CHO is a mammalian cell line originally obtained from chinese hamster ovaries. The cells are grown in RPMI 1640 medium (Invitrogen, Grand Island, NY, USA) with 10% FBS (Gibco, Grand Island, NY, USA), 100 units/ml penicillin (PAA Laboratories GmbH) and 100 µg/ml streptomycin (PAA Laboratories GmbH) and incubated at 37 °C and 5% CO<sub>2</sub>. Confluent cells are split 1:4 every 3-4 days.

#### 3.3.3 COS-7 Cell Line

COS-7 is a simian cell line originally obtained from the kidney of the african green monkey *Chlorocebus aethiops*, by transformation with an origin defective mutant of the SV-40 virus. The cells are grown in *Dulbecco's modified Eagle's medium* (DMEM) (Invitrogen, Grand Island, NY, USA) with 10% FBS (Gibco, Grand Island, NY, USA), 100 units/ml penicillin (PAA Laboratories GmbH), and 100 µg/ml streptomycin (PAA Laboratories GmbH) and incubated at 37 °C and 5% CO<sub>2</sub>. Confluent cells are split 1:4 every 3-4 days.

#### 3.3.4 HeLa Cell Line

HeLa is a human cell line originally cultured from an adenocarcinoma. It is characterized by an adherent, epithelial growth in monolayers. The cells are grown in RPMI 1640 medium (PAA Laboratories GmbH, Pasching, Austria), supplemented with 100 units/ml penicillin (PAA Laboratories GmbH), 100 µg/ml streptomycin (PAA Laboratories GmbH), 2 mmol/l L-glutamin (PAA Laboratories GmbH), 10% FBS (Gibco, Grand Island, NY, USA), 1% non-92 essential amino acids (PAA Laboratories GmbH) and 1 mmol/l sodium pyruvate (PAA Laboratories GmbH) and incubated at 37 °C and 5% CO<sub>2</sub>. Confluent cells are split 1:4 every 3-4 days.

#### 3.3.5 U2OS Cell Line

U2OS is a human cell line cultured from an osteosarcoma in the tibia. The cells are grown in DMEM (Invitrogen, Grand Island, NY, USA) with 10% FBS (Gibco, Grand Island, NY, USA), 100 units/ml penicillin (PAA Laboratories GmbH), and 100 µg/ml streptomycin (PAA Laboratories GmbH) and incubated at 37 °C and 5% CO<sub>2</sub>. Confluent cells are split 1:4 every 3-4 days.

### 3.4 Labeling Cellular Structures

#### 3.4.1 Formaldehyde Fixation

Cells were plated and grown on 8-well microscope cover glass chambers (Sarstedt) up to 80% confluency. Cells were rinsed 3 times with PBS and fixed by incubation in 4% formaldehyde in PBS for 10 min at room temperature. After fixation the cells were rinsed 3 times in PBS and permeabilized by incubation in permeabilization buffer (0.5% Triton X-100 (Sigma), 0.2%

Tween (Sigma) in PBS). After 3 additional washing steps with PBS the cells were stored at 4 °C for further use.

### 3.4.2 Glutaraldehyde Fixation

Cells were plated and grown on 8-well microscope cover glass chambers (Sartstedt) up to 80% confluency. Cells were rinsed 3 times with PBS and extracted by incubation in extraction buffer (0.5% Triton X-100 (Sigma), 4 mmol/l *ethylene glycol tetraacetic acid*) (EGTA) (Sigma) in Brinkley Buffer 1980) for 30 s at room temperature. After extraction the cells were fixed by incubation in extraction buffer with 0.5% glutaraldehyde (Sigma) for 10 min at room temperature. After 3 additional washing steps with PBS the cells were stored at 4 °C for further use.

### 3.4.3 Immunohistochemistry

Indirect immunohistochemistry was used to label cellular structures. Hereby, a sandwich-like structure is formed by two antibodies to label the POI comprising a primary antibody, from a species different than the sample species, against a POI specific epitope structure and a secondary antibody against the primary antibody labeled with an organic dye.

After fixation the cells were rinsed 3 times with TBS (150 mmol/l *NaCl* (Sigma), 20 mmol/l Tris (pH 8) (Sigma)). Unspecific binding sites were blocked by incubation in blocking solution (TBS, 0.1% Triton X-100 (Sigma), 2% BSA) for 10 min at room temperature. The blocked cells were incubated with a primary antibody against the POI at a concentration  $\approx 2 \mu\text{g/ml}$  in blocking solution for 30 min to 24 h. The cell were rinsed 3 times with TBS and incubated with the secondary antibody at a concentration  $\approx 4 \mu\text{g/ml}$  in blocking solution for 1 h at room temperature. After 3 additional washing steps with TBS the cells were stored in PBS at 4 °C for further use.

### 3.4.4 Actin Labeling with Phalloidin

Phalloidin is a bicyclic peptide from the poison repertoire of the death cap *Amantia phalloides*. It stabilizes the actin-actin binding and increases the polymerization constant from g-actin to f-actin<sup>102</sup>. Coupled to an organic dye phalloidin is broadly used to label the actin skeleton of cells achieving a labeling degree up to one per molecule<sup>102</sup>.

After fixation the cells were rinsed 3 times with PBS and incubated in blocking solution (PBS, 0.1% Triton X-100 (Sigma), 2% BSA) for 10 min at room temperature. The blocked cells were incubated with phalloidin-Alexa Fluor 647 (Invitrogen) at a concentration  $\approx 1 \mu\text{g/ml}$  in block-

ing solution for 20 min at room temperature. The cells were rinsed 3 times with PBS at 4 °C for further use.

#### 3.4.5 Click Chemistry

Click chemistry enables direct labeling of *deoxyribonucleic acid* (DNA)<sup>103</sup>. During the DNA replication cycle thymidine is replaced by a structural analogue termed *5-ethynyl-2'-deoxyuridine* (EdU). EdU has a terminal alkyne group instead of a methyl group in the 5-position. Alkynes bind covalently to azides in a Cu(I) catalyzed [3+2] cyclo-addition.

Cells were plated and grown on 8-well microscope cover glass chambers (Sartstedt) over night and incubated in medium containing 10 µmol/l EdU for 15 min to 24 h. After incubation cells were fixed according to the formaldehyde fixation protocol (see chapter 3.4.1). EdU was labeled with an azide derivative of Alexa Fluor 647 using the Click-iT EdU Alexa Fluor 647 Imaging Kit (Invitrogen) by incubating the cells in click reaction buffer (100 mmol/l HEPES (pH 8.2), 1 mmol/l  $CuSO_4$ , 50 mmol/l aminoguanidine, 25 mmol/l AA) for 15 min at room temperature. The cells were rinsed 3 times with PBS at 4 °C for further use.

### 3.5 Transient Transfection

A genetically modified POI may be introduced into a cell by transiently transfecting *complementary deoxyribonucleic acid* (cDNA), in form of a plasmid, into the eukaryotic cell. It is not introduced into the cellular genome but stays for a period of 24 to 96 h while the POI gets expressed. The plasmid is designed prior to the experiment to code for a fusion protein consisting of the POI, a short linker sequence, and a label. The process of designing the fusion protein includes the verification that the fused label does not affect the POI function. The introduction of foreign proteins into cells may influence the cell cycle and has to be proceeded with care, if the POI is not expressed natively by the cell. If the fusion protein is co-expressed with the native form of the POI from the genome, the rate of co-expression is set by the plasmid promotor and the DNA copy numbers within the cytosol. The fusion of a POI to a fluorescent label by transient transfection is achieved in a biological and a chemical way.

The biological way is the expression of a FP as a label. If the POI is not expressed natively by the cell, this method achieves a reliable one to one labeling of the POI in the sample.

An indirect biological way combines characteristics of the transient transfection protocols with immunohistochemistry to label the POI with an organic fluorescent probe. The POI is genetically tagged to a single GFP which specific epitopes are unique in mammalian cell lines. A

primary anti-GFP antibody labeled with an organic dye binds the GFP at the POI. This technique is often combined with camelian antibodies with high affinity to GFP ( $K_d = 0.59$  nM). The camelian antibodies have a size of about 13 kD (1.5 nm · 2.5 nm) and are termed nanobodies<sup>104</sup>.

The chemical way is to label the POI with a chemical tag sequence. A prominent chemical tag is the SNAP-tag, a derivate of the ubiquitous human *O*<sup>6</sup>-alkylguanine-DNA alkyltransferase (hAGT) that repairs *O*<sup>6</sup>-alkylated guanine in DNA by transferring an alkyl group to one of its reactive cysteine residues<sup>105</sup>. hAGT also reacts with the cell permeable *O*<sup>6</sup>-benzylguanine (BG)<sup>106</sup>. An organic dye coupled to an NHS-ester is attached to a BG derivate containing an additional amino group. By separating the guanine via the hAGT, the organic dye is covalently bound to the protein.

### 3.5.1 Transient Transfection with Turbofect

Cells were plated and grown on 8-well microscope cover glass chambers (Sartstedt) up to 80% confluency. The cells were rinsed 3 times in PBS and transferred to Opti-MEM (Life Technologies). Cationic plasmid complex formation was induced by incubating 8 µg of plasmid in 800 µl Opti-MEM containing 16 µl TurboFect (Thermo Scientific) for 20 min at room temperature. For transfection the cells were incubated in Cationic plasmid complex diluted 1:3 with Opti-MEM at 37 °C and 5% CO<sub>2</sub> for 2 h. The cells were rinsed 3 times in PBS and incubated in Opti-MEM at 37 °C and 5% CO<sub>2</sub> over night.

### 3.5.2 Transient Transfection with FugeneHD

Cells were plated and grown on 8-well microscope cover glass chambers (Sartstedt) up to 80% confluency. The plasmid was diluted in water to a concentration of 1 µg/µl. A transfection solution was prepared containing 98 µl medium, 2 µg plasmid, and 6 µl FugeneHD (Promega) and incubated at room temperature for 20 min. For transfection the cells were incubated in transfection solution diluted 1:3 with medium at 37 °C and 5% CO<sub>2</sub> over night.

### 3.5.3 Transient Transfection by Electroporation

Cells were harvested and rinsed with PBS once. The cell pellet was resuspended to a concentration of  $1.3 \cdot 10^7$  cells/ml in serum-free medium containing 10 mmol/l dextrose (Sigma), 0.1 mmol/l dithiothreitol (Sigma) and 10 µg plasmid. 500 µl cell suspension were transferred to a 0.4 cm cuvette (Invitrogen) and electroporated by a Gene Pulser Xcell System (Bio Rad) at

300 V with a capacity of 950  $\mu\text{F}$ . Transfected cells were incubated at 37 °C and 5%  $\text{CO}_2$  over night washed twice in PBS and transferred to an 8-well microscope cover glass for fixation.

## 3.6 Optical Setups

Three optical setups were built during this thesis, and will be described in the following.

### 3.6.1 Wide Field Setup

The wide field setup consist of a laser unit (see figure 3.1, a), a microscope (IX71, Olympus or Eclipse Ti, Nikon) and a detection unit (see figure 3.1, b and c). It is aligned on an air damped optical table (Opta). Within the laser unit the different laser lines of a water cooled argon-krypton laser (2.5 W multi line spectrum, 476, 488, 514, 521, 531, 568, 647 nm (lines above 100 mW), Innova 70 C, Coherent) can be selected by an *acousto optic tunable filter* (AOTF) (A.A. Opto Electronic). Additional band pass filters (AHF) are used for clean up. The laser line of a diode laser emitting at *ultra-violet* (UV) wavelengths (405 nm diode laser, Cube 405-100C, 100 mW, Coherent) is coupled into an optical fiber (Thorlabs) and aligned with the argon-krypton laser lines by an appropriate dichroic beam splitter (AHF) behind the AOTF. The overlaid laser beams are expanded by a Galilei telescope consisting of two achromatic lenses (Linos), resulting in a laser beam with short Rayleigh length. The laser beam is coupled into the microscope through the back port by a mobile 45° mirror (Thorlabs) that enables the parallel translation of the laser beam and allows for infinitely adjustable illumination angles from wide field over HILO into TIR. The microscope itself consists of a filter wheel containing several dichroic beam splitters that separate the illumination light from the fluorescence light, a second filter wheel containing clean up filters and additional reflective optics that direct the fluorescence light to one of the side ports. The selected dichroic beam splitter reflects the illumination light onto the sample and lets pass the fluorescence emission. The beam waist of the short Rayleigh length illumination light is placed onto the BFP of the objective (60x, NA = 1.45, Olympus or 100x, NA = 1.49, Nikon, both oil immersion and suitable for TIR illumination) by the Galilei telescope, resulting in a nearly parallel illumination with a long Rayleigh length. The fluorescence emission is collected by the objective, passes the dichroic beam splitter, and the second filter wheel containing several filters that select the desired range of the fluorescence spectrum. An insertable optovar lens may increase the microscopic magnification by the factor of 1.6.



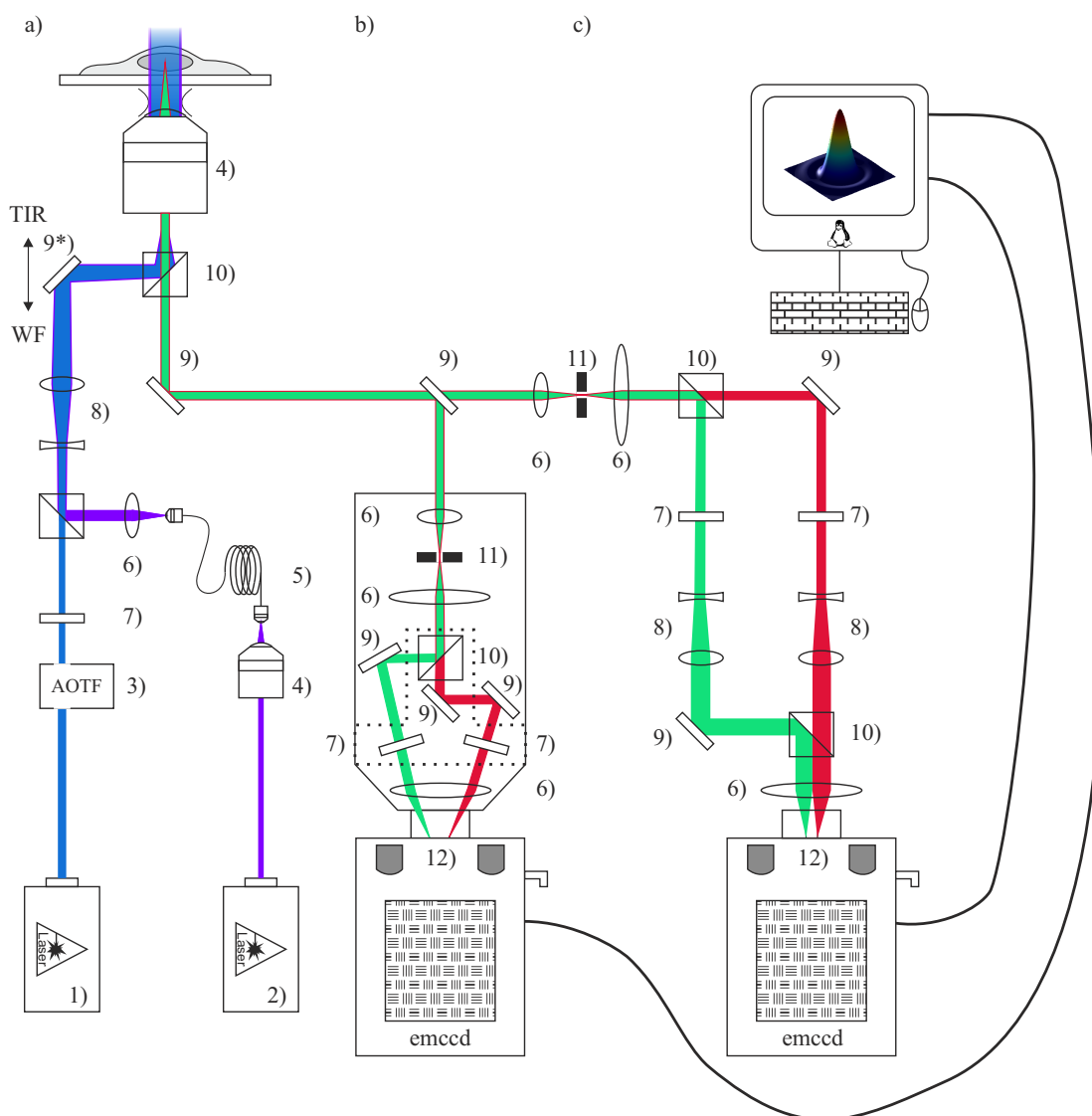


Figure 3.1: **Wide field setup**

The custom-built multi-channel wide field setup for single molecule fluorescence detection is split into two different parts. The illumination unit a), and either a detection unit, comprising a dual view and an EMCCD camera b), or a custom build two-color detection unit c).

1) argon-krypton laser, 2) UV-laser, 3) AOTF, 4) objective, 5) optical fiber, 6) lens, 7) filter, 8) Galilei telescope, 9) mirror, 10) dichroic, 11) aperture, 12) EMCCD camera

The detection unit is attached to the side port of the microscope, consisting of a dualview (DV2, Photometrics) and an air cooled EMCCD camera (Ixon DU 897 (512\*512 pixel, 16  $\mu\text{m}$ , Andor). The dualview can be switched between two operating states. With no further optics inserted (optics within the dotted frame in figure 3.1 b) it directs the fluorescence light to the EMCCD camera resulting in a single image on the entire chip. By inserting an additional dichroic beam

splitter and two clean up filters the fluorescence light is separated in two spectral by channels that are imaged next to each other on the EMCCD chip. This enables parallel two-color imaging.

By inserting a cylindrical lens (10 m CVI, Laser Optics and Melles Griot) into the fluorescence light path after the second filter wheel, an astigmatic distortion of the microscope PSF is achieved used for *three dimensional* (3D) imaging. The degree of PSF distortion depends on the axial position of the emitter, and therefore can be used to obtain information on the 3D distribution of fluorophores (see chapter 2.9.3).

The fully automatic microscope is controlled by the open source software platform micro manager ( $\mu$ manager)<sup>107</sup>. Sample temperature control is achieved by a custom build heating chamber located at the sample table.

#### 3.6.2 Ensemble Spectrometer

By introducing a flexible mirror in the illumination unit of the wide field setup, laser light is guided into a cuvette carrier (Thorlabs). The fluorescence emission propagating orthogonal to the illumination light is filtered by a band pass filter and coupled into a fiber spectrometer (CCS 200, Thorlabs) by a collimator (Thorlabs).

Absorption spectra of biomolecules were measured with a commercial absorption spectrometer (Cary 100 UV-Vis, Agilent-Technologies) to determine the degree of labeling, and the protein concentration.

#### 3.6.3 Confocal Setup

The confocal setup consists of a laser unit, a custom built microscope, a detection unit, and a correlation unit. It is aligned on two separated breadboards fixed on an air damped optical table (Opta) (see figure 3.2). Within the laser unit a red emitting diode laser (640 nm, 100 mW, Coherent) and a green emitting Nd-YAG laser (532 nm, 45 mW, Coherent) are passing a clean-up filter (AHF) and are overlaid by a dichroic mirror (AHF). The desired wavelength and intensity may be chosen by an AOTF (A.A. Opto Electronic). Afterwards the beam is coupled into a fiber (Thorlabs) by an air immersion objective (10x, NA = 0.25, Olympus). The illumination light from the fiber is coupled into the microscope pathway by a collimator (6 mm), and reflected onto the back focal plane of a water immersion objective (60x, NA = 1.20, Olympus). The collimated beam has a broad Rayleigh length and thus the objective achieves a focussed illumination of the sample. The fluorescence emission is collected by the same water objective. It is separated from the excitation light by a dichroic mirror and mediated as parallel

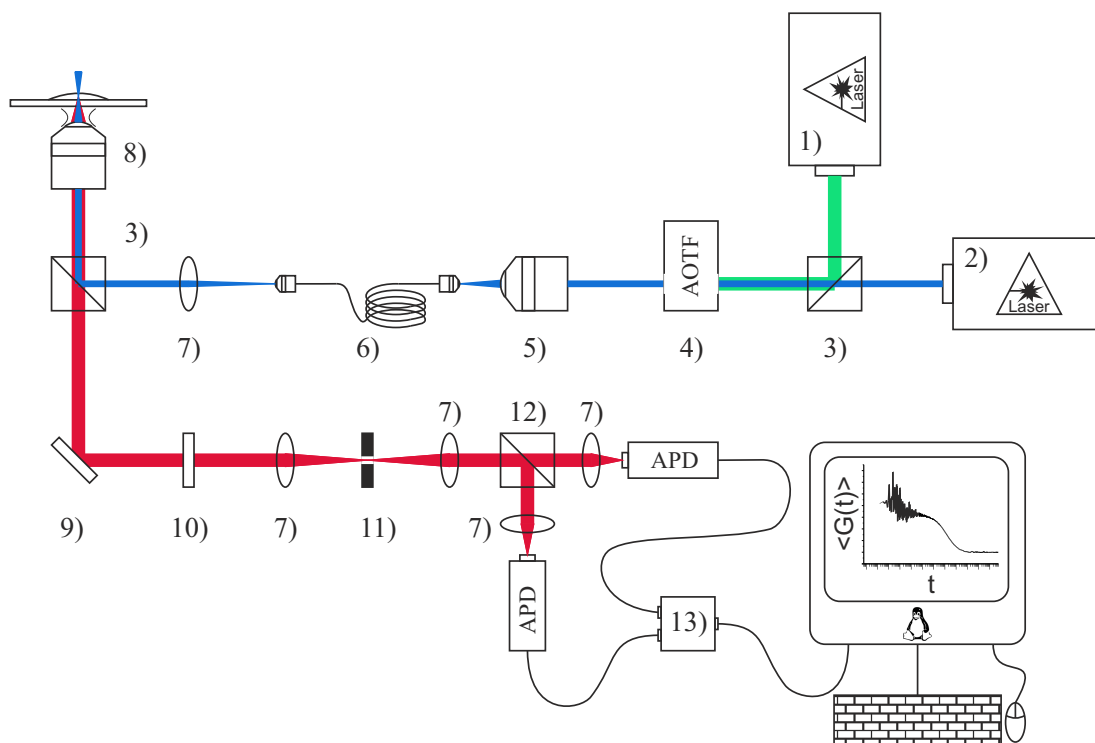


Figure 3.2: **Confocal setup**

The custom-built multi-channel confocal setup allows for auto- or cross-correlation analysis of the fluorescence signal occurring from the confocal volume.

1) green laser, 2) red-laser, 3) dichroic, 4) AOTF, 5) objective, 6) optical fiber, 7) lens, 8) microscope objective, 9) mirror, 10) filter, 11) pinhole, 12) 50/50 beam splitter, 13) external correlator card

light to the detection unit. The effective detection volume is formed by a two lens Kepler telescope ( $f_1 = 100$  mm,  $f_2 = 100$  mm) placed in the distance  $d = f_1 + f_2$ , and a pinhole (diameter = 100  $\mu$ m) at the Fourier transform plane of the telescope that is confocal with the focal plane of the microscope objective. After passing the pinhole, the detection light is split by a 50/50 beam splitter (AHF), cleaned by additional band pass filters (AHF) and focussed by a convex lens ( $f_3 = 25.5$  mm) onto an APD detector (PerkinElmer, Optoelectronics). The intensity time signal from the two APD detectors are cross-correlated by an external correlator card (Flex03LQ, Correlator.com). To identify the focal plane of the objective within the sample, a part of the non filtered detection light is directed to a *charge-coupled device* (CCD) camera. The sample temperature was controlled by cooling the water immersion objective and the sample table with a custom-built closed water cooling circuit.

## 3.7 Acquisition of Single Molecule Localization Microscopy Data

### 3.7.1 Composition of dSTORM Switching Buffer

Controlled photo-switching conditions were achieved by a switching buffer comprising a pH-stabilizing buffer system, a reduction reagent (e.g. MEA, or AA) and, if necessary, an enzymatic oxygen scavenging system. As each fluorophore needs individual buffer conditions to achieve a switching behavior appropriate for dSTORM imaging, the switching buffer was prepared as a three-component stock solution system (glucose solution, MEA solution, and enzyme solution), that allows for fluorophore-individual buffer compositions.

Glucose Solution		
5	g	glucose
45	ml	PBS
5	ml	glycerine > 99 %
MEA Solution		
1	M	MEA-HCL
10	ml	PBS
Enzyme Solution		
100	$\mu$ l	catalase 40k – 60k units/mg
200	$\mu$ l	TCEP 1 M
25	ml	glycerine > 99 %
22.5	ml	<i>dH<sub>2</sub>O</i>
1.25	ml	KCL 1 M
1	ml	Tris-HCL pH 7,5
50	mg	glucose oxidase

Stock solution aliquots were stored at  $-20$  °C and thawed on ice before use. The composition of 1 ml/litre switching buffer appropriate for dSTORM experiments with Alexa Fluor 647 can be found in table 3.1.

### 3.7.2 Acquisition of dSTORM Data

Acquisition of dSTORM data was performed on a wide field setup suitable for TIR illumination (see chapter 3.6.1), using a fluorophore specific switching buffer (see table 3.2). For each dSTORM image 3,000 to 10,000 frames were recorded with a frequency of 10 to 100 Hz. The sample was illuminated by continuous irradiation with a read out laser with a power density

**Table 3.1: Switching Buffer for Alexa Fluor 647:**

Specific compilation of a switching buffer from stock solutions, appropriate for dSTORM experiments with Alexa Fluor 647

Ingediant	Volume
PBS	350 $\mu$ l
glucose solution	500 $\mu$ l
MEA solution	100 $\mu$ l
KOH	to adjust pH to 7.5 – 8
enzyme solution	50 $\mu$ l

of 1 to 4 kW/cm<sup>2</sup>, and if necessary a switching laser with a power density of 0.2 to 1 kW/cm<sup>2</sup>. The appropriate illumination conditions for the used organic dyes are summarized in table 3.3.

**Table 3.2: Switching Buffer Compilations:**

Fluorophore specific compilation of switching buffer

Dye	Reduction Reagent	Oxigen Depletion	pH
Alexa Fluor 488	100 mmol/l MEA	–	7.5
Alexa Fluor 532	100 mmol/l MEA	+ / –	8
Cy 5	100 mmol/l MEA	+	7.5 – 8
Alexa Fluor 647	100 mmol/l MEA	+	7.5 – 8
ATTO 655	10 mmol/l MEA	–	8
ATTO 655	50 $\mu$ mol/l AA in D <sub>2</sub> O	–	8

### 3.7.3 Acquisition of PALM Data

Acquisition of PALM data was performed on a wide field setup suitable for TIR illumination (see chapter 3.6.1). For each PALM image 3,000 to 10,000 frames were recorded with a frequency of 10 to 100 Hz. The sample labeled with either mEOS2, or tdEOS were illuminated continuously with  $\lambda_{\text{read}} = 568$  nm with a power density of 1 to 2 kW/cm<sup>2</sup>. Photo-conversion was performed by irradiation with  $\lambda_{\text{conv}} = 378$  nm or 405 nm. The power density of the photo-

Table 3.3: **dSTORM Illumination conditions:**

Fluorophore specific illumination conditions for dSTORM experiments

Dye	Family	$\lambda_{switch}$ [ nm ]	$\lambda_{read}$ [ nm ]
Alexa Fluor 488	Rhodamine	405	488
Alexa Fluor 532	Rhodamine	–	532
Cy 5	Cyanine	488	647
Alexa Fluor 647	Cyanine	488	647
ATTO 655	Oxazine	–	647

conversion light was increased during the measurement in order to achieve a stable number of photo-converted fluorophores per frame.

#### 3.7.4 Acquisition of sptPALM Data

Acquisition of sptPALM data was performed at 37 °C on a wide field setup suitable for TIR illumination (see chapter 3.6.1). Cells transfected with a tdEOS-fusion protein were identified by the native tdEOS fluorescence emission at  $\lambda_{nat} = 506$  nm with irradiation at 488 nm. For each PALM image 15,000 to 90,000 frames were recorded with a frequency of 50 Hz. The sample was illuminated continuously with  $\lambda_{read} = 568$  nm with a power density of 1 to 2 kW/cm<sup>2</sup>. Photo-conversion was performed by constant irradiation with  $\lambda_{conv} = 378$  nm or 405 nm. The power density of the photo-conversion light was kept sufficiently low in order to achieve a stable number of photo-converted fluorophores per frame.

### 3.8 Single Fluorescent Probe Localization Algorithms

All SMLM raw data consist of multi-image stacks with up to millions of spatiotemporal separated PSFs. In order to achieve a fast and robust molecule detection most localization algorithms are based on two steps. A fast pre-selecting routine that identifies candidates for being possible fluorophore PSFs, followed by a time consuming PSF fitting routine that verifies true fluorophore PSFs and estimates their coordinates. Here, two localization algorithms used in this thesis shall be explained in more detail.

### 3.8.1 The rapidSTORM Algorithm

The *rapid yet accurate program implementing the direct stochastic optical reconstruction microscopy* (rapidSTORM) algorithm is optimized for static SMLM experiments that are characterized by long-lasting equilibria, such as they occur in dSTORM experiments with no need for further irradiation adjustments during the experiment. But in principle it is capable of analyzing every sort of SMLM experiment. Heart of rapidSTORM is the rapidSTORM engine (see algorithm 2) that converts an image stack of a SMLM experiment into a single molecule localization list by *maximum likelihood estimate* (MLE).

rapidSTORM comprises a large toolbox of functions to analyze static SMLM experiments. To list all of these functions would go far beyond the scope of this chapter. The interested reader will find additional information about rapidSTORM in<sup>108-111</sup>

### 3.8.2 The PALM Tracer Algorithm Part I

An alternative to MLE based Gaussian fitting of single emitter PSFs is based on wavelet segmentations followed by centroid estimation<sup>112</sup>. The PALM Tracer engine (see algorithm 3) uses an "à trous" wavelet transform which reliably filters noise and background<sup>113</sup>, allowing a precise threshold based object segmentation followed by a centroid extraction. An optional watershed algorithm can be used for additional segmentation of sparse overlapping PSFs. A comparison of the two techniques revealed that on the one hand the wavelet segmentation needs a far lower number of computing operations than MLE, which is an iterative algorithm consisting of at least 30 iterations to estimate 6 parameters ( $x, y, \sigma_x, \sigma_y, \text{intensity, offset}$ ). On the other hand MLE exceeds the wavelet segmentation in localization accuracy of static samples<sup>112</sup>.

### 3.8.3 The PALM Tracer Algorithm Part II

sptPALM data is processed via the PALM Tracer routine<sup>114</sup>. It is achieved by target segmentation and identification by the previously described wavelet segmentation (see chapter 3.8.2) followed by a *multidimensional image analysis* (MIA) (see algorithm 4). Single fluorophores are imaged in multiple adjacent frames and identified by matching different photo-physical char-

---

**Algorithm 2:** rapidSTORM engine

---

**Data:** image stack  $S$ ;

**Data:** assumed intensity of Gaussian PSF envelope  $A_0$ ;

**Data:** assumed standard deviations of Gaussian PSF envelope  $\sigma_x$  and  $\sigma_y$ ;

**Result:** single molecule localization list  $L$ ;

```

1 create list of localizations L;
2 for all source images I in S do
    /* fast pre-selection of possible candidates */
3 blurr images I;
4 identify local maxima by non-maximum suppression;
5 write local maxima in candidate list C;
6 sort C by quality;
    /* precise coordinate estimation of fluorescent probes */
7 for all candidates in C do
8     check quality of candidate;
9     if candidate is of sufficient quality then
10         fit Gaussian envelope to the raw image PSF of the candidate by least square
            fitters resulting in a fit F;
11         evaluate likelihood G of F describing a true Gaussian PSF envelope with  $A_0$ ,  $\sigma_x$ 
            and  $\sigma_y$ ;
12         if G likely describes a true Gaussian PSF envelope then
13             write candidate coordinates to L;
14             remove candidate from C;
15         else
16             remove remaining candidates from C;

```

---

acteristics, that are depending on the fluorescent protein's PSF:

$$C(PSF) = (C_x(PSF), C_y(PSF)) \quad (3.3)$$

$$I(PSF) = \sum_{pxl \in PSF} I(pxl) \quad (3.4)$$

$$A(PSF) = \sum_{pxl \in PSF} 1 \quad (3.5)$$

$$\langle I(PSF) \rangle = \frac{1}{\sum_{pxl \in PSF} 1} \sum_{pxl \in PSF} I(pxl) = \frac{1}{A(PSF)} I(PSF) \quad (3.6)$$



---

**Algorithm 3:** PALM Tracer localization engine

---

**Data:** image stack  $S$ ;  
**Data:** assumed size of Gaussian PSF  $A_0$ ;  
**Result:** single molecule localization list  $L$ ;

- 1 create list of localizations  $L$ ;
- 2 **for all source images  $I$  in  $S$  do**
  - 3 fast noise and background reduction by "à trous" wavelet filtering;
  - 4 threshold based image segmentation;
  - 5 watershed based segmentation of sparse overlapping PSFs;
  - 6 write segments in candidate list  $C$ ;
  - 7 **for all candidates in  $C$  do**
    - 8 check candidate size;
    - 9 **if candidate has approximately size  $A_0$  then**
      - 10 centroid estimation of candidate;
      - 11 write candidate centroids to  $L$ ;
    - 12 remove candidate from  $C$ ;

---

With  $C(PSF)$  indicating the center of mass for every dimension,  $I(PSF)$  indicating the absolute intensity by the sum of the pixel intensity  $I(px, l)$  covered by the PSF,  $A(PSF)$  indicating the area covered by the PSF in  $px, l$ , and  $\langle I(PSF) \rangle$  indicating the absolute intensity  $I(PSF)$  standardized according to  $A(PSF)$ . For each identified localization  $n$  during the measurement these characteristics are measured and stored in a vertex  $V^n$ . By using PC-FPs the transitions between different fluorescent states have to be taken into account. Fluorescent labels may convert to the bright state, further referred to as *birth effect*, or they might photobleach, further referred to as *death effect*. For this purpose an empty vertex  $V^0$  is generated.

The diffusive characteristics of the measured particles however are defined by the biophysical behavior of membrane proteins at the single molecule level. Being integrated in the cell membrane, only lateral diffusion is allowed. With no additional further event this will be referred to as *continuous*. Membrane proteins may change their organization during the observation time. Monomers for example may reorganize into dimers or multimers, which would lead to the overlap of two PSFs, further referred to as *fusion event*. Dimeric structures on the other hand may dissociate into monomers, which would lead to a splitting of one PSF into two. This will be further referred to as *splitting event*. For the sake of completeness it should be mentioned

that the origin of *birth* and *death* events may also be a biological one, if particles are integrated into the membrane or vice versa membrane proteins are internalized and may no longer be detected using TIR illumination.

On the basis of this biophysical model for membrane integrated fusion proteins the temporally measured data can be analyzed for the energetically most probable displacement of every  $V^h$ , with  $A \subset V_n$  and  $B \subset V_{n+1}$  being the proper subset of all vertexes that belong to a trajectory lasting from frame  $n$  to frame  $n + 1$ . Therefore, each  $A$  and  $B$  may contain  $m_V = 1$  to  $m_V = 3$  vertexes and are defined in table 3.4.

Table 3.4: **Vertex Transitions:**

List of possible vertex transitions between adjacent frames

event	frame $n$	frame $n + 1$	#vertexes
birth event:	$A = V^0$	$B = V_{n+1}^j$	$m_V = 1$
death event:	$A = V_n^h$	$B = V^0$	$m_V = 1$
continuous event:	$A = V_n^h$	$B = V_{n+1}^j$	$m_V = 2$
fusion event:	$A = V_n^h + V_n^i$	$B = V_{n+1}^j$	$m_V = 3$
splitting event:	$A = V_n^h$	$B = V_{n+1}^j + V_{n+1}^k$	$m_V = 3$

The trajectory energy of a single event calculates to:

$$\sum(A, B) = m_V \left( \sum_{C(PSF)} (A, B) + \sum_{I(PSF)} (A, B) + \sum_{\langle I(PSF) \rangle} (A, B) \right) \quad (3.7)$$

The sum of all individual event energies over the complete single molecule experiment gives the global energy  $J(E_a)$  of a distinct possible diffusion behavior of the complete vertex set  $E_a$ . Possible errors within  $E_a$  caused by false vertex connections are minimized by a simulated annealing algorithm<sup>115</sup> exceeding high energy barriers in the energy landscape by insertion of random mutations of random selected vertex connections followed by an energy minimization. The overall number of possible vertex interactions is limited by a distance threshold  $r_{max}$ , that only allows vertex connections over adjacent frames at a distance lower than  $r_{max}$ , to reduce computing time. In the optimal case the vertex connection set  $E_{opt}$  returned by the simulated annealing routine represents the global minimal energy  $J(E_{opt})$  and most likely yields the real diffusion of the detected particles.

---

**Algorithm 4:** PALM Tracer MIA engine

---

**Data:** Vertex list  $V_n^h(C_{PSF}, I_{PSF}, \langle I_{PSF} \rangle)$ ;

**Data:** estimated diffusion threshold  $r_{max}$ ;

**Result:** energy optimized vertex connection set  $E_{opt}$ ;

```

1 create empty vertex connection set  $E_{opt}$ ;
2 create initial vertex connection set  $E_1$ ;
3 set  $E_{opt} = E_1$ ;
4 repeat
5   | change  $E_1$  by point mutation concerning  $r_{max}$  resulting in  $E_1^*$ ;
6   | calculate  $\Delta J = J(E_1^*) - J(E_1)$ ;
7   | if  $\Delta J < 0$  then
8   |   | set  $E_1 = E_1^*$ ;
9   |   minimize  $J(E_1)$  by simulated annealing;
10  | if  $J(E_1) < J(E_{opt})$  then
11  |   | set  $E_{opt} = E_1$ ;
12 until  $J(E_{opt})$  converges ;

```

---

### 3.9 Acquisition of FCS Data

For sample preparation soluble TNF $\alpha$  labeled with Alexa Fluor 647 N was diluted to a concentration of 5 nmol/l in PBS containing 0.05% Tween-20. For FCS measurements 75  $\mu$ l sample solution were transferred into the cavity of Menzel microscope cover glasses (Thermo Scientific). Each measurement was performed in a depth of 40  $\mu$ m. Acquisition of FCS data was performed at  $\approx 21$   $^{\circ}$ C on a confocal setup (see chapter 3.6.3). The sample was irradiated at 647 nm with a power of 40 mW AOTF transmission. The intensity-time signal was recorded for 60 s to 600 s. The split fluorescence emission was cross correlated. The cross correlation signal between  $\tau = 10^{-6}$  s and  $\tau = 10^{-1}$  s was fit to a model of two-dimensional diffusion by a custom written Levenberg-Marquardt algorithm (see chapter 2.10.1). The diffusion coefficient of freely diffusing proteins was determined by diffusion time analysis of ATTO 655 molecules with known diffusion coefficient  $\tau_D = 404 \pm 10$   $\mu$ m<sup>2</sup>/s at 23  $^{\circ}$ C<sup>77,116</sup>.

---

## Chapter 4. | Results and Discussion I: Publications

The developmental process of the imaging-systems for localization-based super-resolution light-microscopy in physical biology from first two color approaches to their application in systems biology have been published step by step in the following publications (\* indicates an equal contribution of the authors to this work):

1. U. Endesfelder, **S. Malkusch**, B. Flottmann, J. Mondry, P. Liguzinski, P. J. Verveer and M. Heilemann, "Chemically induced photoswitching of fluorescent probes—a general concept for super-resolution microscopy", *Molecules*, vol. 16, no. 4, pp. 3106-3118, 2011, doi: 10.3390/molecules16043106  
**Author Contribution:** Design of optical setups, experimental design of dual color experiments, development of post processing algorithms, partially wrote the paper
2. **S. Malkusch\***, U. Endesfelder\*, J. Mondry, M. Gelléri, P. J. Verveer and M. Heilemann, "Coordinate-based colocalization analysis of single-molecule localization microscopy data", *Histochemistry and Cell Biology*, vol.137, no. 1, pp. 1-10, 2012, doi: 10.1007/s00418-011-0880-5  
**Author Contribution:** Design of optical setups, experimental design of dual color experiments, performance of experiments, simulation design, development of post processing algorithms, data analysis, wrote the paper
3. M. Heidbreder, C. Zander, **S. Malkusch**, D. Widera, B. Kaltschmidt, C. Kaltschmidt, D. Nair, D. Choquet, J. B. Sibarita and M. Heilemann, "TNF- $\alpha$  influences the lateral dynamics of TNF receptor I in living cells", *Biochimica et Biophysica Acta (BBA) Molecular Cell Research*, vol. 1823, no. 10, pp. 1984-1989, 2012, doi: 10.1016/j.bbamcr.2012.06.026  
**Author Contribution:** Design of optical setups, data analysis

4. **S. Malkusch\***, W. Muranyi\*, B. Müller, H. G. Kräusslich and M. Heilemann, "Single-molecule coordinate-based analysis of the morphology of HIV-1 assembly sites with near-molecular spatial resolution", *Histochemistry and Cell Biology*, vol. 139, no. 1, pp. 173-179, 2013, doi: 10.1007/s00418-012-1014-4  
**Author Contribution:** Experimental design, development of post processing algorithms, data analysis, simulation design, wrote the paper
5. W. Muranyi, **S. Malkusch**, B. Müller, M. Heilemann and H. G. Kräusslich, "Super-resolution microscopy reveals specific recruitment of HIV-1 envelope proteins to viral assembly sites dependent on the envelope C-terminal tail", *PLoS Pathogens*, vol. 9, no. 2, 2013, doi: 10.1371/journal.ppat.1003198  
**Author Contribution:** Development of post processing algorithms, data analysis
6. P. J. M. Zessin\*, C. L. Krüger\*, **S. Malkusch\***, U. Endesfelder and M. Heilemann, "A hydrophilic gel matrix for single-molecule super-resolution microscopy", *Optical Nanoscopy*, vol. 2, no. 1, 2013, doi: 10.1186/2192-2853-2-4  
**Author Contribution:** Experimental design of dual color experiments, development of post processing algorithms, simulation design, data analysis, partially wrote the paper
7. Z. Truan\*, L. Tarancón Díez\*, C. Bönsch, **S. Malkusch**, U. Endesfelder, M. Munteanu, O. Hartley, M. Heilemann and Fürstenberg A, "Quantitative morphological analysis of arrestin2 clustering upon G protein-coupled receptor stimulation by super-resolution microscopy", *Journal of Structural Biology*, vol. 184, no. 2, pp. 329-334, 2013, doi: 10.1016/j.jsb.2013.09.019  
**Author Contribution:** Development of post processing algorithms, data analysis
8. U. Endesfelder, **S. Malkusch**, F. Fricke and M. Heilemann, "A simple method to estimate the average localization precision of a single molecule localization microscopy experiment", *Histochemistry and Cell Biology*, [Epub ahead of print] , 2014, doi: 10.1007/s00418-014-1192-3  
**Author Contribution:** Experimental design, development of post processing algorithms, simulation design, data analysis, partially wrote the paper
9. L. Tarancón Díez, C. Bönsch, **S. Malkusch**, Z. Truan, M. Munteanu, M. Heilemann , O. Hartley, U. Endesfelder and A. Fürstenberg, "Coordinate-based co-localization-mediated analysis of arrestin clustering upon stimulation of the C-C chemokine receptor 5 with RANTES analogues", *Histochemistry and Cell Biology*, [Epub ahead of print] , 2014, doi:

10. F. Fricke\*, **S. Malkusch\***, G. Wangorsch, J. F. Greiner, B. Kaltschmidt, C. Kaltschmidt, D. Widera, T. Dandekar and M. Heilemann, "Quantitative single molecule localization microscopy combined with rule-based modeling reveals ligand induced TNF-R1 reorganization towards higher order oligomers", *Histochemistry and Cell Biology*, [Epub ahead of print], 2014, doi: 10.1007/s00418-014-1195-0

**Author Contribution:** Experimental design of dual color experiments, performance of experiments, development of post processing algorithms, simulation design, model design, data analysis, performance of rule based modeling, partially wrote the paper

*Molecules* **2011**, *16*, 3106-3118; doi:10.3390/molecules16043106

OPEN ACCESS

*molecules*

ISSN 1420-3049

www.mdpi.com/journal/molecules

Article

## Chemically Induced Photoswitching of Fluorescent Probes—A General Concept for Super-Resolution Microscopy

Ulrike Endesfelder <sup>1</sup>, Sebastian Malkusch <sup>1</sup>, Benjamin Flottmann <sup>2</sup>, Justine Mondry <sup>3</sup>,  
Piotr Liguzinski <sup>3</sup>, Peter J. Verveer <sup>3</sup> and Mike Heilemann <sup>1,2,\*</sup>

<sup>1</sup> Biotechnology & Biophysics, Julius-Maximilians-University Würzburg, Am Hubland, 97074 Würzburg, Germany

<sup>2</sup> Bioquant Centre, University of Heidelberg, INF 297, 69120 Heidelberg, Germany

<sup>3</sup> Department of Systemic Cell Biology, Max Planck Institute of Molecular Physiology, Otto-Hahn-Strasse 11, 44227 Dortmund, Germany

\* Author to whom correspondence should be addressed; E-Mail: mike.heilemann@uni-wuerzburg.de; Tel.: +49-931-31-84649; Fax: +49-931-31-84509.

*Received: 18 March 2011; in revised form: 8 April 2011 / Accepted: 12 April 2011 /*

*Published: 13 April 2011*

---

**Abstract:** We review fluorescent probes that can be photoswitched or photoactivated and are suited for single-molecule localization based super-resolution microscopy. We exploit the underlying photochemical mechanisms that allow photoswitching of many synthetic organic fluorophores in the presence of reducing agents, and study the impact of these on the photoswitching properties of various photoactivatable or photoconvertible fluorescent proteins. We have identified mEos2 as a fluorescent protein that exhibits reversible photoswitching under various imaging buffer conditions and present strategies to characterize reversible photoswitching. Finally, we discuss opportunities to combine fluorescent proteins with organic fluorophores for dual-color photoswitching microscopy.

**Keywords:** photoswitchable organic fluorophores; fluorescent proteins; super-resolution; PALM; dSTORM

---

## 1. Introduction

The limited resolution of light microscopy has led to the development of a number of technologies that are referred to as super-resolution microscopy [1,2]. The most prominent technologies in this toolbox are stimulated-emission depletion (STED) [3], structured-illumination microscopy (SIM) [4] and single-molecule localization based methods [5-7]. Among the different methods, only the single-molecule localization-based techniques have demonstrated near-molecular resolution in biological samples. Prominent examples for these techniques are photoactivated-localization microscopy (PALM) [6], stochastic optical reconstruction microscopy (STORM) [5] and direct STORM (*d*STORM) [7]. The working principle of all these techniques is a temporal confinement of the fluorescence signal by employing photoswitchable or photoactivatable fluorescent probes, single-molecule localization with high precision and image reconstruction (Figure 1).

**Figure 1.** The principle of localization-based super-resolution microscopy with photoswitchable fluorophores. **(a)** Photoswitchable fluorescent probes exist in a bright (fluorescent) and dark (non-fluorescent) state, and can be interconverted e.g. by irradiation with light. **(b)** The total fluorescence signal is separated in time by activating a sparse subset of fluorophores. Single-molecule coordinates are determined and used to reconstruct a super-resolution image.



The key requirement of all localization-based super-resolution technologies is the availability of fluorescent probes that can be photoactivated or photoswitched [8]. Different concepts for localization microscopy have been introduced. STORM applies carbocyanine fluorophores such as Alexa647 or Cy5 and an additional activator fluorophore [5]. However, photoswitching of carbocyanine fluorophores requires the removal of oxygen [5,9] and is not compatible with live cell imaging. PALM applies photoactivatable or photoconvertible fluorescent proteins [6], has the advantage of genetic co-expression and thus stoichiometric labeling of a target protein, and also can be combined with live cell imaging [10]. The more general *d*STORM approach operates a broad range of synthetic organic fluorophores as photoswitchable units [7,8,11], and in combination with site-specific tagging approaches, can be used inside living cells [12]. A selection of photoswitchable and photoactivatable fluorophores that are nowadays used in the various approaches of super-resolution localization microscopy is presented in Table 1.

In the present paper, we first introduce the mechanisms of photoswitching of organic fluorophores under reducing conditions as they are used in the *d*STORM principle [7,11,13,14]. Building on these findings, we present our studies on how photoactivatable and photoconvertible fluorescent proteins perform under similar imaging conditions as in *d*STORM, which is under reducing buffer conditions and both in the presence and absence of oxygen. Finally, we discuss possible experimental conditions



that allow the combined use of both fluorescent proteins and organic fluorophores in dual-color localization-based super-resolution imaging with photoswitchable probes.

**Table 1.** A selection of fluorescent proteins and organic fluorophores that can be photoactivated or photoswitched and that are used in super-resolution localization microscopy (rev. = reversible, irrev. = irreversible) [7,11,13,15-21].

	Type of fluorophore	Photoactivation/-switching properties	$\lambda_{act}$ [nm]	$\lambda_{ex}$ [nm] (pre/post)	$\lambda_{em}$ [nm] (pre/post)	Reference
bsDronpa	fluorescent protein	rev. photoactivation	405	460	504	[19]
ps-CFP2	fluorescent protein	irrev. photoconversion	405	400/490	468/511	[15]
pa-GFP	fluorescent protein	irrev. photoactivation	413	400/504	515/517	[17]
Alexa 488	rhodamine	rev. photoswitching	/	496	519	[13]
Atto 520	oxazine	rev. photoswitching	/	516	538	[11]
Alexa 532	rhodamine	rev. photoswitching	/	532	553	[13]
Dendra	fluorescent protein	irrev. photoconversion	405/488	490/553	507/573	[18]
TMR	rhodamine	rev. photoswitching	405	554	580	[16]
mEOS2	fluorescent protein	irrev. photoconversion	405	506/573	519/584	[21]
Atto 565	rhodamine	rev. photoswitching		563	592	[11]
PAmCherry1	fluorescent protein	irrev. photoactivation	405	570	596	[20]
Alexa 568	rhodamine	rev. photoswitching	/	578	603	[13]
Atto 590	rhodamine	rev. photoswitching	/	594	624	[13]
Alexa 647	carbocyanine	rev. photoswitching	488/514	650	665	[7]
Atto 655	oxazine	rev. photoswitching	/	663	684	[11]
Atto 700	oxazine	rev. photoswitching	/	700	719	[11]

## 2. Results and Discussion

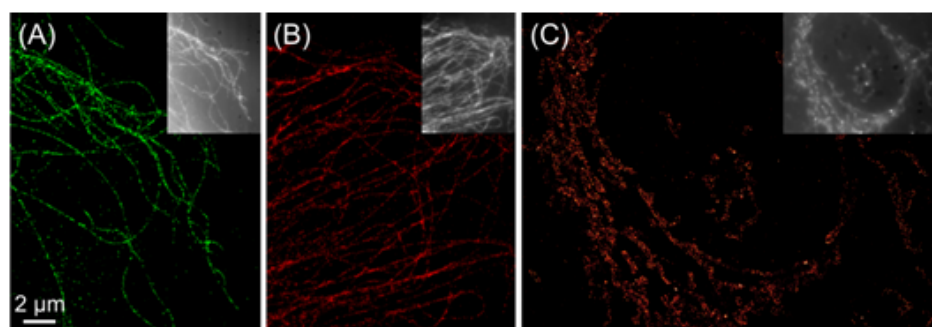
### 2.1. Operating organic fluorophores as photoswitches using redox chemistry

Synthetic organic fluorophores can be operated as photoswitchable fluorophores by exploiting their sensitivity towards reducing agents, e.g. thiol compounds, which lead to fluorescence quenching through the formation of a stable non-fluorescent state [13,14]. For the application in single-molecule localization based super-resolution imaging, a suitable fluorophore should in addition exhibit a high brightness, such that the detection of single molecules is possible. Synthetic organic fluorophores that have successfully been used for localization-based super-resolution imaging using the *d*STORM approach are e.g. the carbocyanine fluorophores (Cy5, Alexa Fluor 647 and others) [5,9], rhodamine fluorophores (Alexa Fluor 488, Alexa Fluor 532 and others) and oxazine fluorophores (e.g. ATTO655) [8,14].

*d*STORM imaging of samples is straightforward as it can be combined with established techniques such as immunofluorescence using commercially available antibodies that carry a suitable fluorophore

that can be operated as a photoswitch. *d*STORM imaging of carbocyanine fluorophores such as Alexa Fluor 647 or Cy5 is performed using an imaging buffer suited for carbocyanine photoswitching and simultaneous irradiation with 514 nm and 647 nm [5,9]. Rhodamine fluorophores, such as Alexa Fluor 532 and others, follow a slightly different mechanism. These fluorophores are also photoswitched in the presence of millimolar concentrations of MEA, but compared to the carbocyanine fluorophores tolerate oxygen. The stable off state of rhodamine fluorophores has been demonstrated to be a radical ion [13,14]. In a similar way as rhodamines, oxazine fluorophores such as ATTO655 can be operated as photoswitches in the presence of oxygen and by adding millimolar concentrations of MEA. The photoproducts in photoswitching of oxazine fluorophores have been studied with electron paramagnetic resonance (EPR) spectroscopy and by Fourier-transform infrared (FT-IR) spectroscopy in combination with theoretical calculations and involve both a radical ion as well as the transition to a fully reduced state [13,14,22]. Exemplary super-resolution images for one representative fluorophore of each of these three classes have been recorded with the *d*STORM approach and are shown in Figure 2. Beyond super-resolution imaging in fixed cells, some organic fluorophores can be operated as photoswitches inside living cells, where fluorescence quenching is caused by intracellular thiols or reducing species like glutathione [12,16]. The necessary site-specific labeling of proteins with organic fluorophores can be realized with the various chemical tags available, such as the SNAP-Tag [23] or trimethoprim tag [12].

**Figure 2.** *d*STORM imaging operating conventional synthetic organic fluorophores as photoswitches through redox-chemical processes: (a) microtubulin labeled with Alexa Fluor 532, (b) microtubulin labeled with ATTO655, (c) endoplasmic reticulum labeled with Alexa Fluor 647.

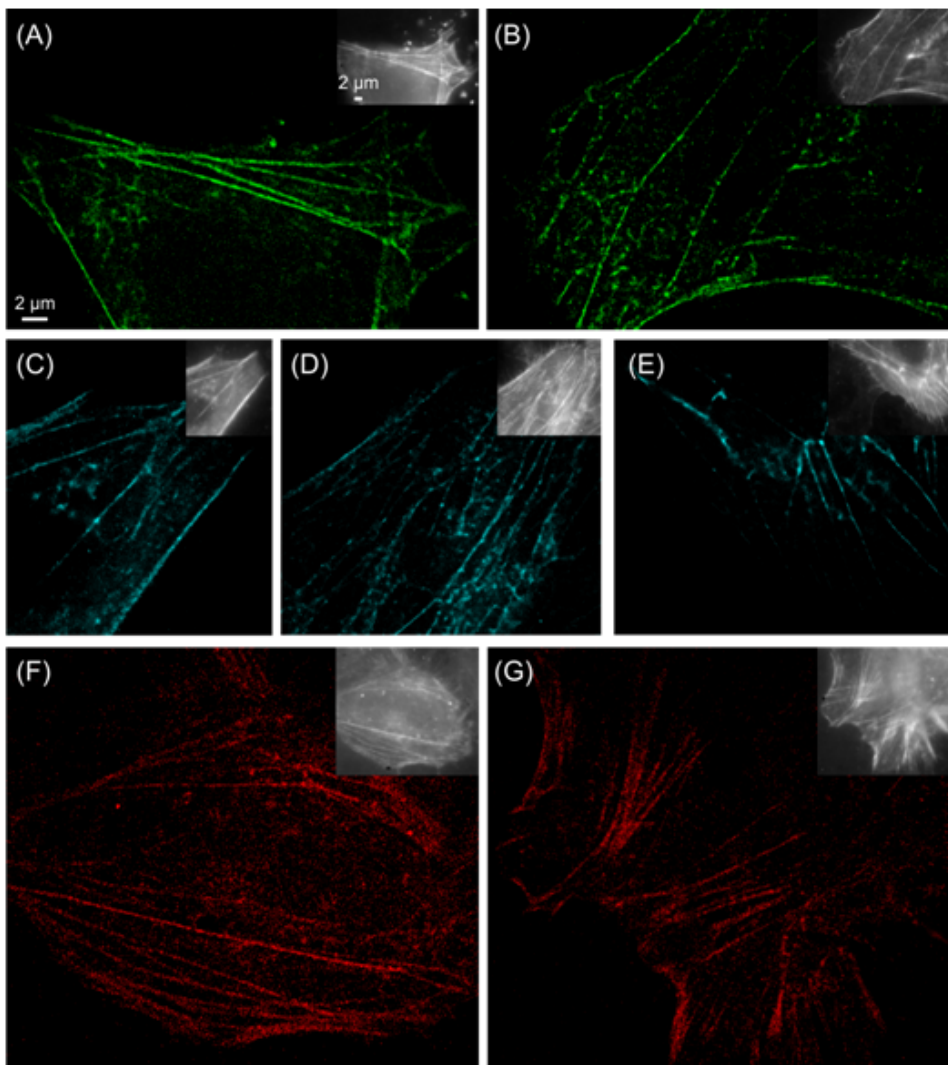


## 2.2. Photoswitching of photoactivatable and photoconvertible fluorescent proteins using redox chemistry

Compared to organic fluorophores, photoswitchable fluorescent proteins have the advantage that they can be genetically attached to a protein of interest and provide stoichiometric labeling. In addition, fluorescent proteins do not require specific imaging buffers and can be used for live-cell PALM imaging in a straightforward manner [10]. A slight disadvantage of fluorescent proteins is their lower brightness or photon yield, which directly translates into the localization accuracy and thus the achievable optical resolution [24]. In addition, experiments that aim to follow dynamic processes require multiple read-out cycles of photoswitchable fluorophores [12,25], and only few

photoswitchable fluorescent proteins are available for this purpose so far [26]. Bright and at the same time reversibly photoswitchable fluorescent proteins are thus rare, and organic fluorophores are sometimes an attractive alternative choice. Beyond these small differences and next to the particular advantages and disadvantages that both organic fluorophores and fluorescent proteins exhibit, it would be desirable to combine their use in two-color super-resolution imaging.

**Figure 3.** PALM imaging of the actin cytoskeleton in HeLa cells. The photoswitchable fluorescent protein Dendra2 (a, b), the reversibly photoswitchable protein bsDronpa (c-e) and the photoactivatable protein PAmCherry1 (f, g) are shown. Images were recorded in PBS buffer (a, c, f), in the presence of 10 mM MEA (b, d, g) and in the presence of 100 mM MEA (e).



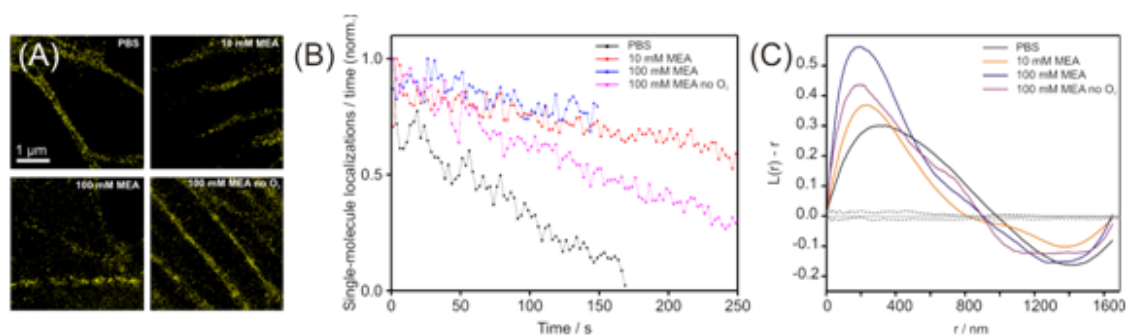
Here, we have studied the photoswitching properties of fluorescent proteins under reducing conditions as they are used for *d*STORM imaging. Therefore, we have compared the photoswitching properties in physiological buffer (PBS), in addition of a reducing agent MEA and in the presence or absence of oxygen. The fundamental initial interest here is to find out whether and how reducing

conditions impact the photoswitching properties of fluorescent proteins *per se*. Beyond this, our motivation is three-fold: first, a combination of a suitable organic dye and fluorescent protein would allow dual-color imaging using both organic fluorophores and fluorescent proteins; second, it would allow using complementary labeling strategies; and third, it could present an attractive route for two-color live-cell super-resolution imaging. We have focused in this study onto a selection of five fluorescent proteins previously used for PALM imaging, which are psCFP2 [15], bsDronpa [19], mEos2 [21], PAmCherry1 [20] and Dendra2 [18], and reducing buffer conditions as they are used for dSTORM imaging [7,13].

We have performed PALM imaging of cells co-expressing one of the fluorescent proteins with actin monomers. We used various imaging conditions for PALM imaging, i.e. in physiological buffer (PBS pH 7.4), under reducing conditions in the presence of 10 mM MEA, by adding 100 mM MEA, and in 100 mM MEA with oxygen removed from the buffer using an enzymatic oxygen scavenger. We found that all photoswitchable fluorescent proteins can be operated both in PBS as well as in PBS with 10 mM MEA added (Figure 3). This finding suggests that any of the fluorescent proteins can be combined with rhodamine and oxazine fluorophores, as these fluorophores can be operated under similar conditions, e.g. ATTO655 [13,14]. Typically, the addition of higher concentrations of MEA did deteriorate the photoswitching capabilities of the fluorescent proteins. The fluorescent proteins bsDronpa (Figure 3e), psCFP2, Dendra2 and mEos2 (Figure 4a) could be operated as photoswitches in 100 mM MEA, i.e. the highest concentration of MEA tested that is required for photoswitching of many rhodamine fluorophores [14]. Both psCFP2 (Supporting Figure 1) and mEos2 also tolerate oxygen removal and thus image buffer conditions as required to photoswitch carbocyanine fluorophores, e.g. Alexa Fluor 647, Alexa Fluor 680, Cy5 and Cy5.5 [7].

The photoswitching properties in different buffer conditions, i.e. PBS only, PBS with 10 mM MEA and PBS with 100 mM MEA and oxygen removed, were characterized in more detail for the fluorescent protein mEos2, as this protein both tolerated all buffer conditions and exhibited the highest photon yield (Figure 4a). For this purpose, two different approaches were used. In a first approach, the number of single-molecule localizations was plotted against time for the different imaging buffer conditions (Figure 4b), while the experimental parameters such as excitation intensities were kept constant. We observe an increase in the number of single-molecule localizations over time in the presence of reducing agents as well as in the presence and absence of oxygen. This finding suggests an increase in reversible photoswitching of mEos2 in the photoconverted form and is in accordance with previous findings [27]. As an alternative approach, we computed Ripley's k-function [28] in order to characterize reversible photoswitching or apparent clustering through an all distance distribution in regions of globular actin monomers (Figure 4c) (for details see experimental section). We observe a shift of the main maximum of Ripley's k-function towards shorter r-values in reducing and oxygen-free buffer. Given that the underlying distributions of fluorescent proteins used to compute the k-function was similar for all four data sets, we interpret this finding as increase in reversibility of photoswitching of mEos2 in the photoconverted form. Beyond the shift in the maximum, we observe a more confined shape of the k-function in the presence of reducing thiols as well as in the absence of oxygen. As the k-function essentially reports on single-molecule distributions over a range of distances [28,29], we interpret this confinement in an increased contribution of multiple single-molecule localizations through reversible switching of the same fluorescent protein.

**Figure 4.** Reversible photoswitching of the fluorescent protein mEos2 under reductive and oxygen-free conditions. (a) PALM images of actin-mEos2 in PBS (HeLa), 10 mM (U2OS), 100 mM MEA (HeLa) and 100 mM MEA with oxygen removed (U2OS). (b) The decay of the relative number of localizations per frame indicates an increased reversible photoswitching of mEos2 in buffers with reducing thiols. (c) Ripley's k-function corroborates reversible switching by indicating a shift to smaller distances between single mEos2 proteins (black line, expectation value, dotted grey lines, 95% confidence level of the expectation value).



### 2.3. Prospectives for dual-color localization-based super-resolution imaging

The photoswitching properties of the fluorescent proteins in the different imaging conditions open a number of possibilities to combine photoswitchable fluorescent proteins with photoswitchable organic fluorophores (summarized in Table 2). Essentially, all five proteins can be operated in combination with rhodamine and oxazine fluorophores in physiological buffer and in the presence of 10 or 100 mM MEA (see Table 2) (Figure 5). In addition, the fluorescent protein mEos2 can even be operated under buffer conditions as used for the carbocyanine fluorophores Alexa Fluor 647 and Cy5.

**Figure 5.** Dual-color imaging of HeLa cells with mEos2-actin (green color) and  $\beta$ -tubulin labeled with ATTO655 (red) via immunofluorescence in 10 mM MEA.

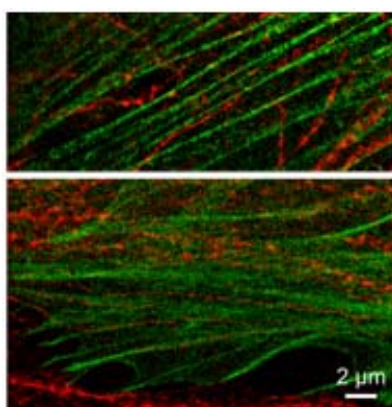


**Table 2.** Summary of suitable buffer conditions for the fluorescent proteins tested and with respect to organic fluorophore photoswitching.

	PBS	Buffer conditions for photoswitching of rhodamine/oxazine dyes 10 mM MEA	Buffer conditions for photoswitching of rhodamine/oxazine dyes 100 mM MEA	Buffer conditions for photoswitching of carbocyanine dyes 100 mM MEA, -O <sub>2</sub>
psCFP2	✓ irreversible, dim	✓ mostly reversible, dim	✓ mostly reversible, dim	✓ mostly reversible, dim
bsDronpa	✓ reversible, dim	✓ reversible, dim	✓ some reversible, dim some diffuse glowing	✗ few reversible, dim some diffuse glowing
Dendra2	✓ irreversible, dim	✓ reversible, dim	✓ some reversible, dim some diffuse glowing	✗ few reversible, dim some diffuse glowing
mEos2	✓ irreversible	✓ reversible	✓ reversible	✓ reversible
PAmCherry1	✓ irreversible	✓ mostly reversible	✗ few reversible some diffuse glowing	✗ few reversible some diffuse glowing

### 3. Experimental

#### 3.1. Sample preparation

HeLa or U2OS cells were plated and grown in Labtek 8-well chambered cover glass (Nunc, Germany) up to 80% confluency. The cells were transiently transfected with a plasmid encoding for one of the fluorescent proteins (mEos2, PAmCherry1, bsDronpa, psCFP2, Dendra2) and actin using the transfection reagent Turbofect (Fermentas, Germany). After overnight expression, the cells were fixed using 4% PFA for 10 minutes and stored in phosphate buffered saline (PBS). Labeling with organic fluorophores was done using standard immunofluorescence protocols. The microtubulin network of COS-7 cells was labeled using a rabbit anti- $\beta$ -tubulin primary antibody (Abcam, Cambridge, UK). The secondary antibody was a goat F(ab')<sub>2</sub> anti rabbit (Invitrogen, USA) that was custom-labeled with ATTO 655 following protocols published by the manufacturer (Atto-Tec, Germany). The degree of labeling was determined to 1.3. Microtubulin of HeLa cells was labeled with monoclonal anti- $\alpha$ -tubulin antibody (MS-581-P1; Thermo Scientific, Waltham, MA) and Alexa Fluor 532 labeled secondary antibody (A11002, Invitrogen, Carlsbad, CA). Staining of the endoplasmatic reticulum of HeLa cells was done using monoclonal antibody against calnexin (ab31290; Abcam, Cambridge, UK) and Alexa Fluor 647 labeled secondary antibody (A21235; Invitrogen, USA).

#### 3.2. Microscopic configuration

A standard epifluorescence microscope operated in total internal reflection fluorescence (TIRF) and equipped with suitable laser sources was used for PALM and dSTORM imaging, essentially configured as published elsewhere [6-8]. Briefly, a multi-line argon-krypton laser (Innova 70C; Coherent, USA) was coupled into an inverted microscope (IX71, Olympus, Japan) equipped with a 60x oil immersion objective (PlanApo 60x, NA 1.45, Olympus). Excitation and fluorescent light was separated using a dichroic mirror. Here either FF560/659-Di01 (AHF, Germany) or



FF410/504/588/669-Di01 (AHF, Germany) or HC576/661 (AHF, Germany) were used. The fluorescence signal was read out with an electron-multiplying CCD camera (EMCCD; Andor Ixon DU 897, Belfast, Ireland). Raw data was processed using the rapidSTORM algorithm [30].

### 3.3. PALM imaging

Fluorescent proteins were imaged with a suitable combination wavelengths provided by various laser sources: 378 nm or 405 nm and 488 nm (psCFP2, bsDronpa), 378 nm or 405 nm and 568 nm (mEos2, PAmCherry1, Dendra2). Typically, irradiation intensities of 20 to 40 mW ( $1\text{--}2\text{ kW cm}^{-2}$ ) for the read-out wavelength (488 nm or 568 nm) were used. A lower intensity of about 10 mW was used for imaging bsDronpa. Filter sets for imaging mEos2, PAmCherry1 and Dendra2 included a 568/10 bandpass filter (AHF, Germany) as clean-up filter in the excitation path, and a combination of a 568LP and a 610/75 (AHF) in the detection path. Filter sets for imaging psCFP2 and bsDronpa included a 488/10 clean-up filter (AHF) in the excitation path, and a combination of a 488LP and a 550/88 (AHF) in the detection path. Typically, 3000–6000 frames were recorded at frame rates of 100 Hz, and the experiment was terminated when all fluorescent proteins were irreversibly photobleached. In experiments that showed reversible photoswitching of the fluorescent proteins, a similar number of frames was recorded and the experiment finished prior to all fluorescent proteins photobleached.

### 3.4. dSTORM imaging

dSTORM imaging was performed in suitable imaging buffers as described elsewhere for carbocyanine [7] and rhodamine or oxazine fluorophores [8]. Briefly, photoswitching of the carbocyanine Alexa 647 was performed with 514 nm and 647 nm radiation in oxygen-depleted PBS buffer and 100 mM MEA added. Photoswitching of ATTO655 was performed in 10 mM MEA and with irradiation at 647 nm. Photoswitching of Alexa Fluor 532 was performed in 100 mM MEA and with irradiation at 514 nm.

### 3.5. Dual color imaging

Dual color imaging of ATTO655 and mEos2 was performed by sequentially imaging first ATTO655 and then mEos2. As imaging buffer, 250 mM  $\text{NaHCO}_3$  (pH8) with 10 mM MEA was used. The filter sets used were a 488/568/647-10 bandpass filter (AHF, Germany) for the excitation path. In the detection paths, a combination of a LP647 and 705/75(AHF) (ATTO655 channel) and a combination of LP568 SP630 and 610/75 (AHF) (mEos2 channel) was used. The two channels were aligned by imaging multi-labeled beads (TetraSpeck, Invitrogen) and calculating the local weighted mean using the local weighted mean function of Matlab (Mathworks, Natick, MA) [31].

### 3.6. Data analysis

Reversible switching was assessed through calculating the distribution of all localization distances within the population of distinct regions of interest (ROI) with the size of  $1.65 \times 1.65\ \mu\text{m}^2$ . In order to have comparable input data, we chose intracellular regions with a high occurrence of globular actin as ROI. Regions with filaments were avoided, because of a variable and dense structure that is typical for

actin multimers. The spatial distribution of all localizations was calculated by Ripley's K-function [28,29]:

$$K(r) = \frac{1}{n^2} \sum_i \sum_j \frac{N_r(d_{ij})}{\lambda} \quad (1)$$

where  $n$  is the total number of localizations within the ROI,  $d_{ij}$  is the distance between the localization  $i$  and  $j$ ,  $N_r$  is the number of localization around localization  $i$  within the distance  $j$  and  $\lambda$  is a weighting factor correcting for the area of the ROI.

The function is linearized:

$$L(r) = \sqrt{\frac{K(r)}{\pi}} \quad (2)$$

and then normalized:

$$H(r) = L(r) - r \quad (3)$$

so that a normal distribution would give an expected value of  $H(r) = 0$  for all  $r$  [32].

In order to account for edge effects we chose the toroidal edge correction [33]. To achieve statistical significance we employed 95% confidence envelopes produced with Monte Carlo methods [32].

#### 4. Conclusions

We have studied the photoswitching properties of the photoactivatable fluorescent protein PAmCherry1, of the photoconvertible fluorescent protein mEos2, Dendra2 and psCFP2 and of the photoswitchable fluorescent protein bsDronpa. We found that all five fluorescent proteins tolerate both physiological buffer conditions (PBS) as well as the addition of a reducing agent MEA at concentrations of 10 mM. Furthermore, we found that all proteins except PAmCherry1 tolerate higher concentrations of 100 mM MEA, as they are required also in photoswitching of some rhodamine fluorophores. Finally, we found that mEos2 and psCFP2 tolerate imaging conditions as used for photoswitching carbocyanine fluorophores, *i.e.* 100 mM MEA and an oxygen-free buffer. We have analyzed the impact of the various buffer conditions on the photoswitching properties for the fluorescent protein mEos2 in more detail using single-molecule localization data, and we identified reversible photoswitching. Overall, this study suggests the combination of fluorescent proteins and organic fluorophores in single-molecule based super-resolution imaging, both in fixed and in live cells.

#### Acknowledgments

The authors are grateful for funding by the German Ministry of Education and Research (BMBF, grants 0315262 to M.H., and 0315257 to P.J.V.). M.H. and B.F. are grateful for funding by the Baden-Württemberg-Stiftung, grant P-LS-SPII/11. P.J.V. is grateful for funding by the DFG as part of the NanoSci-ERA consortium, grant VE 579/1-1.



### Supplementary Materials

Supplementary Materials includes PALM images of actin-psCFP2 and can be accessed at <http://www.mdpi.com/1420-3049/16/4/3106/s1>.

### References

1. Hell, S.W. Microscopy and its focal switch. *Nat. Methods* **2009**, *6*, 24-32.
2. Heilemann, M. Fluorescence microscopy beyond the diffraction limit. *J. Biotechnol.* **2010**, *149*, 243-251.
3. Hell, S.W.; Wichmann, J. Breaking the diffraction resolution limit by stimulated emission: stimulated-emission-depletion fluorescence microscopy. *Opt. Lett.* **1994**, *19*, 780-782.
4. Gustafsson, L.; Sparen, P.; Gustafsson, M.; Pettersson, B.; Wilander, E.; Bergstrom, R.; Adami, H.O. Low efficiency of cytologic screening for cancer in situ of the cervix in older women. *Int. J. Cancer* **1995**, *63*, 804-809.
5. Rust, M.J.; Bates, M.; Zhuang, X. Sub-diffraction-limit imaging by stochastic optical reconstruction microscopy (STORM). *Nat. Methods* **2006**, *3*, 793-795.
6. Betzig, E.; Patterson, G.H.; Sougrat, R.; Lindwasser, O.W.; Olenych, S.; Bonifacino, J.S.; Davidson, M.W.; Lippincott-Schwartz, J.; Hess, H.F. Imaging intracellular fluorescent proteins at nanometer resolution. *Science* **2006**, *313*, 1642-1645.
7. Heilemann, M.; van de Linde, S.; Schuttpelz, M.; Kasper, R.; Seefeldt, B.; Mukherjee, A.; Tinnefeld, P.; Sauer, M. Subdiffraction-resolution fluorescence imaging with conventional fluorescent probes. *Angew. Chem. Int. Ed. Engl.* **2008**, *47*, 6172-6176.
8. Heilemann, M.; Dedecker, P.; Hofkens, J.; Sauer, M. Photoswitches: Key molecules for subdiffraction-resolution fluorescence imaging and molecular quantification. *Laser Photonics Rev.* **2009**, *3*, 180-202.
9. Heilemann, M.; Margeat, E.; Kasper, R.; Sauer, M.; Tinnefeld, P. Carbocyanine dyes as efficient reversible single-molecule optical switch. *J. Am. Chem. Soc.* **2005**, *127*, 3801-3806.
10. Shroff, H.; Galbraith, C.G.; Galbraith, J.A.; Betzig, E. Live-cell photoactivated localization microscopy of nanoscale adhesion dynamics. *Nat. Methods* **2008**, *5*, 417-423.
11. van de Linde, S.; Endesfelder, U.; Mukherjee, A.; Schuttpelz, M.; Wiebusch, G.; Wolter, S.; Heilemann, M.; Sauer, M. Multicolor photoswitching microscopy for subdiffraction-resolution fluorescence imaging. *Photochem. Photobiol. Sci.* **2009**, *8*, 465-469.
12. Wombacher, R.; Heidbreder, M.; van de Linde, S.; Sheetz, M.P.; Heilemann, M.; Cornish, V.W.; Sauer, M. Live-cell super-resolution imaging with trimethoprim conjugates. *Nat. Methods* **2010**, *7*, 717-719.
13. Heilemann, M.; van de Linde, S.; Mukherjee, A.; Sauer, M. Super-resolution imaging with small organic fluorophores. *Angew. Chem. Int. Ed. Engl.* **2009**, *48*, 6903-6908.
14. van de Linde, S.; Krstic, I.; Prisner, T.; Doose, S.; Heilemann, M.; Sauer, M. Photoinduced formation of reversible dye radicals and their impact on super-resolution imaging. *Photochem. Photobiol. Sci.* **2011**, *10*, 499-506.

15. Chudakov, D.M.; Verkhusha, V.V.; Staroverov, D.B.; Souslova, E.A.; Lukyanov, S.; Lukyanov, K.A. Photoswitchable cyan fluorescent protein for protein tracking. *Nat. Biotechnol.* **2004**, *22*, 1435-1439.
16. Klein, T.; Loschberger, A.; Proppert, S.; Wolter, S.; van de Linde, S.; Sauer, M. Live-cell dSTORM with SNAP-tag fusion proteins. *Nat. Methods* **2011**, *8*, 7-9.
17. Patterson, G.H.; Lippincott-Schwartz, J. A photoactivatable GFP for selective photolabeling of proteins and cells. *Science* **2002**, *297*, 1873-1877.
18. Gurskaya, N.G.; Verkhusha, V.V.; Shcheglov, A.S.; Staroverov, D.B.; Chepurnykh, T.V.; Fradkov, A.F.; Lukyanov, S.; Lukyanov, K.A. Engineering of a monomeric green-to-red photoactivatable fluorescent protein induced by blue light. *Nat. Biotechnol.* **2006**, *24*, 461-465.
19. Andresen, M.; Stiel, A.C.; Folling, J.; Wenzel, D.; Schonle, A.; Egner, A.; Eggeling, C.; Hell, S.W.; Jakobs, S. Photoswitchable fluorescent proteins enable monochromatic multilabel imaging and dual color fluorescence nanoscopy. *Nat. Biotechnol.* **2008**, *26*, 1035-1040.
20. Subach, F.V.; Patterson, G.H.; Manley, S.; Gillette, J.M.; Lippincott-Schwartz, J.; Verkhusha, V.V. Photoactivatable mCherry for high-resolution two-color fluorescence microscopy. *Nat. Methods* **2009**, *6*, 153-159.
21. McKinney, S.A.; Murphy, C.S.; Hazelwood, K.L.; Davidson, M.W.; Looger, L.L. A bright and photostable photoconvertible fluorescent protein. *Nat. Methods* **2009**, *6*, 131-133.
22. Kottke, T.; van de Linde, S.; Sauer, M.; Kakorin, S.; Heilemann, M. Identification of the Product of Photoswitching of an Oxazine Fluorophore Using Fourier Transform Infrared Difference Spectroscopy. *J. Phys. Chem. Lett.* **2010**, *1*, 3156-3159.
23. Keppler, A.; Gendreizig, S.; Gronemeyer, T.; Pick, H.; Vogel, H.; Johnsson, K. A general method for the covalent labeling of fusion proteins with small molecules *in vivo*. *Nat. Biotechnol.* **2003**, *21*, 86-89.
24. Thompson, R.E.; Larson, D.R.; Webb, W.W. Precise nanometer localization analysis for individual fluorescent probes. *Biophys. J.* **2002**, *82*, 2775-2783.
25. Endesfelder, U.; van de Linde, S.; Wolter, S.; Sauer, M.; Heilemann, M. Subdiffraction-resolution fluorescence microscopy of myosin-actin motility. *ChemPhysChem* **2010**, *11*, 836-840.
26. Manley, S.; Gillette, J.M.; Patterson, G.H.; Shroff, H.; Hess, H.F.; Betzig, E.; Lippincott-Schwartz, J. High-density mapping of single-molecule trajectories with photoactivated localization microscopy. *Nat. Methods* **2008**, *5*, 155-157.
27. Annibale, P.; Scarselli, M.; Kodiyan, A.; Radenovic, A. Photoactivatable Fluorescent Protein mEos2 Displays Repeated Photoactivation after a Long-Lived Dark State in the Red Photoconverted Form. *J. Phys. Chem. Lett.* **2010**, *1*, 1506-1510.
28. Ripley, B.D. Modelling spatial patterns. *J. Roy. Statist. Soc. B* **1977**, *39*, 172-212.
29. Lillemeier, B.F.; Mortelmaier, M.A.; Forstner, M.B.; Huppa, J.B.; Groves, J.T.; Davis, M.M. TCR and Lat are expressed on separate protein islands on T cell membranes and concatenate during activation. *Nat. Immunol.* **2010**, *11*, 90-96.
30. Wolter, S.; Schuttpelz, M.; Tscherepanow, M.; van de Linde, S.; Heilemann, M.; Sauer, M. Real-time computation of subdiffraction-resolution fluorescence images. *J. Microsc.* **2010**, *237*, 12-22.

31. Churchman, L.S.; Okten, Z.; Rock, R.S.; Dawson, J.F.; Spudich, J.A. Single molecule high-resolution colocalization of Cy3 and Cy5 attached to macromolecules measures intramolecular distances through time. *Proc. Natl. Acad. Sci. USA* **2005**, *102*, 1419-1423.
32. Haase, P. Spatial Pattern-Analysis in Ecology Based on Ripley K-Function - Introduction and Methods of Edge Correction. *J. Vegetation Sci.* **1995**, *6*, 575-582.
33. Ripley, B.D. Tests of 'randomness' for spatial point patterns. *J. Roy. Statist. Soc. B* **1979**, *41*, 368-374.

*Sample Availability:* Not Available.

© 2011 by the authors; licensee MDPI, Basel, Switzerland. This article is an open access article distributed under the terms and conditions of the Creative Commons Attribution license (<http://creativecommons.org/licenses/by/3.0/>).



## TNF- $\alpha$ influences the lateral dynamics of TNF receptor I in living cells

Meike Heidbreder<sup>a</sup>, Christin Zander<sup>b</sup>, Sebastian Malkusch<sup>a</sup>, Darius Widera<sup>b</sup>, Barbara Kaltschmidt<sup>b,c</sup>, Christian Kaltschmidt<sup>b</sup>, Deepak Nair<sup>d</sup>, Daniel Choquet<sup>d</sup>, Jean-Baptiste Sibarita<sup>d,\*</sup>, Mike Heilemann<sup>a,e,\*\*</sup>

<sup>a</sup> Julius-Maximilians-Universität, Department of Biotechnology & Biophysics, 97074 Würzburg, Germany

<sup>b</sup> University of Bielefeld, Faculty of Biology, Department of Cell Biology, 33615 Bielefeld, Germany

<sup>c</sup> University of Bielefeld, Faculty of Biology, Molecular Neurobiology, 33615 Bielefeld, Germany

<sup>d</sup> University of Bordeaux, Interdisciplinary Institute for Neuroscience, CNRS UMR 5297, F-33000 Bordeaux, France

<sup>e</sup> Johann Wolfgang Goethe-University, Institute of Physical and Theoretical Chemistry, 60438 Frankfurt/Main, Germany

### ARTICLE INFO

#### Article history:

Received 25 November 2011  
Received in revised form 31 May 2012  
Accepted 19 June 2012  
Available online 27 June 2012

#### Keywords:

TNF receptor I  
Receptor multimerization  
Photoactivation  
Single-particle tracking  
Single-molecule fluorescence

### ABSTRACT

In mammalian cells, inflammation is mainly mediated by the binding of tumor necrosis factor alpha to tumor necrosis factor receptor 1. In this study, we investigated lateral dynamics of TNF-R1 before and after ligand binding using high-density single-particle tracking in combination with photoactivated localization microscopy. Our single-molecule data indicates the presence of tumor necrosis factor receptor 1 with different mobilities in the plasma membrane, suggesting different molecular organizations. Cholesterol depletion led to a decrease of slow receptor species and a strong increase in the average diffusion coefficient. Moreover, as a consequence of tumor necrosis factor-alpha treatment, the mean diffusion coefficient moderately increased while its distribution narrowed. Based on our observation, we propose a refined mechanism on the structural arrangement and activation of tumor necrosis factor receptor 1 in the plasma membrane.

© 2012 Elsevier B.V. All rights reserved.

### 1. Introduction

Cellular functions can be controlled by external stimuli which induce specific responses such as gene transcription, proliferation or apoptosis; all of which are tightly controlled by the cell to ensure its physiological function. Such signaling is one of the most complex cellular processes, involving the reception of the signal (e.g. ligand binding to its receptor), transduction of the signal and finally the cellular response. This can be further influenced by events such as receptor oligomerization, internalization or even exocytotic release. Tumor necrosis factor-alpha (TNF- $\alpha$ ) is one of the best-characterized mediators of inflammation and binds to the transmembrane receptor TNF receptor 1 (TNF-R1) with high affinity [1,2]. TNF- $\alpha$  is mainly secreted by hematopoietic cells after stimulation with bacterial lipopolysaccharides (LPS), interleukins or interferon  $\gamma$  [3]. TNF-R1 appears to pre-assemble on the cell surface prior to signal initiation, hinting at trimerization and oligomerization [4], a reaction that has already been observed for other members of the TNF superfamily (e.g. Fas/CD95 and CD40 [5,6]). Crystal structures corroborate a trimerization of TNF-R1 to enclose the homotrimeric ligand [7]. Interestingly, it has been reported that TNF-R1 might be arranged in homodimers, which are allosterically activated under

TNF- $\alpha$  addition to produce large, stable receptor–ligand signaling complexes with intracellular partners [8,9].

Through recruitment of internal adapter proteins, TNF-R1 can either induce apoptosis by activation of Caspase-8 or survival via Nuclear Factor-kappa B (NF- $\kappa$ B) (for review see [10]). Compartmentalization seems to play an important role in this dichotomy; recruitment onto lipid rafts and internalization on one hand and cell surface signaling on the other hand are thought to separate the survival- and death-pathways spatially as well as temporally [11,12]. Multimerization events on the cell membrane might provide an additional modulation of the transduced stimulus [6,13,14]. However, *in vitro* studies of receptors by means of lipid raft extraction favor receptor aggregation without molecular interactions, creating complexes that are larger than their native counterparts [15]. In addition to the activation of NF- $\kappa$ B, TNF-R1 can activate neutral sphingomyelinase via the receptor-associated protein FAN [16] and recruitment of the polycomb-group protein EED [17].

Here, we employ photoactivated-localization microscopy in combination with single-particle tracking (sptPALM) [18] to monitor cellular responses with sub-diffraction resolution over long time periods under cell culture conditions. Single-molecule methods provide information on subpopulations and can reveal heterogeneities in TNF-R1 species of different mobility and molecular organization, the influence of ligand binding and interactions with membrane microdomains. We describe for the first time the influence of lipid raft disruption and TNF- $\alpha$  stimulation on lateral mobility of TNF-R1 with nanometric resolution and extract a refined hypothesis on the dynamics of TNF-R1 in living cells.

\* Corresponding author. Tel.: +33 5 57 57 56 06; fax: +33 5 57 57 16 84.

\*\* Corresponding author. Tel.: +49 931 31 84643; fax: +49 931 31 84509.

E-mail addresses: jean-baptiste.sibarita@u-bordeaux2.fr (J.-B. Sibarita), m.heilemann@uni-wuerzburg.de (M. Heilemann).

## 2. Materials and methods

### 2.1. Plasmid vector design

The C-terminal tEoS fusion to TNF-R1 was achieved by digesting the pcDNA3-Flag1-tEosFP vector (MoBiTec) using NotI and XhoI (NEB). TNF-R1 was amplified from the pOTB7-TNFRSF1A vector (MGC Clone Collection), using 5'-AAA AGC GGC CGC TGT CTG GCA TGG GCC TCT CC-3' (NotI) and 5'-TTT TCT CGA GGC CAA ATC TGA GAA GAC TGG GC-3' (XhoI) (Metabion). The resulting amplicon was inserted into the tEos vector to create TNF-R1-tEos (see supplemental Fig. 1). The functionality of the TNF-R1 construct was verified through dual Luciferase reporter assay as described elsewhere [19]. Cells transfected with the construct reacted comparably to TNF $\alpha$  stimulation than native cells, as an induction of NF- $\kappa$ B is still observed.

### 2.2. Cell culture and transfection

HeLa cells were grown in DMEM/F12 supplemented with 10% fetal calf serum (Gibco) and incubated at 37 °C and 5% CO<sub>2</sub>. Fresh medium was supplied every other day. For experiments, cells were transferred into chamber slides (Nunc) and allowed to rest until adhesion was re-established. Cells were transiently transfected with TNF-R1-tEos or tEoS plasmid overnight, using Fugene6 (Roche) according to the manufacturer's suggestions.

### 2.3. Sample preparation

To reset receptor distribution to the cell surface, cells were incubated with fresh medium and incubated at 4 °C for 30 min before imaging. Cells were then washed twice with cold medium and imaged in 37 °C phenol and FCS-free medium. For signal-induction or lipid raft disruption, 10 ng/ml of recombinant, soluble TNF- $\alpha$  (Gibco) and/or 10 mM methyl- $\beta$ -cyclodextrin (Sigma) or 50  $\mu$ M Nystatin (Sigma) was added at 4 °C and washed off with cold medium twice before imaging (see supplemental Fig. 1).

### 2.4. sptPALM imaging

Cells were imaged at 37 °C using a custom-built heating stage that was mounted on an inverted microscope (IX71, Olympus) equipped with a 60 $\times$  1.45NA PlanApo objective (Olympus), allowing acquisition in total internal reflection mode or oblique illumination. A 405 nm laser diode (Coherent) was used for photoactivation of tEos. A multi-line argon-krypton laser (Coherent) was used for read-out of both the native fluorescence of tEos (excitation at 488 nm) as well as for the photoconverted tEos (568 nm). Typical irradiation intensities in the range of 1–5 mW (488 nm), 10–20 mW (568 nm) and <100  $\mu$ W (405 nm) were used. The irradiation intensity was kept constant during acquisition. Appropriate filters (633SP, 610/75, 525/50; Semrock) and a dichroic mirror (DCXR560; AHF) were used to separate the fluorescence signal from the excitation light. The fluorescence emission of single fluorophores was recorded with an electron-multiplying CCD (EMCCD) camera (Ixon DU897, Andor) at 50 fps. Recording times for single cells varied from 5 min to 30 min.

### 2.5. Single molecule segmentation and tracking

Briefly, a single-cell sptPALM experiment generates a set of images from which single molecule localization and dynamics data are extracted. Single molecule fluorescent spots are localized in each image frame and tracked over time using a combination of wavelet segmentation [20] and simulated annealing algorithms [21,22]. The pointing accuracy of the whole system, which depends on the image signal to noise ratio [23,24], was quantified to about 25 nm. It was determined using fixed

samples labeled with tEos from which we analyzed a few tens of 2D distributions of single molecule positions belonging to long trajectories (more than 30 frames) by Gaussian fitting. The software package used to visualize and quantify the data on protein localization and dynamics is custom written as a plug-in for Metamorph (Molecular Devices). We evaluated an average of > 500 trajectories per cell with a minimum trajectory length of 80 ms (4 frames). Standard deviations (SD) were calculated for the mean diffusion coefficients ( $D_{\text{mean}}$ ), which allowed a better comparison with the FCS data of a previous study [35]. Standard errors of the mean (SEM) were calculated for slow fraction of receptors ( $D_{\text{mean}} < 0.005 \mu\text{m}^2/\text{s}$ ), and two-tailed Student's t-tests were performed to test for significance of the results.

## 3. Results and discussion

### 3.1. sptPALM of TNF-R1-tEos

Tracking single receptors in a membrane can provide information on dynamics and biomolecular interaction with single-molecule resolution [25]. However, classic single-particle tracking (SPT) is limited by the small number of labeled proteins that are observed in each experiment, and thus by the sparse statistics.

Recently, SPT has been combined with photoactivation-localization microscopy (PALM) [26] to sptPALM [18]. Here, a protein of interest is genetically fused to a fluorescent protein that can be photoactivated by irradiation with light [27,28]. Illumination is tuned such that only a small stochastic subset of the fluorescent proteins is transferred from an inactive (dark) to an active (fluorescent) state and tracked for up to 400 ms before bleaching (Fig. 1). This cycle is repeated many (few thousands) times profiting from the pool of labeled biomolecules in a sample, and so a large number of single-molecule trajectories are recorded. The dynamics of a protein species can be monitored over long periods of time and with single-molecule resolution, providing information on subpopulations and heterogeneities. The continuous targeting of membrane receptors with fluorophore-labeled ligands at sufficiently low concentrations is a similar concept, termed universal point accumulation for imaging in nanoscale topography (uPAINT) [29].

Here, we used the photoswitchable fluorescent protein tandem-Eos-FP (tEos) whose fluorescence emission can be converted from green (516 nm) to orange (582 nm) by irradiation with 405 nm [27]. tEos was preferred because of its brightness and photostability, and for the fact that the maturation of the protein is compatible with cell culture conditions (37 °C) [30,31]. Previous studies have shown that tEos is well suitable for single-particle tracking in combination with photoactivation [18]. tEos was genetically fused to the intracellular domain of TNF-R1. The functionality of the TNF-R1-tEos construct was shown by luciferase activity assays (see supplemental material).

### 3.2. TNF-R1-tEos is in a dynamic equilibrium

We performed sptPALM experiments in living HeLa cells and recorded several thousands of trajectories per cell over 5 or 30 min (Fig. 2). From single-molecule localization data (Fig. 2B, D), trajectories of individual TNF-R1-tEos were extracted (Fig. 2C, E). The high density of trajectories allows generating a trajectory map, revealing a heterogeneous occupation of the plasma membrane with TNF-R1 (Fig. 2C, E). These might be related to well-known spatial heterogeneities of membranes, such as raft domains or invaginations of the cell. However, we performed the experiments at the lower surface of a settled HeLa cell which is mostly flat [32], and we suggest that lipid rafts or other outer membrane domains are the source of the observed dynamics. A diffusion coefficient was calculated for each trajectory and a histogram of diffusion coefficients was generated (Fig. 2G). The broad distribution of diffusion coefficients indicates that TNF-R1 may exist in different self-assembled molecular complexes of different mobilities,

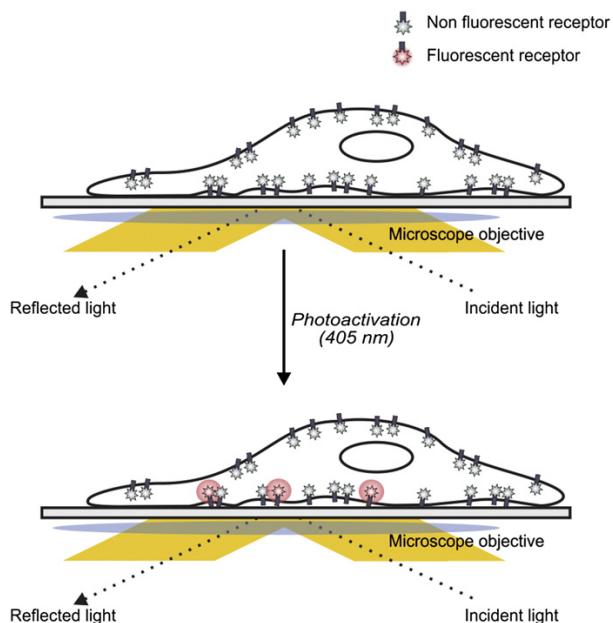


**Fig. 1.** Scheme of a sptPALM experiment to image single-molecule trajectories of membrane receptors. Cells are transfected with a receptor fused to a photoswitchable fluorescent protein. A sparse subset of fluorescent proteins is stochastically activated by photoconversion and tracked at the cell membrane using TIRF illumination. The experiment can be performed for a long duration on the same cell profiting from a large pool of non-activated fluorescent receptors.

or interacts with microdomains in the plasma membrane that affect its mobility. An average diffusion coefficient ( $D_{\text{mean}}$ ) of  $0.14 \mu\text{m}^2/\text{s}$  ( $\text{SD} \pm 0.02$ ) was calculated for uninduced HeLa cells. The average diffusion coefficient appeared constant over time, suggesting that the long-term observation as such does not affect the mobility of TNF-R1 in resting living cells (Fig. 2H). Single-molecule trajectories can further be used to

generate diffusion coefficient maps of whole cells (Fig. 3A–E) and reveal heterogeneous distributions in diffusion coefficients.

### 3.3. Cholesterol depletion induces lateral movement of TNF-R1

To investigate the association to lipid raft domains, we performed sptPALM experiments in the presence and absence of methyl- $\beta$ -cyclodextrin (MCD), a drug which depletes cholesterol from the membrane and thus disrupts lipid rafts and perturbs the actin cytoskeleton [33,34]. In accordance with [35], we observe an increase in the average diffusion coefficient to  $D_{\text{mean}} = 0.20 \mu\text{m}^2/\text{s}$  ( $\text{SD} \pm 0.04$ ) (Table 1). This observation indicates an association of TNF-R1 with lipid rafts or other membrane microdomains which hinder receptor mobility under native conditions. Furthermore, the distribution of the diffusion coefficients of TNF-R1 significantly changed compared to uninduced cells (Fig. 3F). The slow fraction of TNF-R1 receptors ( $D < 0.005 \mu\text{m}^2/\text{s}$ ) was depleted in the presence of MCD (4.9% as compared to 14.0% under native conditions), while the maximum of the distribution shifted to higher values (Fig. 3G). We attribute the slow receptor species to aggregates or networks that are trapped in or associated with a lipid raft, possibly pre-formed receptor multimers as reported before [8,12,36]. Fast species might represent single receptor molecules which are outside of lipid rafts. Note that the distinction of TNF-R1 species of different mobilities is only possible because of the excellent statistics derived from high density single-molecule tracking data, whereas other methods providing information on receptor mobility are not sensitive enough for such small changes [37,38].

### 3.4. Binding of TNF- $\alpha$ depletes slow species of TNF-R1

The addition of TNF- $\alpha$  [39] led to a moderate but not significant increase in the average diffusion coefficient  $D_{\text{mean}}$  to  $0.16 \mu\text{m}^2/\text{s}$  ( $\text{SD} \pm 0.04$ ) (Fig. 4). However, compared to uninduced cells, a significant depletion of the slow receptor species (8.4% as compared to 14.0% for native conditions) was observed, which was less than under cholesterol depleting conditions (Fig. 4A, B). This can be interpreted as the ligand-induced internalization of the slow and

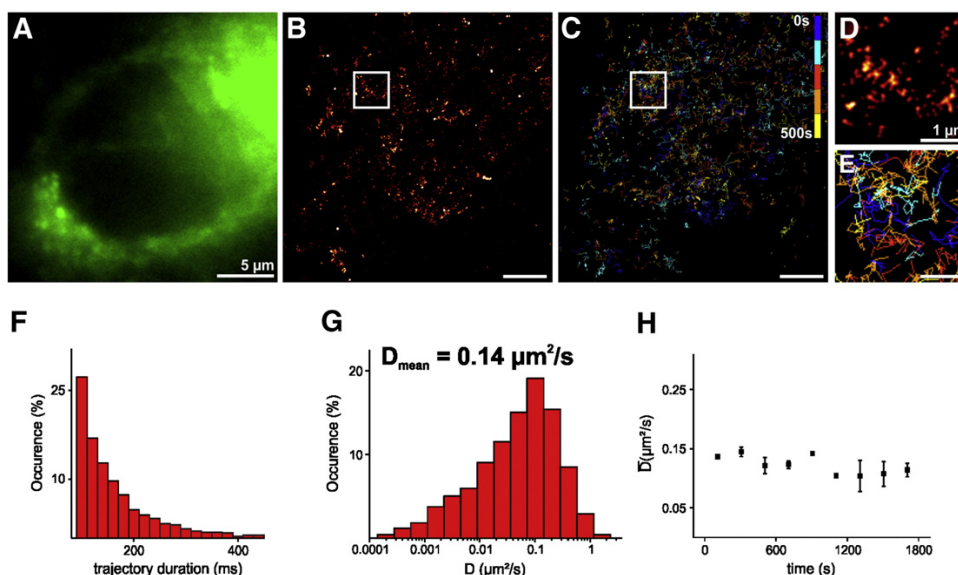


**Fig. 2.** From single-molecule localization to sptPALM. (A) Transfected cells were identified in wide field mode by monitoring the native fluorescence of unconverted tdEos. (B, D) Superresolved intensity images were reconstructed from the sequential localization of photoconverted single tdEos molecules from 5000 frames. (C, E) Map of single particle trajectories reveals heterogeneities on the cell surface. From the trajectories, distributions of trajectory durations (F) and average diffusion coefficients (G) are computed. (H) Average diffusion coefficient  $D_{\text{mean}}$  of TNF-R1-tdEos monitored over time (a representative data set from a single cell is shown).



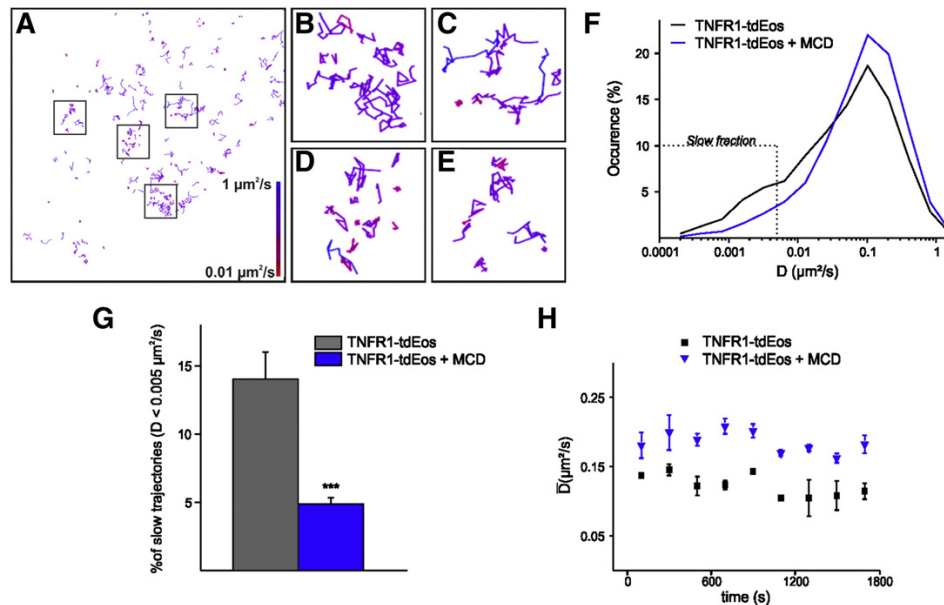


**Fig. 3.** TNF-R1 diffusion after cholesterol depletion. (A) TNF-R1 trajectories in the membrane of a HeLa cell color-coded for the diffusion coefficient (5000 frames, 100 s). (B–E) Heterogeneous diffusion patterns of TNF-R1. (F) Comparison of the diffusion coefficient distribution of TNF-R1-tdEos in the presence (blue) and absence (grey) of MCD reveals a depletion of the slow receptor fraction and a shift towards higher diffusion coefficients (average from 10 cells). (G) The population of slow receptors ( $D < 0.005 \mu\text{m}^2/\text{s}$ ) decreases after cholesterol depletion ( $p$  value  $< 0.0001$ ; error bars are standard errors of the mean (SEM)), and an overall increase in  $D_{\text{mean}}$  was observed. (H) Average diffusion coefficient  $D_{\text{mean}}$  of TNF-R1-tdEos under native conditions and after treatment with MCD monitored over time (a representative data set from a single cell each is shown). (For interpretation of the references to color in this figure legend, the reader is referred to the web version of this article.)

pre-assembled receptors already recruited to lipid rafts, happening only a few minutes after ligand binding [11,40].

We observed again a rather steady diffusion coefficient over 30 min, which suggests that only a particular fraction of TNF-R1 is recruited, presumably the fraction with the slow diffusion coefficient. Ligand addition after cholesterol depletion resulted in a drastic change of  $D_{\text{mean}}$  to  $0.24 \mu\text{m}^2/\text{s}$  ( $\text{SD} \pm 0.03$ ) that seems to have an additive effect on TNF-R1 mobility. In another experiment, we investigated the influence of the cholesterol-sequestering polyene Nystatin. Interestingly, cells treated with Nystatin showed a comparable change in the diffusion coefficient of TNF-R1 as observed for ligand induction with TNF- $\alpha$ : the slow fraction of receptors was depleted (8.7% for Nystatin, 8.4% for TNF- $\alpha$ ), while the overall  $D_{\text{mean}}$  did not increase significantly in comparison to the native condition ( $0.16 \mu\text{m}^2/\text{s}$  ( $\text{SD} \pm 0.05$ ) for Nystatin,  $0.16 \mu\text{m}^2/\text{s}$  ( $\text{SD} \pm 0.04$ ) for TNF- $\alpha$ —see supplemental Fig. 3). This suggests that the major mechanism underlying the depletion of slow receptor fractions is indeed a result of lipid raft disruption, which underscores their importance in TNF-R1 signaling [41,42]. The more drastic increase of the diffusion coefficient observed after MCD addition might then in turn be attributed to further detrimental effects of MCD on the cell, as MCD is known to negatively influence both lipid rafts

and the underlying actin cytoskeleton. A similar observation was made for CD95/Fas, another member of the TNF superfamily, where actin is needed for receptor internalization [43].

The average diffusion coefficients derived by sptPALM are in good accordance to previously published data using fluorescence correlation spectroscopy (FCS) [35] (Table 1). As an additional benefit of sptPALM as a single-molecule method, excellent statistics with single-molecule resolution are provided, particularly revealing subpopulations and heterogeneities. As an imaging method, trajectories of whole cells can be recorded while spatial heterogeneities can be revealed at the same time. Recorded trajectory maps suggest a heterogenic distribution of receptors on the cell surface, with some areas frequented more often, which might represent receptors occupying lipid rafts.

### 3.5. A refined model for TNF-R1

We investigated the dynamics of TNF-R1 on the cell surface of living cells with high-density single molecule tracking experiments. Our findings demonstrated that TNF-R1 associates with lipid rafts, probably to form pre-assembled receptor complexes with a lower mobility. Ligand induction reduced the slow fraction of TNF-R1 immediately, which might be a consequence of internalization of the receptor–ligand complexes [11] removing them from the field of view.

An explanation of these dynamic changes (Fig. 4D, supplemental Fig. 2) must not only incorporate the presence or absence of lipid rafts, but also the possibility of multimerization and internalization of TNF-R1 in response to TNF- $\alpha$ . A resting cell shows a large fraction of nearly immobile receptors (14.0%). Like other members of the TNF superfamily (e.g. Fas), TNF-R1 contains an extracellular pre-ligand assembly domain (PLAD), that facilitates oligomerization prior to ligand binding to enable a fast signal transduction [4]. As TNF-R1 signals cell death by internalization from lipid rafts, this amplifies the possible signal immediately. TNF-R1 molecules in non-raft compartments, exhibiting faster dynamics, might represent the receptor fraction responsible for survival-signaling, which has been shown to be induced on the cell surface directly [40].

**Table 1**

Average diffusion coefficients and standard deviations derived from fluorescence correlation spectroscopy (FCS) experiments (taken from [35]) and this study. The sptPALM data for each condition was averaged from 10 cells. The significance was tested against the native condition using two-tailed Student's  $t$ -test ( $p < 0.05$ ) (#no data on the standard deviation available for these values in the original work [35]).

	$D_{\text{mean}}$ derived from FCS ( $\mu\text{m}^2/\text{s} \pm \text{SD}$ )	$D_{\text{mean}}$ derived from sptPALM ( $\mu\text{m}^2/\text{s} \pm \text{SD}$ )	p value
Native	$0.12 \pm 0.09$	$0.14 \pm 0.02$	
+MCD	$0.16^{\#}$	$0.20 \pm 0.04$	0.001 (**)
+TNF- $\alpha$	$0.11 \pm 0.08$	$0.16 \pm 0.03$	0.089 (n.s.)
+TNF- $\alpha$ + MCD	$0.16^{\#}$	$0.24 \pm 0.03$	0.0001 (***)

p value significance levels were depicted as  $p > 0.05$  = not significant (n.s.);  $p \leq 0.05$  = \*;  $p \leq 0.01$  = \*\* and  $p \leq 0.001$  = \*\*\* (highly significant).

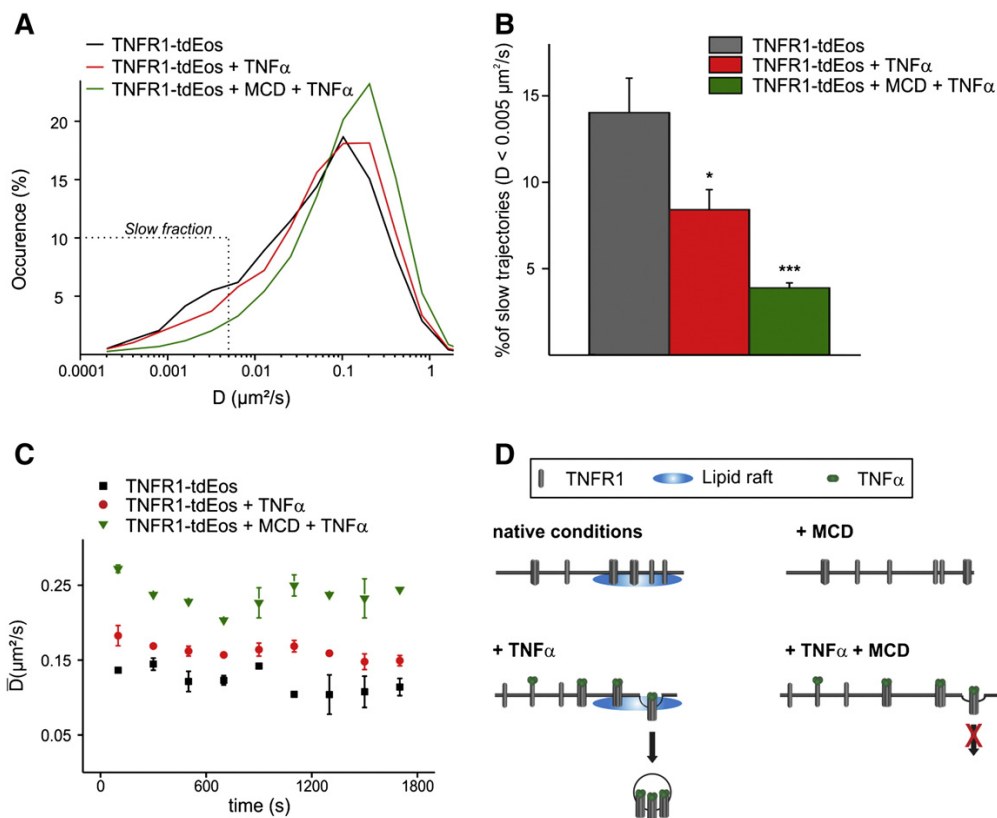


**Fig. 4.** TNF-R1 mobility upon activation by TNF- $\alpha$ . (A)  $D_{\text{mean}}$  distribution of TNF-R1-tdEos in the presence and absence of TNF- $\alpha$  under native conditions and after cholesterol depletion reveals a depletion of the slow receptor population. A shift towards higher diffusion coefficients is observed only upon MCD addition (average from 10 cells). (B) Quantification of the depletion of the slow receptor population ( $p$  value = 0.018 for TNF- $\alpha$  addition and  $p < 0.0001$  for MCD + TNF $\alpha$ ; error bars are standard errors of the mean (SEM)). (C) Average diffusion coefficient  $D_{\text{mean}}$  of TNF-R1-tdEos in the presence of TNF- $\alpha$  under native conditions and after cholesterol depletion (a representative data set from a single cell each is shown).  $D_{\text{mean}}$  is rather constant over time for TNF- $\alpha$  addition under normal ( $0.16 \mu\text{m}^2/\text{s}$ ) and after cholesterol depletion ( $0.20 \mu\text{m}^2/\text{s}$ ). (D) A refined model for TNF-R1 mobility: native cells have many pre-formed TNF-R1 clusters associated to lipid rafts (PLADs). Lipid disruption leads to an increase of TNF-R1 mobility by the lack of recruitment into larger complexes or the absence of sterical hindrances. TNF- $\alpha$  addition leads to a depletion of the slow fraction by fast internalization or the mobilization of induced receptor trimers, while TNF- $\alpha$  addition under lipid disruption stops internalization and recruitment onto lipid rafts.

Whether these receptors are also pre-assembled or present in mono- or trimers cannot be deduced from this data, but the high  $D_{\text{mean}}$  hints at smaller aggregations at most.

Disrupting lipid rafts with MCD or Nystatin might lead to a disassociation of these pre-formed complexes and thus an overall increase in receptor mobility. This could also shift the cellular signaling towards survival via activation of NF- $\kappa$ B in non-raft compartments, as the inhibition of endocytosis (via disruption of clathrin or actin or possibly both [44]) is known to block TNF- $\alpha$ -induced apoptosis [45].

The addition of TNF- $\alpha$  depletes the slow fraction of receptors as well, as the pre-formed complexes might be internalized within minutes [11,40]. Mobilization of new receptors would replace internalized TNF-R1 molecules to secure a constant signal transduction. Thus, the cell membrane is populated with new single receptors that do not form nascent clusters. While the slow fraction disappears upon activation, we do not observe a significant increase in receptor mobility.

#### 4. Conclusions

In summary, we present a refined explanation for association and activation of TNF-R1 in the cell membrane derived from single-molecule fluorescence experiments with nanometer-spatial resolution and extended observation times. We revealed so-far unidentified sub-populations of TNF-R1 molecular aggregates and studied their presence and function under different cellular conditions.

TNF-R1 was found to be present in different species of molecular organization, namely a slow species of presumably lipid raft-bound aggregates and a fast species that might represent receptor trimers or monomers. Moreover, cholesterol depletion reduced the fraction of the slow species, indicating an association of TNF-R1 to lipid, and shifted the diffusion coefficient distribution to higher values, suggesting an overall higher mobility. Signal initiation by TNF- $\alpha$  led to a smaller reduction of the fraction of the slow species of TNF-R1, without a shift of the diffusion coefficient distribution. Based on these findings, we propose a refined model for TNF-R1 association and activation, suggesting the formation of oligomeric TNF-R1 complexes before or after ligand binding and general association and stabilization of receptor-ligand oligomers on lipid rafts.

#### Acknowledgements

We thank the cell culture team at IINS, Bordeaux, for technical assistance. MeH, MiH and SM acknowledge the financial support by the German Ministry of Education and Research (BMBF, grant 0315262) and the German Science Foundation (DFG, grant HE 6166/2-1). BK and CK acknowledge financial support by the BMBF (grant 01GN1006A) and DFG. DW acknowledges financial support by a FiF grant of the University of Bielefeld. DN, DC and JBS acknowledge the financial support from the French Ministry of Research, CNRS, the Regional Council of Aquitaine, the Fondation pour la Recherche



Médicale and the European Union's seventh framework program for research and development for the Marie-Curie-IntraEuropean Fellowship and the ERC grant Nano-Dyn-Syn.

#### Appendix A. Supplementary data

Supplementary data to this article can be found online at <http://dx.doi.org/10.1016/j.bbamcr.2012.06.026>.

#### References

- [1] B.B. Aggarwal, et al., Human tumour necrosis factors: structure and receptor interactions, *CIBA Found. Symp.* 131 (1987) 39–51.
- [2] H. Wajant, K. Pfizenmaier, P. Scheurich, Tumor necrosis factor signaling, *Cell Death Differ.* 10 (1) (2003) 45–65.
- [3] J. Vilcek, T.H. Lee, *Tumor necrosis factor*. New insights into the molecular mechanisms of its multiple actions, *J. Biol. Chem.* 266 (12) (1991) 7313–7316.
- [4] F.K. Chan, et al., A domain in TNF receptors that mediates ligand-independent receptor assembly and signaling, *Science* 288 (5475) (2000) 2351–2354.
- [5] A.S. Varadhachary, et al., Phosphatidylinositol 3'-kinase blocks CD95 aggregation and caspase-8 cleavage at the death-inducing signaling complex by modulating lateral diffusion of CD95, *J. Immunol.* 166 (11) (2001) 6564–6569.
- [6] S.S. Pullen, et al., High-affinity interactions of tumor necrosis factor receptor-associated factors (TRAFs) and CD40 require TRAF trimerization and CD40 multimerization, *Biochemistry* 38 (31) (1999) 10168–10177.
- [7] D.W. Banner, et al., Crystal structure of the soluble human 55 kd TNF receptor-human TNF beta complex: implications for TNF receptor activation, *Cell* 73 (3) (1993) 431–445.
- [8] V. Boschert, et al., Single chain TNF derivatives with individually mutated receptor binding sites reveal differential stoichiometry of ligand receptor complex formation for TNFR1 and TNFR2, *Cell. Signal.* 22 (7) (2010) 1088–1096.
- [9] Q. Yin, et al., E2 interaction and dimerization in the crystal structure of TRAF6, *Nat. Struct. Mol. Biol.* 16 (6) (2009) 658–666.
- [10] H. Wajant, P. Scheurich, TNFR1-induced activation of the classical NF-kappaB pathway, *FEBS J.* 278 (6) (2011) 862–876.
- [11] W. Schneider-Brachert, et al., Compartmentalization of TNF receptor 1 signaling: internalized TNF receptors as death signaling vesicles, *Immunity* 21 (3) (2004) 415–428.
- [12] D.F. Legler, et al., Recruitment of TNF receptor 1 to lipid rafts is essential for TNFalpha-mediated NF-kappaB activation, *Immunity* 18 (5) (2003) 655–664.
- [13] F. Bazzoni, B. Beutler, The tumor necrosis factor ligand and receptor families, *N. Engl. J. Med.* 334 (26) (1996) 1717–1725.
- [14] Y.C. Park, et al., Structural basis for self-association and receptor recognition of human TRAF2, *Nature* 398 (6727) (1999) 533–538.
- [15] T. Friedrichson, T.V. Kurzchalia, Microdomains of GPI-anchored proteins in living cells revealed by crosslinking, *Nature* 394 (6695) (1998) 802–805.
- [16] S. Adam-Klages, et al., FAN, a novel WD-repeat protein, couples the p55 TNF-receptor to neutral sphingomyelinase, *Cell* 86 (6) (1996) 937–947.
- [17] S. Philipp, et al., The Polycomb group protein EED couples TNF receptor 1 to neutral sphingomyelinase, *Proc. Natl. Acad. Sci. U. S. A.* 107 (3) (2010) 1112–1117.
- [18] S. Manley, et al., High-density mapping of single-molecule trajectories with photoactivated localization microscopy, *Nat. Methods* 5 (2) (2008) 155–157.
- [19] S.J. Gould, S. Subramani, Firefly luciferase as a tool in molecular and cell biology, *Anal. Biochem.* 175 (1) (1988) 5–13.
- [20] I. Izeddin, et al., Wavelet analysis for single molecule localization microscopy, *Opt. Express* 20 (3) (2012) 2081–2095.
- [21] V. Racine, et al., Visualization and quantification of vesicle trafficking on a three-dimensional cytoskeleton network in living cells, *J. Microsc.* 225 (Pt 3) (2007) 214–228.
- [22] V. Racine, et al., Multiple-target tracking of 3D fluorescent objects based on simulated annealing, In: 2006 IEEE International Symposium on Biomedical Imaging (ISBI 2006), April 6–9, 2006, Arlington, VA, 2006.
- [23] U. Kubitscheck, U. Homann, G. Thiel, Osmotically evoked shrinking of guard-cell protoplasts causes vesicular retrieval of plasma membrane into the cytoplasm, *Planta* 210 (3) (2000) 423–431.
- [24] M.K. Cheezum, W.F. Walker, W.H. Guilford, Quantitative comparison of algorithms for tracking single fluorescent particles, *Biophys. J.* 81 (4) (2001) 2378–2388.
- [25] G.J. Schutz, H. Schindler, T. Schmidt, Single-molecule microscopy on model membranes reveals anomalous diffusion, *Biophys. J.* 73 (2) (1997) 1073–1080.
- [26] E. Betzig, et al., Imaging intracellular fluorescent proteins at nanometer resolution, *Science* 313 (5793) (2006) 1642–1645.
- [27] J. Wiedenmann, et al., EosFP, a fluorescent marker protein with UV-inducible green-to-red fluorescence conversion, *Proc. Natl. Acad. Sci. U. S. A.* 101 (45) (2004) 15905–15910.
- [28] G.H. Patterson, J. Lippincott-Schwartz, A photoactivatable GFP for selective photolabeling of proteins and cells, *Science* 297 (5588) (2002) 1873–1877.
- [29] G. Giannone, et al., Dynamic superresolution imaging of endogenous proteins on living cells at ultra-high density, *Biophys. J.* 99 (4) (2010) 1303–1310.
- [30] G.U. Nienhaus, et al., Photoconvertible fluorescent protein EosFP: biophysical properties and cell biology applications, *Photochem. Photobiol.* 82 (2) (2006) 351–358.
- [31] S.A. McKinney, et al., A bright and photostable photoconvertible fluorescent protein, *Nat. Methods* 6 (2) (2009) 131–133.
- [32] H.W. Fisher, T.W. Cooper, Electron microscope studies of the microvilli of HeLa cells, *J. Cell Biol.* 34 (2) (1967) 569–576.
- [33] J. Pitha, et al., Drug solubilizers to aid pharmacologists: amorphous cyclodextrin derivatives, *Life Sci.* 43 (6) (1988) 493–502.
- [34] J. Kwik, et al., Membrane cholesterol, lateral mobility, and the phosphatidylinositol 4,5-bisphosphate-dependent organization of cell actin, *Proc. Natl. Acad. Sci. U. S. A.* 100 (24) (2003) 13964–13969.
- [35] M. Gerken, et al., Fluorescence correlation spectroscopy reveals topological segregation of the two tumor necrosis factor membrane receptors, *Biochim. Biophys. Acta* 1798 (6) (2010) 1081–1089.
- [36] F.K.M. Chan, A domain in TNF receptors that mediates ligand-independent receptor assembly and signaling, *Science* 288 (5475) (2000) 2351–2354.
- [37] S.A. Kim, et al., Quantifying translational mobility in neurons: comparison between current optical techniques, *J. Neurosci.* 30 (49) (2010) 16409–16416.
- [38] U. Meseth, et al., Resolution of fluorescence correlation measurements, *Biophys. J.* 76 (3) (1999) 1619–1631.
- [39] M. Grell, et al., The transmembrane form of tumor necrosis factor is the prime activating ligand of the 80 kDa tumor necrosis factor receptor, *Cell* 83 (5) (1995) 793–802.
- [40] S. Schütze, V. Tchikov, W. Schneider-Brachert, Regulation of TNFR1 and CD95 signalling by receptor compartmentalization, *Nat. Rev. Mol. Cell Biol.* 9 (8) (2008) 655–662.
- [41] Y.G. Ko, et al., TNF-alpha-mediated apoptosis is initiated in caveolae-like domains, *J. Immunol.* 162 (12) (1999) 7217–7223.
- [42] J.E. Doan, D.A. Windmiller, D.W. Riches, Differential regulation of TNF-R1 signaling: lipid raft dependency of p42mapk/erk2 activation, but not NF-kappaB activation, *J. Immunol.* 172 (12) (2004) 7654–7660.
- [43] S. Parlato, et al., CD95 (APO-1/Fas) linkage to the actin cytoskeleton through ezrin in human T lymphocytes: a novel regulatory mechanism of the CD95 apoptotic pathway, *EMBO J.* 19 (19) (2000) 5123–5134.
- [44] B. Qualmann, M.M. Kessels, R.B. Kelly, Molecular links between endocytosis and the actin cytoskeleton, *J. Cell Biol.* 150 (5) (2000) F111–F116.
- [45] S. Schütze, et al., Inhibition of receptor internalization by monodansylcadaverine selectively blocks p55 tumor necrosis factor receptor death domain signaling, *J. Biol. Chem.* 274 (15) (1999) 10203–10212.

## Coordinate-based colocalization analysis of single-molecule localization microscopy data

Sebastian Malkusch · Ulrike Endesfelder ·  
Justine Mondry · Márton Gelléri · Peter J. Verveer ·  
Mike Heilemann

Accepted: 19 October 2011 / Published online: 16 November 2011  
© Springer-Verlag 2011

**Abstract** Colocalization of differently labeled biomolecules is a valuable tool in fluorescence microscopy and can provide information on biomolecular interactions. With the advent of super-resolution microscopy, colocalization analysis is getting closer to molecular resolution, bridging the gap to other technologies such as fluorescence resonance energy transfer. Among these novel microscopic techniques, single-molecule localization-based super-resolution methods offer the advantage of providing single-molecule coordinates that, rather than intensity information, can be used for colocalization analysis. This requires adapting the existing mathematical algorithms for localization microscopy data. Here, we introduce an algorithm for coordinate-based colocalization analysis which is suited for single-molecule super-resolution data. In addition, we present an experimental configuration for simultaneous dual-color imaging together with a robust approach to correct for optical aberrations with an accuracy of a few nanometers. We demonstrate the potential of our approach for cellular structures and for two proteins binding actin filaments.

**Keywords** Colocalization · Super-resolution microscopy · Single-molecule fluorescence microscopy · Cellular structures

### Introduction

Fluorescence microscopy is a valuable tool to unravel biomolecular interactions. By applying differently colored labels to biomolecules, interactions can be studied systematically ranging from conventional colocalization down to the 2–10 nm length scale achieved by fluorescence resonance energy transfer (FRET) (Grecco and Verveer 2011). FRET is an excellent choice to study intermolecular interactions on a very short length scale, but requires that two biomolecules come together closely. On a longer length scale, spatial colocalization of the fluorescence signal in different color channels is a standard approach (Bolte and Cordeliers 2006; French et al. 2008; Zinchuk and Zinchuk 2008). However, colocalization of conventional fluorescence microscopy images suffers from a limited spatial resolution of about half the wavelength used and from chromatic errors (Ronneberger et al. 2008), which limits the extractable information and thus interpretation of the data. Here, super-resolution fluorescence microscopy techniques can help, as these methods can reach a spatial resolution down to tens of nanometers (Heilemann 2010; Schermelleh et al. 2010). Colocalization analysis has been applied for instance to stimulated-emission depletion (STED) microscopy (McClatchey and Fehon 2009) and structured illumination microscopy (SIM) (Schermelleh et al. 2008) images. Localization-based super-resolution techniques are somehow different in this context as these are based on coordinates of single-molecules (Betzig et al. 2006; Heilemann et al. 2008; Rust et al.

S. Malkusch and U. Endesfelder contributed equally.

S. Malkusch · U. Endesfelder · M. Heilemann (✉)  
Biotechnology and Biophysics, Julius-Maximilians-University  
Würzburg, Am Hubland, 97074 Würzburg, Germany  
e-mail: m.heilemann@uni-wuerzburg.de

J. Mondry · M. Gelléri · P. J. Verveer  
Department of Systemic Cell Biology, Max Planck Institute  
of Molecular Physiology, Otto-Hahn-Strasse 11,  
44227 Dortmund, Germany

2006). Super-resolution images are obtained by histogramming or blurring all localizations. These intensity-like images can then be processed by common image-based colocalization algorithms (Bolte and Cordelières 2006; French et al. 2008; Zinchuk and Zinchuk 2008). Therefore, they depend on processing parameters chosen for the reconstruction of super-resolution images. Our novel approach starts from the set of single-molecule coordinates of two different species that are derived from a localization microscopy experiment, and applies coordinate-based algorithms to calculate colocalization parameters. In addition, our approach is able to provide information on the environment of each species separately, distinguishing between the questions how a biomolecule of species A is surrounded by a biomolecule of species B, and vice versa.

In the present work, we demonstrate a robust approach for coordinate-based colocalization analysis of dual-color super-resolution imaging based on photoswitching of fluorescent probes independent of specific fluorophores. We introduce an experimental configuration for simultaneous dual-color imaging that overcomes the dynamic range of the camera and is not sensitive to cross talk. We introduce a routine to correct for aberrations with nanometer accuracy, and we developed a coordinate-based colocalization (CBC) analysis method.

## Methods

### Calibration phantom

For calibrating the dual-color setup a calibration phantom has been prepared. The glass surface of a LabTek 8-welled chamber (Nunc, Germany) was etched with 0.05% HF and then incubated with 0.1% poly-L-lysine (Sigma-Aldrich, USA) for 10 min. The surface was incubated with multi-color labeled polystyrene beads (TetraSpeck, Invitrogen, USA) dissolved 1:1,000 in PBS (Sigma-Aldrich, USA) for 15 min. The beads were imaged on both channels by irradiation with 647 nm and with 568 nm. For the calibration several images of different surface areas were taken and the fiducial coordinates were obtained with the rapid-STORM algorithm (Wolter et al. 2011). A correction matrix was generated and used for alignment of the two-color super-resolution data using MatLab (Mathworks, USA).

### Molecular biology

Merlin-EGFP was prepared by polymerase chain reaction (PCR) amplification using a sense primer (CGCGCTAGCATGGCCGGAGCCATCGC) and an anti-sense primer (GCGGTTCGACCGGAGCTCTCAAAGAAGG), which

contain the restriction sites *NheI* and *SalI*, respectively. The synthesized strand was cloned into the Clontech EGFP-N1 vector. Ezrin-EGFP was prepared by PCR using a sense primer (GCCCAAGCTTATGGATACAAGGATGAC) and an anti-sense primer (CGGACTCAGATCTCGAGCTCAAGCTTCGATGCCCAAGCC) which were cloned into the EGFP-N1 Clontech vector. Here, the restriction sites *HindIII* and *SalI* were used which were also included in the primers. To generate the mEos2 variants of merlin and ezrin, a fluorophore exchange was performed via the restriction sites *AgeI* and *NotI*. mEos2 was amplified with the primers CGCACCGGTCGCCACCATGAGTGCATT AAGC (sense) and GCGGCGGCCGCTTTACGTCTGG CATTGTCAG (anti-sense) while EGFP was cut out of the vectors EGFP-N1-merlin and EGFP-N1-ezrin. The DNA-fragments were ligated to maintain the constructs mEos2-merlin and mEos2-ezrin.

### Sample preparation of cells expressing mEos2-actin

HeLa cells were taken from cell culture flasks, seeded out in LabTek 8-welled chambers (Nunc, Germany) and incubated at 37°C and 5% CO<sub>2</sub> until they were 80% confluent. The cells were transiently transfected with mEos2-actin using Turbofect (Fermentas, Germany). After overnight expression at 37°C, the cells were fixed for 10 min in 4% paraformaldehyde (PFA, Sigma, USA) and stored in PBS at 4°C. Prior to imaging, the actin skeleton of the cells was labeled by incubation with Alexa Fluor 647-phalloidin (Invitrogen, USA) for 10 min. Tubulin-stained HeLa cells were prepared using standard immunocytochemistry protocols by a primary rabbit anti- $\beta$ -tubulin antibody (Abcam, UK). The secondary antibody was a goat F(ab')<sub>2</sub> anti rabbit labeled with Alexa Fluor 647 (Invitrogen, USA).

### Sample preparation of cells expressing mEos2-merlin or mEos2-ezrin

COS-7 cells were seeded in LabTek 8-well chambers (Nunc, Germany) and grown in DMEM + 10% fetal calf serum (FCS) + 1% L-glutamin + 1% non-essential amino acids (NEAA). The cells were maintained in culture at 37°C and 5% CO<sub>2</sub>. After cell attachment, transient transfection of mEos2-merlin or mEos2-ezrin was carried out using the transfection reagent Effectene (Qiagen, Germany) according to the protocol of the manufacturer. The transfected cells were incubated 12–15 h at 37°C and 5% CO<sub>2</sub>. Cells were washed two times with PBS, fixed with 4% PFA (paraformaldehyde) for 15 min at room temperature, permeabilized with 0.5% Triton-X 100 for 10 min and incubated with 3% BSA (bovine serum albumin) for 30 min. Finally the cells were stained with 1 unit Alexa

Fluor 647 phalloidin (Invitrogen, USA) in 1% BSA solution for 20 min, and rinsed 3 times with PBS.

#### Microscopic configuration

A multi-line argon–krypton laser (Innova70C, Coherent, USA) was coupled into an inverted microscope (IX71, Olympus, Japan) equipped with a 60× oil immersion objective (PlanApo 60x, Na 1.45, Olympus, Japan) suitable for total internal reflection fluorescence (TIRF) imaging. The excitation and fluorescence light were separated using a dichroic mirror [HC576/661 (AHF, Germany)]. Spectral discrimination of the two different fluorescent probes was achieved by splitting the fluorescence emission in the detection path (custom-modified 650 DCXR, AHF, Germany). Two parallel light paths both containing a Galilei telescope project the fluorescence emission onto two separate regions of the chip of an EMCCD camera (EMCCD, Andor Ixon DU897, Ireland) (Fig. 1). In order to correct for chromatic aberrations in the focal plane of the objective, the length of the Galilei telescope in one beam path was adjusted. Additional filters were placed in the two spectral channels [633SP and 610/75 in the mEos2

channel; 664LP and 700/75 in the Alexa Fluor 647 channel (AHF, Germany)]. An additional longpass filter (568 LP; AHF, Germany) was used for both spectral channels.

#### Super-resolution imaging

Combined PALM and dSTORM imaging was performed using an alternating laser excitation scheme. The sample was prepared in an imaging buffer suitable for both dSTORM and PALM as described elsewhere (Endesfelder et al. 2011; Heilemann et al. 2008). Briefly, the cells were imaged in oxygen-depleted hydrocarbonate with pH 8 and 100 mM MEA added. mEos2 was photoactivated by irradiation with 378 nm and read out by irradiation with 568 nm. Alexa Fluor 647 was reversibly photoswitched by irradiation with 488 nm and read out by irradiation with 647 nm. The alternation of all light sources was triggered by the EMCCD and controlled by a pulse generator (Stanford Research Systems, USA). For each pair of super-resolved images a series of 3,000 frames, 1,500 frames per fluorescent probe in alternation, were recorded with an irradiation time of 99 ms and an acquisition time of 100 ms.

#### Dual-color image acquisition

The recorded image stack contains both dSTORM (Alexa Fluor 647) and PALM data (mEos2) in alternating frames and was separated into two individual image stacks (Fig. 1). Single-molecule localizations in both datasets were calculated using the rapidSTORM algorithm (Wolter et al. 2011). This scheme of alternating excitation and read-out allowed imaging the different fluorophores in separate spectral channels and significantly reduced cross talk. Image alignment was performed by translating single-molecule localizations in the mEos2 channel onto the Alexa Fluor 647 channel. Afterwards, the single-molecule localizations of the mEos2 channel were corrected using the local weighted mean calculated from the calibration phantom (Fig. 2). This procedure generates two super-resolved images that are corrected for optical and chromatic aberrations.

#### Coordinate-based colocalization of single-molecule localization data

The coordinate-based colocalization (CBC) value is calculated from single-molecule localization data of two species (A, B). A CBC value is assigned to each single localization of each species.

To calculate the CBC value for a specific localization  $A_i$  from species A, the distribution of localizations from both species A and B around  $A_i$  is calculated as:

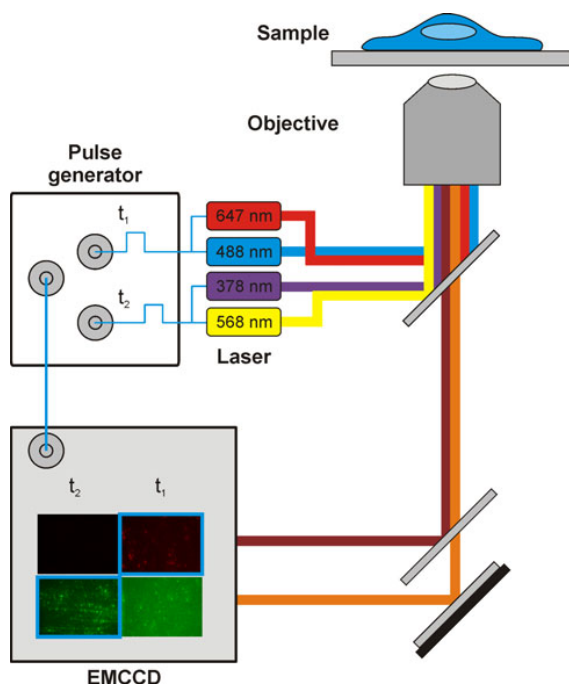


**Fig. 1** Experimental setup for parallel two-color localization-based super-resolution microscopy with alternating laser excitation. The trigger signal of the camera is processed by a frequency generator and used to modulate the different laser lines. In an alternating fashion, the sample was irradiated by either 647 and 488 nm, or by 568 and 378 nm. The fluorescence emission was spectrally separated on the camera

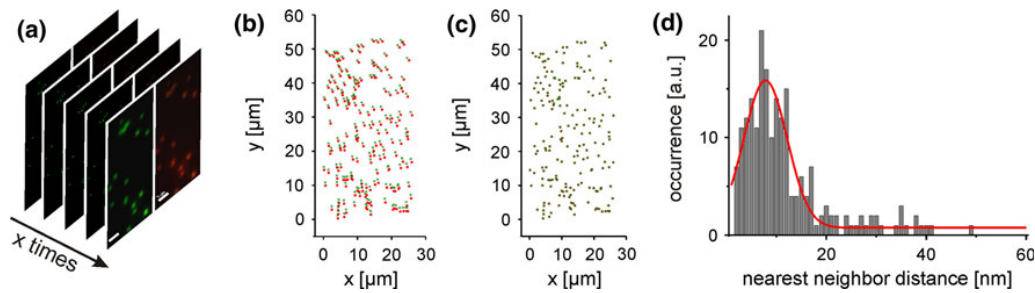


**Fig. 2** Aberration correction for two-color localization-based super-resolution microscopy. **a** A poly-L-lysine coated surface was loaded with Tetraspeck multispectral beads (100 nm diameter, Invitrogen, USA). The emission spectrum was split onto two separate regions of the EMCCD camera. **b** The spectrally separated single-molecule

localizations were overlaid and **c** a local weighted-mean matrix for aberration correction was calculated. **d** The nearest neighbor distribution of paired single-molecule localizations after aberration correction has a maximum at 7.8 nm, representing the correction level that can be reached with this calibration approach

$$D_{A_i,A}(r) = \frac{N_{A_i,A}(r)}{\pi r^2} \cdot \frac{\pi R_{\max}^2}{N_{A_i,A}(R_{\max})} = \frac{N_{A_i,A}(r)}{N_{A_i,A}(R_{\max})} \cdot \frac{R_{\max}^2}{r^2}$$

$$D_{A_i,B}(r) = \frac{N_{A_i,B}(r)}{N_{A_i,B}(R_{\max})} \cdot \frac{R_{\max}^2}{r^2}$$

Here,  $N_{A_i,A}(r)$  is the number of localizations of species A within the distance  $r$  around  $A_i$  and  $N_{A_i,B}(r)$  is the number of localizations of species B within the distance  $r$  around  $A_i$ . These distributions are corrected for the area ( $\pi r^2$ ), normalized by the number of localizations within the largest observed distance  $R_{\max}$  and divided by the largest observed area for species A ( $N_{A_i,A}(R_{\max})/\pi R_{\max}^2$ ) and B ( $N_{A_i,B}(R_{\max})/\pi R_{\max}^2$ ). A uniform distribution would give an expected value of  $D(r) = 1$  for all  $r$ .

From these two distributions, we calculated the rank correlation coefficient (Spearman) using a function available in Matlab (Mathworks, Natick, MA)

$$S_{A_i} = \frac{\sum_{r_j=0}^{R_{\max}} (O_{D_{A_i,A}}(r_j) - \bar{O}_{D_{A_i,A}}) (O_{D_{A_i,B}}(r_j) - \bar{O}_{D_{A_i,B}})}{\sqrt{\sum_{r_j=0}^{R_{\max}} (O_{D_{A_i,A}}(r_j) - \bar{O}_{D_{A_i,A}})^2} \sqrt{\sum_{r_j=0}^{R_{\max}} (O_{D_{A_i,B}}(r_j) - \bar{O}_{D_{A_i,B}})^2}}$$

Here,  $O_{D_{A_i,A}}(r)$  is the rank of  $O_{D_{A_i,A}}(r)$  calculated after Spearman, and  $\bar{O}_{D_{A_i,A}}$  is the arithmetic average of  $O_{D_{A_i,A}}(r)$ . The colocalization value,  $C_{A_i}$ , is calculated as  $C_{A_i} = S_{A_i} \cdot e^{(-\frac{E_{A_i,B}}{R_{\max}})}$ , with  $E_{A_i,B}$  as the distance from  $A_i$  to the nearest neighbor from species B.  $C_{A_i}$  is calculated for every single-molecule localization and can adapt values from  $-1$  to  $1$ .

## Results and discussion

Conventional colocalization algorithms generate an overlay coefficient for each pixel of an image calculated from the fluorescence signal recorded for two different and fluorophore-labeled biomolecules. This approach has two

drawbacks: first, it depends on prior image processing such as thresholding and deconvolution; second, a false positive colocalization value is yielded if one of the biomolecules is distributed randomly. These issues have been addressed in intensity correlation analysis (ICA) (Li et al. 2004a) by also taking into account the spatial distribution of the biomolecules analyzed.

Different from conventional fluorescence microscopy, super-resolution localization microscopy provides coordinates of biomolecules with single-molecule resolution. These coordinates can be used for colocalization analysis without the need of image processing steps. The simplest approach is a nearest-neighbor distance analysis, however, this approach would also yield false positive colocalization in the case of one species being randomly distributed. Therefore, we developed a coordinate-based colocalization (CBC) algorithm that takes into account the spatial distribution of biomolecules and provides a colocalization value for each single-molecule localization of each species separately.

### Dual-color localization microscopy with subdiffraction resolution

Colocalization analysis of single-molecule localization microscopy data first requires a solid approach for simultaneous imaging of two different photoswitchable fluorophores. In our experiments, we have chosen a combination of the monomeric photoactivatable fluorescent protein mEos2 (McKinney et al. 2009) with the photoswitchable carbocyanine fluorophore Alexa Fluor 647 (Heilemann et al. 2005), which both can be photoswitched reliably under identical buffer conditions (Endesfelder et al. 2011). We have applied an alternating scheme which in a first cycle reads out the fluorescence signal of mEos2 applying 378 nm for photoactivation and 568 nm for excitation, and in a second cycle reads out the fluorescence signal of Alexa



Fluor 647 applying 488 nm for photoactivation and 647 nm for excitation. Both signals are recorded on the same detector that is spectrally split on two channels (Fig. 1). Cross-activation of Alexa Fluor 647 by 378 nm will only occur to a low extent because of the comparably low irradiation intensity, but can be neglected as cross talk can be sorted out by the spectral and temporal separation of the fluorescence signal (Endesfelder et al. 2011). Notably, both fluorophores exhibit reversible photoswitching (Heilemann et al. 2005; Radenovic et al. 2010).

#### Superposition of multi-channel single-molecule localization data

Extracting reliable information on molecular proximity from single-molecule localization microscopy data with subdiffraction spatial resolution requires a robust correction for aberration errors at the nanometer level. Several protocols have been developed for this purpose (Churchman et al. 2005; Koyama-Honda et al. 2005). Sub-1 nm chromatic correction has been reported recently (Pertsinidis et al. 2010). Here, we account for chromatic aberrations as well as for nonlinear aberrations in the microscope which arise due to imperfect optical elements. We selected the approach of using multicolor fluorescent beads to record a dense matrix of points on both channels (Fig. 2a) (Churchman et al. 2005). The images were processed such that all points were allocated to pairs (Fig. 2b), and a correction matrix was calculated (Fig. 2c). From this data, we can routinely demonstrate a residual localization error below 10 nm (Fig. 2d).

#### Colocalization based on coordinates of individual molecules

As a next step, we have implemented an algorithm for colocalization which is based on single-molecule coordinates, and which reports on the neighborhood of two species separately. The easiest way to characterize the colocalization of pairs of coordinates would be a simple nearest neighbor analysis where each localization of the observed protein population A is attributed by an individual colocalization value based on the distance to the nearest localization of a protein from population B (Koyama-Honda et al. 2005). However, this method is not reliable for single-molecule localization microscopy, as photoswitching of fluorophores often is reversible and would introduce artifacts (Endesfelder et al. 2011; Heilemann et al. 2005; Radenovic et al. 2010). Our approach corrects for multiple switching cycles of single fluorophores (and thus for multiple detection events) by comparing the spatial distribution of surrounding localizations from both species. For each molecule of a species A, the average number of

molecules of a species B in a given distance is calculated (Fig. 3). Each localization of the observed protein population is attributed an individual colocalization value calculated as Spearman's correlation coefficient between the linearized distribution functions of both protein populations in the neighborhood of the very localization. However, this method alone results in false positive colocalization information for localizations where the nearest neighbor is far away. To overcome this limitation, we weighted the colocalization by the distance to the nearest neighbor (see "Methods" section). As a result and similar to the Spearman correlation coefficient, our colocalization parameter can reach values from  $-1$  for anti-correlated [which are difficult to interpret also in image-based colocalization methods (Adler and Parmryd 2010; Zinchuk and Zinchuk 2008)], through  $0$  for non-correlated distributions (indicating a low probability of colocalization), to  $+1$  for perfectly correlated distributions (indicating a high probability of colocalization). Note that this analysis provides colocalization information for each species separately and with single-molecule resolution.

In a first robust test of this approach, we simulated two identical distributions of two species with a different alignment with respect to each other achieved by rotation (Fig. 3a, e). For this exemplary pattern, we would expect a strong colocalization only in the region where both distributions cross each other. One molecule is chosen from the red population to calculate the linearized distribution function of the neighboring localizations from the red population (Fig. 3b) and the linearized distribution function of the neighboring localizations from the green population (Fig. 3c). Afterwards, the correlation coefficient for the two distribution functions is calculated, weighted by the nearest neighbor distribution from the green population and attributed to the chosen localization. The procedure is repeated for all localizations from the red population (Fig. 3d). This way, we are able to allocate a specific colocalization factor to each localization. The same procedure can be repeated for localizations from the green population with respect to the red population (Fig. 3e–h).

We then applied our approach to cellular structures that can serve as a positive control, in order to evaluate our colocalization algorithm and to compare it to the intensity correlation analysis (ICA) (Li et al. 2004b), which is an image-based colocalization approach that also depends on protein distributions. In a first example, we recorded a super-resolution image of the microtubulin skeleton of a fixed HeLa cell labeled with Alexa Fluor 647 by antibody staining. From this dataset, we generated artificial images by overlaying two identical images with different translational shifts of 0, 10, 50 and 100 nm (Fig. 4). This way, we have the advantage of using experimentally derived distributions of single-molecule localizations instead of Monte

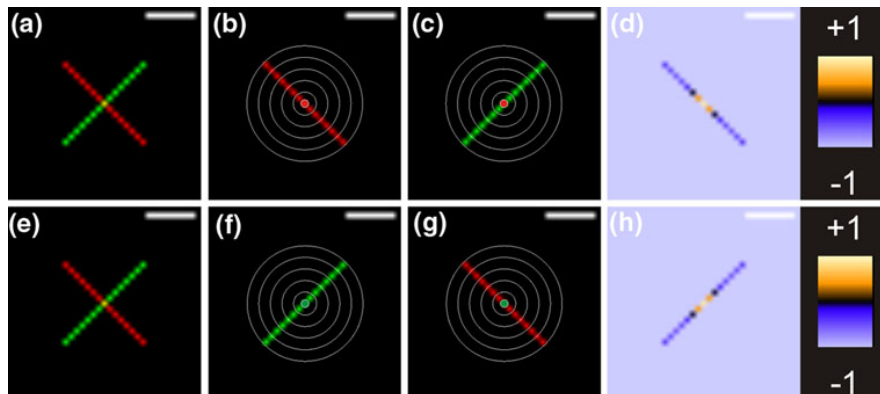
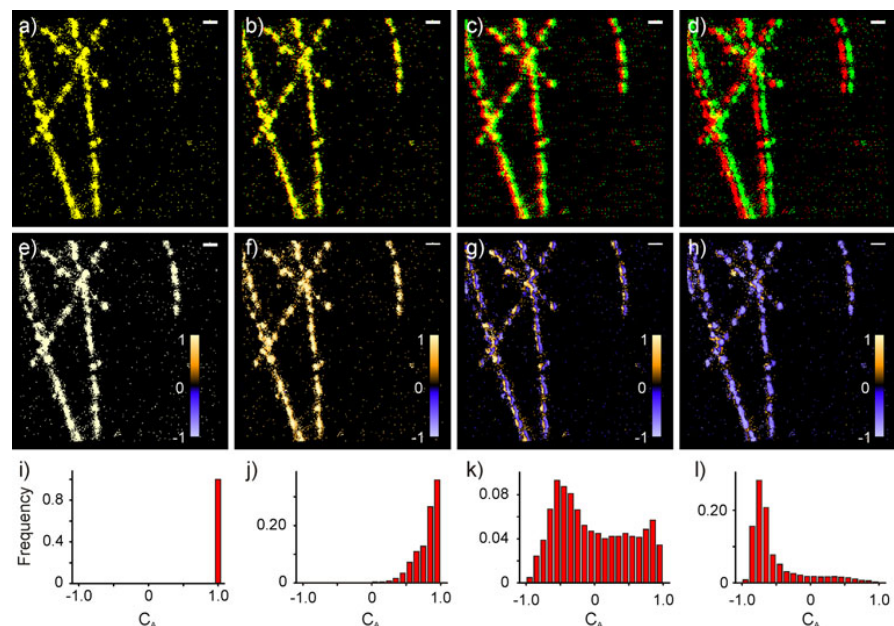


**Fig. 3** **a, e** Coordinate-based colocalization (CBC) for a simulated distribution of single-molecule localizations of two different molecular species, represented as *green and red dots* (scale bar 100 nm). **b, f** In a first step, for each single-molecule localization of either species (*green or red*), the distribution function of the neighboring localizations from the same species is calculated. **c, g** In a second step, the distribution function of the neighboring localizations from

the other population is calculated. **d, h** From the individual distribution functions, a correlation coefficient is calculated and weighted by the distance distribution. As a result, each single-molecule localization of each species is attributed an individual colocalization value, which reports on the local environment of a particular red or green molecule, separately

**Fig. 4** Coordinate-based colocalization (CBC) of a single-stained microtubulin structure recorded with single-molecule super-resolution imaging in fixed HeLa cells (scale bar 200 nm). **a–d** For CBC analysis, the microtubulin structure was doubled, translated in one direction by 0 nm (**a**), 10 nm (**b**), 50 nm (**c**) or 100 nm (**d**), and overlaid with itself (*green and red*, intensity colocalization in *yellow*). **e–h** Corresponding coordinate-based colocalization images of the microtubulin structures. **i–l** The histograms show the single-molecule distributions of the colocalization parameter,  $C_A$



Carlo simulations, where the natural protein distributions would have to be assumed. As expected, the colocalization values for the non-translated image exhibits a perfect colocalization ( $C_{A_i} = +1$ ) throughout, whereas the values start to decrease with increasing distance. Similar to ICA, our method indicates a colocalization for  $0 < C_{A_i} < 1$  and segregated but near localizations for  $-1 < C_{A_i} < 0$ . A coefficient of  $C_{A_i} = 0$  indicates no colocalization at all.

In a second example, we prepared HeLa cells with dual-labeled actin by both genetic labeling with mEos2

(McKinney et al. 2009) as well as chemical labeling with phalloidin-Alexa Fluor 647. We recorded two-color images and applied coordinate-based colocalization analysis to the single-molecule localization data (Fig. 5). The super-resolution image (Fig. 5a, b, g, l) shows unquestionably that both labels target the actin structure, but at the same time, the images reveal that the structure is labeled in different regions by the different fluorophores. This effect is most likely a combination of experimental parameters, such as differences in the labeling molecule and mechanism as well

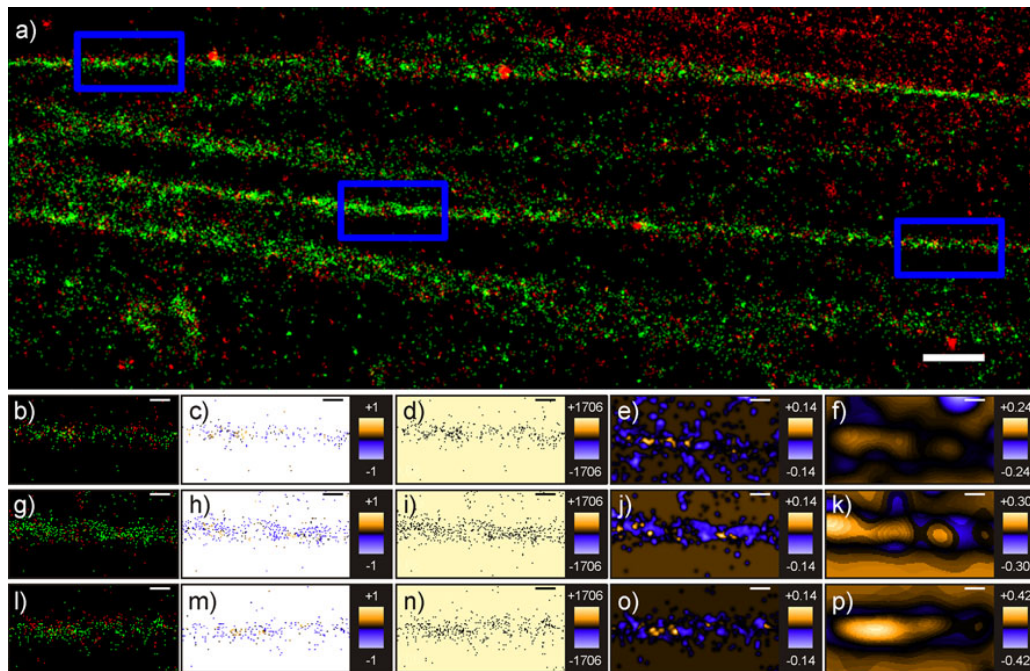


**Fig. 5** Coordinate-based colocalization (CBC) of a dual-stained actin structure recorded with single-molecule super-resolution imaging in fixed HeLa cells. **a** Dual-color super-resolution image of dual-stained actin (green mEos2-actin, red actin labeled with phalloidin-Alexa Fluor 647; scale 1  $\mu\text{m}$ ). **b**, **g**, **l** Magnified view of three selected regions from the super-resolution images (scale bar 200 nm) which were analyzed for single-molecule colocalization with the CBC

algorithm (**c**, **h**, **m**). The results are compared to conventional intensity-based colocalization with three image representations of the super-resolution data used: **d**, **i**, **n** displays the intensity-based colocalization of our raw localization data given in a 10-nm grid; **e**, **j**, **o** displays the intensity-based colocalization of Gaussian-blurred localization data; **f**, **k**, **p** displays the intensity-based colocalization of the same regions but blurred mathematically to confocal resolution

as spatial constraints. A strong colocalization signal (Fig. 5c, h, m) is evident for the inner regions of the actin filaments, whereas the outer regions of the filaments show predominant negative values thus pointing to segregated localization distributions. This data indicate that at a near-molecular level, our colocalization method is highly sensitive to the strategy of labeling, especially when the same structure is labeled in two different ways that also might interfere with each other. For comparison, we also analyzed the data with conventional intensity-based colocalization algorithms in three different ways (Fig. 5d–f, i–k, n–p). First, we calculate the ICA for the raw super-resolution images generated by binning single-molecule localizations into sub-pixels of 11 nm (Fig. 5d, i, n). These images show nearly no correlation, as very few single-molecule localizations of the two different species colocalize in one sub-pixel. This demonstrates that this approach is based on the sub-pixel size chosen for binning, and thus biased and inappropriate. A common strategy to convert raw super-resolution localization images into intensity-like images is to blur each single-molecule localization by a Gaussian function, with the width of the

Gaussian function accounting for the localization accuracy (Betzig et al. 2006; Smith et al. 2010). These images were generated and intensity-based colocalization analysis (Fig. 5e, j, o) shows regions with high colocalization of both biomolecules. The results obtained here are similar to the results obtained by coordinate-based analysis (Fig. 5b, g, l), however, the colocalization parameter cannot be given for each species separately. In a final approach, we calculated artificial images with confocal resolution from the localization microscopy data by Gaussian blurring, to demonstrate the results that would have been achieved with confocal microscopy (Fig. 5f, k, p). Large regions with strong colocalization values and much less structural information are observed, which is due to the lower spatial resolution.

#### Colocalization of the actin-binding proteins merlin and ezrin on a molecular level

In a second approach, we tested our experimental setup and quantitative analysis on two actin-binding cellular proteins, merlin and ezrin. Both merlin and ezrin are playing an



important role in membrane–cytoskeletal interactions. Ezrin and merlin are closely related and exhibit large portions of similar conserved sequences like the FERM N-terminal domain, but the binding specificity of the two proteins towards actin is different. Ezrin exhibits a C-terminal ERM-association domain (C-ERMAD) that binds F-actin. The access to this domain is regulated by head-to-tail folding of ezrin from a dormant closed conformation to an active open conformation by phosphorylation and phospholipid binding. Merlin lacks this C-terminal actin-binding domain, but recent studies in mammalian cells suggest that the N-terminal 18 amino acids of merlin mediate actin binding (McClatchey and Fehon 2009).

Both proteins were tagged with the photoswitchable fluorescent protein mEos2 (McKinney et al. 2009) and transiently transfected into COS-7 cells. The actin cytoskeleton was labeled with phalloidin-Alexa Fluor 647.

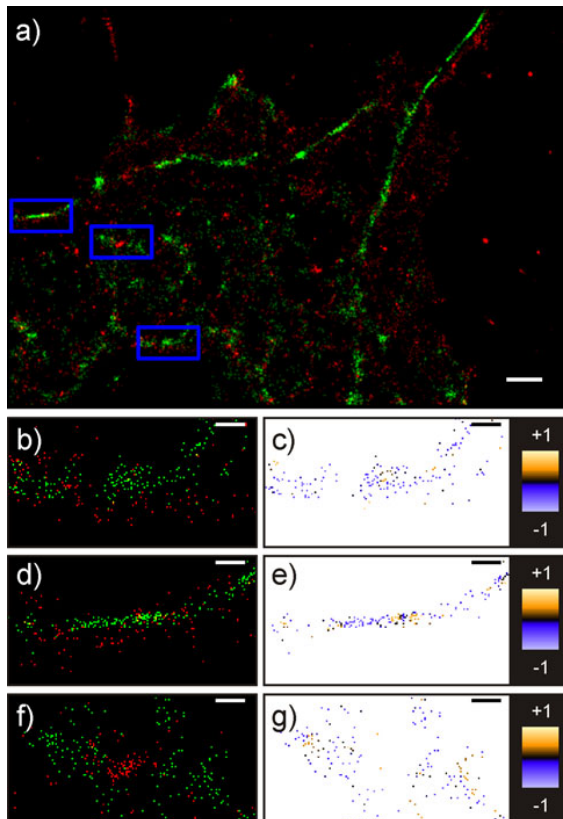


**Fig. 6** Coordinate-based colocalization (CBC) of single-molecule super-resolution data of actin and the actin-binding protein ezrin in fixed COS-7 cells. **a** Dual-color super-resolution image of ezrin-mEos2 (green) and actin labeled with phalloidin-Alexa Fluor 647 (red) (scale bar 1  $\mu$ m). **b, d, f** Selected regions (scale bar 200 nm) were analyzed by CBC. **(c, e, g)** The colocalization of ezrin with respect to actin is shown, reporting for the proximity of single-molecule localizations of actin around single ezrin molecules

Dual-color super-resolution images that were recorded and corrected for aberrations are shown in Figs. 6 and 7. From this data, we could identify major differences in the structural organization of ezrin and merlin: while ezrin is organized in large tube-like structures similar to actin (Fig. 6a), merlin is typically found in small clusters (Fig. 7a). As expected, both protein organization units are found close to actin filaments. While the actin skeleton is partly enclosed by the small merlin clusters (Fig. 7a, b, d, f), ezrin and actin filaments coil up to a helical structure (Fig. 6a, b, d, f). Due to the fact that ezrin structures appear denser than merlin cluster, the density distribution of  $C_A$  for ezrin (Fig. 8a) looks quite different to the one for merlin (Fig. 8b). Both distributions show a clear maximum in the negative range ( $-0.45$  for ezrin and  $-0.55$  for merlin). Contrary to merlin, only ezrin also shows a clear maximum on the positive side (0.25), which corroborates that ezrin has a higher binding affinity to actin than merlin which is attributed to the C-ERMAD of ezrin (Fehon et al. 2010).

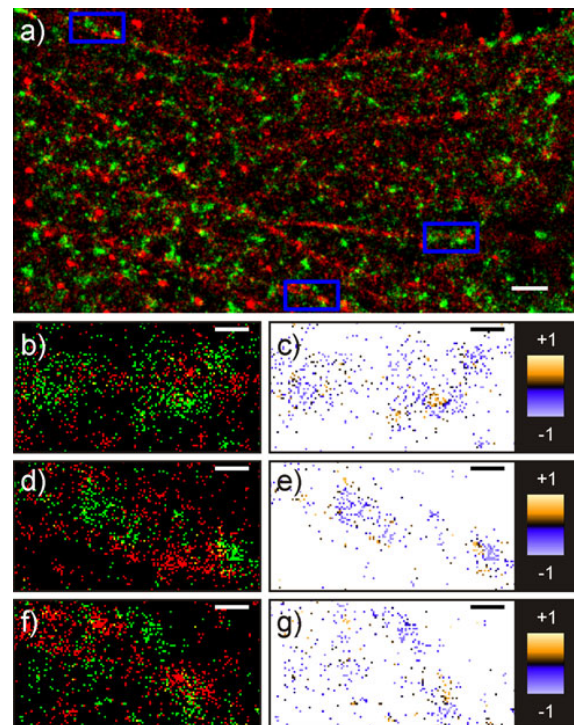


**Fig. 7** Coordinate-based colocalization (CBC) of single-molecule super-resolution data of actin and the actin-binding protein merlin in fixed COS-7 cells. **a** Dual-color super-resolution image of merlin-mEos2 (green) and actin labeled with phalloidin-Alexa Fluor 647 (red) (scale bar 1  $\mu$ m). **b, d, f** Selected regions (scale bar 200 nm) were analyzed by CBC **(c, e, g)**. The colocalization of merlin with respect to actin is shown, reporting for the proximity of single-molecule localizations of actin around single merlin molecules

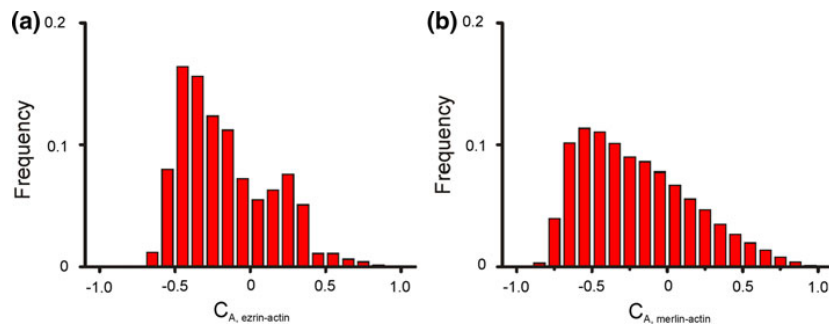


**Fig. 8** Distribution of the colocalization parameter  $C_A$  for the actin-binding proteins ezrin and merlin with respect to actin (calculated from the data shown in Figs. 6 and 7). The distributions were derived from single-molecule localization data that were analyzed by CBC.

**a** The colocalization analysis for ezrin reveals two maxima, one for negative  $C_A$  ( $m_- = -0.45$ ) and one for positive  $C_A$  ( $m_+ = 0.25$ ). **b** The colocalization analysis for merlin exhibits a broad distribution with a maximum at  $m_- = -0.55$

## Conclusions

We report a robust and straightforward solution to derive colocalization information from single-molecule localization microscopy data. We presented a microscopic configuration for alternated-excitation imaging of two spectral channels and therefore overcome dynamic range problems of the EMCCD camera. We introduced a solid correction approach for chromatic errors that reaches on average less than 10 nm errors over a whole field of view. We presented different positive controls using simulations, a cellular structure with exact identical protein distributions and a dual-labeled cellular structure. We applied the method to two proteins that interact differently with the actin cytoskeleton and confirmed the different binding affinity. As several inorganic dyes can be operated as photoswitches in a live cell (Wombacher et al. 2010) together with the wealth of available photoactivatable fluorescent proteins, it is possible to use this approach for live cell imaging. Finally, the CBC approach can be extended to a third dimension in a straightforward way.

**Acknowledgments** M.H. is grateful for funding by the German Ministry of Education and Research (BMBF; FORSYS initiative, grant nr. 0315262) and the German Science Foundation (DFG, grant nr. HE 6166/2-1). P.J.V is grateful for funding by the German Ministry of Education and Research (BMBF; FORSYS initiative, grant nr. 0315257) and by the German Science Foundation, as part of the NanoSci-ERA consortium (grant nr. VE 579/1-1).

## References

- Adler J, Parmryd I (2010) Quantifying colocalization by correlation: the Pearson correlation coefficient is superior to the Mander's overlap coefficient. *Cytom A* 77:733–742
- Betzig E, Patterson GH, Sougrat R, Lindwasser OW, Olenych S, Bonifacino JS, Davidson MW, Lippincott-Schwartz J, Hess HF (2006) Imaging intracellular fluorescent proteins at nanometer resolution. *Science* 313:1642–1645

- Bolte S, Cordelieres FP (2006) A guided tour into subcellular colocalization analysis in light microscopy. *J Microsc* 224:213–232
- Churchman LS, Okten Z, Rock RS, Dawson JF, Spudich JA (2005) Single molecule high-resolution colocalization of Cy3 and Cy5 attached to macromolecules measures intramolecular distances through time. *Proc Natl Acad Sci USA* 102:1419–1423
- Endesfelder U, Malkusch S, Flottmann B, Mondry J, Liguzinski P, Verveer PJ, Heilemann M (2011) Chemically induced photoswitching of fluorescent probes—a general concept for super-resolution microscopy. *Molecules* 16:3106–3118
- Fehon RG, McClatchey AI, Bretscher A (2010) Organizing the cell cortex: the role of ERM proteins. *Nat Rev Mol Cell Biol* 11:276–287
- French AP, Mills S, Swarup R, Bennett MJ, Pridmore TP (2008) Colocalization of fluorescent markers in confocal microscope images of plant cells. *Nat Protoc* 3:619–628
- Grecco HE, Verveer PJ (2011) FRET in cell biology: still shining in the age of super-resolution? *Chemphyschem* 12:484–490
- Heilemann M (2010) Fluorescence microscopy beyond the diffraction limit. *J Biotechnol* 149:243–251
- Heilemann M, Margeat E, Kasper R, Sauer M, Tinnefeld P (2005) Carbocyanine dyes as efficient reversible single-molecule optical switch. *J Am Chem Soc* 127:3801–3806
- Heilemann M, van de Linde S, Schuttpelz M, Kasper R, Seefeldt B, Mukherjee A, Tinnefeld P, Sauer M (2008) Subdiffraction-resolution fluorescence imaging with conventional fluorescent probes. *Angew Chem Int Ed Engl* 47:6172–6176
- Koyama-Honda I, Ritchie K, Fujiwara T, Iino R, Murakoshi H, Kasai RS, Kusumi A (2005) Fluorescence imaging for monitoring the colocalization of two single molecules in living cells. *Biophys J* 88:2126–2136
- Li Q, Lau A, Morris TJ, Guo L, Fordyce CB, Stanley EF (2004a) A syntaxin 1, Galpha(o), and N-type calcium channel complex at a presynaptic nerve terminal: analysis by quantitative immunocolocalization. *J Neurosci* 24:4070–4081
- Li Q, Lau A, Morris TJ, Guo L, Fordyce CB, Stanley EF (2004b) A syntaxin 1, Galpha(o), and N-type calcium channel complex at a presynaptic nerve terminal: analysis by quantitative immunocolocalization. *J Neurosci* 24:4070–4081
- McClatchey AI, Fehon RG (2009) Merlin and the ERM proteins—regulators of receptor distribution and signaling at the cell cortex. *Trends Cell Biol* 19:198–206
- McKinney SA, Murphy CS, Hazelwood KL, Davidson MW, Looger LL (2009) A bright and photostable photoconvertible fluorescent protein. *Nat Methods* 6:131–133

- Pertsinidis A, Zhang Y, Chu S (2010) Subnanometre single-molecule localization, registration and distance measurements. *Nature* 466:647–651
- Radenovic A, Annibale P, Scarselli M, Kodiyan A (2010) Photoactivatable fluorescent protein mEos2 displays repeated photoactivation after a long-lived dark state in the red photoconverted form. *J Phys Chem Lett* 1:1506–1510
- Ronneberger O, Baddeley D, Scheipl F, Verveer PJ, Burkhardt H, Cremer C, Fahrmeir L, Cremer T, Joffe B (2008) Spatial quantitative analysis of fluorescently labeled nuclear structures: problems, methods, pitfalls. *Chromosome Res* 16:523–562
- Rust MJ, Bates M, Zhuang X (2006) Sub-diffraction-limit imaging by stochastic optical reconstruction microscopy (STORM). *Nat Methods* 3:793–795
- Schermelleh L, Carlton PM, Haase S, Shao L, Winoto L, Kner P, Burke B, Cardoso MC, Agard DA, Gustafsson MG, Leonhardt H, Sedat JW (2008) Subdiffraction multicolor imaging of the nuclear periphery with 3D structured illumination microscopy. *Science* 320:1332–1336
- Schermelleh L, Heintzmann R, Leonhardt H (2010) A guide to super-resolution fluorescence microscopy. *J Cell Biol* 190:165–175
- Smith CS, Joseph N, Rieger B, Lidke KA (2010) Fast, single-molecule localization that achieves theoretically minimum uncertainty. *Nat Methods* 7:373–375
- Wolter S, Endesfelder U, van de Linde S, Heilemann M, Sauer M (2011) Measuring localization performance of super-resolution algorithms on very active samples. *Optics Express* 19:7020–7033
- Wombacher R, Heidbreder M, van de Linde S, Sheetz MP, Heilemann M, Cornish VW, Sauer M (2010) Live-cell super-resolution imaging with trimethoprim conjugates. *Nat Methods* 7:717–719
- Zinchuk V, Zinchuk O (2008) Quantitative colocalization analysis of confocal fluorescence microscopy images. *Curr Protoc Cell Biol* Chapter 4:4–19

## Single-molecule coordinate-based analysis of the morphology of HIV-1 assembly sites with near-molecular spatial resolution

Sebastian Malkusch · Walter Muranyi ·  
Barbara Müller · Hans-Georg Kräusslich ·  
Mike Heilemann

Accepted: 31 July 2012 / Published online: 23 August 2012  
© Springer-Verlag 2012

**Abstract** We apply single-molecule super-resolution microscopy and coordinate-based cluster analysis to extract information on the distribution and on the morphology and size of clusters of the human immunodeficiency virus (HIV-1) Gag polyprotein in fixed cells. Three different patterns of Gag distribution could be distinguished. A major type of assembly observed was in accordance with previous electron microscopy analyses revealing ~140 nm-sized HIV-1 buds at the plasma membrane of virus-producing cells. The distribution of Gag molecules in the 2D projection at these sites was consistent with a semi-spherical 3D assembly. We compared different methods of cluster analysis and demonstrated that we can reliably distinguish different distribution patterns of the Gag polyprotein. These methods were applied to extract information on the properties of the different Gag clusters.

**Keywords** Super-resolution microscopy · Single-molecule fluorescence microscopy · Cluster analysis · Cellular structures · Human immunodeficiency virus · Gag

### Abbreviations

CA	Capsid domain
dSTORM	Direct stochastic optical reconstruction microscopy
EMCCD	Electron-multiplying charge device
HIV-1	Human immunodeficiency virus type 1
MA	Matrix domain
MEA	Mercaptoethylamine
NC	Nucleocapsid domains
ROI	Region of interest
Ryr	Ryanodine receptors
TIRF	Total internal reflection fluorescence

S. Malkusch and W. Muranyi contributed equally.

**Electronic supplementary material** The online version of this article (doi:10.1007/s00418-012-1014-4) contains supplementary material, which is available to authorized users.

S. Malkusch · M. Heilemann  
Biotechnology and Biophysics, Julius-Maximilians-University  
Würzburg, Würzburg, Germany

W. Muranyi · B. Müller · H.-G. Kräusslich  
Department of Infectious Diseases, Virology,  
University Hospital Heidelberg, Heidelberg, Germany

M. Heilemann (✉)  
BIOQUANT Centre, University of Heidelberg,  
Heidelberg, Germany  
e-mail: m.heilemann@uni-wuerzburg.de

### Introduction

The Gag polyprotein is the major structural component of the HIV-1 particle. It is targeted to the inner leaflet of the plasma membrane to form virions with an average diameter of about 140 nm (Briggs and Kräusslich 2011). In its unprocessed form, Gag consists of four major functional domains. The N-terminal matrix domain (MA) is required for attaching Gag to the plasma membrane via a myristoylation anchor and a cluster of basic residues. The capsid domain (CA) plays an essential role in Gag multimerization and the nucleocapsid domain (NC) binds to the viral RNA genome. The C-terminal p6 domain of Gag is needed for virus release via interaction with cellular cofactors (Ono 2009).

To visualize transport and assembly processes of Gag at the plasma membrane with conventional fluorescence microscopy in the cellular context, fusion proteins of Gag with EGFP were generated in the complete viral context. When expressed together with wild-type Gag at an equimolar ratio, these fusions gave rise to assembly- and entry-competent particles (Muller et al. 2004). The studies with Gag.EGFP revealed a punctuate staining in the cytosol and at the plasma membrane. Plasma membrane resident puncta of Gag.EGFP represent individual viral assembly sites, at which Gag molecules were found to accumulate over a period of  $\sim 10$  min (Ivanchenko et al. 2009; Jovenet et al. 2008). HIV-1 budding sites and extracellular particles have an average diameter of ca. 140 nm with significant size variability as determined by cryo-electron microscopy (Briggs et al. 2009; Carlson et al. 2008; Larson et al. 2005; Wright et al. 2007).

Super-resolution microscopy extends beyond the limits of conventional light microscopy, providing information on levels of protein organization, from single proteins to small clusters and large aggregates. Stochastic methods employing a temporal separation of individual fluorescence signals using photoswitchable fluorescent probes which are localized as single molecules are particularly valuable for super-resolution microscopy: they yield so far the best spatial resolution in biological samples, reaching a near-molecular level (Mortensen et al. 2010; Schermelleh et al. 2010). Recently, a dual-objective approach has demonstrated a lateral optical resolution of about 10 nm (Xu et al. 2012). As single-molecule methods, they provide access to quantitative information (van de Linde et al. 2008), and as coordinate-based approaches, they are compatible with established algorithms to study biomolecular aggregation and clustering (Baddeley et al. 2009; Williamson et al. 2011).

In the present work, we applied single-molecule localization microscopy (Betzig et al. 2006; Heilemann et al. 2008, 2009; Rust et al. 2006) to study the distribution of the HIV-1 Gag protein at the plasma membrane of a transfected T-cell line with single-molecule sensitivity and a spatial resolution of about 20 nm. A previous study employed a fusion of HIV-1 Gag to a photoswitchable fluorescent protein to analyze the dynamic behavior of Gag, revealing clusters of immobilized Gag molecules at the plasma membrane (Manley et al. 2008). More recently, Lehmann et al. (2011) applied dual-color super-resolution microscopy to investigate the co-localization of the cellular restriction factor tetherin with assemblies of HIV-1 Gag labeled with a photoswitchable protein. However, a detailed analysis of Gag distribution patterns on the surface of cells expressing Gag in the viral context has not been reported so far. In order to exploit the enhanced sensitivity and improved spatial resolution provided by the higher

photon yield of organic fluorophores, we used an HIV-1 derivative carrying a SNAP-tag within the Gag polyprotein, which has been shown to display a wild-type assembly phenotype upon co-expression with its untagged counterpart (Eckhardt et al. 2011). The SNAP-tag is an altered version of the DNA repair protein O<sup>6</sup>-alkylguanine-DNA alkyltransferase which catalyzes a self-labeling reaction with fluorescently labeled benzylguanine (BG) substrates. Insertion of the SNAP-tagged label into an almost complete (non-infectious) HIV genome in combination with super-resolution microscopy allows us to draw a comprehensive picture of the distribution and morphology of Gag assemblies at the plasma membrane of virus-producing T cells.

## Methods

### Cell culture, plasmids and transfection

The T-cell line A3.01 was grown in RPMI 1640 medium supplemented with 10 % fetal calf serum (FCS), 100 U/ml penicillin and 100  $\mu$ g/ml streptomycin. Cells were maintained at 37 °C and 5 % CO<sub>2</sub>.

Plasmids pCHIV and pCHIV<sup>SNAP</sup> were described previously (Eckhardt et al. 2011; Lampe et al. 2007). For the analysis of Gag assembly sites, an equimolar amount of the wild-type pCHIV and tagged pCHIV<sup>SNAP</sup> constructs were used in order to ensure wild-type assembly properties (Eckhardt et al. 2011). The electroporation and staining procedure was described previously (Eckhardt et al. 2011). In brief,  $5 \times 10^6$  A3.01 cells were electroporated with 10  $\mu$ g of each plasmid. At 24-h post-electroporation, cells were washed twice with phosphate buffered saline (pH 7.4; PBS) and transferred to LabTek 8-well chambered cover glasses. Cells were fixed with 3 % paraformaldehyde (PFA) in PBS for 15 min, washed and permeabilized with 0.1 % Triton X-100 in PBS for 10 min. After blocking the cells with 2 % bovine serum albumin (BSA) solution, cells were stained with 5  $\mu$ M SNAP-surface Alexa Fluor 647 (Invitrogen, Carlsbad, USA) according to the manufacturer's instructions. After staining, cells were washed with PBS containing 0.1 % Tween 20 (Sigma, USA) and PBS.

### Super-resolution fluorescence microscopy

Super-resolution imaging was performed using the *d*STORM approach and has been described elsewhere (Heilemann et al. 2008). Briefly, fluorophore read-out and photoswitching of the carbocyanine fluorophore Alexa Fluor 647 were performed using the 647 and 514 nm laser lines of an argon-krypton laser (Innova 70C, Coherent, USA) that were directed through an oil immersion



objective (60×, NA = 1.45; Olympus, Japan) which was mounted on an inverted microscope (IX71, Olympus, Japan). The microscope was operated in total internal reflection fluorescence (TIRF) mode. Fluorescence emission was spectrally separated from the excitation light using appropriate dichroic beamsplitters and filters (AHF, Germany) and directed onto the active area of an electron-multiplying charge-coupled device (EMCCD) (Ixon, Andor, Ireland). Additional optics was used to set the image pixel size to 110 nm.

Reversible photoswitching of Alexa Fluor 647 was performed in PBS in the presence of 50–100 mM mercaptoethylamine (MEA) and an enzymatic oxygen scavenging system (for details, see Heilemann et al. 2008). Typically, irradiation intensities of 1–4 kW/cm<sup>2</sup> (647 nm) and 0.2–1 kW/cm<sup>2</sup> (514 nm) were applied. Image stacks consisting of 4,000–10,000 individual frames with an integration time of 20–50 ms were recorded. Single-molecule localization and image reconstruction was performed using the rapidSTORM algorithm (Wolter et al. 2010) (available free of charge at [www.super-resolution.de](http://www.super-resolution.de)), applying appropriate intensity thresholds.

#### Coordinate-based cluster analysis

Distance distribution analysis of defined regions of interest (ROI) with the dimension of 2 μm by 2 μm was performed as described earlier (Endesfelder et al. 2011). Briefly, we calculated Ripley's K-function,  $K(r)$ , (Ripley 1977) for the ROI and compared it with a toroidal edge correction to account for edge effects against a 95 % confidence envelope of uniform distributions simulated with Monte Carlo methods using Matlab (Mathworks, Natick, MA, USA). We used a linearized form,  $L(r)$ , of Ripley's K-function that has been normalized such that a uniform distribution would give an expected value of  $L(r) - r = 0$  for all  $r$ , in order to distinguish between different spatial patterns of Gag protein at the plasma membrane (Haase 1995; Ripley 1979):

$$K(r) = \frac{1}{n^2} \sum_i \sum_j \frac{N_r(d_{ij})}{\lambda} \quad (1)$$

$$L(r) = \sqrt{\frac{K(r)}{\pi}} \quad (2)$$

where  $n$  is the total number of localizations within the ROI,  $d_{ij}$  is the distance between two localizations  $i$  and  $j$ ,  $N_r$  is the number of localizations around localization  $i$  within the distance  $j$ , and  $\lambda$  is a weighting factor correcting for the area of the ROI. The maximum of the normalized K-function is a measure of cluster size and lies between the radius and the diameter of the cluster, yet also depends on the distance between individual clusters. We have

performed simulations on single-molecule localization data for illustration (supplemental Fig. 2).

#### Morphological cluster analysis

Morphological cluster analysis was performed by first generating a reconstructed image by binning all single-molecule localizations into a two-dimensional histogram with a bin size of 11 nm per sub-pixel. In these images, the information on each pixel represents the relative single-molecule densities in this area. The cluster size was examined with an image-based approach using the intensity plot plugin of ImageJ (Abramoff et al. 2004) and an intensity threshold. In a second approach, we applied a nearest neighbor analysis to extract the cluster size using custom-written software in Matlab (Mathworks, Natick, MA, USA). For all single-molecule localizations which were found within a cluster, the nearest neighbor has been identified and the distance to it was determined. The mean value of nearest neighbor distances was plotted against the distance of the very location to the center of the cluster. The derivative of the nearest neighbor distance does not depend on a threshold and was used to discriminate single-molecule localizations inside the cluster from the ones outside or around the cluster.

## Results and discussion

We studied the assembly of HIV-1 at the plasma membrane of the A3.01 T-cell line using a localization-based super-resolution microscopy setup with stochastically photoswitchable organic fluorophores (Heilemann et al. 2008). Since Gag is the major structural polyprotein of the virus, we focused on its distribution and morphology analyzing all assembly sites of an entire cell. This was achieved by labeling the MA domain of Gag fused to a SNAP-tag (Eckhardt et al. 2011) with the carbocyanine fluorophore Alexa Fluor 647 and performing single-molecule localization microscopy with subdiffraction spatial resolution (Heilemann et al. 2008). From the single-molecule data, we generated reconstructed images (Fig. 1) that typically showed a localization precision of ~20 nm (see supplementary Fig. S1) in the imaging plane and thus about one order of magnitude below the diffraction limit of visible light. Importantly, single-molecule based microscopy provides two-dimensional coordinates which allowed the analysis of shape and spatial distribution of the Gag protein, from individual molecules to complex clusters at the plasma membrane.

Conventional fluorescence microscopy has revealed Gag proteins to be organized in different aggregation states at the plasma membrane (Jouvenet et al. 2011). Our aim was

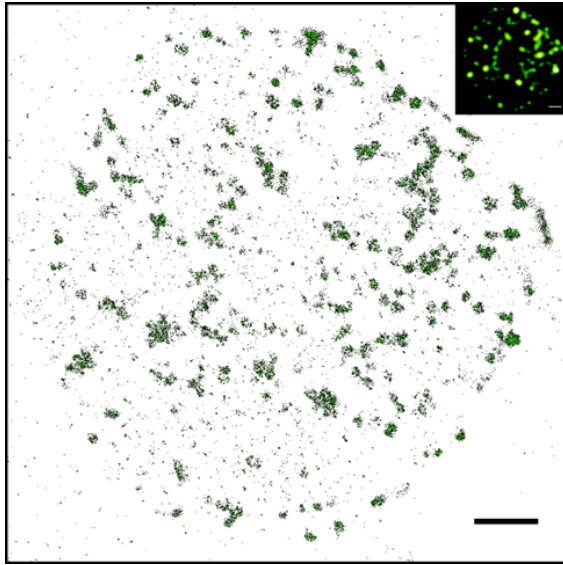


**Fig. 1** Super-resolution fluorescence image of an A3.01 cell expressing Gag.SNAP labeled with Alexa Fluor 647 and recorded with the *d*STORM approach. The *inset* shows the fluorescence image with diffraction-limited spatial resolution. The *d*STORM image shows individual clusters of the Gag protein, representing putative HIV assembly sites (scale bar 1  $\mu$ m)

to characterize organization states profiting from molecular coordinates provided by stochastic single-molecule super-resolution data, which are an ideal basis for cluster analysis. Such algorithms are routinely used in electron microscopy (Mayhew et al. 2004), yet are still not established in fluorescence microscopy. Recently, the spatial organization of the ryanodine receptors (Ryr) was investigated using a cluster algorithm that determines morphology and shape parameters (Baddeley et al. 2009). Clustering of a T-cell receptor was studied from single-molecule super-resolution data (Owen et al. 2010) using Ripley's K-function (Ripley 1977), a cluster analysis approach that starts off with single-object coordinates. The K-function provides information on cluster size and distribution, with the maximum of the K-function approaching the diameter of an individual cluster at large inter-cluster distances (Kiskowski et al. 2009).

We applied Ripley's K-function to characterize the Gag protein distribution in different ROI of the plasma membrane and a simulated data set with a dimension of  $2 \mu\text{m} \times 2 \mu\text{m}$  (Fig. 2, supplemental Fig. 2). We distinguished three forms of protein organization: (i) a diffusely distributed organization (Fig. 2a, b) with a broad maximum of the mean K-function at 173 nm; (ii) organization into small dense clusters (Fig. 2c, d) with a sharp maximum of the mean K-function at 40 nm; (iii) organization into clusters suggested to correspond to viral assembly sites

(Fig. 2e, f) with a mean K-function exhibiting a maximum at 120 nm. It is important to note that the maximum of a mean K-function indicates the cluster size, but does not exactly provide a radius or a diameter of a cluster. The maximum of the K-function lies between the radius and the diameter of particles, and also depends on the average distance between particles, a fact that is often neglected in data interpretation (an according analysis of simulated data is available as supplemental Fig. 2). Commonly, the K-function is used to differentiate spatial distributions or aggregation states of proteins (see e.g., Williamson et al. 2011). However, the rather sharp peak of the K-function (Fig. 2f) indicates a regular size, compared, for example, with the more diffuse distribution found for those Gag proteins (Fig. 2a), with a K-function exhibiting a broad peak (Fig. 2b). From the analysis of our experimental data with the K-function, we conclude that we can distinguish a first group of Gag molecules appearing as small clusters (Fig. 2c), which might represent initial stages of virus bud formation and/or mobile Gag proteins as described by Manley et al. (2008). The second, most prominent group of Gag engaged in late assembly sites with a characteristic shape and diameter (Fig. 2e), and a third group of Gag molecules organized in larger and less well-defined platforms (Fig. 2a). These latter platforms (Fig. 2a) were less frequently detected than the cluster types (ii) and (iii) and were only observed in a subset of cells analyzed. Larger accumulations of Gag have also been seen in images generated by diffraction-limited fluorescence microscopy in cells expressing HIV-1 Gag tagged with fluorescent proteins (e.g., Hermida-Matsumoto and Resh 2000; Ivanchenko et al. 2009; Jouvenet et al. 2006). Live-cell TIRF microscopy revealed that larger clusters, presumably representing aggregated budding sites and cell-attached particles, appeared at a late stage ( $>1$  h) after the onset of budding site formation in the respective cell (Ivanchenko et al. 2009). Based on this observation, we propose that the diffuse Gag.SNAP clusters detected in some cells may represent a late stage of Gag accumulation upon prolonged viral protein expression.

Next, we described the shape of single HIV assembly sites [exemplary intensity profiles are shown in (Fig. 3a–l) in two different ways]. First, we performed an image-based analysis and generated an average intensity profile (Fig. 3m) from 25 individual assembly sites. From this average intensity profile, we determined a full-width half-maximum (FWHM) of 118 nm, which corresponds to the diameter of the assembly sites. This value is in good accordance with the size of HIV budding sites determined by electron tomography (Carlson et al. 2008). Notably, we observed a local minimum in the center of the intensity profile (Fig. 3m, supplemental Fig. 3), which can be explained by the spherical structure of the assembly site: the distribution of

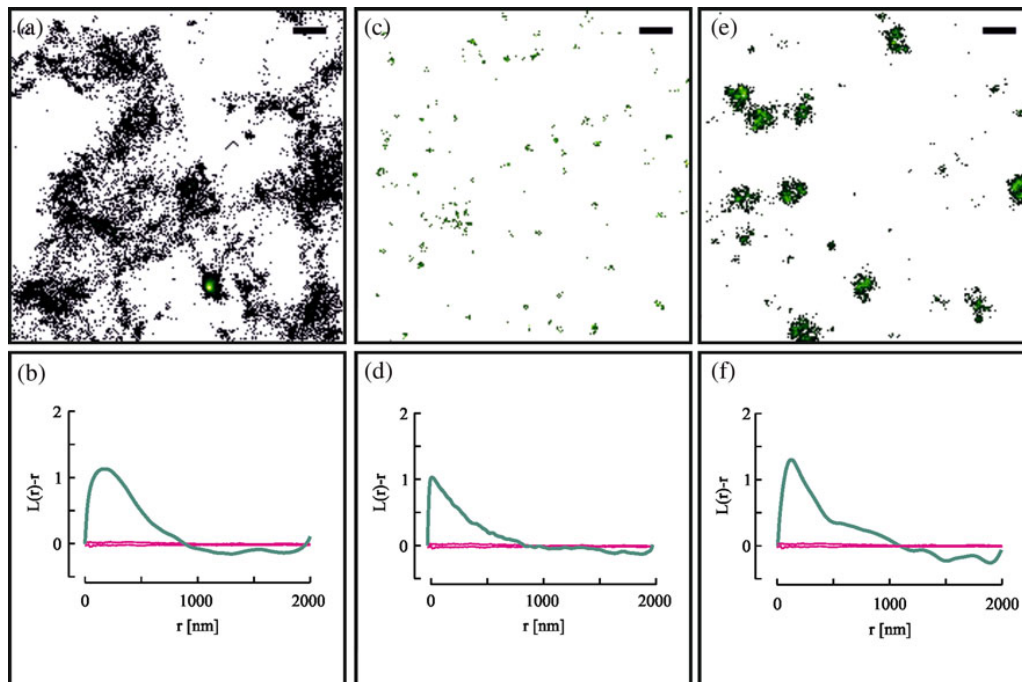


**Fig. 2** **a, c, e** Distributions of Gag proteins recorded with localization-based super-resolution imaging (scale bars 200 nm). **b, d, f** Single-molecule distributions were analyzed for clustering with Ripley's K-function. The normalized function,  $L(r) - r$ , indicates different levels of Gag protein organization on the plasma membrane (green curve) relative to a random distribution indicated by a 95 % confidence envelope (magenta curve). The diffuse Gag protein (**a, b**) is non-randomly distributed and exhibits a maximum of clustering at

$r = 173$  nm. Single Gag molecules together with small and dense Gag clusters (**c, d**) are non-randomly distributed, the maximum of clustering lies at  $r = 40$  nm. **e, f** Clusters considered to correspond to viral assembly sites are non-randomly distributed, and the normalized Ripley function exhibits a maximum at  $r = 120$  nm which correlates with the size of the putative assembly sites. Data analysis was performed from 16 different experimental data sets

Gag molecules on the surface of a sphere results in a higher fluorophore density at the edges in a 2D projection of the data (see supplemental Fig. 4). The local minimum shown here had not been observed in a recent study, which used photoactivated-localization microscopy (PALM) to visualize assembly sites of Gag labeled with a photoswitchable protein (Lehmann et al. 2011). This apparent discrepancy can be explained by the higher photon yield of the organic fluorophore used here, resulting in a higher localization accuracy (Heilemann 2010). This improvement made it possible to resolve the 3D projection of the semi-spherical Gag shell (see supplementary Figs. S3, S4).

In a second approach, we performed a nearest neighbor analysis of single-molecule localization data of circular assembly sites in HIV expressing A3.01 cells. The distance from the localization of every single molecule of Gag to its nearest neighbor was calculated and the distribution was plotted with respect to the distance to the center of a putative Gag assembly site (Fig. 3n). This nearest neighbor distribution revealed two distinct populations: the first group of Gag molecules was observed within a radius of 0–70 nm from the center, with a constant distance to its

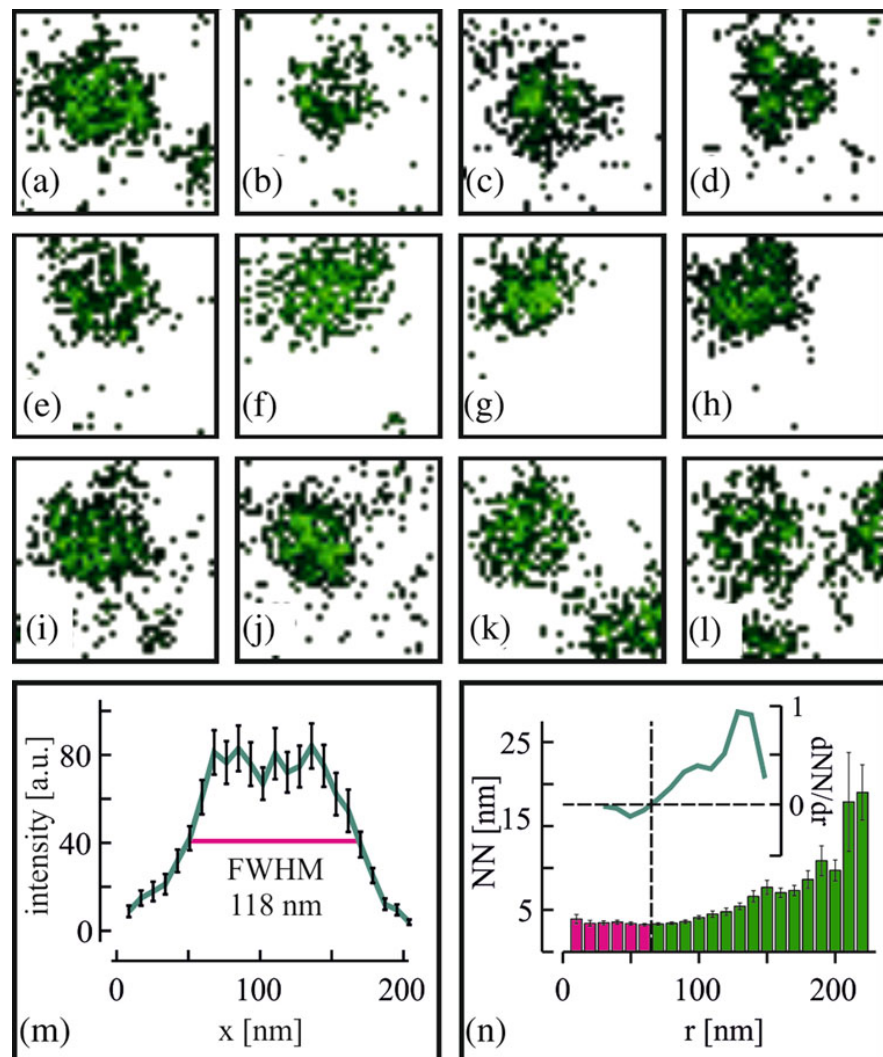
nearest neighbor, indicating a homogeneous molecular density representing tightly packed Gag molecules inside a cluster (highlighted in magenta in Fig. 3n). This tightly packed Gag cluster represents nascent virus budding sites with an average radius of 70 nm, a value which is slightly larger than determined by averaging of single budding sites (Fig. 3a–l). The second group of Gag molecules exhibited an increase in the distance to their respective nearest neighbor, indicating that Gag molecules are not part of an assembly site but of a protein pool located in its vicinity. In contrast to the image-based cluster analysis, the coordinate-based analysis does not require thresholding or other image processing procedures (e.g., deconvolution). In addition, we can differentiate different patterns of spatial organizations of Gag molecules in the immediate vicinity of an assembling HIV-1 particle.

## Conclusion and outlook

In conclusion, we demonstrate how structural information on protein aggregation can be derived by cluster analysis of



**Fig. 3** **a–l** Examples of super-resolution fluorescence images of single Gag protein clusters (300 nm × 300 nm). **m** Average intensity profile of putative assembly sites derived from 25 Gag clusters exhibit a FWHM of 118 nm, corresponding to the size of the putative budding sites. **n** Distribution of the average distance of each single-molecule localization to its nearest neighbor scaled to the center of the assembly site and derived from 25 Gag clusters (*error bars* indicate standard error). The *pink color* highlights a region with a constant nearest neighbor distance (about 4–5 nm), which indicates a dense packing and thus represents the radius of a budding site; at larger distance from the center of the clusters, the average distance to the nearest neighbor increases, indicating Gag proteins that are outside of a cluster (*inset* derivative of the nearest neighbor distance to the radius)



single-molecule super-resolution data. Specifically, we have studied the distribution of the HIV-1 Gag protein on the plasma membrane of an entire particle-producing cell. We found three different states of cluster distribution: (i) small Gag clusters, (ii) Gag clusters of a defined size of ~140 nm and (iii) patchy aggregation of Gag proteins. Furthermore, we have used coordinate-based algorithms to derive information on the size of single assembly sites and obtained results for the size of putative assembly sites that are in good accordance with prior electron microscopy data. This analysis provides a framework to analyze and describe the localization of other viral or cellular proteins with respect to HIV-1 Gag assembly sites. The adaption to other cellular structures is also possible, as well as the extension to live-cell super-resolution imaging (van de Linde et al. 2011; Wombacher et al. 2010).

**Acknowledgments** This work was supported by the Systems Biology Initiative (FORSYS) of the German Ministry of Research and Education (BMBF), Project VIROQUANT and Grant No. 0315262.

### References

- Abramoff MDM, Paulo J, Ram, Sunanda J (2004) Image processing with ImageJ. *Biophotonics Int* 11:36–42
- Baddeley D, Jayasinghe ID, Lam L, Rossberger S, Cannell MB, Soeller C (2009) Optical single-channel resolution imaging of the ryanodine receptor distribution in rat cardiac myocytes. *Proc Natl Acad Sci USA* 106:22275–22280
- Betzig E, Patterson GH, Sougrat R, Lindwasser OW, Olenych S, Bonifacino JS, Davidson MW, Lippincott-Schwartz J, Hess HF (2006) Imaging intracellular fluorescent proteins at nanometer resolution. *Science* 313:1642–1645

- Briggs JA, Krausslich HG (2011) The molecular architecture of HIV. *J Mol Biol* 410:491–500
- Briggs JA, Riches JD, Glass B, Bartonova V, Zanetti G, Krausslich HG (2009) Structure and assembly of immature HIV. *Proc Natl Acad Sci USA* 106:11090–11095
- Carlson LA, Briggs JA, Glass B, Riches JD, Simon MN, Johnson MC, Muller B, Grunewald K, Krausslich HG (2008) Three-dimensional analysis of budding sites and released virus suggests a revised model for HIV-1 morphogenesis. *Cell Host Microbe* 4:592–599
- Eckhardt M, Anders M, Muranyi W, Heilemann M, Krijnse-Locker J, Muller B (2011) A SNAP-tagged derivative of HIV-1—a versatile tool to study virus-cell interactions. *PLoS ONE* 6:e22007
- Endesfelder U, Malkusch S, Flottmann B, Mondry J, Liguzinski P, Verveer PJ, Heilemann M (2011) Chemically induced photoswitching of fluorescent probes—a general concept for super-resolution microscopy. *Molecules* 16:3106–3118
- Haase P (1995) Spatial pattern analysis in ecology based on Ripley K-function: introduction and methods of edge correction. *J Veg Sci* 6:575–582
- Heilemann M (2010) Fluorescence microscopy beyond the diffraction limit. *J Biotechnol* 149:243–251
- Heilemann M, van de Linde S, Schuttpelz M, Kasper R, Seefeldt B, Mukherjee A, Tinnefeld P, Sauer M (2008) Subdiffraction-resolution fluorescence imaging with conventional fluorescent probes. *Angew Chem Int Ed Engl* 47:6172–6176
- Heilemann M, van de Linde S, Mukherjee A, Sauer M (2009) Super-resolution imaging with small organic fluorophores. *Angew Chem Int Ed Engl* 48:6903–6908
- Hermida-Matsumoto L, Resh MD (2000) Localization of human immunodeficiency virus type 1 Gag and Env at the plasma membrane by confocal imaging. *J Virol* 74:8670–8679
- Ivanchenko S, Godinez WJ, Lampe M, Krausslich HG, Eils R, Rohr K, Brauchle C, Muller B, Lamb DC (2009) Dynamics of HIV-1 assembly and release. *PLoS Pathog* 5:e1000652
- Jouvenet N, Neil SJ, Bess C, Johnson MC, Virgen CA, Simon SM, Bieniasz PD (2006) Plasma membrane is the site of productive HIV-1 particle assembly. *PLoS Biol* 4:e435
- Jouvenet N, Bieniasz PD, Simon SM (2008) Imaging the biogenesis of individual HIV-1 virions in live cells. *Nature* 454:236–240
- Jouvenet N, Simon SM, Bieniasz PD (2011) Visualizing HIV-1 assembly. *J Mol Biol* 410:501–511
- Kiskowski MA, Hancock JF, Kenworthy AK (2009) On the use of Ripley's K-function and its derivatives to analyze domain size. *Biophys J* 97:1095–1103
- Lampe M, Briggs JA, Endress T, Glass B, Riegelsberger S, Krausslich HG, Lamb DC, Brauchle C, Muller B (2007) Double-labelled HIV-1 particles for study of virus-cell interaction. *Virology* 360:92–104
- Larson DR, Johnson MC, Webb WW, Vogt VM (2005) Visualization of retrovirus budding with correlated light and electron microscopy. *Proc Natl Acad Sci USA* 102:15453–15458
- Lehmann M, Rocha S, Mangeat B, Blanchet F, Uji IH, Hofkens J, Piguet V (2011) Quantitative multicolor super-resolution microscopy reveals tetherin HIV-1 interaction. *PLoS Pathog* 7:e1002456
- Manley S, Gillette JM, Patterson GH, Shroff H, Hess HF, Betzig E, Lippincott-Schwartz J (2008) High-density mapping of single-molecule trajectories with photoactivated localization microscopy. *Nat Methods* 5:155–157
- Mayhew TM, Griffiths G, Lucocq JM (2004) Applications of an efficient method for comparing immunogold labelling patterns in the same sets of compartments in different groups of cells. *Histochem Cell Biol* 122:171–177
- Mortensen KI, Churchman LS, Spudich JA, Flyvbjerg H (2010) Optimized localization analysis for single-molecule tracking and super-resolution microscopy. *Nat Methods* 7:377–381
- Muller B, Daecke J, Fackler OT, Dittmar MT, Zentgraf H, Krausslich HG (2004) Construction and characterization of a fluorescently labeled infectious human immunodeficiency virus type 1 derivative. *J Virol* 78:10803–10813
- Ono A (2009) HIV-1 assembly at the plasma membrane: Gag trafficking and localization. *Future Virol* 4:241–257
- Owen DM, Rentero C, Rossy J, Magenau A, Williamson D, Rodriguez M, Gaus K (2010) PALM imaging and cluster analysis of protein heterogeneity at the cell surface. *J Biophotonics* 3:446–454
- Ripley BD (1977) Modelling spatial patterns. *J R Stat Soc* 39:172–212
- Ripley BD (1979) Tests of 'randomness' for spatial point patterns. *J R Stat Soc* 41:368–374
- Rust MJ, Bates M, Zhuang X (2006) Sub-diffraction-limit imaging by stochastic optical reconstruction microscopy (STORM). *Nat Methods* 3:793–795
- Schermelleh L, Heintzmann R, Leonhardt H (2010) A guide to super-resolution fluorescence microscopy. *J Cell Biol* 190:165–175
- van de Linde S, Sauer M, Heilemann M (2008) Subdiffraction-resolution fluorescence imaging of proteins in the mitochondrial inner membrane with photoswitchable fluorophores. *J Struct Biol* 164:250–254
- van de Linde S, Loschberger A, Klein T, Heidbreder M, Wolter S, Heilemann M, Sauer M (2011) Direct stochastic optical reconstruction microscopy with standard fluorescent probes. *Nat Protoc* 6:991–1009
- Williamson DJ, Owen DM, Rossy J, Magenau A, Wehrmann M, Gooding JJ, Gaus K (2011) Pre-existing clusters of the adaptor Lat do not participate in early T cell signaling events. *Nat Immunol* 12:655–662
- Wolter S, Schuttpelz M, Tscherepanow M, Van De Linde S, Heilemann M, Sauer M (2010) Real-time computation of subdiffraction-resolution fluorescence images. *J Microsc* 237:12–22
- Wombacher R, Heidbreder M, van de Linde S, Sheetz MP, Heilemann M, Cornish VW, Sauer M (2010) Live-cell super-resolution imaging with trimethoprim conjugates. *Nat Methods* 7:717–719
- Wright ER, Schooler JB, Ding HJ, Kieffer C, Fillmore C, Sundquist WI, Jensen GJ (2007) Electron cryotomography of immature HIV-1 virions reveals the structure of the CA and SP1 Gag shells. *EMBO J* 26:2218–2226
- Xu K, Babcock HP, Zhuang X (2012) Dual-objective STORM reveals three-dimensional filament organization in the actin cytoskeleton. *Nat Methods* 9:185–188

# Super-Resolution Microscopy Reveals Specific Recruitment of HIV-1 Envelope Proteins to Viral Assembly Sites Dependent on the Envelope C-Terminal Tail

Walter Muranyi<sup>1</sup>, Sebastian Malkusch<sup>2</sup>, Barbara Müller<sup>1</sup>, Mike Heilemann<sup>3,4</sup>, Hans-Georg Kräusslich<sup>1\*</sup>

**1** Department of Infectious Diseases, Virology, University Hospital Heidelberg, Heidelberg, Germany, **2** Department of Biotechnology & Biophysics, Theodor-Boveri-Institute, Julius-Maximilians-University, Würzburg, Germany, **3** Institute of Physical & Theoretical Chemistry, Goethe University, Frankfurt am Main, Germany, **4** Bioquant, University of Heidelberg, Heidelberg, Germany

## Abstract

The inner structural Gag proteins and the envelope (Env) glycoproteins of human immunodeficiency virus (HIV-1) traffic independently to the plasma membrane, where they assemble the nascent virion. HIV-1 carries a relatively low number of glycoproteins in its membrane, and the mechanism of Env recruitment and virus incorporation is incompletely understood. We employed dual-color super-resolution microscopy visualizing Gag assembly sites and HIV-1 Env proteins in virus-producing and in Env expressing cells. Distinctive HIV-1 Gag assembly sites were readily detected and were associated with Env clusters that always extended beyond the actual Gag assembly site and often showed enrichment at the periphery and surrounding the assembly site. Formation of these Env clusters depended on the presence of other HIV-1 proteins and on the long cytoplasmic tail (CT) of Env. CT deletion, a matrix mutation affecting Env incorporation or Env expression in the absence of other HIV-1 proteins led to much smaller Env clusters, which were not enriched at viral assembly sites. These results show that Env is recruited to HIV-1 assembly sites in a CT-dependent manner, while Env( $\Delta$ CT) appears to be randomly incorporated. The observed Env accumulation surrounding Gag assemblies, with a lower density on the actual bud, could facilitate viral spread *in vivo*. Keeping Env molecules on the nascent virus low may be important for escape from the humoral immune response, while cell-cell contacts mediated by surrounding Env molecules could promote HIV-1 transmission through the virological synapse.

**Citation:** Muranyi W, Malkusch S, Müller B, Heilemann M, Kräusslich H-G (2013) Super-Resolution Microscopy Reveals Specific Recruitment of HIV-1 Envelope Proteins to Viral Assembly Sites Dependent on the Envelope C-Terminal Tail. *PLoS Pathog* 9(2): e1003198. doi:10.1371/journal.ppat.1003198

**Editor:** Alexandra Trkola, University of Zurich, Switzerland

**Received:** August 18, 2012; **Accepted:** January 3, 2013; **Published:** February 28, 2013

**Copyright:** © 2013 Muranyi et al. This is an open-access article distributed under the terms of the Creative Commons Attribution License, which permits unrestricted use, distribution, and reproduction in any medium, provided the original author and source are credited.

**Funding:** This work was supported by the Systems Biology Initiative (FORSYS) of the German Ministry of Research and Education (BMBF), project VIROQUANT and grant number 0315262. The funders had no role in study design, data collection and analysis, decision to publish, or preparation of the manuscript.

**Competing Interests:** The authors have declared that no competing interests exist.

\* E-mail: hans-georg.krausslich@med.uni-heidelberg.de

## Introduction

Human immunodeficiency virus type 1 (HIV-1) acquires its lipid envelope by budding through the plasma membrane of an infected cell. Virus morphogenesis is directed by the viral Gag polyprotein, which is sufficient for release of virus-like particles, and also facilitates the incorporation of the viral genome and other important factors including the viral envelope (Env) glycoproteins (reviewed in [1]). Env plays an essential role in virus replication by mediating the fusion between viral and cellular membranes during virus entry. The Env proteins are synthesized as a polyprotein precursor (gp160) that is cleaved to the mature surface glycoprotein gp120 and the transmembrane glycoprotein gp41 by cellular proteases. During virus assembly at the plasma membrane, the gp120/gp41 complex is incorporated into the lipid bilayer of nascent particles as a trimer of heterodimers. Within the virion, these trimeric complexes project from the membrane surface as highly glycosylated spikes (reviewed in [2]). HIV-1 exhibits a relatively low density of glycoprotein spikes on its surface compared to other enveloped viruses with only 7–14 Env

complexes per virion [3,4]. Virus entry is initiated by gp120 binding to the viral receptor CD4 and a chemokine receptor, and completed by insertion of a fusion peptide into the host membrane and conformational changes in gp41 mediating membrane fusion (reviewed in [2]).

HIV-1 Env is transported to the cell surface via the secretory pathway and inserts into the lipid membrane through the gp41 transmembrane domain. However, the mechanism by which the Env glycoprotein complex is incorporated into virus particles remains incompletely understood. Genetic and biochemical evidence points to an important role of the N-terminal, membrane-apposed matrix (MA) domain of the viral Gag polyprotein and the unusually long (151 amino acids) C-terminal tail of gp41 (CT), projecting into the interior of the virion, for Env incorporation [5–10]. HIV-1 derivatives lacking their cognate Env proteins can incorporate heterologous viral glycoproteins, thereby adopting their distinctive entry properties, however ('pseudotyping'; reviewed in [11]). Furthermore, deletion of the Env CT has only minor effects on virion incorporation of Env and viral infectivity in certain permissive cell lines, while strongly reducing

### Author Summary

Newly formed HIV-1 particles assemble at the plasma membrane of virus producing cells. The inner structural protein Gag and the envelope glycoprotein Env, which are both essential components of infectious virus particles, traffic to the membrane via different pathways. Attached to the inner side of the membrane, Gag assembles into spherical particles that incorporate Env proteins in their surrounding lipid envelope. The mechanism of Env incorporation is incompletely understood, however. Here, we have exploited recently developed super-resolution fluorescence microscopy techniques that yield a near-molecular spatial resolution to analyze HIV-1 Gag and Env distribution patterns at the surface of virus producing cells. We observed recruitment of Env to the surroundings of Gag assembly sites, dependent on the presence of its cytoplasmic domain. A large proportion of Env was found in the vicinity of the Gag assembly sites rather than directly co-localizing with it. These results support an indirect mechanism of Env recruitment, presumably mediated through virus induced changes in the environment of the nascent Gag assembly. Furthermore, they suggest a role for the Env protein in HIV-1 transmission that goes beyond its well-characterized function as an entry protein on the viral surface.

Env incorporation and abolishing infectivity in non-permissive cells [12–15]. Although these results are consistent with an important role of the CT, they show that an HIV-1 specific signal is dispensable for glycoprotein incorporation.

Four mutually non-exclusive models have been proposed to explain Env incorporation into retroviral particles: (i) random incorporation of plasma membrane proteins including Env, (ii) specific incorporation of Env into the virus by direct protein-protein interactions, (iii) co-targeting of Gag and Env to the same region of the plasma membrane and (iv) indirect incorporation via a bridging factor (reviewed in [2]). There is experimental evidence supporting, or at least consistent with each of these models. Efficient pseudotyping by heterologous glycoproteins and the large number of cellular membrane proteins incorporated into HIV-1 (reviewed in [16,17]) indicate that there is no exclusion of non-specific proteins. Incorporation may thus be influenced by surface density of the respective protein. A direct interaction between MA and Env CT *in vitro* has been reported [10] and there is strong genetic evidence supporting this interaction [5–8,18]. HIV-1 assembly is believed to occur at specific, raft-like membrane lipid microdomains, and both Gag and Env have been reported to be associated with detergent-resistant membranes (reviewed in [19]). Furthermore, co-expression of HIV-1 Gag with both HIV-1 Env and Ebola virus glycoproteins in the same cells showed efficient incorporation of both glycoproteins, but segregation into separate particle populations suggesting their spatial separation in virus producing cells [20]. Finally, a number of cellular proteins have been found to interact with HIV-1 Env proteins and may act as bridging factors for Env incorporation [2].

Fluorescence microscopy of HIV-1 producing cells shows patchy signals of both Gag and Env at the plasma membrane, while the majority of Env appears to reside in intracellular membrane compartments [21]. Confocal microscopy provided evidence for some colocalisation of Gag and Env at the plasma membrane [21], but reported correlation coefficients are low [20] and the resolution of light microscopy is not sufficient to discern adjacent individual budding sites. Immunostaining of surface glycoproteins and visualization with scanning electron microscopy

provided convincing evidence for a specific recruitment of Rous sarcoma virus (RSV) Env proteins to RSV but not to HIV-1 budding sites [22]; this study did not include HIV-1 glycoproteins, however.

Studying the distribution of viral proteins at small spatial scales requires an optical resolution which is beyond the limit of light microscopy (~200 nm). New super-resolution fluorescence microscopy techniques [23–25] have bypassed this resolution limit, providing spatial resolution reaching a near-molecular level. These include single-molecule localization techniques such as photoactivated localization microscopy (PALM) [23] and direct stochastic optical reconstruction microscopy (dSTORM) [26]. PALM and STORM microscopy have been employed to investigate the distribution of viral proteins upon HIV-1 cell entry [27,28] and to detect Gag assemblies at the plasma membrane [29–31]. Lehmann et al. [30] used multicolor super-resolution microscopy to investigate co-localization of the cellular restriction factor tetherin with HIV-1 budding sites. These authors also reported scattered Env distribution at Gag assembly sites, but did not further characterize Env localization [30]. Here, we performed dual-color super-resolution microscopy to analyze HIV-1 Gag and Env distribution patterns in HIV-1 producing cells. We show a CT dependent recruitment of Env to the viral budding site, with Env molecules concentrating around the Gag assemblies and in their periphery.

### Results

For detection of HIV-1 Gag in the viral context, we made use of a construct carrying the photoconvertible protein mEosFP inserted between the MA and capsid (CA) domains of Gag [32]. Proviral constructs carrying a gene encoding an autofluorescent protein at this position yield fluorescently labeled HIV-1 particles with wild-type morphology and infectivity upon co-transfection with equal amounts of their unlabeled counterpart [32]. Since fully assembled HIV-1 buds comprise ~2,400 molecules of Gag [33], 1,200 molecules of mEosFP are expected to accumulate on average at viral budding sites. In this study we employed constructs based on pCHIV [34] that encodes all HIV-1<sub>NL4-3</sub> proteins except Nef, but is replication deficient due to deletion of the viral long terminal repeats. The ratio of Env to Gag in transfected cells is thus comparable to that found in HIV-1 infected cells. Env molecules at the cell surface were detected by indirect immunolabeling using a human monoclonal antibody against gp120 (MAb 2G12; [35]). Primary antibody binding was revealed by a secondary antibody coupled to Alexa Fluor 647 followed by dSTORM imaging. Due to the higher photon yield of organic fluorophores, dSTORM imaging yields improved single-molecule localization and thus higher spatial resolution than PALM. The combination of PALM for detection of the abundant Gag molecules with a known lattice structure [1] and dSTORM for detection of the much rarer Env molecules [3] thus appeared ideally suited for the purpose of this study.

Total internal fluorescence (TIRF) microscopy and TIRF-PALM imaging of Gag.mEosFP at the plasma membrane of transfected HeLa cells was performed for detection of HIV-1 assembly sites. At the conditions used, Gag.mEosFP was detected with a localization accuracy of ~28 nm in PALM mode (Figure S1). TIRF microscopy revealed punctuate structures of Gag-mEosFP at the plasma membrane as described previously for Gag.eGFP [36] (Figure 1A). These punctae could be clearly resolved into individual assembly sites by super-resolution imaging (PALM; Figure 1B–D). Compact round assemblies with a diameter of ~130 nm (Figure 1D), closely resembling assembly

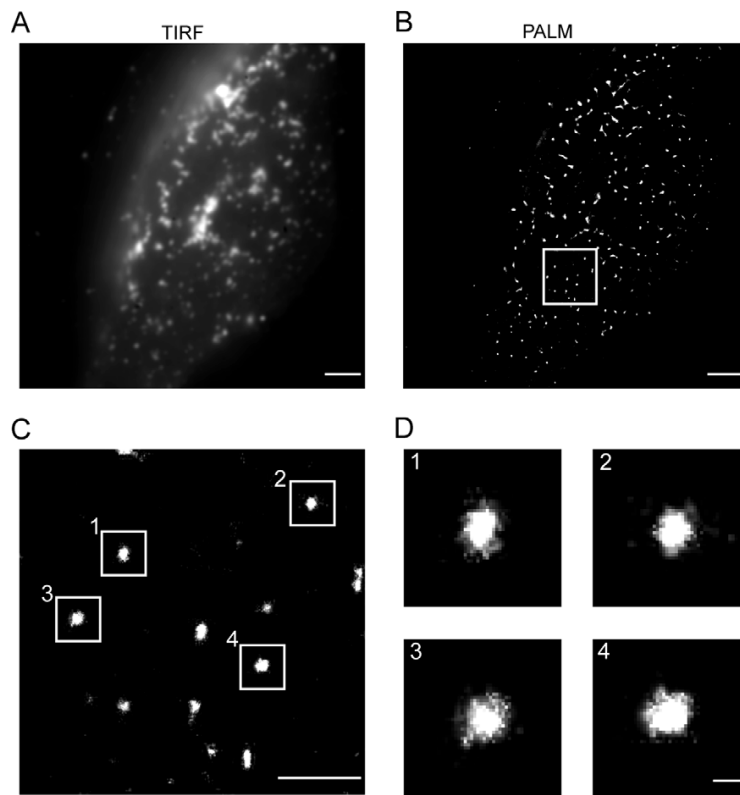


**Figure 1. Distribution of Gag.mEosFP at the plasma membrane of HeLa cells imaged by super-resolution TIRF microscopy.** HeLa cells were transfected with equimolar amounts of pCHIV and pCHIV<sup>mEosFP</sup>. At 24 hpt, cells were fixed and HIV-1 assembly sites were imaged by PALM as described in Materials and Methods. Summed intensity TIRF (A) and high resolution PALM (B) microscopy images of a representative cell are displayed. Scale bars correspond to 2  $\mu$ m. The boxed region in (B) corresponds to the region of interest shown as an enlarged high resolution image in (C). Scale bar in (C) corresponds to 1  $\mu$ m. (D) Four individual HIV-1 assembly sites from the boxed regions shown in (C). Scale bar corresponds to 100 nm.

doi:10.1371/journal.ppat.1003198.g001

sites detected by dSTORM or PALM in previous studies [29,30] were considered to represent HIV-1 budding structures. The PALM resolution achieved here was not sufficient to detect the semi-spherical architecture of individual Gag shells, which we have recently shown at higher resolution ( $\sim$ 18 nm) by dSTORM imaging of Gag.SNAP assembly sites labelled with a bright synthetic fluorophore [31].

HeLa cells transfected as above were fixed and subjected to immunostaining for HIV-1 Env, followed by TIRF- and TIRF-dSTORM microscopy. Alexa Fluor 647, coupled to the protein of interest through the primary and secondary antibody, was detected with a localization accuracy of  $\sim$ 15 nm in dSTORM mode (Figure S2). TIRF microscopy showed a multi-clustered Env distribution (Figure 2A), similar to previously reported results [21]. Env clusters of various sizes were observed by dSTORM imaging (Figure 2B). These clusters appeared larger and less compact than the Gag.mEosFP assemblies detected in the same cells (compare Figure 1). Dual-color super-resolution microscopy was performed on HeLa cells expressing HIV<sup>mEosFP</sup> to determine the relative localization of Env with respect to viral Gag assemblies. As shown in the representative images in Figures 2C and 2D, Env clusters surrounding Gag assembly sites were often round and sometimes displayed a doughnut-like shape. A similar pattern was observed

when another antibody against gp120 (MAb b12, [37]) was used (Figure S3), or when a harsher fixation protocol reported to block membrane protein motility [38] was applied (Figure S4). Env clusters of similar morphology were also observed in regions lacking a detectable Gag.mEosFP signal (Figure 2C), and only  $\sim$ 50% of Env clusters were associated with obvious HIV-1 budding sites. Env clusters not associated with characteristic Gag assemblies may correspond to early budding sites with a low number of Gag molecules. Furthermore, co-transfection with a wt plasmid encoding unlabeled Gag was performed in our experiments, and some assembly sites may thus contain a low number of Gag.mEosFP molecules. To address this issue, HeLa cells were transfected with pCHIV<sup>mEosFP</sup> alone and subsequently processed and analyzed as above. Similar Gag assembly sites surrounded by larger Env clusters were observed, but  $\sim$ 90% of Env clusters were found to be associated with Gag assemblies in this case (Figure S3).

Parallel control experiments showed that omitting the primary antibody from the staining solution or analysis of cells expressing a virus derivative lacking the viral Env protein yielded only few dense Alexa Fluor 647 signals, while the Env clusters were completely lost (Figure S5). The remaining non-specific signals presumably represent aggregates of secondary antibody. Env clusters overlapping HIV-1 budding sites showed a scattered



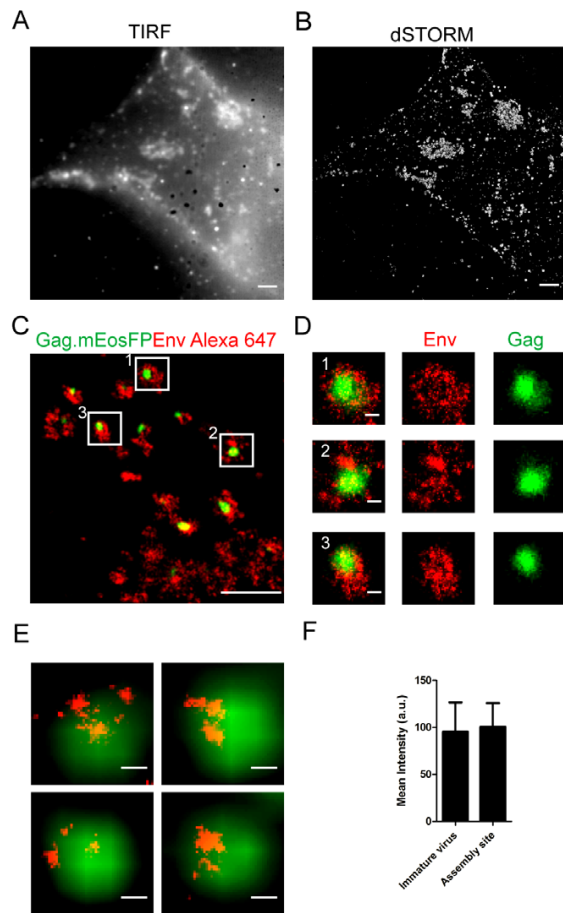


**Figure 2. Distribution of HIV-1 Env at the plasma membrane of HeLa cells visualized by super-resolution TIRF microscopy.** HeLa cells were transfected with equimolar amounts of pCHIV and pCHIV<sup>mEosFP</sup>. Cells were fixed 24 hpt, stained by indirect immunofluorescence using MAb 2G12 and goat anti-human Alexa Fluor 647 and imaged by dSTORM as described in Materials and Methods. Summed intensity TIRF (A) and high resolution dSTORM (B) microscopy images of a representative cell are displayed. Scale bars correspond to 2  $\mu$ m. (C) Region from the plasma membrane of a representative cell, showing the superposition of a PALM image for Gag.mEosFP (green) and the corresponding dSTORM image of Env stained with Alexa Fluor 647 (red), respectively. HeLa cells transfected with equimolar amounts of pCHIV and pCHIV<sup>mEosFP</sup> were fixed and stained by indirect immunofluorescence using MAb 2G12 and goat anti-human Alexa Fluor 647. Cells were subjected to dual-color super-resolution microscopy as described in Materials and Methods. Scale bar corresponds to 1  $\mu$ m. (D) Individual HIV-1 assembly sites from the boxed regions are shown. Scale bar corresponds to 100 nm. (E) Env surface distribution on extracellular immature HIV-1 particles. Particles were purified from the supernatant of 293T cells transfected with pCHIV carrying a point mutation in the HIV-1 protease active site [39]. An eGFP-tagged version of the accessory protein Vpr [63] was included as a marker to localize the position of individual virions in diffraction limited images. Virions were adhered to fibronectin-coated coverslips, fixed and immunostained with MAb 2G12 and goat anti-human Alexa Fluor 647. The panel shows images of four individual particles with the eGFP signal (green) recorded in diffraction limited mode and the Alexa Fluor 647 (red) signal recorded by dSTORM. Scale bars correspond to 100 nm. (F) Comparison of the Env signal intensities on single extracellular immature particles with the Env signal intensities colocalizing with HIV-1 assembly sites defined by the

dSTORM signal for Gag.mEosFP. Fluorescence intensities of the Alexa Fluor 647 signals were determined for the super-resolution images of ten individual particles each. The histogram shows the average values and SD of the fluorescence intensity. doi:10.1371/journal.ppat.1003198.g002

distribution and always extended beyond the area, in which Gag.mEosFP molecules were detected (Figure 2C, D). Furthermore, the density of Env localization events was not enriched at the position of the Gag.mEosFP assembly compared to the directly adjacent membrane area, but often appeared lower over the actual Gag assembly site (Figure 2C, D; see below). A comparative quantitative analysis of the Env signal on budding sites and released immature virions was performed to determine whether the comparatively low proportion of Env signals directly colocalizing with Gag constitutes the full complement of Env on the virion or whether peripheral Env clusters also contribute to the Env signal on the virus. Immature virions were used for this comparison, since the Gag lattice at the budding site is also immature and the Env distribution pattern on the viral surface is altered by proteolytic maturation of the inner virion structure [39]. Purified immature viral particles were fixed, stained with 2G12 as described for virus producing HeLa cells, and analyzed by dSTORM. Env signals distributed in multiple clusters were detected on the viral surface (Figure 2E) in agreement with recent results obtained by stimulated emission depletion microscopy [39]. Quantitative assessment revealed a similar intensity of the total Env signal on extracellular immature virions compared to the Env signal directly co-localizing with the Gag assembly site (Figure 2F). Accordingly, the Env content of the virion appears to be derived from the relatively low number of Env molecules directly overlapping the Gag assembly sites, while the larger Env cluster surrounding nascent assembly sites is not incorporated into the virion. Env recruitment was also investigated in the A3.01 T-cell line, since T-cells represent a natural target cell of HIV-1. A similar distribution of Gag assembly sites with overlapping Env clusters, but increased Env density at the periphery and surrounding the actual budding site was observed by super-resolution dual-color imaging of A3.01 cells producing HIV-1<sup>mEosFP</sup> (Figure S6A, 6B).

The experiments described were carried out employing fixed cells stained with complete IgG molecules, which could potentially affect distribution and detection of the molecules of interest. To exclude potential artifacts, all further experiments (except for those with the MA(mut) constructs, see below) were performed using unfixed cells (stained at 16°C to prevent membrane protein internalization) and immunostaining with Fab fragments. The distribution pattern for Gag assembly sites and Env molecules was largely unaltered when HeLa cells expressing HIV<sup>mEosFP</sup> were analyzed in this way (Figure 3A) compared to the initial protocol (Figure 2C). Tightly packed clusters of Gag.mEosFP with a diameter of ~130 nm marked HIV-1 assembly sites, which were overlaid by less dense Env clusters that commonly exhibited enrichment in the periphery and surrounding the Gag budding site (Figure 3B). To investigate whether the membrane distribution of HIV-1 Env was determined by the Env protein itself or was altered by the co-expression of other viral proteins, comparative dSTORM microscopy was performed on HeLa cells expressing either HIV<sup>mEosFP</sup> as before or only HIV-1 Env in the absence of other viral proteins. Super-resolution imaging of Env alone yielded a clearly different pattern compared to Env in the viral context. The large and distinctive round or doughnut shaped Env clusters, which frequently marked HIV-1 assembly sites (Figure 3C), were not seen in the absence of other viral proteins. Instead, much

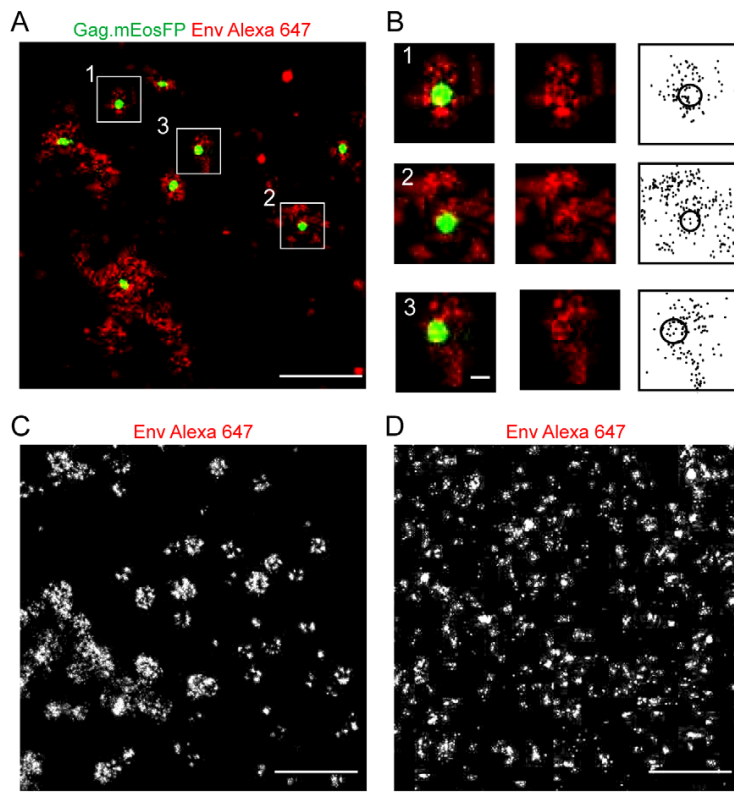


**Figure 3. Comparative analysis of Env(wt) distribution expressed in the viral context or alone.** (A, B) Distribution of HIV-1 Gag and Env at the plasma membrane of HeLa cells transfected with equimolar amounts of pCHIV and pCHIV<sup>mEosFP</sup>. Unfixed cells were stained by indirect immunofluorescence using Fab 2G12 and Fab goat anti-human Alexa Fluor 647, fixed, and subjected to dual-color super-resolution microscopy as described in Materials and Methods. (A) Region from the plasma membrane of a representative cell, showing the superposition of a PALM image for Gag.mEosFP (green) and the corresponding dSTORM image of Env stained with Alexa Fluor 647 (red), respectively. Scale bar corresponds to 1  $\mu$ m. (B) Enlargement of three individual assembly sites from the boxed regions indicated in (A). The figure shows merged super-resolution images (left panels), the dSTORM Env Alexa Fluor 647 image (middle panels) and individual Alexa Fluor 647 localizations from all images recorded in the defined area as black dots, with a black circle representing the rims of the Gag cluster (right panels), respectively. Scale bar corresponds to 100 nm. (C, D) Env distribution patterns in the presence (C) and absence (D) of other HIV-1 derived proteins. HeLa cells were transfected with equimolar amounts of pCHIV and pCHIV<sup>mEosFP</sup> (C) or with pEnv(wt) (D), respectively. Unfixed cells were stained with 2G12 Fab and Alexa Fluor 647 Fab, fixed, and visualized by dual-color super-resolution microscopy as described in Materials and Methods. Scale bars represent 1  $\mu$ m.  
doi:10.1371/journal.ppat.1003198.g003

smaller and more dispersed clusters were observed when Env was expressed alone (Figure 3D). These results demonstrate a clear influence of the other HIV-1 proteins, most likely Gag, on the membrane distribution of HIV-1 Env.

To investigate whether the long Env CT and its presumed interaction with the underlying Gag lattice are important for Env distribution on the surface of HIV-1 producing cells, we performed dual-color super-resolution microscopy on HeLa cells expressing HIV<sup>mEosFP</sup>Env( $\Delta$ CT). Tightly packed clusters of Gag.mEosFP as described above were detected in this case as well and identified *bona fide* HIV-1 budding sites (Figure 4A). Clusters of Env( $\Delta$ CT) appeared much smaller than observed for wild-type (wt) Env, however. In contrast to (wt) Env clusters, Env( $\Delta$ CT) clusters were not enriched at HIV-1 budding sites, but appeared to be more randomly distributed (Figure 4A, B). Furthermore, the characteristic Env clusters observed for the wt protein (compare Figure 3C) were not observed in this case. Similar results were obtained in HIV<sup>mEosFP</sup> expressing A3.01 cells (Figure S6). Comparison of Env distribution patterns in cells

expressing either HIV<sup>mEosFP</sup>Env( $\Delta$ CT) (Figure 4C) or only Env( $\Delta$ CT) (Figure 4D) using super-resolution microscopy revealed no apparent difference with similar cluster size and distribution in both cases. Thus, the characteristic Env distribution appeared to depend on the presence of other viral proteins and on the Env CT.

The most likely viral protein responsible for the observed specific Env distribution pattern in the full viral context is Gag since several mutations in its MA domain have been shown to affect Env incorporation [5–7,9]. To directly address this issue, we made use of a panel of proviral constructs carrying either the wt sequence or two point mutations (L8S/S9R) within the MA domain of Gag [8,40] (designated here as MA(mut)) in the context of Env(wt) or Env( $\Delta$ CT). These point mutations have been shown to affect Env(wt) particle incorporation and thereby viral infectivity; both defects are alleviated by truncation of the Env CT [8]. Transfected HeLa cells were fixed and immunostained with antibodies against MA and Env followed by dual-color dSTORM analysis (Figure 5, S7). Typical Gag assembly sites were readily detected in all cases and were associated with Env clusters

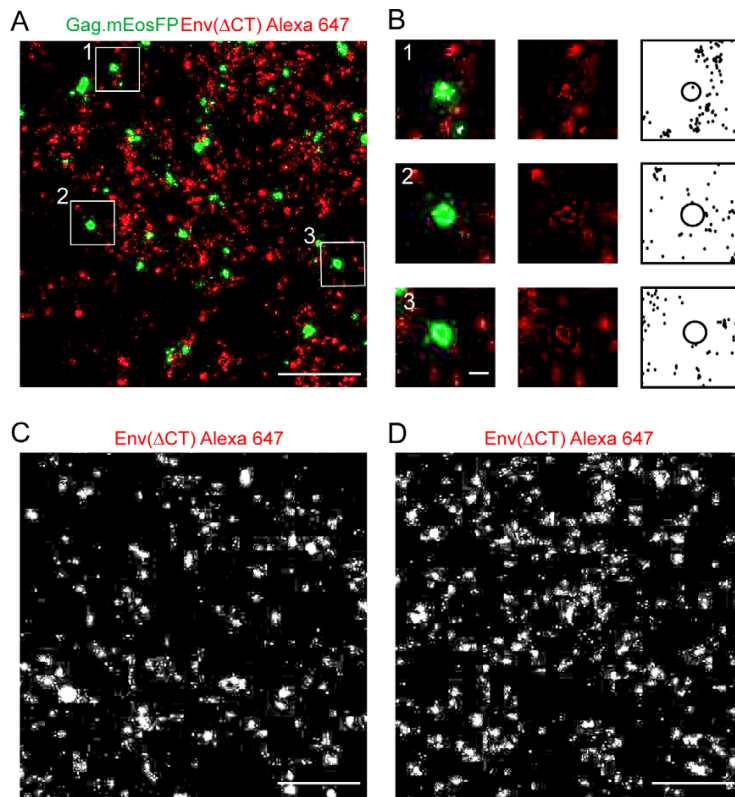


**Figure 4. Comparative analysis of Env( $\Delta$ CT) distribution expressed in the viral context or alone.** (A, B) Distribution of HIV-1 Gag and Env at the plasma membrane of HeLa cells transfected with equimolar amounts of pCHIV.Env( $\Delta$ CT) and pCHIV<sup>mEosFP</sup>.Env( $\Delta$ CT). Unfixed cells were stained by indirect immunofluorescence using Fab 2G12 and Fab goat anti-human Alexa Fluor 647, fixed, and subjected to dual-color super-resolution microscopy as described in Materials and Methods. (A) Region from the plasma membrane of a representative cell, showing the superposition of a PALM image for Gag.mEosFP (green) and the corresponding dSTORM image of Env( $\Delta$ CT) stained with Alexa Fluor 647 (red), respectively. Scale bar corresponds to 1  $\mu$ m. (B) Enlargement of three individual assembly sites from the boxed regions indicated in (A). The figure shows merged super-resolution images (left panels), the dSTORM Env Alexa Fluor 647 image (middle panels) and individual Alexa Fluor 647 localizations from all images recorded in the defined area as black dots, with a black circle representing the rims of the Gag cluster (right panels), respectively. Scale bar corresponds to 100 nm. (C, D) Comparison of Env( $\Delta$ CT) distribution patterns in the presence (C) and absence (D) of other HIV-1 derived proteins. HeLa cells were transfected with equimolar amounts of pCHIV.Env( $\Delta$ CT) and pCHIV<sup>mEosFP</sup>.Env( $\Delta$ CT) (C) or with pEnv( $\Delta$ CT) (D), respectively. Unfixed cells were stained with 2G12 Fab and Alexa Fluor 647 Fab, fixed, and visualized by dSTORM as described. Scale bars represent 1  $\mu$ m. doi:10.1371/journal.ppat.1003198.g004

extending beyond the assembly site for the wt construct (Figure 5A, S7A). These Gag associated Env clusters were absent for MA(wt) in the context of Env( $\Delta$ CT) (Figure 5B, S7B) consistent with the results observed above. A similar phenotype was observed for Env(wt) in the context of the MA(mut) virus (Figure 5C, S7C), indicating that the reported Env incorporation defect is due to a loss of Env recruitment to the assembly site. The combination of both mutations displayed an intermediate phenotype, with the overall Env distribution pattern (Figure S7D) resembling the pattern observed for the individual MA or Env mutants, but a slightly more pronounced Env-Gag co-localization revealed upon inspection of individual assembly sites (Figure 5D).

To describe the different Env distribution patterns at the cell membrane in an objective and quantitative manner, we performed mathematical cluster analysis using two complementary approaches. Data sets were derived from transfected HeLa or A3.01 cells, respectively; at least three cells per condition were included in the analysis. In a first approach, we used an image-based morphological cluster analysis (Figure 6A) to determine the average cluster

size of Env in whole cells. The average cluster size of Env(wt) in virus producing cells was significantly larger than observed for Env(wt) expressed alone or for clusters formed in cells expressing Env( $\Delta$ CT) (with or without other viral proteins). The distribution of cluster sizes of Env(wt) in HeLa cells was also analyzed by subtracting values obtained for cells expressing only Env from those obtained for HIV-1 producing cells (Figure 6B). Positive values in this analysis indicate an enrichment of the respective cluster size in virus-producing cells. This analysis revealed that smaller clusters with a radius <50 nm are much more prominent in cells expressing only Env, while larger clusters with a radius of 50 to 150 nm predominate in virus-producing cells.

In an independent second approach, a coordinate-based distance distribution analysis using Ripley's H-function [41] was applied (Figure 6C, 6D and S8). This approach compares the measured distribution of single-molecule localizations to a simulated random distribution, and provides information whether clustering occurs. The maximum of the H function reflects the average size of clusters. The amplitude of the H-function is a



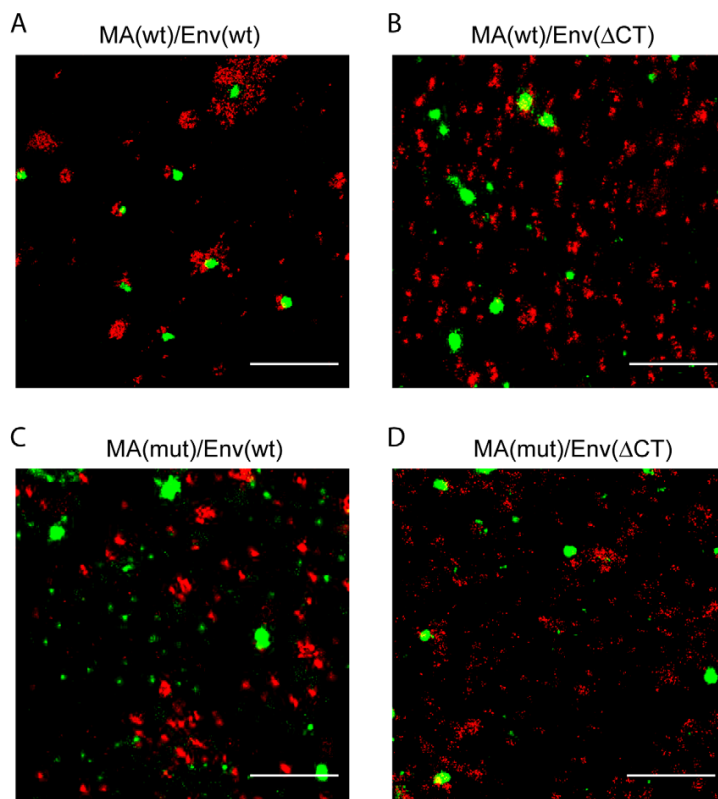


**Figure 5. Distribution of Env(wt) or Env( $\Delta$ CT) in the context of an Env-interaction deficient Gag variant.** HeLa cells were transfected with proviral constructs carrying both wt Gag and wt Env (A), wt Gag and Env( $\Delta$ CT) (B), Gag carrying the MA mutation and wt Env (C), or comprising both mutated MA and Env( $\Delta$ CT) (D), respectively. Fixed cells were stained by indirect immunofluorescence using MAb APR342 and goat anti-mouse Alexa Fluor 532 and MAb 2G12 and goat anti-human Alexa Fluor 647, and subjected to dual-color dSTORM. Scale bar corresponds to 1  $\mu$ m. An overview of respective cells is presented in Figure S7. doi:10.1371/journal.ppat.1003198.g005

measure of the degree of clustering. The variance of the amplitude reflects the variance of the spatial organization of proteins within a cluster. Unbiased analysis of clustering confirmed the larger size of Env(wt) clusters in virus producing cells compared to expression of Env alone or Env( $\Delta$ CT) (with or without other viral proteins) (Figure 6C). Furthermore, clusters of Env(wt) in HIV-1 producing cells exhibited a much smaller variation in cluster size (Figure S8) and a higher degree of homogeneity of clustering (Figure 6D) than observed for any of the other conditions. This result shows that Env(wt) clusters in HIV-1 producing cells are mostly homogenous and organized and most Env(wt) molecules are likely to be found in a single type of arrangement. The results of both cluster analyses were similar for HeLa and A3.01 cells, and corroborated the results of visual inspection of the spatial distribution of HIV-1 Env. Because whole cells were analyzed in this case and no pre-selection of particular regions was made, the results of the computational analyses represent average values and provide a more general and unbiased pattern.

While providing a view on the whole cell, these computational analyses were not suitable to decipher differences in the Env distribution pattern at specific localizations, e.g. HIV-1 budding sites. To obtain quantitative information on the spatial distribution of Env at such sites, it was required to analyze preselected regions. This was performed by aligning and averaging the intensity

distribution of Gag.mEosFP and Env at seven HIV-1 assembly sites each from HeLa cells producing either HIV<sup>mEosFP</sup> or HIV<sup>mEosFP</sup>Env( $\Delta$ CT). This procedure should enhance features common to the respective assembly sites, while deemphasizing random distributions. The averaged images of assembly sites from cells producing HIV-1 containing Env(wt) or Env( $\Delta$ CT), respectively, showed a very similar pattern for the respective Gag assembly sites but a dramatic difference for the Env distribution pattern (Figure 7). The full-length Env protein (Figure 7A) exhibited a doughnut-shaped average pattern, reflected by a bimodal distribution of Env with a local intensity minimum at the position of the peak of the Gag intensity distribution (Figure 7A). In contrast, Env( $\Delta$ CT) (Figure 7B) displayed a more random distribution without any significant enrichment at or close to the actual budding site. The averaged intensity profiles recorded for cells producing the Env( $\Delta$ CT) virus revealed no distinctive pattern of Env and no enrichment of Env density in the region of the Gag assembly site (Figure 7B), again confirming the qualitative results obtained by visual inspection of the images.

## Discussion

Here, we employed dual-color super-resolution microscopy to investigate the distribution of HIV-1 Env glycoproteins at the cell

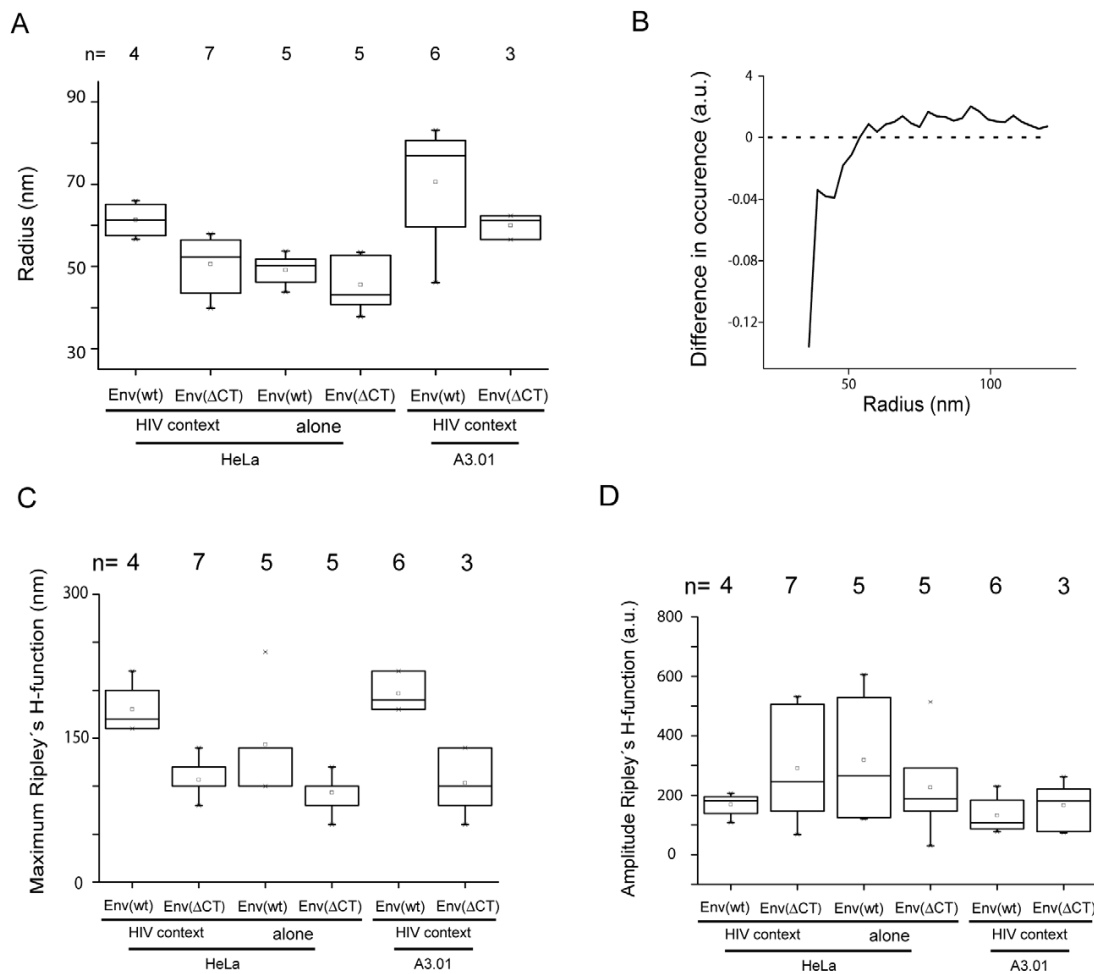


**Figure 6. Computational cluster analysis of HIV-1 Env membrane distribution.** Global cluster analysis of Env distribution at the plasma membrane was performed based on super-resolution images of HeLa cells transfected with pCHIV/pCHIV<sup>mEosFP</sup>, pCHIV.Env(ΔCT)/pCHIV<sup>mEosFP</sup>Env(ΔCT), pEnv(wt) or pEnv(ΔCT), or of A3.01 T-cells nucleofected with pCHIV/pCHIV<sup>mEosFP</sup> or pCHIV.Env(ΔCT)/pCHIV<sup>mEosFP</sup>Env(ΔCT), respectively. **(A)** Image-based, morphological cluster analysis of entire cells. **(B)** Differential distribution of cluster size for Env(wt) on the surface of HeLa cells in the presence and absence of other viral proteins. The curve was derived by subtraction of the normalized distribution of cluster size obtained by image-based cluster analysis for Env(wt) expressed in the HIV-1 context from that obtained upon expression of Env(wt) alone. **(C)** Coordinate based all-distance distribution analysis by Ripley's H-function. Statistical evaluation of the maximal H-values [nm] was performed as a correlate of the average cluster diameter. **(D)** Statistical evaluation of the amplitude of the H-function [a.u.] as a measure of the average degree of clustering. Box plots display 5<sup>th</sup> percentile, 25<sup>th</sup> percentile, median (straight line), mean (square), 75<sup>th</sup> percentile and 95<sup>th</sup> percentile. doi:10.1371/journal.ppat.1003198.g006

surface of virus-producing and Env expressing cells. A combination of PALM imaging of an autofluorescent HIV-1 Gag derivative with dSTORM imaging of Env immunostained with a fluorescent dye appeared to be the optimal strategy. In general, synthetic fluorophores have a higher photon yield than fluorescent proteins, thereby providing increased spatial resolution in single-molecule based super-resolution imaging [26]. Accordingly, dSTORM imaging of Gag assemblies had revealed spherical edge effects [31] which were obscured in previous PALM images of Gag fused to autofluorescent proteins [30]. However, the structure of the Gag lattice at HIV-1 budding sites has already been characterized by electron tomography [33], and Gag staining with synthetic fluorophores requires cell fixation and immobilization that might affect Env protein distribution. In contrast, the cell

surface protein Env can be detected on native cells by immunolabeling and subsequent detection using organic fluorophores. Thus, we applied PALM for detection of Gag, while the higher localization accuracy of dSTORM was exploited for the detailed characterization of Env surface distribution.

Using this system, we have analyzed Env localization in the presence and absence of other viral proteins as well as for a variant with mutations in the MA region of Gag and determined the role of the CT for HIV-1 Env membrane distribution. The results clearly revealed a CT- and MA dependent recruitment of Env proteins to the vicinity of Gag assembly sites. Env proteins accumulated around Gag clusters, concentrating at their periphery, while the bud center displayed reduced Env density. These results are consistent with Gag-dependent Env accumulation

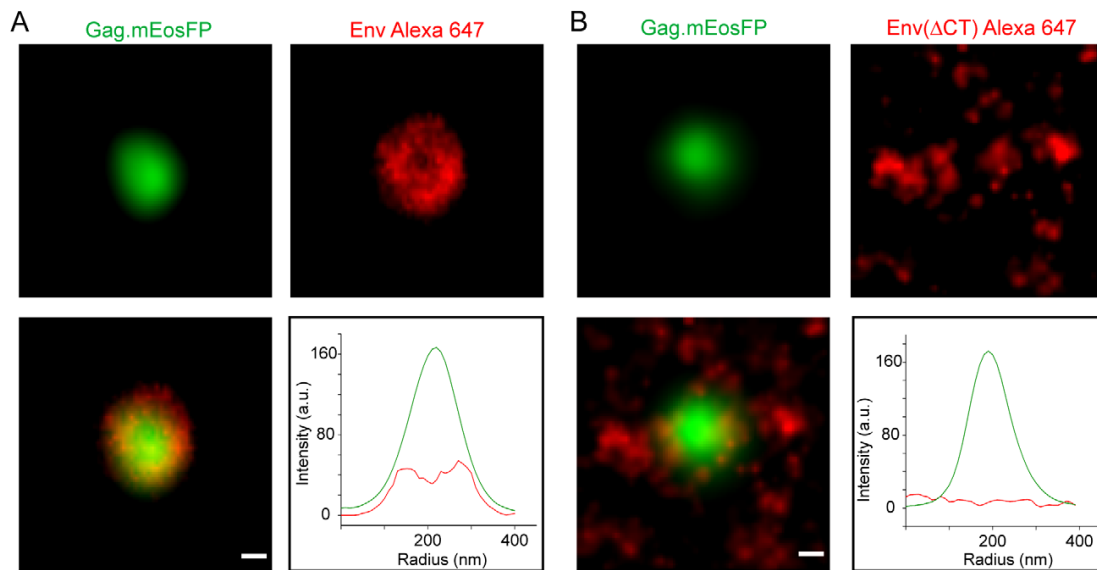


**Figure 7. Averaged super-resolution intensity distribution of Env at HIV-1 assembly sites.** Image-based, averaged assembly site analysis performed on super-imposed high-resolution images of individual Gag.mEosFP clusters (green) from cells transfected with pCHIV/pCHIV<sup>mEosFP</sup> (A) or pCHIV.Env(ΔCT)/pCHIV<sup>mEosFP</sup>Env(ΔCT) (B), respectively (n=7 assembly sites per condition) and the averaged Env Alexa Fluor 647 signal in the respective area (red). Graphs show the profile of intensity through the center of the averaged, overlaid intensity images: green line, Gag.mEosFP; red line, Env. Scale bars represent 50 nm. doi:10.1371/journal.ppat.1003198.g007

surrounding individual sites of HIV-1 particle formation, while the observed larger extension of Env clusters compared to that of Gag assemblies suggests that other factors than direct Gag-Env interaction may contribute to Env recruitment.

Comparing Env distribution on cells producing HIV-1 particles with the distribution of Env expressed in the absence of other viral components revealed a difference that was clearly recognizable even without co-detection of the HIV-1 Gag protein. A scattered membrane distribution of Env with small clusters was seen in cells expressing Env alone, while larger accumulations were detected in virus producing cells. The appearance of the larger clusters was dependent on the Env CT and was disrupted by a MA mutation that abolishes Env incorporation. Dual color analysis revealed that larger Env clusters were commonly (~90%) associated with *bona fide* HIV-1 assembly sites, and Env structures with the characteristic round or doughnut-like shape were absent in cells expressing Env alone. The remaining ~10% of larger Env clusters apparently lacking Gag association could correspond to nascent HIV-1 assembly sites with a low number of Gag molecules or constitute remnants of prior assembly sites after extracellular release of the viral particle. Alternatively, they could be induced by HIV-1 mediated changes of the membrane environment leading to membrane areas conducive for Env accumulation.

Unbiased computational intensity-based cluster analysis from whole-cell data confirmed that the average cluster size was largest for Env(wt) in the presence of other HIV-1 proteins. This was supported by subtractive distribution of cluster sizes showing that Env(wt) expressed alone was mainly found in small clusters ( $r < 50$  nm), whereas the same protein formed clusters with a radius of 50 to 150 nm in HIV-1 producing cells. While image-based cluster analysis can be performed on whole-cell data and generates distributions of cluster sizes, it depends on the spatial resolution and pixel size of the image and requires setting intensity

thresholds. Thus, we applied Ripley's H-function [41] as a complementary approach for cluster analysis. This method can only analyze regions of interest rather than whole cells and does not provide information on the distribution of cluster sizes, but it is independent of thresholds. The maximum of the H-function, which correlates with the average cluster size, again demonstrated that the largest clusters were formed by Env(wt) in HIV-1 producing cells. In addition, Ripley's-H function provides information on the heterogeneity of clustering through the variance of its amplitude. A very small variance was observed for Env(wt) in HIV-1 producing cells suggesting a single type of cluster. The sharper peak of the H-function in this case compared to the other three conditions (Figure S8) further indicated more regular clustering. Thus, evaluation of the data sets by two independent types of computational cluster analysis yielded a complete and consistent picture, confirming and extending the results of visual inspection of the super-resolution images.

Considering the four described models for Env incorporation, the reported data clearly argue for specific recruitment and against random incorporation for wt HIV-1. In contrast, random incorporation appears to be likely for Env(ΔCT). Averaging the Env signal at multiple HIV-1 budding sites revealed no distinctive features for the Env(ΔCT) virus, confirming the visual impression. Env(ΔCT) incorporation into HIV-1 particles may thus occur randomly and only depend on its cell surface concentration. This interpretation is consistent with its observed reduced incorporation compared to Env(wt) [7,9] and the cell type dependence of the mutant phenotype [12–15]. Loss of apparent accumulation of Env at viral budding sites was also observed when a RSV variant with a truncated Env CT was analyzed by scanning electron microscopy of immunostained cells [22]. Thus, CT dependent specific recruitment of Env to the assembly site may be a general feature of retroviruses rather than being determined by the long lentiviral

CT. Random incorporation may also be expected for pseudotyping with other viral glycoproteins. However, Jorgenson et al. [22] reported accumulation of at least some heterologous viral glycoproteins at RSV and HIV assembly sites, arguing for specific recruitment even in the absence of the cognate Gag-Env pair.

Genetic data from multiple studies support a direct interaction of the HIV-1 Env CT with the membrane-apposed MA layer [6–9,18] even though biochemical evidence for this interaction is weak. Here, we observed that a mutation in MA that had been shown to disrupt virion incorporation of Env [8,40] abolished formation of Env clusters at HIV-1 assembly sites. This observation is consistent with MA-dependent recruitment of Env to the viral budding site. On the other hand, Env clusters in the case of wt HIV-1 significantly extended beyond the respective Gag assembly sites. Even close inspection revealed no detectable enrichment of Gag signals surrounding *bona fide* budding sites, consistent with the proposition that recruitment of Gag to the nascent bud occurs mostly from a cytoplasmic pool [36]. The majority of Env signals within the respective cluster were detected in the region surrounding the bud, however. Thus, Gag density in the vicinity of HIV-1 budding sites did not appear to differ significantly from its density in other plasma membrane regions, while Env density clearly did. Furthermore, Env density within the cluster appeared lowest at the center of the viral bud, where Gag is most concentrated. These results do not rule out a direct Gag-Env interaction, but argue that an indirect mode may at least contribute to Env concentration at HIV-1 assembly sites. This function clearly depends on HIV-1 Gag since Env accumulation was not seen in the absence of other viral proteins or in the case of the MA mutant. Co-targeting of Gag and Env to pre-existing membrane microdomains with special properties could therefore also not explain our results. Conceivably, accumulation of HIV-1 Gag and possibly of other viral proteins may induce an altered membrane micro-environment which attracts Env(wt) molecules. Alternatively, Env may be recruited by a proteinaceous bridging factor, which directs the viral glycoproteins to the assembly site, but does not immobilize them at this position. A specific membrane environment at the viral budding site is consistent with the raft-like lipid composition of HIV-1 particles [42,43] and the association of budding sites with tetraspanin-enriched microdomains (reviewed in [44]). The hypothesis that Gag assembly at the plasma membrane alters or induces a specific lipid environment is also consistent with results from several recent studies using fluorescence recovery after photobleaching, fluorescence resonance energy transfer or antibody co-patching of membrane proteins to reveal Gag dependent changes in marker protein mobility or distribution (reviewed in [45]). Dual- or triple-color super-resolution microscopy using marker membrane proteins or lipid dyes could in the future provide direct evidence regarding the size and colocalization of such domains with viral Gag and Env clusters, and may further clarify the mechanism of Env recruitment.

At first glance, the accumulation of large amounts of Env surrounding, but not co-localizing with, Gag assemblies appears surprising for viral production sites. The observed bimodal shape of the Env density profile with a minimum in the central region of the HIV-1 bud is consistent with the low density of Env trimers detected on HIV-1 virions [3,4], however, and may be explained by limited compatibility of the trimeric CT with the tightly packed Gag lattice. Many cellular membrane proteins are incorporated into HIV-1 particles [16,17], but efficiency dependent on the CT length has been described, suggesting steric hindrance [46], and exclusion due to interaction of CTs with cytoplasmic factors has been observed [47]. The low number of viral glycoproteins on the

particle surface has been suggested to provide a selective advantage by allowing escape of the virus from the humoral immune response [48]. Concentrating surplus Env proteins not required for infectious particle formation around viral buds, on the other hand, could play an important role in forming and maintaining the virological synapse during cell-to-cell transmission. The formation of contacts between infected and uninfected T-cells is induced by Env [49], and viral spread through such synapses is considered to be the major mode of HIV-1 transmission *in vivo* (reviewed in [50]). The observed large HIV-1 Env clusters may thus play an important role in viral spread and pathogenesis. Visualization of the architecture of virological synapse structures using 3D multicolor super-resolution microscopy will therefore be an important goal of future research.

## Materials and Methods

### Cell lines and plasmids

HeLa cells and A3.01 T-cells [51] were grown at 37°C and 5% CO<sub>2</sub> in Dulbecco's modified Eagle's medium (DMEM; Invitrogen) and RPMI-1640 medium, respectively. Media were supplemented with 10% fetal calf serum (FCS), 100 U/ml penicillin and 100 µg/ml streptomycin. Plasmid pCHIV, expressing all HIV-1 proteins except for Nef under the control of a CMV promoter and its derivative pCHIV<sup>ΔEosFP</sup> have been described previously [36]. pCHIVEnv(ΔCT) and pCHIV<sup>ΔEosFP</sup> Env(ΔCT) were constructed by exchanging an AgeI/XhoI fragment of the respective parental plasmid with a corresponding fragment covering the *env* coding region from plasmid pNL4-3CTdel144-2 [14]. The HIV-1 Env expression vector pCAGGS.NL4-3-Xba, designated here as pEnv(wt), has been described previously [52]. pEnv(ΔCT) was kindly provided by Nikolas Herold. It was constructed based on pEnv(wt) by exchanging an Acc65I/XhoI restriction fragment against the corresponding fragment from an Env(ΔCT) expression vector kindly provided by Valerie Bosch [15]. HIV-1 proviral constructs carrying wt Gag or the MA L8S/S9R mutant defective in Env interaction [8,40] in combination with either Env(wt) or Env(ΔCT) were kindly provided by F. Mammano.

### Transfection and immunofluorescence staining

HeLa cells were seeded at a density of  $1 \times 10^4$  cells in 8-well chambered cover glasses (LabTek) and transfected with 0.2 µg of plasmid/well on the following day using the FuGene HD transfection reagent (Roche Diagnostics). Nucleofection of A3.01 cells was performed as described previously [29]. In brief:  $5 \times 10^6$  cells were electroporated with 10 µg of each plasmid in a 0.4 cm cuvette (Invitrogen) in a volume of 500 µl of serum-free medium using a Gene Pulser Xcell (BioRad). Parameters were: capacity 950 µF and 300 V. After 24 hours, cells were seeded on 8-well chambered cover glasses (LabTek) coated with fibronectin at a concentration of 5 µg/ml. After sedimentation, cells were fixed with 3% paraformaldehyde (PFA) followed by permeabilization and blocking with 2% BSA.

Two staining approaches for Env were applied: fixation followed by staining, or staining followed by fixation. For the first approach, cells were fixed at 24 h post transfection (hpt) with 3% PFA, washed and blocked for 10 min with 2% BSA in phosphate buffered saline (PBS). Harsher fixation of samples was performed using 4% PFA/0.2% glutaraldehyde for 30 min [38]. Cells were incubated with the monoclonal anti-gp120 antibody 2G12 ([35], Polymun Scientific) for 45 min. To confirm the specificity of 2G12 staining, the anti-gp120 MAb b12 ([37], Polymun Scientific) was used. The washing and blocking procedures were repeated before incubation with goat anti-human Alexa Fluor 647 secondary

antibody (Invitrogen). To exclude antibody induced Env clustering and fixation artifacts, we performed staining prior to fixation and used Fab fragments of the respective antibodies (kindly provided by J. Chojnacki). All steps were performed at 16°C to block endocytic uptake of surface molecules. Cells were washed with PBS and samples were blocked with 2% BSA for 10 min, followed by incubation with 2G12 Fab for 40 min. Subsequently, cells were incubated with goat anti-human Alexa Fluor 647 Fab (Dianova) for 40 min. Stained cells were fixed with 3% PFA for 20 min and washed with PBS. Staining of the MA domain of HIV was performed using the MAb APR342 [53] (CFAR, UK) followed by goat-anti-mouse Alexa Fluor 532 antibody.

Immature eGFP.Vpr-labelled viruses [39], kindly provided by J. Chojnacki, were adhered to LabTek chamber slides coated with 5 µg/ml fibronectin, fixed with 3% PFA and stained with MAb 2G12 and goat anti-human Alexa Fluor 647 and subjected to dSTORM imaging.

### Super-resolution microscopy

Super-resolution microscopy was performed using a custom-built microscope setup as described elsewhere [54]. Briefly, a multi-line argon-krypton laser (Innova70C, Coherent, USA) and a 405 nm diode laser (Cube, Coherent, USA) were coupled into an inverted microscope (IX71, Olympus, Japan) equipped with a 63× oil immersion objective (PlanApo 63×, NA 1.45, Olympus, Japan) suitable for total internal reflection fluorescence (TIRF) imaging. The excitation and emission beams were separated using appropriate dichroic mirrors and filters (AHF, Germany). The fluorescence emission was detected by an EM-CCD camera (Ixon, Andor, Ireland).

Combined PALM and dSTORM imaging was performed sequentially, using an imaging buffer which is suitable for both photoswitching the fluorescent protein mEosFP as well as the organic fluorophore Alexa Fluor 647 or Alexa Fluor 532 [55]. Briefly, the cells were imaged in oxygen-depleted hydrocarbonate buffer (pH 8) supplemented with 100 mM mercaptoethylamine (MEA). First, Alexa Fluor 647 was reversibly photoswitched by irradiation with 488 nm (photoactivation) and 647 nm (read-out). For each channel, 8,000 to 10,000 images were recorded with an integration time of 50 ms. Then mEosFP was photoactivated by irradiation with 405 nm and imaged using an excitation wavelength of 568 nm. Alternatively, Alexa Fluor 532 was photoactivated by irradiation with 514 nm. Single-molecule localization and image reconstruction was performed using the *rapidSTORM* software [56]. The localization accuracy of single-molecule super-resolution microscopy was evaluated experimentally as described earlier [57] using a custom written software (Python and Scipy) [58]. For each localized fluorophore, the distance to its nearest neighbor fluorophore in an adjacent frame was calculated. As the majority of fluorophores are detected in multiple adjacent frames, the maximum of the nearest neighbor distance distribution represents the error of localization. A prerequisite for using this approach is a statistically significant number of events ( $n > 4,000$ ). Dual-color images were recorded by adding multi-spectral beads (Invitrogen) to the sample and post-aligning the individual images [59].

### Cluster analysis

All-distance distributions are a common tool for cluster analysis of single-molecule super-resolution data [31,60,61]. We used Ripley's K-function [41] (1) in its linearized (2) and normalized form (3) (Ripley's H-function):

$$K(r) = \frac{1}{n^2} \sum_i \sum_j \frac{N_r(d_{ij})}{\lambda} \quad (1)$$

$$L(r) = \sqrt{\frac{K(r)}{\pi}} \quad (2)$$

$$H(r) = L(r) - r \quad (3)$$

where  $r$  is the observation radius,  $n$  is the total number of localizations within a region of interest (ROI),  $d_{ij}$  is the distance between two localizations  $i$  and  $j$ ,  $N_r$  is the number of localizations around localization  $i$  within the distance  $r$ , and  $\lambda$  is a weighting factor correcting for the area of the ROI. We calculated Ripley's H-function for ROIs of  $2 \times 2 \mu\text{m}^2$ . In order to account for edge effects, we used a toroidal edge correction. The results were tested against a 95% confidence envelope of uniform distributions generated by Monte Carlo methods. All calculations and simulations were performed using custom software written in Matlab (Mathworks, Natick, MA).

Image-based cluster analysis was performed on super-resolution images by identifying cohesive regions of protein populations and determining their area. For this, a 'quantitative' super-resolution image with a pixel size of 10 nm was generated, in which the pixel value represents the number of localizations found at this position (custom software written in Matlab (Mathworks, Natick, MA)). Cohesive regions in these quantitative images were identified and measured using an algorithm based on the analyze particles function from FIJI [62].

To analyze the protein distribution, we calculated average images by overlaying multiple images of individual clusters using an image pixel size of 5 nm. The individual images were aligned using the center of mass of the Gag protein distribution. Image averaging was performed using a custom software written in Matlab (Mathworks, Natick, USA), intensity profiles were extracted using FIJI.

### Supporting Information

**Figure S1 Experimental determination of the localization accuracy of mEosFP by a coordinate-based algorithm.** The nearest neighbor distribution of a single-molecule data set of Gag.mEosFP ( $n = 7,522$  single-molecule localizations) was calculated. The maximum, representing localization accuracy, was found at 28 nm. (TIF)

**Figure S2 Experimental determination of the localization accuracy of Alexa Fluor 647 by a coordinate-based algorithm.** The nearest neighbor distribution of a single-molecule data set of Alexa Fluor 647 ( $n = 4,196$  single-molecule localizations) was calculated. The maximum, representing fluorophore localization accuracy, was found at 15 nm. (TIF)

**Figure S3 Increased sensitivity of Gag assembly site detection.** HeLa cells were transfected with pCHIV<sup>mEosFP</sup>, fixed 24 hpt, stained by indirect immunofluorescence using MAb b12 and goat anti-human Alexa Fluor 647, and imaged by super-resolution TIRF microscopy as described in Materials and Methods. A representative region from the plasma membrane, showing the superposition of a PALM image for Gag.mEosFP (green) and the corresponding dSTORM image of Env stained with Alexa Fluor 647 (red), respectively. Scale bars represent 1 µm. (TIF)

**Figure S4 Env immunostaining following harsher chemical fixation.** HeLa cells were transfected with equimolar amounts of pCHIV and pCHIV<sup>mEosFP</sup>. At 24 hpt cells were fixed with 4% PFA/0.2% glutaraldehyde for 30 min. Subsequently samples were stained by immunofluorescence using MAb 2G12 and goat anti-human IgG Alexa Fluor 647 and imaged by dSTORM as described in Materials and Methods. Scale bar represents 1  $\mu$ m.

(TIF)

**Figure S5 Specificity of Env immunostaining.** (A) HeLa cells were transfected with equimolar amounts of pCHIV.Env(-) and pCHIV<sup>mEosFP</sup>.Env(-). Cells were fixed, immunostained using MAb 2G12 and goat anti-human IgG Alexa Fluor 647, and imaged as in Materials and Methods. (B) HeLa cells were transfected with an equimolar mixture of pCHIV and pCHIV<sup>mEosFP</sup> and stained only with goat anti-human Alexa Fluor 647 without the primary antibody. Scale bars represent 1  $\mu$ m.

(TIF)

**Figure S6 Distribution of Gag and Env at the plasma membrane of A3.01 cells analyzed by dual-color super-resolution microscopy.** (A) A3.01 cells were nucleofected with equimolar amounts of pCHIV and pCHIV<sup>mEosFP</sup>. At 24 h post nucleofection, cells were fixed, stained by indirect immunofluorescence using MAb 2G12 and goat anti-human Alexa Fluor 647 and imaged by dual-color super-resolution microscopy as described in Materials and Methods. An image of a representative cell is shown. Green, mEosFP; red, Alexa Fluor 647. Scale bar represents 2  $\mu$ m. (B) Enlargement of three individual assembly sites from the boxed regions indicated in (A). The figure shows merged super-resolution images (left panels), the dSTORM Env Alexa Fluor 647 image (middle panels) and individual Alexa Fluor 647 localizations from all images recorded in the defined area as black dots, with a black circle representing the rims of the Gag cluster (right panels), respectively. Scale bars correspond to 100 nm. (C) Distribution of HIV-1 Gag and Env at the plasma membrane of A3.01 cells nucleofected with equimolar amounts of pCHIV.Env( $\Delta$ CT) and pCHIV<sup>mEosFP</sup>.Env( $\Delta$ CT). Cells were fixed and stained by indirect immunofluorescence using MAb 2G12 and goat anti-human Alexa Fluor 647, and subjected to dual-color super-resolution microscopy as described in Materials and Methods. Region from the plasma membrane of a representative cell, showing the superposition of a PALM image for Gag.mEosFP (green) and the corresponding dSTORM image of Env( $\Delta$ CT) stained with Alexa Fluor 647 (red), respectively. Scale bar represents 2  $\mu$ m. (D) Enlargement of three individual assembly sites from the boxed regions indicated in (C). The figure shows merged super-resolution images (left panels), the dSTORM Env Alexa Fluor 647 image (middle panels) and individual Alexa Fluor 647 localizations from all images recorded in the defined area as black dots, with a black circle representing the rims of the Gag

cluster (right panels), respectively. Scale bars correspond to 100 nm.

(TIF)

**Figure S7 Overview of Gag and Env distribution for proviral constructs expressing wt or mutated MA and wt or CT truncated Env.** Distribution of HIV-1 Gag and Env at the plasma membrane of HeLa cells transfected with the respective proviral constructs carrying both wt Gag and wt Env (A), wt Gag and Env( $\Delta$ CT) (B), Gag carrying the MA mutation and wt Env (C), or comprising both mutated MA and Env( $\Delta$ CT) (D). Expanded sections from these images highlighting individual sites are shown in main Figure 5. Scale bar represents 2  $\mu$ m.

(TIF)

**Figure S8 Coordinate based all distance distribution analysis using Ripley's H-function.** The graphs show a comparison of relative Env clustering on the membrane of HeLa cells (A–D) or A3.01 cells (E–F) transfected with pCHIV/pCHIV<sup>mEosFP</sup> (A, E), pCHIV.Env( $\Delta$ CT)/pCHIV<sup>mEosFP</sup>.Env( $\Delta$ CT) (B, F), pEnv(wt) (C) and pEnv( $\Delta$ CT) (D), respectively. Two regions of interest (ROI) of 2  $\mu$ m $\times$ 2  $\mu$ m from three cells per transfection condition were examined. The maximal H-value [nm] reflects the average cluster diameter. The amplitude of the H-function [a.u.] indicates the average degree of clustering. Six ROIs per condition were selected from the central region of the cells in order to avoid edge effects. For each ROI, Ripley's H-function was calculated. The solid red line shows the mean value for the 6 measurements and red error bars indicate the standard deviation. As a control 19 Monte Carlo simulations of a uniform distribution within a ROI were calculated in order to create a 95% confidence envelope for Ripley's H-function in case of non-cluster forming distributions (magenta and blue lines).

(TIF)

## Acknowledgments

We gratefully acknowledge Benjamin Flottmann for help with dual-color PALM/dSTORM imaging. We thank Nikolas Herold for providing plasmid pEnv( $\Delta$ CT), Fabrizio Mammano (Hôpital Saint-Louis, Paris) and Valerie Bosch (DKFZ, Heidelberg) for providing proviral constructs and Jakub Chojnacki for purified Fab fragments and eGFP.Vpr labeled virions. MAb APR342 was obtained from the Centre for AIDS Reagents, NIBSC HPA UK, supported by the EC FP6/7 Europrise Network of Excellence, and NGIN consortia and the Bill and Melinda Gates GHRC-CAVD Project and was donated by Division of Infection and Immunity, University College London, London, UK. We are grateful to Steeve Boulant and Jakub Chojnacki for helpful discussions.

## Author Contributions

Conceived and designed the experiments: HGK BM WM. Performed the experiments: WM MH. Analyzed the data: WM SM MH HGK. Contributed reagents/materials/analysis tools: WM SM BM MH HGK. Wrote the paper: WM BM MH HGK.

## References

- Sundquist WI, Krausslich HG (2012) HIV-1 Assembly, Budding, and Maturation. *Cold Spring Harb Perspect Med* 2: a006924.
- Checkley MA, Lutttge BG, Freed EO (2011) HIV-1 envelope glycoprotein biosynthesis, trafficking, and incorporation. *J Mol Biol* 410: 582–608.
- Chertova E, Bess JW, Jr., Crise BJ, Sowder IR, Schaden TM, et al. (2002) Envelope glycoprotein incorporation, not shedding of surface envelope glycoprotein (gp120/SU), is the primary determinant of SU content of purified human immunodeficiency virus type 1 and simian immunodeficiency virus. *J Virol* 76: 5315–5325.
- Zhu P, Chertova E, Bess J, Jr., Lifson JD, Arthur LO, et al. (2003) Electron tomography analysis of envelope glycoprotein trimers on HIV and simian immunodeficiency virus virions. *Proc Natl Acad Sci U S A* 100: 15812–15817.
- Dorfman T, Mammano F, Haseltine WA, Gottlinger HG (1994) Role of the matrix protein in the virion association of the human immunodeficiency virus type 1 envelope glycoprotein. *J Virol* 68: 1689–1696.
- Freed EO, Martin MA (1995) Virion incorporation of envelope glycoproteins with long but not short cytoplasmic tails is blocked by specific, single amino acid substitutions in the human immunodeficiency virus type 1 matrix. *J Virol* 69: 1984–1989.
- Freed EO, Martin MA (1996) Domains of the human immunodeficiency virus type 1 matrix and gp41 cytoplasmic tail required for envelope incorporation into virions. *J Virol* 70: 341–351.
- Mammano F, Kondo E, Sodroski J, Bukovsky A, Gottlinger HG (1995) Rescue of human immunodeficiency virus type 1 matrix protein mutants by envelope glycoproteins with short cytoplasmic domains. *J Virol* 69: 3824–3830.

HIV-1 Envelope Proteins at Viral Assembly Sites

9. Yu X, Yuan X, Matsuda Z, Lee TH, Essex M (1992) The matrix protein of human immunodeficiency virus type 1 is required for incorporation of viral envelope protein into mature virions. *J Virol* 66: 4966–4971.
10. Cosson P (1996) Direct interaction between the envelope and matrix proteins of HIV-1. *Embo J* 15: 5783–5788.
11. Johnson MC (2011) Mechanisms for Env glycoprotein acquisition by retroviruses. *AIDS Res Hum Retroviruses* 27: 239–247.
12. Akari H, Fukumori T, Adachi A (2000) Cell-dependent requirement of human immunodeficiency virus type 1 gp41 cytoplasmic tail for Env incorporation into virions. *J Virol* 74: 4891–4893.
13. Iwatani Y, Ueno T, Nishimura A, Zhang X, Hattori T, et al. (2001) Modification of virus infectivity by cytoplasmic tail of HIV-1 TM protein. *Virus Res* 74: 75–87.
14. Murakami T, Freed EO (2000) The long cytoplasmic tail of gp41 is required in a cell type-dependent manner for HIV-1 envelope glycoprotein incorporation into virions. *Proc Natl Acad Sci U S A* 97: 343–348.
15. Wilk T, Pfeiffer T, Bosch V (1992) Retained in vitro infectivity and cytopathogenicity of HIV-1 despite truncation of the C-terminal tail of the env gene product. *Virology* 189: 167–177.
16. Cantin R, Methot S, Tremblay MJ (2005) Plunder and stowaways: incorporation of cellular proteins by enveloped viruses. *J Virol* 79: 6577–6587.
17. Ott DE (2008) Cellular proteins detected in HIV-1. *Rev Med Virol* 18: 159–175.
18. Murakami T, Freed EO (2000) Genetic evidence for an interaction between human immunodeficiency virus type 1 matrix and alpha-helix 2 of the gp41 cytoplasmic tail. *J Virol* 74: 3548–3554.
19. Ono A (2010) Relationships between plasma membrane microdomains and HIV-1 assembly. *Biol Cell* 102: 335–350.
20. Leung K, Kim JO, Ganesh L, Kabat J, Schwartz O, et al. (2008) HIV-1 assembly: viral glycoproteins segregate quantally to lipid rafts that associate individually with HIV-1 capsids and virions. *Cell Host Microbe* 3: 285–292.
21. Hermida-Matsumoto L, Resh MD (2000) Localization of human immunodeficiency virus type 1 Gag and Env at the plasma membrane by confocal imaging. *J Virol* 74: 8670–8679.
22. Jorgenson RL, Vogt VM, Johnson MC (2009) Foreign glycoproteins can be actively recruited to virus assembly sites during pseudotyping. *J Virol* 83: 4060–4067.
23. Betzig E, Patterson GH, Sougrat R, Lindwasser OW, Olenych S, et al. (2006) Imaging intracellular fluorescent proteins at nanometer resolution. *Science* 313: 1642–1645.
24. Heilemann M (2010) Fluorescence microscopy beyond the diffraction limit. *J Biotechnol* 149: 243–251.
25. Hell SW (2007) Far-field optical nanoscopy. *Science* 316: 1153–1158.
26. Heilemann M, van de Linde S, Schüttelpelz M, Kasper R, Seefeldt B, et al. (2008) Subdiffraction-resolution fluorescence imaging with conventional fluorescent probes. *Angew Chem Int Ed Engl* 47: 6172–6176.
27. Lelek M, Di Nunzio F, Henriques R, Chameau P, Arhel N, et al. (2012) Superresolution imaging of HIV in infected cells with FLASH-PALM. *Proc Natl Acad Sci U S A* 109: 8564–8569.
28. Pereira CF, Rossy J, Owen DM, Mak J, Gaus K (2012) HIV taken by STORM: super-resolution fluorescence microscopy of a viral infection. *Virology* 439: 84.
29. Eckhardt M, Anders M, Muranyi W, Heilemann M, Krijne-Locker J, et al. (2011) A SNAP-tagged derivative of HIV-1—a versatile tool to study virus-cell interactions. *PLoS One* 6: e22007.
30. Lehmann M, Rocha S, Manganet B, Blanchet F, Uji IH, et al. (2011) Quantitative multicolor super-resolution microscopy reveals tetherin HIV-1 interaction. *PLoS Pathog* 7: e1002456.
31. Malkusch S, Muranyi W, Muller B, Krausslich HG, Heilemann M (2012) Single-molecule coordinate-based analysis of the morphology of HIV-1 assembly sites with near-molecular spatial resolution. *Histochem Cell Biol* 139: 173–9.
32. Muller B, Daecke J, Fackler OT, Dittmar MT, Zentgraf H, et al. (2004) Construction and characterization of a fluorescently labeled infectious human immunodeficiency virus type 1 derivative. *J Virol* 78: 10803–10813.
33. Carlson LA, Briggs JA, Glass B, Riches JD, Simon MN, et al. (2008) Three-dimensional analysis of budding sites and released virus suggests a revised model for HIV-1 morphogenesis. *Cell Host Microbe* 4: 592–599.
34. Lampe M, Briggs JA, Endress T, Glass B, Riegelsberger S, et al. (2007) Double-labelled HIV-1 particles for study of virus-cell interaction. *Virology* 360: 92–104.
35. Trkola A, Purtscher M, Muster T, Ballaun C, Buchacher A, et al. (1996) Human monoclonal antibody 2G12 defines a distinctive neutralization epitope on the gp120 glycoprotein of human immunodeficiency virus type 1. *J Virol* 70: 1100–1108.
36. Ivanchenko S, Godinez WJ, Lampe M, Krausslich HG, Eils R, et al. (2009) Dynamics of HIV-1 assembly and release. *PLoS Pathog* 5: e1000652.
37. Roben P, Moore JP, Thali M, Sodroski J, Barbas CF, 3rd, et al. (1994) Recognition properties of a panel of human recombinant Fab fragments to the CD4 binding site of gp120 that show differing abilities to neutralize human immunodeficiency virus type 1. *J Virol* 68: 4821–4828.
38. Tanaka KA, Suzuki KG, Shirai YM, Shibutani ST, Miyahara MS, et al. (2010) Membrane molecules mobile even after chemical fixation. *Nat Methods* 7: 865–866.
39. Chojnacki J, Staudt T, Glass B, Bingen P, Engelhardt J, et al. (2012) Maturation-dependent HIV-1 surface protein redistribution revealed by fluorescence nanoscopy. *Science* 338: 524–528.
40. Monel B, Beaumont E, Vendrame D, Schwartz O, Brand D, et al. (2012) HIV cell-to-cell transmission requires the production of infectious virus particles and does not proceed through env-mediated fusion pores. *J Virol* 86: 3924–3933.
41. Ripley B (1977) Modelling spatial patterns. *Journal of the Royal Statistical Society* 39: 172–212.
42. Brugger B, Glass B, Haberkant P, Leibrecht I, Wieland FT, et al. (2006) The HIV lipidome: a raft with an unusual composition. *Proc Natl Acad Sci U S A* 103: 2641–2646.
43. Chan R, Uchil PD, Jin J, Shui G, Ott DE, et al. (2008) Retroviruses human immunodeficiency virus and murine leukemia virus are enriched in phosphoinositides. *J Virol* 82: 11228–11238.
44. Thali M (2011) Tetraspanin functions during HIV-1 and influenza virus replication. *Biochem Soc Trans* 39: 529–531.
45. Hogue IB, Llewellyn GN, Ono A (2012) Dynamic Association between HIV-1 Gag and Membrane Domains. *Mol Biol Int* 2012: 979765.
46. Henriksson P, Pfeiffer T, Zentgraf H, Alke A, Bosch V (1999) Incorporation of wild-type and C-terminally truncated human epidermal growth factor receptor into human immunodeficiency virus-like particles: insight into the processes governing glycoprotein incorporation into retroviral particles. *J Virol* 73: 9294–9302.
47. Henriksson P, Bosch V (1998) Inhibition of cellular glycoprotein incorporation into human immunodeficiency virus-like particles by coexpression of additional cellular interaction partner. *Virology* 251: 16–21.
48. Klein JS, Bjorkman PJ (2010) Few and far between: how HIV may be evading antibody avidity. *PLoS Pathog* 6: e1000908.
49. Jolly C, Kashefi K, Hollinshead M, Sattentau QJ (2004) HIV-1 cell to cell transfer across an Env-induced, actin-dependent synapse. *J Exp Med* 199: 283–293.
50. Sattentau QJ (2010) Cell-to-Cell Spread of Retroviruses. *Viruses* 2: 1306–1321.
51. Folks T, Bemm S, Rabson A, Theodore T, Hoggan MD, et al. (1985) Characterization of a continuous T-cell line susceptible to the cytopathic effects of the acquired immunodeficiency syndrome (AIDS)-associated retrovirus. *Proc Natl Acad Sci U S A* 82: 4539–4543.
52. Bozek K, Eckhardt M, Sierra S, Anders M, Kaiser R, et al. (2012) An expanded model of HIV cell entry phenotype based on multi-parameter single-cell data. *Retrovirology* 9: 60.
53. Ferns RB, Partridge JC, Spence RP, Hunt N, Tedder RS (1989) Epitope location of 13 anti-gag HIV-1 monoclonal antibodies using oligopeptides and their cross reactivity with HIV-2. *Aids* 3: 829–834.
54. Nanguneri S, Flottmann B, Horstmann H, Heilemann M, Kuner T (2012) Three-dimensional, tomographic super-resolution fluorescence imaging of serially sectioned thick samples. *PLoS One* 7: e38098.
55. Endesfelder U, Malkusch S, Flottmann B, Mondry J, Liguzinski P, et al. (2011) Chemically induced photoswitching of fluorescent probes—a general concept for super-resolution microscopy. *Molecules* 16: 3106–3118.
56. Wolter S, Endesfelder U, van de Linde S, Heilemann M, Sauer M (2011) Measuring localization performance of super-resolution algorithms on very active samples. *Opt Express* 19: 7020–7033.
57. Lando D, Endesfelder U, Berger H, Subramanian L, Dunne PD, et al. (2012) Quantitative single-molecule microscopy reveals that CENP-A(Cnp1) deposition occurs during G2 in fission yeast. *Open Biol* 2: 120078.
58. Jones E, Oliphant T, Peterson P (2001) SciPy: Open source scientific tools for Python.
59. Malkusch S, Endesfelder U, Mondry J, Gelleri M, Vermeer PJ, et al. (2012) Coordinate-based colocalization analysis of single-molecule localization microscopy data. *Histochem Cell Biol* 137: 1–10.
60. Lillemeyer BF, Mortelmaier MA, Forstner MB, Huppa JB, Groves JT, et al. (2010) TCR and Lat are expressed on separate protein islands on T cell membranes and concatenate during activation. *Nat Immunol* 11: 90–96.
61. Williamson DJ, Owen DM, Rossy J, Magenau A, Wehrmann M, et al. (2011) Pre-existing clusters of the adaptor Lat do not participate in early T cell signaling events. *Nat Immunol* 12: 655–662.
62. Schindelin J, Arganda-Carreras I, Frise E, Kaynig V, Longair M, et al. (2012) Fiji: an open-source platform for biological-image analysis. *Nat Methods* 9: 676–682.
63. McDonald D, Vodicka MA, Lucero G, Svitkina TM, Borisy GG, et al. (2002) Visualization of the intracellular behavior of HIV in living cells. *J Cell Biol* 159: 441–452.

ORIGINAL ARTICLE

Open Access

# A hydrophilic gel matrix for single-molecule super-resolution microscopy

Patrick JM Zessin<sup>†</sup>, Carmen L Krüger<sup>†</sup>, Sebastian Malkusch<sup>†</sup>, Ulrike Endesfelder and Mike Heilemann<sup>\*</sup>

## Abstract

**Background:** Novel microscopic techniques which bypass the resolution limit in light microscopy are becoming routinely established today. The higher spatial resolution of super-resolution microscopy techniques demands for precise correction of drift, spectral and spatial offset of images recorded at different axial planes.

**Methods:** We employ a hydrophilic gel matrix for super-resolution microscopy of cellular structures. The matrix allows distributing fiducial markers in 3D, and using these for drift correction and multi-channel registration. We demonstrate single-molecule super-resolution microscopy with photoswitchable fluorophores at different axial planes. We calculate a correction matrix for each spectral channel, correct for drift, spectral and spatial offset in 3D.

**Results and discussion:** We demonstrate single-molecule super-resolution microscopy with photoswitchable fluorophores in a hydrophilic gel matrix. We distribute multi-color fiducial markers in the gel matrix and correct for drift and register multiple imaging channels. We perform two-color super-resolution imaging of click-labeled DNA and histone H2B in different axial planes, and demonstrate the quality of drift correction and channel registration quantitatively. This approach delivers robust microscopic data which is a prerequisite for data interpretation.

**Keywords:** Single-molecule localization microscopy; Super-resolution microscopy; Drift correction; Registration

## Background

Various techniques that bypass the resolution limit in light microscopy were established for cellular imaging (Galbraith and Galbraith 2011, Heilemann 2010, Hell 2009). These techniques, commonly summarized as super-resolution microscopy, resolve cellular structures up to the near-molecular level and still profit from the advantages of fluorescence microscopy, such as high contrast and live cell compatibility. However, at these small spatial scales, accurate correction for drift and spatial or spectral offsets is required. Single-molecule localization microscopy techniques (Betzig et al. 2006, Folling et al. 2008, Heilemann et al. 2008, Hess et al. 2006, Rust et al. 2006) are particularly prone to drift, as many thousands of images and thus long acquisition times are required.

Drift can be minimized by hardware, e.g. with temperature chambers that enclose the microscope (Adler and Pagakis 2003), devices which uncouple the sample

from the sample holder (van de Linde et al. 2011) or by implementing feedback loops (Carter et al. 2007, Pertsinidis et al. 2010). Drift was reported to be minimized to 0.64 nm for an acquisition time of several hours (Pertsinidis et al. 2010). Software-based drift correction can be achieved by image correlation of bright-field (Mennella et al. 2012) or super-resolution images (Huang et al. 2008, Mlodzianoski et al. 2011). This approach works particularly well in the presence of structured or dense features. In a dual-objective configuration, anti-correlated changes of the point-spread function (PSF) were analyzed and used for drift correction (Xu et al. 2012). Alternatively, fiducial markers can be added to the sample (Betzig et al. 2006, Rust et al. 2006), and tracking their position over time can be used to correct for drift. This approach is independent of the structure or density of the sample. In addition, multi-spectral markers offer the additional advantage to correct for chromatic offset and register multi-color super-resolution images (Churchman et al. 2005, Malkusch et al. 2012). Fiducial markers are added to the sample and distributed at the surface of the cover slip. The level of lateral drift can be assessed by the standard deviation of the localization of the markers and were

\* Correspondence: heilemann@chemie.uni-frankfurt.de

<sup>†</sup>Equal contributors

Institute of Physical and Theoretical Chemistry, Goethe-University Frankfurt, Max-von-Laue-Str. 7, 60438, Frankfurt, Germany



Springer

© 2013 Zessin et al.; licensee Springer. This is an Open Access article distributed under the terms of the Creative Commons Attribution License (<http://creativecommons.org/licenses/by/2.0>), which permits unrestricted use, distribution, and reproduction in any medium, provided the original work is properly cited.



reported between 8 and 10 nm (Quan et al. 2010, Rust et al. 2006, Shtengel et al. 2009). Recently, drift correction through image correlation was demonstrated for 3D single-molecule localization microscopy (McGorothy et al. 2013).

Here, we introduce a simple experimental protocol to distribute fiducial markers in three dimensions using a hydrophilic extracellular matrix (ECM). Such hydrogels were developed for cell culture to support cell growth in 3D and serve as a scaffold (Lee et al. 2008), and comprise biocompatible compounds such as fibrin (Blomback 2004 #212), collagen (Bell et al. 1979) or alginate (Augst et al. 2006). Adding fiducial markers to the ECM gel and embedding the cells in the gel matrix leads to a distribution of the fiducial markers in 3D. We perform single-molecule localization microscopy of DNA and histone H2B in different axial planes, and use the fiducial markers to correct for both drift and spectral offset. A sufficiently dense distribution of fiducial markers further allows registering super-resolution images recorded in different axial planes.

## Materials and methods

### Cell culture

HeLa cells (300194, Cell Line Service, Eppelheim, Germany) were seeded into 8 chamber cell culture dishes with coverslip bottom (Sarstedt) and cultured at 37°C, 5% CO<sub>2</sub> in RPMI 1640 (PAA Laboratories GmbH, Pasching, Austria) supplemented with 1% penicillin-streptomycin (PAA Laboratories GmbH, Germany), 2 mM L-glutamin (PAA Laboratories GmbH), 10% fetal bovine serum (FBS, Gibco/Invitrogen, Grand Island, NY, USA), 1% non-essential amino acids (PAA Laboratories GmbH) and 1 mM sodium pyruvate (PAA Laboratories GmbH).

### Cloning and transfection

H2B was fused to mEos2 and cloned into a CMV promoter driven backbone (Clontech C2). 24 hours after seeding, HeLa cells were transiently transfected with this plasmid, using FugeneHD (Promega Corporation, Madison, WI, USA).

### DNA labelling

24 hours after seeding, 5-ethynyl-2'-deoxyuridine (EdU, Invitrogen, Eugene, Oregon, USA) was added to a final concentration of 10 µM. 15 minutes after incubation cells were fixed for 15 minutes with 4% formaldehyde (FA) solution in phosphate buffered saline (PBS, Sigma) pH 7, which was freshly prepared from 38% stock solution (Sigma). Subsequently, cells were permeabilized with 0.5% Triton X-100 (Sigma) and washed with PBS containing 3% (w/v) BSA (bovine serum albumin, Sigma). Click chemistry labeling of EdU with dye azide was performed in a reaction buffer based on protocol published by Qu et al. (2011) which was further

optimized to preserve fluorescence emission of fluorescence proteins (100 mM HEPES pH 8.2, 1 mM CuSO<sub>4</sub>, 50 mM aminoguanidine and 25 mM ascorbic acid). HeLa cells were incubated in the reaction buffer for 15 minutes, and washed with PBS. Labeling of EdU was performed with either Alexa Fluor 647 solely or Alexa Fluor 647 and Alexa Fluor 488 in equal amounts.

### Sample preparation

Extracellular matrix (ECM) gel from Engelbreth-Holm-Swarm murine sarcoma (Sigma, protein concentration 7–9 mg/mL, index of refraction 1.34) was thawed on ice. Fiducial markers (TetraSpecks, 100 nm, Invitrogen) were sonicated for 1 minute and diluted 1:5 in water. 29 µl of the liquid ECM gel and 1 µl of the fiducial marker solution were mixed, sonicated and carefully added to the fixed cells and incubated at 37°C until solidification (~1-2 h). The samples were post-fixed with 4% FA in PBS for 15 minutes to obtain a stable, temperature-independent solidification. The sample preparation is illustrated in Additional file 1: Figure S1a.

### Single-molecule localization microscopy

Super-resolution imaging was performed either on a commercial system (N-STORM, Nikon) equipped with a cylindrical lens for 3D imaging and a feedback loop driven axial stabilizing system (Perfect Focus System, Nikon) or a custom-built microscope essentially described earlier (Endesfelder et al. 2013). Dual-color imaging of Alexa Fluor 647 and Alexa Fluor 488 was performed in PBS with 100 mM beta-mercaptoethylamine (MEA, Sigma) added and pH set to 7.5. Dual-color imaging of Alexa Fluor 647 and mEos2 was performed in 0.5 mg/ml (100 units/ml) glucose oxidase (Sigma), 40 mg/ml (2000 units/ml) catalase (Roche Applied Science), 10% w/v glucose and 10 mM MEA in PBS at pH 8 (Endesfelder et al. 2011). Imaging in different axial planes was realized with a highly inclined and laminated optical sheet (HILO) illumination mode (Tokunaga et al. 2008). The different spectral channels were recorded sequentially.

### Drift correction and image registration

Single-molecule localization data was analyzed with *rapidSTORM* (Wolter et al., 2010) or the N-STORM software (STORM plugin, NIS, Nikon). As the fiducial markers are found in a large number of frames, we obtain the coordinates of the markers over time, which we want to call trajectory. The trajectories of fiducial markers were extracted using either the “track emission” filter of *rapidSTORM* or custom-written software.

Trajectories which did not span sufficient long time periods were rejected. All other trajectories were rendered with a Gaussian low pass filter. Drift correction

was performed with affine matrices (see Additional file 1: Figure S1b and Additional file 2: Figure S2). The registration of different spectral channels was performed by identifying fiducial markers that were present in both spectral data sets. A non-linear translation matrix was calculated from all fiducial markers in both channels. All coordinate processing routines were written in Python, Scipy and Numpy (Peterson 2009) (Additional file 1: Figure S1b). Super-resolution images were generated with *rapidSTORM* and overlaid in Fiji (Schindelin et al. 2012); 3D data was visualized using PyMol (Delano 2004).

### Theory of drift correction error analysis

An accurate metric for testing the quality of image registration with fiducial markers is the target registration error (TRE) (Fitzpatrick and West 2001, Maurer et al. 1997). Here, we adopted the TRE approach to quantify the quality of drift correction. In a first step, the coordinates from  $N$  fiducial markers were separated from the coordinates of the fluorophore-labeled biomolecules. Next, the set of trajectories of fiducial markers was separated into two subpopulations, where the first subpopulation  $x_1$  contained the trajectory of one fiducial marker, and subpopulation  $x_2$  contained the trajectories of all other fiducial markers. A correction matrix was calculated from  $x_2$ , and  $x_1$  was transformed with that matrix for every point in time,  $t$  (n.b.:  $x_1$  did not contribute to its own transformation matrix). To calculate the error, the difference between the transformed trajectory,  $f_{trans}\{x_1\}$ , and the local weighted mean  $f_{LWM}\{x_1\}$  from  $f_{trans}\{x_1\}$  over time, was calculated. This procedure was repeated for all  $N$  fiducial markers, and for all frames,  $T$ , according to:

$$TRE = \sqrt{\left(\frac{1}{NT} \sum_{n=1}^N \sum_{t=1}^T (f_{n,t,trans}\{x_{n,t,1}\} - f_{n,LWM}\{x_{n,1}\})^2\right)}$$

### Theory of image registration error analysis

The 3D coordinate-based colocalization (CBC) algorithm (Malkusch et al. 2012) was used to quantify the error of the registration of different channels (offset correction). For this purpose, we calculated the distribution of single fluorophores around a center molecule using an all-distances function related to Ripley's K-function (Ripley 1977). We calculated the distribution of (i) single molecules detected in channel one around the center molecule and of (ii) single molecules detected in channel two around the same center molecule. The two distributions were correlated (Spearman) and weighted, yielding a CBC value for the center molecule which can serve as a measure of colocalization with neighboring molecules. This procedure was repeated for every single molecule detected in the image. We applied this approach to

fiducial markers to estimate the quality of the image registration (fiducial markers which were used for quality control were not used to calculate the registration matrix).

## Results and discussion

### Distribution of fiducial markers in 3D

Fiducial markers were frequently used for drift correction and image registration in single-molecule localization microscopy (Betzig et al. 2006, Churchman et al. 2005, Rust et al. 2006, Shtengel et al. 2009). Typically, the markers were added to the sample and distributed on the glass surface. This approach often limits their usefulness when imaging away from the surface. Other approaches involved attaching fiducial markers to a cell (e.g. membrane), which in turn can affect single-molecule detection in the area of the fiducial marker. For drift correction and image registration, fiducial markers should be available in every imaging plane, and should not be attached to the target structure to avoid artifacts in single-molecule localization. Here, we employed a hydrophilic extracellular matrix (ECM), which is commonly used in cell culture (Kleinman and Martin 2005), for super-resolution microscopy. We added the fiducial markers to the ECM gel, embedded the specimen in the matrix and observed the distribution of the markers in 3D (Figure 1).

For drift correction in super-resolution localization microscopy, the spatial position of fiducial markers had to be particularly stable within the gel matrix for the whole acquisition time. We verified this by tracking the

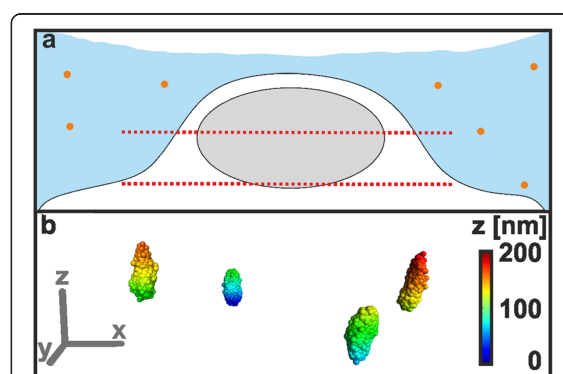


**Figure 1** Sample embedding in hydrophilic matrix gel. (a) Fiducial markers can be distributed in an ECM gel in 3D space, and can be used for correction of drift and channel offsets in super-resolution microscopy. The distribution in 3D allows recording images in different focal planes; a sufficient density of the same markers in two imaging planes allows 3D registration of super-resolution images. (b) The positions of four fiducial markers distributed in the ECM gel were tracked in 3D for an acquisition of 10,000 frames, and are color-coded for the axial position. After drift correction, a localization precision of 6.9 nm (s.d., lateral) and 18.1 nm (axial) was determined (scale bars 100 nm).

trajectory of single fiducial markers with respect to the trajectories of the other markers. For that purpose, the distance of a specific fiducial marker to the center of mass of the remaining fiducial markers was calculated. This procedure was repeated for every fiducial marker, and allowed us identifying and removing those that showed an independent movement with respect to the other fiducial markers. In a representative experiment with 33 fiducial markers, we found two which matched these criteria and removed them from further analysis (Additional file 3: Figure S3).

#### Non-linear drift correction

In contrast to diffraction-limited microscopy, super-resolution images even suffer from drift in the nanometer range which reduces the spatial resolution (Mlodzianoski *et al.* 2011). Drift often comprises several non-linear components (Adler and Pagakis 2003). Linear drift correction is not suitable, and more sophisticated methods are needed, for example by using affine or non-linear matrices (see Materials and Methods, Additional file 2: Figure S2) (Betzig *et al.* 2006, Malkusch *et al.* 2012).

To first demonstrate drift correction we prepared a sample of fiducial markers immobilized on a glass surface, which was imaged under normal conditions and showed a high level of non-linear drift (an exemplary trajectory is shown in Additional file 2: Figure S2a). From the coordinates of the fiducial markers over time, trajectories were generated which contained information on the movement of the markers. These trajectories were split into spatial dimensions (Additional file 2: Figure S2b) and were convolved with a Gaussian low pass filter (Additional file 2: Figure S2c and S2d). From these trajectories, an affine transfer matrix was calculated for each frame and applied to the uncorrected coordinates of fiducial markers (Additional file 2: Figure S2e). In a second experiment, we embedded fiducial markers in the gel matrix in 3D. Lateral drift was described as above (Additional file 4: Figure S4), axial drift was controlled actively by hardware (see Methods).

#### Multi-channel image registration

Imaging more than one spectral channel, focal plane or time point always leads to a spatial offset. A correction of this offset requires multi-channel image registration. To test the suitability of fiducial markers embedded in ECM gel for multi-channel image registration, we prepared a sample in which we visualized three fiducial markers. The sample was imaged in one color, and the image stack was split in two halves. From the two resulting image stacks, two uncorrected super-resolution images were reconstructed (Figure 2a). In the absence of drift, these images should show a colocalization near 100%. By applying drift correction (Figure 2b) and

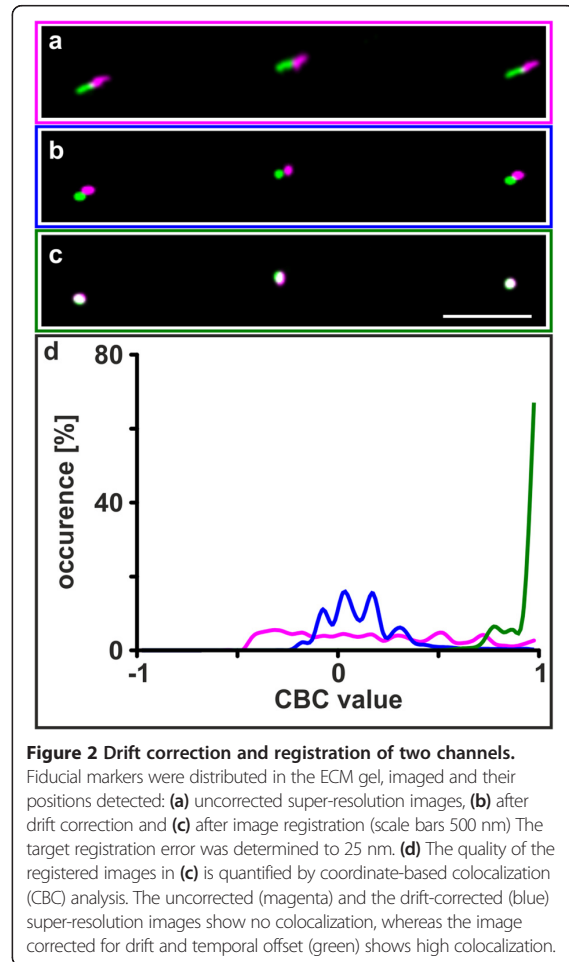


**Figure 2** Drift correction and registration of two channels. Fiducial markers were distributed in the ECM gel, imaged and their positions detected: (a) uncorrected super-resolution images, (b) after drift correction and (c) after image registration (scale bars 500 nm). The target registration error was determined to 25 nm. (d) The quality of the registered images in (c) is quantified by coordinate-based colocalization (CBC) analysis. The uncorrected (magenta) and the drift-corrected (blue) super-resolution images show no colocalization, whereas the image corrected for drift and temporal offset (green) shows high colocalization.

channel registration (Figure 2c), the mean CBC value is approaching 1 (representing perfect colocalization) (Figure 2d). In contrast, the uncorrected images showed a near uniform distribution of CBC values. The CBC values of the drift corrected, but unregistered images on the other hand showed an expected distribution around 0 (representing no colocalization) caused by the spatial offset (Figure 2d). A target registration error analysis for the registration of the two spectral channels yielded a mean registration error of 25 nm (see Methods).

HeLa cells were labeled for DNA (15 minutes pulse) with both Alexa Fluor 488 and Alexa Fluor 647, and imaged with super-resolution microscopy (Figure 3). Before drift correction and image registration, the fluorescence signal in the two spectral channels showed little overlap (Figures 3a, 3c). After drift-correction and image registration, the spatial pattern of the fluorescence signal recorded for DNA was largely similar and overlapping (Figures 3b, 3d).

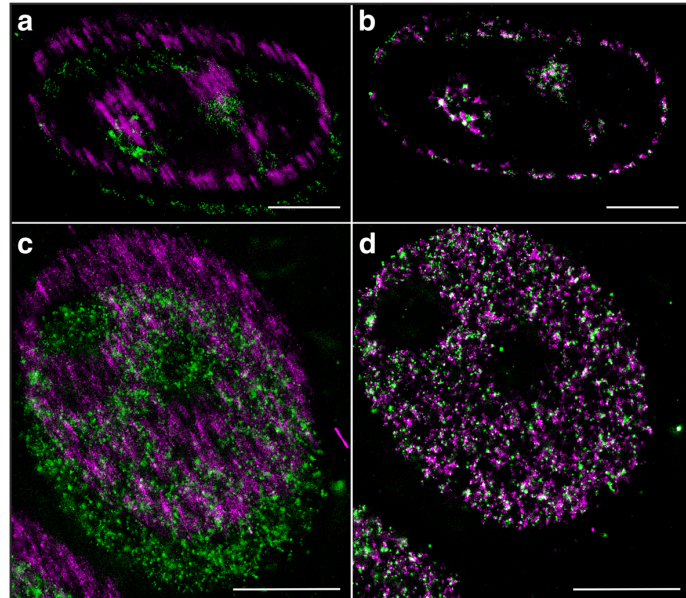


**Figure 3** Drift correction and registration of super-resolution images of cells. Cells were treated with the thymidine analogue EdU for 15 minutes, DNA was labeled with both Alexa Fluor 647 (magenta) and Alexa Fluor 488 (green) using click chemistry. HeLa cells were imaged in mid stage (**a, b**) and early stage (**c, d**), both original images (**a, c**) and corrected images (**b, d**) are shown (drift and spectral offset was increased for demonstration purpose in (**a, c**)). The corrected images (**b, d**) show colocalization of DNA labeled with two fluorophores (scale bars 5  $\mu\text{m}$ ).

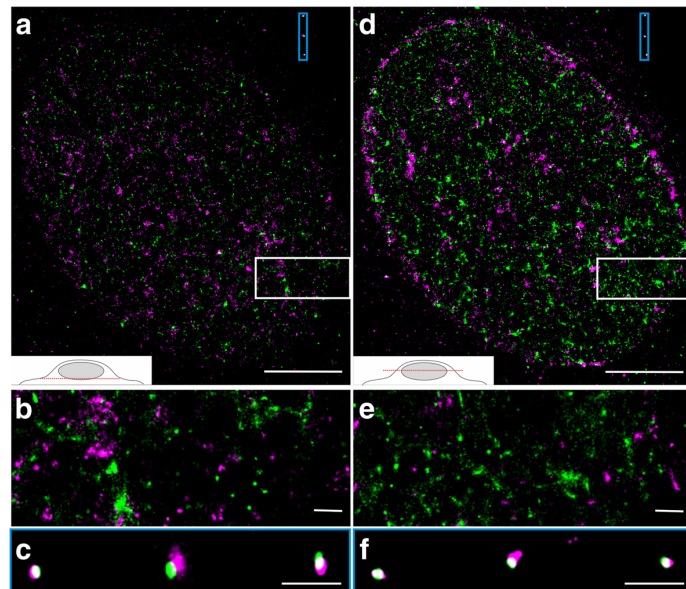


**Figure 4** Super-resolution imaging of histone H2B and nascent DNA at different axial planes. Replicated DNA (EdU-Alexa Fluor 647, magenta) and H2B (mEos2-H2B, green) were imaged (**a**) at the bottom and (**d**) at the middle of a HeLa cell. The nascent DNA shows the typical distribution for a mid S phase nucleus. A magnified view of selected regions (white boxes, (**b, e**)) highlights that the distribution of DNA and H2B is different at this stage of the cell cycle. (**c, f**) Fiducial markers which were not used for correction of drift and chromatic offset are colocalized and demonstrate the quality of image registration (scale bars 5  $\mu\text{m}$  (**a, d**), 500 nm (**b, c, e, f**)).



**Influence of illumination on image registration**

A possible error source in multi-channel image registration is the use of TIRF or HILO excitation. Both methods are well suited for single-molecule localization microscopy due to the increase in signal-to-noise ratio by background reduction. Still, with both methods, experiments might suffer from non-uniform illumination and light scattering, which get more prominent when imaging with multiple channels deep inside the sample (Oheim and Schapper 2005, Rohrbach 2000, van 't Hoff et al., 2008). Multi-channel imaging with super-resolution microscopy benefits from homogeneous TIRF and HILO illumination by scanning the focused laser spot in a circular orbit on the back focal plane (van 't Hoff et al., 2008). Another approach is light sheet illumination, which is decoupling the illumination pathway from the detection pathway (Gao et al. 2012, Keller et al. 2008, Planchon et al. 2011).

**3D imaging of histone H2B and chromosomal DNA**

Super-resolution images of the histone protein H2B (labeled with the fluorescent protein mEos2) and chromosomal DNA (labeled with Alexa Fluor 647) were recorded at two different axial focal planes of the cell nucleus (Figure 4 and Additional file 5: Figure S5), each providing a 3D section with an axial range of about 1  $\mu\text{m}$ . Notably, we observed similar photoactivation (mEos2) and photoswitching (Alexa Fluor 647) properties as in aqueous buffers. The super-resolution images were corrected for drift and registered (Figure 4). The spatial pattern of DNA matched typical patterns for the mid (Figure 4a, b) and early (Figure 4c, d) S phase of replication (Nakayasu and Berezney 1989, Zessin et al. 2012). We note that we observe a higher registration error at the limits of the depth of field, which might be due to aberrations (see for example Figure 4c, fiducial marker in the middle, and Additional file 6: Figure S6).

For the generation of a 3D super-resolution image from two 3D sections, we selected fiducial markers in the overlapping space between both planes (300 nm) (Additional file 6: Figure S6). This resulted in a 3D image with an axial range of 1.7  $\mu\text{m}$ . The acquisition of more 3D sections will further increase the axial range, and whole cells can be visualized. The quality of drift correction and image registration is visualized by 3 fiducial markers at the upper right of the image (Figure 4a, d and Additional file 6: Figure S6). These fiducial markers were not part of the drift correction and registration matrix.

**Conclusions**

We introduce a hydrophilic gel matrix for single-molecule super-resolution microscopy. This matrix matches the index of refraction of aqueous buffers (1.34), and is compatible with photoswitching of synthetic fluorophores in appropriate switching buffers. We

demonstrate that single-molecule super-resolution microscopy can be performed in the ECM gel, and that fiducial markers can be added to the ECM gel prior to sample embedding. These fiducial markers are distributed in 3D in the gel matrix, and can be used to correct for drift and image registration. The fiducial markers can be used for imaging away from the cover glass. In addition, this approach allows registration of images recorded in different axial planes, making use of fiducial markers that were recorded in multiple planes. In the future, this approach can be combined with a light sheet illumination scheme and a piezo-driven scanning mode, to allow for automated whole-cell imaging in 3D.

**Additional files**

**Additional file 1: Figure S1.** Sample preparation and data processing. (a) Fiducial markers are added to the hydrophilic gel matrix (extracellular matrix (ECM)) and applied to the specimen. (b) Drift correction and image registration workflow. (TIFF 593 kb)

**Additional file 2: Figure S2.** Non-linear drift correction in 2D. We demonstrate the robustness of drift correction with a sample containing 13 fiducial markers which exhibit non-linear drift. (a) Coordinates (before (black) and after (red) drift correction) and calculated centre (triangle, before (blue) and after (magenta) drift correction) of a single fiducial marker. (b) Trajectories (coordinates of fiducial markers over time) were split in x and y and (c) convolved with a Gaussian low pass filter to eliminate high frequencies. (d) Smoothed trajectories of 12 fiducial markers were used to calculate the transfer matrix and applied to correct for the non-linear drift of the selected fiducial marker shown in (a) (the fiducial marker in (a) was not used to generate the transfer matrix). This procedure was repeated for all 13 fiducial markers. (e) Distance distribution (left) from all fiducial marker coordinates to its center shown in (a) before (black) and after (red) drift correction. The peak of the distance distribution, which is a measure of the quality of drift control, moved from 40.1 nm (s.d., uncorrected) to 6.2 nm (corrected) (respective values for each dimension: 23.5 nm (before) and 4.5 nm (after drift correction) in x-direction, 32.5 nm and 4.2 nm in y-direction). A further and different measure for the quality of drift correction is the covariance matrix (right, distribution of covariances for x (dashed line) and y (straight line) for both uncorrected (black) and corrected (red) coordinates of all fiducial markers). The average covariance decreases from 360.7 nm<sup>2</sup> (x, uncorrected) and 698 nm<sup>2</sup> (y, uncorrected) to 31.2 nm<sup>2</sup> and 24.8 nm<sup>2</sup> (corrected).

**Additional file 3: Figure S3.** Stability of fiducial markers in gel matrix. The stability of fiducial markers (N = 31) in the gel matrix was measured over 10,000 frames. The distance variation of a single fiducial marker with respect to the centre of gravity of all other fiducial markers (i.e. 30) over time was calculated. This procedure was repeated for each marker and histogrammed over time, which results in the distributions shown for x (top), y (middle) and z (bottom) (the centre position was set to zero for better comparison). The histograms (right) show the distance variation summed over all frames. The histograms were approximated with a Gaussian function and yielded an s.d. of 3.5 nm (x), 4.9 nm (y) and 11.3 nm (z).

**Additional file 4: Figure S4.** Drift correction of single fiducial markers. Coordinates of four fiducial markers obtained from one super-resolution image (x (red), y (blue) and z (green)) are shown before (left panel) and after (right panel) drift correction. Drift in x and y was corrected as described, drift in z was corrected by hardware stabilization (for details, see Materials and Methods).

**Additional file 5: Figure S5.** Super-resolution imaging of DNA and histone H2B. Replicated DNA (EdU-Alexa Fluor 647, magenta) and H2B (mEos2-H2B, green) were imaged (a) at the bottom and (b) at the

middle of a HeLa cell. Drift was not corrected here (see Figure 4 for drift corrected images) (scale bar 5  $\mu\text{m}$ ).

**Additional file 6: Figure S6.** Registration of two 3D stacks. A HeLa cell stained for DNA (EdU-Alexa Fluor 647) was imaged at two different planes (see Additional file 5: figure S5) using 3D super-resolution localization microscopy. The two sets of 3D images were registered by using fiducial markers present in both imaging planes (highlighted in boxes, top right), generating a new 3D stack which spans 1.7  $\mu\text{m}$  along the axial direction (scale bar 5  $\mu\text{m}$ , color coding for c coordinate).

#### Competing interests

The authors declare no competing interests.

#### Authors' contributions

PJMZ, CLK, SM, UE and MH designed experiments. PJMZ, UE and CLK acquired data. SM, UE and MH designed the software and analyzed the data. All authors analyzed the data, designed figures and wrote the manuscript. All authors read and approved the final manuscript.

#### Acknowledgements

We thank Sven Proppert and Daniela Wengler for their support with initial experiments. The authors gratefully acknowledge financial support by the BMBF (FORSYS, research grant 0315262), the DFG (EXC 115) and the Goethe-University Frankfurt.

Received: 13 March 2013 Accepted: 29 August 2013

Published: 10 September 2013

#### References

- Adler J, Pagakis SN (2003) Reducing image distortions due to temperature-related microscope stage drift. *J Microsc* 210:131–137
- Augst AD, Kong HJ, Mooney DJ (2006) Alginate hydrogels as biomaterials. *Macromol Biosci* 6:623–633
- Bell E, Ivarsson B, Merrill C (1979) Production of a tissue-like structure by contraction of collagen lattices by human fibroblasts of different proliferative potential in vitro. *Proc Natl Acad Sci USA* 76:1274–1278
- Betzig E, Patterson GH, Sougrat R, Lindwasser OW, Olenych S, Bonifacino JS, Davidson MW, Lippincott-Schwartz J, Hess HF (2006) Imaging intracellular fluorescent proteins at nanometer resolution. *Science* 313:1642–1645
- Blomback B, Bark N (2004) Fibrinopeptides and fibrin gel structure. *Biophys Chem* 112:147–151
- Carter AR, King GM, Ulrich TA, Halsey W, Alchenberger D, Perkins TT (2007) Stabilization of an optical microscope to 0.1 nm in three dimensions. *Appl Opt* 46:421–427
- Churchman LS, Okten Z, Rock RS, Dawson JF, Spudis JA (2005) Single molecule high-resolution colocalization of Cy3 and Cy5 attached to macromolecules measures intramolecular distances through time. *Proc Natl Acad Sci USA* 102:1419–1423
- Delano WL (2004) Use of PYMOL as a communications tool for molecular science. *Abstr Pap Am Chem Soc* 228:U313–U314
- Endesfelder U, Malkusch S, Flottmann B, Mondry J, Liguzinski P, Verwee PJ, Heilemann M (2011) Chemically induced photoswitching of fluorescent probes—a general concept for super-resolution microscopy. *Molecules* 16:3106–3118
- Endesfelder U, Finan K, Holden SJ, Cook PR, Kapanidis AN, Heilemann M (2013) Multiscale Spatial Organization of RNA Polymerase in *Escherichia coli*. *Biophys J* 105:172–181
- Fitzpatrick JM, West JB (2001) The distribution of target registration error in rigid-body point-based registration. *IEEE Trans Med Imaging* 20:917–927
- Folling J, Bossi M, Bock H, Medda R, Wurm CA, Hein B, Jakobs S, Eggeling C, Hell SW (2008) Fluorescence nanoscopy by ground-state depletion and single-molecule return. *Nat Methods* 5:943–945
- Galbraith CG, Galbraith JA (2011) Super-resolution microscopy at a glance. *J Cell Sci* 124:1607–1611
- Gao L, Shao L, Higgins CD, Poulton JS, Peifer M, Davidson MW, Wu X, goldstein B, Betzig E (2012) Noninvasive imaging beyond the diffraction limit of 3D dynamics in thickly fluorescent specimens. *Cell* 151:1370–1385
- Heilemann M (2010) Fluorescence microscopy beyond the diffraction limit. *J Biotechnol* 149:243–251
- Heilemann M, van de Linde S, Schuttpelz M, Kasper R, Seefeldt B, Mukherjee A, Tinnefeld P, Sauer M (2008) Subdiffraction-resolution fluorescence imaging with conventional fluorescent probes. *Angew Chem Int Ed Engl* 47:6172–6176
- Hell SW (2009) Microscopy and its focal switch. *Nat Methods* 6:24–32
- Hess ST, Girirajan TP, Mason MD (2006) Ultra-high resolution imaging by fluorescence photoactivation localization microscopy. *Biophys J* 91:4258–4272
- Huang B, Wang W, Bates M, Zhuang X (2008) Three-dimensional super-resolution imaging by stochastic optical reconstruction microscopy. *Science* 319:810–813
- Keller PJ, Schmidt AD, Wittbrodt J, Stelzer EH (2008) Reconstruction of zebrafish early embryonic development by scanned light sheet microscopy. *Science* 322:1065–1069
- Kleinman HK, Martin GR (2005) Matrigel: basement membrane matrix with biological activity. *Semin Cancer Biol* 15:378–386
- Lee J, Cuddihy MJ, Kotov NA (2008) Three-dimensional cell culture matrices: state of the art. *Tissue Eng Part B Rev* 14:61–86
- Malkusch S, Endesfelder U, Mondry J, Gelleri M, Verwee PJ, Heilemann M (2012) Coordinate-based colocalization analysis of single-molecule localization microscopy data. *Histochem Cell Biol* 137:1–10
- Maurer Cr JR, Fitzpatrick JM, Wang MY, Galloway RLJR, Maciunas RJ, Allen GS (1997) Registration of head volume images using implantable fiducial markers. *IEEE Trans Med Imaging* 16:447–462
- Mcgorthy R, Kamiyama D, Huang B (2013) Active microscope stabilization in three dimensions using image correlation. *Optical Nanoscopy* 2:2–3
- Mennella V, Keszthelyi B, McDonald KL, Chhun B, Kan F, Rogers GC, Huang B, Agard DA (2012) Subdiffraction-resolution fluorescence microscopy reveals a domain of the centrosome critical for pericentriolar material organization. *Nat Cell Biol* 14:1159–1168
- Mlodzianoski MJ, Schreiner JM, Callahan SP, Smolkova K, Dlaskova A, Santorova J, Jezek P, Bewersdorff J (2011) Sample drift correction in 3D fluorescence photoactivation localization microscopy. *Opt Express* 19:15009–15019
- Nakayasu H, Berezney R (1989) Mapping replicational sites in the eucaryotic cell nucleus. *J Cell Biol* 108:1–11
- Oheim M, Schapper F (2005) Non-linear evanescent-field imaging. *J Phys D-Appl Phys* 38:R185–R197
- Pertsinidis A, Zhang Y, Chu S (2010) Subnanometre single-molecule localization, registration and distance measurements. *Nature* 466:647–651
- Peterson P (2009) F2PY: a tool for connection Fortran and Python programs. *J Comput Sci Eng* 4:296–305
- Planchon TA, Gao L, Milkie DE, Davidson MW, Galbraith JA, Galbraith CG, Betzig E (2011) Rapid three-dimensional isotropic imaging of living cells using Bessel beam plane illumination. *Nat Methods* 8:417–423
- Qu D, Wang G, Wang Z, Zhou L, Chi W, Cong S, Ren X, Liang P, Zhang B (2011) 5-Ethynyl-2'-deoxycytidine as a new agent for DNA labeling: detection of proliferating cells. *Anal Biochem* 417:112–121
- Quan T, Li P, Long F, Zeng S, Luo Q, Hedde PN, Nienhaus GU, Huang ZL (2010) Ultra-fast, high-precision image analysis for localization-based super resolution microscopy. *Opt Express* 18:11867–11876
- Ripley BD (1977) Modeling Spatial Patterns. *J R Stat Soc Ser B-Methodological* 39:172–212
- Rohrbach A (2000) Observing secretory granules with a multiangle evanescent wave microscope. *Biophys J* 78:2641–2654
- Rust MJ, Bates M, Zhuang X (2006) Sub-diffraction-limit imaging by stochastic optical reconstruction microscopy (STORM). *Nat Methods* 3:793–795
- Schindelin J, Arganda-Carreras I, Frise E, Kaynig V, Longair M, Pietzsch T, Preibisch S, Rueden C, Saalfeld S, Schmid B, Tinevez JY, White DJ, Hartenstein V, Eliceiri K, Tomancak P, Cardona A (2012) Fiji: an open-source platform for biological-image analysis. *Nat Methods* 9:676–682
- Shtengel G, Galbraith JA, Galbraith CG, Lippincott-Schwartz J, Gillette JM, Manley S, Sougrat R, Waterman CM, Kanchanawong P, Davidson MW, Fetter RD, Hess HF (2009) Interferometric fluorescent super-resolution microscopy resolves 3D cellular ultrastructure. *Proc Natl Acad Sci USA* 106:3125–3130
- Tokunaga M, Imamoto N, Sakata-Sogawa K (2008) Highly inclined thin illumination enables clear single-molecule imaging in cells. *Nat Methods* 5:159–161
- van de Linde S, Loschberger A, Klein T, Heidbreder M, Wolter S, Heilemann M, Sauer M (2011) Direct stochastic optical reconstruction microscopy with standard fluorescent probes. *Nat Protoc* 6:991–1009
- Van T, Hoff M, De Sars V, Oheim M (2008) A programmable light engine for quantitative single molecule TIRF and HILO imaging. *Opt Express* 16:18495–18504

Zessin *et al.* *Optical Nanoscopy* 2013, **2**:4  
<http://www.optnano.com/content/2/1/4>

Page 8 of 8

- Wolter S, Schüttelpeiz M, Tscherepanow M, Van de Linde S, Heilemann M, Sauer M (2010) Real-time computation of subdiffraction-resolution fluorescence images. *J Microsc* 237:12–22
- Xu K, Babcock HP, Zhuang X (2012) Dual-objective STORM reveals three-dimensional filament organization in the actin cytoskeleton. *Nat Methods* 9:185–188
- Zessin PJ, Finan K, Heilemann M (2012) Super-resolution fluorescence imaging of chromosomal DNA. *J Struct Biol* 177:344–348

doi:10.1186/2192-2853-2-4

**Cite this article as:** Zessin *et al.*: A hydrophilic gel matrix for single-molecule super-resolution microscopy. *Optical Nanoscopy* 2013 **2**:4.

**Submit your manuscript to a SpringerOpen<sup>®</sup> journal and benefit from:**

- ▶ Convenient online submission
- ▶ Rigorous peer review
- ▶ Immediate publication on acceptance
- ▶ Open access: articles freely available online
- ▶ High visibility within the field
- ▶ Retaining the copyright to your article

---

Submit your next manuscript at ▶ [springeropen.com](http://springeropen.com)

---



## Regular Article

## Quantitative morphological analysis of arrestin2 clustering upon G protein-coupled receptor stimulation by super-resolution microscopy



Zinnia Truan<sup>a,1</sup>, Laura Tarancón Díez<sup>a,1</sup>, Claudia Bönsch<sup>b</sup>, Sebastian Malkusch<sup>c</sup>, Ulrike Endesfelder<sup>c</sup>, Mihaela Munteanu<sup>b</sup>, Oliver Hartley<sup>b</sup>, Mike Heilemann<sup>c,\*</sup>, Alexandre Fürstenberg<sup>a,\*</sup>

<sup>a</sup> Department of Human Protein Sciences, University of Geneva, CMU, Rue Michel-Servet 1, 1211 Genève 4, Switzerland

<sup>b</sup> Department of Pathology and Immunology, University of Geneva, CMU, Rue Michel-Servet 1, 1211 Genève 4, Switzerland

<sup>c</sup> Institute for Physical and Theoretical Chemistry, Goethe-University Frankfurt, Max-von-Laue-Str. 7, 60438 Frankfurt, Germany

## ARTICLE INFO

## Article history:

Received 1 April 2013

Received in revised form 20 September 2013

Accepted 24 September 2013

Available online 30 September 2013

## Keywords:

Super-resolution microscopy

Clustering

Arrestin

G-protein coupled receptor

Single-molecule fluorescence microscopy

## ABSTRACT

Clustering of arrestins upon G protein-coupled receptor stimulation is a phenomenon that is well-known but difficult to describe quantitatively due to the size of the clusters close to the diffraction limit of visible light. We introduce a general method to quantitatively investigate the clustering of arrestin following stimulation of the C–C chemokine receptor 5 (CCR5) using single-molecule super-resolution imaging and coordinate and image-based cluster analysis. We investigated the effect of potent anti-HIV ligands of CCR5 with different pharmacological profiles on arrestin2 cluster formation and found that only the ligands capable of inducing CCR5 internalization induced arrestin2 recruitment and clustering. We further demonstrate that the fraction of arrestin2 molecules found in clusters larger than 100 nm correlates with the magnitude of ligand-induced CCR5 internalization, but not with G protein activation, indicating that recruitment of arrestin2 to CCR5 is independent of G protein activation. Pre-treatment of the cells with the drug cytochalasin D, which blocks actin polymerization, led to the formation of larger clusters, whereas the inhibitor of microtubule polymerization nocodazole had little effect on arrestin2 recruitment, suggesting an active role of actin in the organization and dynamics of these aggregates.

© 2013 Elsevier Inc. All rights reserved.

## 1. Introduction

G protein-coupled receptors (GPCRs) are proteins with seven transmembrane domains that have been extensively investigated owing to the fact that they are targeted by a third of currently marketed medicines (Rosenbaum et al., 2009). They mediate a wide variety of signals across the cell membrane as diverse as ions, small molecules, peptides, or hormones that regulate important physiological processes ranging from heart beat to smell to taste through the recruitment and activation of an array of adapter proteins inside the cell. They are however not simple 'on-off' switches, since chemically very similar ligands that bind the same receptor often trigger distinct pharmacological outcomes. The detailed underlying activation mechanism is still poorly understood and likely related to the existence of various receptor conformations inducing differential recruitment of cytosolic partners (Kenakin, 2009; Kobilka and Deupi, 2007). Upon agonist binding, GPCRs are stabilized in an ensemble of active conformations which catalyze the exchange

of GDP for GTP on the  $\alpha$  subunit of a cytoplasmic heterotrimeric G protein, promoting dissociation of  $G\alpha$ . Free  $G\alpha$ -GTP and  $G\beta\gamma$  subunits subsequently mediate effector functions through second messengers that control the activity of key cellular enzymatic processes. In parallel, GPCR stimulation leads to the recruitment of arrestin proteins which block the interaction of receptors with their G protein, thereby arresting downstream second-messenger signaling (Lefkowitz and Shenoy, 2005). Independently of G protein signaling, arrestins also induce clathrin-mediated endocytosis of the GPCRs, which are internalized and then either targeted to lysosomes for degradation or recycled to the cell surface after ligand dissociation in endosomal compartments (Moore et al., 2007). Endocytosis of cell-surface receptors renders the cell less responsive to subsequent stimuli and is part of the desensitization process widespread among GPCRs.

There are four known arrestins, two of which are localized primarily in visual sensory tissue. The two others, arrestin2 and arrestin3, are ubiquitously expressed and interact with most GPCRs, but are also involved in the endocytosis of other proteins, suggesting a general role of arrestins in clathrin-mediated endocytosis (Luttrel and Gesty-Palmer, 2010). Upon stimulation, arrestins are recruited from cytosolic pools to the plasma membrane where they bind to clathrin and AP-2 components of the endocytic machinery and

\* Corresponding authors. Fax: +49 6979829560 (M. Heilemann), +41 223795502 (A. Fürstenberg).

E-mail addresses: [heilemann@chemie.uni-frankfurt.de](mailto:heilemann@chemie.uni-frankfurt.de) (M. Heilemann), [alexandre.fuerstenberg@unige.ch](mailto:alexandre.fuerstenberg@unige.ch) (A. Fürstenberg).

<sup>1</sup> These authors contributed equally to this work.



induce clustering of GPCRs in preexisting coated pits (Santini et al., 2002). Whereas arrestins 2 and 3 facilitate the internalization of all class A and class B GPCRs (which were divided into these classes based on their agonist-dependent arrestin binding profile), they dissociate from class A receptors after internalization close to the plasma membrane and maintain a stable association with class B receptors (Oakley et al., 2000).

Although arrestin2 clustering upon GPCR stimulation and fusion of coated pits has been reported before (Laporte et al., 2000; Santini et al., 2002), very little is known about the fate of arrestin clusters after dissociation from the receptor. They seem to form in zones that are connected to an actin cytoskeleton subdomain, but their size close to the diffraction limit (~200 nm) and the difficulty of finding well-working arrestin antibodies for immunofluorescence experiments has prevented detailed morphological studies by fluorescence microscopy. Recent modifications of single-molecule wide-field imaging techniques however enable optical resolutions as small as a few tens of nanometers to be routinely achieved with blinking fluorescent probes by reconstruction of a pointillist image with the coordinates of individually localized fluorophores (Fürstenberg and Heilemann, 2013; Moerner, 2012). Here we introduce a general method to evaluate the size of arrestin clusters using the combination of a GFP fusion tag, fluorophore-tagged anti-GFP nanobodies, and the super-resolution imaging technique of direct stochastic optical reconstruction microscopy (dSTORM) (Heilemann et al., 2009). Nanobodies are single-domain antibodies derived from camelidae with much smaller size (~13 kDa) than regular antibodies whose usefulness and simplicity has been recently demonstrated in the context of single-molecule super-resolution imaging (Ries et al., 2012). They allow high labeling densities and can access densely packed cellular structures.

We chose the C–C chemokine receptor 5 (CCR5), principal co-receptor used by HIV to infect cells, as a model class A GPCR and investigated the effect of the chemokine ligands RANTES/CCL5, PSC-RANTES, 5P12-RANTES, and 5P14-RANTES (differing by only a few residues among the first 9 of the 68 amino acids) on arrestin2 recruitment. These N-terminal analogues of the natural CCR5 ligand RANTES were previously shown to be able to efficiently block HIV infection although their pharmacological profiles in terms of receptor activation and internalization is very different (Gaertner et al., 2008b; Hartley et al., 2004; Lederman et al., 2004) (Table 1). Molecules such as RANTES and PSC-RANTES behave like classical agonists by inducing G protein activation and it is thought that PSC-RANTES owes its greatly enhanced anti-HIV potency over RANTES to its capacity not only to induce CCR5 internalization but also long-term sequestration of the receptor inside the cell (Escola et al., 2010; Hartley et al., 2004). Molecules such as 5P12-RANTES and 5P14-RANTES display the same anti-HIV potency as PSC-RANTES, but neither of them activates G protein signaling via CCR5 and, while 5P12-RANTES does not induce endocytosis of CCR5, 5P14-RANTES does partially (Gaertner et al., 2008b) and has therefore been suggested to act as a biased ligand (Zidar, 2011). The precise mechanisms by which these different ligands are capable of potentially blocking HIV infection while displaying dif-

ferent pharmacological profiles is currently not understood and likely related to stabilization of CCR5 by the ligands in different conformational ensembles. We therefore explored the effect of these ligands on arrestin2 recruitment and cluster formation to see if differential mobilization and clustering of arrestin could relate to the pharmacological profiles of the ligands. Here, by applying super-resolution microscopy techniques to evaluate the relative number of arrestin2 molecules getting recruited into clusters and to determine the cluster size using coordinate and image-based approaches (Malkusch et al., 2013), we demonstrate a correlation between the number of arrestin2 molecules recruited into clusters and the capacity of the chemokine analogues to induce receptor internalization.

## 2. Materials and methods

### 2.1. Materials

RANTES and its analogues were synthesized as previously described (Gaertner et al., 2008b). H<sub>2</sub>O was purified using a Milli-Q system (Millipore). DMSO was obtained from Sigma–Aldrich. PBS (composition: NaCl 155.17 mM, KH<sub>2</sub>PO<sub>4</sub> 1.06 mM, Na<sub>2</sub>HPO<sub>4</sub> 2.97 mM, pH 7.4) and other cell culture reagents were purchased from Life Technologies.

### 2.2. Cell lines and cell culture

Plasmids pEGFP-NI with bovine arrestin2 were obtained from Jeffrey Benovic (Jefferson University). Chinese hamster ovary cells stably expressing CCR5 (Hartley et al., 2004) were grown to 80% confluence in 12 well plates and transfected with 0.25 µg p-arrestin1–GFP using X-treme GENE HP DNA transfection reagent (Roche) according to the manufacturer's instructions. Stable clones were selected and maintained in RPMI 10% supplemented with 0.75 mg/ml neomycin (G-418, PAA Laboratories). Media were subsequently replaced every 3 days with complete media containing 0.75 mg/ml neomycin. Stably transfected cells were isolated 3 weeks after transfection by fluorescence-assisted cell sorting (MoFlo<sup>®</sup> Astrios<sup>™</sup>) into 96-well plates. Clonal expression was confirmed by examining cells grown on coverslips by fluorescent microscopy.

Cells were cultured at 37 °C with 5% CO<sub>2</sub> in phenol-red free RPMI supplemented with 10% fetal bovine serum, 100 units/ml penicillin, and 100 µg/ml streptomycin. For single-molecule imaging experiments, they were grown for 48–72 h on glass-bottom Petri dishes (FluoroDish<sup>™</sup>, World Precision Instruments, Inc.) coated with 10 µg/ml of fibronectin (Calbiochem) in full medium for 45 min at 37 °C and washed with PBS.

### 2.3. Nanobody labeling

50 µl (3.8 nmol) of GFP-Trap<sup>®</sup> nanobody (ChromoTek) stock solution (1 mg/ml) were diluted with 50 µl of PBS and the buffer was exchanged against 0.1 M NaHCO<sub>3</sub> buffer at pH 8.3 using a spin concentrator with a 10-kDa molecular weight cutoff (Microcon-10, Millipore). 5 M equivalents of ATTO655-NHS ester (ATTO-Tec GmbH) from a 1-mM stock solution in DMSO were added and left to react for 1 h at room temperature on a rotating wheel. Excess dye was removed by washing the sample 5 times with 100 µl of PBS on another Microcon-10 spin concentrator. The degree of labeling of the nanobody was determined to be 1.5 by absorption spectroscopy (Genesis 10S UV–Vis spectrophotometer, Thermo Scientific) using a measured extinction coefficient at 280 nm of 25,280 cm<sup>-1</sup> M<sup>-1</sup> for the pure nanobody and of 125,000 cm<sup>-1</sup> M<sup>-1</sup> at the absorption maximum of ATTO655.

**Table 1**

Functional characterization of RANTES (Gaertner et al., 2008a; Hartley et al., 2004) and its analogues (Gaertner et al., 2008b). Signaling activity (intracellular release of Ca<sup>2+</sup>) and CCR5 internalization are expressed using PSC-RANTES as a reference (100%).

Ligand	Anti-HIV potency	G protein signaling (%)	CCR5 internalization (%)
RANTES	~1 µM	50	64
PSC-RANTES	25 pM	100	100
5P12-RANTES	28 pM	<5	3
5P14-RANTES	26 pM	<5	47

#### 2.4. Immunofluorescence

For immunofluorescence staining, cells were fixed with a 4% aqueous paraformaldehyde (Sigma) solution for 20 min at 4 °C and then washed once with PBS. Free aldehydes were quenched with a 50 mM NH<sub>4</sub>Cl (Merck) solution and subsequently washed 3 times with PBS. Membranes were permeabilized for 30 min with a 0.1% (w/w) solution of saponin (Sigma) in PBS containing 1% (w/v) bovine serum albumin (BSA, Sigma). Samples were then washed twice with PBS and incubated for 45 min with a 1:100-fold dilution of ATTO655-labeled GFP-Trap nanobody in PBS in the presence of 1% BSA. The cells were then washed 3 times with PBS and stored dry in the dark at 4 °C. When required, samples were incubated with 100 nM RANTES analogues 90 min prior to fixation and 15 μM nocodazole (Sigma) or 1 μM cytochalasin D (Sigma) 120 min prior to fixation in full medium.

#### 2.5. Confocal microscopy

Stacks of confocal microscopy images were acquired on a Zeiss LSM700 microscope with a X63/1.4NA PlanApoChromat oil-immersion objective using the 488 nm line of an Ar/Kr laser and GFP filters and maximum intensity projections were obtained using the ZEN 2011 software.

#### 2.6. Wide-field microscopy

Wide-field images and movies were acquired on an Olympus IX71 inverted epi-fluorescence microscope equipped with an oil-immersion objective (Olympus, PlanApoChromat, 60 × 1.42 NA) and detected on a 512 × 512 pixel EMCCD (Andor iXonEM + DU897). Excitation was performed at 488 or 640 nm with the spectrally filtered (BrightLine HC 482/18 or MaxDiode LD01-640/8, Semrock) output of an Oxxius LaserBoxx LBX-488-50 or a Coherent Cube 640-100-C laser, respectively. Wide-field illumination was achieved by focusing the spatially expanded and filtered laser beams onto the back-aperture of the objective using a 500-mm focal length lens placed at the back of the microscope. Fluorescence was collected through the objective and filtered by a 491/639-nm dual line dichroic beam splitter (z491/639rpc, Chroma) and a 500-nm (Edge Basic 488LP, Semrock) or a 660-nm (HQ660LP, Chroma) long-pass filter, before going through a 2.5× magnifier (Olympus, PE2.5x). Each pixel on the camera corresponded to a 109 × 109 nm<sup>2</sup> square in the sample plane.

#### 2.7. Super-resolution microscopy

Super-resolution imaging was performed on the wide-field microscope described above using the dSTORM technique (Heilemann et al., 2009). Blinking of ATTO655 was induced in the presence of 50 μM ascorbic acid (Merck) added from a freshly prepared 1-mM stock solution (Cordes et al., 2010) and imaging was performed in heavy water (D<sub>2</sub>O, 99.8% D-atom content, Armar Chemicals) (Lee et al., 2013). In a typical experiment, movies of 6000 frames were acquired with a 15 ms exposure time at an excitation wavelength of 640 nm and an illumination intensity of ~3 kW/cm<sup>2</sup>. Individual emitters were localized and super-resolution images were reconstructed using the rapidSTORM software (Wolter et al., 2010).

#### 2.8. Cluster analysis

All-distance distributions are commonly calculated for coordinate-based cluster analysis of single-molecule super-resolution data (Malkusch et al., 2013; Williamson et al., 2011). We used Rip-

ley's *K*-function (Ripley, 1977) (1) in its linearized (2) and normalized form (3) (Ripley's *H*-function):

$$K(r) = \frac{1}{n^2} \sum_i \sum_j \frac{N_r(d_{ij})}{\lambda} \quad (1)$$

$$L(r) = \sqrt{\frac{K(r)}{\pi}} \quad (2)$$

$$H(r) = L(r) - r \quad (3)$$

where *r* is the observation radius, *n* is the total number of localizations within a region of interest (ROI), *d<sub>ij</sub>* is the distance between two localizations *i* and *j*, *N<sub>r</sub>* is the number of localizations around localization *i* within the distance *r*, and *λ* is a weighting factor correcting for the area of the ROI. We calculated Ripley's *H*-function for large ROIs and molecules closer than 1 μm from the edge of the ROI were not taken into account into the calculations in order to account for edge effects. All calculations and simulations were performed in Matlab (The MathWorks, Inc.).

For image-based cluster analysis, "quantitative" super-resolution images with a pixel size of 10 nm were generated with pixel values representing the number of localizations (custom software written in Python, Scipy and Numpy (Peterson, 2009)). The obtained images were blurred with a Gaussian filter of 15 nm and cohesive regions were extracted and used as binary mask to obtain localization intensities within these areas from the original super-resolution data (ImageJ, <http://rsb.info.nih.gov/ij/>). The radius from spheres coextensive to the measured cluster areas was calculated. The cluster maps shown in Fig. 2 were obtained by superimposing the extracted cohesive regions with a wide-field image of the same cell whose shape was obtained with a binary filter.

### 3. Results

The formation of arrestin2 clusters upon stimulation of GPCRs has been reported by various groups (Laporte et al., 2000; Santini et al., 2002). These clusters appear at a size that is in the order of the diffraction limit of light microscopy (~200 nm in the imaging plane), which restricts the characterization of size and protein numbers. In order to overcome the resolution limit, we use here single-molecule localization-based super-resolution microscopy, which typically achieves a lateral resolution of ~20–30 nm (Kamiyama and Huang, 2012). Individual protein clusters which might overlap in a conventional microscopy image can thereby be discerned (van de Linde et al., 2008). In addition, this method provides single-molecule coordinates which can be used for secondary data analysis, such as coordinate-based cluster analysis (Malkusch et al., 2013; Williamson et al., 2011), and report on cluster size and relative protein numbers within these clusters.

In agreement with previous observations (Laporte et al., 2000; Santini et al., 2002), Fig. 1 illustrates how stimulation of the class A GPCR CCR5 with the agonist RANTES in stably transfected CHO cells induced arrestin2 carrying a GFP fusion tag (arrestin2-GFP) to cluster, whereas it is uniformly distributed in the cytoplasm of unstimulated cells. The full agonist PSC-RANTES induced even stronger clustering, whereas the amount of clustering was comparable with the non-signaling ligand 5P14-RANTES. 5P12-RANTES, which does not activate CCR5 nor leads to its internalization, failed to cause any arrestin2 clustering above background level. Qualitatively similar observations were made in living CHO-CCR5 cells (data not shown).

The confocal microscopy images demonstrate arrestin2 cluster formation with ligands capable of inducing receptor internalization; yet, at the same time, they show that a robust analysis of size and protein numbers is difficult due to extensive spatial overlap-

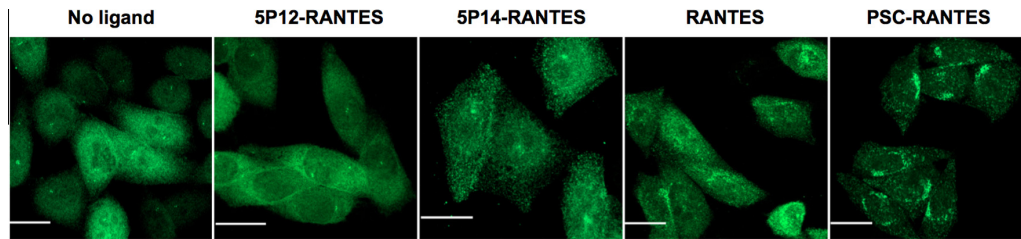


**Fig. 1.** Representative confocal microscopy images of arrestin2-GFP in fixed CHO-CCR5 cells in the absence of ligand and after 90 min of treatment with different chemokine analogues. Scale bar: 20  $\mu\text{m}$ .

ping of the fluorescent proteins. In order to investigate arrestin2 clusters with better resolution, we used a versatile and simple approach to obtain super-resolution images from GFP-labeled structures by targeting them with GFP-specific fluorophore-labeled nanobodies. We recorded super-resolution images of arrestin2 for unstimulated CCR5 and CCR5 exposed to the different chemokine ligands (Fig. S1), which allowed us to visualize single and independent clusters of arrestin2. Inspection of these images at higher magnification (Fig. 2) showed that arrestin2 clusters dramatically change in size, from individual proteins and small structures in the absence of ligand or after treatment with 5P12-RANTES, to medium-sized clusters upon CCR5 stimulation with 5P14-RANTES and RANTES, and even larger clusters upon addition of PSC-RANTES.

We next aimed to provide a more advanced analysis of the microscopy data, in order to make the crucial transition from simple qualitative visualization to quantitative information. Single-molecule super-resolution methods have proven particularly useful in this context, and have provided protein numbers (Lando et al., 2012; Sengupta et al., 2011) and quantitative information on nano-sized molecular patterns (Mennella et al., 2012; Muranyi et al., 2013; Williamson et al., 2011). Here, we used two approaches for quantitative cluster analysis, the first one by calculating Ripley's  $H$ -function (Ripley, 1977) from the coordinates of the localized molecules and the second one by image-based analysis (Endesfelder et al., 2013; Malkusch et al., 2013; Muranyi et al., 2013).

Image-based cluster analysis was carried out by generating cluster maps from the super-resolution images (Fig. 2) and extracting cohesive regions (see Section 2). We determined the area of each cluster and weighted it by its integrated detected fluorescence intensity, such that information on relative arrestin2 molecule numbers could be obtained. Fig. 3 shows for each ligand the fraction of arrestin2 molecules which were recruited into clusters with an area corresponding to a circle of 100 nm in radius or larger. This threshold was selected as it matched the maximum of the Ripley function in the case of untreated cells (see below). In the absence of ligand, 96% of the detected arrestin2 molecules were in clusters that had a radius below 100 nm, in agreement with the observation that arrestin2 is distributed throughout the cytoplasm in the absence of receptor stimulation (Fig. 1). These clusters can mainly be accounted for by the average degree of labeling (1.5) of the nanobodies, by the blinking characteristics of ATTO655 molecules which are detected several times during a typical dSTORM acquisition scheme, and by the experimental scheme which involves random (but not uniform) bleaching of fluorophores before actual acquisition during the step in which the concentration of fluorophores in their on-state is reduced. This apparent "self-clustering" therefore also reports on the localization accuracy obtained in the individual experiments, determined to 27 nm (Fig. S2) (Lando et al., 2012).

Upon stimulation of CCR5 with 5P12-RANTES, no major increase in the recruitment of arrestin2 was observed (12% of the

molecules). On the other hand, with 5P14-RANTES (27%) and RANTES (37%), we observed that a significant fraction of arrestin2 molecules were recruited into larger clusters, the fraction rising even to 87% with the strong agonist PSC-RANTES.

Further statistical analysis confirmed a global increase in cluster sizes upon stimulation with ligands that are able to induce CCR5 internalization (see Table 1), especially with PSC-RANTES, by a shift of the maximum of the Ripley function towards larger distances (Fig. 4). The Ripley function is a measure of the randomness of a spatial distribution, with positive values indicating that molecules are statistically closer to each other (clustered) than in a perfectly random sample. The observed broadening of the function with some ligands, again especially with PSC-RANTES, can be attributed to a more heterogeneous distribution of cluster sizes (Malkusch et al., 2013).

Interestingly, in many cells the spatial distribution of arrestin2 clusters did not appear to follow a random pattern (Fig. S3), but the clusters tended to arrange along lines resembling cytoskeletal structure such as microtubuli or the actin cytoskeleton known to be involved in GPCR internalization (Santini et al., 2002). Similar patterns can be observed in previous studies but have not been commented (Laporte et al., 2000; Santini et al., 2002). We therefore investigated the effect of the drugs nocodazole (Noc) and cytochalasin D (CytD), inhibitors of microtubule and actin polymerization, respectively. Cells were pre-treated with either of the drugs 30 min before incubation with 5P14-RANTES or PSC-RANTES and super-resolution images were recorded (Fig. S4) and analyzed according to the same procedure as described above (Fig. 5). Nocodazole had little effect by itself on the distribution of arrestin2 in the absence and in the presence of the chemokines, with a small increase in the fraction of arrestin2 molecules recruited into clusters being observed. On the other hand, with cytochalasin D, large clusters could be observed both with 5P14-RANTES and PSC-RANTES, but not in the absence of chemokine, and the majority of arrestin2 molecules were recruited into these large clusters. These observations suggest a role for the actin cytoskeleton dynamics in the formation of these clusters and in the initial steps of GPCR internalization.

#### 4. Discussion

We have introduced a general method to study arrestin2 clustering quantitatively and have exemplified it on a model GPCR using single-molecule localization-based super-resolution microscopy with a lateral localization precision of about 27 nm. We used the versatile approach of fluorophore-labeled nanobodies targeting GFP, which allow for high-density labeling of GFP-tagged proteins and super-resolution imaging (Ries et al., 2012). We found that the ligands RANTES, 5P14-RANTES, and PSC-RANTES induced arrestin2 clustering, whereas 5P12-RANTES, the only one in this study which is not able to internalize the receptor (Table 1) and to induce arrestin2 recruitment (Figs. 1 and 2), did not. The amount of cluster-



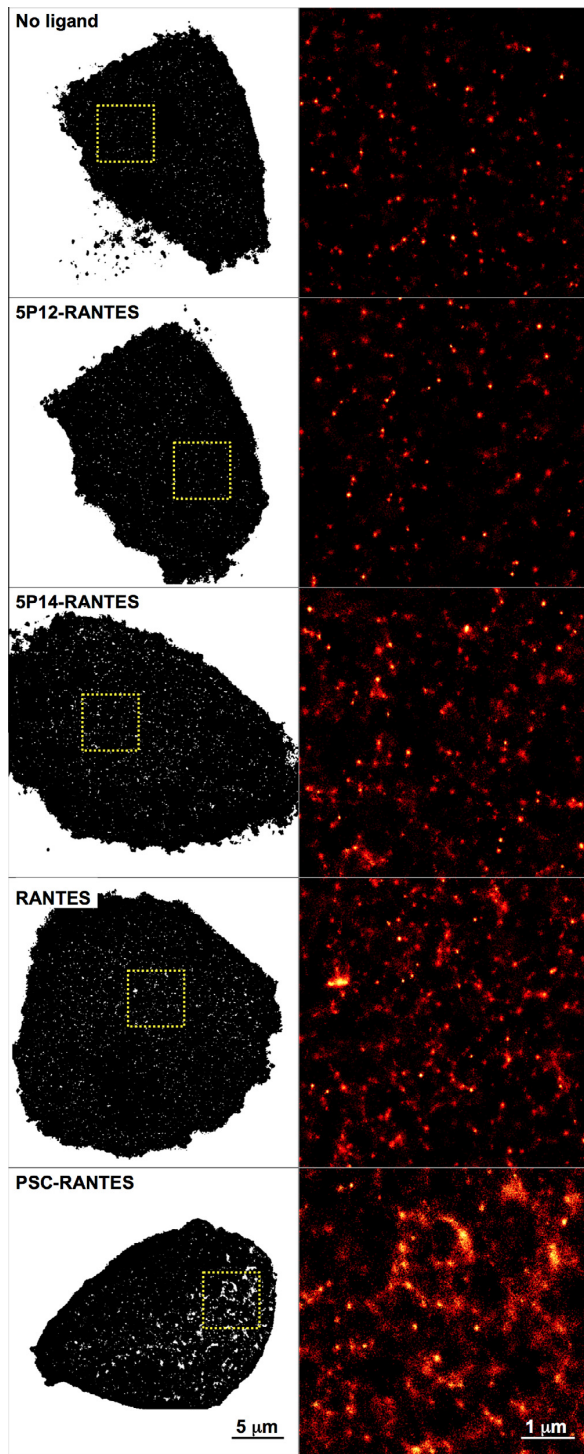


**Fig. 2.** (Left) Cluster maps obtained from the full dSTORM images. The yellow squares show the zoomed-in area displayed in the right part of the figure. Scale bar: 5  $\mu\text{m}$ . (Right) dSTORM images of arrestin2 in fixed CHO-CCR5 cells in the absence of ligand and after 90 min of treatment with different chemokine analogues. Scale bar: 1  $\mu\text{m}$ . (For interpretation of the references to colour in this figure legend, the reader is referred to the web version of this article.)

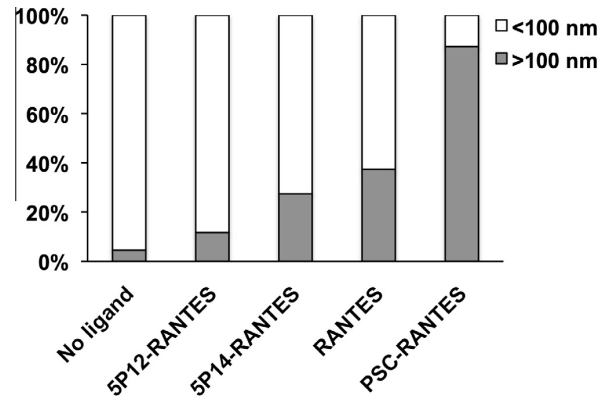


**Fig. 3.** Global morphological cluster analysis. Total fraction of arrestin2 molecules found in clusters with an area corresponding to a radius larger than 100 nm (grey bars) in untreated cells and in cells exposed to the different chemokine analogues.

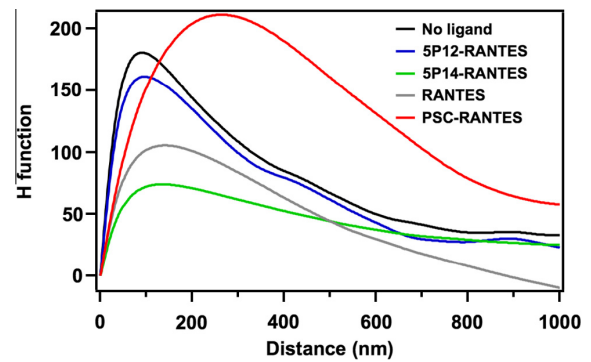


**Fig. 4.** All-distances analysis of arrestin2 clusters using Ripley's H function. The peak of each distribution is indicative of an average clustering size with its value lying between the average cluster radius and diameter (Malkusch, 2013).

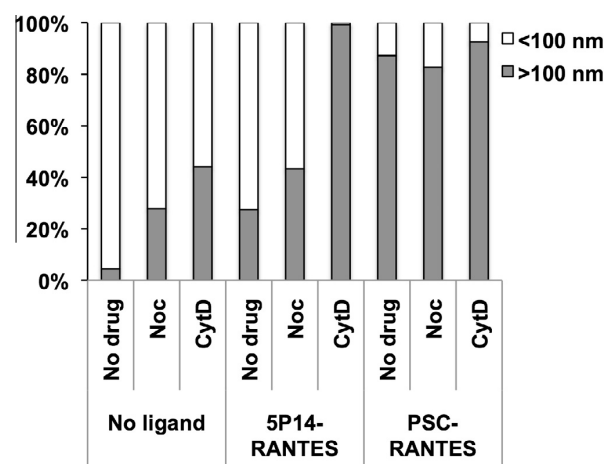


**Fig. 5.** Total fraction of arrestin2 molecules found in clusters with an area corresponding to a radius larger than 100 nm (grey bars) in untreated cells and in cells exposed to various combinations of drugs and chemokine analogues.

ing and the cluster size was further shown to increase with the capacity of the ligands to cause CCR5 internalization. We further observed even larger clusters and a high level of arrestin2 recruitment to those entities upon blocking actin polymerization with cytochalasin D, whereas disruption of the microtubules with nocodazole had little effect on the clustering.

Arrestins are known to interact with several endocytic elements such as clathrin, AP-2, or the N-ethylmaleimide-sensitive fusion protein (Lefkowitz and Shenoy, 2005). Furthermore, endocytic vesicles are transferred from coated pits to endosomes along actin filaments with the help of myosins (Spudich and Sivaramakrishnan, 2010). The high level of arrestin2 molecules found in large clusters upon blocking actin polymerization thus hints at the active role of actin in the formation and dynamics of arrestin2 clusters.

This work furthermore represents the first demonstration that 5P14-RANTES, a non-G protein-signaling ligand (Gaertner et al., 2008b), is able to induce arrestin2 recruitment by CCR5. Arrestin2 recruitment to CCR5 therefore seems to be independent of G protein activation, as it has been observed with other GPCRs (Reiter et al., 2012), and the clear correlation found between the amount of arrestin2 clustering and the capacity of the ligands to induce CCR5 internalization strongly suggests that arrestin2 recruitment is at the origin of the internalization of CCR5. Advanced microscopy techniques such as quantitative localization-based microscopy therefore seem promising in order to further help elucidate the unusual inhibitory mechanisms of RANTES analogues and the activation and desensitization mechanisms of GPCRs in general.

#### Acknowledgments

We are grateful to Jeffrey Benovic (Thomas Jefferson University) for the arrestin2-GFP plasmid. This work was supported by the Swiss National Science Foundation through Ambizione fellowship PZ00P3\_131935 (A.F.) and project number 310030\_143789 (O.H.), as well as by Dormeur Investment Service Ltd (O.H. and A.F.). M.H. acknowledges funding by the Bundesministerium für Bildung und Forschung (Grant Number 0315262) and the German Science Foundation (EXC 115).

#### Appendix A. Supplementary data

Supplementary data associated with this article can be found, in the online version, at <http://dx.doi.org/10.1016/j.jsb.2013.09.019>.

#### References

Cordes, T., Strackham, M., Stahl, S.W., Summerer, W., Steinhauer, C., Forthmann, C., Puchner, E.M., Vogelsang, J., Gaub, H.E., Tinnefeld, P., 2010. Resolving single-molecule assembled patterns with superresolution blink-microscopy. *Nano Lett.* 10, 645–651.

Endesfelder, U., Finan, K., Holden, S.J., Cook, P.R., Kapanidis, A.N., Heilemann, M., 2013. Multi-scale spatial organization of RNA polymerase in *Escherichia coli*. *Biophys. J.* 105, 172–181.

Escola, J.-M., Kuenzi, G., Gaertner, H., Foti, M., Hartley, O., 2010. CC chemokine receptor 5 (CCR5) desensitization – cycling receptors accumulate in the trans-Golgi network. *J. Biol. Chem.* 285, 41772–41780.

Fürstenberg, A., Heilemann, M., 2013. Single-molecule localization microscopy – near-molecular spatial resolution in light microscopy with photoswitchable fluorophores. *Phys. Chem. Chem. Phys.* 15, 14919–14930.

Gaertner, H., Lebeau, O., Borlat, I., Cerini, F., Dufour, B., Kuenzi, G., Melotti, A., Fish, R.J., Offord, R., Springael, J.Y., Parmentier, M., Hartley, O., 2008a. Highly potent HIV inhibition: engineering a key anti-HIV structure from PSC-RANTES into MIP-1 beta/CCL4. *Protein Eng. Des. Sel.* 21, 65–72.

Gaertner, H., Cerini, F., Escola, J.-M., Kuenzi, G., Melotti, A., Offord, R., Rossitto-Borlat, I., Nedellec, R., Salkowitz, J., Gorochov, G., Mosier, D., Hartley, O., 2008b. Highly potent, fully recombinant anti-HIV chemokines: reengineering a low-cost microbicide. *Proc. Natl. Acad. Sci. USA* 105, 17706–17711.

Hartley, O., Gaertner, H., Wilken, J., Thompson, D., Fish, R., Ramos, A., Pastore, C., Dufour, B., Cerini, F., Melotti, A., Heveker, N., Picard, L., Alizon, M., Mosier, D., Kent, S., Offord, R., 2004. Medicinal chemistry applied to a synthetic protein: development of highly potent HIV entry inhibitors. *Proc. Natl. Acad. Sci. USA* 101, 16460–16465.

Heilemann, M., van de Linde, S., Mukherjee, A., Sauer, M., 2009. Super-resolution imaging with small organic fluorophores. *Angew. Chem. Int. Ed.* 48, 6903–6908.

Kamiyama, D., Huang, B., 2012. Development in the STORM. *Dev. Cell* 23, 1103–1110.

Kenakin, T.P., 2009. Cellular assays as portals to seven-transmembrane receptor-based drug discovery. *Nat. Rev. Drug Discov.* 8, 617–626.

Kobilka, B.K., Deupi, X., 2007. Conformational complexity of G-protein-coupled receptors. *Trends Pharmacol. Sci.* 28, 397–406.

Lando, D., Endesfelder, U., Berger, H., Subramanian, L., Dunne, P.D., McColl, J., Klenerman, D., Carr, A.M., Sauer, M., Allshire, R.C., Heilemann, M., Laue, E.D., 2012. Quantitative single-molecule microscopy reveals that CENP-A(Cnp1) deposition occurs during G2 in fission yeast. *Open Biol.* 2, 120078.

Laporte, S.A., Oakley, R.H., Holt, J.A., Barak, L.S., Caron, M.G., 2000. The interaction of beta-arrestin with the AP-2 adaptor is required for the clustering of beta(2)-adrenergic receptor into clathrin-coated pits. *J. Biol. Chem.* 275, 23120–23126.

Lederman, M.M., Veazey, R.S., Offord, R., Mosier, D.E., Dufour, J., Mefford, M., Piatak Jr., M., Lifson, J.D., Salkowitz, J.R., Rodriguez, B., Blauvelt, A., Hartley, O., 2004. Prevention of vaginal SHIV transmission in rhesus macaques through inhibition of CCR5. *Science* 306, 485–487.

Lee, S.F., Vérolet, Q., Fürstenberg, A., 2013. Improved super-resolution microscopy with oxazine fluorophores in heavy water. *Angew. Chem. Int. Ed.* 52, 8948–8951.

Lefkowitz, R.J., Shenoy, S.K., 2005. Transduction of receptor signals by beta-arrestins. *Science* 308, 512–517.

Luttrell, L.M., Gesty-Palmer, D., 2010. Beyond desensitization: physiological relevance of arrestin-dependent signaling. *Pharmacol. Rev.* 62, 564.

Malkusch, S., Muranyi, W., Muller, B., Krausslich, H.G., Heilemann, M., 2013. Single-molecule coordinate-based analysis of the morphology of HIV-1 assembly sites with near-molecular spatial resolution. *Histochem. Cell Biol.* 139, 173–179.

Mennella, V., Keszthelyi, B., McDonald, K.L., Chhun, B., Kan, F., Rogers, G.C., Huang, B., Agard, D.A., 2012. Subdiffraction-resolution fluorescence microscopy reveals a domain of the centrosome critical for pericentriolar material organization. *Nat. Cell Biol.* 14, 1159–1168.

Moerner, W.E., 2012. Microscopy beyond the diffraction limit using actively controlled single molecules. *J. Microsc.* 246, 213–220.

Moore, C.A.C., Milano, S.K., Benovic, J.L., 2007. Regulation of receptor trafficking by GRKs and arrestins. *Annu. Rev. Physiol.* 69, 451–482.

Muranyi, W., Malkusch, S., Muller, B., Heilemann, M., Krausslich, H.G., 2013. Super-resolution microscopy reveals specific recruitment of HIV-1 envelope proteins to viral assembly sites dependent on the envelope C-terminal tail. *PLoS Pathog.* 9, e1003198.

Oakley, R.H., Laporte, S.K., Holt, J.A., Caron, M.G., Barak, L.S., 2000. Differential affinities of visual arrestin, beta arrestin1, and beta arrestin2 for G protein-coupled receptors delineate two major classes of receptors. *J. Biol. Chem.* 275, 17201–17210.

Peterson, P., 2009. F2PY: a tool for connecting Fortran and Python programs. *Int. J. Comput. Sci. Eng.* 4, 296–305.

Reiter, E., Ahn, S., Shukla, A.K., Lefkowitz, R.J., 2012. Molecular mechanism of beta-arrestin-biased agonism at seven-transmembrane receptors. *Annu. Rev. Pharmacol. Toxicol.* 52, 179–197.

Ries, J., Kaplan, C., Platonova, E., Eghlidi, H., Ewers, H., 2012. A simple, versatile method for GFP-based super-resolution microscopy via nanobodies. *Nat. Methods* 9, 582–584.

Ripley, B.D., 1977. Modelling spatial patterns. *J. R. Stat. Soc.* 39, 172–212.

Rosenbaum, D.M., Rasmussen, S.G.F., Kobilka, B.K., 2009. The structure and function of G-protein-coupled receptors. *Nature* 459, 356–363.

Santini, F., Gaidarov, I., Keen, J.H., 2002. G protein-coupled receptor/arrestin3 modulation of the endocytic machinery. *J. Cell Biol.* 156, 665–676.

Sengupta, P., Jovanovic-Taliman, T., Skoko, D., Renz, M., Veatch, S.L., Lippincott-Schwartz, J., 2011. Probing protein heterogeneity in the plasma membrane using PALM and pair correlation analysis. *Nat. Methods* 8, 969–975.

Spudich, J.A., Sivaramakrishnan, S., 2010. Myosin VI: an innovative motor that challenged the swinging lever arm hypothesis. *Nat. Rev. Mol. Cell Biol.* 11, 128–137.

van de Linde, S., Sauer, M., Heilemann, M., 2008. Subdiffraction-resolution fluorescence imaging of proteins in the mitochondrial inner membrane with photoswitchable fluorophores. *J. Struct. Biol.* 164, 250–254.

Williamson, D.J., Owen, D.M., Rossy, J., Magenau, A., Wehrmann, M., Gooding, J.J., Gaus, K., 2011. Pre-existing clusters of the adaptor lat do not participate in early T cell signaling events. *Nat. Immunol.* 12, 655–662.

Wolter, S., Schuttpelz, M., Tscherepanov, M., Van de Linde, S., Heilemann, M., Sauer, M., 2010. Real-time computation of subdiffraction-resolution fluorescence images. *J. Microsc.* 237, 12–22.

Zidar, D.A., 2011. Endogenous ligand bias by chemokines: implications at the front lines of infection and leukocyte trafficking. *Endocr. Metab. Immun. Disord. Drug Targets* 11, 120–131.

## Coordinate-based co-localization-mediated analysis of arrestin clustering upon stimulation of the C–C chemokine receptor 5 with RANTES/CCL5 analogues

Laura Tarancón Díez · Claudia Bönsch · Sebastian Malkusch · Zinnia Truan · Mihaela Munteanu · Mike Heilemann · Oliver Hartley · Ulrike Endesfelder · Alexandre Fürstenberg

Accepted: 25 February 2014  
© Springer-Verlag Berlin Heidelberg 2014

**Abstract** G protein-coupled receptor activation and desensitization leads to recruitment of arrestin proteins from cytosolic pools to the cell membrane where they form clusters difficult to characterize due to their small size and further mediate receptor internalization. We quantitatively investigated clustering of arrestin 3 induced by potent anti-HIV analogues of the chemokine RANTES after stimulation of the C–C chemokine receptor 5 using single-molecule localization-based super-resolution microscopy. We determined arrestin 3 cluster sizes and relative fractions of arrestin 3 molecules in each cluster through image-based analysis of the localization data by adapting a method originally developed for co-localization analysis from molecular coordinates. We found that only classical agonists in the set of tested ligands were able to efficiently recruit arrestin 3 to clusters mostly larger than 150 nm in size and compare our results with existing data on arrestin 2 clustering induced by the same chemokine analogues.

**Electronic supplementary material** The online version of this article (doi:10.1007/s00418-014-1206-1) contains supplementary material, which is available to authorized users.

L. Tarancón Díez · Z. Truan · A. Fürstenberg (✉)  
Department of Human Protein Sciences, University of Geneva,  
CMU, Rue Michel-Servet 1, 1211 Geneva 4, Switzerland  
e-mail: alexandre.fuerstenberg@unige.ch

C. Bönsch · M. Munteanu · O. Hartley  
Department of Pathology and Immunology,  
University of Geneva, CMU, Rue Michel-Servet 1,  
1211 Geneva 4, Switzerland

S. Malkusch · M. Heilemann · U. Endesfelder  
Institute for Physical and Theoretical Chemistry,  
Goethe-University Frankfurt, Max-von-Laue-Str. 7,  
60438 Frankfurt, Germany

**Keywords** Clustering · Super-resolution microscopy · Single-molecule localization microscopy · G protein-coupled receptors · Arrestin · CCR5

### Introduction

G protein-coupled receptors (GPCRs) are membrane proteins that mediate a wide range of chemical signals across the cell membrane and thereby control important physiological processes. Not surprisingly, they have therefore been major drug targets (Rask-Andersen et al. 2011). Activation of a GPCR through agonist binding (ions, small molecules, hormones,...) induces dissociation of its cytosolic G protein, leading to downstream second messenger signalling (Rosenbaum et al. 2009). In parallel, arrestin proteins are recruited from cytosolic pools (Lefkowitz and Shenoy 2005). They arrest coupling between G proteins and their receptor and, independently of G protein signalling, also induce clathrin-mediated endocytosis as part of a desensitization process common to GPCRs (Moore et al. 2007). Not all agonists trigger, however, the full signalling repertoire of GPCRs and there are now numerous examples of ligands that bias the receptor response either towards G protein coupling or towards non-G protein effectors such as arrestins (Gesty-Palmer and Luttrell 2011). This ability of different ligands binding to the same GPCR to trigger various pharmacological outcomes is related to the diversity of conformational states in which GPCRs exist (Kobilka and Deupi 2007; Bockenhauer et al. 2011) and has become an attractive feature for drug discovery (Kenakin and Christopoulos 2013).

The C–C chemokine receptor 5 (CCR5) is a prototypical GPCR for which the existence of biased ligands has been suggested (Zidar 2011; Kenakin et al. 2012).

**Table 1** Functional characterization of RANTES (Hartley et al. 2004; Gaertner et al. 2008b) and of some of its analogues (Gaertner et al. 2008a)

Ligand	Anti-HIV potency	G protein signalling (%)	CCR5 internalization (%)
RANTES	~1 $\mu$ M	50	64
PSC-RANTES	25 pM	100	100
6P4-RANTES	21 pM	88	93
5P12-RANTES	28 pM	<5	3
5P14-RANTES	26 pM	<5	47

G protein signalling activity (release of  $\text{Ca}^{2+}$ ) and CCR5 internalization are expressed relatively to PSC-RANTES, which displays maximal response in these assays

It is further an important drug target by being the major co-receptor used by HIV to infect target cells, and it can be efficiently blocked to prevent person-to-person virus transmission (Kuhmann and Hartley 2008; Karim et al. 2010). Analogues of the natural CCR5 ligand RANTES were previously shown to efficiently prevent HIV infection (Lederman et al. 2004; Hartley et al. 2004; Gaertner et al. 2008a). Interestingly, however, the pharmacological profiles of these ligands differing by only a few amino acids among the first 9 of 68 residues (Table S1) display large variations (Table 1). Molecules such as RANTES, 6P4-RANTES, or PSC-RANTES act like classical partial or full agonists by causing both strong G protein activation and CCR5 internalization. The increased anti-HIV potency of PSC-RANTES over RANTES has been ascribed to additional long-term sequestration of CCR5 inside target cells (Escola et al. 2010). On the other hand, analogues such as 5P12-RANTES and 5P14-RANTES display the same anti-HIV activity as PSC-RANTES or 6P4-RANTES but do not trigger G protein signalling and induce CCR5 internalization only partially (5P14-RANTES) or not at all (5P12-RANTES). It is currently not understood how these chemokine analogues all potently block HIV infection despite their very different pharmacological profiles, but stabilization of CCR5 into various conformational ensembles is likely involved. We recently characterized the effect of some of these ligands on arrestin 2 recruitment upon stimulation of CCR5 to test whether arrestin 2 mobilization could relate to their pharmacology and found that only those ligands capable of recruiting arrestin 2 also induced receptor internalization (Truan et al. 2013).

Among the arrestin protein family, both arrestin 2 and arrestin 3 are ubiquitously expressed. These proteins interact with most GPCRs and cluster around clathrin-coated pits upon GPCR stimulation (Santini et al. 2002; Laporte et al. 2000; Luttrell et al. 1999). It has, however, traditionally been difficult to study the formation, the dimension, or the fate of such clusters by standard imaging procedures because of their size near or below the diffraction limit. Standard techniques applied to obtain information on

biomolecular interactions such as Förster resonance energy transfer (FRET) or two-colour co-localization of differently labelled molecules by fluorescence microscopy indeed suffer from a spatial resolution limited to typically ~200 nm because of the wave-like nature of visible light. The recent introduction of super-resolution microscopy techniques has enabled to overcome this limit (Rust et al. 2006; Betzig et al. 2006; Hess et al. 2006; Hell 2007) and opened up new avenues to resolve small objects and monitor protein–protein interaction scales closer to the molecular resolution. Super-resolution methods based on the localization of single molecules (Fürstenberg and Heilemann 2013; Moerner 2012) have the advantage of providing not only an image (which means pixels with an intensity information) but also molecular coordinates that can be directly used in novel schemes for co-localization and clustering analysis (Sengupta et al. 2011; Malkusch et al. 2012; Owen et al. 2013; Truan et al. 2013; Endesfelder et al. 2013; Specht et al. 2013).

Clustering and oligomerization are frequent types of functionally relevant protein–protein interaction in which two or several proteins of the same kind interact together. From an analysis point of view, they are, however, only a particular case of molecular entities interacting together, so that existing co-localization analysis methods based on molecular coordinates can readily be adapted to monitor clustering processes. We present here a simple modification to a recently introduced coordinate-based co-localization (CBC) analysis method (Malkusch et al. 2012) that enables to evaluate the spatial distribution of a protein recorded in a single channel and provides a physical basis for setting a threshold in image-based cluster analysis. We apply CBC-mediated cluster analysis to evaluate the dimension of arrestin 3 clusters upon stimulation of CCR5 by RANTES analogues in order to test the hypothesis that these ligands induce differential arrestin 3 recruitment and relate this observation to their pharmacological profile. We further compare our results with recently obtained information on arrestin 2 mobilization by a similar set of ligands (Truan et al. 2013) and find that most ligands causing arrestin 2



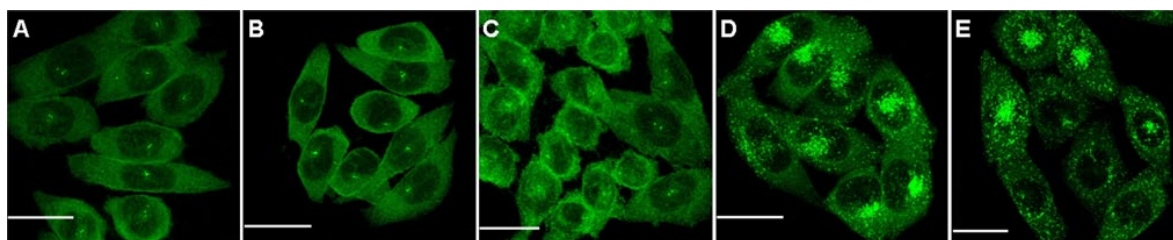


**Fig. 1** Confocal microscopy images (maximum intensity projection) of arrestin 3-GFP in fixed CHO-CCR5 cells in the absence of ligand (**a**) or after 90 min of stimulation with 5P12-RANTES (**b**), 5P14-RANTES (**c**), RANTES (**d**), or PSC-RANTES (**e**). Scale bar 20  $\mu\text{m}$

clustering also cause arrestin 3 clustering, except 5P14-RANTES. This compound might thereby represent the first example of a ligand inducing recruitment of selectively one type of arrestin upon stimulation of CCR5.

## Materials and methods

### Materials, cell lines, and cell culture

All cell culture reagents were obtained from Life Technologies. Water was purified using a Milli-Q system (Millipore). RANTES and its analogues were prepared by total chemical synthesis as previously published (Gaertner et al. 2008a).

Plasmids pEGFP-N1 with bovine arrestin 3 (Mundell et al. 2000) were a gift from Jeffrey Benovic (Thomas Jefferson University). Chinese hamster ovary cells stably expressing CCR5 (hereafter CHO-CCR5) (Hartley et al. 2004) were transfected with 0.5  $\mu\text{g}$  arrestin 3-GFP plasmid, and stable clones were obtained as described before (Truan et al. 2013).

Cells were cultured at 37  $^{\circ}\text{C}$  with 5 %  $\text{CO}_2$  in phenol-red free RPMI supplemented with 10 % foetal bovine serum, 100 units/ml penicillin, and 100  $\mu\text{g}/\text{ml}$  streptomycin. For super-resolution experiments, they were plated 36–72 h beforehand on glass-bottom petri dishes (FluoroDish<sup>TM</sup>, World Precision Instruments, Inc.) coated with fibronectin (Calbiochem).

### Immunofluorescence

Samples for confocal microscopy and for super-resolution imaging were prepared by fixation in 4 % paraformaldehyde as previously described (Truan et al. 2013). For super-resolution imaging, samples were further stained with a GFP-specific ATTO655-labelled GFP-Trap<sup>®</sup> nanobody (ChromoTek) (Truan et al. 2013). When desired, samples were treated with 100 nM chemokine analogues in full medium 90 min before fixation.

### Confocal microscopy

Stacks of confocal microscopy images were recorded on a Zeiss LSM700 microscope with an X63/1.4NA Plan Apochromat oil-immersion objective. Excitation was performed with the 488 nm line of an Ar/Kr laser, and GFP filters were used for detection. Maximum intensity projections as displayed in Fig. 1 were obtained using the ZEN 2011 software.

### Super-resolution microscopy

Super-resolution experiments were performed on a wide-field epi-fluorescence microscope (Truan et al. 2013) with the *d*STORM (direct stochastic optical reconstruction microscopy) technique (Heilemann et al. 2009) using 640 nm excitation ( $\sim 3 \text{ kW}/\text{cm}^2$ , Coherent Cube 640-100-C laser). Blinking of ATTO655 was induced with a 50  $\mu\text{M}$  solution of ascorbic acid (Merck) (Cordes et al. 2010) in heavy water ( $\text{D}_2\text{O}$ , 99.8 % D-atom content, Armar Chemicals) (Lee et al. 2013) prepared from a 1-mM stock solution in  $\text{H}_2\text{O}$ . Single emitters were localized, and super-resolution images (10  $\times$  10  $\text{nm}^2$  per pixel) were reconstructed with the *rapid*STORM software (version 2.13) (Wolter et al. 2010). Each pixel on the EMCCD camera (Andor iXonEM+ DU8987) corresponded to a 109  $\times$  109  $\text{nm}^2$  area in the sample plane.

### Cluster analysis

Ripley's H-function (normalized form of the K-function) (Ripley 1977) was calculated as previously described (Truan et al. 2013) for 5  $\times$  5  $\mu\text{m}^2$  regions of interest using a self-written MATLAB (The MathWorks, Inc.) routine, and edge effects were taken into account by omitting molecules closer than 1  $\mu\text{m}$  from the edge of the region of interest in the calculations.

Coordinate-based co-localization (CBC)-mediated cluster analysis was performed using an algorithm described elsewhere (Malkusch et al. 2012). Because the algorithm



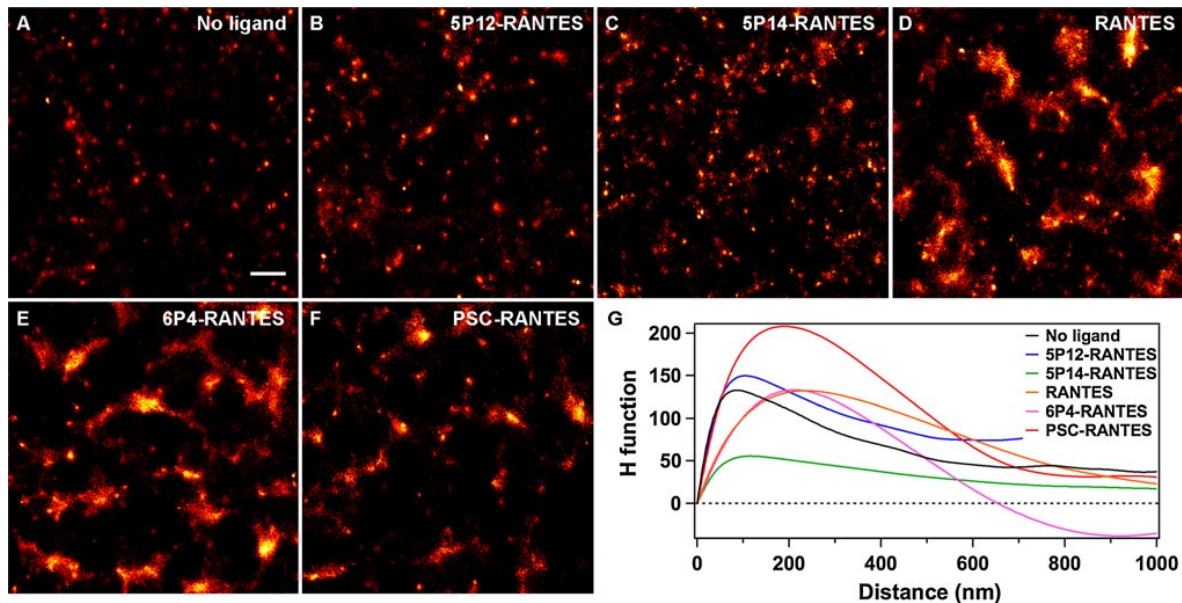


**Fig. 2** Representative super-resolution images of ATTO655-nanobody-labelled arrestin 3-GFP in fixed CHO-CCR5 in the absence of ligand (a) and after treatment with different chemokine analogues for 90 min (b–f). Scale bar 0.5  $\mu\text{m}$ . g Ripley analysis of the *d*STORM

experiments demonstrating clustering of arrestin 3 upon stimulation of CCR5 with RANTES, 6P4-RANTES, and PSC-RANTES, but not with 5P12-RANTES or 5P14-RANTES. The peak position is indicative of the typical cluster size

was originally written to determine co-localization of two molecules, it requires data from two channels as an input. Our data was, however, recorded in a single channel since our goal was to measure clustering of a single species. We therefore performed pre-sorting of the detected arrestin 3 molecules into molecules that were localized in odd frames and molecules that were localized in even frames, resulting in two localization files that both contain information about the distribution of the same molecules within the range of the localization accuracy (Banterle et al. 2013; Nieuwenhuizen et al. 2013). By correlating the circular distributions of the arrestin 3 molecule, localizations from both localization lists around a single arrestin 3 molecule with each other (Malkusch et al. 2012), a clustering value characterizing the degree of clustering could be determined for every localization. This parameter can vary between  $-1$  and  $1$ , a value of  $1$  indicating the highest probability of clustering.

Localizations with clustering values above  $0.7$  were kept for morphological cluster analysis (custom-written software), which was performed by applying a  $15\text{-nm}$  Gaussian filter and a binary mask to the filtered data. Cluster sizes were extracted from cohesive regions in the mask, and the area of every cluster was further weighted by the integrated fluorescence intensities within every cluster to determine the fraction of arrestin 3 molecules per cluster. Cluster radii were calculated from spheres coextensive to the measured clusters.

## Results

In order to visualize arrestin 3, we stably transfected CHO cells expressing CCR5 with a plasmid for arrestin 3 carrying a GFP fusion tag (Mundell et al. 2000). Like arrestin 2, arrestin 3 proteins are randomly distributed in the cytoplasm of resting cells (Fig. 1a). The distribution did not change when cells were exposed to a saturating concentration of 5P12-RANTES or of 5P14-RANTES (Fig. 1b, c). However, upon CCR5 stimulation with the agonists RANTES and PSC-RANTES (Fig. 1d, e), arrestin 3 molecules were recruited from the cytosolic pool to the plasma membrane where they formed clusters (Laporte et al. 2000) with dimensions around the diffraction limit, making it difficult to investigate their morphology in a robust way by classical microscopy techniques.

We, thus, turned to super-resolution microscopy so as to quantify the magnitude of arrestin 3 recruitment by determining the size of these clusters and the relative number of arrestin 3 molecules within each cluster, using an approach that we recently successfully applied to the investigation of arrestin 2 clustering and that relies on dye-labelled nanobodies selective for GFP (Truan et al. 2013; Ries et al. 2012). Super-resolution images of arrestin 3 were obtained in untreated cells and in cells exposed to the different chemokine analogues (Fig. 2a–f, Fig. S1). Images of cells treated with no ligand, with 5P12-RANTES, or

with 5P14-RANTES display mainly individual proteins and small clusters, whereas much larger clusters are frequently visualized in cells stimulated with RANTES, 6P4-RANTES, or PSC-RANTES. In order to quantify clustering, we calculated Ripley's H-function from the single-molecule coordinates obtained in the super-resolution experiment (Fig. 2g). This function is a straightforward way of characterizing the randomness of a spatial distribution. Positive values indicate that molecules are closer to each other than if they were homogeneously distributed, which denotes clustering, and the value at which the function peaks is indicative of the average cluster size (its value is comprised between the average cluster radius and diameter). Displacement of the peak to larger values with RANTES, 6P4-RANTES, and PSC-RANTES compared with untreated cells, but not with 5P12-RANTES or 5P14-RANTES, confirmed that the former 3 ligands selectively induce strong arrestin 3 clustering.

We next aimed at quantifying the dimensions of arrestin 3 clusters by image-based analysis of the super-resolution data (Malkusch et al. 2013; Endesfelder et al. 2013; Truan et al. 2013). The goal of such analysis is to generate from each super-resolution image a binary cluster map in which every cohesive region represents a cluster whose size can then be determined by integration. Creating a binary map from a super-resolution image, which contains intensity information, requires, however, the application of an intensity threshold to the *d*STORM image to define cluster boundaries. In order to identify which localizations are part of a cluster based on a clustering parameter that can be calculated, we adapted an algorithm originally developed to assess co-localization from single-molecule coordinates (Malkusch et al. 2012), considering that clustering is only a special case of co-localization in which all the information is collected in a single colour channel instead of two. Our coordinate-based co-localization (CBC)-mediated clustering algorithm (Fig. 3a) splits the list of coordinates obtained from a *d*STORM experiment (which is also used to reconstruct super-resolution images such as in Fig. 3b, c) into two, as if the data had been recorded in two channels, and calculates a clustering value for every localization, which takes into account its direct neighbourhood (for details, see "Materials and methods" section). This clustering value can vary from  $-1$  for anti-correlated distributions through  $0$  for uncorrelated distributions up to  $1$  for perfectly correlated distributions, which would indicate a high probability of clustering. It was previously shown for co-localization analysis that overlaying two identical images with a translational shift of  $10$  nm results in the largest fraction of the distribution of co-localization values (analogous to the clustering values here) being above  $0.7$  (Malkusch et al. 2012). Given the typical localization precision in our super-resolution experiments of about  $20$  nm,

we used a minimal clustering value of  $0.7$  as a threshold to consider a localization as being part of a cluster and filtered out localizations with a clustering value below this threshold. CBC-mediated clustering images (Fig. 3d, e, Fig. S2) in which localizations with a clustering value above threshold are displayed in green and those below threshold in red show that rejected localizations mostly either form a cloud-like pattern throughout the cell indicative of single or spurious localizations or can be found at the edges of higher intensity clustered areas, thereby defining the border of clusters.

After application of the CBC-mediated clustering filter to all images, cluster maps were extracted (Fig. 3f, g, Fig. S3) by applying a  $15$ -nm Gaussian blur filter, reflecting the finite experimental localization precision (for this reason, the clusters in the binary map, Fig. 3g, appear slightly larger than in the filtered image, Fig. 3e) (Smith et al. 2010). The area of each cohesive region was then calculated and weighted by its integrated fluorescence intensity to gain information on relative arrestin 3 molecule numbers per cluster. Figure 4 shows for each chemokine analogue the fraction of arrestin 3 as a function of cluster size. Cluster radii were calculated from spheres coextensive to the measured cluster area. In untreated cells, most arrestin 3 molecules were found in domains with a radius smaller than  $120$  nm, and no significant change was noticed when cells were exposed to either 5P12-RANTES or 5P14-RANTES, in agreement with the confocal microscopy observations (Fig. 1). The fact that clusters, albeit of small size, are observed for these three conditions for which one could expect to find arrestin 3 homogeneously distributed throughout the cytoplasm can be ascribed to an average number of fluorophores per nanobody higher than one ( $1.5$ ), to multiple detection of the same molecules due to fluorophore blinking, and to the experimental scheme requiring fluorophores to be first put into a dark state at the beginning of the experiment, inevitably leading to random but non-uniform photobleaching of dye molecules before the start of the acquisition. Similar observations were previously made with arrestin 2 (Truan et al. 2013). On the other hand, upon treatment of the cells with the agonists RANTES, 6P4-RANTES, or PSC-RANTES, the largest fraction of arrestin 3 molecules was found in clusters with a radius larger than  $150$  nm, confirming that these ligands that are all classical agonists (that is, they cause G protein activation) lead to strong clustering of arrestin 3 via CCR5.

## Discussion

We have quantitatively investigated the recruitment of arrestin 3 to CCR5 using single-molecule localization microscopy and morphological cluster analysis after

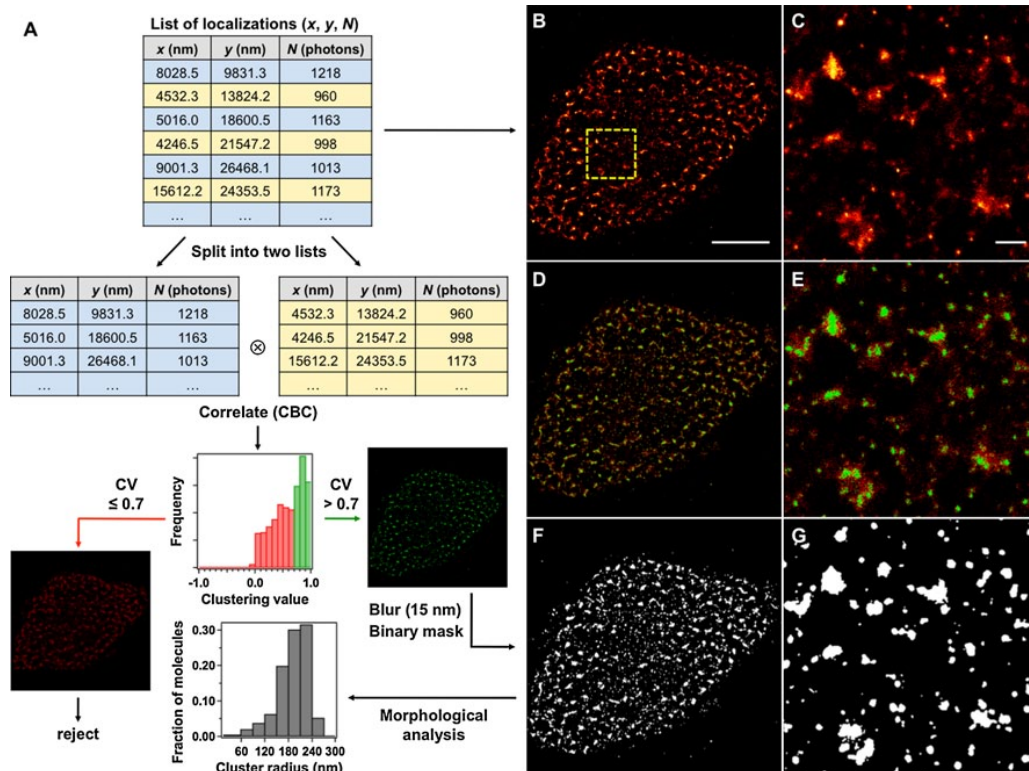
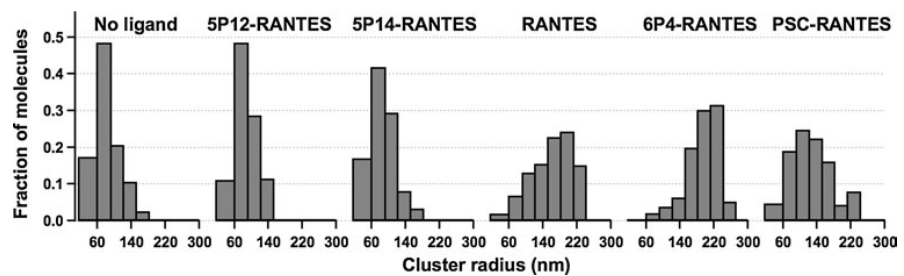


**Fig. 3** a Flow chart of CBC-mediated cluster analysis. In CBC-mediated cluster analysis, the table of localizations from the *d*STORM experiment, which is used to reconstruct super-resolution images **b**, **c** is split into two equally long tables of coordinates. A clustering value (CV) is calculated for every localization. Localizations with a clustering value below a 0.7 threshold are discarded. The others are kept to reconstruct a CBC-mediated clustering filtered image which is then blurred with a Gaussian filter to take into account the finite localization precision of the experiment. The resulting binary image (**f**, **g**)

undergoes morphological analysis for cluster sizes and relative molecule numbers from every cluster to be extracted. **b**, **c** Super-resolution images of a cell exposed to 6P4-RANTES. **d**, **e** CBC-mediated clustering filtered images in which every localization with a clustering value below threshold is displayed in *red* and with a clustering value above threshold in *green*. **f**, **g** Binary cluster maps extracted from the blurred CBC-mediated clustering filtered images. The *yellow box* in **b** represents the area blown up in **c**, **e**, and **g**. Scale bar 5  $\mu\text{m}$  in **b**, **d**, **f**; 0.5  $\mu\text{m}$  in **c**, **e**, **g**

**Fig. 4** Distribution of arrestin 3 molecules as a function of cluster size determined from CBC-mediated morphological cluster analysis



stimulation of the receptor with different chemokine analogues. We observed that a saturating concentration of the ligands RANTES, 6P4-RANTES, and PSC-RANTES, which induce both G protein signalling and lead to receptor internalization, induced strong arrestin 3 clustering (Figs. 1, 2), whereas no arrestin 3 recruitment above

background level was observed with 5P12-RANTES and 5P14-RANTES, two ligands that do not activate the G protein and induce no or only partial receptor internalization (Table 1). In order to extract quantitative information from the super-resolution experiments, we introduced a coordinate-based clustering filter derived from a coordinate-based

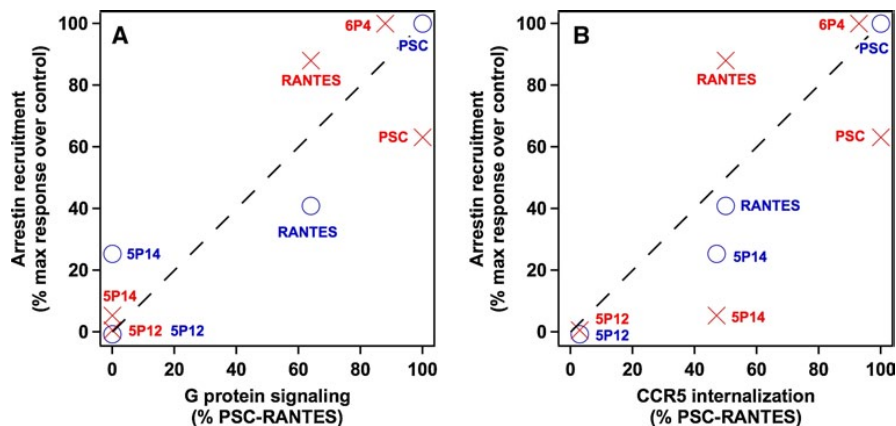


**Fig. 5** Relative arrestin 2 (blue) and arrestin 3 (red) recruitment versus CCR5 internalization (a) or G protein signalling efficiency (b) for the different chemokine analogues. The magnitude of arrestin recruitment was calculated by comparing the fraction of arrestin 3 molecules found in clusters larger than 100 nm (Truan et al. 2013) compared with the control level (0 %), which is defined by observations

in untreated cells. Arrestin 2 data were taken from (Truan et al. 2013) and reanalyzed with the CBC-mediated cluster analysis for proper quantitative comparison (differences for the values obtained by CBC-mediated cluster analysis to the originally published values lie within experimental errors and thus revalidate the visually set threshold values used before)

co-localization analysis method (Malkusch et al. 2012). It enables to sort localizations based on a calculated clustering value that takes into account the spatial distribution around every localization and that can be used as a threshold for image-based cluster analysis (Fig. 3) instead of relying on a visually set manual threshold. We successfully applied this filter to the determination of arrestin 3 cluster sizes and arrestin 3 distribution within these clusters. In agreement with qualitative observations, we found that the largest fraction of arrestin 3 molecules was recruited to domains with a radius of 150 nm or larger with RANTES, 6P4-RANTES, and PSC-RANTES, whereas the distribution stayed unaltered with 5P12-RANTES and 5P14-RANTES compared with cells not exposed to chemokine analogues for which the domains are mostly smaller than 120 nm in radius (Fig. 4).

The finding that, within the tested set of ligands, only classical agonists induce arrestin 3 clustering might suggest a link between arrestin 3 recruitment and G protein activation. The magnitude of arrestin 3 recruitment, calculated as the fraction of molecules found in clusters larger than 100 nm relatively to the control experiment (no ligand) and the maximal response (here 6P4-RANTES), indeed correlates well with the relative magnitude of G protein signalling (Fig. 5a, red crosses). This conclusion differs from our recent observations on ligand-induced arrestin 2 clustering (Truan et al. 2013), where a connection between arrestin 2 clustering and CCR5 internalization had been established (Fig. 5b, blue circles). Arrestin 2 and arrestin 3 have been found to be interchangeable with respect to their function in many instances, in particular regarding receptor

desensitization and internalization (Pierce and Lefkowitz 2001). In the case of CCR5, Aramori et al. (1997) demonstrated that both arrestin 2 and arrestin 3 are sufficient (in conjunction with G protein-coupled receptor kinases) for the chemokine agonist MIP-1 $\beta$ /CCL4 to induce CCR5 internalization, with arrestin 3 being slightly more efficient than arrestin 2. Functional differences between the two homologues depending on some particular GPCR have, however, also been described (Pierce and Lefkowitz 2001). Arrestin 3 has, for example, been shown to induce  $\beta_2$ -adrenergic receptor internalization upon binding of the full agonist isoproterenol 100 times more efficiently than arrestin 2 (Kohout et al. 2001).

With CCR5 and the tested set of ligands, differences in the relative magnitude of arrestin 2 and arrestin 3 recruitment are actually minor but for one case: RANTES and PSC-RANTES, which induce strong arrestin 2 clustering, also lead to strong arrestin 3 clustering, and 5P12-RANTES does not cause mobilization of either of them; 5P14-RANTES, however, appears capable of mediating selectively clustering of arrestin 2, not of arrestin 3. One caveat to this observation is the background clustering detected in our assay (cells not exposed to any ligand), and one cannot totally exclude that 5P14-RANTES elicits an arrestin 3 response, which is too weak to be measured. This background level is, however, not significantly different from what was observed with arrestin 2 (Truan et al. 2013). 5P14-RANTES might, therefore, represent the first CCR5 ligand that is biased for one arrestin over another or G proteins, which would only hint again (Gaertner et al. 2008a; Truan et al. 2013) to the ability of this molecule to stabilize



a very special set of CCR5 conformations in comparison with other ligands. Biochemical experiments or other biophysical assays based on the bioluminescence resonance energy transfer (BRET) technology (Bertrand et al. 2002) might be able to provide a more definitive answer to this question in the future.

**Acknowledgments** We thank Jeffrey Benovic (Thomas Jefferson University) for the arrestin 3-GFP plasmid. This work was supported by the Swiss National Science Foundation through *Ambizione* fellowship PZ00P3\_131935 (A.F.) and project number 310030\_143789 (O.H.), as well as by Fondation Dormeur (O.H. and A.F.). M.H. acknowledges funding by the Bundesministerium für Bildung und Forschung (Grant Number 0315262) and the German Science Foundation (EXC 115).

## References

- Aramori I, Zhang J, Ferguson SSG, Bieniasz PD, Cullen BR, Caron MG (1997) Molecular mechanism of desensitization of the chemokine receptor CCR-5: receptor signaling and internalization are dissociable from its role as an HIV-1 co-receptor. *EMBO J* 16(15):4606–4616
- Banterle N, Khanh Huy B, Lemke EA, Beck M (2013) Fourier ring correlation as a resolution criterion for super-resolution microscopy. *J Struct Biol* 183(3):363–367
- Bertrand L, Parent S, Caron M, Legault M, Joly E, Angers S, Bouvier M, Brown M, Houle B, Menard L (2002) The BRET2/arrestin assay in stable recombinant cells: a platform to screen for compounds that interact with G protein-coupled receptors (GPCRs). *J Recept Signal Transduct Res* 22(1–4):533–541
- Betzig E, Patterson GH, Sougrat R, Lindwasser OW, Olenych S, Bonifacino JS, Davidson MW, Lippincott-Schwartz J, Hess HF (2006) Imaging intracellular fluorescent proteins at nanometer resolution. *Science* 313(5793):1642–1645
- Bockenbauer S, Fürstenberg A, Yao XJ, Kobilka BK, Moerner WE (2011) Conformational dynamics of single G protein-coupled receptors in solution. *J Phys Chem B* 115(45):13328–13338
- Cordes T, Strackharn M, Stahl SW, Summerer W, Steinhauer C, Forthmann C, Puchner EM, Vogelsang J, Gaub HE, Tinnefeld P (2010) Resolving single-molecule assembled patterns with super-resolution blink-microscopy. *Nano Lett* 10(2):645–651
- Endesfelder U, Finan K, Holden SJ, Cook PR, Kapanidis AN, Heilemann M (2013) Multi-scale spatial organization of RNA polymerase in *Escherichia coli*. *Biophys J* 105(1):172–181
- Escola J-M, Kuenzi G, Gaertner H, Foti M, Hartley O (2010) CC chemokine receptor 5 (CCR5) desensitization—cycling receptors accumulate in the trans-golgi network. *J Biol Chem* 285(53):41772–41780
- Fürstenberg A, Heilemann M (2013) Single-molecule localization microscopy—near-molecular spatial resolution in light microscopy with photoswitchable fluorophores. *Phys Chem Chem Phys* 15(36):14919–14930
- Gaertner H, Cerini F, Escola J-M, Kuenzi G, Melotti A, Offord R, Rossitto-Borlat I, Nedellec R, Salkowitz J, Gorochoy G, Mosier D, Hartley O (2008a) Highly potent, fully recombinant anti-HIV chemokines: reengineering a low-cost microbicide. *Proc Natl Acad Sci USA* 105(46):17706–17711
- Gaertner H, Lebeau O, Borlat I, Cerini F, Dufour B, Kuenzi G, Melotti A, Fish RJ, Offord R, Springael JY, Parmentier M, Hartley O (2008b) Highly potent HIV inhibition: engineering a key anti-HIV structure from PSC-RANTES into MIP-1 beta/CCL4. *Protein Eng Des Sel* 21(2):65–72
- Gesty-Palmer D, Luttrell LM (2011) Refining efficacy: exploiting functional selectivity for drug discovery. *Adv Pharmacol* 62:79–107
- Hartley O, Gaertner H, Wilken J, Thompson D, Fish R, Ramos A, Pastore C, Dufour B, Cerini F, Melotti A, Heveker N, Picard L, Alizon M, Mosier D, Kent S, Offord R (2004) Medicinal chemistry applied to a synthetic protein: development of highly potent HIV entry inhibitors. *Proc Natl Acad Sci USA* 101(47):16460–16465
- Heilemann M, van de Linde S, Mukherjee A, Sauer M (2009) Super-resolution imaging with small organic fluorophores. *Angew Chem Int Ed* 48(37):6903–6908
- Hell SW (2007) Far-field optical nanoscopy. *Science* 316(5828):1153–1158
- Hess ST, Girirajan TPK, Mason MD (2006) Ultra-high resolution imaging by fluorescence photoactivation localization microscopy. *Biophys J* 91(11):4258–4272
- Karim QA, Karim SSA, Frohlich JA, Grobler AC, Baxter C, Mansoor LE, Kharsany ABM, Sibeko S, Mlisana KP, Omar Z, Gengiah TN, Maarschalk S, Arulappan N, Mlotshwa M, Morris L, Taylor D, Grp CT (2010) Effectiveness and safety of tenofovir gel, an antiretroviral microbicide, for the prevention of HIV infection in women. *Science* 329(5996):1168–1174
- Kenakin T, Christopoulos A (2013) Signalling bias in new drug discovery: detection, quantification and therapeutic impact. *Nat Rev Drug Discov* 12(3):205–216
- Kenakin T, Watson C, Muniz-Medina V, Christopoulos A, Novick S (2012) A simple method for quantifying functional selectivity and agonist bias. *ACS Chem Neurosci* 3(3):193–203
- Kobilka BK, Deupi X (2007) Conformational complexity of G-protein-coupled receptors. *Trends Pharmacol Sci* 28(8):397–406
- Kohout TA, Lin FT, Perry SJ, Conner DA, Lefkowitz RJ (2001) Beta-arrestin 1 and 2 differentially regulate heptahelical receptor signaling and trafficking. *Proc Natl Acad Sci USA* 98(4):1601–1606
- Kuhmann SE, Hartley O (2008) Targeting chemokine receptors in HIV: A status report. *Annu Rev Pharmacol Toxicol* 48:425–461
- Laporte SA, Oakley RH, Holt JA, Barak LS, Caron MG (2000) The interaction of beta-arrestin with the AP-2 adaptor is required for the clustering of beta(2)-adrenergic receptor into clathrin-coated pits. *J Biol Chem* 275(30):23120–23126
- Lederman MM, Veazey RS, Offord R, Mosier DE, Dufour J, Mefford M, Piatak M Jr, Lifson JD, Salkowitz JR, Rodriguez B, Blauevelt A, Hartley O (2004) Prevention of vaginal SHIV transmission in rhesus macaques through inhibition of CCR5. *Science* 306(5695):485–487
- Lee SF, Vérolet Q, Fürstenberg A (2013) Improved super-resolution microscopy with oxazine fluorophores in heavy water. *Angew Chem Int Ed Engl* 52(34):8948–8951
- Lefkowitz RJ, Shenoy SK (2005) Transduction of receptor signals by beta-arrestins. *Science* 308(5721):512–517
- Luttrell LM, Ferguson SSG, Daaka Y, Miller WE, Maudsley S, Della Rocca GJ, Lin FT, Kawakatsu H, Owada K, Luttrell DK, Caron MG, Lefkowitz RJ (1999) Beta-arrestin-dependent formation of beta(2) adrenergic receptor Src protein kinase complexes. *Science* 283(5402):655–661
- Malkusch S, Endesfelder U, Mondry J, Gelleri M, Verwee PJ, Heilemann M (2012) Coordinate-based colocalization analysis of single-molecule localization microscopy data. *Histochem Cell Biol* 137(1):1–10
- Malkusch S, Muranyi W, Muller B, Krausslich HG, Heilemann M (2013) Single-molecule coordinate-based analysis of the morphology of HIV-1 assembly sites with near-molecular spatial resolution. *Histochem Cell Biol* 139(1):173–179
- Moerner WE (2012) Microscopy beyond the diffraction limit using actively controlled single molecules. *J Microsc* 246(3):213–220
- Moore CAC, Milano SK, Benovic JL (2007) Regulation of receptor trafficking by GRKs and arrestins. *Annu Rev Physiol* 69:451–482

- Mundell SJ, Matharu AL, Kelly E, Benovic JL (2000) Arrestin isoforms dictate differential kinetics of A(2B) adenosine receptor trafficking. *Biochemistry* 39(42):12828–12836
- Nieuwenhuizen RP, Lidke KA, Bates M, Puig DL, Grunwald D, Stallinga S, Rieger B (2013) Measuring image resolution in optical nanoscopy. *Nat Methods* 10:557–562
- Owen DM, Williamson DJ, Boelen L, Magenau A, Rossy J, Gaus K (2013) Quantitative analysis of three-dimensional fluorescence localization microscopy data. *Biophys J* 105(2):L05–L07
- Pierce KL, Lefkowitz RJ (2001) Classical and new roles of beta-arrestins in the regulation of G-protein-coupled receptors. *Nat Rev Neurosci* 2(10):727–733
- Rask-Andersen M, Almen MS, Schioth HB (2011) Trends in the exploitation of novel drug targets. *Nat Rev Drug Discov* 10(8):579–590
- Ries J, Kaplan C, Platonova E, Eghlidi H, Ewers H (2012) A simple, versatile method for GFP-based super-resolution microscopy via nanobodies. *Nat Methods* 9(6):582–584
- Ripley BD (1977) Modelling spatial patterns. *J Roy Statist Soc B* 39:172–212
- Rosenbaum DM, Rasmussen SGF, Kobilka BK (2009) The structure and function of G-protein-coupled receptors. *Nature* 459(7245):356–363
- Rust MJ, Bates M, Zhuang XW (2006) Sub-diffraction-limit imaging by stochastic optical reconstruction microscopy (STORM). *Nat Methods* 3(10):793–795
- Santini F, Gaidarov I, Keen JH (2002) G protein-coupled receptor/arrestin3 modulation of the endocytic machinery. *J Cell Biol* 156(4):665–676
- Sengupta P, Jovanovic-Talisman T, Skoko D, Renz M, Veatch SL, Lippincott-Schwartz J (2011) Probing protein heterogeneity in the plasma membrane using PALM and pair correlation analysis. *Nat Methods* 8(11):969–975
- Smith CS, Joseph N, Rieger B, Lidke KA (2010) Fast, single-molecule localization that achieves theoretically minimum uncertainty. *Nat Methods* 7(5):373–375
- Specht CG, Izeddin I, Rodriguez PC, El Beheiry M, Rostaing P, Darzacq X, Dahan M, Triller A (2013) Quantitative nanoscopy of inhibitory synapses: counting gephyrin molecules and receptor binding sites. *Neuron* 79(2):308–321
- Truan Z, Tarancón Díez L, Bönsch C, Malkusch S, Endesfelder U, Munteanu M, Hartley O, Heilemann M, Fürstenberg A (2013) Quantitative morphological analysis of arrestin 2 clustering upon G protein-coupled receptor stimulation by super-resolution microscopy. *J Struct Biol* 184(2):329–334
- Wolter S, Schüttelz M, Tscherepanow M, Van de Linde S, Heilemann M, Sauer M (2010) Real-time computation of subdiffraction-resolution fluorescence images. *J Microsc* 237(1):12–22
- Zidar DA (2011) Endogenous ligand bias by chemokines: implications at the front lines of infection and leukocyte trafficking. *Endocr Metab Immune Disord Drug Targets* 11(2):120–131

## A simple method to estimate the average localization precision of a single-molecule localization microscopy experiment

Ulrike Endesfelder · Sebastian Malkusch ·  
Franziska Fricke · Mike Heilemann

Accepted: 26 January 2014  
© Springer-Verlag Berlin Heidelberg 2014

**Abstract** The localization precision is a crucial and important parameter for single-molecule localization microscopy (SMLM) and directly influences the achievable spatial resolution. It primarily depends on experimental imaging conditions and the registration potency of the algorithm used. We propose a new and simple routine to estimate the average experimental localization precision in SMLM, based on the nearest neighbor analysis. By exploring different experimental and simulated targets, we show that this approach can be generally used for any 2D or 3D SMLM data and that reliable values for the localization precision  $\sigma_{\text{SMLM}}$  are obtained. Knowing  $\sigma_{\text{SMLM}}$  is a prerequisite for consistent visualization or any quantitative structural analysis, e.g., cluster analysis or colocalization studies.

**Keywords** Single-molecule localization microscopy · Fluorescence microscopy · Resolution · Localization precision · Single-molecule fluorescence

### Introduction

After the successful first observation of a single molecule (Moerner and Kador 1989) and the first detection of

single-molecule fluorescence (Orrit and Bernard 1990), today, the huge field of single-molecule biophysics emerged. This includes single-molecule localization microscopy (SMLM) techniques (Betzig et al. 2006; Rust et al. 2006; Heilemann et al. 2008), in which the total fluorescence signal is detected as subsets of single fluorophores employing photoswitching. An important parameter for SMLM experiments is how accurate the positions of the detected fluorescent emitters can be determined, which directly influences the achievable resolution. For the quantification of the localization precision, several strategies were proposed. The obtained precision primarily depends on experimental imaging conditions (setup-dependent, e.g., objective and optics, and sample-dependent, e.g., signal-to-noise ratio (SNR), photon rates, blinking performances) and the registration potency of the single-molecule localization algorithm used. Characterizing whether a fundamental precision limit exists has already been targeted since the first single-molecule studies were conducted and has been addressed in several theoretical approaches.

Ober et al. (2004) calculate a general variance limit from the Cramér–Rao Lower Bound (CRLB), which is derived from the Fisher information matrix. The complexity can be reduced by assumptions, e.g., by applying a Gaussian model and experimental parameters to yield explicit expressions of the precision limit (Bobroff 1986; Kubitscheck et al. 2000; Thompson et al. 2002; Ober et al. 2004; DeSantis et al. 2010; Jia et al. 2010; Mortensen et al. 2010). However, the theoretical lower bound is normally not reached under experimental conditions. Furthermore, CRLB does not take into account further loss in accuracy of the localization positions by common post-processing routines, e.g., drift corrections or multi-channel registration. The experimental localization precision for a particular experiment is usually determined by characterizing the distribution of the multiple localizations arising from a single, isolated molecule. The approximation to a

**Electronic supplementary material** The online version of this article (doi:10.1007/s00418-014-1192-3) contains supplementary material, which is available to authorized users.

U. Endesfelder (✉) · S. Malkusch · F. Fricke ·  
M. Heilemann (✉)  
Institute of Physical and Theoretical Chemistry, Johann Wolfgang  
Goethe University Frankfurt am Main, Frankfurt am Main, Germany  
e-mail: endesfelder@chemie.uni-frankfurt.de

M. Heilemann  
e-mail: Heilemann@chemie.uni-frankfurt.de

Gaussian allows measuring the full-width at half-maximum (FWHM) to extract the standard deviation  $\sigma_{\text{SMLM}}$ . The statistics can be improved by overlaying multiple molecules by their center of mass (Rust et al. 2006; Heilemann et al. 2008; Huang et al. 2008). This approach cannot be used for dense targets where single-molecule distributions are not resolved. Experiments using fluorophores that are not localized many times (e.g., irreversibly switching fluorophores used for photoactivated localization microscopy (PALM)) or time-critical experiments where, e.g., fast dynamics of living cells are involved, hinder accurate determination of  $\sigma_{\text{SMLM}}$ . Different approaches make use of known distances of structures, e.g., the 2D-projected walls of microtubules (Vaughan et al. 2012, 2013; Olivier et al. 2013), the central channel of a nuclear pore (Loschberger et al. 2012) or DNA-based synthetic molecular rulers (Ram et al. 2006; Steinhauer et al. 2009). This method, however, presupposes fundamental knowledge about the dimensions of the imaged structure. It yields the spatial resolution of the very calibration measurement dependent on its specific experimental conditions that are not automatically transferable to a different experiment.

It is important to note that the overall resolution of a SMLM image is not only given by the spatial resolution determined by the localization precision. Also labeling density (Shannon 1949), fitting performances (Small 2009; Wolter et al. 2011) or temporal shifts (Endesfelder et al. 2010; Yau et al. 2011; Deschout et al. 2012) are key factors that affect the overall achieved resolution. Measuring the SMLM resolution has been targeted via spatial-frequency-dependent data analysis. First work determined a cutoff parameter for the frequency-dependent SNR, which needs prior information on localization precision, labeling density and structure (Fitzgerald et al. 2012). Other work built an information transfer function on the spatial frequency analysis including photon statistics and labeling density (Mukamel and Schnitzer 2012), and very recently, the spatial frequencies were explored by spatial Fourier ring correlation analysis (Banterle et al. 2013; Nieuwenhuizen et al. 2013).

In this complex context, we here introduce a method, named NeNA (nearest neighbor based analysis), that directly rates the experimental localization precision for any localization microscopy experiment in a very general context and that includes parameters such as time dependence, alignment registration and structural labeling factors.

## Materials and methods

### mEos2 purification and preparation of single-molecule surfaces

*E. coli* BL21ai cells (Invitrogen) were transformed with the pRSetA-mEos2-6his vector (Addgene). For protein

expression, BL21ai cell stocks frozen at  $-80\text{ }^{\circ}\text{C}$  were thawed on ice and transferred into sterile LB medium (0.5 mL, 100  $\mu\text{g/ml}$  ampicillin) over night at  $37\text{ }^{\circ}\text{C}$  shaking at 220 rpm. The starter culture was transferred to the main culture. At  $\text{OD}_{600\text{nm}} = 0.5$ , the expression of mEos2-6his was induced by the application of 0.5 % arabinose (Sigma). After 80 min of incubation at  $30\text{ }^{\circ}\text{C}$  shaking at 220 rpm, cells were harvested via centrifugation at 3,500  $g$  for 40 min at  $4\text{ }^{\circ}\text{C}$  and lysed under native conditions. The cell lysate was sonicated on ice (30 GHz, 6 pulses each for 10 s) and centrifuged at 3,500  $g$  for 40 min at  $4\text{ }^{\circ}\text{C}$ . The supernatant was purified by standard protocol in a Ni-NTA agarose system (Merck Millipore). The degree of mEos2-6his purity was quantified by loading the different collected fractions onto a SDS-gel. mEos2-6his proteins were biotinylated with *N*-hydroxysuccinimide-polyethylene glycol 12-biotin (NHS-Peg<sub>12</sub>-Biotin, Thermo Scientific) and short-term stored using protease inhibitor (SigmaFAST™, Sigma) in phosphate-buffered saline (PBS pH 7.4, Sigma) at  $4\text{ }^{\circ}\text{C}$ .

The glass surface of microscopic cover chambers (Labtek, Nunc) was etched by 0.5 % hydrofluoric acid (HF) for 10 s and washed 3 times with PBS. The chambers were incubated with a 5 mg/ml bovine serum albumin (BSA, Sigma) and 1 mg/ml BSA-biotin (Sigma) solved in PBS for 4 h at  $4\text{ }^{\circ}\text{C}$ . Remaining BSA was removed by 3 washing steps with PBS. The BSA/BSA-biotin surfaces were incubated with 0.1 mg/ml streptavidin (Sigma) solved in PBS for 15 min at room temperature. Freely diffusing streptavidin was removed by three additional washing steps with PBS. mEos2-6his-Peg<sub>12</sub>-biotin was incubated until the single fluorescent protein concentration at the chamber surface was suitable for single-molecule fluorescence experiments. Free mEos2-6his-Peg<sub>12</sub>-biotin molecules were removed by three additional washing steps with PBS. For short-term storage, the immobilized mEos2 surface was stored in PBS at  $4\text{ }^{\circ}\text{C}$ .

### Cell culture, fixation and immunostaining

HeLa cells were cultured in RPMI 1640 (Gibco) supplemented with 100 units/ml penicillin, 100  $\mu\text{g/ml}$  streptomycin, 2 mM L-glutamine and 10 % fetal calf serum at  $37\text{ }^{\circ}\text{C}$  with 5 %  $\text{CO}_2$ . For imaging, cells were seeded in 8-well cover glass chamber slides (Sarstedt), fixed and immunostained based on a protocol from Desai (2012). In brief, cells were extracted for 2 min in extraction buffer containing 80 mM Pipes, 1 mM  $\text{MgCl}_2$ , 5 mM EGTA, 0.5 % Triton X-100 (all from Sigma), with the pH adjusted to 6.9. For fixation, glutaraldehyde (Sigma, EM grade) is added to the extraction buffer to a final concentration of 0.5 % and cells were incubated for another 10 min. After washing in TBS (150 mM NaCl (Sigma), 20 mM Tris (pH 8) (Sigma)) and



treatment with blocking buffer (TBS, 0.1 % Triton X-100 and 2 % BSA (Sigma)) for 10 min, cells were incubated by the primary mouse anti- $\beta$ -tubulin monoclonal antibody (Novex, 32-2600) at a concentration of 2  $\mu\text{g}/\text{ml}$  in blocking buffer for 2 h, followed by an extensive rinse of the cells in TBS. Alexa Fluor 647 dye labeled  $F(ab')_2$  fragment of goat anti-mouse IgG (Molecular Probes, A-21237) is added at a concentration of 4  $\mu\text{g}/\text{ml}$  in blocking buffer for the secondary antibody incubation of 1 h, followed by extensive rinsing in TBS. For buffers requiring pH adjustment, we used 1 M aqueous KOH.

#### Single-molecule localization microscopy

Imaging experiments were performed on two custom-built localization microscopy setups as described elsewhere (Heilemann et al. 2008). Chamber slides were mounted on an Olympus IX71 inverted microscope equipped with 60 $\times$  or 100 $\times$  oil immersion objective lenses (PlanApo 60x for single-molecule surfaces and PLAPO 100x TIRFM for cells, NA  $\geq$  1.45, Olympus). By translation of a mirror, the setup was operated in wide field or TIR illumination. A 405-nm diode laser (CUBE 405-100C, Coherent), the 568-nm line of a multiline argon krypton mixed gas ion laser (Innova70C, Coherent) or a 643-nm diode laser (iBeam smart, Toptica) were coupled into the microscope by a quad-band dichroic mirror (F73-888, AHF). Fluorescence light was collected by the objective, spectrally separated from excitation light by filters (F76-568, F39-617 for mEos2; F47-700 for Alexa Fluor 647, all from AHF) and projected on the 512  $\times$  512 pixel chip of an electron-multiplying charge-coupled device EMCCD (iXon, Andor).

For single-molecule imaging, immobilized mEos2 fluorophores in PBS (pH 7.5) or in 100 mM MEA in PBS (pH 7.5) were photoconverted by 405-nm illumination (1–5  $\mu\text{W}$ ) and read out by the 568-nm laser (40 mW). Videos of the single-molecule fluorescence traces were recorded with a 100 ms exposure time for 5 min using different blinking conditions (Endesfelder et al. 2011). Cells with immunostained microtubules were briefly washed with PBS and then placed in imaging buffer consisting of PBS (Gibco), 100 mM MEA (Sigma) and the pH adjusted to 8. Alexa Fluor 647 molecules were excited by the 643-nm laser (70 mW). Fluorescence signals were recorded using an exposure time of 30 ms over a recording time of 50 min. Bleached dye molecules were reactivated by 405-nm laser illumination. The density of active, fluorescent Alexa Fluor 647 molecules is kept constant by slowly increasing the 405-nm laser power with a neutral density filter wheel.

Single-molecule image reconstruction was done with the open source evaluation tool rapidSTORM (Wolter et al. 2010). Localization data and super-resolution images were further analyzed with Fiji (Schindelin et al. 2012),

OriginPro 8.5G (Texas Instruments) and a custom-written, standalone program (Python based with Numpy and Scipy packages (Oliphant 2007), see supplementary text and .py software code package).

#### Simulation methods

##### *Monte Carlo simulation of single molecules*

The Monte Carlo simulations made are all based on the three following assumptions: (1) fluorophores of the same type behave in the same way; (2) the distribution of localizations measured from a single fluorophore results in a two-dimensional Gaussian distribution; (3) SMLM patterns were simulated using the standard random generator for normal distributions implemented in Numpy (Oliphant 2007) with a fixed variance for all fluorophores, which we assume to generate reliable random normal distributions.

Every simulated fluorophore is localized 3,000 times in the theoretical experiment (except the single-molecule simulation exploring the dependency on the number of localizations where the input was varied from 100 to 900). The on-time  $\tau_{\text{on}}$  of the molecules was set to match the integration time of the camera, as it should be under ideal experimental conditions to collect the maximal number of detected photons for a fluorophore in one camera frame. Note that every molecule can be detected in two adjacent frames, as fluorescence emission and the detection by the camera are not synchronized.

##### *Simulation of microtubule filaments*

The measured localization precision of 8.6 nm and the density (4,000 loc/ $\mu\text{m}$ ) are used as the input parameters for the simulation. As staining with antibodies occurs outside the tube structure, the microtubule size increases by labeling. Under the chosen parameters of immunostained microtubules in SMLM experiments ( $r_{\text{Tubulin}} = 12.5$  nm,  $d_{\text{IgG}} = 15.0$  nm,  $d_{F(ab)} = 7.5$  nm,  $\tau_{\text{on}} = 2.5$  frames, active density of ROI: 2 fluorophores in on-state, total of 800 molecules, each 5 localizations), a simulated localization data set for a 1  $\mu\text{m}$  microtubule was generated.

## Results and discussion

The distribution  $NN_{\text{adfr}}$  of nearest neighbor distances from adjacent imaging frames

The raw data of localization microscopy are obtained by identifying and fitting single fluorescent spots, which generates a “localization list” that contains spatial coordinates, a time stamp and fitting parameters (number of

photons, variances, etc.) (Fig. 1a). The fluorescent spots are typically fitted by a Gaussian rather than the exact Airy distribution (which itself possesses an infinite standard deviation  $\sigma$ ). This Gaussian approximation is valid for isotropic symmetric single-molecule signals, when effects like light scattering in thicker samples, a large refraction index mismatch, dipole orientations or diffraction rings due to, e.g., larger imaging depths are excluded (Cheezum et al. 2001). The precision of the position determination by Gaussian approximation can be obtained by several methods. A theoretical limit of precision (Fig. 1b. 1) can be calculated for each localization, depending on the size (e.g.,  $\sigma_{\text{PSF}}$ ) and strength (photon number  $N_{\text{phot}}$ ) of the signal (Bobroff 1986; Thompson et al. 2002; Ober et al. 2004; Mortensen et al. 2010). Experimentally, the localization precision  $\sigma_{\text{SMLM}}$  is obtained from multiple positions of a single molecule or several molecules overlaid in their center of mass (Fig. 1b. 2, upper part). In the approach presented here, we characterize the positional variability of the distribution by the pairwise displacement between repetitive localizations (Fig. 1b. 2, lower part). Churchman et al. analytically described the distribution of relative distances between two Gaussian-distributed spots by a non-Gaussian distribution of pairwise distances (Churchman et al. 2006). As the true distance between multiple localizations of the same molecule in SMLM equals zero, this distribution of pairs of different molecules can be simplified to a single-molecule distribution with repeat localizations:

$$p(d_{ij}) = \left( \frac{d_{ij}}{2\sigma_{\text{SMLM}}^2} e^{-\frac{(d_{ij})^2}{4\sigma_{\text{SMLM}}^2}} \right)$$

$p(d_{ij})$  gives the probability for a positional displacement in two dimensions and is further referred to as the pairwise displacement distribution. Here, the distance between an arbitrary pair of localizations  $i$  and  $j$  is given by  $d_{ij}$ , while  $\sigma_{\text{SMLM}}$  is the Gaussian standard deviation characterizing the localization precision.

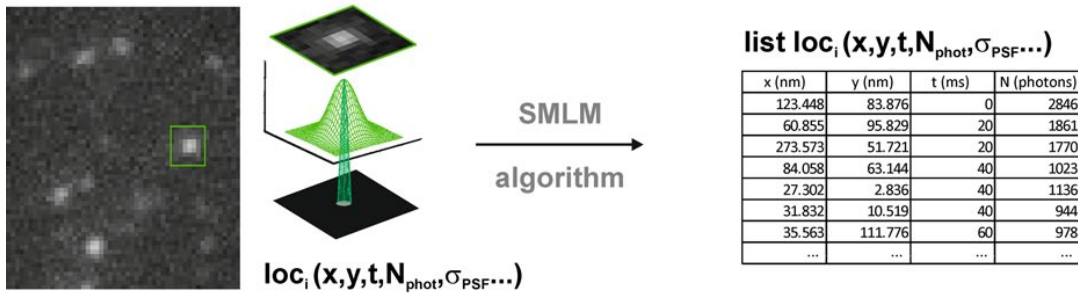
Importantly, the pairwise displacement distribution yields improved statistics compared to the Gaussian localization distribution as the distance between all possible pairs of localizations is determined. The total number of measured distances then equals the sum  $n = \sum_{i=1}^{n_{\text{loc}}-1} i$ , where  $n_{\text{loc}}$  is the total number of localizations. In comparison, only one measurement per localization ( $n = n_{\text{loc}}$ ) is made for the Gaussian distribution, namely the position relative to the center of mass. This is also reflected in the statistics of simulations for different  $n_{\text{loc}}$  in the supplementary figure 1.

In localization microscopy experiments, the localization distributions of single fluorophores marking super-resolved structures typically overlap, thus single-molecule

**Fig. 1** SMLM localization precision. **a** The raw data of localization microscopy are obtained by identifying and fitting *single spots* of the acquisition images (*green box*). A typical localization list contains spatial coordinates, a time stamp and fitting parameters (number of photons, variances, etc.) for each fitted spot. **b** The precision of the SMLM data can be obtained by several methods. (*b1*) A theoretical limit of precision can be calculated for each localization dependent on the PSF of the spot ( $\sigma_{\text{PSF}}$ ) and the photon number  $N_{\text{phot}}$ . (*b2*) Further, individual molecules can be used to determine an experimental precision. A highly blinking molecule localized repeatedly or several molecules overlaid by their center of mass can be fitted by a Gaussian to obtain  $\sigma_{\text{SMLM}}$ . Additionally relative pairwise distances of all localizations can be measured and fitted by the non-Gaussian pairwise displacement fit (Churchman et al. 2006). (*b3*) When multiple molecules are in close proximity, no distributions from individual molecules can be received (*red* molecule positions, *black* localizations). As a fluorescence event normally spans several imaging frames, a displacement fit  $p(d)$  of the nearest neighbor distribution  $\text{NN}_{\text{adfr}}$  of localizations in adjacent frames yields an experimental precision. Nevertheless, a correction term for contributions of nearest neighbors of different molecules (false nearest neighbor, marked by a *red dotted circle*) has to be included (*red fit curve* standard non-Gaussian pairwise displacement distribution  $p(d_{ij})$ , *green fit curve* non-Gaussian pairwise displacement distribution including correction terms  $p(d)$ )

distributions with repeat localizations of the same molecule usually cannot be identified. We therefore take advantage of the fact that the assembly of all relative pairwise distances between the Gaussian-distributed localizations of a single, frequently localized molecule (e.g., a highly reversibly blinking dye) in fact equals the collection of randomly chosen discrete relative pairwise distances from few localizations of a single molecule, which are summed up for many different molecules of the same type of fluorophore. As normally one fluorescent burst is detected on several adjacent imaging frames, it is therefore possible to determine the mean Gaussian standard deviation  $\sigma_{\text{SMLM}}$  of any localization microscopy data set. This approach also holds for fluorophores that are only localized a few times or for overlapping fluorophores (Fig. 1b. 3). We further make use of the fact that a specific localization  $\text{loc}_i(r_i, t_i)$  in one imaging frame possesses a nearest neighbor localization  $\text{NN}_i(\text{nn}_{r_i}, t_{i+1})$  in the next imaging frame  $t_{i+1}$  that likely originates from the same fluorophore. It is therefore possible to calculate the pairwise displacement  $d = \text{loc}_i(r_i, t_i) - \text{NN}_i(\text{nn}_{r_i}, t_{i+1})$  of single molecules. As a result, the obtained relative distances of nearest neighbors can be histogrammed in a single distribution without the need of any alignment (Lando et al. 2012; Muranyi et al. 2013; Truan et al. 2013). Nevertheless, a certain percentage of these nearest neighbors of adjacent frames originate from different molecules in close proximity. Also, at the first and last imaging frame of a single fluorescent burst, no nearest neighbor belonging to the same molecule can be found. Here, the distance to another molecule makes up the nearest neighbor (Fig. 1b. 3). Thus, this nearest neighbor distribution in adjacent frames  $\text{NN}_{\text{adfr}}$  cannot be described

(a) SMLM localization data



(b) SMLM localization precision

1 Estimation theory

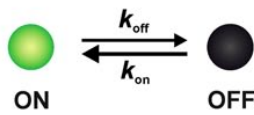
**list loc<sub>i</sub>(x,y,t,N<sub>phot</sub>,σ<sub>PSF</sub>...)**

x (nm)	y (nm)	t (ms)	N (photons)
123.448	83.876	0	2846
60.855	95.829	20	1861
273.573	51.721	20	1770
84.058	63.144	40	1023
27.302	2.836	40	1136
31.832	10.519	40	944
35.563	111.776	60	978
...	...	...	...

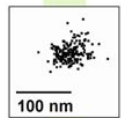
localization  
→  
each localization

$$\sigma_{SMLM} \propto \frac{\sigma_{PSF}}{\sqrt{N_{phot}}}$$

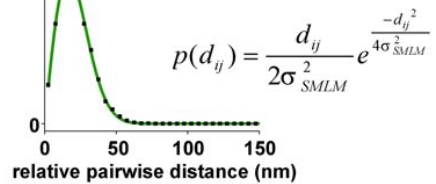
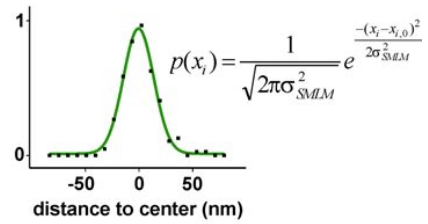
2 Individual molecules



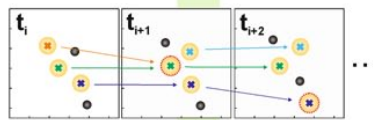
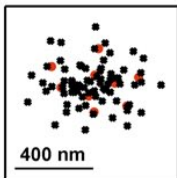
molecule



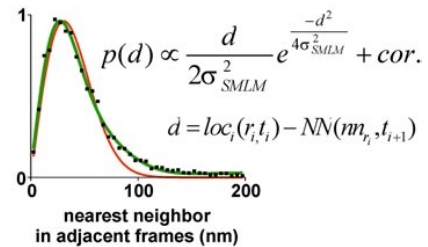
multiple localizations



3 Multiple molecules



$$\sum loc = \sum_{i=1}^{molecules} \left( \sum_{j=1}^{blinks} loc(r_j, t_j) \right)$$



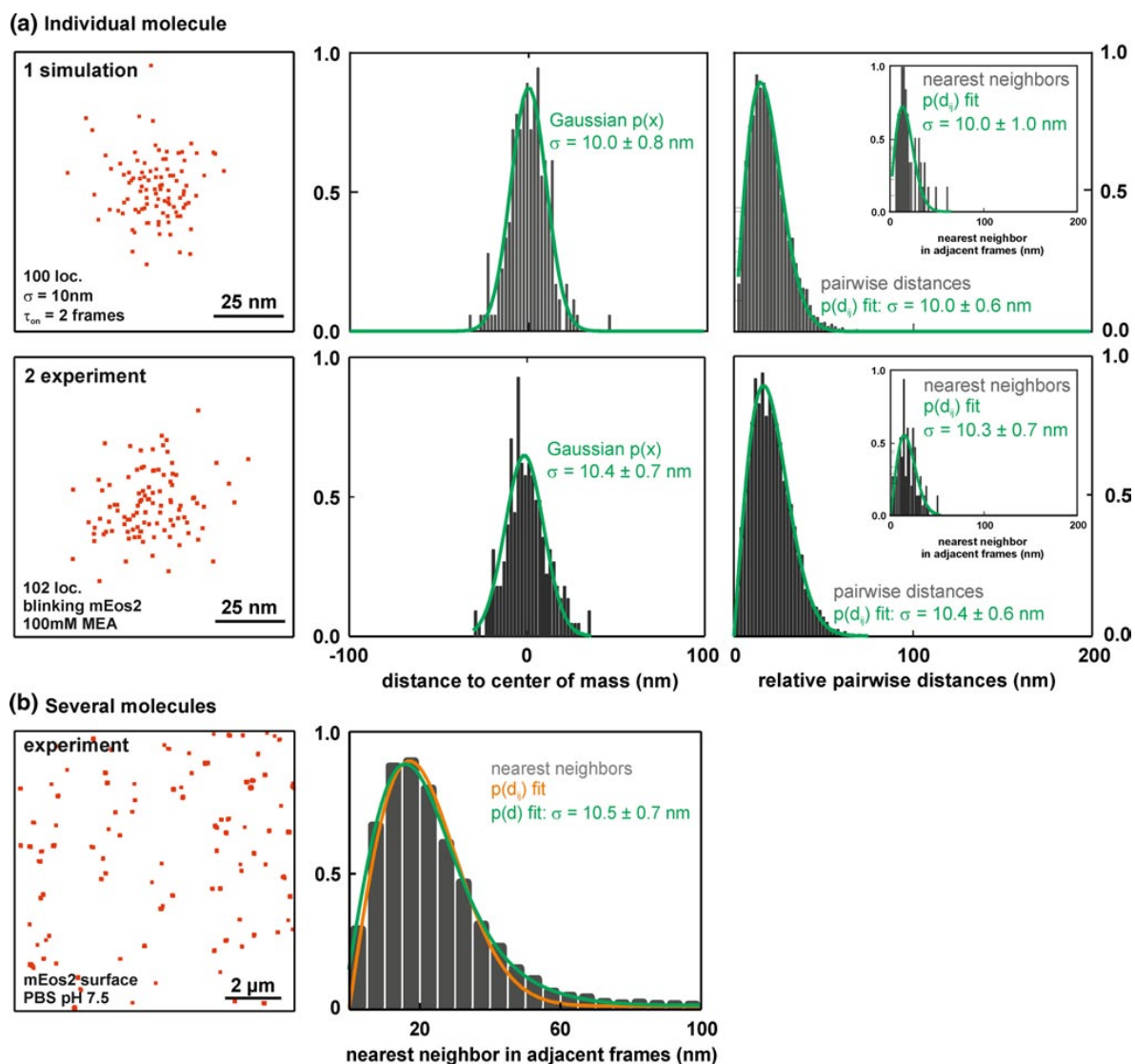


**Fig. 2** Retrieving  $\sigma_{\text{SMLM}}$  by different distributions. **a** Comparison between Gaussian and pairwise distance distributions for individual molecules. *a1* Simulation of a Gaussian-distributed localization list of a single molecule (100 localizations,  $\sigma = 10\text{ nm}$ ,  $\tau_{\text{on}} = 2\text{ frames}$ ). *a2* Distribution of 102 measured localizations of an individual blinking molecule [mEos2, 100 mM MEA in PBS, pH 7.5, conditions from (Endesfelder et al. 2011)]. Both spatial localization distributions are evaluated by measuring the absolute distances of all localizations to the center of mass, the distribution of the relative pairwise

distances of all localizations and the nearest neighbor in adjacent frame distribution  $\text{NN}_{\text{adfr}}$  (*inset*) and are fitted with a Gaussian  $p(x)$  or  $p(d_{ij})$ , respectively, to obtain  $\sigma_{\text{SMLM}}$  values. **b** For several overlapping molecules, no distributions on individual molecule statistics can be obtained. Thus, solely the distribution  $\text{NN}_{\text{adfr}}$  can be calculated as a fluorescent event spans several imaging frames. The pairwise displacement fit  $p(d_{ij})$  (*orange curve*) is extended by a correction term to account for contributions of nearest neighbors of different molecules yielding  $p(d)$  (*green curve*)

by  $p(d_{ij})$  (*orange curve* in Fig. 1b. 3) but needs correction terms to account for the above effects.

To evaluate our approach, we first simulated SMLM data with defined parameters. In Fig. 2a (upper part), the simulated distribution of a single molecule consisting of 100 localizations with 10 nm standard deviation is shown.

A standard deviation  $\sigma_{\text{SMLM}}$  of  $10.0 \pm 0.8\text{ nm}$  determined by Gaussian fitting and of  $10.0 \pm 0.6\text{ nm}$  determined by fitting the pairwise displacement distribution with  $p(d_{ij})$  were obtained, both reflecting the a priori simulated value. By including an on-time  $\tau_{\text{on}}$  of the fluorophores, the nearest neighbor in adjacent frames distance distribution

$NN_{\text{adfr}}$  yields  $10.0 \pm 1.0$  nm for the case of  $\tau_{\text{on}}$  equaling the frame rate, which results in a maximum photon count per spot and spreads the detection of every molecule in two adjacent frames.

In a next step, we imaged single mEos2 fluorophores immobilized on a glass surface and localized about 100 times by redox-induced blinking in 100 mM MEA (Endesfelder et al. 2011). We determined a standard deviation of  $10.4 \pm 0.7$  nm for the Gaussian distribution and of  $10.4 \pm 0.6$  nm determined by the pairwise displacement analysis. The nearest neighbor distance distribution  $NN_{\text{adfr}}$  yields  $10.3 \pm 0.7$  nm (Fig. 2a, lower part). Comparing the measured values of  $\sigma_{\text{SMLM}}$ , 100 localizations are already sufficient to obtain a reliable value for  $\sigma_{\text{SMLM}}$ . Statistics for  $\sigma_{\text{SMLM}}$  for different numbers of  $n_{\text{loc}}$  are depicted in the box plots of supplementary figure 1 and show the limit of experimental precision for the Gaussian (red) and pairwise displacement distribution (black).

For a single-molecule surface, the distribution of localization positions with respect to their overall center of mass is no longer Gaussian-distributed. Similarly, the pairwise displacement distribution majorly comprises distances of different molecules rendering both distributions unsuitable for localization precision determination. The distribution  $NN_{\text{adfr}}$  for a single-molecule surface of immobilized mEos2 fluorophores in Fig. 2b also possesses nearest neighbor distances far beyond the expected resolution, arising from false nearest neighbors of different molecules. The pairwise displacement fit  $p(d_{ij})$  is no longer well defined for the distribution (orange curve) and replaced by the fit  $p(d)$  (green curve) that includes correction terms for false nearest neighbors. Nevertheless, it should be noted that the distribution  $NN_{\text{adfr}}$  is minorly affected by false nearest neighbors and gives a good estimate of the average localization precision ( $\sigma_{\text{SMLM}} = 10.5 \pm 0.7$  nm) of the mEos2 surface.

The impact and nature of this second underlying distribution of false nearest neighbor distances generally depends on the fluorophore labeling density, the structure of the labeled target molecules and imaging parameters ( $N_{\text{phot}}$ , frame rate/ $\tau_{\text{on}}$  ratio, etc.). On the other hand, it is not dependent on blinking characteristics of fluorophores as blinking events from a single molecule do not influence an approach measuring events in adjacent frames. Very general, this second distribution of distances between different molecules can in theory be described as a sum of all non-Gaussian distributions by the original formula from Churchman et al. (2006) of pairwise distances between all possible partners of the different molecules which are in close proximity. This analytical distribution nevertheless is different for each single experiment and can only be described by knowing the number and photophysical properties of molecules marking the specific structure and assigning every individual localization to its originating molecule.

In reality, typical SMLM localization distributions overlap, and for small distances, nearest neighbors originating from the same molecule cannot be distinguished from false nearest neighbor distances. By choosing the imaging frame rate with respect to the mean fluorescence lifetime  $\tau_{\text{on}}$ , the individual fluorescent bursts are spread onto few imaging frames. It is therefore possible to obtain a sufficient number of nearest neighbor distances of adjacent imaging frames, which originate from the same molecule. The correction terms of the  $NN_{\text{adfr}}$ -fit function  $p(d)$  describe the interfering contribution from different molecules (false nearest neighbors) and thus the impact of the background disturbance on the single-molecule distribution. For identifying appropriate correction terms, we explored these dependences using detailed Monte Carlo simulations (supplementary text and supplementary figures 2–4). We found that the interference from other molecules within the diffraction-limited region (DLR) can be approximated by a Gaussian term correcting for short-range order and a second linear part correcting for long-range order:

$$p(d) = p(\text{single molecule}) + \text{cor}(\text{short}_{\text{DLR}}) + \text{cor}(\text{long}_{\text{DLR}})$$

$$p(d) = A_1 \left( \frac{d}{2\sigma_{\text{SMLM}}^2} e^{-\frac{d^2}{4\sigma_{\text{SMLM}}^2}} \right) + A_2 \left( \frac{1}{\sqrt{2\pi}\omega^2} e^{-\frac{(d-d_c)^2}{2\omega^2}} \right) + A_3 d$$

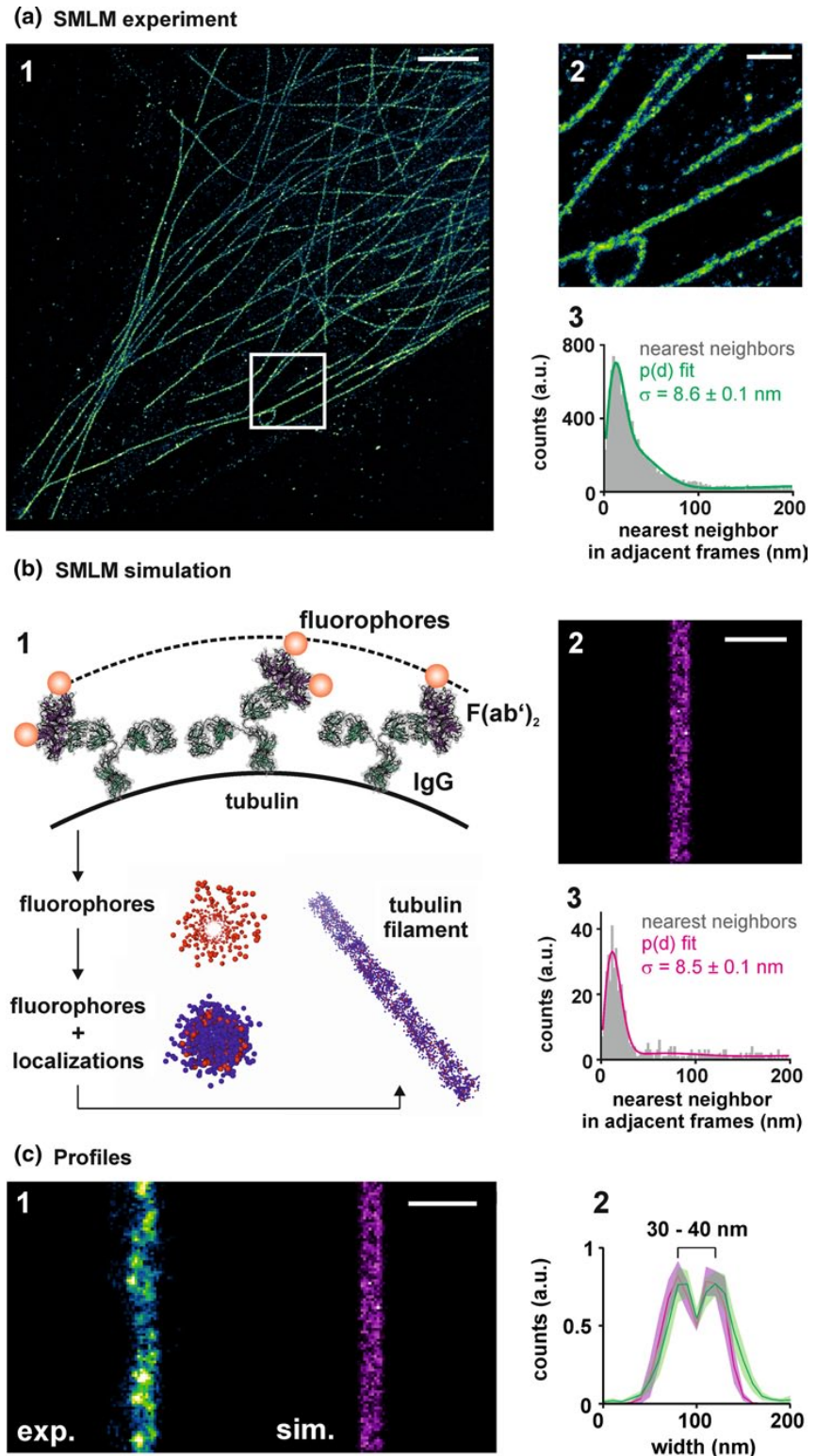
$p(d)$  gives the probability for a positional displacement. The distance  $d$  is calculated between a specific localization  $\text{loc}_i(r_i, t_i)$  in one imaging frame and its nearest neighbor localization  $\text{NN}_i(\text{nn}_{r_i}, t_{i+1})$  in the next imaging frame  $t_{i+1}$  ( $d = \text{loc}_i(r_i, t_i) - \text{NN}_i(\text{nn}_{r_i}, t_{i+1})$ ),  $\sigma_{\text{SMLM}}$  is the Gaussian standard deviation characterizing the localization precision,  $A_1, A_2, A_3$  are the amplitudes of each term, and  $\omega$  is the Gaussian standard deviation characterizing the short-range correction term centering at  $d_c$ . For further details see supplementary text.

#### Microtubule filament measurement and simulation

To quantify the localization precision and evaluate the goodness of the fit  $p(d)$  on the distribution  $NN_{\text{adfr}}$  of a biological sample, we imaged HeLa cells with immunostained microtubules under standard *d*STORM conditions (Fig. 3a). Fluorescently tagged microtubules are commonly used as standard biological targets to test the performance of SMLM imaging techniques or labeling strategies. The FWHM of a single microtubule intensity profile has often been considered to be a good estimate of the effective image resolution, when microtubule diameter and fluorescent tag size are taken into account. As recently shown by Vaughan et al. (2012, 2013), Olivier et al. (2013) and in Fig. 3a, c, the 2D-projected tubulin consists in fact of two peaks as a consequence of projecting a 3D tube onto



**Fig. 3** Structure of single microtubule filaments. **a** Microtubule filaments in a HeLa cell (*a1*) are used as intrinsic test target. SMLM images of Alexa Fluor 647 immunostained microtubules reveal the typical double-peaked radial filament profile, stemming from the hollow tubule structure (*a2*). The localization precision of 8.6 nm obtained by fitting the distribution  $NN_{\text{adfr}}$  by  $p(d)$  (*a3*) and the density (4,000 loc/ $\mu\text{m}$ ) are used as input parameters for the simulated filament (**b**). As staining with antibodies can be obtained solely externally of the tubule, the microtubule size increases by labeling (*b1*). The simulated filament (parameters of simulation:  $r_{\text{Tubulin}} = 12.5$  nm,  $d_{\text{IgG}} = 15.0$  nm,  $d_{\text{F(ab)'}_2} = 7.5$  nm,  $\tau_{\text{on}} = 2.5$  frames, active density of ROI: 2 fluorophores in on-state) yields a precision of  $8.5 \pm 0.1$  nm (*b3*) and is compared to the experimental filament (*c1*, experiment *green*, simulation *magenta*). The cross sections including the 95 % confidence interval (*shaded area*) of the microtubules are obtained by averaging 23 (experiment, *green*) and 16 (simulation, *magenta*) cross sections (*c2*), respectively, and reveal a separation of 30–40 nm



a 2D image. This provides an even better estimate for spatial resolution, as the distance of the two parallel lines is in the range of the typical spatial resolution in SMLM. The obtained  $NN_{\text{adfr}}$  distribution exhibits a strong single-molecule contribution as well as short- and long-range order disturbances (Fig. 3a. 3). To test whether fitting with  $p(d)$  including all correction terms yields a good approximation of  $NN_{\text{adfr}}$ , the obtained localization precision of 8.6 nm from the fit  $p(d)$  (Fig. 3a. 3) and the density of localizations ( $4,000/\mu\text{m}$ ) are used as input parameters for simulating a tubule filament as depicted in Fig. 3b. Staining with antibodies can be obtained solely externally of the microtubule, thus its size increases by labeling as sketched in Fig. 3b. 1. Choosing these parameters for the SMLM experiment simulation ( $r_{\text{Tubulin}} = 12.5$  nm,  $d_{\text{lgG}} = 15.0$  nm,  $d_{\text{F(ab)}} = 7.5$  nm,  $\tau_{\text{on}} = 2.5$  frames, active density of ROI: 2 fluorophores in on-state), intensity profiles including the 95 % confidence interval of the simulated and experimentally measured microtubules were generated. Averaging 23 (experiment, green) and 16 (simulation, magenta) cross sections (Fig. 3c. 2) yielded a typical separation of 30–40 nm of the two peaks. It should be noted that some microtubules do not show a two-peaked intensity profile throughout the whole filament (Fig. 3a. 1), which illustrates that the spatial resolution can be different in each region of an image.

## Conclusion

Knowing  $\sigma_{\text{SMLM}}$  for an experiment is crucial for reliable SMLM data interpretation, visualization or any further quantitative structural analysis, e.g., cluster analysis or colocalization studies. Evidently, even for SMLM images of relatively simple structures such as microtubules, there exists no practical solution for reliable localization precision determination, except for theoretical estimates or by searching for isolated individual fluorophores in the data set. Here, we proposed a simple, more independent and general routine, termed NeNA, for localization precision estimation. For that purpose, we identify the distance distribution  $NN_{\text{adfr}}$  of nearest neighbors in adjacent frames. It is closely related to the pairwise displacement distribution of Gaussian-distributed localizations of a single, frequently localized molecule and directly yields the localization precision  $\sigma_{\text{SMLM}}$  of SMLM experiments. By testing different experimental and simulated conditions, we investigated the influence of false nearest neighbors from different molecules. Under all conditions tested, the fitting of the nearest neighbor in adjacent frames distribution with a defined function  $p(d)$  is robust and yields reliable values for the localization precision  $\sigma_{\text{SMLM}}$ . The distribution  $NN_{\text{adfr}}$  can be obtained for any 2D or 3D data set, in whole or for defined subsets. Furthermore, the quality of

post-processing routines can be quantified by comparing the calculated values of  $\sigma_{\text{SMLM}}$  before and after application. The routine is simple to use and easily implemented for data analysis of all sorts of SMLM experiments. Notably, it does not require structural knowledge of the biological probe and may be extended to general single-molecule approaches, when the localization precision is of interest. We conclude that our proposed NeNA routine can accurately assess SMLM image quality and will help to improve and optimize SMLM studies.

**Acknowledgments** We thank Steve Wolter for helpful discussions. We acknowledge funding by the German Ministry of Education and Research (Grants 0315262 and 0316170D) and the cluster of excellence “Macromolecular Complexes” (CEF, DFG cluster of excellence (EXC 115)).

## References

- Banterle N, Bui KH et al (2013) Fourier ring correlation as a resolution criterion for super-resolution microscopy. *J Struct Biol* 183(3):363–367
- Betzig E, Patterson GH et al (2006) Imaging intracellular fluorescent proteins at nanometer resolution. *Science* 313:1642–1645
- Bobroff N (1986) Position measurement with a resolution and noise-limited instrument. *Rev Sci Instrum* 57(6):1152–1157
- Cheezum MK, Walker WF et al (2001) Quantitative comparison of algorithms for tracking single fluorescent particles. *Biophys J* 81(4):2378–2388
- Churchman LS, Flyvbjerg H et al (2006) A non-Gaussian distribution quantifies distances measured with fluorescence localization techniques. *Biophys J* 90(2):668–671
- Desai A (2012) Fluorescence procedures for the actin and tubulin cytoskeleton in fixed cells. <http://mitchison.med.harvard.edu/protocols/general/Fluorescence%20Procedures%20for%20the%20Actin%20and%20Tubulin%20Cytoskeleton%20in%20Fixed%20Cells.pdf>
- DeSantis MC, DeCenzo SH et al (2010) Precision analysis for standard deviation measurements of immobile single fluorescent molecule images. *Opt Express* 18(7):6563–6576
- Deschout H, Neyts K et al (2012) The influence of movement on the localization precision of sub-resolution particles in fluorescence microscopy. *J Biophotonics* 5(1):97–109
- Endesfelder U, van de Linde S et al (2010) Subdiffraction-resolution fluorescence microscopy of myosin-actin motility. *ChemPhysChem* 11(4):836–840
- Endesfelder U, Malkusch S et al (2011) Chemically induced photoswitching of fluorescent probes—a general concept for super-resolution microscopy. *Molecules* 16(4):3106–3118
- Fitzgerald JE, Lu J et al (2012) Estimation theoretic measure of resolution for stochastic localization microscopy. *Phys Rev Lett* 109(4):048102
- Heilemann M, van de Linde S et al (2008) Subdiffraction-resolution fluorescence imaging with conventional fluorescent probes. *Angew Chem Int Ed* 47(33):6172–6176
- Huang B, Wang W et al (2008) Three-dimensional super-resolution imaging by stochastic optical reconstruction microscopy. *Science* 319(5864):810–813
- Jia H, Yang J et al (2010) Minimum variance unbiased subpixel centroid estimation of point image limited by photon shot noise. *J Opt Soc Am A Opt Image Sci Vis* 27(9):2038–2045

- Kubitscheck U, Kuckmann O et al (2000) Imaging and tracking of single GFP molecules in solution. *Biophys J* 78(4):2170–2179
- Lando D, Endesfelder U et al (2012) Quantitative single-molecule microscopy reveals that CENP-A(Cnp1) deposition occurs during G2 in fission yeast. *Open Biol* 2(7):120078
- Loschberger A, van de Linde S et al (2012) Super-resolution imaging visualizes the eightfold symmetry of gp210 proteins around the nuclear pore complex and resolves the central channel with nanometer resolution. *J Cell Sci* 125(Pt 3):570–575
- Moerner WE, Kador L (1989) Optical detection and spectroscopy of single molecules in a solid. *Phys Rev Lett* 62(21):2535–2538
- Mortensen KI, Churchman LS et al (2010) Optimized localization analysis for single-molecule tracking and super-resolution microscopy. *Nat Methods* 7(5):377–381
- Mukamel EA, Schnitzer MJ (2012) Unified resolution bounds for conventional and stochastic localization fluorescence microscopy. *Phys Rev Lett* 109(16):168102
- Muranyi W, Malkusch S et al (2013) Super-resolution microscopy reveals specific recruitment of HIV-1 envelope proteins to viral assembly sites dependent on the envelope C-terminal tail. *PLoS Pathog* 9(2):e1003198
- Nieuwenhuizen RPJ, Lidke KA et al (2013) Measuring image resolution in optical nanoscopy. *Nat Methods* 10(6):557
- Ober RJ, Ram S et al (2004) Localization accuracy in single-molecule microscopy. *Biophys J* 86(2):1185–1200
- Oliphant TE (2007) Python for scientific computing. *Comput Sci Eng* 9(3):10–20
- Olivier N, Keller D et al (2013) Resolution doubling in 3D-STORM imaging through improved buffers. *PLoS ONE* 8(7):e69004
- Orrit M, Bernard J (1990) Single pentacene molecules detected by fluorescence excitation in a p-terphenyl crystal. *Phys Rev Lett* 65(21):2716–2719
- Ram S, Ward ES et al (2006) Beyond Rayleigh's criterion: a resolution measure with application to single-molecule microscopy. *Proc Natl Acad Sci USA* 103(12):4457–4462
- Rust MJ, Bates M et al (2006) Sub-diffraction-limit imaging by stochastic optical reconstruction microscopy (STORM). *Nat Methods* 3(10):793–795
- Schindelin J, Arganda-Carreras I et al (2012) Fiji: an open-source platform for biological-image analysis. *Nat Methods* 9(7):676–682
- Shannon CE (1949) Communication in the presence of noise. *Proc Inst Radio Eng* 37(1):10–21
- Small AR (2009) Theoretical limits on errors and acquisition rates in localizing switchable fluorophores. *Biophys J* 96(2):L16–L18
- Steinhauer C, Jungmann R et al (2009) DNA origami as a nanoscopic ruler for super-resolution microscopy. *Angew Chem Int Ed* 48(47):8870–8873
- Thompson RE, Larson DR et al (2002) Precise nanometer localization analysis for individual fluorescent probes. *Biophys J* 82:2775–2783
- Truan Z, Tarancon Diez L et al (2013) Quantitative morphological analysis of arrestin2 clustering upon G protein-coupled receptor stimulation by super-resolution microscopy. *J Struct Biol* 184(2):329–334
- Vaughan JC, Jia S et al (2012) Ultrabright photoactivatable fluorophores created by reductive caging. *Nat Methods* 9(12):1181–1184
- Vaughan JC, Dempsey GT et al (2013) Phosphine quenching of cyanine dyes as a versatile tool for fluorescence microscopy. *J Am Chem Soc* 135(4):1197–1200
- Wolter S, Schuttpelz M et al (2010) Real-time computation of subdiffraction-resolution fluorescence images. *J Microsc* 237(1):12–22
- Wolter S, Endesfelder U et al (2011) Measuring localization performance of super-resolution algorithms on very active samples. *Opt Express* 19(8):7020–7033
- Yau W, Zhiping L et al (2011) Limit of the accuracy of parameter estimation for moving single molecules imaged by fluorescence microscopy. *Signal Process IEEE Trans* 59(3):895–911



## Quantitative single-molecule localization microscopy combined with rule-based modeling reveals ligand-induced TNF-R1 reorganization toward higher-order oligomers

Franziska Fricke · Sebastian Malkusch · Gaby Wangorsch · Johannes F. Greiner · Barbara Kaltschmidt · Christian Kaltschmidt · Darius Widera · Thomas Dandekar · Mike Heilemann

Accepted: 28 January 2014  
© Springer-Verlag Berlin Heidelberg 2014

**Abstract** We report on the assembly of tumor necrosis factor receptor 1 (TNF-R1) prior to ligand activation and its ligand-induced reorganization at the cell membrane. We apply single-molecule localization microscopy to obtain quantitative information on receptor cluster sizes and copy numbers. Our data suggest a dimeric pre-assembly of TNF-R1, as well as receptor reorganization toward higher oligomeric states with stable populations comprising three to six TNF-R1. Our experimental results directly serve as input parameters for computational modeling of the ligand–receptor interaction. Simulations corroborate

the experimental finding of higher-order oligomeric states. This work is a first demonstration how quantitative, super-resolution and advanced microscopy can be used for systems biology approaches at the single-molecule and single-cell level.

**Keywords** Super-resolution microscopy · TNF receptor I · Receptor clustering · Systems biology · Modeling · PALM · dSTORM

Franziska Fricke and Sebastian Malkusch have contributed equally.

**Electronic supplementary material** The online version of this article (doi:10.1007/s00418-014-1195-0) contains supplementary material, which is available to authorized users.

F. Fricke · S. Malkusch · M. Heilemann (✉)  
Institute for Physical and Theoretical Chemistry,  
Johann-Wolfgang-Goethe-University Frankfurt,  
Frankfurt am Main, Germany  
e-mail: heilemann@chemie.uni-frankfurt.de

G. Wangorsch · T. Dandekar  
Bioinformatics, Biocenter, Julius-Maximilians-University  
Würzburg, Würzburg, Germany

J. F. Greiner · C. Kaltschmidt · D. Widera  
Department of Cell Biology, Faculty of Biology, University  
of Bielefeld, Bielefeld, Germany

B. Kaltschmidt  
Molecular Neurobiology, Faculty of Biology, University  
of Bielefeld, Bielefeld, Germany

M. Heilemann  
BIOQUANT Centre, University of Heidelberg,  
Heidelberg, Germany

### Introduction

Activation of tumor necrosis factor receptor 1 (TNF-R1) is broadly described to result in strong cellular responses ranging from inflammation and proliferation to different forms of programmed cell death including apoptosis and necroptosis (Vandenabeele et al. 2010; Wajant and Scheurich 2011). Triggered by the discovery of the two TNF receptors, TNF-R1 and TNF-R2, their activation and signaling have been intensively studied for more than two decades (Brockhaus et al. 1990; Hohmann et al. 1989). TNF-R1 consists of four cysteine-rich domains (CRDs) on the extracellular side and a cytoplasmic death domain (Chan 2007). TNF receptors and other members of the TNF receptor superfamily including Fas and TRAIL (TNF related apoptosis-inducing ligand) receptors bind non-covalently homotrimeric ligands that exist in a membrane bound and soluble form (Eck and Sprang 1989). Crystallographic data revealed that receptors are recruited to the groove between two ligand protomers resulting in a 3:3 receptor–ligand-binding stoichiometry in a cell-free system (Banner et al. 1993; Hymowitz et al. 1999). The soluble form of tumor necrosis factor alpha (TNF $\alpha$ ) was shown to strongly induce signaling via TNF-R1 but not TNF-R2 (Boschert

et al. 2010; Grell et al. 1995). TNF $\alpha$ -binding to TNF-R1 initiates two major pathways: apoptosis via cleavage of procaspases or activation of nuclear factor- $\kappa$ B (NF- $\kappa$ B) (Wajant and Scheurich 2011). Both pathways require binding of adapter proteins to the intracellular death domain of the receptor, mainly TNF receptor-associated death domain protein (TRADD) and receptor-interacting protein 1 (RIP1), which in turn serve as a platform for further protein recruitment.

However, the initial steps during ligand-induced signaling at the plasma membrane remain unclear. Several studies for members of the TNF receptor superfamily promote the theory of a receptor homodimer formation prior to ligand activation caused by the pre-ligand assembly domain (PLAD) located at the membrane-distal CRD1 (Chan et al. 2000; Naismith et al. 1995). Receptor pre-assembly is argued to be essential for ligand binding which then induces a conformational change of the receptor dimer required for signal initiation (Chan 2007; Lewis et al. 2012). Another possible consequence of receptor dimerization may be a formation of large ligand–receptor clusters that were already proposed by (Naismith et al. 1995) as highly organized hexagonal structures and supported by cross-linking studies and confocal microscopy data (Chan et al. 2000; Henkler et al. 2005; Krippner-Heidenreich et al. 2002; Siegel et al. 2004; Valley et al. 2012). These oligomeric structures are associated with strong signaling (Krippner-Heidenreich et al. 2002), but whether receptor clustering as opposed to ligand-induced activation of receptor dimers is essential for signal transduction remains to be seen. Also, the stoichiometry of PLAD-mediated receptor assembly is still controversial (Boschert et al. 2010).

Recent advances in light microscopy helped our understanding of protein organization and cellular architecture at the near-molecular level (Gould et al. 2012). A spatial resolution of 20 nm and higher is now routinely achieved with single-molecule localization microscopy techniques. Photoactivated-localization microscopy (PALM) (Betzig et al. 2006), one of the earliest methods, has carried single-molecule imaging toward quantitative microscopy where spatial organization is related to molecule copy numbers. Examples include protein counting in cells with PALM based on elaborate quantification methods correcting for overcounting due to fluorophore blinking (Annibale et al. 2011; Lando et al. 2012; Lee et al. 2012; Ori et al. 2013; Sengupta et al. 2011) and undercounting owing to impaired fluorescent protein (FP) maturation or undetected FP emissions (Puchner et al. 2013).

Predictive computational simulations of receptor signaling strongly support the understanding of signal initiation, outcome, and cell fate. Today's molecular systems biology toolbox comprises detailed modeling of receptor activation and protein recruitment at the cell membrane as well

as complex circuits of signaling hubs determining downstream events. Few quantitative models of the initial steps of ligand binding by TNF-R1 or other members of the TNF receptor superfamily exist (Jackson and Lai 2004; Winkel et al. 2012). The models reported in the literature focus on the first few steps of ligand–receptor binding, but do not implement higher-order ligand–receptor complexes consisting of more than three receptors.

Here, we investigate the organization of TNF-R1 in the plasma membrane before and after ligand binding and the following receptor rearrangement. By combining experimental data from quantitative super-resolution microscopy of TNF-R1 and binding studies with network-free rule-based modeling of the receptor–ligand complex, we provide first evidence of receptor dimerization on the plasma membrane of intact cells followed by receptor reorganization toward small clusters after ligand binding.

## Materials and methods

### Plasmids and cells

Plasmid construct encoding for TNF-R1-tEOS was described elsewhere (Heidbreder et al. 2012). VSVG-tEOS vector was produced by replacing PAGFP in VSVG-PAGFP with tEOS using *Bam*HI and *Bsp*1407I restriction sites. VSVG-PAGFP plasmid was obtained from Addgene (Addgene plasmid 11915) (Presley et al. 1997). HeLa cells were grown in chamber slides (Sarstedt) in RPMI 1640 medium containing 100 IU/mL penicillin, 100  $\mu$ g/mL streptomycin, 2 mM L-glutamine, and 5 % fetal calf serum (Gibco). Human U251 glioblastoma cells were cultured in tissue culture dishes (TPP Techno Plastic Products) and DMEM high glucose (Biochrom) containing 200 mM L-glutamine (Sigma), amphotericin B (1 mL (0.25 mg)/100 mL; PAA), penicillin/streptomycin (1 mL (2 mg)/100 mL; PAA), and 10 % fetal calf serum (Sigma).

### Fluorescent labeling of TNF $\alpha$

Recombinant human soluble TNF $\alpha$  (Gibco) was fluorescently labeled with ATTO647N NHS-ester (ATTO-TEC) and recombinant human soluble TNF $\alpha$  (Immunotools) was coupled with Cy5 (GE Healthcare) as described in (Dietz et al. 2013a). A degree of labeling (DOL) of 0.8 was obtained for TNF $\alpha$ -ATTO647N and 1.1 for TNF $\alpha$ -Cy5, as measured by absorption spectroscopy (Cary 100 UV–VIS, Jasco). For both, no loss of biological activity was observed as determined by activity assays (Fig. S1 b). Visualization of exposed amino groups of TNF $\alpha$  for possible NHS-ester binding was performed on a homology model (Fig. S1 c).

### TNF $\alpha$ activity assay

Biological activity of labeled TNF $\alpha$  was measured according to (Dietz et al. 2013a; Greiner et al. 2013; Widera et al. 2006). See the Supplemental Material and Fig. S1 for detailed experimental information.

### Microscopy sample preparation

Hela cells were transiently transfected with Fugene HD Transfection Reagent (Promega). After 24 h, cells were washed in PBS and fixed in 4 % FA for 15 min. For ligand activation, 1 day after transfection cells were washed in ice-cold, serum-free medium three times, followed by 1 h of ligand incubation using 10 nM TNF $\alpha$  (Gibco) labeled with ATTO647N in serum-free medium at 4 °C to prevent receptor internalization. Cells were then washed in PBS and fixed in 4 % FA for 15 min.

### Single-molecule localization microscopy

The principle of sequential dual-color localization microscopy is described elsewhere (Muranyi et al. 2013). Single-molecule and super-resolution PALM imaging was performed on a custom-built wide-field microscope as described in (Dietz et al. 2013a). Briefly, a 647 nm (iBeam smart, Toptica Photonics), a 568 nm (Sapphire 568 LP, Coherent), a 488 nm (Sapphire 488 LP, Coherent), and a 405 nm laser (CUBE 405-50C, Coherent) were combined by appropriate dichroic mirrors (LaserMUX 561-594R, LaserMUX 514-543R, LaserMUX 473-491R, 1064R, LaserMUX 427-25, AHF) and coupled into an inverted microscope (IX71, Olympus) equipped with an 100 $\times$  oil immersion objective (PLAPO 100 $\times$  TIRFM, NA  $\geq$ 1.45, Olympus) and a nose piece to avoid drift. A translational mirror within the illumination pathway allowed for a continuous adjustment of the illumination light field angle from wide-field to total internal reflection (TIR) illumination. The 643, 568, and 488 nm laser were addressed separately by use of an acousto-optic tunable filter (AAOptics). Fluorescent light was collected by the objective and spectrally separated from excitation light by a dichroic mirror (HC Quad 410/504/582/669, AHF) inside the microscope and bandpass filters (ET 525/50 for the green state of tEOS FP, BrightLine HC 590/20 for the red state of tEOS FP; ET 700/75 for ATTO647N, all from AHF) situated in the emission pathway. Filtered fluorescent light was projected on an EMCCD (iXon3, Andor).

Hela cells were briefly washed in PBS and mounted on the microscope. Cells transiently expressing TNF-R1-tEOS were spotted in the green tEOS channel by low light illumination with the 488 nm laser. After TIR illumination was established, the signal of TNF $\alpha$ -ATTO647N

was read out first by recording image sequences of about 5,000 images with a frame rate of 33 Hz under continuous 643 nm laser illumination (2 kW/cm<sup>2</sup>). Lasers and filters were then rearranged for photoactivating and detecting the red state of tEOS-FPs. Image stacks were collected at 10 Hz under constant 568 nm laser excitation (0.5 kW/cm<sup>2</sup>) and adjustable 405 nm laser illumination (0–20 W/cm<sup>2</sup>) for photoactivation until all tEOS-FPs were irreversibly photobleached.

For single-color PALM, transiently expressing Hela cells were spotted in the green channel and imaged in the red channel as described above.

### Single-molecule data processing

Fluorescent label positions were calculated by fitting their point spread functions (PSFs) from single-molecule emissions to a two-dimensional Gaussian intensity distribution using rapidSTORM (Wolter et al. 2012). Coordinates of fluorescent labels were stored in charts, further referred to as localization lists. Based on the localization lists, images were reconstructed using either rapidSTORM or a python-based custom written software (Endesfelder et al. 2014; Jones et al. 2001; Malkusch et al. 2012). The mean localization accuracy of an experiment was evaluated directly from the localization list using a custom written software (Jones et al. 2001; Malkusch et al. 2013). Gold beads were used for spatial alignment of dual-color images.

### Coordinate-based colocalization

The coordinate-based colocalization (CBC) algorithm (Malkusch et al. 2012) was used to identify ligand-bound TNF-R1 molecules at the cell membrane. Briefly, the circular distribution of TNF-R1s around a single receptor was determined from the localization list and compared with the distribution of TNF $\alpha$  molecules around the same receptor by correlation, resulting in a colocalization value for every TNF-R1 localization. By setting a threshold for the colocalization value, the TNF-R1 localizations were pre-sorted into subpopulations of ligand-bound and ligand-free TNF-R1 molecules before further data processing. Colocalization images of TNF-R1 were rendered as described previously (Malkusch et al. 2012).

### Morphological cluster analysis

Super-resolution PALM images were reconstructed by binning localizations into 10 nm pixel and scaling the brightness with the number of localizations. Images were analyzed for clusters using the Analyze Particles ImageJ-plugin in FIJI (Schindelin et al. 2012). Receptor or VSVG accumulations of  $\geq$ 13 cohesive pixels were identified as

valid clusters corresponding to a minimum cluster radius of 20 nm, which exceeds the calculated localization accuracy of all PALM images.

By combining CBC results with cluster analysis, TNF-R1 accumulations were sorted into free (no colocalization) and ligand-bound clusters (predominant colocalization) yielding quantitative information (e.g., cluster radius, localizations per cluster) for both free and ligand-bound receptor species.

#### Microscale thermophoresis

Binding affinities were measured with microscale thermophoresis (MST). Thermophoresis describes the movement of molecules along a temperature gradient (Dühr and Braun 2006). The thermophoretic effect mainly depends on molecular size, charge and solvation shell and allows for precise measurement of binding affinities. For more detail on MST, see (Baaske et al. 2010; Jerabek-Willemsen et al. 2011).

Binding experiments were performed on a commercial MST device (Monolith.NT115, Nanotemper) at 22 °C. For MST, TNF $\alpha$ -Cy5 was diluted in PBS containing 0.2 M NaCl and 0.05 % Tween (Sigma) with a pH of 7.4 to a final concentration of 0.5 nM and a total volume of 100  $\mu$ L. The ectodomain of the TNF-R1 (ProSpec) was added to different final concentration in a range, where binding is expected (40 pM–2.8  $\mu$ M). All binding reactions were performed in reaction tubes supplied by Nanotemper and incubated at room temperature until the reaction equilibrium was reached. The protein solution was transferred to standard capillaries (Nanotemper) and transferred to the MST instrument (Monolith.NT115, Nanotemper). Final average binding data with SEM were obtained by averaging 20 binding experiments. The dissociation constant  $K_d$  was obtained by fitting the binding curve with the Hill function.

$$\text{Bound ligand} = \frac{[\text{receptor}]}{K_d + [\text{receptor}]}$$

Here, bound ligand is the fraction of bound ligand in percent and [receptor] is the receptor concentration.

#### Network-free rule-based modeling

Receptor organization and ligand binding at the cell membrane were modeled by a varied trivalent ligand/bivalent–receptor interaction model using the free and open-source Network-Free stochastic simulator (NFsim) (Sneddon et al. 2011).

#### Statistical analysis

Respective  $N$  values are noted in the figure captions. Statistical analysis was performed with OriginPro 9 (OriginLab).

For statistical significance testing,  $P$  values were computed with Mann–Whitney  $U$  tests and are indicated in the figures.

## Results

### Single-molecule localization microscopy of TNF-R1 and TNF $\alpha$

TNF-R1 expression levels were found to be in the range of 1,500–2,900 receptors on the cell membrane of HeLa cells (Dietz et al. 2013b). Corresponding receptor densities challenge the applicability of diffraction limited light microscopy to resolve single-receptor structures. Single-molecule localization imaging techniques including PALM can overcome this barrier, thereby allowing for investigating receptor organization on intact cells. We tagged TNF-R1 with the photoconvertible fluorescent protein tdEOS and applied PALM on HeLa cells transiently transfected with TNF-R1-tdEOS to resolve receptor structures on the basal membrane with super-resolution. Figure 1a shows the reconstructed super-resolution image of TNF-R1-tdEOS at the lower cell membrane. PALM image resolution was assessed from the experimental localization precision. A mean localization precision of  $(14 \pm 3 \text{ SD})$  nm was obtained for TNF-R1 images ( $N = 5$ ) ensuring TNF-R1 observation with near-molecular accuracy.

TNF-R1 is suggested to undergo reorganization toward a signaling state in response to ligand activation. We investigated TNF $\alpha$ -binding to TNF-R1-tdEOS using single-molecule localization microscopy. For in vitro experiments, TNF $\alpha$  applied in the low nM to pM concentration range is known to be sufficient for receptor signal induction e.g., initiation of apoptosis, NF- $\kappa$ B-activation (Nelson et al. 2002). Under these conditions, ligand-binding sites of TNF-R1 are far from being saturated (Dietz et al. 2013a). To spatially distinguish ligand-bound TNF-R1-tdEOS complexes from free TNF-R1-tdEOS under near-physiological conditions, ATTO647N-labeled TNF $\alpha$  (10 nM) was applied to the cells prior to imaging. Ligand incubation lasted 1 h during which cells were cooled to avoid ligand-induced receptor internalization (Schneider-Brachert et al. 2004). Dual-color super-resolution images of TNF $\alpha$ -ATTO647N (Fig. 1b, c, magenta) and TNF-R1-tdEOS (Fig. 1b, c, green) at the basal membrane of fixed HeLa cells showed specific colocalization of certain receptor complexes with TNF $\alpha$ , indicating ligand–receptor binding (Fig. 1b, c).

### Quantitative PALM of TNF-R1 after TNF $\alpha$ -binding

In reconstructed PALM images, TNF-R1 assembles in defined nanoscale-sized units. These receptor clusters were

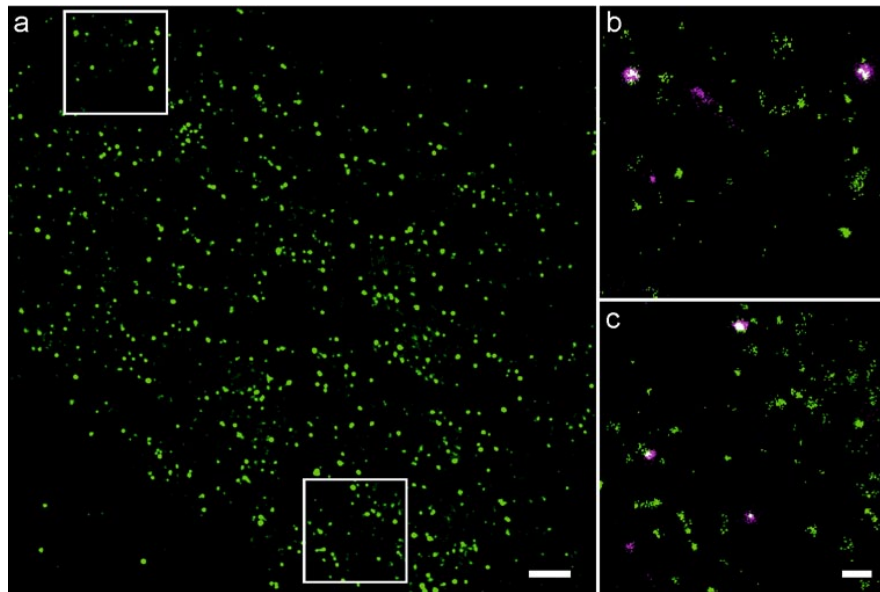


**Fig. 1** Single-molecule imaging of TNF $\alpha$  and its receptor TNF-R1-tdEOS at the cell surface of HeLa cells stimulated with TNF $\alpha$ -ATTO647N for 1 h at 4 °C (scale bar 1  $\mu$ m). **a** Super-resolution

PALM image of TNF-R1-tdEOS distribution. **b, c** Magnifications of the boxed regions in **a** show dual-color images of TNF-R1-tdEOS in green and TNF $\alpha$ -ATTO647N in magenta (scale bar 250 nm)

evaluated for size and localizations per cluster with the Analyze Particles ImageJ-plugin (Schindelin et al. 2012). Additionally, localization lists of corresponding TNF $\alpha$  and TNF-R1 images (Fig. 2a) were subjected to coordinate-based colocalization analysis assigning a colocalization value to each localization. The colocalization value-based image demonstrates spatial correlation of a TNF-R1-tdEOS cluster with TNF $\alpha$ , directly determined from positive colocalization values (Fig. 2b).

For receptor PALM images, colocalization values were used to sort clusters into two subgroups: free TNF-R1-tdEOS clusters and receptor clusters bound to TNF $\alpha$ , which we presume to be activated. We compared cluster radii obtained from receptor PALM images of unstimulated (TNF-R1) and ligand-stimulated HeLa cells after sorting into free and ligand-bound TNF-R1 clusters (Fig. 2c, d). Cluster size and localizations per cluster distributions of free TNF-R1 were similar for unstimulated cells and ligand-stimulated cells (Fig. S2), validating our CBC-based sorting approach and morphological cluster analysis. Ligand binding led to a slight increase in TNF-R1-tdEOS cluster size and a distinguished peak with a fitted maximum at 33 nm in the radii distribution (Fig. 2d). Notably, we rarely observed the formation of large receptor aggregates, corroborating studies of TNF-R1-Fas chimera, Fas and death receptor 5, where incubations at 37 °C but not 4 °C lead to extended ligand-receptor oligomerization (Krippner-Heidenreich et al. 2002; Siegel et al. 2004; Valley et al. 2012).

Next, we evaluated the number of tdEOS localizations per receptor cluster, which correlates with the TNF-R1-tdEOS copy number per assembly site. The ligand-free clusters feature a single peak distribution, whereas ligand-bound receptors assemble in higher-order arrangements with two maxima corresponding to about 1.5 and 3 times the amount of receptors per cluster as compared to free TNF-R1-tdEOS. These findings suggest receptor reorganization toward oligomeric states triggered by the ligand-binding event even at 4 °C. Since cluster sizes only increase marginally, we conclude that ligand-induced TNF-R1 assemblies primarily appear as tightly packed units. Large clusters with more than 200 localizations were observed 2.5 times more frequently for ligand-bound TNF-R1-tdEOS compared with ligand-free clusters (data not shown).

To further quantify TNF-R1-tdEOS amounts in clusters, we used the vesicular stomatitis virus G protein (VSVG) as a calibration protein. VSVG localizes at the cell membrane as a predominantly trimeric transmembrane protein as predicted by biochemical studies (Zagouras and Rose 1993). Pair-correlation analysis of PALM data, namely using the distance distribution of arbitrary pairs of localizations for fluorophore overcounting correction, experimentally confirmed VSVG trimerization on the cell membrane by direct protein counting with PALM (Sengupta et al. 2011). VSVG as calibration protein has further the advantage of residing in a similar cellular environment as TNF-R1, since the photochemical behavior of many fluorescent probes is majorly



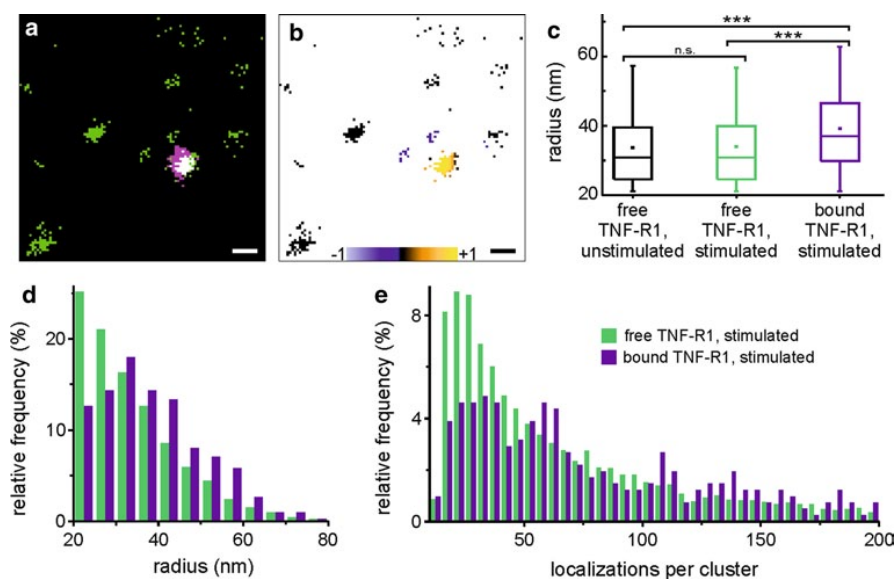


**Fig. 2** Quantitative analysis of ligand–receptor colocalization reveals reorganization of spatially correlated TNF-R1 with TNF $\alpha$ . **a** Binary two-color image of TNF-R1-tdEOS (green) colocalizing with its ligand TNF $\alpha$ -ATTO647N (magenta). **b** Corresponding single-molecule colocalization image obtained from CBC-analysis (scale bar 100 nm). The color-code ranges from high colocalization (+1) to anticolocalization (–1) and allows for receptor sorting into ligand-bound and ligand-free subgroups on a single-molecule level. Morphological cluster analysis of quantitative PALM images yields radius

and single-receptor localizations per TNF-R1 cluster for unstimulated HeLa cells (free TNF-R1, unstimulated,  $N = 4$ ) and ligand-free/ligand-bound TNF-R1 clusters for stimulated cells (free/bound TNF-R1, stimulated,  $N = 8$ ). **c** Box plot of receptor cluster radius displays 5th percentile, 25th percentile, median (line), mean (square), 75th percentile, and 95th percentile ( $P$  values: n.s.,  $P > 0.05$ ;  $*0.05 > P > 0.01$ ;  $**0.01 > P > 0.001$ ;  $***0.001 > P$ ). Frequency distributions of cluster radius (**d**) and localizations per cluster (**e**)

influenced by environmental factors as well as buffer conditions and excitation power (Endesfelder et al. 2011).

We transiently expressed VSVG tagged with tEOS in HeLa cells and performed PALM under equal experimental conditions as TNF-R1 imaging. PALM images of VSVG-tdEOS were subjected to morphological cluster analysis, yielding a distinct peak in the localizations per cluster distribution (Fig. S3), which we assume stems from VSVG trimers, resulting in 10–11 localizations per tEOS molecule. The peak is situated at about 1.5 times the value of that of TNF-R1-tdEOS clusters (Fig. S3), inferring a primarily dimeric TNF-R1 pre-assembly. TNF $\alpha$ -bound TNF-R1 clusters exhibit one maximum at similar values and a second one at about twice as many localizations per cluster, arguing for stable receptor organizations as ligand-bound trimeric complexes and higher-order organizations with five to six receptors per cluster.

#### Binding affinity of TNF-R1 for TNF $\alpha$

Determination of the TNF-R1 binding affinity to its ligand TNF $\alpha$  is crucial for interpretation of the receptor activation event. For example, computational models can only make reliable predictions, when the initial input parameters, e.g.,

dissociation constants, are correct. For TNF $\alpha$ , reported binding affinities in different cell lines and in aqueous solution range from 0.003 to 290 nM (Day et al. 2012; Dietz et al. 2013a; Kull et al. 1985; MacEwan 2002; Yoshida et al. 2006). We therefore investigated receptor binding to TNF $\alpha$  labeled with Cy5 using MST. Binding experiments in solution using the purified ectodomain of TNF-R1 clearly revealed binding of TNF $\alpha$ -Cy5 to TNF-R1 (Fig. 3). Fitting of the sigmoidal binding curve yielded a dissociation constant  $K_D$  of ( $16.6 \pm 3.3$ ) nM, which is in good agreement with the binding affinity of ( $15.69 \pm 0.03$ ) nM measured directly on the membrane of intact HeLa cells (Dietz et al. 2013a). These findings suggest that the obtained moderate-affinity binding reflects the receptor–ligand system as it was confirmed by two independent methods.

#### Modeling TNF-R1-TNF $\alpha$ -binding and cluster formation

Modeling of receptor–ligand interactions at the cell membrane helps to interpret experimental results and allows for predicting receptor–ligand assembly and stable organizations. A potential TNF-R1 dimerization complicates matters: Dimeric receptors can link ligand-bound TNF-R1 complexes to larger oligomeric structures and should

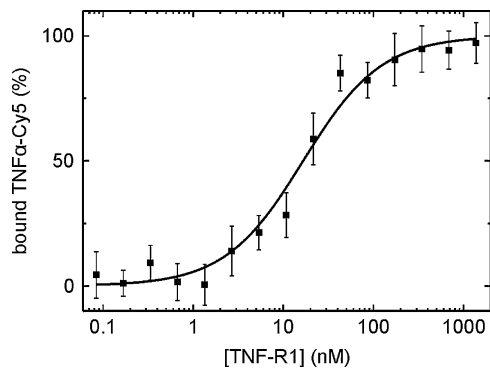


**Fig. 3** Moderate-binding affinity of TNF-R1 ectodomain for its ligand TNF $\alpha$  determined by microscale thermophoresis. Data from  $N = 20$  experiments were normalized to the fraction of bound ligand and averaged. The *sigmoidal shape* implies ligand binding. By fitting with the Hill function, a  $K_d$  of  $(16.6 \pm 3.3)$  nM was obtained

be considered in computational models. The process of ligand–receptor binding and cluster formation results in a substantial number of molecular compounds and interactions. This combinatorial complexity of molecular interactions complicates predictive modeling of biological systems. To overcome this obstacle, we use NFsim, where a biologically intuitive representation based on molecular objects, here receptor and ligand entities, with specific binding and modification sites is applied (Sneddon et al. 2011). These sites are acted on directly by defined reaction rules specified in the BioNetGen language. By network-free rule-based modeling, stochastic results are obtained without expanding the system into equations. Therefore, NFsim performance stays unaffected by the size of the

reaction network rendering it ideal for modeling polymerization and aggregation processes.

The stoichiometry of our model features TNF $\alpha$  trimers exhibiting three receptor binding sites (Banner et al. 1993; Eck and Sprang 1989). Based on our own results and published structural data (Naismith et al. 1995), receptor pre-assembly as TNF-R1 dimers is permitted. We assess TNF-R1–TNF $\alpha$ –binding and subsequent receptor oligomerization by two models. The first model (model 1) postulates that only receptor dimers are able to bind ligand molecules (Fig. 4, without insert), as supported in the literature (Chan 2007; Winkel et al. 2012). The second model (model 2) permits ligand binding by both monomeric and dimeric receptors (complete Fig. 4). Both models allow for all kinds of aggregation and cluster formation but also incorporate TNF-R1 dimer decay, when ligand-bound. Dissociation constants  $K_{PLAD}$  and  $K_{LIG}$  determine TNF-R1 dimerization and ligand-binding kinetics, respectively. It should be noted that solely the initial steps of TNF-R1 activation are modeled. Internalization, adapter protein recruitment or a conformational change of TNF-R1 as postulated by (Lewis et al. 2012; Richter et al. 2013) are not considered. All modeling was performed until the simulation system reached a steady state.

TNF-R1 organization after TNF $\alpha$  binding at equilibrium conditions

First, we identified input parameters for the two models. TNF-R1 numbers were obtained from quantitative PALM data and converted to an initial receptor concentration  $R_0$ . TNF $\alpha$  concentration was given by the experimental conditions as  $L_0 = 10$  nM. The dissociation constants

**Fig. 4** Proposed models for TNF-R1-binding of TNF $\alpha$  and oligomerization. For model 1, receptor dimers exclusively bind TNF $\alpha$ , but may decay after ligand binding. Model 2 includes ligand binding by TNF-R1 monomers. Both models allow for ligand–receptor aggregation. TNF-R1-bound TNF $\alpha$  was obtained from homology modeling and visualized with PyMOL (PDB: 1FT4, 1TNR)

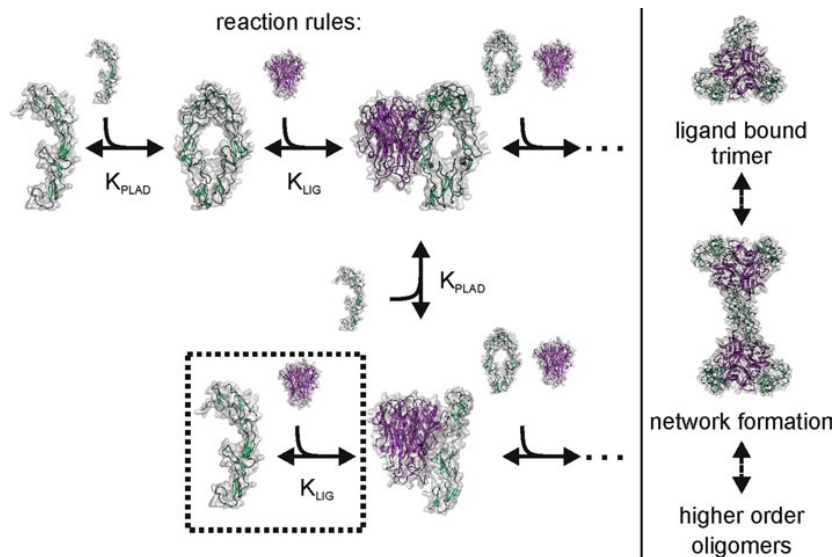


**Table 1** Input parameters for model simulation

Parameter	Value
$[R]_0$	$6 \times 10^{-7} \text{ M}^a$
$[L]_0$	$1 \times 10^{-8} \text{ M}^a$
$K_{\text{PLAD}}$	$10^{-8}$ – $10^{-4} \text{ M}^b$
$k_{\text{PLAD,on}}$	$6 \times 10^3 \text{ M}^{-1} \text{ min}^{-1c}$
$K_{\text{LIG}}$	$10^{-12}$ – $10^{-6} \text{ M}^b$
$k_{\text{LIG,on}}$	$1.3 \times 10^7 \text{ M}^{-1} \text{ min}^{-1c}$

<sup>a</sup> Determined from experimental data

<sup>b</sup> Parameter screened for model analysis

<sup>c</sup> Taken from (Winkel et al. 2012)

for dimerization  $K_{\text{PLAD}}$  and ligand-binding  $K_{\text{LIG}}$  were screened by the model within a range relevant for binding. For example, screened  $K_{\text{LIG}}$  starts in the micromolar

range, proceeding to picomolar values as predicted by radioligand-binding studies (MacEwan 2002). The respective rate constants  $k_{i,\text{on}}$  ( $i = \text{PLAD, LIG}$ ) were extracted from published data (Winkel et al. 2012). With  $k_{i,\text{off}} = K_i \cdot k_{i,\text{on}}$ , all necessary input parameters were determined. Reactions were modeled in a constant reaction volume given by the space between the lower cell membrane and the microscopic cover slip further described in the Supplemental Material. For the sake of simplicity, physical parameters were eliminated so that both models had a common, dimensionless form.

For model evaluation, we analytically assessed dimerization kinetics of TNF-R1 for exemplary values of  $K_{\text{PLAD}} = 10 \text{ nM}$  and  $R_0 = 6 \times 10^{-7} \text{ M}$  as shown in Table 1. We calculated equilibrium concentrations and obtained  $7.3 \times 10^{-8} \text{ M}$  receptor monomers and  $2.6 \times 10^{-7} \text{ M}$  dimers, matching the equilibrium values

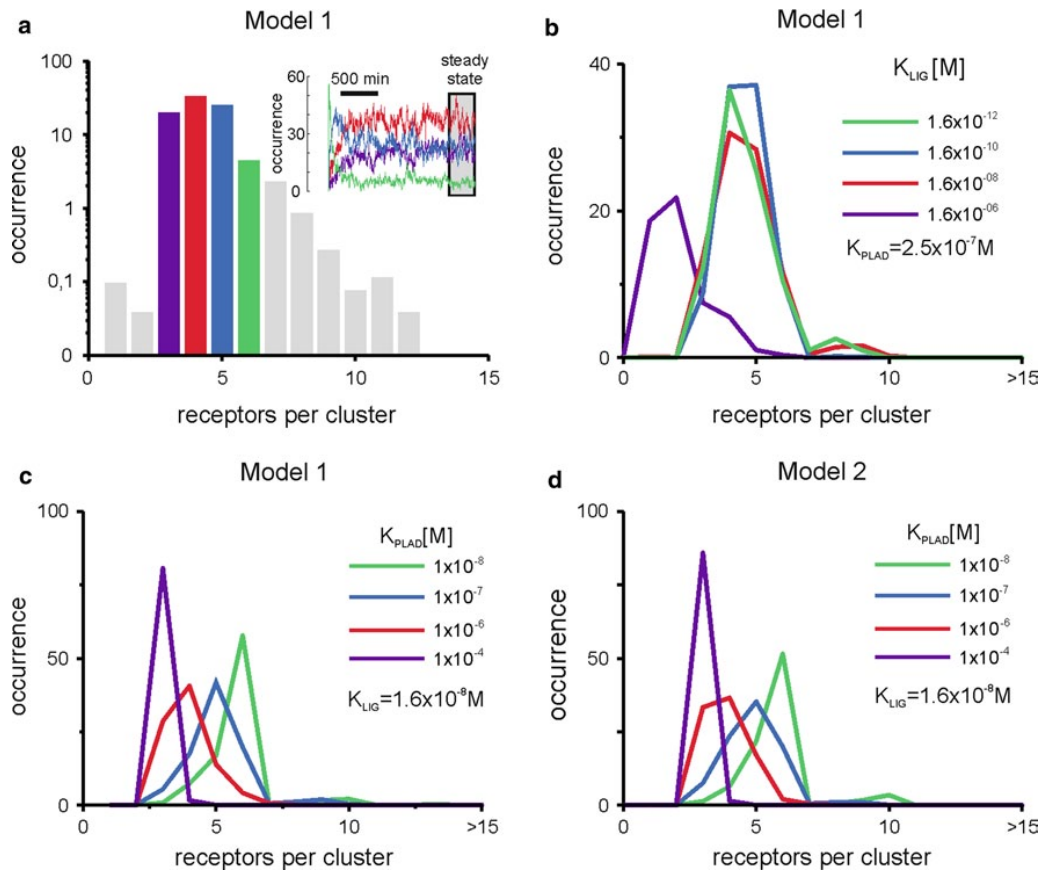


**Fig. 5** TNF $\alpha$ -induced TNF-R1 oligomerization by network-free rule-based modeling. TNF $\alpha$ -induced TNF-R1 oligomerization up to 20 receptors per complex was simulated until equilibrium was reached. **a** Clusters with equal receptor amounts were grouped and their concentration time traces are plotted (*inset*). The distribution of receptors per

cluster was obtained by averaging the steady state population (four species are highlighted by *color code*). **b–d** Parameter scans of  $K_{\text{LIG}}$  and  $K_{\text{PLAD}}$  for model 1 and 2 result in different receptors per cluster distributions favoring three to six receptors per cluster



when modeled with NFsim (see Supplemental Material for detailed information).

Modeling of receptor aggregation after ligand binding was performed to maximum aggregate sizes composed of 20 TNF-R1. Simulations of model 1 and 2 were evaluated for TNF-R1 amounts per ligand–receptor complex at equilibrium conditions. Therefore, we grouped complexes with the same amount of receptors into 20 species (comprising 1–20 receptors) and computed species-specific concentrations over time. When steady states were reached for all species, time averages of each species were plotted as a histogram (Fig. 5a). Species distributions were generated for different sets of scanning parameters  $K_{LIG}$  and  $K_{PLAD}$  for both models (Fig. 5b–d). For a fixed  $K_{PLAD} = 250$  nM, clusters with more than three receptors become favorable as soon as  $K_{PLAD}$  exceeds  $K_{LIG}$  shifting the maximum to higher-order structures, for which TNF-R1 dimer associated ligand binding is essential (Fig. 5b). Further increase of the ligand-binding affinity neither affects the distribution nor promotes oligomerization. The same holds true for model 2 (data not shown). We therefore decided to fix the TNF-R1-TNF $\alpha$  dissociation constant at  $K_{LIG} = 16$  nM, a value obtained on intact cells by single-molecule studies (Dietz et al. 2013a) and reconfirmed in vitro by thermophoresis (Fig. 3). Stepwise screening of  $K_{PLAD}$  in the physiological range of  $10^{-4}$ – $10^{-8}$  M (Lee et al. 2005) reveals similar behaviors for model 1 and 2 (Fig. 5c, d). Decreasing  $K_{PLAD}$  values result in a broader species distribution, shifting to higher-order organization forms. Overall, both models indicate stable complex formation predominantly consisting of three to six TNF-R1 per cluster.

## Discussion

TNF superfamily receptor organization at the cell membrane is still a controversial topic in the scientific community (Chan et al. 2000; Henkler et al. 2005; Jackson and Lai 2004; Krippner-Heidenreich et al. 2002; Lewis et al. 2012; Naismith et al. 1995; Ozsoy et al. 2008; Richter et al. 2013; Siegel et al. 2004; Valley et al. 2012; Winkel et al. 2012). Although addressed by several recent studies, the signaling competent receptor complex is only poorly understood. In this regard, ligand-induced supramolecular clusters active dimer formation as well as a trimeric receptor complex are discussed.

Our study elucidates TNF-R1 pre-assembly and reorganization after ligand binding. Quantitative single-molecule localization microscopy reveals TNF-R1 dimerization at the membrane of intact HeLa cells in the absence of its ligand TNF $\alpha$ . After ligand application, we observed cluster formation with 3–6 receptors, which we confirmed experimentally as well as theoretically. Our models indicate that

clusters comprising more than four TNF-R1 are in favor, when the dimerization dissociation constant ( $K_{PLAD}$ ) is sufficiently low, e.g., in the range of 1–10  $\mu$ M as obtained for TRAIL receptors (Lee et al. 2005) or lower. This necessitates at least one TNF-R1 dimer bound to TNF $\alpha$  within the cluster. We therefore assume that ligand-bound TNF-R1 dimers are required for a signaling competent receptor complex. This hypothesis is in accordance with the potential role of conformational changes of the ligand-bound receptor dimer for inducing receptor signaling, as postulated for TNF superfamily receptors (Lewis et al. 2012; Ozsoy et al. 2008; Richter et al. 2013; Valley et al. 2012). Demonstrably, large oligomeric structures were not observed for the chosen experimental and modeling conditions.

In conclusion, our study indicates that TNF-R1 pre-assembled as dimer forms oligomers of higher order after ligand binding, thereby emphasizing the enormous potential of quantitative single-molecule data as input values for computational models for improvement and extension of current molecular systems biology approaches.

**Acknowledgments** We thank Markus Braner for help with microscale thermophoresis measurements. M. Heilemann, F. Fricke and S. Malkusch acknowledge the financial support by the German Ministry of Education and Research (BMBF, Grant 336314) and the cluster of excellence “Macromolecular Complexes” (CEF, DFG cluster of excellence (EXC 115)). T. Dandekar and G. Wangorsch acknowledge the financial support by the German Science Foundation (DFG, Da 208/12-1 and SFB688/A2). D. Widera, C. Kaltschmidt, B. Kaltschmidt and J. Greiner were supported by the BMBF and Cassella Med, Cologne.

## References

- Annibale P, Vanni S, Scarselli M, Rothlisberger U, Radenovic A (2011) Quantitative photo activated localization microscopy: unraveling the effects of photoblinking. *PLoS One* 6:e22678. doi:10.1371/journal.pone.0022678
- Baaske P, Wienken CJ, Reineck P, Duhr S, Braun D (2010) Optical thermophoresis for quantifying the buffer dependence of aptamer binding. *Angew Chem Int Ed Engl* 49:2238–2241. doi:10.1002/ange.200903998
- Banner DW, D’Arcy A, Janes W, Gentz R, Schoenfeld H-J, Broger C, Loetscher H, Lesslauer W (1993) Crystal structure of the soluble human 55 kd TNF receptor-human TNF $\beta$  complex: implications for TNF receptor activation. *Cell* 73:431–445. doi:10.1016/0092-8674(93)90132-A
- Betzig E, Patterson GH, Sougrat R, Lindwasser OW, Olenych S, Bonifacino JS, Davidson MW, Lippincott-Schwartz J, Hess HF (2006) Imaging intracellular fluorescent proteins at nanometer resolution. *Science* 313:1642–1645. doi:10.1126/science.1127344
- Boschert V, Krippner-Heidenreich A, Branschädel M, Tepperink J, Aird A, Scheurich P (2010) Single chain TNF derivatives with individually mutated receptor binding sites reveal differential stoichiometry of ligand receptor complex formation for TNFR1 and TNFR2. *Cell Signal* 22:1088–1096. doi:10.1016/j.cellsig.2010.02.011
- Brockhaus M, Schoenfeld HJ, Schlaeger EJ, Hunziker W, Lesslauer W, Loetscher H (1990) Identification of two types of tumor

- necrosis factor receptors on human cell lines by monoclonal antibodies. *Proc Natl Acad Sci* 87:3127–3131
- Chan FK (2007) Three is better than one: pre-ligand receptor assembly in the regulation of TNF receptor signaling. *Cytokine* 37:101–107. doi:10.1016/j.cyto.2007.03.005
- Chan FK, Chun HJ, Zheng L, Siegel RM, Bui KL, Lenardo MJ (2000) A domain in TNF receptors that mediates ligand-independent receptor assembly and signaling. *Science* 288:2351–2354. doi:10.1126/science.288.5475.2351
- Day ES, Cote SM, Whitty A (2012) Binding efficiency of protein–protein complexes. *Biochemistry* 51:9124–9136. doi:10.1021/bi301039t
- Dietz MS, Fricke F, Krüger CL, Niemann HH, Heilemann M (2013a) Receptor–ligand interactions: binding affinities studied by single-molecule and super-resolution microscopy on intact cells. *ChemPhysChem*. doi:10.1002/cphc.201300755
- Dietz MS, Haße D, Ferraris DM, Göhler A, Niemann HH, Heilemann M (2013b) Single-molecule photobleaching reveals increased MET receptor dimerization upon ligand binding in intact cells. *BMC Biophys* 6:6. doi:10.1186/2046-1682-6-6
- Duhr S, Braun D (2006) Why molecules move along a temperature gradient. *Proc Natl Acad Sci* 103:19678–19682. doi:10.1073/pnas.0603873103
- Eck MJ, Sprang SR (1989) The structure of tumor necrosis factor- $\alpha$  at 2.6 Å resolution. *J Biol Chem* 264:17595–17605
- Endesfelder U, Malkusch S, Flottmann B, Mondry J, Liguzinski P, Verwee PJ, Heilemann M (2011) Chemically induced photo-switching of fluorescent probes—a general concept for super-resolution microscopy. *Molecules* 16:3106–3118. doi:10.3390/molecules16043106
- Endesfelder U, Malkusch S, Fricke F, Heilemann M (2014) A simple method to estimate the average localization precision of a single-molecule localization microscopy experiment. *Histochem Cell Biol*. doi:10.1007/s00418-014-1192-3
- Gould TJ, Hess ST, Bewersdorf J (2012) Optical nanoscopy: from acquisition to analysis. *Annu Rev Biomed Eng* 14:231–254. doi:10.1146/annurev-bioeng-071811-150025
- Greiner JF-W, Müller J, Zeuner M-T, Hauser S, Seidel T, Klenke C, Grunwald L-M, Schomann T, Widera D, Sudhoff H, Kaltschmidt B, Kaltschmidt C (2013) 1,8-Cineol inhibits nuclear translocation of NF- $\kappa$ B p65 and NF- $\kappa$ B-dependent transcriptional activity. *Biochim Biophys Acta* 1833:2866–2878. doi:10.1016/j.bbamcr.2013.07.001
- Grell M, Douni E, Wajant H, Löhden M, Clauss M, Maxeiner B, Georgopoulos S, Lesslauer W, Kollias G, Pfizenmaier K, Scheurich P (1995) The transmembrane form of tumor necrosis factor is the prime activating ligand of the 80 kDa tumor necrosis factor receptor. *Cell* 83:793–802. doi:10.1016/0092-8674(95)90192-2
- Heidbreder M, Zander C, Malkusch S, Widera D, Kaltschmidt B, Kaltschmidt C, Nair D, Choquet D, Sibarita J-B, Heilemann M (2012) TNF- $\alpha$  influences the lateral dynamics of TNF receptor I in living cells. *Biochim Biophys Acta* 1823:1984–1989. doi:10.1016/j.bbamcr.2012.06.026
- Henkler F, Behrle E, Dennehy KM, Wicovsky A, Peters N, Warnke C, Pfizenmaier K, Wajant H (2005) The extracellular domains of FasL and Fas are sufficient for the formation of supramolecular FasL–Fas clusters of high stability. *J Cell Biol* 168:1087–1098. doi:10.1083/jcb.200501048
- Hohmann H, Remy R, Brockhaus M, van Loon APGM (1989) Two different cell types have different major receptors for human tumor necrosis factor (TNF $\alpha$ ). *J Biol Chem* 264:14927–14934
- Hymowitz SG, Christinger HW, Fuh G, Ultsch M, O’Connell M, Kelley RF, Ashkenazi A, de Vos AM (1999) Triggering cell death. *Mol Cell* 4:563–571. doi:10.1016/S1097-2765(00)80207-5
- Jackson TL, Lai R (2004) A mathematical model of receptor-mediated apoptosis: dying to know why FasL is a trimer. *Math Biosci Eng* 1:325–338. doi:10.3934/mbe.2004.1.325
- Jerabek-Willemsen M, Wienken CJ, Braun D, Baaske P, Duhr S (2011) Molecular interaction studies using microscale thermophoresis. *Assay Drug Dev Technol* 9:342–353. doi:10.1089/adt.2011.0380
- Jones E, Oliphant T, Peterson P et al (2001) SciPy: open source scientific tools for Python. <http://www.scipy.org/>
- Krippner-Heidenreich A, Tübing F, Bryde S, Willi S, Zimmermann G, Scheurich P (2002) Control of receptor-induced signaling complex formation by the kinetics of ligand/receptor interaction. *J Biol Chem* 277:44155–44163. doi:10.1074/jbc.M207399200
- Kull FC, Jacobs S, Cuatrecasas P (1985) Cellular receptor for 125I-labeled tumor necrosis factor: specific binding, affinity labeling, and relationship to sensitivity. *Proc Natl Acad Sci* 82:5756–5760
- Lando D, Endesfelder U, Berger H, Subramanian L, Dunne PD, McColl J, Klenerman D, Carr AM, Sauer M, Allshire RC, Heilemann M, Laue ED (2012) Quantitative single-molecule microscopy reveals that CENP-A(Cnp1) deposition occurs during G2 in fission yeast. *Open Biol* 2:120078. doi:10.1098/rsob.120078
- Lee H-W, Lee S-H, Lee H-W, Ryu Y-W, Kwon M-H, Kim Y-S (2005) Homomeric and heteromeric interactions of the extracellular domains of death receptors and death decoy receptors. *Biochem Biophys Res Commun* 330:1205–1212. doi:10.1016/j.bbrc.2005.03.101
- Lee S-H, Shin JY, Lee A, Bustamante C (2012) Counting single photoactivatable fluorescent molecules by photoactivated localization microscopy (PALM). *Proc Natl Acad Sci* 109:17436–17441. doi:10.1073/pnas.1215175109
- Lewis AK, Valley CC, Sachs JN (2012) TNFR1 signaling is associated with backbone conformational changes of receptor dimers consistent with overactivation in the R92Q TRAPS mutant. *Biochemistry* 51:6545–6555. doi:10.1021/bi3006626
- MacEwan DJ (2002) TNF ligands and receptors—a matter of life and death. *Br J Pharmacol* 135:855–875. doi:10.1038/sj.bjp.0704549
- Malkusch S, Endesfelder U, Mondry J, Gelléri M, Verwee PJ, Heilemann M (2012) Coordinate-based colocalization analysis of single-molecule localization microscopy data. *Histochem Cell Biol* 137:1–10. doi:10.1007/s00418-011-0880-5
- Malkusch S, Muranyi W, Müller B, Kräusslich H-G, Heilemann M (2013) Single-molecule coordinate-based analysis of the morphology of HIV-1 assembly sites with near-molecular spatial resolution. *Histochem Cell Biol* 139:173–179. doi:10.1007/s00418-012-1014-4
- Muranyi W, Malkusch S, Müller B, Heilemann M, Kräusslich H-G (2013) Super-resolution microscopy reveals specific recruitment of HIV-1 envelope proteins to viral assembly sites dependent on the envelope C-terminal tail. *PLoS Pathog* 9:e1003198. doi:10.1371/journal.ppat.1003198
- Naismith JH, Devine TQ, Brandhuber BJ, Sprang SR (1995) Crystallographic evidence for dimerization of unliganded tumor necrosis factor receptor. *J Biol Chem* 270:13303–13307. doi:10.1074/jbc.270.22.13303
- Nelson G, Paraoan L, Spiller DG, Wilde GJC, Browne MA, Djali PK, Unitt JF, Sullivan E, Floettmann E, White MRH (2002) Multi-parameter analysis of the kinetics of NF- $\kappa$ B signalling and transcription in single living cells. *J Cell Sci* 115:1137–1148
- Ori A, Banterle N, Iskar M, Andrés-Pons A, Escher C, Khanh Bui H, Sparks L, Solis-Mezarino V, Rinner O, Bork P, Lemke EA, Beck M (2013) Cell type-specific nuclear pores: a case in point for context-dependent stoichiometry of molecular machines. *Mol Syst Biol* 9:648. doi:10.1038/msb.2013.4
- Ozsoy HZ, Sivasubramanian N, Wieder ED, Pedersen S, Mann DL (2008) Oxidative stress promotes ligand-independent

- and enhanced ligand-dependent tumor necrosis factor receptor signaling. *J Biol Chem* 283:23419–23428. doi:[10.1074/jbc.M802967200](https://doi.org/10.1074/jbc.M802967200)
- Presley JF, Cole NB, Schroer TA, Hirschberg K, Zaal KJ, Lippincott-Schwartz J (1997) ER-to-Golgi transport visualized in living cells. *Nature* 389:81–85. doi:[10.1038/38001](https://doi.org/10.1038/38001)
- Puchner EM, Walter JM, Kasper R, Huang B, Lim WA (2013) Counting molecules in single organelles with superresolution microscopy allows tracking of the endosome maturation trajectory. *Proc Natl Acad Sci* 110:16015–16020. doi:[10.1073/pnas.1309676110](https://doi.org/10.1073/pnas.1309676110)
- Richter F, Liebig T, Guenzi E, Herrmann A, Scheurich P, Pfizenmaier K, Kontermann RE (2013) Antagonistic TNF receptor one-specific antibody (ATROSAB): receptor binding and in vitro bioactivity. *PLoS One* 8:e72156. doi:[10.1371/journal.pone.0072156](https://doi.org/10.1371/journal.pone.0072156)
- Schindelin J, Arganda-Carreras I, Frise E, Kaynig V, Longair M, Pietzsch T, Preibisch S, Rueden C, Saalfeld S, Schmid B, Tinevez J-Y, White DJ, Hartenstein V, Eliceiri K, Tomancak P, Cardona A (2012) Fiji: an open-source platform for biological-image analysis. *Nat Methods* 9:676–682. doi:[10.1038/nmeth.2019](https://doi.org/10.1038/nmeth.2019)
- Schneider-Brachert W, Tchikov V, Neumeyer J, Jakob M, Winoto-Morbach S, Held-Feindt J, Heinrich M, Merkel O, Ehrenschwender M, Adam D, Mentlein R, Kabelitz D, Schütze S (2004) Compartmentalization of TNF receptor 1 signaling: internalized TNF receptors as death signaling vesicles. *Immunity* 21:415–428. doi:[10.1016/j.immuni.2004.08.017](https://doi.org/10.1016/j.immuni.2004.08.017)
- Sengupta P, Jovanovic-Taliman T, Skoko D, Renz M, Veatch SL, Lippincott-Schwartz J (2011) Probing protein heterogeneity in the plasma membrane using PALM and pair correlation analysis. *Nat Methods* 8:969–975. doi:[10.1038/nmeth.1704](https://doi.org/10.1038/nmeth.1704)
- Siegel RM, Muppidi JR, Sarker M, Lobito A, Jen M, Martin D, Straus SE, Lenardo MJ (2004) SPOTS: signaling protein oligomeric transduction structures are early mediators of death receptor-induced apoptosis at the plasma membrane. *J Cell Biol* 167:735–744. doi:[10.1083/jcb.200406101](https://doi.org/10.1083/jcb.200406101)
- Sneddon MW, Faeder JR, Emonet T (2011) Efficient modeling, simulation and coarse-graining of biological complexity with NFsim. *Nat Methods* 8:177–183. doi:[10.1038/nmeth.1546](https://doi.org/10.1038/nmeth.1546)
- Valley CC, Lewis AK, Mudaliar DJ, Perlmutter JD, Braun AR, Karim CB, Thomas DD, Brody JR, Sachs JN (2012) Tumor necrosis factor-related apoptosis-inducing ligand (TRAIL) induces death receptor 5 networks that are highly organized. *J Biol Chem* 287:21265–21278. doi:[10.1074/jbc.M111.306480](https://doi.org/10.1074/jbc.M111.306480)
- Vandenabeele P, Galluzzi L, Vanden Berghe T, Kroemer G (2010) Molecular mechanisms of necroptosis: an ordered cellular explosion. *Nat Rev Mol Cell Biol* 11:700–714. doi:[10.1038/nrm2970](https://doi.org/10.1038/nrm2970)
- Wajant H, Scheurich P (2011) TNFR1-induced activation of the classical NF- $\kappa$ B pathway. *FEBS J* 278:862–876. doi:[10.1111/j.1742-4658.2011.08015.x](https://doi.org/10.1111/j.1742-4658.2011.08015.x)
- Widera D, Mikenberg I, Elvers M, Kaltschmidt C, Kaltschmidt B (2006) Tumor necrosis factor alpha triggers proliferation of adult neural stem cells via IKK/NF-kappaB signaling. *BMC Neurosci* 7:64. doi:[10.1186/1471-2202-7-64](https://doi.org/10.1186/1471-2202-7-64)
- Winkel C, Neumann S, Surulescu C, Scheurich P (2012) A minimal mathematical model for the initial molecular interactions of death receptor signalling. *Math Biosci Eng* 9:663–683. doi:[10.3934/mbe.2012.9.663](https://doi.org/10.3934/mbe.2012.9.663)
- Wolter S, Löscherberger A, Holm T, Aufmkolk S, Dabauvalle M, van de Linde S, Sauer M (2012) rapidSTORM: accurate, fast open-source software for localization microscopy. *Nat Methods* 9:1040–1041. doi:[10.1038/nmeth.2224](https://doi.org/10.1038/nmeth.2224)
- Yoshida A, Kohchi C, Inagawa H, Nishizawa T, Hori H, Soma G (2006) A soluble 17 kDa tumour necrosis factor (TNF) mutein, TNF-SAM2, with membrane-bound TNF-like biological characteristics. *Anticancer Res* 26:4003–4008
- Zagouras P, Rose J (1993) Dynamic equilibrium between vesicular stomatitis virus glycoprotein monomers and trimers in the Golgi and at the cell surface. *J Virol* 67:7533–7538

---

# Chapter 5. | Results and Discussion II: SMLM Setup Performance

## 5.1 Localization Accuracy

In order to characterize the quality of an SMLM experiment, the localization accuracy is a crucial parameter, as it is directly linked to the achievable spatial resolution. It depends on several aspects, as the intensity of the utilized fluorescent probes, the quality of the optics equipment, and the localization performance of the localization algorithm. During this thesis the localization accuracy of SMLM experiments has been determined in two different ways.

### 5.1.1 Theoretical Localization Accuracy

The theoretical localization accuracy of a single fluorophore can be calculated from the number of photons detected within the area of its PSF after the methods of Thompson et al.<sup>82</sup>, and Mortensen et al.<sup>83</sup> as described in chapter 2.9.1. These methods calculate the achieved localization accuracy for every detected localization and therefore fulfill the spirit of single molecule experiments, by enabling the detection of different subspecies within the ensemble of measured data. However, by assuming an ideal microscope without aberrations except for a noise and a spatial inaccuracy caused by the pixelation of the EMCCD, they give a rather optimistic value for the achieved localization accuracy.

### 5.1.2 Experimental Localization Accuracy

In order to account for every possible kind of aberrations resulting from the microscopic setup an experimental way of determining the localization accuracy has been developed. The algo-

rithm estimates the average localization accuracy directly from the measured data set without the need for an additional calibration phantom. It is based on analyzing the distribution of pairwise distances  $d_{ij}$  between the localizations resulting from the same fluorescent probe, that are imaged in adjacent frames (see figure 5.1)<sup>117</sup>. By assuming that the nearest neighbor of a specific localization within the adjacent frame is originated most likely from the very same fluorescent probe and by approximating the localization distribution arising from every multiple detected fluorescent probes being identical, it is possible to calculate the pairwise distance distribution  $p(d_{ij})$  of an averaged fluorophore. The technique is therefore termed *Nearest Neighbor Approach* (NeNA).

$$p(d_{ij}) = \left( \frac{d_{ij}}{2\sigma^2} e^{-\frac{d_{ij}^2}{4\sigma^2}} \right) \quad (5.1)$$

Here,  $p(d_{ij})$  describes the probability for a positional displacement  $d_{ij}$  in two dimensions and  $\sigma$  represents the standard deviation of the Gaussian distributed localizations. Nevertheless, a

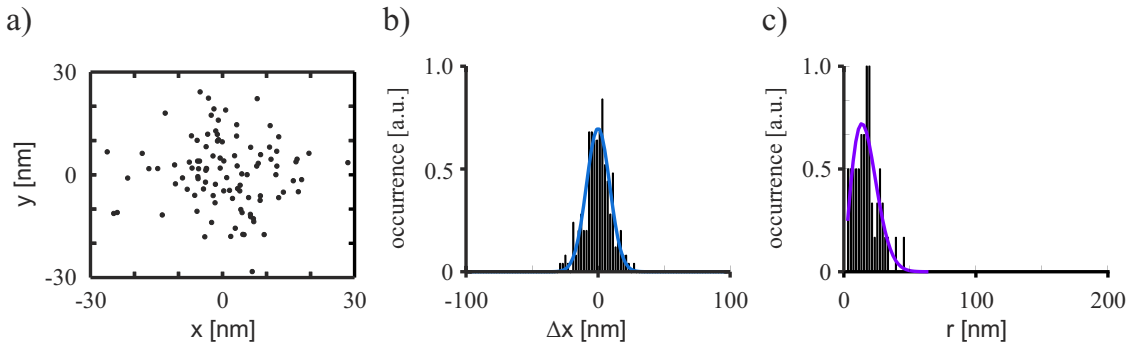


Figure 5.1: **Determining the average single-molecule localization accuracy**

a) Simulation of 100 localizations of a single molecule. The error caused by the fitting algorithm is approximated by a normal distribution. b) The distance distribution from all localizations to the origin is described by a Gaussian function with  $\sigma = 10.0 \pm 0.7$  nm. c) The pairwise distance distribution between all localizations is described by equation 5.1 with  $\sigma = 10.1 \pm 0.5$  nm (input parameter: 100 simulations, each with 100 Gaussian-distributed localizations with  $\sigma = 10$  nm).

certain fraction of the nearest neighbors from adjacent frames might originated from a different molecule. These inter-molecular distances are larger than the expected localization accuracy and will distort the distribution. For an accurate fitting two correction terms were conceived and tested by Monte Carlo simulations to correct for short-range distortions occurring from molecules within the direct neighborhood ( $corr_{short}$ ) and long-range distortions ( $corr_{long}$ ),

which include also background noise (see equation equation 5.3).

$$P(d_{ij}) = p(\text{singlemolecule}) + \text{corr}_{short} + \text{corr}_{long} \quad (5.2)$$

$$P(d_{ij}) = A_1 \left( \frac{d_{ij}}{2\sigma^2} e^{-\frac{(d_{ij}^2)}{4\sigma^2}} \right) + A_2 \frac{1}{\sqrt{2\pi\omega^2}} e^{-\frac{(d_{ij}-d_c)^2}{2\omega^2}} + A_3 d_{ij} \quad (5.3)$$

Here,  $A_x$  is a free fitting parameter that describes the amplitude of every summand and  $\omega$  describing the width of  $\text{corr}_{short}$ .

Determining the localization accuracy by the experimental method has the drawback that an average localization accuracy is calculated, such that subpopulations with different localization accuracy are not accessible.

On the other hand the experimental method overcomes the theoretical one in three main aspects. It includes the microscopic setup performance, it can be extended for the localization accuracy in axial dimension, and it can be used to define the quality of drift correction (see chapter 5.2) and image registration. These Corrections add an additional localization inaccuracy to the post-processed data set. Detailed information about NeNA can be found in chapter 4<sup>118</sup>

## 5.2 Sample Drift Quantification

The overall resolution of a SMLM data set is not only characterized by the localization accuracy, but also depends on temporal shifts<sup>119–121</sup>. SMLM experiments take 10 to 20 minutes, and therefore demand setup stability. The near molecular resolution in combination with long image acquisition times makes the setup prone for drift, even when in the range of only a few nm/min. In order to characterize the sample drift during SMLM experiments, a drift characterization routine has been developed (see figure 5.2 a).

The drift characterization routine determines the directed displacement of fiducial markers with fixed relative positions. In order to access nonlinear components of the sample drift, the fiducial markers need to be detected over a complete image stack in order to work well as a molecular ruler for drift quantification<sup>122</sup>. TetraSpeck beads (Invitrogen) for example are polymer spheres filled with organic fluorophores, that fulfill these requirements, by exhibiting a long-lasting and stable fluorescence. Time trajectories are calculated from the SMLM data sets. These time trajectories may be incomplete, if the localization software misses some fiducial marker positions during data acquisition, e.g caused by blinking effects. Therefore, the drift characterization routine estimates missing bead localizations by linear drift approximation. Trajectories from fiducial markers are identified by their fluorescence endurance (see figure 5.2

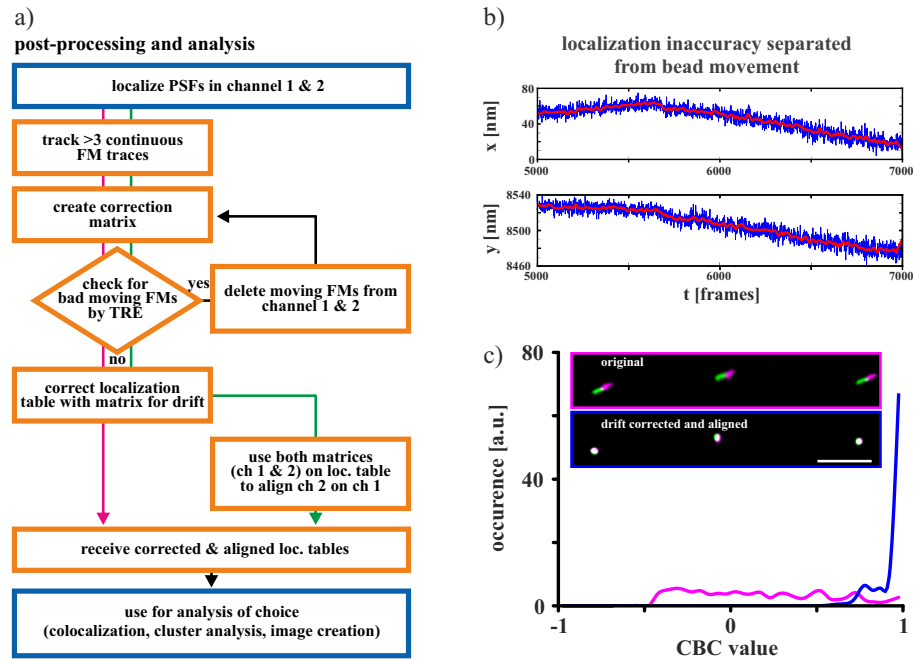


Figure 5.2: **Nonlinear drift correction and channel registration**

a) Flow chart of the drift correction and channel registration algorithm. b) Trajectories of fiducial markers were split in x and y and convolved with a Gaussian low pass filter to eliminate high frequencies. Smoothed trajectories are used to calculate the transfer matrix to correct for the non-linear drift of the selected fiducial marker. c) Images of three fiducial marker that were not used to generate the transfer matrix before and after drift correction and channel registration. The *coordinate-based colocalization* (CBC) approach was used to quantify the quality of channel registration.

b, blue time trace). The directed drift signal for each dimension is extracted from the trajectories by eliminating higher spatial frequencies, caused by localization inaccuracy, by Gaussian low pass filtering in the Fourier space (see figure 5.2 a and b, red time trace). Non-fixed fiducial marker are identified by an undirected diffusion compound and rejected.

### 5.2.1 Drift Correction

Measuring a set of fiducial markers, comprising at least three beads, yields sufficient information to correct the SMLM data set for drift. The spatiotemporal displacement of the fiducial marker set from its initial position can be described by a time series of affine transformation matrices. These matrices are further used to filter the drift of the raw SMLM data set (see figure 5.2 c).



### 5.2.2 Error Estimation

The quality of the drift correction can be calculated by the *target registration error* (TRE) (see figure 5.3)<sup>123</sup>. Briefly, the trajectory  $x_n$  of each fiducial marker ( $N$ ) was corrected for drift by a time series of affine transformation matrices for all frames ( $T$ ), determined from the directed spatiotemporal displacement of the residual fiducial markers. This procedure guarantees that  $x_n$  does not contribute to its own transformation matrix. The TRE is further characterized by the distance distribution of all localizations  $f_{trans}\{x_{n,t}\}$  with respect to the *local weighted mean* (LWM)  $f_{LWM}\{x_n\}$  of the trajectory (see figure 5.3 b):

$$TRE = \sqrt{\left(\frac{1}{NT} \sum_{n=1}^N \sum_{t=1}^T (f_{trans}\{x_{n,t}\} - f_{LWM}\{x_n\})^2\right)} \quad (5.4)$$

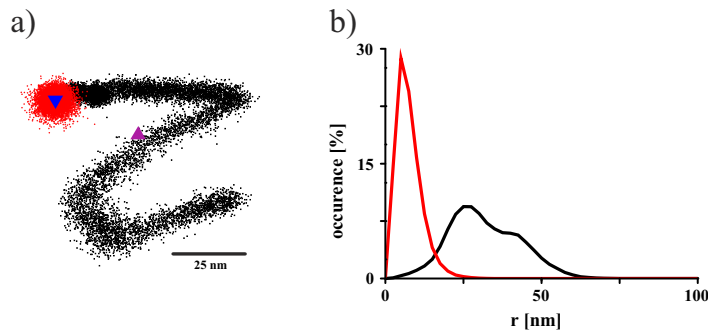


Figure 5.3: **Target registration error estimation of drift correction**

Robustness of drift correction with a sample containing 13 fiducial markers which exhibit non-linear drift. a) Coordinates before (black) and after (red) drift correction. The calculated centre (triangle, before (blue) and after (magenta) drift correction) of a single fiducial marker trajectory is calculated exemplarily. b) TRE distribution from all fiducial marker coordinates to the local weighted mean of the particular trajectory before (black) and after (red) drift correction. The peak of the distance distribution, which is a measure of the quality of drift control, moved from 40.1 nm (uncorrected) to 6.2 nm (corrected).

### 5.2.3 A Hydrophilic Gel Matrix for Spatial Drift Correction

Estimating the setup focus stability during 3D SMLM experiments, as well as expanding the drift correction methods introduced in chapter 5.2 to the third dimension, requires a spatial distribution of the fiducial markers. For this purpose, cells and fiducial markers are embedded in a hydrophilic *extra cellular matrix* (ECM) gel<sup>124</sup>. The ECM gel matches the refraction index of aqueous buffers ( $n = 1.34$ ), and is accessible for photoswitching buffers. Fiducial markers



are added to the ECM gel before sample embedding, resulting in a random distribution in the extra-cellular space (see figure 5.4).

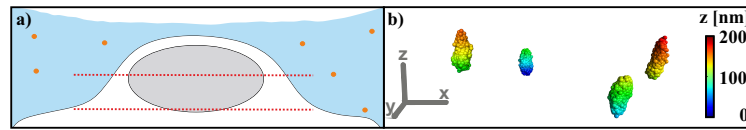


Figure 5.4: **A hydrophilic gel matrix for three dimensional fiducial marker distributions**

a) Protocol for 3D fiducial marker placement. The extracellular matrix gel (blue) is prepared with fiducial markers (orange) before sample preparation. b) 3D localization distribution of fiducial markers embedded in an ECM gel.

In order to verify the spatial stability of the fiducial marker positions within the ECM gel, an ensemble containing 33 randomly-distributed fiducial markers was imaged for 10,000 frames. The relative position of each fiducial marker with respect to the LWM of the remaining fiducial markers was determined over time, resulting in a time series of distance distributions (see figure 5.5, left side of each dimension). For comparison the distance distribution time series are normalized to their center of mass (see figure 5.5, right side of each dimension). Spatial stable beads were identified by defining a threshold of maximum displacement from the LWM in lateral ( $Thr_{xy} = 55$  nm) and axial dimension ( $Thr_z = 100$  nm). As a result, 94% of all beads (31 of 33) are confirmed as stable during the measuring procedure.

## 5.3 Multi Color Imaging

By labeling biomolecules with differently-colored photoswitchable fluorophores, SMLM can be used to study colocalization with near molecular resolution. The quality of such multicolor SMLM studies strongly depends as well on the switching behavior of the deployed fluorescent probes, as it depends on the spatial offset between the spectrally separated SMLM data sets.

### 5.3.1 Fluorescent Proteins under switching buffer conditions

The impact of different switching buffers on the activation / conversion mechanism of different PA/PC-FP were investigated. The conversion mechanism of *mEOS2* was identified to be still working under most switching buffer conditions (see table 5.1). Nevertheless, it develops reversible transitions between its two fluorescent states. This has to be taken into account for further data post processing in order to avoid an overestimation of the FP population within

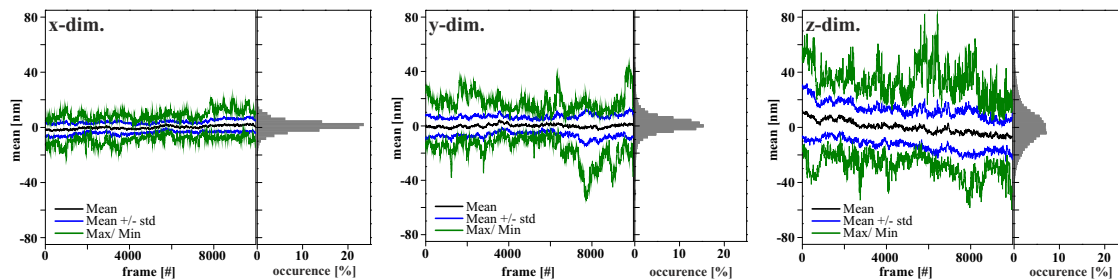


Figure 5.5: **Spatial stability of 3D distributed fiducial markers embedded in ECM gel**

Relative position of 31 spatial stable fiducial markers over time in comparison to the LWM of the residual fiducial markers embedded in an ECM gel. For the sake of simplicity, separate plots for the three dimensions are shown and normalized to their center of mass. The distributions of each time step are indicated by the mean (black), the standard deviation (blue) and the extremal values (green). On the right side, the distance distribution over the whole acquisition time is shown. Fitting the distance distribution to a Gaussian distribution results in standard deviations of  $\sigma_x = 3.52$  nm,  $\sigma_y = 4.94$  nm,  $\sigma_z = 11.25$  nm, verifying the spatial stability of the fiducial markers within the ECM gel.

the sample<sup>92</sup>.

Table 5.1: **Fluorescent proteins under switching buffer conditions**

Impact of different switching buffer conditions on the fluorescence signal of different PA/PC-FPs. (+) indicates a working conversion mechanism, (-) indicates a non working conversion mechanism.

Protein	PBS	10 mM MEA	100 mM MEA	100 mM MEA without O <sub>2</sub>
<i>psCFP2</i>	+ (irreversible)	+ (reversible)	+/- (reversible)	+/- (reversible)
<i>bsDRONPA</i>	+ (reversible)	+ (reversible)	+/- (reversible)	-
<i>Dendra2</i>	+ (irreversible)	+ (reversible)	+/- (reversible)	-
<i>mEOS2</i>	+ (irreversible)	+ (reversible)	+ (reversible)	+ (reversible)
<i>PAmCherry1</i>	+ (irreversible)	+ (reversible)	-	-

The detailed results about the switching buffer effects on PA/PC-FPs can be found in chapter 4<sup>125</sup>, which provides a basic concept for the combination of organic fluorescent probes and FPs in further dual color SMLM experiments.

### 5.3.2 Channel Registration

Due to the near molecular resolution and large image acquisition periods, SMLM data sets are not only prone to drift but also to spatial offsets if more than one spectral channel, focal plane,

or time point of the same sample is imaged. In order to correct for such spatial offsets, a multi channel registration approach was developed. The routine uses multicolor fiducial markers that are localized in both channels. The fiducial marker localizations from both channels are identified and allocated to their appendant localization within the respectively other channel (see figure 5.6 a and b). From all identified localization pairs a non-linear transformation matrix is calculated and applied for channel registration (see figure 5.6 c and d). This approach can

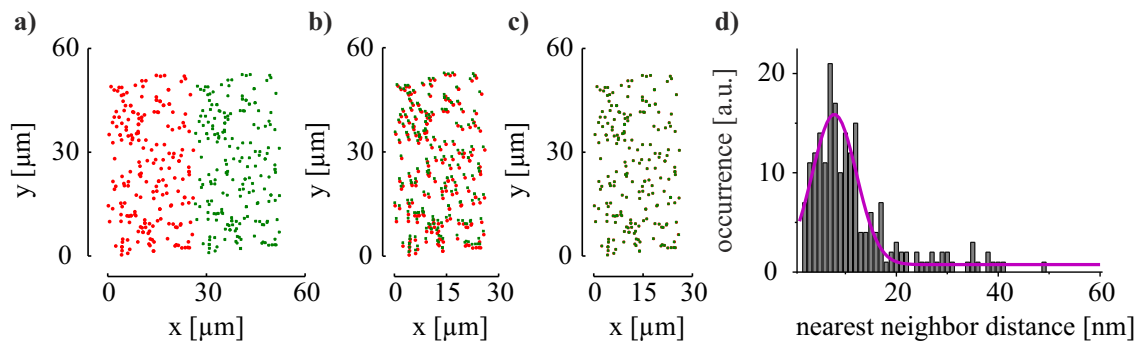


Figure 5.6: **Image registration**

Registration of a two color SMLM data set by a non linear transformation matrix calculated from fiducial marker displacements. a) The fluorescence signal of a random distribution of fix multicolor fiducial marker on a glass surface are recorded by two spectrally separated optical detection pathways and imaged on two spatial separated regions on the EMCCD camera. b) Linear channel transformation shows the need for a non linear channel registration. c) Result of a non linear channel registration. d) Quality control of the channel registration routine. The distribution of the displacement between appendant fiducial marker localizations of both channels after channel registration shows a mean displacement of 7.8 nm.

also be combined with fiducial marker-based drift correction by registering each frame of one channel to the first frame of the respective channel (see figure 5.2 c). Detailed information about SMLM data set registration can be found in in chapter 4<sup>126,127</sup>.

---

# Chapter 6. | Results and Discussion

## III:

### Post-Processing of SMLM Data

Parameters obtained by SMLM are quantitative parameters, that can be directly used for further data processing and data comparison with quantitative data obtained from different methods. As SMLM data differ significantly from the data obtained by conventional fluorescence microscopy, several image post-processing algorithms do not fit satisfactorily. Therefore, the following section deals with the development of SMLM-specific post-processing algorithms in order to extract quantitative information from SMLM data and maximize the data interpretation.

#### 6.1 Cluster Analysis

Proteins of the plasma membrane of eucaryotic cells are an ideal target for SMLM performed with TIR illumination. An important question on membrane proteins is their oligomeric state, which can be analyzed with cluster analysis algorithms.

##### 6.1.1 Image Reconstruction

In order to analyze SMLM data by conventional image processing software tools like ImageJ, the localization list has to be transformed into a super resolved image. A simple visualization is a 2D histogram of the localization coordinates. The 2D histogram function results in an 8-bit gray scale image. The desired pixel size of the super resolved image can be chosen as desired with a pixel intensity depending proportionally on the number of comprised localizations. If

the proportionality constant is defined as 1, the respective gray value of a pixel is increased by 1 for every binned localization.

### 6.1.2 Morphological Cluster Analysis

*Morphological Cluster Analysis* is an image-based approach. Starting with the reconstructed image, a binary mask of cohesive regions is calculated by choosing an intensity threshold. Due to the high localization accuracy, SMLM-based morphological cluster analysis routines have no need for further morphological image processing as erosion or dilation, as they could distort the image. Cohesive regions obtained from the binary mask are further analyzed for their size, usually given by the radius of a circle coextensive to the regions area, and their shape by a circularity measurement. So far the morphological cluster analysis routine equals conventional image-based cluster algorithms like the *objects counter* plugin in ImageJ<sup>128</sup>. The strength lies in the possibility of analyzing the number of localizations within each cluster, by referring to the original localizations list. The Morphological Cluster Analysis routine was tested on the HIV-1 Gag polyprotein assembly cites<sup>129,130</sup> of known size at the cell membrane<sup>131-134</sup>. It was applied to investigate the clustering of *viral envelope* (ENV) glycoproteins<sup>130</sup>, as well as arrestin2<sup>135</sup> and arrestin3<sup>136</sup> proteins at the cell membrane.

### 6.1.3 Ripley's K-Function

*Ripley's K-Function* calculates a second order statistic over the variance of all intermolecular distances  $r$  up to a maximal distance  $r_{max}$ <sup>137</sup>. It tests a two dimensional localization pattern against the null hypothesis of a uniform distribution and characterizes the degree of clustering.  $K(r)$  calculates to:

$$K(r) = \frac{1}{n^2} \sum_i \sum_j \frac{N_r(d_{ij})}{\lambda} \quad (6.1)$$

With  $r$  being the investigated neighborhood distance,  $n$  being the total number of investigated localizations,  $i$  being the walk parameter over the pool of investigated localizations,  $j$  being the walk parameter over the pool of possible neighbors,  $\lambda$  being a weighting factor for the area of investigated  $i$ , and  $N_r(d_{ij})$  being the number of neighbor localizations within the distance  $r$  summed over all  $i$  and  $j$ . For the sake of intuitive interpretation, the K-function is linearized to the L-function:

$$L(r) = \sqrt{\frac{K(r)}{\pi}} \quad (6.2)$$

A further normalization to the L-function with the distances  $r$  calculates to the H-function:

$$H(r) = L(r) - r \quad (6.3)$$

Equation 6.3 turns 0 for all  $r$  if the localization pattern is uniformly distributed. For all other distributions the distance  $r_{\max}$  at which  $H(r)$  has its maximum defines the average degree of clustering within the *region of interest* (ROI) (see figure 6.1 a). Typically  $r_{\max}$  lies between the average cluster radius and the average cluster diameter, depending on the mean distance between the clusters (see figure 6.1)<sup>138</sup>.

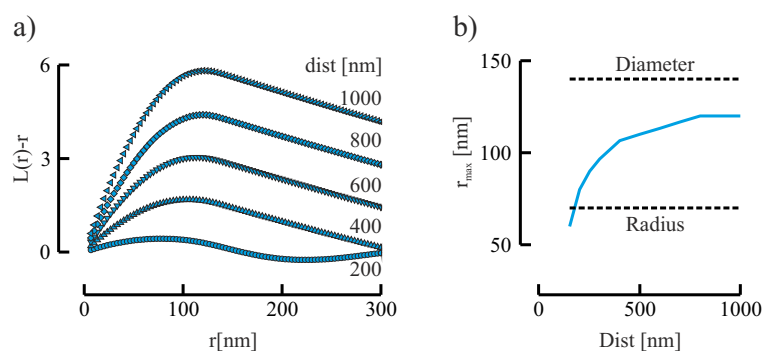


Figure 6.1: Using Ripley's H-function to identify the average cluster size

a)  $H(r)$  was calculated for simulated clusters at different inter-cluster distances, ranging from 200 nm to 1  $\mu\text{m}$ , leading to a shift in the maximum with increased inter-cluster distance. b)  $r_{\max}$  is plotted against the inter-cluster distance. The graph shows that  $H(r)$  yields a measure for the cluster size which depends also on the inter-cluster distance, and which generally scales between the cluster radius and the cluster diameter<sup>129</sup>.

Ripley's K-Function has been applied to characterize different types of cluster formation. For example, to characterize the photoswitching properties by analyzing the small localization distributions of isolated reversible switching fluorophores<sup>125</sup>. A more common application of Ripley's K-function is the characterization of membrane protein distributions<sup>139–141</sup>.

A weakness of the second order statistic function is the appearance of edge effects. If the distance of the investigated neighborhood exceeds the borders of the ROI, a part of the neighborhood localization would be located outside the ROI and would therefore not exist in the pool of available neighboring candidates  $j$ . As a consequence, the number of detected neighbors would be underestimated. Edge corrections needs to be applied to correct for this, before using Ripley's K-function. Possible methods of edge correction are the introduction of a buffer zone, the calculation of a passepartout containing a contineous localization pattern, or the adaption of the detected neighbors  $N_r(d_{ij})$  by a weighting factor  $\omega$  to the effectively observed neighbor-

ing area<sup>142</sup>.

### Buffer Zones

The introduction of a buffer zone is based on decoupling the pool of investigated localizations  $i$  located in ROI <sub>$i$</sub>  from the pool of possible neighboring localizations  $j$  located in ROI <sub>$j$</sub> <sup>143</sup>. By enlarging the area of ROI <sub>$j$</sub>  in comparison to the area of ROI <sub>$i$</sub>  a buffer zone is introduced containing additional possible neighboring localizations. In order to correct for edge effects, ROI <sub>$i$</sub>  has to be dislocated at least by a distance of  $r_{max}$  from all edges of ROI <sub>$j$</sub> . Therefore, the radius of a circular distribution ROI <sub>$j$</sub>  has to exceed the radius of ROI <sub>$i$</sub>  by a factor of  $r_{max}$ . For squared ROIs the area  $A_j$  of ROI <sub>$j$</sub>  is related to the area  $A_i$  of ROI <sub>$i$</sub>  defined by an edge length of  $a_i$  by:

$$A_j = (a_i + 2r_{max})^2 \quad (6.4)$$

This method of edge correction describes a pattern in the most realistic way, as no assumption or annealing has to be calculated. The main drawback of introducing a buffer zone is the limitation in ROI selection to the inner part of a structure. Buffer zones cannot guarantee a satisfying correction for edge effects if the ROI <sub>$i$</sub>  is located at the edges of a structure. This may hinder the investigation of larger ROI <sub>$i$</sub> . A minor drawback of a buffer zone is that an increasing pool of possible neighbor localizations  $j$  also increases the computing time. Buffer zones were deployed to analyze the degree of clustering of arrestin2<sup>135</sup> and arrestin3<sup>136</sup> proteins at the cell membrane.

### Weighting Factor

A weighting factor works on a ROI <sub>$i$</sub>  identical to ROI <sub>$j$</sub> , which gives two identical pools  $i$  and  $j$  of investigated localizations and possible neighbors. If the area of the investigated neighborhood exceeds the boundaries of the ROI, the division by a weighting factor  $\omega$  may correct the detected number of neighbors  $N_r(d_{ij})$  out of  $j$  around a localization  $i$  within a distance  $r$  for the effectively observed area<sup>142,144,145</sup>.  $\omega$  is based upon the assumption that the distribution pattern outside the ROI is exactly the same as inside.  $\omega$  has to be considered for four different cases.

1. If the observed distance  $r$  around  $i$  is smaller than the distance to the nearest ROI boundary, no additional weighting is necessary as all possible neighbors are existing within  $j$ .

2. If the observed distance  $r$  around  $i$  is bigger than the distance to the nearest ROI boundary  $b_1$ ,  $\omega$  calculates to:

$$\omega_r = 1 - \frac{\cos^{-1}\left(\frac{b_1}{r}\right)}{\pi} \quad (6.5)$$

3. If the observed distance  $r$  around  $i$  is bigger than the distance to two ROI boundaries  $b_1$  and  $b_2$ ,  $\omega$  calculates to:

$$\omega_r = 1 - \left[ \cos^{-1}\left(\frac{b_1}{r}\right) + \cos^{-1}\left(\frac{b_2}{r}\right) + \frac{\pi}{2} \right] 2\pi \quad (6.6)$$

4. If the observed distance  $r$  around  $i$  is bigger than the distance to two ROI boundaries  $b_1$  and  $b_2$  and  $r$  is smaller than the distance between  $i$  and the nearest corner,  $\omega$  calculates to:

$$\omega_r = 1 - \left[ 2 \cos^{-1}\left(\frac{b_1}{r}\right) + 2 \cos^{-1}\left(\frac{b_2}{r}\right) \right] 2\pi \quad (6.7)$$

As a main advantage of this technique, the ROI can be chosen freely within the area of the imaged cell membrane, because ROI<sub>*i*</sub> is identical to ROI<sub>*j*</sub>. As a disadvantage, the weighting factor assumes that the localization pattern within the full distance  $r$  around  $i$  is of a similar distribution. This assumption only holds for a uniform distribution. Correcting for edge effects via a weighting factor is the method of choice in samples exhibiting localization patterns near a uniform distribution, but it may lead to a general underestimation of the degree of clustering in highly-clustered samples. This effect correlates with the inverse of the weighting factor.

### Toroidal Edge Correction

Toroidal edge correction combines the two methods described above. The degree of clustering is assumed as consistent within a large area around the ROI. The distribution of investigated localizations  $i$  within the ROI is projected onto a three dimensional surface with no existing ROI boundaries. As a result, localizations that were located at opposing boundaries before are now located in close neighborhood (see figure 6.2). Toroidal edge correction is realized by computing a passepartout from 8 identical copies of the ROI around the original ROI<sup>146</sup>. This passepartout serves as an artificial buffer zone. As toroidal edge correction enlarges the pool of possible neighbors  $j$ , it also requires high computation time. It provides the user with the opportunity to freely choose the ROI as the weighting factor method does. The fictional buffer zone might, as well as the weighting factor, lead to misinterpretations on the degree of clustering.



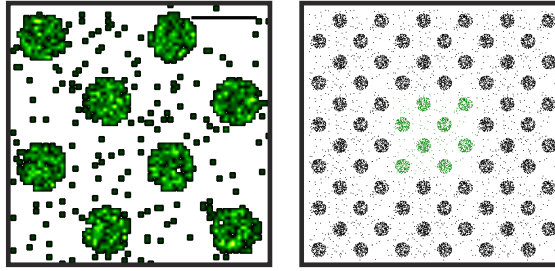


Figure 6.2: **Toroidal edge correction**

Simulation of single-molecule localization data and analysis with Ripley's K-function. Single-molecule localization data of clusters with a diameter of 140 nm were simulated and background noise was added. The clusters were spaced in a regular pattern with the same average distance (scale bar: 200 nm). For cluster analysis using the K-function, the simulated data were extended to a 3 x 3 area to minimize edge effects.

Toroidal edge correction was applied to test the degree of HIV-1 Gag protein clustering at the cell membrane. This was done by a 95% confidence envelope resulting from the calculated maxima and minima of 19 simulations of a uniform distribution with identical number of  $i$  in an identical ROI<sup>147</sup>. The method seems sufficient, because HIV-1 Gag proteins explicitly show a high degree of clustering, as well as a similar degree of clustering all over the cell membrane<sup>129,130</sup>.

## 6.2 Coordinate Based Colocalization

"The introduction of sub-diffraction-limited, super-resolution microscopy techniques has engendered a paradigm shift in approaching the colocalization analysis of single molecules."

*The histochemistry and cell biology compendium: a review of 2012* by Douglas J. Taatjes and Jürgen Roth<sup>148</sup>

Conventional colocalization analysis routines operate on overlapping PSFs in diffraction-limited fluorescence images of spectrally separate channels as an overall ensemble measurement. SMLM data consist of the accurate localization of each biomolecule. Therefore, neither of the conventional methods of measuring colocalization suites SMLM data. As a defined space may only be populated by one molecule, no colocalization in the original meaning will be measured. An alternative would be to redefine colocalization as the probability of protein-protein

interaction which, for short range interactions, is accessible by FRET experiments (see chapter 2.4). By performing a cross-correlation analysis the contribution of different biomolecules to mixed cluster formation can be determined by *pair-correlation photo-activated localization microscopy* (PC-PALM)<sup>149</sup>. For example, the PC-PALM approach was used to study the ethanol mediated membrane reorganization by a colocalizing the glycosylphosphatidylinositol distribution with actin<sup>150</sup>. PC-PALM directly determines the general colocalization of two protein species from SMLM data, but it does not provide spatial data in form of a colocalization coded image, indicating possible subpopulations of protein colocalization like FRET<sup>151</sup>. Therefore, a coordinate based colocalization (CBC)<sup>126</sup> algorithm was developed to close the gap between diffraction limited fluorescence imaging and single-molecule FRET measurements.

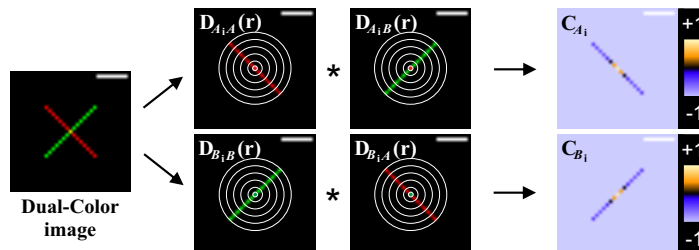


Figure 6.3: **The CBC concept**

CBC for a simulated distribution of single-molecule localizations. For each single-molecule localization of either species (green or red), the distribution function of the neighboring localizations from the same species is calculated. Like Pearson's colocalization coefficient<sup>152</sup>, the CBC can therefore reach from 1 (high colocalization) over 0 (no colocalization) to  $-1$  (anti-colocalization). In a second step, the distance to the nearest localization from the other population is calculated. The correlation coefficient is weighted by the distance factor. As a result, an individual colocalization value is attributed to each localization of each species.

The CBC routine calculates a value  $C_{A_i}$  for each localization  $A_i$ . The neighborhood distributions of two spectrally separated single-molecule localization lists ( $A$  and  $B$ ) around each localization  $A_i$  are correlated within the distance  $R_{\max} \approx 200$  nm to  $S_{A,B}(i)$  (see figure 6.3). With  $\bar{E}_{A_i,B}$  being the distance between  $A_i$  to its nearest neighbor from channel  $B$ , the  $C_{A_i}$  value for a single localization  $A_i$  calculates to:

$$C_{A_i} = S_{A,B}(i) \cdot e^{\frac{\bar{E}_{A_i,B}}{R_{\max}}} \quad (6.8)$$

This way, each localization can be sorted into two categories by introducing a threshold: colocalized or not colocalized. By diversifying the CBC weighting factor  $\bar{E}_{A_i,B}$ , one can define if the

CBC analysis should be more weighted on the distance factor or on the neighborhood correlation factor. These factors have to be chosen for every type of data set and need to be identical for the sake of comparability of different measurements.

Like SMLM data the CBC coordinate lists can be transferred into super resolved two or three dimensional colocalization distribution maps (see figure 6.4 e-h). Similar to the PC-PALM ap-

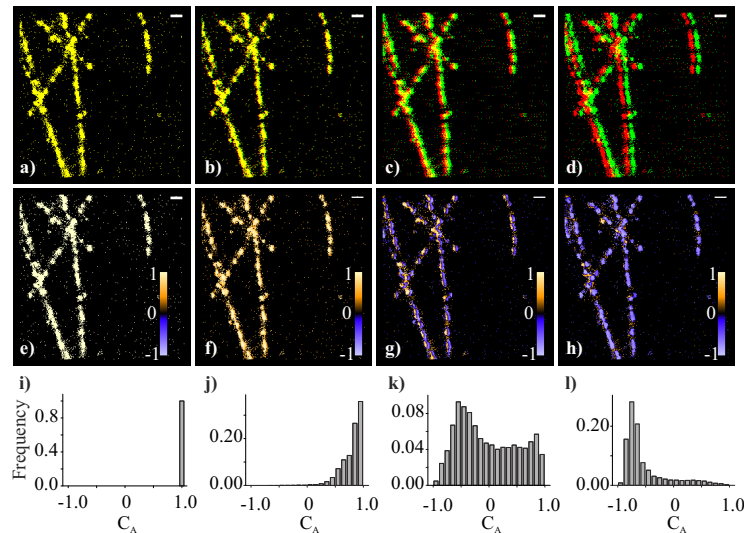


Figure 6.4: **Calibrating the CBC algorithm**

CBC of a singly labeled microtubulin in a fixed HeLa cell (scale bar 200 nm). a) The SMLM data set of the microtubule structure is duplicated, overlaid on each other (green and red), and the CBC is calculated (e). The structures are displaced stepwise (b-d) in one dimension and the CBC is calculated (f-h): b, f) 10 nm, c, g) 50nm, d, h) 100 nm. i-l) The histograms show the single-molecule distributions of the colocalization parameter  $C_A$ .

proach, the CBC data can be used to determine the general degree of colocalization from a  $C_A$  value distribution (see figure 6.4 i-l).

The CBC approach was applied to characterize the degree of molecular interaction between TNF-R1 and TNF $\alpha$  (see chapter 8).

### 6.2.1 CBC-mediated cluster analysis

By splitting the localization list in even and odd frame numbers, the CBC algorithm can be used to correlate each localization's neighborhood with itself (see figure 6.5). The result is a  $C_A$  value that indicates the degree of clustering. This index can be used to sort every localization into two categories: arranged within a cluster, or not. This way, the CBC algorithm also offers the possibility for a coordinate-based cluster analysis that, compared to Ripley's K-function<sup>137</sup>

or the pair correlation PALM algorithm<sup>153</sup>, additionally contains spatial information.

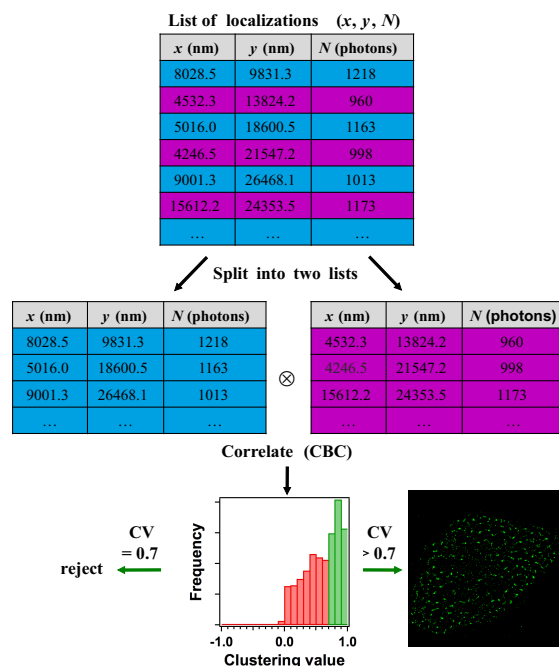


Figure 6.5: **CBC-mediated cluster analysis**

The localization list is split into two lists comprising only localizations with even, or odd frame numbers. The resulting localization lists are correlated by the CBC algorithm in order to determine each localization's degree of clustering. By applying a threshold, a binary clustering map is calculated from all localizations characterized by a  $C_A > 0.7$ .

## 6.3 Single Particle Diffusion Analysis

The PALM-Tracer algorithm (see chapter 3.8.2 - 3.8.3)<sup>112,114</sup> was used to analyze the diffusion of single membrane proteins. It fits a 2D Brownian motion model (see chapter 2.10.2) to the first four time points of the  $MSD(t)$  curve, obtaining the two dimensional diffusion coefficient<sup>154</sup>. Annealing the diffusion of all measured molecules with the model of Brownian motion is legitimate because nearly all membrane proteins show a freely diffusing behavior within the first four time steps of the  $MSD(t)$  curve (see figure 6.6)<sup>97</sup>. The sptPALM approach was tested on the diffusion of membrane bound TNF-R1, as this system was previously studied by FCS<sup>155</sup>. The mean diffusion coefficient of TNF-R1-tdEos molecules at the membrane of HeLa cells, determined by quantitative FCS measurements<sup>155</sup>, could be verified by sptPALM (see table 6.1).

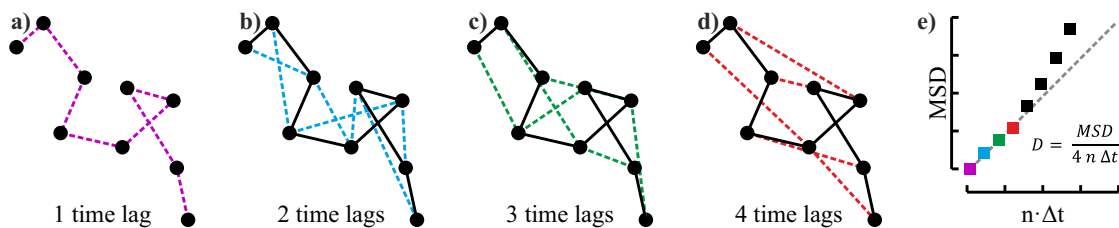


Figure 6.6: **Determining diffusion coefficients from single-molecule trajectories**

Single-molecule localizations are connected to trajectories. The MSD is calculated as the average distance between localizations of the same molecule for a certain time lag  $n \cdot \Delta t$ . With  $\Delta t$  being the integration time. a) distances with  $n = 1$ , b)  $n = 2$ , c)  $n = 3$ , and d)  $n = 4$ . e) The diffusion coefficient  $D$  is extracted from the MSD vs. time plot by fitting the first four time points to a 2D diffusion model of Brownian motion, indicated by the dotted line.

Table 6.1: **Mean diffusion coefficient of membrane bound TNF-R1 measured with FCS<sup>155</sup> and sptPALM**

TNF-R1	D from FCS $\mu\text{m}^2/\text{s}$	D from sptPALM $\mu\text{m}^2/\text{s}$
Native	$0.12 \pm 0.09$	$0.14 \pm 0.02$
+ methyl- $\beta$ -cyclodextrin (MCD)	$0.16 \pm n.a.$	$0.20 \pm 0.04$
+TNF $\alpha$	$0.11 \pm 0.08$	$0.16 \pm 0.03$
+ MCD + TNF $\alpha$	$0.16 \pm n.a.$	$0.24 \pm 0.03$

---

# Chapter 7. | Results and Discussion IV: Applied Cell Biology and Biophysical Projects

## 7.1 Morphology of HIV-1 Assembly Sites and Specific Recruitment of the Envelope Protein

HIV-1 virions released from the cell membrane, are formed in budding sites with an average diameter of 140 nm, as determined by cryo electron microscopy<sup>131-134</sup>. The main structural component of HIV-1 virions is the Gag poly-protein<sup>156</sup>. The dynamic of the Gag poly-protein fused to a PC-FP was determined by sptPALM measurements, revealing an immobile Gag fraction organized in assembly sites<sup>97</sup>. A wild-type like protein association of the assembly sites can be achieved by cotransfecting the fusion protein with an equimolar concentration of the wild-type Gag<sup>157</sup>.

To draw a comprehensive picture of the HIV-1 Gag distribution at the cell membrane A3.01 T-cells, morphological and coordinate-based clustering post processing routines were applied to SMLM data. Cells were either cotransfected with HIV-1 Gag.mEosFP, or HIV-1 Gag.SNAP, which was labeled to Alexa Fluor 647. The average localization accuracy of the SMLM experiments was calculated by NeNA to 28 nm for HIV-1 Gag.mEosFP and 18 nm for HIV-1 Gag.SNAP.

By post processing the SMLM data with Ripley's K-function, three different organization forms of HIV-1 Gag at the cell membrane could be identified: A diffusive distribution forming broad

coherent clusters ( $R_{\max} = 173$  nm), a distribution with small dense clusters ( $R_{\max} = 40$  nm), and bigger clusters ( $R_{\max} = 120$  nm) that likely represent the viral budding sites (see figure 7.1).

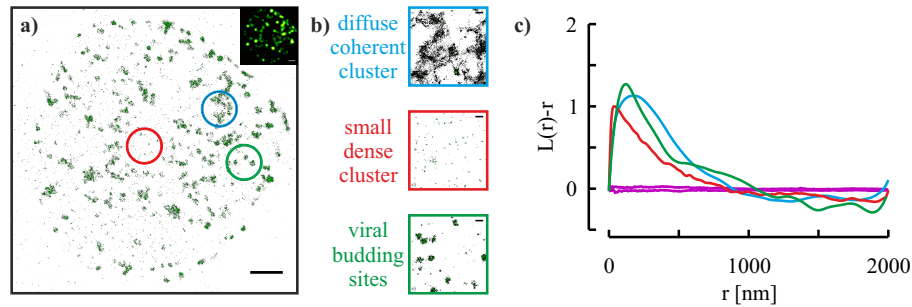


Figure 7.1: **Quantitative cluster analysis of HIV-1 Gag distribution at the cell membrane by Ripley's K-function**

a) SMLM image of a A3.01 cell expressing HIV-1 Gag.SNAP labeled with Alexa Fluor 647. The insert shows the diffraction-limited image (scale bar 1  $\mu\text{m}$ ). Different types of HIV-1 Gag distributions (b) are analyzed quantitatively for clustering with Ripley's K-function against the hypothesis of forming a uniform distribution (95% confidence interval shown in magenta) (c). The diffusive HIV-1 Gag distribution has its maximum at  $R_{\max} = 173$  nm (blue). Regions of HIV-1 Gag molecules forming small dense clusters exhibit a maximum at  $R_{\max} = 40$  nm (red). Clusters considered to correspond to viral budding sites exhibit a maximum at  $R_{\max} = 120$  nm (green).

To further characterize the shape of viral budding sites, 25 clusters were identified and analyzed. The FWHM of the average intensity profile plot gives a mean budding site diameter of  $R_{\text{FWHM}} = 59$  nm. By plotting the nearest neighbor distribution of all localized HIV-1 Gag proteins within an assembly site against the distance of the localizations to the center, the molecular density was determined. Two forms of HIV-1 Gag organization are identified by their difference in their molecular density. A circular area around the assembly site center with a diameter of  $R_{\text{NN}} = 70$  nm, characterized by a constant molecular density, representing the viral budding site. With increasing distance to center the molecular density decreases, indicating for a protein pool which appears likely to be located in the vicinity of the budding site.

HIV-1 Gag assembly sites show different shapes with an intensity minimum at each respective cluster center. Modeling the detected distribution of fluorophores onto the surface of 3D sphere with a radius of 70 nm, as known from electron microscopy<sup>131-134</sup>, indicates that the different shapes result from the projection of particles at different developmental stages (see figure 7.3).

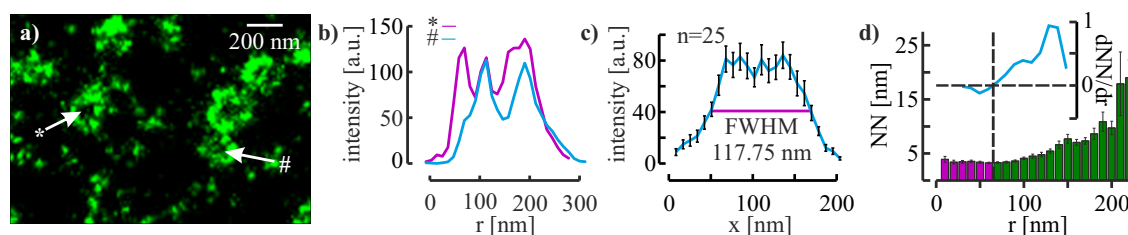


Figure 7.2: **Determination of the average dimension of HIV-1 Gag budding sites**

a) SMLM image of HIV-1 Gag assembly sites that are suggested to represent the viral budding sites (scale bar 200 nm). b) intensity distribution two exemplary single viral budding sites. c) Average intensity distribution of viral budding site calculated from 25 single budding sites reveals a FWHM at 118 nm. d) Distribution of the average distance between single HIV-1 Gag molecules plotted against the molecules' distance to the cluster center reveals two different organization forms of HIV-1 Gag molecules within a protein assembly site (insert shows the derivate of the distribution with respect to the distance to the cluster center). A population equidistant to its respective nearest neighbor molecule, characterized by a derivation around 0, closely approximated to the cluster center indicates an organized protein distribution (magenta). This population circular arranged around the cluster center is considered to represent the organization of HIV-1 Gag proteins within a viral budding site. A second population with an increasing distance dependency to its respective nearest neighbor as a function of distance to the cluster center is characterized by a derivation larger than 0 (green).

This semi-spherical architecture of Gag assembly sites could only be detected with Gag.SNAP labeled with Alexa Fluor 647, as the localization accuracy achieved for Gag.mEOSFP was not sufficient to resolve projection effects.

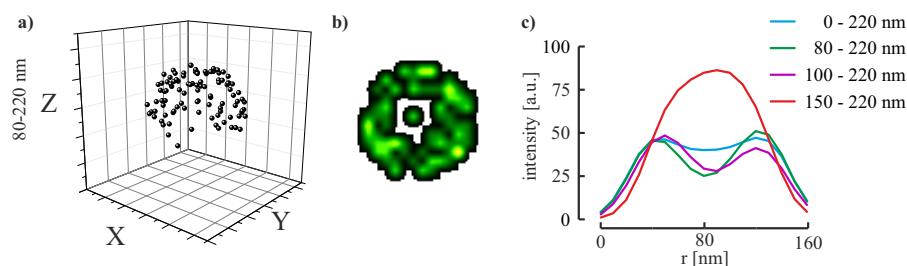


Figure 7.3: **Modeling HIV-1 Gag budding sites at different developmental stages**

Simulation of fluorophore localizations onto the surface of 3D spherical caps ( $r = 70$  nm) at different plane heights. a) 3D model of a spherical cap which is nearly closed. b) Reconstruction of the resulting SMLM image of the nearly closed cap projected onto the X-Y plane. c) Intensity profiles from reconstructed SMLM images of spherical caps with different plane heights.



The HIV-1 glycoprotein ENV mediates the virus entry by binding the viral receptor CD14<sup>158</sup>. In average a HIV-1 virion comprises 7-14 Env complexes<sup>159,160</sup>. Former confocal microscopy studies determined a colocalization of ENV and Gag proteins at the cell membrane<sup>161</sup> with low correlation coefficients<sup>162</sup>. The recruitment of the envelope protein ENV to HIV-1 Gag assembly sites in virus producing cells was studied with dual-color SMLM experiments on cells coexpressing HIV-1 Gag.mEosFP, HIV-1 Gag wild-type and HIV-1 Env. The average localization accuracy of HIV-1 Env Alexa Fluor 647 was calculated by NeNA to 15 nm. Env was observed to largely be located around Gag assembly sites, but not colocalized (see figure 7.4 a-c). Cells expressing HIV-1 Env exhibit smaller clusters which were rather uniformly distributed. SMLM experiments on cells coexpressing HIV-1 Gag with a HIV-1 Env mutation in which the *cytoplasmic tail* (CT) was truncated ( $\Delta$ CT) show no cluster formation around HIV-1 Gag assembly sites (see figure 7.4 d-f). Coexpression of HIV-1 Gag containing two point mutations within the *matrix associated* (MA) domain (L8S/S9R) with the HIV-1 Env wild type results in a similar phenotype than Gag wild type coexpressed with Env ( $\Delta$ CT). Thus, SMLM experiments identified the MA domain of the HIV-1 Gag protein, as well as the CT of the HIV-1 Env to be essential for specific recruitment of HIV-1 envelope proteins, while for both mutants random incorporation appears to be more likely. These results conform with the reduced incorporation of Env ( $\Delta$ CT) into virions comprising Gag wild type<sup>163</sup>, as well as the reduced incorporation of Env wild type into virions comprising Gag with a mutated MA domain<sup>164</sup>.

## 7.2 Arrestin Clustering Upon Stimulation of the C-C Chemokine Receptor 5 with RANTES Analogues

Arrestin2 and arrestin3 are ubiquitously expressed cytosolic proteins that are involved in the clathrin-mediated endocytosis of the *G-protein-coupled receptor* (GPCR). Upon stimulation of GPCR, cytosolic arrestins are recruited to the plasma membrane and organize clustering of GPCRs and internalization<sup>165-168</sup>. The major GPCR used by HIV to infect target cells is the C-C chemokine receptor (CCR)5<sup>169,170</sup>. Several analogues of the CCR5 ligand RANTES are known to reduce HIV infection<sup>171-173</sup>. Therefore, the characterization of these RANTES analogues is of essential pharmacological interest.

Clustering in arrestin2/3 in *chinese hamster ovary* (CHO) was studied for several GPCR ligand analogues (RANTES, PSC-RANTES, 6P4-RANTES, 5P12-RANTES, 5P14-RANTES). CHO cells stably expressing GPCR<sup>172</sup>, obtained by lentiviral vector transduction<sup>174</sup>, were further stably transfected with either arrestin2-GFP or arrestin3-GFP fusion protein<sup>175</sup>. The cells were treated

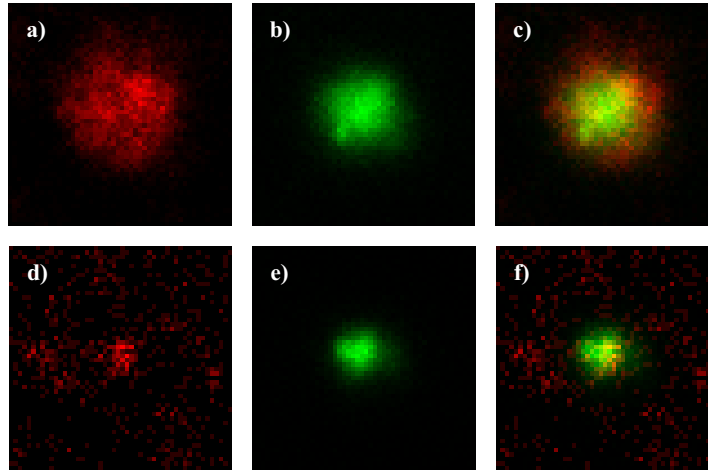


Figure 7.4: **Averaged distribution of Env in context to Gag assembly sites**

Average of high-resolution images of HIV-1 Gag assembly sites and the respective Env distribution ( $n = 7$ , image width is 500 nm). Viral context (a-c): Cells coexpressing Env wild type (a) and HIV-1 Gag wild type (b). Without viral context (d-f): Cells coexpressing Env ( $\Delta$ CT) (d) and HIV-1 Gag wild type (e). The restrictive overlay of the Env and HIV-1 Gag channel is shown in c and f.

with 100 nM of the particular RANTES analogue for 90 min before fixation. Fixed samples were immuno-stained with a GFP-specific nanobody labeled with Atto655. The average experimental achieved localization accuracy was determined to be 27 nm for arrestin2 and 20 nm for arrestin3, both determined by NeNA.

Cluster analysis was performed by a CBC-mediated pre-sorting into cluster-associated localizations ( $C_A > 0.7$ ) and diffuse distributed localizations (see chapter 6.2.1 figure 6.5). Cluster-associated arrestin localizations were further analyzed by a morphological cluster analysis. For this purpose, super-resolution images with a pixel size of 10 nm were reconstructed from all localizations with a  $C_A > 0.7$  (see figure 7.5). The images were convolved by a Gaussian low pass to reflect the average localization accuracy of the image. Cohesive regions were identified and characterized by the radius of a circle with coextensive area, further referred to as cluster radius. As a control, the arrestin clustering of untreated cells was investigated. For both arrestin2 and arrestin3, it was found that most molecules were organized in domains with a radius  $r < 120$  nm. The incubation with 5P12-RANTES shows a similar result for both arrestins. Incubation with native RANTES as well as PSC-RANTES results in a reorganization of both arrestins into assembly domains with a radius  $r > 150$  nm. Most RANTES analogues show a similar effect on arrestin2 as well as arrestin3, except for 5P14-RANTES, which only induces ar-

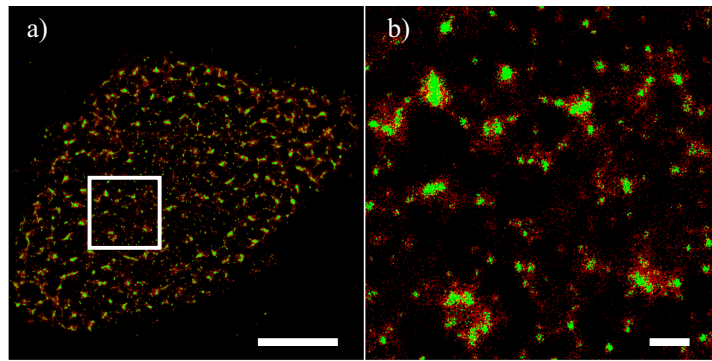


Figure 7.5: **CBC-mediated cluster analysis of arrestin3 clusters**

Super-resolution image of the arrestin3 distribution at the plasma membrane of a cell exposed to 6P4-RANTES. CBC-mediated cluster analysis was used to sort localizations into states by applying a threshold of  $C_A = 0.7$ . Localizations with  $C_A > 0.7$  are indicated in green. Localizations with  $C_A \leq 0.7$  are indicated in red. The green localizations are further used for morphological cluster analysis (Scale bar:  $a) = 5 \mu\text{m}$ ,  $b) = 0.5 \mu\text{m}$ ).

restin2 clustering. This result may be the first example of a ligand-induced recruitment of only one type of arrestin to CCR5, as former studies on different chemokine agonists indicate for an interchangeable ability of both arrestins regarding to receptor internalization<sup>176</sup>, especially for CCR5<sup>177</sup>. The effect of 6P14-RANTES was only tested on arrestin3 and leads to a similar reorganization as native RANTES and PSC-RANTES. A comparison of ligand-induced cluster formation to the pharmacological ligand activity (G-Protein signalling, GPCR5 internalization, taken from<sup>171,172,178</sup>) is summarized in figure 7.6.

### 7.3 sptPALM reveals morphological and dynamical heterogeneities of membrane-bound TNF-R1 at the single molecule level

TNF  $\alpha$  is a potent mediator of inflammation in mammalian cells<sup>179</sup>. It is secreted from hematopoietic cells after stimulation with bacterial lipopolysaccharides, interleukins, or interferon  $\gamma$ , and binds to TNF-R1 with high affinity<sup>180</sup>. The lateral diffusion dynamics of TNF-R1 before and after ligand application were investigated by sptPALM.

HeLa cells were transiently transfected with the fusion protein TNF-R1-tdEOS. To synchronize internalization upon by ligand application cells were incubated in fresh medium at  $4^\circ\text{C}$  for 30 min<sup>181</sup>. Signal-induction was introduced by applying 10 ng/ml TNF $\alpha$  to the cold medium. To further investigate the impact of membrane compartmentalization, cells were additionally

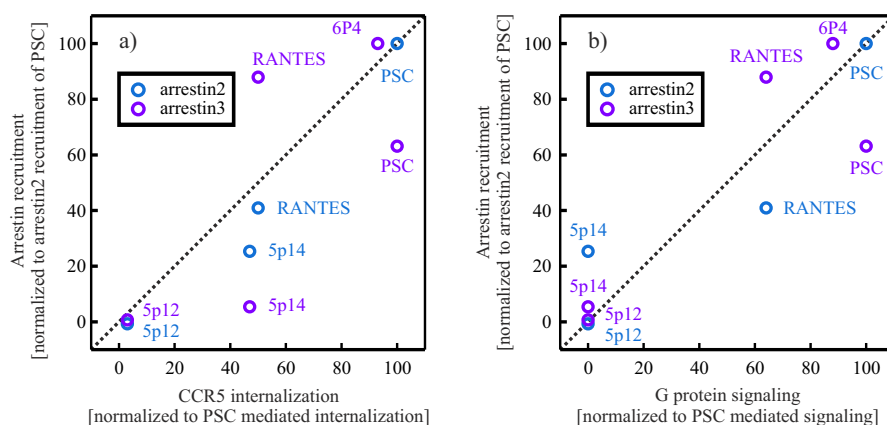


Figure 7.6: Comparison of RANTES analogues effects on arrestin recruitment, G protein signaling, and CCR5 internalization

Cells treated with RANTES analogues were analyzed by CBC-mediated cluster analysis with a threshold of  $C_A = 0.7$ , followed by a morphological cluster analysis. Arrestin recruitment was calculated by comparing the absolute number of arrestin molecules found in clusters with a radius  $r > 100$  nm. The values from cells treated with RANTES analogues were normalized by the value obtained from native cells as a control (0%). Values for G protein signaling, and CCR5 internalization were taken from<sup>171,172,178</sup> and normalized to the effect of PSC-RANTES (100%).

treated with 10 mmol/l MCD, to deplete cholesterol from the membrane, and disrupt membrane microdomains<sup>182,183</sup>.

All sptPALM experiments were made in living cells with phenol- and fetal calf-serum free medium at 37 °C. Imaging procedures took 5 to 30 min, during which thousands of single-molecule trajectories were recorded<sup>112,114</sup>. The high density of TNF-R1-tdEos trajectories permitted the reconstruction of a super-resolution trajectory map of the plasma membrane. These maps reveal information on subpopulations in diffusive states as well as spatial heterogeneities at the cell membrane (see figure 7.7). By calculating the MSD of a trajectory and fitting the first 4 time steps to a model of Brownian motion, the lateral diffusion coefficient was determined. This procedure was repeated for each trajectory, resulting in a distribution of diffusion coefficients. From the sptPALM experiments, two subpopulations of diffusive states were identified: A fast diffusing population, and a slow diffusing population. The slow diffusing population could be depleted by the application of MCD, suggesting for association with cholesterol-rich domains in the membrane (see figure 7.8). The effect of MCD on the slow diffusion species was not further affected by ligand application. TNF $\alpha$ -mediated signal-induction alone, however, results in a smaller reduction of the slow species, without significant changes in the diffusion coefficient

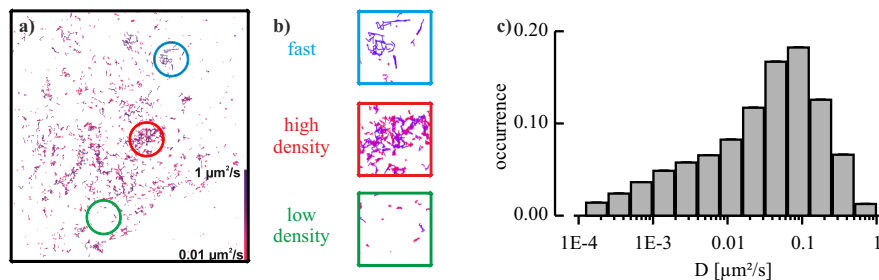


Figure 7.7: **Super-resolution trajectory map of single TNF-R1 molecules on a HeLa cell membrane**

- a) Super-resolution high density trajectory map of single TNF-R1 molecules on a HeLa cell membrane.  
b) Inserts reveal population heterogeneities and subpopulations in the mean regional diffusion coefficient  $D$ .  
c) Diffusion coefficient distribution from all detected trajectories of a single cell.

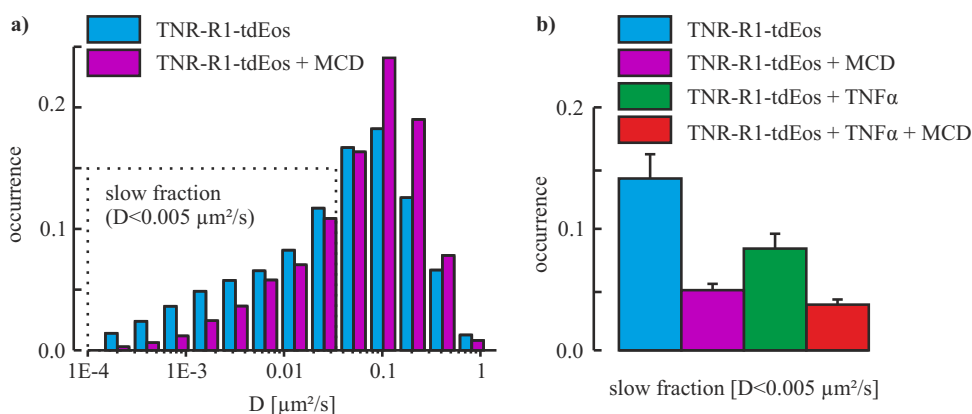


Figure 7.8: **TNF-R1 diffusion coefficients in single cells**

- a) Diffusion coefficients of TNF-R1 in native cells (blue) and cells pre-incubated with MCD (magenta) calculated from a model of lateral Brownian motion. Molecules diffusing with  $D < 0.005 \mu\text{m}^2$  were characterized as the slow diffusing population. b) Mean fraction of slow diffusing TNF-R1 molecules (error bars indicate the standard errors of the mean).

distribution of the fast diffusing population. To further characterize the different diffusion populations, the sptPALM data were analyzed by a model of anomalous lateral diffusion<sup>184</sup>. This allowed sorting single trajectories into different types of diffusion, by the exponent  $\alpha$  of the anomalous diffusion coefficient  $\Gamma$ .

$$\text{MSD} = 4\Gamma t^\alpha \quad (7.1)$$

Single molecule trajectories were grouped into four different diffusion types: directed ( $\alpha > 1.1$ ), free ( $1.1 > \alpha > 0.9$ ), confined ( $0.9 > \alpha > 0.1$ ), and immobile ( $\alpha < 0.1$ ) (see figure 7.9). The model of anomalous diffusion indicates that the slow diffusing fraction is mainly populated by immobile or confined diffusing particles. Thus, future sptPALM data might allow to elab-

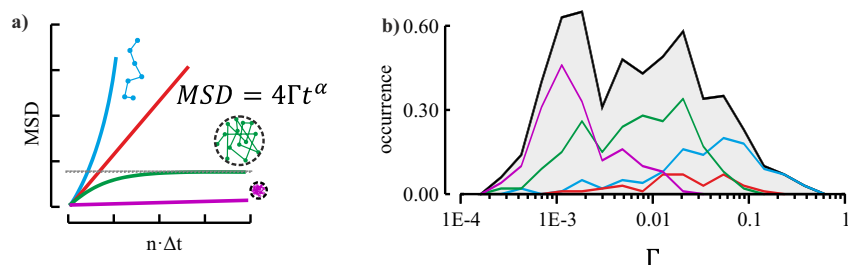


Figure 7.9: **Sorting single particle trajectories into different diffusion states**

Analysis of sptPALM data from a native cell by an anomalous diffusion model. a) Single-molecule trajectories are sorted into four different types: directed (blue), free (red), and confined (green) diffusing, and immobile (purple) molecules. b) Resulting diffusion coefficient distributions for TNF-R1-tdEos (black is the sum over all different coefficients).

orate the role of membrane microdomains for the internalization of TNF $\alpha$ -TNF-R1 complexes mediating the inflammation.

# Chapter 8. | Outlook: From Single Molecule Biophysics to Systems Biology

With single molecule fluorescence techniques fluorescently labeled biological probes can be investigated in a quantitative way at a localization accuracy in near molecular range. Data determined from single molecule fluorescence experiments are perfectly suitable as input parameters for detailed mathematical modeling of intermolecular interactions at a single molecule scale<sup>4,185–187</sup>. Here, two ongoing research projects are presented briefly, dealing with the development of new, or refinement of existing mathematical models of the initiation of the TNF $\alpha$  induced TNF-R1 signaling pathway. The models will be based on quantitative data obtained by the single molecule fluorescence techniques, especially on the coordinate based post processing algorithms developed within the work of this thesis. SMLM and FCS experiments will allow for subpopulation detection that remain hidden when imaged with conventional fluorescence microscopy.

## 8.1 Interpreting Static Single-Molecule Data by Rule-Based Modeling

The assembly of TNF-R1 prior to ligand activation and its ligand induced reorganization at the cell membrane was studied by several research groups<sup>188–190</sup>. The molecular stoichiometry of free TNF-R1 and the activated signaling complex still remains unknown. By using single molecule fluorescence techniques quantitative information about receptor clustering (e.g. size,

and number of molecules per cluster) were obtained and further use as input parameters for a rule based-model of ligand induced reorganization of TNF-R1.

### 8.1.1 Pre-Ligand TNF-R1 Organization

PALM experiments were made in HeLa cells, transiently transfected with TNF-R1-tdEOS<sup>191</sup>. Absolute copy numbers of TNF-R1 at the plasma membrane of HeLa cells were found to be in the range of 1,500 – 2,900 measured by SMLM<sup>98</sup>. The number of receptor molecules per cluster was calculated by comparing the SMLM data obtained from TNF-R1-tdEOS to SMLM data obtained from *vesicular stomatitis virus G protein* (VSVG)-tdEOS, which is a trimeric transmembrane protein<sup>149,192</sup>. The weighted average number of VSVG localizations per cluster exceeded the weighted average number of TNF-R1 molecules per cluster by a factor of 1.5, inferring a primarily dimeric TNF-R1 pre-assembly (see figure 8.1). This finding is compatible with the formation of a *pre ligand association domain* (PLAD)<sup>193,194</sup>.

### 8.1.2 Binding Affinity of TNF $\alpha$ for TNF-R1

TNF $\alpha$  was labeled with ATTO647N (DOL = 0.8) or Cy5 (DOL = 1.1). The biological activity of the labeled TNF $\alpha$  was confirmed by a luciferase activity assay<sup>100</sup> and the binding of freely diffusing TNF $\alpha$ -ATTO647N to membrane bound TNF-R1 was determined by SMLM experiments performed directly at the cell membrane<sup>98</sup> to  $K_{LIG} = 15.69 \pm 0.03$  nM. This value was confirmed for freely diffusing TNF $\alpha$ -Cy5 binding to soluble ectodomain TNF-R1 by micro-scale thermophoresis measurements to  $K_{LIG} = 16.6 \pm 3.3$  nM<sup>195-197</sup>.

### 8.1.3 Ligand-Induced Reorganization of TNF-R1

Ligand-induced reorganization of TNF-R1 occurred upon application of TNF $\alpha$ -ATTO647N. Receptor internalization was prevented by incubating the cells with TNF $\alpha$ -ATTO647N at 4 °C for 1 h before fixation<sup>181</sup>. Dual-color SMLM was performed on an inverted wide field microscope. CBC analysis of the two channels enabled sorting localizations into free TNF-R1-tdEOS molecules and TNF-R1-tdEOS molecules colocalizing with TNF $\alpha$ -ATTO647N, which were presumed to be activated (see figure 8.1 a, b). A morphological cluster analysis revealed that cluster size (see figure 8.1 c) and the localizations per cluster distribution of the free TNF-R1-tdEOS subpopulation were similar to the distribution obtained from unstimulated cells (see figure 8.1 d). For the ligand-stimulated subpopulation the localizations per cluster distribu-



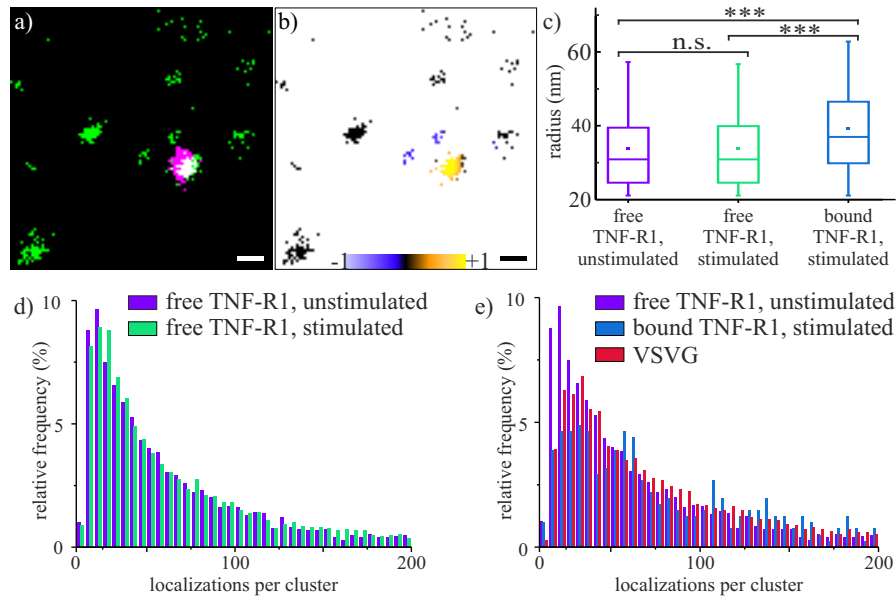


Figure 8.1: **Quantitative analysis of ligand-receptor interaction**

a) Binary two-color image of TNF-R1-tdEOS (green) and TNF $\alpha$ -ATTO647N (magenta) reveals moderate colocalization (white). b) Pre-sorting of colocalizing and non colocalizing cluster in the CBC space. The color code ranges from high anti-colocalization (-1), over no colocalization (0), to high colocalization values (+1) (scale bar 100 nm). c) Box plot of receptor cluster radius pre-sorted by CBC displays 5th percentile, 25th percentile, median (line), mean (square), 75th percentile and 95th percentile (P values by Mann-Whitney U tests: n.s.  $P > 0.05$ ; highly significant (\*\*\*)  $P < 0.01$ ). d) Morphological TNF-R1-tdEOS cluster analysis of unstimulated (free TNF-R1, unstimulated) and ligand-stimulated HeLa cells, that are characterized as not colocalized with TNF $\alpha$ -ATTO647N by CBC (free TNF-R1, stimulated), shows no significant difference in localization population per cluster. e) Morphological TNF-R1-tdEOS cluster analysis with no colocalization (free TNF-R1, unstimulated) and ligand-colocalized (bound TNF-R1, stimulated) compared to VSVG reveals reorganization of TNF-R1 spatially correlated with TNF $\alpha$  towards higher order oligomers.

tion exhibited two maxima, corresponding to about 1.5 and 3 times the amount of receptors per non-ligand induced cluster (see figure 8.1 e). The cluster size increased only marginally, indicating that ligand-induced TNF-R1 assembly primarily leads to tightly packed units.

#### 8.1.4 A Rule-Based Model for Ligand-Induced TNF-R1 Reorganization

The quantitative data obtained by SMLM experiments, served as input parameters for two minimal rule-based models<sup>199,200</sup> for the TNF-R1-TNF $\alpha$  interaction<sup>190</sup> (The unknown PLAD dissociation constant  $K_{PLAD}$  was obtained by parameter screening, see figure 8.2).

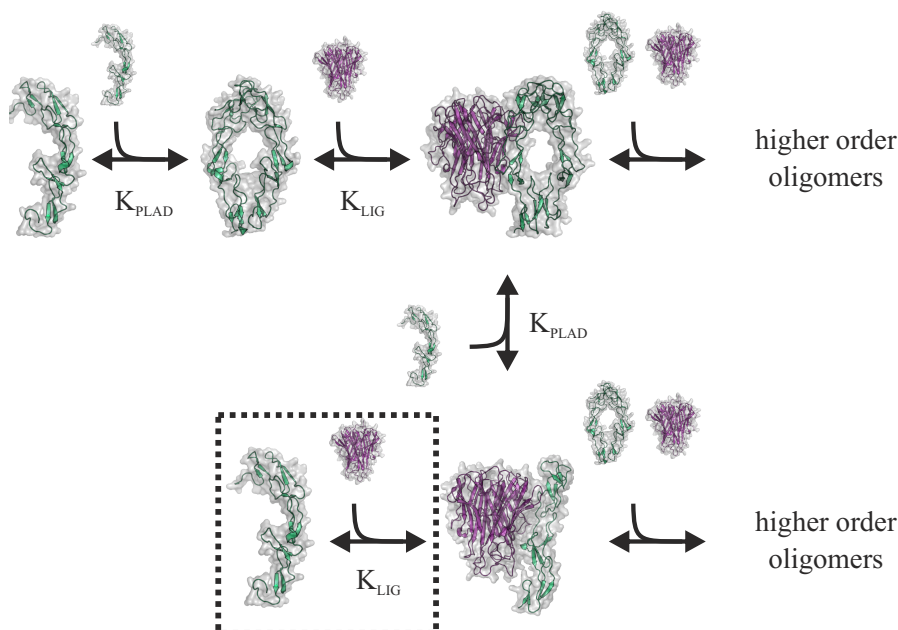


Figure 8.2: **Two minimal rule based models for the TNF-R1-TNF $\alpha$  interaction**

Model 1) Receptor dimers (green) explicitly bind trimeric TNF $\alpha$  (red) but pre-ligand associated TNF-R1 dimers may dissociate after ligand binding. Model 2) extends the first model by allowing additional ligand-receptor association between TNF $\alpha$  and TNF-R1 monomers (box in lower left). Both models allow for aggregation to higher order oligomers. TNF-R1-bound TNF $\alpha$  structure was obtained by homology modeling (MODELLER<sup>198</sup>) and visualized with PyMOL (PDB: 1FT4, 1TNF, TNR).

Up to now, both experiments and simulations indicate receptor reorganization after ligand-induction towards higher oligomeric states. The stable populations, postulated by the model, comprise three to six TNF-R1 per cluster. This is in good agreement with the experimentally obtained distribution of localizations per cluster (see figure 8.3). This outlook is a first demonstration how quantitative single molecule fluorescence techniques can be used for systems biology approaches.

## 8.2 Interpreting Dynamic Single-Molecule Data by Hidden Markov Modeling

So far, the rule-based model of TNF-R1-TNF $\alpha$  interaction is based solely on static SMLM data. As reactions between two molecules are diffusion limited, the diffusion coefficient of

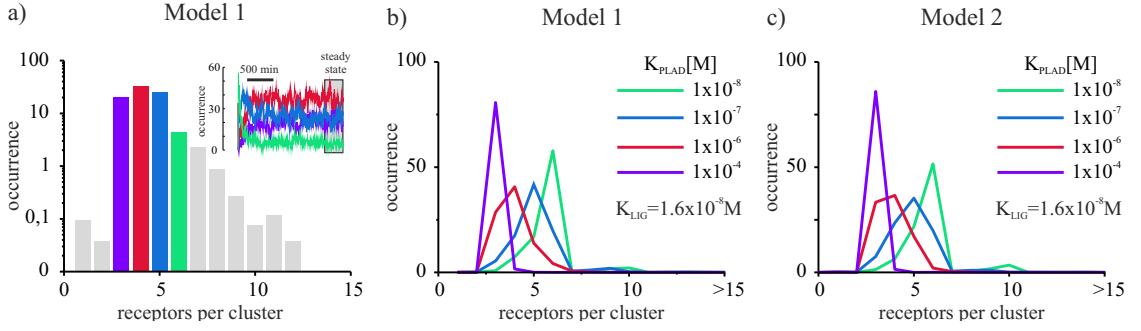


**Figure 8.3: TNF $\alpha$ -induced TNF-R1 oligomerization by network minimal rule-based modeling**

The rule-based model is simulated until the equilibrium is reached. The equilibrium state is highlighted by the gray box (Insert). TNF $\alpha$  induced TNF-R1 oligomerization is developed for clusters consisting of up to 20 receptors. a) TNF-R1 cluster size distribution averaged over the equilibrium state. b)-c) Averaged TNF-R1 cluster size distribution of the equilibrium state for model 1 and model 2 for indicated  $K_{PLAD}$  values.

the molecules has to be taken into account by calculating the reaction velocity constant<sup>23</sup>.

$$k_{D_{ij}} = 4\pi R_0 D_{ij} N_A \quad (8.1)$$

With  $R_0$  being the distance of the two molecules  $i$  and  $j$  at which a reaction takes place, and  $D_{ij}$  being the sum of their diffusion coefficients. The diffusion coefficient of freely diffusing TNF $\alpha$  can be obtained from the diffusion time of TNF $\alpha$ -ATTO647N by FCS. First measurements were made at room temperature ( $T \approx 25^\circ\text{C}$ ) without temperature control. The dimension of the confocal volume was estimated by measuring the diffusion time of the fluorophore ATTO655 ( $\tau_{\text{ATTO655}} = 0.412 \pm 0.008$  ms) with known diffusion coefficient ( $D_{\text{ATTO655}} = 426 \pm 8 \mu\text{m}^2/\text{s}$ <sup>116</sup>) as a reference. For TNF $\alpha$ -ATTO647N a diffusion time of  $\tau_{\text{TNF}} = 2.42 \pm 0.14$  ms was measured. As both samples are irradiated under the same conditions (excitation wavelength, intensity) the observed confocal volume is equal for both measurements. By approximating a lateral diffusion, the diffusion coefficient of TNF $\alpha$ -ATTO647N can be calculated by equation (2.196) to:

$$4 \cdot D_{\text{ATTO655}} \cdot \tau_{\text{ATTO655}} = 4 \cdot D_{\text{TNF}} \cdot \tau_{\text{TNF}} \quad (8.2)$$

$$D_{\text{TNF}} = \frac{D_{\text{ATTO655}} \cdot \tau_{\text{ATTO655}}}{\tau_{\text{TNF}}} \quad (8.3)$$

The error propagates to:

$$\sigma D_{\text{TNF}} = \sqrt{\left(\frac{\partial D_{\text{TNF}}}{\partial D_{\text{ATTO655}}} \cdot \sigma D_{\text{ATTO655}}\right)^2 + \left(\frac{\partial D_{\text{TNF}}}{\partial \tau_{\text{ATTO655}}} \cdot \sigma \tau_{\text{ATTO655}}\right)^2 + \left(\frac{\partial D_{\text{TNF}}}{\partial \tau_{\text{TNF}}} \cdot \sigma \tau_{\text{TNF}}\right)^2} \quad (8.4)$$

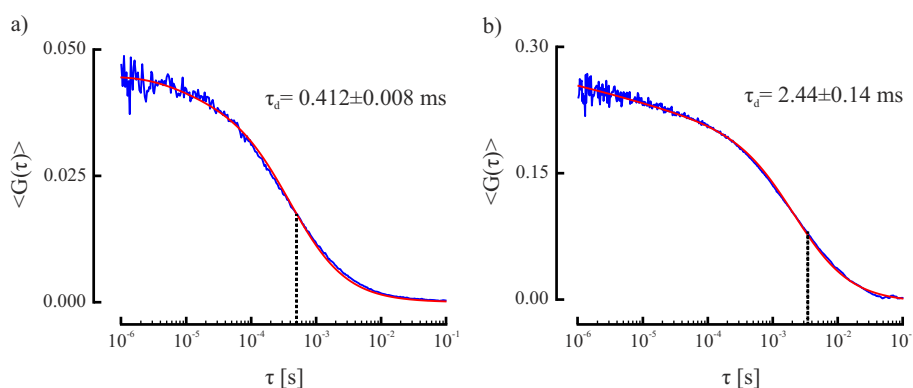


Figure 8.4: FCS measurements of ATTO655 and TNF $\alpha$ -ATTO647N

Preliminary FCS measurements were made without active temperature control at  $T \approx 25$  °C. The FCS data were fitted with a model of lateral Brownian motion to obtain the diffusion time. The average diffusion time  $\tau_d$  was obtained by calculating the mean diffusion time from  $n$  measurements. The error indicates the standard deviation. a) FCS measurements of freely diffusing ATTO655 ( $n=3$ ,  $\tau_d = 0.412 \pm 0.008$  ms). b) FCS measurements of freely diffusing TNF $\alpha$ -ATTO647N ( $n=7$ ,  $\tau_d = 2.44 \pm 0.14$  ms).

The diffusion coefficient of TNF $\alpha$ -ATTO647N was calculated by equations (8.3) and (8.4) to  $D_{\text{TNF}} = 71 \pm 4$   $\mu\text{m}^2/\text{s}$ . For more accurate experiments the dimension of the confocal volume has to be characterized with an actively controlled sample temperature<sup>77</sup>.

The distribution of diffusion coefficients for TNF-R1-tdEOS molecules at the cell membrane was determined by sptPALM experiments (see chapter 7.3)<sup>191</sup>. Parameters still unknown are the reaction rates of two TNF-R1-tdEOS molecules forming a pre-ligand dimer and the reaction rates of the TNF-R1-tdEOS-TNF $\alpha$ -ATTO647N complex binding another TNF-R1-tdEOS molecule. A promising solution to this problem seems to be the *variational Bayes SPT* (vbSPT) approach<sup>186</sup>, that was designed to identify different oligomeric and diffusive states and transition rates from short single-molecule trajectories by a HMM for intracellular diffusion. A key will be the refinement of the vbSPT algorithm to 2D membrane diffusion systems, as well as determining the number of hidden states as the introduction of an additional state always leads to a better fit<sup>186</sup>. To reduce the number of states, the obtained sptPALM data can be pre-sorted by the model of anomalous diffusion (see chapter 7.3). Therefore, only molecules characterized by Brownian motion will be further investigated by the vbSPT approach.

The high accuracy of the quantitative data, as well as the information about molecular sub-populations, that have been masked by averaging routines of conventional ensemble measure-

ments by now, provided by SMLM experiments will help to create detailed models with low degree of abstraction of the initiation process of transmembrane signaling processes. Such models are further expected to be used for drug discovery<sup>201</sup>.

## Chapter A. | Acronyms

**3D** *three dimensional*

**AA** *ascorbic acid*

**AOTF** *acousto optic tunable filter*

**APD** *avalanche photodiode*

**AU** *Airy unit*

**BaLM** *bleaching/blinking assisted localization microscopy*

**BFP** *back focal plane*

**BG** *O<sup>6</sup>-benzylguanine*

**BSA** *bovine serum albumin*

**CBC** *coordinate-based colocalization*

**CCD** *charge-coupled device*

**CCR** *C-C chemokine receptor*

**cDNA** *complementary deoxyribonucleic acid*

**CHO** *chinese hamster ovary*

**CLSM** *confocal laser scanning microscopy*

**CPU** *central processor unit*

**CT** *cytoplasmic tail*

**CV** *confocal volume*

**Cy** *cyanine*

**DMEM** *Dulbecco's modified Eagle's medium*

**DNA** *deoxyribonucleic acid*

**DOL** *degree of labeling*

**dSTORM** *direct stochastic optical reconstruction microscopy*

**ECM** *extra cellular matrix*

**E. coli** *Escherichia coli*

**EdU** *5-ethynyl-2'-deoxyuridine*

**e.g.** *exempli gratia*

**EGTA** *ethylene glycol tetraacetic acid)*

**EMCCD** *electron multiplying charge-coupled device*

**ENV** *viral envelope*

**FBS** *fetal bovine serum*

**FCS** *fluorescence correlation spectroscopy*

**FFP** *front focal plane*

**FIONA** *fluorescence imaging with one nanometer accuracy*

**FP** *fluorescent protein*

**F-PALM** *fluorescence photo-activated localization microscopy*

**FRET** *Foerster resonance energy transfer*

**FT** *Fourier transformation*

**FWHM** *full width at half maximum*

**GFP** *green fluorescent protein*

**GPCR** *G-protein-coupled receptor*

**GSDIM** *ground state depletion microscopy followed by individual molecule return*

**hAGT** *O<sup>6</sup>-alkylguanine-DNA alkyltransferase*

- HF** *hydrofluoric acid*
- HILO** *highly inclined and laminated optical sheet*
- HIV** *human immunodeficiency virus*
- HMM** *hidden Markov model*
- HOMO** *highest occupied molecular orbital*
- HPLC** *high performance liquid chromatography*
- IC** *internal conversion*
- ISC** *intersystem crossing*
- laser** *light amplification by stimulated emission of radiation*
- LUMO** *lowest unoccupied molecular orbital*
- LWM** *local weighted mean*
- MA** *matrix associated*
- MCD** *methyl- $\beta$ -cyclodextrin*
- ME**  *$\beta$ -mercapto-ethanol*
- MEA**  *$\beta$ -mercapto-ethylamine*
- MIA** *multidimensional image analysis*
- MLE** *maximum likelihood estimate*
- MSD** *mean squared displacement*
- MV** *methylviologen*
- MW** *molecular weight*
- NA** *numerical aperture*
- NeNA** *Nearest Neighbor Approach*
- NHS** *N-hydroxysuccinimide*
- OTF** *optical transfer function*



**PA** *photo-activatable*

**PALM** *photo-activated localization microscopy*

**PALMIRA** *photo-activated localization microscopy with independently running acquisition*

**PBS** *phosphate buffered saline*

**PC** *photo-convertible*

**PC-PALM** *pair-correlation photo-activated localization microscopy*

**PEG** *polyethylene glycol*

**PET** *photoinduced electron transfer*

**Phe** *phenylalanine*

**PLAD** *pre ligand association domain*

**PMT** *photomultiplier tube*

**POI** *protein of interest*

**PSF** *point-spread function*

**QY** *quantum yield*

**rapidSTORM** *rapid yet accurate program implementing the direct stochastic optical reconstruction microscopy*

**ROI** *region of interest*

**ROS** *highly reactive oxygen species*

**ROX** *reducing and oxidizing*

**rpm** *rounds per minute*

**RPMI** *Roswell Park Memorial Institute*

**SMLM** *single-molecule localization microscopy*

**SNR** *signal to noise ratio*

**spt** *single particle tracking*

**sptPALM** *single particle tracking photo-activated localization microscopy*

**STORM** *stochastic optical reconstruction microscopy*

**TIR** *totally internal reflection*

**TNF** *tumor necrosis factor*

**TNF-R1** *tumor necrosis factor receptor type I*

**TRE** *target registration error*

**Trp** *tryptophan*

**TRX** *trolox*

**Tyr** *tyrosine*

**UV** *ultra-violet*

**vbSPT** *variational Bayes SPT*

**VR** *vibrational relaxation*

**VSVG** *vesicular stomatitis virus G protein*

## Chapter B. | References

- [1] L. Thims, *Human chemistry (Volume One)*. Lulu. com, 2007.
- [2] A. Yildiz and P. R. Selvin, "Fluorescence imaging with one nanometer accuracy: application to molecular motors," *Accounts of Chemical Research*, vol. 38, no. 7, pp. 574–582, 2005.
- [3] P. R. Selvin, T. Loughheed, M. T. Hoffman, H. Park, H. Balci, B. H. Blehm, and E. Toprak, "Fluorescence Imaging with One-Nanometer Accuracy (FIONA)," *Cold Spring Harbor Protocols*, vol. 2007, no. 10, 2007.
- [4] Y. Sako, M. Hiroshima, C.-G. Pack, K. Okamoto, K. Hibino, and A. Yamamoto, "Live cell single-molecule detection in systems biology," *Wiley Interdisciplinary Reviews: Systems Biology and Medicine*, vol. 4, no. 2, pp. 183–192, 2012.
- [5] J. Vogelsang, R. Kasper, C. Steinhauer, B. Person, M. Heilemann, M. Sauer, and P. Tinnefeld, "A reducing and oxidizing system minimizes photobleaching and blinking of fluorescent dyes," *Angewandte Chemie International Edition*, vol. 47, no. 29, pp. 5465–5469, 2008.
- [6] G. T. Dempsey, M. Bates, W. E. Kowtoniuk, D. R. Liu, R. Y. Tsien, and X. Zhuang, "Photo-switching mechanism of cyanine dyes," *Journal of the American Chemical Society*, vol. 131, no. 51, pp. 18192–18193, 2009.
- [7] A. Le Gall, D. Dulin, G. Clavier, R. Méallet-Renault, P. Bouyer, K. Perronet, and N. Westbrook, "Improved photon yield from a green dye with a reducing and oxidizing system," *European Journal of Chemical Physics and Physical Chemistry (ChemPhysChem)*, vol. 12, no. 9, pp. 1657–1660, 2011.
- [8] E. Betzig, G. H. Patterson, R. Sougrat, O. W. Lindwasser, S. Olenych, J. S. Bonifacino, M. W. Davidson, J. Lippincott-Schwartz, and H. F. Hess, "Imaging intracellular fluorescent proteins at nanometer resolution," *Science*, vol. 313, no. 5793, pp. 1642–1645, 2006.

- [9] M. J. Rust, M. Bates, and X. Zhuang, "Sub-diffraction-limit imaging by stochastic optical reconstruction microscopy (STORM)," *Nature Methods*, vol. 3, no. 10, pp. 793–796, 2006.
- [10] M. Heilemann, S. van de Linde, M. Schüttpelz, R. Kasper, B. Seefeldt, A. Mukherjee, P. Tinnefeld, and M. Sauer, "Subdiffraction-resolution fluorescence imaging with conventional fluorescent probes," *Angewandte Chemie International Edition*, vol. 47, no. 33, pp. 6172–6176, 2008.
- [11] S. Malkusch, U. Endesfelder, M. Heidbreder, and M. Heilemann, "Fluorescence nanoscopy with photoswitchable fluorophores: Super-resolution fluorescence microscopy and single-molecule detection offer new insights into cellular processes," *Systembiologie.de*, vol. 3, pp. 20–23, 2011.
- [12] W. Hallwachs, "Ueber die Electricisirung von Metallplatten durch Bestrahlung mit elektrischem Licht," *Annalen der Physik*, vol. 270, no. 8A, pp. 731–734, 1888.
- [13] M. Planck, "On the law of distribution of energy in the normal spectrum," *Annalen der Physik*, vol. 4, pp. 553–563, 1901.
- [14] A. Einstein, "Zur Quantentheorie der Strahlung," *Physikalische Zeitschrift*, vol. 18, pp. 121–128, 1917.
- [15] J. Franck and E. Dymond, "Elementary processes of photochemical reactions," *Transactions of the Faraday Society*, vol. 21, no. February, pp. 536–542, 1926.
- [16] E. Condon, "A theory of intensity distribution in band systems," *Physical Review*, vol. 28, no. 6, p. 1182, 1926.
- [17] M. Born and R. Oppenheimer, "Zur quantentheorie der molekeln," *Annalen der Physik*, vol. 389, no. 20, pp. 457–484, 1927.
- [18] H. Haken and H. Wolf, *Atom- und Quantenphysik*. Physics and astronomy online library, Springer Berlin Heidelberg, 2003.
- [19] M. Kasha, "Characterization of electronic transitions in complex molecules," *Discussions of the Faraday Society*, vol. 9, pp. 14–19, 1950.
- [20] J. B. Birks and D. Dyson, "The relations between the fluorescence and absorption properties of organic molecules," *Proceedings of the Royal Society of London. Series A. Mathematical and Physical Sciences*, vol. 275, no. 1360, pp. 135–148, 1963.

- [21] A. Jaboski, "Efficiency of anti-Stokes fluorescence in dyes," *Nature*, vol. 131, pp. 839–840, 1933.
- [22] C. M. Marian, "Spin-orbit coupling and intersystem crossing in molecules," *Wiley Interdisciplinary Reviews: Computational Molecular Science*, vol. 2, no. 2, pp. 187–203, 2012.
- [23] P. W. Atkins, A. Höpfner, A. Schleitzer, and M. Bär, *Physikalische Chemie*, vol. 2. VCH Weinheim, 1987.
- [24] J. R. Lakowicz, *Principles of fluorescence spectroscopy*. Springer, 2009.
- [25] O. Stern and M. Volmer, "Über die Abklingzeit der Fluoreszenz," *Physikalische Zeitschrift*, vol. 20, pp. 183–188, 1919.
- [26] D. Evans, "Perturbation of singlet–triplet transitions of aromatic molecules by oxygen under pressure," *Journal of the Chemical Society*, pp. 1351–1357, 1957.
- [27] J. Weiss, "Photochemical reactions connected with the quenching of fluorescence of dyestuffs by ferrous ions in solution," *Nature*, vol. 136, pp. 794–795, 1935.
- [28] M. Montalti, A. Credi, L. Prodi, and M. T. Gandolfi, *Handbook of photochemistry*. CRC press, 2006.
- [29] R. Bonnett and G. Martinez, "Photobleaching of sensitizers used in photodynamic therapy," *Tetrahedron*, vol. 57, no. 47, pp. 9513–9547, 2001.
- [30] N. J. Turro, V. Ramamurthy, and J. C. Scaiano, "Modern molecular photochemistry of organic molecules," 2012.
- [31] Q. Zheng, S. Jockusch, Z. Zhou, and S. C. Blanchard, "The Contribution of Reactive Oxygen Species to the Photobleaching of Organic Fluorophores," *Photochemistry and Photobiology*, 2013.
- [32] C. Schweitzer and R. Schmidt, "Physical mechanisms of generation and deactivation of singlet oxygen," *Chemical Reviews*, vol. 103, no. 5, pp. 1685–1758, 2003.
- [33] T. Förster, "Zwischenmolekulare energiewanderung und fluoreszenz," *Annalen der Physik*, vol. 437, no. 1-2, pp. 55–75, 1948.
- [34] J. Longworth, "Luminescence of polypeptides and proteins," in *Excited states of proteins and nucleic acids*, pp. 319–484, Springer, 1971.

- [35] H. Kuhn, "The electron gas theory of the color of natural and artificial dyes: problems and principles," in *Fortschritte der Chemie Organischer Naturstoffe/Progress in the Chemistry of Organic Natural Products/Progrès dans la Chimie des Substances Organiques Naturelles*, pp. 169–205, Springer, 1958.
- [36] W. R. Hamilton, "On a general method in dynamics: by which the study of the motions of all free systems of attracting or repelling points is reduced to the search and differentiation of one central relation, or characteristic function," *Philosophical Transactions of the Royal Society of London*, vol. 124, pp. 247–308, 1834.
- [37] W. R. Hamilton, "Second Essay on a General Method in Dynamics," *Philosophical Transactions of the Royal Society of London*, vol. 125, pp. 95–144, 1835.
- [38] E. Schrödinger, "Quantisierung als Eigenwertproblem," *Annalen der Physik*, vol. 385, no. 13, pp. 437–490, 1926.
- [39] E. Schrödinger, "Der Grundgedanke der Wellenmechanik," *Physikalische Blätter*, vol. 22, no. 1, pp. 3–12, 1966.
- [40] M. Klessinger, "Konstitution und Lichtabsorption organischer Farbstoffe," *Chemie in unserer Zeit*, vol. 12, no. 1, pp. 1–11, 1978.
- [41] M. Heilemann, S. van de Linde, A. Mukherjee, and M. Sauer, "Super-Resolution Imaging with Small Organic Fluorophores," *Angewandte Chemie International Edition*, vol. 48, no. 37, pp. 6903–6908, 2009.
- [42] I. H. Stein, S. Capone, J. H. Smit, F. Baumann, T. Cordes, and P. Tinnefeld, "Linking Single-Molecule Blinking to Chromophore Structure and Redox Potentials," *European Journal of Chemical Physics and Physical Chemistry (ChemPhysChem)*, vol. 13, no. 4, pp. 931–937, 2012.
- [43] W. Pauli, "Über den Einfluss der Geschwindigkeitsabhängigkeit der Elektronenmasse auf den Zeemaneffekt," *Zeitschrift für Physik*, vol. 31, no. 1, pp. 373–385, 1925.
- [44] W. Pauli, "Über den Zusammenhang des Abschlusses der Elektronengruppen im Atom mit der Komplexstruktur der Spektren," *Zeitschrift für Physik*, vol. 31, no. 1, pp. 765–783, 1925.

- [45] G. E. Uhlenbeck and S. Goudsmit, "Ersetzung der Hypothese vom unmechanischen Zwang durch eine Forderung bezüglich des inneren Verhaltens jedes einzelnen Elektrons," *Naturwissenschaften*, vol. 13, no. 47, pp. 953–954, 1925.
- [46] C. E. Shannon, "Communication in the presence of noise," *Proceedings of the IRE*, vol. 37, no. 1, pp. 10–21, 1949.
- [47] L. E. Baum and T. Petrie, "Statistical inference for probabilistic functions of finite state Markov chains," *The Annals of Mathematical Statistics*, vol. 37, no. 6, pp. 1554–1563, 1966.
- [48] S. Cox, E. Rosten, J. Monypenny, T. Jovanovic-Talisman, D. T. Burnette, J. Lippincott-Schwartz, G. E. Jones, and R. Heintzmann, "Bayesian localization microscopy reveals nanoscale podosome dynamics," *Nature Methods*, vol. 9, no. 2, pp. 195–200, 2011.
- [49] R. H. Goldsmith and W. Moerner, "Watching conformational- and photodynamics of single fluorescent proteins in solution," *Nature Chemistry*, vol. 2, no. 3, pp. 179–186, 2010.
- [50] S. W. Englander, D. B. Calhoun, and J. J. Englander, "Biochemistry without oxygen," *Analytical Biochemistry*, vol. 161, no. 2, pp. 300–306, 1987.
- [51] Y. Harada, K. Sakurada, T. Aoki, D. D. Thomas, and T. Yanagida, "Mechanochemical coupling in actomyosin energy transduction studied by in vitro movement assay," *Journal of Molecular Biology*, vol. 216, no. 1, pp. 49–68, 1990.
- [52] S. van de Linde, I. Krstić, T. Prisner, S. Doose, M. Heilemann, and M. Sauer, "Photoinduced formation of reversible dye radicals and their impact on super-resolution imaging," *Photochemical & Photobiological Sciences*, vol. 10, no. 4, pp. 499–506, 2011.
- [53] S. H. Bokman and W. W. Ward, "Renaturation of *Aequorea* green-fluorescent protein," *Biochemical and Biophysical Research Communications*, vol. 101, no. 4, pp. 1372–1380, 1981.
- [54] R. Heim, A. B. Cubitt, and R. Y. Tsien, "Improved green fluorescence," *Nature*, vol. 373, no. 6516, p. 663, 1995.
- [55] M. Ormö, A. B. Cubitt, K. Kallio, L. A. Gross, R. Y. Tsien, and S. J. Remington, "Crystal structure of the *Aequorea victoria* green fluorescent protein," *Science*, vol. 273, no. 5280, pp. 1392–1395, 1996.
- [56] F. Yang, L. G. Moss, and G. N. Phillips Jr, "The molecular structure of green fluorescent protein," *Nature Biotechnology*, vol. 14, no. 10, p. 1246, 1996.

- [57] G. H. Patterson and J. Lippincott-Schwartz, "A photoactivatable GFP for selective photolabeling of proteins and cells," *Science*, vol. 297, no. 5588, pp. 1873–1877, 2002.
- [58] K. Nienhaus, G. U. Nienhaus, J. Wiedenmann, and H. Nar, "Structural basis for photo-induced protein cleavage and green-to-red conversion of fluorescent protein EosFP," *Proceedings of the National Academy of Sciences of the United States of America*, vol. 102, no. 26, pp. 9156–9159, 2005.
- [59] M. Andresen, A. C. Stiel, J. Fölling, D. Wenzel, A. Schönle, A. Egner, C. Eggeling, S. W. Hell, and S. Jakobs, "Photoswitchable fluorescent proteins enable monochromatic multicolor imaging and dual color fluorescence nanoscopy," *Nature Biotechnology*, vol. 26, no. 9, pp. 1035–1040, 2008.
- [60] D. M. Chudakov, V. V. Verkhusha, D. B. Staroverov, E. A. Souslova, S. Lukyanov, and K. A. Lukyanov, "Photoswitchable cyan fluorescent protein for protein tracking," *Nature Biotechnology*, vol. 22, no. 11, pp. 1435–1439, 2004.
- [61] N. G. Gurskaya, V. V. Verkhusha, A. S. Shcheglov, D. B. Staroverov, T. V. Chepurnykh, A. F. Fradkov, S. Lukyanov, and K. A. Lukyanov, "Engineering of a monomeric green-to-red photoactivatable fluorescent protein induced by blue light," *Nature Biotechnology*, vol. 24, no. 4, pp. 461–465, 2006.
- [62] J. Wiedenmann, S. Ivanchenko, F. Oswald, F. Schmitt, C. Röcker, A. Salih, K.-D. Spindler, and G. U. Nienhaus, "EosFP, a fluorescent marker protein with UV-inducible green-to-red fluorescence conversion," *Proceedings of the National Academy of Sciences of the United States of America*, vol. 101, no. 45, pp. 15905–15910, 2004.
- [63] S. A. McKinney, C. S. Murphy, K. L. Hazelwood, M. W. Davidson, and L. L. Looger, "A bright and photostable photoconvertible fluorescent protein," *Nature Methods*, vol. 6, no. 2, pp. 131–133, 2009.
- [64] F. V. Subach, G. H. Patterson, S. Manley, J. M. Gillette, J. Lippincott-Schwartz, and V. V. Verkhusha, "Photoactivatable mCherry for high-resolution two-color fluorescence microscopy," *Nature Methods*, vol. 6, no. 2, pp. 153–159, 2009.
- [65] C. Huygens, *Traite de la lumiere. Où sont expliquées les causes de ce qui luy arrive dans la reflexion, & dans la refraction. Et particulierment dans l'etrange refraction du cristal d'Islande, par CHDZ Avec un Discours de la cause de la pesanteur.* chez Pierre Vander Aa marchand libraire, 1967.



- [66] E. Abbe, "Beiträge zur Theorie des Mikroskops und der mikroskopischen Wahrnehmung," *Archiv für mikroskopische Anatomie*, vol. 9, no. 1, pp. 413–418, 1873.
- [67] G. B. Airy, "On the diffraction of an object-glass with circular aperture," *Transactions of the Cambridge Philosophical Society*, vol. 5, p. 283, 1835.
- [68] L. Rayleigh, "On the theory of optical images, with special reference to the microscope," *The London, Edinburgh, and Dublin Philosophical Magazine and Journal of Science*, vol. 42, no. 255, pp. 167–195, 1896.
- [69] R. Descartes, *Discourse on method and the meditations*. Penguin UK, 1968.
- [70] O. Heimstadt, "Das Fluoreszenzmikroskop," *Zeitschrift für wissenschaftliche Mikroskopie*, vol. 28, pp. 330–337, 1911.
- [71] H. Kogelnik and T. Li, "Laser beams and resonators," *Proceedings of the IEEE*, vol. 54, no. 10, pp. 1312–1329, 1966.
- [72] M. Tokunaga, N. Imamoto, and K. Sakata-Sogawa, "Highly inclined thin illumination enables clear single-molecule imaging in cells," *Nature Methods*, vol. 5, no. 2, pp. 159–161, 2008.
- [73] E. Ambrose, "A surface contact microscope for the study of cell movements," *Nature*, vol. 178, p. 1194, 1956.
- [74] D. Axelrod, "Cell-substrate contacts illuminated by total internal reflection fluorescence," *The Journal of Cell Biology*, vol. 89, no. 1, pp. 141–145, 1981.
- [75] M. Minsky, "Microscopy apparatus," Dec. 19 1961. US Patent 3,013,467.
- [76] S. T. Hess and W. W. Webb, "Focal volume optics and experimental artifacts in confocal fluorescence correlation spectroscopy," *Biophysical Journal*, vol. 83, no. 4, pp. 2300–2317, 2002.
- [77] V. Buschmann, B. Krämer, F. Koberling, R. Macdonald, and S. Rüttinger, "Quantitative FCS: Determination of the Confocal Volume by FCS and Bead Scanning with the Micro-Time 200," *Application Note. PicoQuant GmbH, Berlin*, 2009.
- [78] S. Wilhelm, B. Grobler, M. Gluch, and H. Heinz, "Confocal laser scanning microscopy. Principles," 2003.

- [79] T. Hirschfeld, "Optical microscopic observation of single small molecules," *Applied Optics*, vol. 15, no. 12, pp. 2965–2966, 1976.
- [80] P. Schwille, J. Bieschke, and F. Oehlenschläger, "Kinetic investigations by fluorescence correlation spectroscopy: the analytical and diagnostic potential of diffusion studies," *Biophysical Chemistry*, vol. 66, no. 2, pp. 211–228, 1997.
- [81] B. Zhang, J. Zerubia, and J.-C. Olivo-Marin, "Gaussian approximations of fluorescence microscope point-spread function models," *Applied Optics*, vol. 46, no. 10, pp. 1819–1829, 2007.
- [82] R. E. Thompson, D. R. Larson, and W. W. Webb, "Precise nanometer localization analysis for individual fluorescent probes," *Biophysical Journal*, vol. 82, no. 5, pp. 2775–2783, 2002.
- [83] K. I. Mortensen, L. S. Churchman, J. A. Spudich, and H. Flyvbjerg, "Optimized localization analysis for single-molecule tracking and super-resolution microscopy," *Nature Methods*, vol. 7, no. 5, pp. 377–381, 2010.
- [84] R. P. Nieuwenhuizen, K. A. Lidke, M. Bates, D. L. Puig, D. Grünwald, S. Stallinga, and B. Rieger, "Measuring image resolution in optical nanoscopy," *Nature Methods*, vol. 10, no. 6, pp. 557–562, 2013.
- [85] N. Banterle, K. H. Bui, E. A. Lemke, and M. Beck, "Fourier ring correlation as a resolution criterion for super resolution microscopy," *Journal of Structural Biology*, vol. 183, no. 3, pp. 363–367, 2013.
- [86] S. T. Hess, T. P. Girirajan, and M. D. Mason, "Ultra-high resolution imaging by fluorescence photoactivation localization microscopy," *Biophysical Journal*, vol. 91, no. 11, pp. 4258–4272, 2006.
- [87] A. Egner, C. Geisler, C. Von Middendorff, H. Bock, D. Wenzel, R. Medda, M. Andresen, A. C. Stiel, S. Jakobs, C. Eggeling, *et al.*, "Fluorescence nanoscopy in whole cells by asynchronous localization of photoswitching emitters," *Biophysical Journal*, vol. 93, no. 9, pp. 3285–3290, 2007.
- [88] D. T. Burnette, P. Sengupta, Y. Dai, J. Lippincott-Schwartz, and B. Kachar, "Bleaching/blinking assisted localization microscopy for superresolution imaging using standard fluorescent molecules," *Proceedings of the National Academy of Sciences of the United States of America*, vol. 108, no. 52, pp. 21081–21086, 2011.

- [89] S. W. Hell and M. Kroug, "Ground-state-depletion fluorescence microscopy: A concept for breaking the diffraction resolution limit," *Applied Physics B*, vol. 60, no. 5, pp. 495–497, 1995.
- [90] J. Fölling, M. Bossi, H. Bock, R. Medda, C. A. Wurm, B. Hein, S. Jakobs, C. Eggeling, and S. W. Hell, "Fluorescence nanoscopy by ground-state depletion and single-molecule return," *Nature Methods*, vol. 5, no. 11, pp. 943–945, 2008.
- [91] P. Annibale, S. Vanni, M. Scarselli, U. Rothlisberger, and A. Radenovic, "Quantitative photo activated localization microscopy: unraveling the effects of photoblinking," *PloS One*, vol. 6, no. 7, 2011.
- [92] D. Lando, U. Endesfelder, H. Berger, L. Subramanian, P. D. Dunne, J. McColl, D. Klenerman, A. M. Carr, M. Sauer, R. C. Allshire, *et al.*, "Quantitative single-molecule microscopy reveals that CENP-ACnp1 deposition occurs during G2 in fission yeast," *Open Biology*, vol. 2, no. 7, 2012.
- [93] S.-H. Lee, J. Y. Shin, A. Lee, and C. Bustamante, "Counting single photoactivatable fluorescent molecules by photoactivated localization microscopy (PALM)," *Proceedings of the National Academy of Sciences of the United States of America*, vol. 109, no. 43, pp. 17436–17441, 2012.
- [94] B. Huang, W. Wang, M. Bates, and X. Zhuang, "Three-dimensional super-resolution imaging by stochastic optical reconstruction microscopy," *Science*, vol. 319, pp. 810–813, Feb 2008.
- [95] S. J. Singer and G. L. Nicolson, "The fluid mosaic model of the structure of cell membranes," *Science*, vol. 175, no. 23, pp. 720–731, 1972.
- [96] D. Magde, E. Elson, and W. Webb, "Thermodynamic Fluctuations in a Reacting System \char22 {} Measurement by Fluorescence Correlation Spectroscopy," *Physical Review Letters*, vol. 29, no. 11, pp. 705–708, 1972.
- [97] S. Manley, J. M. Gillette, G. H. Patterson, H. Shroff, H. F. Hess, E. Betzig, and J. Lippincott-Schwartz, "High-density mapping of single-molecule trajectories with photoactivated localization microscopy," *Nature Methods*, vol. 5, no. 2, pp. 155–157, 2008.
- [98] M. S. Dietz, F. Fricke, C. L. Krüger, H. H. Niemann, and M. Heilemann, "Receptor-Ligand Interactions: Binding Affinities Studied by Single-Molecule and Super-Resolution Mi-

- croscopy on Intact Cells," *European Journal of Chemical Physics and Physical Chemistry (ChemPhysChem)*, vol. 15, no. 4, pp. 671–676, 2014.
- [99] J. F.-W. Greiner, J. Müller, M.-T. Zeuner, S. Hauser, T. Seidel, C. Klenke, L.-M. Grunwald, T. Schomann, D. Widera, H. Sudhoff, *et al.*, "1, 8-Cineol inhibits nuclear translocation of NF- $\kappa$ B p65 and NF- $\kappa$ B-dependent transcriptional activity," *Biochimica et Biophysica Acta (BBA)-Molecular Cell Research*, vol. 1833, no. 12, pp. 2866–2878, 2013.
- [100] D. Widera, I. Mikenberg, M. Elvers, C. Kaltschmidt, and B. Kaltschmidt, "Tumor necrosis factor  $\alpha$  triggers proliferation of adult neural stem cells via IKK/NF- $\kappa$ B signaling," *BMC Neuroscience*, vol. 7, no. 1, pp. 1–18, 2006.
- [101] O. Piestert, H. Barsch, V. Buschmann, T. Heinlein, J.-P. Knemeyer, K. D. Weston, and M. Sauer, "A single-molecule sensitive DNA hairpin system based on intramolecular electron transfer," *Nano Letters*, vol. 3, no. 7, pp. 979–982, 2003.
- [102] M. O. Steinmetz, D. Stoffler, S. A. Müller, W. Jahn, B. Wolpensinger, K. N. Goldie, A. Engel, H. Faulstich, and U. Aebi, "Evaluating atomic models of F-actin with an undecagold-tagged phalloidin derivative," *Journal of Molecular Biology*, vol. 276, no. 1, pp. 1–6, 1998.
- [103] A. Salic and T. J. Mitchison, "A chemical method for fast and sensitive detection of DNA synthesis in vivo," *Proceedings of the National Academy of Sciences of the United States of America*, vol. 105, no. 7, pp. 2415–2420, 2008.
- [104] J. Ries, C. Kaplan, E. Platonova, H. Eghlidi, and H. Ewers, "A simple, versatile method for GFP-based super-resolution microscopy via nanobodies," *Nature Methods*, vol. 9, no. 6, pp. 582–584, 2012.
- [105] A. Keppler, M. Kindermann, S. Gendreizig, H. Pick, H. Vogel, and K. Johnsson, "Labeling of fusion proteins of O<sup>6</sup>-alkylguanine-DNA alkyltransferase with small molecules in vivo and in vitro," *Methods*, vol. 32, no. 4, pp. 437–444, 2004.
- [106] A. Keppler, S. Gendreizig, T. Gronemeyer, H. Pick, H. Vogel, and K. Johnsson, "A general method for the covalent labeling of fusion proteins with small molecules in vivo," *Nature Biotechnology*, vol. 21, no. 1, pp. 86–89, 2002.
- [107] A. Edelstein, N. Amodaj, K. Hoover, R. Vale, and N. Stuurman, "Computer control of microscopes using  $\mu$ Manager," *Current Protocols in Molecular Biology*, pp. 14–20, 2010.

- [108] S. Wolter, M. Schüttpelz, M. Tscherepanow, S. Van de Linde, M. Heilemann, and M. Sauer, "Real-time computation of subdiffraction-resolution fluorescence images," *Journal of Microscopy*, vol. 237, no. 1, pp. 12–22, 2010.
- [109] S. Wolter and M. Sauer, "Follow-up to paper by S. Wolter, M. Schüttpelz, M. Tscherepanow, S. van de Linde, M. Heilemann and M. Sauer, entitled Real-Time Computation of Subdiffraction-Resolution Fluorescence Images," *Journal of Microscopy*, vol. 245, no. 1, pp. 109–109, 2012.
- [110] S. Wolter, A. Löschberger, T. Holm, S. Aufmkolk, M.-C. Dabauvalle, S. van de Linde, and M. Sauer, "rapidSTORM: accurate, fast open-source software for localization microscopy," *Nature Methods*, vol. 9, no. 11, pp. 1040–1041, 2012.
- [111] S. van de Linde, A. Löschberger, T. Klein, M. Heidbreder, S. Wolter, M. Heilemann, and M. Sauer, "Direct stochastic optical reconstruction microscopy with standard fluorescent probes," *Nature Protocols*, vol. 6, pp. 991–1009, Jul 2011.
- [112] I. Izeddin, J. Boulanger, V. Racine, C. Specht, A. Kechkar, D. Nair, A. Triller, D. Choquet, M. Dahan, and J. Sibarita, "Wavelet analysis for single molecule localization microscopy," *Optics Express*, vol. 20, no. 3, pp. 2081–2095, 2012.
- [113] M. Holschneider, R. Kronland-Martinet, J. Morlet, and P. Tchamitchian, *A real-time algorithm for signal analysis with the help of the wavelet transform*. Springer, 1990.
- [114] V. Racine, A. Hertzog, J. Jouanneau, J. Salamero, C. Kervrann, and J.-B. Sibarita, "Multiple-target tracking of 3d fluorescent objects based on simulated annealing," in *Biomedical Imaging: Nano to Macro, 2006. 3rd IEEE International Symposium on*, pp. 1020–1023, IEEE, 2006.
- [115] S. Kirkpatrick, D. G. Jr., and M. P. Vecchi, "Optimization by simulated annealing," *Science*, vol. 220, no. 4598, pp. 671–680, 1983.
- [116] T. Dertinger, V. Pacheco, I. von der Hocht, R. Hartmann, I. Gregor, and J. Enderlein, "Two-focus fluorescence correlation spectroscopy: A new tool for accurate and absolute diffusion measurements," *European Journal of Chemical Physics and Physical Chemistry (ChemPhysChem)*, vol. 8, no. 3, pp. 433–443, 2007.
- [117] L. S. Churchman, H. Flyvbjerg, and J. A. Spudich, "A non-Gaussian distribution quantifies distances measured with fluorescence localization techniques," *Biophysical Journal*, vol. 90, no. 2, pp. 668–671, 2006.

- [118] U. Endesfelder, S. Malkusch, F. Fricke, and M. Heilemann, "A simple method to estimate the average localization precision of a single-molecule localization microscopy experiment," *Histochemistry and Cell Biology*, pp. 1–10, 2014.
- [119] U. Endesfelder, S. van de Linde, S. Wolter, M. Sauer, and M. Heilemann, "Subdiffraction-Resolution Fluorescence Microscopy of Myosin–Actin Motility," *European Journal of Chemical Physics and Physical Chemistry (ChemPhysChem)*, vol. 11, no. 4, pp. 836–840, 2010.
- [120] Y. Wong, Z. Lin, and R. J. Ober, "Limit of the accuracy of parameter estimation for moving single molecules imaged by fluorescence microscopy," *IEEE Transactions on Signal Processing*, vol. 59, no. 3, pp. 895–911, 2011.
- [121] H. Deschout, K. Neyts, and K. Braeckmans, "The influence of movement on the localization precision of sub-resolution particles in fluorescence microscopy," *Journal of Biophotonics*, vol. 5, no. 1, pp. 97–109, 2012.
- [122] J. Adler and S. Pagakis, "Reducing image distortions due to temperature-related microscope stage drift," *Journal of Microscopy*, vol. 210, no. 2, pp. 131–137, 2003.
- [123] J. M. Fitzpatrick and J. B. West, "The distribution of target registration error in rigid-body point-based registration," *IEEE Transactions on Medical Imaging*, vol. 20, no. 9, pp. 917–927, 2001.
- [124] H. K. Kleinman and G. R. Martin, "Matrigel: basement membrane matrix with biological activity," *Seminars in Cancer Biology*, vol. 15, no. 5, pp. 378–386, 2005.
- [125] U. Endesfelder, S. Malkusch, B. Flottmann, J. Mondry, P. Liguzinski, P. J. Verveer, and M. Heilemann, "Chemically induced photoswitching of fluorescent probes—a general concept for super-resolution microscopy," *Molecules*, vol. 16, no. 4, pp. 3106–3118, 2011.
- [126] S. Malkusch, U. Endesfelder, J. Mondry, M. Gelléri, P. J. Verveer, and M. Heilemann, "Coordinate-based colocalization analysis of single-molecule localization microscopy data," *Histochemistry and Cell Biology*, vol. 137, pp. 1–10, 2012.
- [127] P. Zessin, C. Kruger, S. Malkusch, U. Endesfelder, and M. Heilemann, "A hydrophilic gel matrix for single-molecule super-resolution microscopy," *Optical Nanoscopy*, vol. 2, no. 1, p. 4, 2013.
- [128] S. Bolte and F. Cordelieres, "A guided tour into subcellular colocalization analysis in light microscopy," *Journal of Microscopy*, vol. 224, no. 3, pp. 213–232, 2006.

- [129] S. Malkusch, W. Muranyi, B. Müller, H.-G. Kräusslich, and M. Heilemann, "Single-molecule coordinate-based analysis of the morphology of HIV-1 assembly sites with near molecular spatial resolution," *Histochemistry and Cell Biology*, vol. 139, pp. 173–179, 2013.
- [130] W. Muranyi, S. Malkusch, B. Müller, M. Heilemann, and H.-G. Kräusslich, "Super-resolution microscopy reveals specific recruitment of HIV-1 envelope proteins to viral assembly sites dependent on the envelope C-terminal tail," *PLoS Pathogens*, vol. 9, Feb 2013.
- [131] J. Briggs, J. Riches, B. Glass, V. Bartonova, G. Zanetti, and H.-G. Kräusslich, "Structure and assembly of immature HIV," *Proceedings of the National Academy of Sciences of the United States of America*, vol. 106, no. 27, pp. 11090–11095, 2009.
- [132] L.-A. Carlson, J. A. Briggs, B. Glass, J. D. Riches, M. N. Simon, M. C. Johnson, B. Müller, K. Grünwald, and H.-G. Kräusslich, "Three-dimensional analysis of budding sites and released virus suggests a revised model for HIV-1 morphogenesis," *Cell Host & Microbe*, vol. 4, no. 6, pp. 592–599, 2008.
- [133] E. R. Wright, J. B. Schooler, H. J. Ding, C. Kieffer, C. Fillmore, W. I. Sundquist, and G. J. Jensen, "Electron cryotomography of immature HIV-1 virions reveals the structure of the CA and SP1 Gag shells," *The EMBO Journal*, vol. 26, no. 8, pp. 2218–2226, 2007.
- [134] D. R. Larson, M. C. Johnson, W. W. Webb, and V. M. Vogt, "Visualization of retrovirus budding with correlated light and electron microscopy," *Proceedings of the National Academy of Sciences of the United States of America*, vol. 102, no. 43, pp. 15453–15458, 2005.
- [135] Z. Truan, L. Tarancón Díez, C. Bönsch, S. Malkusch, U. Endesfelder, M. Munteanu, O. Hartley, M. Heilemann, and A. Fürstenberg, "Quantitative morphological analysis of arrestin2 clustering upon G protein-coupled receptor stimulation by super-resolution microscopy," *Journal of Structural Biology*, vol. 184, no. 2, pp. 329–334, 2013.
- [136] L. T. Díez, C. Bönsch, S. Malkusch, Z. Truan, M. Munteanu, M. Heilemann, O. Hartley, U. Endesfelder, and A. Fürstenberg, "Coordinate-based co-localization-mediated analysis of arrestin clustering upon stimulation of the C–C chemokine receptor 5 with RANTES/CCL5 analogues," *Histochemistry and Cell biology*, pp. 1–9, 2014.
- [137] B. D. Ripley, "The second-order analysis of stationary point processes," *Journal of Applied Probability*, pp. 255–266, 1976.

- [138] M. A. Kiskowski, J. F. Hancock, and A. K. Kenworthy, "On the use of Ripley's K-function and its derivatives to analyze domain size," *Biophysical Journal*, vol. 97, no. 4, pp. 1095–1103, 2009.
- [139] N. H. Roy, J. Chan, M. Lambelé, and M. Thali, "Clustering and mobility of HIV-1 Env at viral assembly sites predict its propensity to induce cell-cell fusion," *Journal of Virology*, vol. 87, no. 13, pp. 7516–7525, 2013.
- [140] J. Rossy, D. M. Owen, D. J. Williamson, Z. Yang, and K. Gaus, "Conformational states of the kinase Lck regulate clustering in early T cell signaling," *Nature Immunology*, vol. 14, no. 1, pp. 82–89, 2013.
- [141] D. M. Owen, C. Rentero, J. Rossy, A. Magenau, D. Williamson, M. Rodriguez, and K. Gaus, "PALM imaging and cluster analysis of protein heterogeneity at the cell surface," *Journal of Biophotonics*, vol. 3, no. 7, pp. 446–454, 2010.
- [142] P. Haase, "Spatial pattern analysis in ecology based on Ripley's K-function: Introduction and methods of edge correction," *Journal of Vegetation Science*, vol. 6, no. 4, pp. 575–582, 1995.
- [143] R. W. Sterner, C. A. Ribic, and G. E. Schatz, "Testing for life historical changes in spatial patterns of four tropical tree species," *The Journal of Ecology*, vol. 74, no. 3, pp. 621–633, 1986.
- [144] A. Getis and J. Franklin, "Second-order neighborhood analysis of mapped point patterns," *Ecology*, vol. 68, no. 3, pp. 473–477, 1987.
- [145] M. Andersen, "Spatial analysis of two-species interactions," *Oecologia*, vol. 91, no. 1, pp. 134–140, 1992.
- [146] B. Ripley, "Tests of randomness' for spatial point patterns," *Journal of the Royal Statistical Society. Series B (Methodological)*, pp. 368–374, 1979.
- [147] R. Leemans, "Canopy gaps and establishment patterns of spruce (*Picea abies* (L.) Karst.) in two old-growth coniferous forests in central Sweden," *Vegetatio*, vol. 93, no. 2, pp. 157–165, 1991.
- [148] D. J. Taatjes and J. Roth, "The Histochemistry and Cell Biology compendium: a review of 2012," *Histochemistry and Cell biology*, pp. 1–32, 2013.



- [149] P. Sengupta, T. Jovanovic-Taliman, D. Skoko, M. Renz, S. L. Veatch, and J. Lippincott-Schwartz, "Probing protein heterogeneity in the plasma membrane using PALM and pair correlation analysis," *Nature Methods*, vol. 8, no. 11, pp. 969–975, 2011.
- [150] S. J. Tobin, E. E. Cacao, D. W. W. Hong, L. Terenius, V. Vukojevic, and T. Jovanovic-Taliman, "Nanoscale Effects of Ethanol and Naltrexone on Protein Organization in the Plasma Membrane Studied by Photoactivated Localization Microscopy (PALM)," *PLoS One*, vol. 9, no. 2, 2014.
- [151] J. A. Brzostowski, T. Meckel, J. Hong, A. Chen, and T. Jin, "Imaging Protein-Protein Interactions by Förster Resonance Energy Transfer (FRET) Microscopy in Live Cells," *Current Protocols in Protein Science*, pp. 19–5, 2009.
- [152] J. Adler and I. Parmryd, "Quantifying colocalization by correlation: the Pearson correlation coefficient is superior to the Mander's overlap coefficient," *Cytometry Part A*, vol. 77, no. 8, pp. 733–742, 2010.
- [153] P. Sengupta and J. Lippincott-Schwartz, "Quantitative analysis of photoactivated localization microscopy (PALM) datasets using pair-correlation analysis," *Bioessays*, vol. 34, no. 5, pp. 396–405, 2012.
- [154] O. Rossier, V. Oceau, J.-B. Sibarita, C. Leduc, B. Tessier, D. Nair, V. Gatterdam, O. Destaing, C. Albigès-Rizo, R. Tampé, *et al.*, "Integrins  $\beta 1$  and  $\beta 3$  exhibit distinct dynamic nanoscale organizations inside focal adhesions," *Nature Cell Biology*, vol. 14, no. 10, pp. 1057–1067, 2012.
- [155] M. Gerken, A. Krippner-Heidenreich, S. Steinert, S. Willi, F. Neugart, A. Zappe, J. Wrachtrup, C. Tietz, and P. Scheurich, "Fluorescence correlation spectroscopy reveals topological segregation of the two tumor necrosis factor membrane receptors," *Biochimica et Biophysica Acta (BBA)-Biomembranes*, vol. 1798, no. 6, pp. 1081–1089, 2010.
- [156] J. A. Briggs and H.-G. Kräusslich, "The molecular architecture of HIV," *Journal of Molecular Biology*, vol. 410, no. 4, pp. 491–500, 2011.
- [157] B. Müller, J. Daecke, O. T. Fackler, M. T. Dittmar, H. Zentgraf, and H.-G. Kräusslich, "Construction and characterization of a fluorescently labeled infectious human immunodeficiency virus type 1 derivative," *Journal of Virology*, vol. 78, no. 19, pp. 10803–10813, 2004.

- [158] M. A. Checkley, B. G. Luttmann, and E. O. Freed, "HIV-1 envelope glycoprotein biosynthesis, trafficking, and incorporation," *Journal of Molecular Biology*, vol. 410, no. 4, pp. 582–608, 2011.
- [159] P. Zhu, E. Chertova, J. Bess, J. D. Lifson, L. O. Arthur, J. Liu, K. A. Taylor, and K. H. Roux, "Electron tomography analysis of envelope glycoprotein trimers on HIV and simian immunodeficiency virus virions," *Proceedings of the National Academy of Sciences of the United States of America*, vol. 100, no. 26, pp. 15812–15817, 2003.
- [160] E. Chertova, J. W. Bess Jr, B. J. Crise, R. C. Sowder II, T. M. Schaden, J. M. Hilburn, J. A. Hoxie, R. E. Benveniste, J. D. Lifson, L. E. Henderson, *et al.*, "Envelope glycoprotein incorporation, not shedding of surface envelope glycoprotein (gp120/SU), is the primary determinant of SU content of purified human immunodeficiency virus type 1 and simian immunodeficiency virus," *Journal of Virology*, vol. 76, no. 11, pp. 5315–5325, 2002.
- [161] L. Hermida-Matsumoto and M. D. Resh, "Localization of human immunodeficiency virus type 1 Gag and Env at the plasma membrane by confocal imaging," *Journal of Virology*, vol. 74, no. 18, pp. 8670–8679, 2000.
- [162] K. Leung, J.-O. Kim, L. Ganesh, J. Kabat, O. Schwartz, and G. J. Nabel, "HIV-1 assembly: viral glycoproteins segregate quantally to lipid rafts that associate individually with HIV-1 capsids and virions," *Cell Host & Microbe*, vol. 3, no. 5, pp. 285–292, 2008.
- [163] E. O. Freed and M. A. Martin, "Domains of the human immunodeficiency virus type 1 matrix and gp41 cytoplasmic tail required for envelope incorporation into virions," *Journal of Virology*, vol. 70, no. 1, pp. 341–351, 1996.
- [164] X. Yu, X. Yuan, Z. Matsuda, T. Lee, and M. Essex, "The matrix protein of human immunodeficiency virus type 1 is required for incorporation of viral envelope protein into mature virions," *Journal of Virology*, vol. 66, no. 8, pp. 4966–4971, 1992.
- [165] L. M. Luttrell and D. Gesty-Palmer, "Beyond desensitization: physiological relevance of arrestin-dependent signaling," *Pharmacological Reviews*, vol. 62, no. 2, pp. 305–330, 2010.
- [166] F. Santini, I. Gaidarov, and J. H. Keen, "G protein-coupled receptor/arrestin3 modulation of the endocytic machinery," *The Journal of Cell Biology*, vol. 156, no. 4, pp. 665–676, 2002.
- [167] S. A. Laporte, R. H. Oakley, J. A. Holt, L. S. Barak, and M. G. Caron, "The interaction of  $\beta$ -arrestin with the AP-2 adaptor is required for the clustering of  $\beta$ 2-adrenergic receptor

- into clathrin-coated pits," *Journal of Biological Chemistry*, vol. 275, no. 30, pp. 23120–23126, 2000.
- [168] L. Luttrell, S. Ferguson, Y. Daaka, W. Miller, S. Maudsley, G. Della Rocca, F.-T. Lin, H. Kawakatsu, K. Owada, D. Luttrell, *et al.*, " $\beta$ -Arrestin-dependent formation of  $\beta$ 2 adrenergic receptor-Src protein kinase complexes," *Science*, vol. 283, no. 5402, pp. 655–661, 1999.
- [169] Q. A. Karim, S. S. A. Karim, J. A. Frohlich, A. C. Grobler, C. Baxter, L. E. Mansoor, A. B. Kharsany, S. Sibeko, K. P. Mlisana, Z. Omar, *et al.*, "Effectiveness and safety of tenofovir gel, an antiretroviral microbicide, for the prevention of HIV infection in women," *Science*, vol. 329, no. 5996, pp. 1168–1174, 2010.
- [170] S. E. Kuhmann and O. Hartley, "Targeting chemokine receptors in HIV: a status report," *Annual Review of Pharmacology and Toxicology*, vol. 48, pp. 425–461, 2008.
- [171] H. Gaertner, O. Lebeau, I. Borlat, F. Cerini, B. Dufour, G. Kuenzi, A. Melotti, R. J. Fish, R. Offord, J.-Y. Springael, *et al.*, "Highly potent HIV inhibition: engineering a key anti-HIV structure from PSC-RANTES into MIP-1 $\beta$ /CCL4," *Protein Engineering Design and Selection*, vol. 21, no. 2, pp. 65–72, 2008.
- [172] O. Hartley, H. Gaertner, J. Wilken, D. Thompson, R. Fish, A. Ramos, C. Pastore, B. Dufour, F. Cerini, A. Melotti, *et al.*, "Medicinal chemistry applied to a synthetic protein: development of highly potent HIV entry inhibitors," *Proceedings of the National Academy of Sciences of the United States of America*, vol. 101, no. 47, pp. 16460–16465, 2004.
- [173] M. M. Lederman, R. S. Veazey, R. Offord, D. E. Mosier, J. Dufour, M. Mefford, M. Piatak, J. D. Lifson, J. R. Salkowitz, B. Rodriguez, *et al.*, "Prevention of vaginal SHIV transmission in rhesus macaques through inhibition of CCR5," *Science*, vol. 306, no. 5695, pp. 485–487, 2004.
- [174] L. Naldini, U. Blömer, P. Gallay, D. Ory, R. Mulligan, F. H. Gage, I. M. Verma, and D. Trono, "In vivo gene delivery and stable transduction of nondividing cells by a lentiviral vector," *Science*, vol. 272, no. 5259, pp. 263–267, 1996.
- [175] S. J. Mundell, A.-L. Matharu, E. Kelly, and J. L. Benovic, "Arrestin isoforms dictate differential kinetics of A2B adenosine receptor trafficking," *Biochemistry*, vol. 39, no. 42, pp. 12828–12836, 2000.

- [176] K. L. Pierce and R. J. Lefkowitz, "Classical and new roles of  $\beta$ -arrestins in the regulation of G-protein-coupled receptors," *Nature Reviews Neuroscience*, vol. 2, no. 10, pp. 727–733, 2001.
- [177] I. Aramori, J. Zhang, S. S. Ferguson, P. D. Bieniasz, B. R. Cullen, and M. G. Caron, "Molecular mechanism of desensitization of the chemokine receptor CCR-5: receptor signaling and internalization are dissociable from its role as an HIV-1 co-receptor," *The EMBO Journal*, vol. 16, no. 15, pp. 4606–4616, 1997.
- [178] H. Gaertner, F. Cerini, G. Kuenzi, A. Melotti, R. Offord, I. Rossitto-Borlat, R. Nedellec, J. Salkowitz, G. Gorochov, D. Mosier, *et al.*, "Highly potent, fully recombinant anti-HIV chemokines: reengineering a low-cost microbicide," *Proceedings of the National Academy of Sciences of the United States of America*, vol. 105, no. 46, pp. 17706–17711, 2008.
- [179] H. Wajant, K. Pfizenmaier, and P. Scheurich, "Tumor necrosis factor signaling," *Cell Death & Differentiation*, vol. 10, no. 1, pp. 45–65, 2003.
- [180] J. Vilcek and T. H. Lee, "Tumor necrosis factor. New insights into the molecular mechanisms of its multiple actions," *Journal of Biological Chemistry*, vol. 266, no. 12, pp. 7313–7316, 1991.
- [181] W. Schneider-Brachert, V. Tchikov, J. Neumeyer, M. Jakob, S. Winoto-Morbach, J. Held-Feindt, M. Heinrich, O. Merkel, M. Ehrenschwender, D. Adam, *et al.*, "Compartmentalization of TNF receptor 1 signaling: internalized TNF receptosomes as death signaling vesicles," *Immunity*, vol. 21, no. 3, pp. 415–428, 2004.
- [182] J. Kwik, S. Boyle, D. Fooksman, L. Margolis, M. P. Sheetz, and M. Edidin, "Membrane cholesterol, lateral mobility, and the phosphatidylinositol 4, 5-bisphosphate-dependent organization of cell actin," *Proceedings of the National Academy of Sciences of the United States of America*, vol. 100, no. 24, pp. 13964–13969, 2003.
- [183] J. Pitha, T. Irie, P. B. Sklar, and J. S. Nye, "Drug solubilizers to aid pharmacologists: amorphous cyclodextrin derivatives," *Life Sciences*, vol. 43, no. 6, pp. 493–502, 1988.
- [184] B. M. Regner, D. Vučinić, C. Domnisoru, T. M. Bartol, M. W. Hetzer, D. M. Tartakovsky, and T. J. Sejnowski, "Anomalous Diffusion of Single Particles in Cytoplasm," *Biophysical Journal*, vol. 104, no. 8, pp. 1652–1660, 2013.
- [185] Y. Sako, "Imaging single molecules in living cells for systems biology," *Molecular Systems Biology*, vol. 2, no. 1, 2006.

- [186] F. Persson, M. Lindén, C. Unoson, and J. Elf, "Extracting intracellular diffusive states and transition rates from single-molecule tracking data," *Nature Methods*, vol. 10, no. 3, pp. 265–269, 2013.
- [187] F. Persson, I. Barkefors, and J. Elf, "Single molecule methods with applications in living cells," *Current Opinion in Biotechnology*, vol. 24, no. 4, pp. 737–744, 2013.
- [188] D. W. Banner, A. D'Arcy, W. Janes, R. Gentz, H.-J. Schoenfeld, C. Broger, H. Loetscher, and W. Lesslauer, "Crystal structure of the soluble human 55 kd TNF receptor-human TNF $\beta$  complex: implications for TNF receptor activation," *Cell*, vol. 73, no. 3, pp. 431–445, 1993.
- [189] A. K. Lewis, C. C. Valley, and J. N. Sachs, "TNFR1 signaling is associated with backbone conformational changes of receptor dimers consistent with overactivation in the R92Q TRAPS mutant," *Biochemistry*, vol. 51, no. 33, pp. 6545–6555, 2012.
- [190] C. Winkel, S. Neumann, C. Surulescu, and P. Scheurich, "A minimal mathematical model for the initial molecular interactions of death receptor signalling," *Mathematical Biosciences and Engineering (MBE)*, vol. 9, no. 3, p. 663, 2012.
- [191] M. Heidbreder, C. Zander, S. Malkusch, D. Widera, B. Kaltschmidt, C. Kaltschmid, D. Nair, D. Choquet, J.-B. Sibarita, and M. Heilemann, "TNF $\alpha$  influences the lateral dynamics of TNF receptor I in living cells," *Biochimica et Biophysica Acta (BBA)-Molecular Cell Research*, vol. 1823, no. 10, pp. 1984–1989, 2012.
- [192] P. Zagouras and J. K. Rose, "Dynamic equilibrium between vesicular stomatitis virus glycoprotein monomers and trimers in the Golgi and at the cell surface," *Journal of Virology*, vol. 67, no. 12, pp. 7533–7538, 1993.
- [193] J. H. Naismith, T. Q. Devine, B. J. Brandhuber, and S. R. Sprang, "Crystallographic evidence for dimerization of unliganded tumor necrosis factor receptor," *Journal of Biological Chemistry*, vol. 270, no. 22, pp. 13303–13307, 1995.
- [194] F. K.-M. Chan, H. J. Chun, L. Zheng, R. M. Siegel, K. L. Bui, and M. J. Lenardo, "A domain in TNF receptors that mediates ligand-independent receptor assembly and signaling," *Science Signaling*, vol. 288, no. 5475, p. 2351, 2000.
- [195] S. Duhr and D. Braun, "Why molecules move along a temperature gradient," *Proceedings of the National Academy of Sciences of the United States of America*, vol. 103, no. 52, pp. 19678–19682, 2006.

- [196] P. Baaske, C. J. Wienken, P. Reineck, S. Duhr, and D. Braun, "Optical thermophoresis for quantifying the buffer dependence of aptamer binding," *Angewandte Chemie International Edition*, vol. 49, no. 12, pp. 2238–2241, 2010.
- [197] M. Jerabek-Willemsen, C. J. Wienken, D. Braun, P. Baaske, and S. Duhr, "Molecular interaction studies using microscale thermophoresis," *Assay and Drug Development Technologies*, vol. 9, no. 4, pp. 342–353, 2011.
- [198] N. Eswar, B. Webb, M. A. Marti-Renom, M. Madhusudhan, D. Eramian, M.-y. Shen, U. Pieper, and A. Sali, "Comparative protein structure modeling using Modeller," *Current Protocols in Bioinformatics*, pp. 5–6, 2006.
- [199] M. W. Sneddon, J. R. Faeder, and T. Emonet, "Efficient modeling, simulation and coarse-graining of biological complexity with NFsim," *Nature Methods*, vol. 8, no. 2, pp. 177–183, 2010.
- [200] A. M. Smith, W. Xu, Y. Sun, J. R. Faeder, and G. E. Marai, "RuleBender: integrated modeling, simulation and visualization for rule-based intracellular biochemistry," *BMC Bioinformatics*, vol. 13, 2012.
- [201] A. Bullen, "Microscopic imaging techniques for drug discovery," *Nature Reviews Drug Discovery*, vol. 7, no. 1, pp. 54–67, 2008.

## Chapter C. | Acknowledgements

"Habe ich nun, ach! *Physik, Biologie* und *Chemie*, und leider auch *Laborumzüge* durchaus studiert."

frei nach J. W. Goethe, Faust, der Tragödie erster Teil

The last years were a wonderful trip through the scientific landscape of Germany: From Bielefeld via Würzburg to Frankfurt, or from the department of Applied Laser-Physics and Spectroscopy via Biotechnology and Biophysics to Physical and Theoretical Chemistry. There are many people that accompanied me during the whole journey, or at least for a short episode that I would like to thank:

First of all, I would like to thank my supervisor Mike Heilemann for giving me the opportunity to start working in the field of quantitative SMLM in his group of single molecule biophysics. I am very grateful for all the support, challenges, and freedom you offered. Thank you so much for constantly encouraging me to follow my own path.

I also thank Martin Grininger for taking the part of the second referee.

I would like to thank all of our interdisciplinary collaborators, who gave so much scientific input:

1. Walter Muranyi, Bianca Nouvertne, Barbara Müller, and Hans-Georg Kräusslich from the Department of Infectious Diseases and Virology of the University of Heidelberg.
2. The quantitative Imaging of the Cell group of Jean-Baptiste Sibarita from the Interdisciplinary Institute for Neurosciences Bordeaux.
3. The group of Alexandre Fürstenberg at the Department of Human Protein Sciences from the University of Geneva.
4. The group of Peter Verveer from Department of Systemic Cell Biology at the Max Planck Institute of Molecular Physiology Dortmund.

5. Darius Widera, Barbara Kaltschmidt, Christian Kaltschmidt from the Department of Cell Biology at the University of Bielefeld.
6. Gaby Wangorsch, and Thomas Dandekar from the department of Bioinformatics at the University of Würzburg.
7. Markus Sauer and his gorgeous group of Biotechnology and Biophysics at the University of Würzburg.
8. Gerd Wiebusch from the former group of Applied Laser-Physics and Spectroscopy at the University of Bielefeld.

I would have never been able to manage all tasks without the fundamental education in biophysics from the University of Kaiserslautern. Therefore I would like to thank my scientific mentors that inspired me: Joachim W. Deitmer, Volker Schünemann, Rolf Diller, Herbert Urbassek, and Wolfgang Demtröder.

I would like to thank everyone in the fast growing Heilemann Group for being more than just colleagues, especially Ulrike Endesfelder and Meike Heidbreder.

Last but not least, I would like to thank my family and friends:

1. My Parents, who inspired my scientific curiosity already in my early childhood and supported me during the whole journey, even through latin.
2. The Bunker-Welt Apple-Beach Gang from the Silo-Nation for supporting me with BBQ, Beer, Booze and Bouncing Beatz, whenever there was need.
3. Simone for being the most awesome, kick-ass girl in the world and always cheering me up, I love you.

And Volkswagen, for manufacturing the Bulli.



# Chapter D. | Curriculum Vitae

## PERSONAL DATES

Name:	Malkusch, Sebastian	Address:	Tabaksmühlenweg 6
Date of Birth:	12.11.1982 in Dortmund		61440 Oberursel (Taunus), Germany
Marital status:	not married	Mail:	malkusch@chemie.uni-frankfurt.de

## EDUCATION

2003 - 2008: Diploma in Biophysics at the Technical University of Kaiserslautern

## EMPLOYMENT AND RESEARCH EXPERIENCE

2009: Research assistant at the Technical University of Kaiserslautern, with focus on ion sensitive fluorescence microscopy and calcium imaging

2009 - 2010: Research assistant at the university medical center of Schleswig-Holstein facility Kiel, with focus on molecular oncology and molecular biophysics

## Doctoral Research Study

2010 - 2011: Research assistant at the Institute of Applied Laser Physics and Laser Spectroscopy at the Technical University of Bielefeld

2011 - 2012: Research assistant at the Institute of Biotechnology and Biophysics at the Julius-Maximilians University Wuerzburg

2012: Visiting research assistant at the Institute of Infectious Diseases and Virology at the Medical Faculty of the University of Heidelberg

Since 2013: Research assistant at the Institute of Physical and Theoretical Chemistry at the Goethe University of Frankfurt am Main

## Honors and Awards:

2014: Fellowship for Systems Biologists of the Federal Ministry of Education and Research Germany